STATUS OF THESIS

Title of thesis: SYNTHESIS, CHARACTERIZATION AND ACTIVITY OF IRON OXIDE NANOCATALYSTS FOR AMMONIA PRODUCTION

I SHIKH MOHD SHAHRUL NIZAN SHIKH ZAHARI
(CAPITAL LETTERS)

hereby allow my thesis to be placed at the Information Resource Center (IRC) of Universiti Teknologi PETRONAS (UTP) with the following conditions:

1. The thesis becomes the property of UTP
2. The IRC of UTP may make copies of the thesis for academic purposes only.
3. This thesis is classified as

☑ Confidential

☐ Non-confidential

If this thesis is confidential, please state the reason:

The contents of the thesis will remain confidential for 6 years.

Remarks on disclosure:

Effect of magnetic field on the ammonia synthesis reaction is a new innovation in heterogeneous catalysis field. Enhancement in the ammonia yield and minimization in reaction condition were successfully achieved in this study.

	Endorsed by
Signature of Author	Signature of Supervisor
Permanent address:	Name of Supervisor
No 8, Lorong 29, R.R.M Balok Baru,	Assoc. Prof. Dr. Noor Asmawati
26100 Kuantan, Pahang Darul Makmur.	Mohd Zabidi
Date:	Date:

UNIVERSITI TEKNOLOGI PETRONAS

SYNTHESIS, CHARACTERIZATION AND ACTVITY OF IRON OXIDE NANOCATALYSTS FOR AMMONIA PRODUCTION

by

SHIKH MOHD SHAHRUL NIZAN SHIKH ZAHARI

The undersigned certify that they have read, and recommend to the Postgraduate Studies Programme for acceptance this thesis for the fulfilment of the requirements for the degree stated.

Signature:	____________________
Main Supervisor:	ASSOC. PROF. DR. NOOR ASMAWATI MOHD ZABIDI
Signature:	____________________
Co-Supervisor:	PROF. DR. NOORHANA YAHYA
Signature:	____________________
Head of Department:	ASSOC. PROF. DR. SUHAIMI MAHADZIR
Date:	____________________

SYNTHESIS, CHARACTERIZATION AND ACTIVITY OF IRON OXIDE NANOCATALYST FOR AMMONIA PRODUCTION

by

SHIKH MOHD SHAHRUL NIZAN SHIKH ZAHARI

A Thesis

Submitted to the Postgraduate Studies Programme

as a Requirement for the Degree of

MASTER OF SCIENCE

CHEMICAL ENGINEERING DEPARTMENT

UNIVERSITI TEKNOLOGI PETRONAS

BANDAR SERI ISKANDAR,

PERAK

MAY 2011

DECLARATION OF THESIS

Title of thesis	SYNTHESIS, CHARACTERIZATION AND ACTIVITY OF IRON OXIDE NANOCATALYSTS FOR AMMONIA PRODUCTION

I SHIKH MOHD SHAHRUL NIZAN SHIKH ZAHARI

(CAPITAL LETTERS)

hereby declare that the thesis is based on my original work except for quotations and citations which have been duly acknowledged. I also declare that it has not been previously or concurrently submitted for any other degree at UTP or other institutions.

	Witnessed by
________________________________	______________________________
Signature of Author	Signature of Supervisor
Permanent address:	Name of Supervisor
No 8, Lorong 29, R.R.M Balok Baru,	Assoc. Prof. Dr. Noor Asmawati
26100 Kuantan, Pahang Darul Makmur.	Mohd Zabidi
Date : _________________________	Date : ________________________

ACKNOWLEDGEMENT

Bismillahirrahmanirrahim…

Alhamdulillah and thanks to ALLAH S.W.T for giving me such a huge blessing in completing this master research successfully. This thesis symbolizes hard work and dedication that have been paid to this project accompanied with the support from family and friends.

Highly appreciation is firstly dedicated to my supervisor, Assoc. Prof. Dr. Noor Asmawati Mohd Zabidi and co-supervisor, Prof. Dr. Noorhana Yahya for their willingness and kindness in guiding me throughout this project. Great support and encouragement from both of them are priceless and will not be forgotten. To my research partner, Poppy Puspitasari, her good cooperation and assistant are also appreciated.

I would also like to acknowledge The Ministry of Science, Technology and Innovation of Malaysia and Universiti Teknologi PETRONAS for the funding (E-Science Fund Code: 03-02-02-SF0031) and facilities provided. Also not to be missed staffs and technicians from Chemical Engineering Department, Fundamental & Applied Sciences Department, Mechanical Engineering Department, Nanotechnology Laboratory and Centralized Laboratory who had given me opinion, suggestion and technical knowledge.

Finally, for those who had threw out constructive comments and ideas as well as assisted directly or indirectly, thank you very much.

ABSTRACT

Ammonia synthesis was evaluated in the presence of α-Fe_2O_3, Fe_3O_4 and 5% α-Fe_2O_3/γ-Al_2O_3 nanocatalysts. The nanocatalysts were prepared via sol-gel and sol gel-hydrothermal methods. The variables studied for synthesis using sol gel method were stirring period and annealing temperature. Samples were characterized using x-ray diffraction (XRD), raman spectroscopy, field emission scanning electron microscopy (FESEM), energy dispersed x-ray (EDX), temperature programmed reduction (TPR), vibration sample magnetometer (VSM) and N_2 adsorption. Extending synthesis period from 1 day to 1 month in the sol gel method reduced the size of α-Fe_2O_3 nanocatalyst particles from 60 nm to 27 nm. Particle size increased from 21 nm to 60 nm when the annealing temperature was increased from 300^oC to 700^oC. The sol gel-hydrothermal produced a well crystallined Fe_3O_4 nanocatalyst at synthesis temperature of 160^oC. The 5% α-Fe_2O_3/γ-Al_2O_3 prepared using sol gel-hydrothermal method at iron nitrate to sodium bis(2-ethylhexyl) sulfucinnate surfactant ratio of 2:3 exhibited better particles dispersion compared to those prepared at other ratios. The TPR profiles for the nanocatalysts exhibited two reduction stages for the transformations of α-Fe_2O_3 to Fe_3O_4 and Fe_3O_4 to α-Fe. For the unsupported α-Fe_2O_3, reduction peaks were observed at 400^oC to 460^oC and 680^oC to 780^oC regions whereas for the γ-Al_2O_3-supported α-Fe_2O_3, the reduction peaks shifted to 350^oC to 400^oC and 550^oC to 650^oC. The catalytic study was conducted in a fixed bed microreactor at 30^oC to 200^oC under atmospheric pressure with a total feed flow rate of 40 cm^3/min and H_2/N_2 volume ratio of 3:1. The amount of ammonia was determined using an acid-base titration method. The ammonia yield over α-Fe_2O_3 and 5% α-Fe_2O_3/γ-Al_2O_3 catalysts at 110^oC measured in the absence of magnetic field was 2.65 %/g_{Fe} and 26.3 %/g_{Fe}, respectively. Applying magnetic field at 1 Tesla to the α-Fe_2O_3 catalyst resulted in two orders of magnitude increase in the ammonia yield while using Fe_3O_4 nanocatalyst further enhanced the ammonia yield by about 14% greater than that of α-Fe_2O_3. The performance of nanocatalysts for the ammonia synthesis in the absence and presence of magnetic field can be ranked as 5% α-Fe_2O_3/γ-Al_2O_3> α-Fe_2O_3 and Fe_3O_4> α-Fe_2O_3, respectively.

ABSTRAK

Sintesis ammonia telah dinilai dengan kehadiran pemangkin-pemangkin nano α-Fe_2O_3, Fe_3O_4 dan 5% α-Fe_2O_3/γ-Al_2O_3. Pemangkin-pemangkin nano ini telah dihasilkan menggunakan kaedah-kaedah sol gel dan sol gel-hidrotermal. Pembolehubah-pembolehubah yang telah diuji bagi sintesis menggunakan kaedah sol- gel adalah tempoh pengacauan dan suhu pemanasan haba. Sifat-sifat bagi sampel-sampel telah diuji menggunakan pembelauan x-ray (XRD), spektroskopi raman, mikroskopi pengesanan medan pemancaran elektron (FESEM), tenaga penaburan x-ray (EDX), program suhu penurunan (TPR), magnetometer sampel bergetar (VSM) dan penjerapan N_2. Pemanjangan tempoh pengacauan dari 1 hari ke 1 bulan bagi kaedah sol gel telah mengecilkan saiz zarah-zarah pemangkin nano α-Fe_2O_3 daripada 60 nm ke 27 nm. Saiz zarah-zarah juga turut meningkat dari 21 nm kepada 60 nm apabila suhu pemanasan haba telah ditingkatkan daripada 300^oC ke 700^oC. Kaedah sol gel-hidrotermal telah menghasilkan pemangkin nano Fe_3O_4 dengan tahap pengkristalan yang bagus pada suhu 160^oC. Bagi pemangkin nano 5% α-Fe_2O_3/γ-Al_2O_3 yang telah dihasilkan melalui kaedah sol gel-hidrotermal pada nisbah 2:3 bagi ferum nitrate kepada natrium bis(2-etilhexil) sulfucinnate, ianya telah menunjukkan penyerakan zarah-zarah yang bagus jika dibandingkan dengan sampel-sampel yang telah dihasilkan menggunakan nisbah-nisbah yang lain. Profil-profil TPR untuk kesemua pemangkin-pemangkin nano telah menunjukkan dua peringkat proses penurunan bagi transformasi α-Fe_2O_3 kepada Fe_3O_4 dan Fe_3O_4 kepada α-Fe. Bagi pemangkin nano α-Fe_2O_3 yang tidak disokong, puncak-puncak penurunan telah dilihat pada 400^oC ke 460^oC dan 680^oC ke 780^oC manakala bagi γ-Al_2O_3 yang menyokong α-Fe_2O_3, puncak-puncak penurunan telah teranjak kepada 350^oC ke 400^oC and 550^oC ke 650^oC. Penilaian pemangkinan telah dijalankan dalam satu lapisan tetap mikroreaktor pada suhu 30^oC ke 200^oC pada tekanan atmosferik dengan jumlah kadar aliran suapan gas pada 40 cm^3/min dan nisbah isipadu H_2/N_2 adalah 3:1. Kuantitit ammonia yang terhasil diperolehi menggunakan kaedah pentitratan asid-bes. Penghasilan ammonia bagi pemangkin-pemangkin α-Fe_2O_3 dan 5% α-Fe_2O_3/γ-Al_2O_3 pada 110^oC

diukur dalam ketidakhadiran medan magnet adalah masing-masing 2.65 $\%/g_{Fe}$ and 26.3 $\%/g_{Fe}$. Pengenalan medan magnet pada 1 Tesla kepada pemangkin α-Fe_2O_3 telah meningkatkan penghasilan ammonia dengan urutan dua magnitud manakala penggunaan Fe_3O_4 turut meningkatkan penghasilan ammonia 14% lebih banyak berbanding α-Fe_2O_3. Prestasi pemangkin-pemangkin nano dalam ketidakhadiran dan kehadiran medan magnet masing-masing boleh didisusun seperti berikut $5\%\alpha\text{-}Fe_2O_3/\gamma\text{-}Al_2O_3 > \alpha\text{-}Fe_2O_3$ dan $Fe_3O_4 > \alpha\text{-}Fe_2O_3$.

In compliance with the terms of the Copyright Act 1987 and the IP Policy of the university, the copyright of this thesis has been reassigned by the author to the legal entity of the university,

Institute of Technology PETRONAS Sdn Bhd.

Due acknowledgement shall always be made of the use of any material contained in, or derived from, this thesis.

© Shikh Mohd Shahrul Nizan Shikh Zahari, January 2011
Institute of Technology PETRONAS Sdn Bhd
All rights reserved.

TABLE OF CONTENTS

CHAPTER 1: INTRODUCTION

CHAPTER 2: THEORY AND LITERATURE REVIEW

CHAPTER 3: METHODOLOGY

CHAPTER 4: RESULTS AND DISCUSSION

CHAPTER 5 CONCLUSION

LIST OF TABLES

LIST OF FIGURES

LIST OF ABBREVIATIONS

GNP	-	Gross national product
PASB	-	PETRONAS Ammonia Sdn. Bhd.
PFK	-	PETRONAS Fertilizer Kedah
KAAP	-	Kellog Advanced Ammonia Process
TCD	-	Thermal conductivity detector
PPM	-	Part per million
XRD	-	X-ray diffraction
H_2-TPR	-	Temperature-programmed reduction (Hydrogen)
FESEM	-	Field emission scanning electron microscopy
EDX	-	Energy dispersed x-ray
TEM	-	Transmission electron microscopy
BET	-	Brunauer-Emmett-Teller Method
VSM	-	Vibration sample magnetometer
GC	-	Gas chromatography
H_2	-	Hydrogen gas
CO	-	Carbon monoxide
N_2	-	Nitrogen gas
SYN	-	Synthesis
CHARAC	-	Characterization
ACT	-	Activity
FE	-	Iron
NANOCAT	-	Nanocatalyst
PROD	-	Production

LIST OF SYMBOLS

^{o}C - Degree Celsius

φ - Work function

π - Pie orbital

π^{*} - Pie antibonding orbital

M_s - Saturation magnetization

M_r - Remanence magnetization

H_c - Coercivity force

T_c - Curie temperature

ΔE - Energy barrier

K_s - Anisotropy constant

S - Surface area

δ - Charge

$\bar{\chi}$ - Electronegativity

p - Proton released

Z - Formal charge

N - Coordination number

E^{o} - Standard reduction potential

H_{ads} - Heat of adsorption

θ - Bragg angle

k - Shape factor

λ - Wavelength

β - Full width half maximum

I.D - Internal diameter

O.D - Outer diameter

I - Intensity

T_{max} - Maximum temperature

R - Gas constant

X_A - Mole fraction of component A

K_{eq} - Equilibrium constant

CHAPTER 1

INTRODUCTION

1.1 Background

Catalysis is an important discipline in reaction engineering and its application covers many areas such as natural gas conversion, chemical synthesis and refining. Catalysis can be divided into two categories namely homogeneous and heterogeneous catalysis. Heterogeneous catalysis refers to a chemical reaction between two phases such as solid (catalyst) and gas (reactant) phases. Heterogeneous catalysts offer several advantages to industrial syntheses such as higher resistivity to severe reaction conditions and no extra steps required for product separation [1]. In terms of economy aspect, the role of heterogeneous catalysis in generating nation income cannot be discounted. The involvement of this field contributes about $ 5 trillion per year of world's GNP [2].

Ammonia or NH_3 is a useful chemical substance particularly for agriculture activities. It has a boiling point and a melting point of $-33.35^{o}C$ and $-77.7^{o}C$, respectively. Ammonia exists as a colourless gas at room temperature having sharp and intensely irritating odours [3].

Many industrial products contain ammonia as one of the raw ingredients. Figure 1.1 summarizes the use of ammonia in several applications [4].

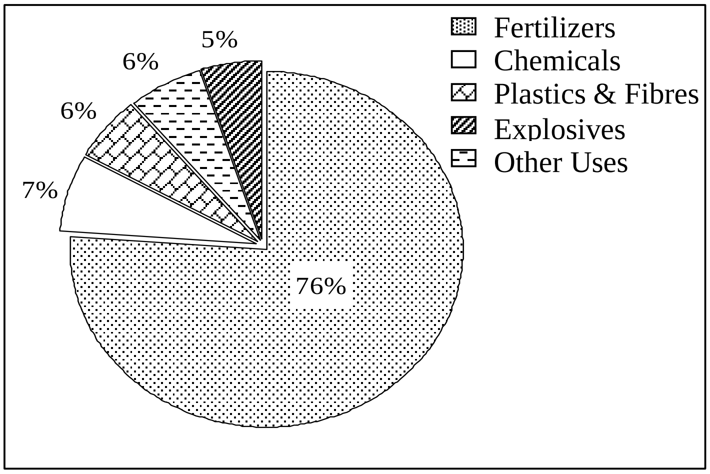

Figure 1.1: Industrial ammonia applications [4]

Ammonia production in Asia has been extensively growing every year. Table 1.1 describes the ammonia production involving some Asian countries in the year of 2003 until 2007 [5].

Table 1.1: Ammonia production in Asia [5].

Country	Thousand metric tons of contained nitrogen				
	2003	**2004**	**2005**	**2006**	**2007**
Malaysia	910	843	920	950	960
India	10048	10718	10800	10900	11000
Indonesia	4250	4120	4400	4300	4400
Iran	1115	1088	1020	1020	2000
Japan	1061	1101	1083	1091	1090
Pakistan	2357	2114	2114	2200	2250
Saudi Arabia	1743	1726	1780	2000	2600

Malaysia has two ammonia production plants namely PETRONAS Ammonia (PASB), located in Kerteh, Terengganu and PETRONAS Fertilizer (PFK) in Gurun, Kedah.

Haber Bosch is a well known process for synthesis of ammonia. A huge appreciation has to be paid to Fritz Haber and Carl Bosch who discovered and introduced this remarkable process at the beginning of 19th century. Generally, ammonia is attained by reacting a mixture of hydrogen and nitrogen gases at a ratio of 3:1 (H_2:N_2) over magnetite (Fe_3O_4) fused-catalyst, at 300-500^oC and 100-200 atm [4], [6]-[7].

1.2 Problem Statement

The well known drawbacks in the ammonia synthesis using Haber Bosch process are the low ammonia yield as well as capital and energy intensive of production operations [4], [6]-[7]. Due to thermodynamic factor, the Haber Bosch process is commonly performed under high temperature (300-500^oC) and pressure (100-200atm) environments. Under this condition, yield of ammonia was only 10-20%. Unfortunately, these facts remain unsolved and controversial until today, thus overcoming steps are highly desirable [4], [6]-[7].

The application of nanotechnology has potential to overcome the drawbacks on ammonia synthesis. Using nanoscale particles in the presence of magnetic field is expected to reduce severity of ammonia synthesis process condition and improve the ammonia yield.

1.3 Hypothesis

Nanosize catalyst provides high surface area which will enhance the chance of reactant molecules to interact with the surface of the catalyst. Employing magnetic field throughout the reaction could minimize the difficulty of interaction between the electrons within the catalyst particles and reactant molecules. The enhanced interaction could lead to higher ammonia yield as well as reduce the severity of the reaction condition.

1.4 Objective

The objectives of this study are:

1. To synthesize unsupported and supported iron oxide nanocatalysts for ammonia production.
2. To characterize the physicochemical properties of the prepared iron oxide nanocatalysts.
3. To evaluate the performance in terms of the rate and ammonia yield of the prepared nanocatalysts in ammonia production in the absence and presence of magnetic field.

1.5 Scope of Work

The scope of work included synthesis, characterization and catalytic study of unsupported and supported iron oxide nanocatalysts in ammonia synthesis. Iron nanocatalysts have been synthesized using sol gel, self assembly, self combustion, hydrothermal, precipitation and sol gel-hydrothermal methods. Three groups of nanocatalysts were prepared, namely hematite (α-Fe_2O_3), magnetite (Fe_3O_4) and hematite supported on alumina, (α-Fe_2O_3/γ-Al_2O_3). Nanocatalysts were characterized using x-ray diffraction (XRD), raman spectroscopy, field emission scanning electron microscopy (FESEM), energy dispersed x-ray (EDX), temperature programmed reduction (TPR), vibration sample magnetometer (VSM) and N_2 adsorption.

The performance of iron nanocatalysts was studied in a microreactor at temperature 30^oC to 200^oC, feed flow rate 28 cm^3/min to 120 cm^3/min, space velocity 8400 $cm^3/g_{cat}.h$ to 30000 $cm^3/g_{cat}.h$, H_2/N_2 volume ratio 3:1 to 5:1 and under atmospheric pressure. The effect of magnetic field on the ammonia yield was also investigated.

1.6 Overview of Thesis

This thesis consists of five main chapters. Chapter 1 provides an overview about ammonia synthesis industries. Chapter 2 elaborates on theories and reviews several works that have been carried out previously. Methodology used in carrying out the research is covered in Chapter 3. Chapter 4 presents the results and discussion of the work. The work is summarized in Chapter 5.

CHAPTER 2

REVIEW OF LITERATURE

2.1 The Role of Transition Metal in Catalysis

Transition metals are important in catalysis. Certain chemical syntheses use transition metals to catalyze the reaction such as Haber Bosch and Fischer-Tropsch reactions [8]-[9]. In general, elements which have d-orbital as the outermost orbital are categorized as transition metals [1], [10].

Iron, Fe is a part of transition metal elements. It possesses 26 electrons with electronic configuration of $1s^2\ 2s^2\ 2p^6\ 3s^2\ 3p^6\ 4s^2\ 3d^6$ or $[Ar]\ 4s^2\ 3d^6$ [1], [10]. The use of iron as a catalyst especially in ammonia synthesis is crucial. Ammonia may not be formed or reaction has to be carried out in severe conditions if iron catalyst is not used.

In ammonia synthesis reaction, atomization is an initial step which has to be experienced by nitrogen and hydrogen molecules before proceeding to the next steps. It allows molecules to dissociate, eventually forming nitrogen and hydrogen monoatomics. This step occurs once reactant molecules are bonded onto metal surface. This bonding is called surface bond. Moreover, the strength of this bonding determines the energy that is required to accomplish the overall mechanism**.** This energy is recognized as a thermodynamic driving force. The strength of the surface bond and the thermodynamic driving force are greatly influenced by the number electrons in the d-orbital of the transition metals**.** These factors could predict how fast the atomization, subsequently influencing the ammonia production process as elaborated in [8], [11]. A diagram called "Volcano Curve" can be cited which explains the dependency of ammonia produced on the number of electrons in d orbital as illustrated in Figure 2.1.

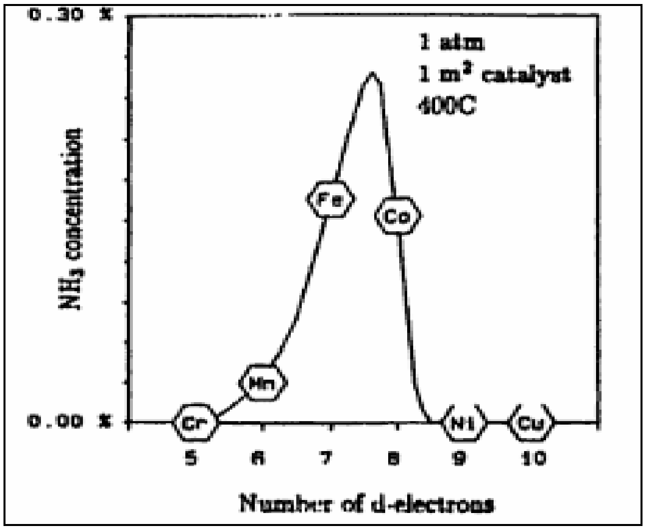

Figure 2.1: Dependency of ammonia yield on transition metals [8], [11].

The curve in Figure 2.1 clearly emphasizes that ammonia concentration depends on the number of electrons in the d-orbital of transition metals. Interestingly, the highest concentration is achieved using iron as a catalyst (Figure 2.1) which has six valence electrons in the d-orbital [8], [11].

Theoretically, metals with fewer d-electrons will create a strong surface bond. It will prolong the residence time of adsorbed nitrogen and hydrogen molecules on the metal surfaces, thus blocking the adsorption of incoming molecules during reaction intermediates. As a consequence, the reaction may stop early and low ammonia concentration might be attained. These explained the trend observed for Cr and Mn (Figure 2.1). Conversely, the necessary surface bond may not be present for Ni and Cu due to full occupancy of the d-orbital forbidding the catalytic activity of the metals (Figure 2.1). Iron gives highest ammonia yield as compared to other elements (Figure 2.1) due to partial occupancy of the d-orbital. Therefore, intermediate-strength surface bond is formed which is sufficient to induce the dissociation steps especially for nitrogen molecules. Herein, residence time for the intermediate process is shortened, hence accelerating the desorption of ammonia [8], [12].

Surface property is an important aspect in catalysis. Ammonia synthesis is a structural sensitive reaction. Figure 2.2 shows the rate of ammonia synthesis over different iron surfaces. Fe (111) and Fe (211) are active surfaces for the ammonia synthesis. Both of them reveal higher ammonia production rate as compared to those other surfaces (Figure 2.2). Few possible factors were suggested to account for this trend which includes surface roughness, work function, φ and C_7 active site.

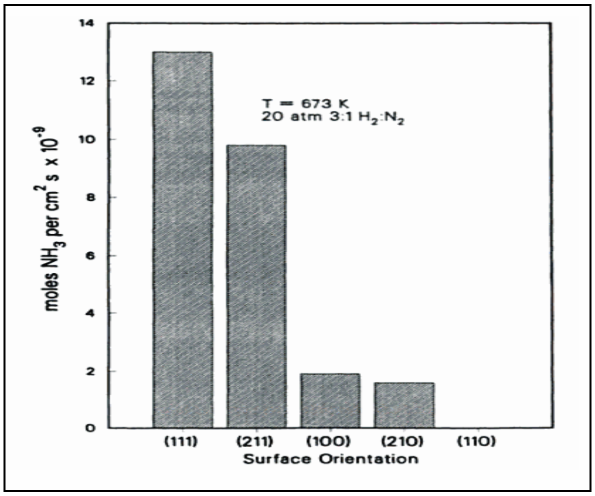

Figure 2.2: Rate of ammonia synthesis over different iron surfaces [8], [11].

Figure 2.3 illustrates the schematic orientation for different iron surfaces which are Fe(111), Fe(210), Fe(100), Fe(211) and Fe(110).

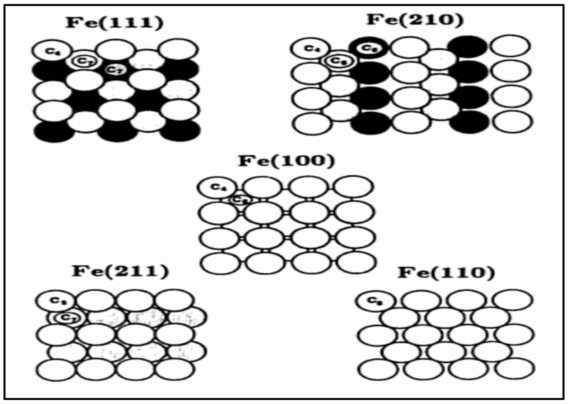

Figure 2.3: Iron (Fe) surfaces [8], [11].

Fe (111) surface has high roughness as it has open face structure which exposes the second and third layers of atoms. Meanwhile, low surface roughness is anticipated for Fe (110) surface. The atoms for the Fe(110) are arranged in close packing manner and only first layer of atoms are exposed (Figure 2.3). Surface roughness is inversely proportional to work function, φ. Low work function is required for inducing electrons transfer process from d-orbital of iron to 2π* antibonding orbital in nitrogen molecules. This process is called "π back donation". The triple bond within nitrogen molecules becomes weaker, thus encouraging the dissociation process. Highest activity for Fe (111) surface (Figure 2.2) is possibly due to high surface roughness and low work function, φ. The same deduction can also be applied to Fe (110) surface [8], [11].

Fe (210) should exhibit higher activity than Fe (211) as it also exposes second and third layers of atoms. However, that is not the case here which suggests that the presence of C_7 active site is important. The C_7 site exists when the central atom is surrounded by seven nearest atoms. The existence of this site in Fe (211) surface increases the catalytic activity due to low energy fluctuations of highly coordinated surface atoms (Figure 2.3) [8], [13].

The importance of iron-based catalyst in ammonia synthesis has been elaborated previously. However, the performance of conventional catalyst remains questionable. It was reported that, current industries are only capable of generating approximately 10-20% ammonia yield under severe synthesis conditions [4]. Recent studies showed that ruthenium is a good catalyst for ammonia synthesis. The activity increased by 10-fold when Ru was promoted with alkali metal and supported on carbon catalyst [7]. Kellogg Advanced Ammonia Process (KAAP) applied Ru- based catalyst and produced about 600 t NH_3/day. This yield was attained under slightly lower pressure (70-105 bar) compared to 150 – 300 bar for iron based catalyst system [7], [14].

Figure 2.4 shows the activity of various transition metals for synthesizing ammonia as a function of the degree of d-band electron filling.

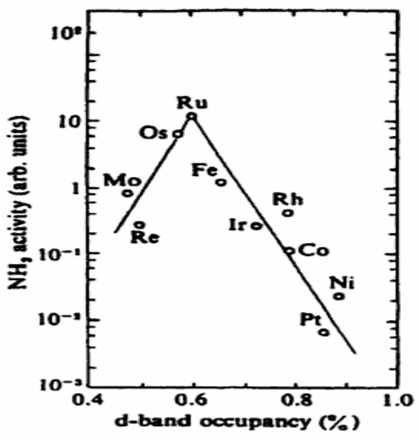

Figure 2.4: Activity of various transition metals on ammonia synthesis [8], [11].

The highest activity is given by Ru catalyst (Figure 2.4). One of the factors contributing to this trend is the presence of small number of the so-called B-5 sites in the ruthenium structure. The B-5 site is found to be extremely active for nitrogen dissociation in rate determining-step, which eventually controls the overall reaction rate. However turning to ruthenium is uneconomical due to its high price compared to other elements, as summarized in Table 2.1 [14]. Plant-scale ammonia synthesis usually involves high cost of productions and the use ruthenium-based catalyst as investigated by Liang [7] and Rosowski [14], could escalate the operational cost as well.

Table 2.1: Transition metal prices in 2010 [15].

Element	Purity (%)	Price (USD)/gram
Iron (Fe)	99.97	0.06
Ruthenium (Ru)	99.95	53.3
Nickel (Ni)	99.90	0.26
Cobalt (Co)	99.90	0.44

2.2 Nanocatalyst

Nanotechnology is a study of controlling the matter so that the size of its structure lies at 100 nm and below. Nanocatalyst is a part of these technology applications [16]. The most essential property of a nanocatalyst is the large surface area than those of bulky materials [17]. These features could enhance the catalytic activity. Study on performance of iron-based nanocatalysts over ammonia synthesis has been actively conducted nowadays. Fe_3O_4 catalyst with the size 8.0 nm was utilized by Jacobsen et al. [18] in ammonia synthesis. Other investigation [19] synthesized ammonia using 31 nm of iron particles supported on an activated carbon.

2.3 Ammonia Synthesis Catalyst

Typical ammonia synthesis catalyst is developed by combining metal crystallite (active phase), textural and electronic promoters [9], [20].

2.3.1 Active phase

Metal that can catalyze the reaction is called the active phase. Intermediate surface bond strength, low work function and high roughness are desired characteristics for active phase which usually exists as oxide compounds. This oxide will initially undergo reduction process to form metallic phase. The reduction can be performed using reducing agents such as hydrogen, H_2 or carbon monoxide, CO gases at specific conditions [8], [21]-[22]. Hematite, α-Fe_2O_3 and magnetite, Fe_3O_4 are two typical oxides for ammonia synthesis catalyst.

α-Fe_2O_3 is evolved by the arrangement of Fe^{3+} and O^{2-} ions in hexagonal unit cell (Figure 2.5 (a)). These ions are arrayed as hexagonal close-packed where every Fe^{3+} cation is surrounded by six O^{2-} anions, forming an octahedral site (Figure 2.5 (b)). The unit cell has lattice parameters of a = 0.5034 nm and c = 1.3572 nm. Moreover, each octahedron shares edges with three neighbouring octahedral in the same plane and also one face with an octahedron in the adjacent plane (Figure 2.5 (c)).

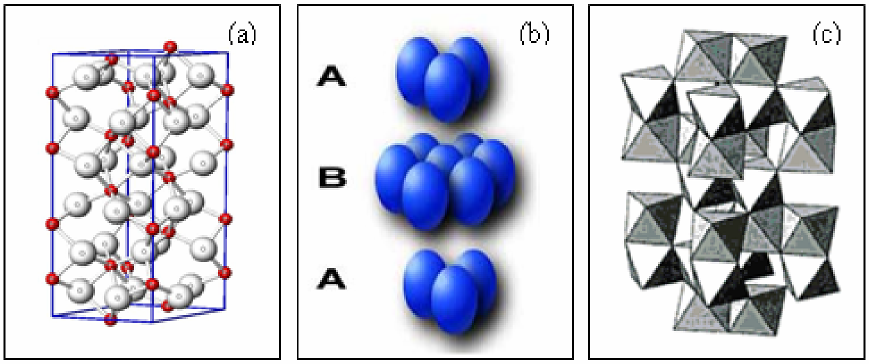

Figure 2.5: Structure of hematite, α-Fe_2O_3 (a) ball and stick model of ions arrangement in unit cell [23] (b) hexagonal close-packed system of ionic arrangement [24] and (c) arrangement of octahedron [20].

On the other hand, Fe_3O_4 encompasses a mixture of α-Fe_2O_3, and $Fe_{1-x}O$. The structure consists of two sites namely octahedral and tetrahedral. Octahedral is occupied by Fe^{3+} and Fe^{2+}, while tetrahedral is filled by Fe^{2+} ions (Figure 2.6 (a)). The presence of these sites gives inverse spinel behavior to Fe_3O_4. Furthermore, all ions are arrayed as cubic closed packed in cubic unit cell with edge length, α of 0.839 nm [20].

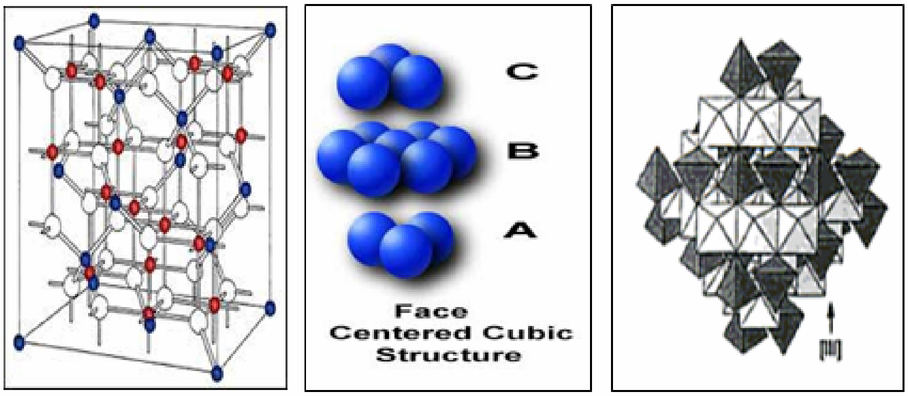

Figure 2.6: Structure of magnetite, Fe_3O_4 (a) ball and stick model of ions arrangement in unit cell [20] (b) face centred-cubic close-packed system of ionic arrangement [24] and (c) arrangement of octahedron [20].

2.3.2 Textural Promoter

Active phase or pure metal will not be stable by itself. It tends to agglomerate with neighbouring particles especially at high temperature due to high surface energy. As a consequence, bulky particles are formed hence reducing the surface area. Thus, fewer sites are available for the catalytic reaction to take place. Therefore, a component that can hold the particles and prevent agglomeration is needed. This component is known as a textural promoter. Textural promoter should have few interesting characteristics such as highly porous, high surface area and significant pore volumes which can improve dispersion of the active phase. A typical textural promoter in ammonia synthesis catalyst is alumina, γ-Al_2O_3. It offers several benefits such as excellent thermal stability and wide range of chemical, physical and catalytic properties. Table 2.2 summarizes some physical properties of γ-Al_2O_3 [9].

Table 2.2: Common physical properties of alumina, γ-Al_2O_3 [9].

BET surface area (m^2/g)	Pore Volume (cm^3/g)	Pore Diameter (nm)
100-300	0.4-0.5	6-40

2.3.3 Electronic Promoter

The main reason of including promoter is to provide excess electron to the catalyst system. This could enhance and accelerate the dissociation of reactant molecules. Electronic promoter is usually included with relatively small quantities (e.g. 1-5%). Excess amount will inhibit the catalytic activity as it can cover the surface area of active phase, hence blocking the adsorption of incoming molecules. Potassium oxide, K_2O is a typical electronic promoter for ammonia synthesis catalyst [9]

2.4 Magnetic Material

Magnetic material refers to any material that exhibits magnetic behavior. Three facts must be considered when discussing this topic. Firstly, some materials may have natural magnetic behavior and become more magnetic with introduction of magnetic field. Secondly, materials will lose its magnetic behavior when the temperature is above their critical temperature. Thirdly, an opposite behavior towards external magnetic field can also be observed for some materials [25].

2.4.1 Magnetic Domain

Magnetic domain can be described as the region within the magnetic material. Their existence can minimize the magnetic free energy. In addition, magnetic materials could possess a single or multi domains. Each domain is separated by domain walls and has a uniform magnetization which is equal to saturation magnetization, Ms. Different domains show diverse magnetization directions [26]. Figure 2.7 illustrates the alignment of magnetic moments in multi domains without magnetic field influence [27].

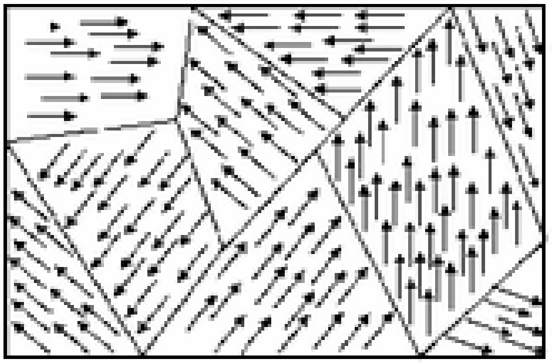

Figure 2.7: Schematic illustration of magnetic moments alignments in multi domains [27].

2.4.2 Classification of Magnetic Materials

Magnetic materials can be divided into several classes which depend on the way of moments alignment in the domain. Few typical classes include ferromagnetic, antiferromagnetic, ferrimagnetic and paramagnetic [20]. Figure 2.8 illustrates the alignments of magnetic moments in the domain.

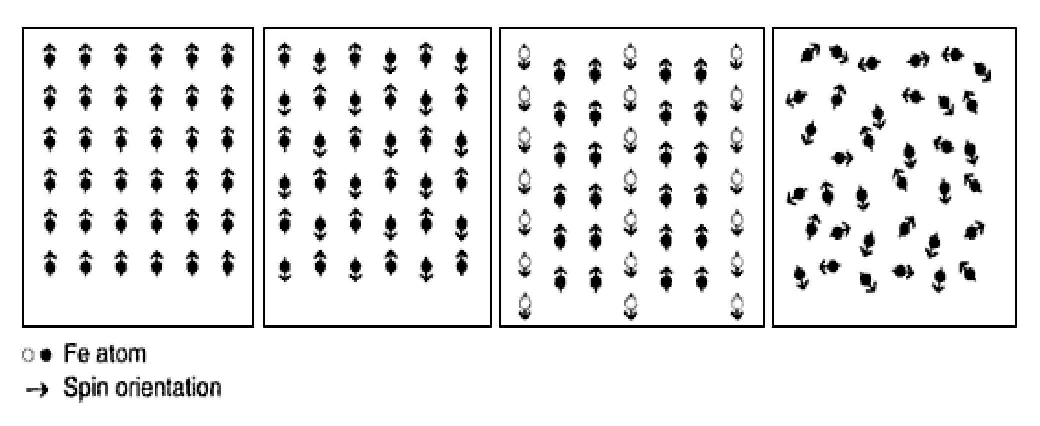

Figure 2.8: Schematic illustration of magnetic moments alignments in (a) ferromagnetic, (b) antiferromagnetic, (c) ferrimagnetic and (d) paramagnetic materials [20].

For some iron oxides, the moments are aligned either in parallel or antiparallel manners (Figure 2.8). It is due to the super exchange interaction which exists when unpaired electrons in e_g orbital of Fe^{3+} and p orbital of O^{2-} are magnetically interacted. Consequently, the Fe-O bond distance becomes shorter, thus enhancing the electron-coupling process [20], [26].

2.4.3 Magnetic Field Strength

The magnetic behavior becomes more pronounced even in weak magnetic field strength. This is due to the existence of a “torque” experienced by the moments as a result of introducing external magnetic field, hence permitting the moments to be aligned in the direction of exerted field. The degree of alignment can be computed as the total of magnetic moments per unit volume or commonly refers to magnetization (M) [25]. In addition, magnetization is also found to be related to the strength of the applied field (H) as expressed in Equation 2.1 [25] where χ refers to the magnetic susceptibility of the materials.

$$M = \chi H \tag{2.1}$$

Under a weak field, the moments begun to orient in the direction of exerted field. The movement of domain walls is also initiated at this point. Meanwhile, increasing the strength of exerted field can speed up the walls movement; eventually constructing a single large domain. At present, all moments are thought to align in a parallel manner. This occurrence designates that the saturation magnetization has been attained. Figure 2.9

demonstrates the effect of magnetic field strength on the magnetic behavior of materials [28].

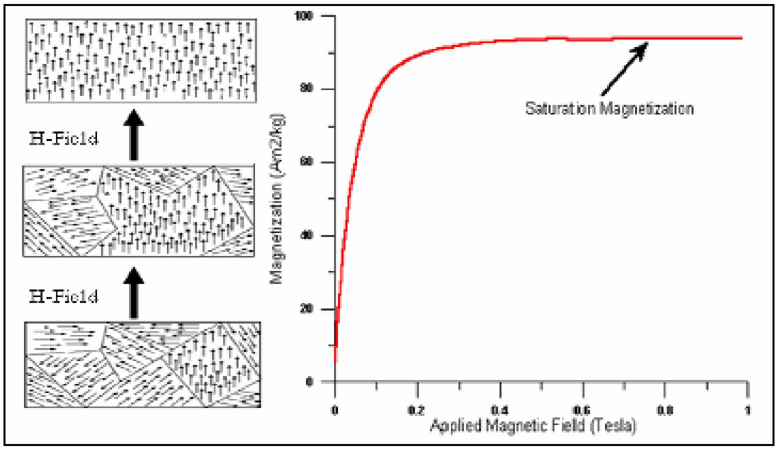

Figure 2.9: Orientation of magnetic moments in the domains with increasing magnetic field strength [28].

A loop called “Hysteresis” is commonly used to study the response of material with a change in the applied field using the vibration sample magnetometer (VSM) equipment. The curve patterns are varied depending on the type of magnetism [25]-[26]. Figure 2.10 demonstrates the typical hysteresis loops for magnetic materials [29].

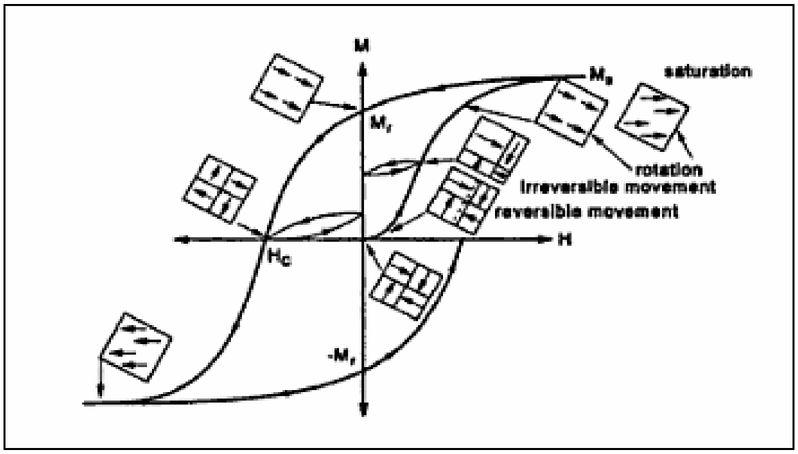

Figure 2.10: Typical hysteresis loop for magnetic material [29].

As illustrated in Figure 2.10, the moments are aligned antiparallel in the absence of external field. However, increasing the strength of the magnetic field will provide sufficient energy for the moments to overcome the randomizing effect. Consequently, all moments can be eventually aligned in parallel manner and the material has achieved saturation magnetization which is labelled as M_s (Figure 2.10). On the other hand, some moments remain aligned when reducing the exerted field strength to zero. This point is called remanence magnetization, M_r. Therefore; further reduction of exerted field strength to negative values is required to restore the moments to be aligned equally as their initial position. Herein, the measured strength is named as coercivity force, H_c [25]-[30].

2.4.4 Effect of Environmental Temperature

Material can reveal various magnetic characters in different temperature environments. It will exhibit superparamagnetic character when the temperature is increased beyond the critical point. This point is called Curie temperature or T_c [31]. At this point, the alignment of moments is no longer in a parallel manner but randomly oriented. Thus an opposite respond towards applied field is obtained. Figure 2.11 reveals the dependency of magnetic character on the temperature of the environment [28].

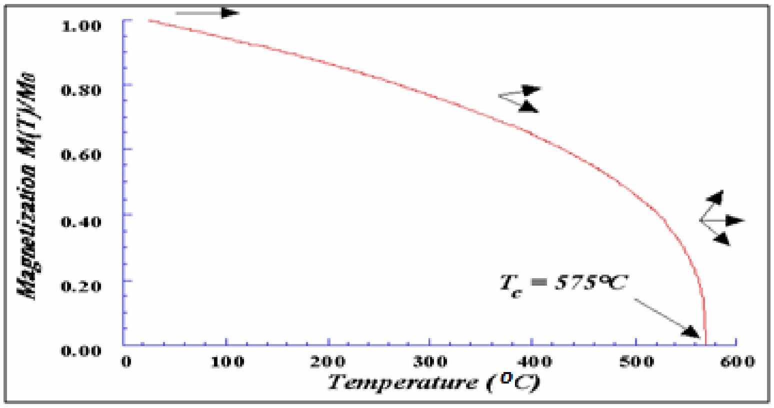

Figure 2.11: Effect of temperature on magnetic characters [28].

α-Fe_2O_3 exhibits weak ferromagnetic at room temperature and transforms to antiferromagnetic at the Morin temperature, T_m of 260 K. The Morin temperature, T_m is defined as a point where the magnetic character of a material turns to be antiferromagnetic. Furthermore, it also reveals paramagnetic above the Curie temperature, T_c of 950 K. On the other hand, ferrimagnetic character is displayed by magnetite at room temperature with Curie temperature, T_c of 850 K [20]. The existence of ferrimagnetic behavior is related to the unique alignment of magnetic moments in the internal structure. Fe_3O_4 contains Fe^{2+} and Fe^{3+} ions. The Fe^{2+} ions occupy tetrahedral site while Fe^{3+} ions are partially distributed to octahedral and tetrahedral sites. The electron spins for Fe^{3+} in both sites are aligned antiparallel, thus giving no net magnetic moments. The appearance of Fe^{2+} ions in octahedral site gives parallel spins alignment with neighbouring Fe^{3+} spins, hence revealing a net magnetic moment [32]. The spins arrangement in magnetite structure can be written as $Fe^{3+}\downarrow [Fe^{3+}\uparrow Fe^{2+}\uparrow] O_4$ [20].

2.4.5 Effect of Particle Size

Magnetic character is found to vary with particles size. Several works examined a consistent increase in magnetization saturation value, M_s; as a result of enlarging the size of particle [32]-[36]. Increasing particle size will increase the fraction of magnetism phase, thus growing the domain from a single to multidomains. Therefore, more magnetic moments are available to respond to the exerted field. In addition, large coercivity force, H_c may be required to completely demagnetize the remaining aligned moments [31]-[32]. The synthesized particles ought to come with the size beyond finite point. Particles with or below than finite point often exhibit superparamagnetic phase. Previous studies investigated that the critical size for most of iron oxides was approximately 10 nm [20], [31], [33], [37]-[39]. These particles displayed small saturation magnetization, M_s and large coercivity, H_c as reported elsewhere [31], [40]-[41]. Theoretically, materials with fewer or no domains will exhibit higher coercivity than those of multidomains [42]. This trend is related to the energy barrier (ΔE) for the rotation of magnetic moments, as elaborated in literatures [40]-[41]. It was discovered that there is a significant relation between surface area, S and energy barrier for the moments rotation, ΔE (J) as described by Equation 2.2 where K_s is the anisotropy constant (J/m^2) [40]-[41].

$$\Delta E = K_s S \tag{2.2}$$

Large surface area particles may possess greater energy barrier for the moment's rotation. However when particles having size equal or less than critical point, domain which is smaller than the single domain can be evolved. As investigated previously, single domain existed for those spherical particles with the size of ~15 – 100 nm [37], [39]. Herein, the available space may be insufficient to allow moments orientation, thus requiring stronger magnetic force to accomplish complete demagnetization. Consequently, higher coercivity value can also be expected. The relation between particles size with coercivity force is expressed in Equation 2.3 [40]-[41] where H_c corresponds to coercivity force (Oe) and *d* is the particle size.

$$H_c \sim 1/d \tag{2.3}$$

2.5 Nanocatalyst Preparation Method

The typical methods to synthesize iron oxide nanocatalysts are sol gel, precipitation and hydrothermal.

2.5.1 Theory of Preparation Method

2.5.1.1 Hydroxylation Step

Hydroxylation is the earliest step in many synthesis methods such as sol gel, precipitation and hydrothermal. The hydroxylation or hydrolysis is defined as a process to introduce hydroxyl ligand, OH^- in the structure of metal complex [43].

The hydroxylation step depends on two factors. Firstly is the formation of a soluble precursor. Iron (III) nitrate nonahydarates, $Fe\ (NO_3)_3.9H_2O$ salt is highly soluble in many solvents such as water, ethylene glycol, as well as nitric acid [43]. Secondly is the dissociation of undesired counter ions. Figure 2.12 illustrates the chemical structure of $Fe(NO_3)_3.9H_2O$ in an aqueous state [44].

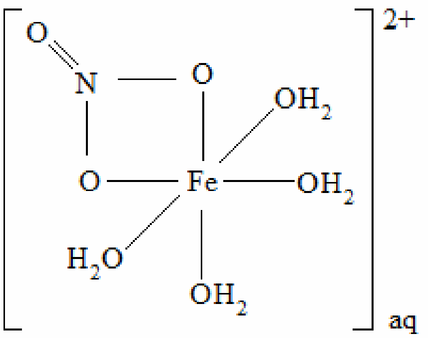

Figure 2.12: Chemical structure of the $Fe(NO_3)_3.9H_2O$ in aqueous state [44].

Nitrate, NO_3^- is a bidentate ligand [1], [44] which is able to replace two H_2O ligands [44]. On the other hand, NO_3^- is also a π donor ligand while H_2O behaves as a donor ligand and a good nucleophile. When NO_3^- and H_2O are coordinated around the Fe center, the electrons within these ligands are transferred to the Fe center, thus enriching the electron density of Fe. However, both NO_3^- and H_2O tend to compete so as to remain coordinated at the Fe center. Hence, electronegativity factor is taken into account which determines the ability of these ligands to remain coordinated or dissociated at the Fe center. The electronegativity, $\bar{\chi}$ for H_2O and NO_3^- is 2.49 and 2.76, respectively. Because NO_3^- has a slightly higher electronegativity, it favors to attract the electrons from the high electron density of the Fe center. This increases the negative charge of NO_3^- to a value of -0.84. The π back donation process increases, hence raising the electron density of NO_3^-. The $Fe-ONO_2^-$ bonds become weaker which subsequently reduces the ability of the NO_3^- to complex with the Fe center. The NO_3^- is finally dissociated, leaving two vacant sites which are then filled by the H_2O ligands. The ionic dissociation process shifts to the right side, eliminating the NO_3^- from the Fe-complex structure as described in Equation 2.4 [44].

$$[Fe(NO_3)(OH_2)_4]^{2+}{}_{(aq)} \leftrightarrow Fe(OH_2)_6]^{3+}{}_{(aq)} + NO_3^-{}_{(aq)} \qquad (2.4)$$

Equation 2.5 [44] describes the general chemical equation for the hydroxylation process, where p is the number of acidic proton released, Z is the formal charge and N is the coordination number.

$$[MO_NH_{2N}]^{z+} + pH_2O \leftrightarrow [MO_NH_{2N-p}]^{(z-p)+} + pH_3O^+ \qquad (2.5)$$

Water is amphiprotic which means that the process of transferring a proton, H_3O^+ happened even in the absence of acid or base. The H^+ is transferred from one water molecule to another and this occurrence is named as autoionization. Equation 2.6 [1], [10] describes the autoionization process.

$$2H_2O_{(aq)} \leftrightarrow H_3O^+{}_{(aq)} + OH^-{}_{(aq)} \qquad (2.6)$$

2.5.1.2 Sol Gel Method

The sol gel method is based on hydroxylation and condensation processes. The hydroxylation process has been elaborated in Section 2.5.1.1. The $[Fe(H_2O)_6]^{3+}$ complex must be entirely converted to zero valence charge complex, $[Fe(OH)_3(OH_2)_3]^o$ for the condensation process to take place. This can be accomplished by adding oxidizing agent such as the HNO_3 or hydrogen peroxide, H_2O_2 [44]. Nitric acid, HNO_3 is a strong oxidizing agent [1], [10] that can dissolve most metal precursors [43]. The mixture must be heated to initiate the condensation due to enthalpy change, ΔH is positive [44].

Condensation process comprises olation, gelation and oxolation steps. The olation is a process where the hydroxo or "ol" bridge, Fe-OH-Fe is formed via nucleophilic substitution (SN). This step is initiated when the $[Fe(OH)_3(OH_2)_3]^o$ has been successfully formed. In this step, iron-hydroxyl, Fe-OH acts as the nucleophile while water, H_2O

operates as the leaving group. The “ol” bridges can be formed via several ways as demonstrated in Equations 2.7-2.10 [44].

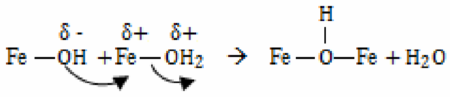

(2.7)

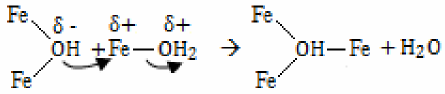

(2.8)

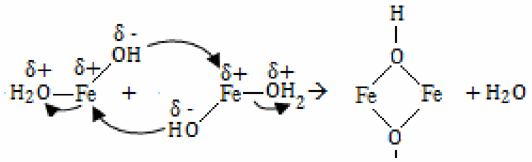

(2.9)

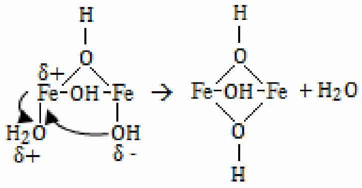

(2.10)

The olation step is ended when all H_2O ligands are entirely removed from the coordination sphere. The next step is the gelation which involves prototropic reaction whereby a proton jumps in between two adjacent OH^- ligands as illustrated in Equation 2.11.

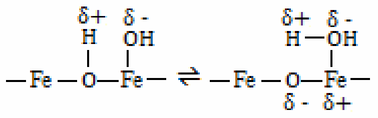

(2.11)

The occurrence of protonic reaction mainly depends on electronegativity of the H_2O ligand, $\delta(H_2O)$ and type of transition metal. The electronegativity of H_2O, $\delta(H_2O)$ value for the Fe complexes is tabulated in Table 2.3.

Table 2.3: Stability of hydroxide $M(OH)_z$ for Fe complexes calculated from Partial Charge Model [44].

Soluble precursor	$\delta(H_2O)$	Solid hydroxide formed by pure olation	$\delta(H_2O)$
$[Fe(OH)_3(H_2O)_3]^o$	+ 0.03	$Fe(OH)_3$	+ 0.07

As shown in Table 2.3, the electronegativity of $\delta(H_2O)$ for the Fe complexes is greater than zero, ($\delta(H_2O)>0$), resulting in a net repulsion force between the Fe (δ+) and H_2O ligand (δ+). This ensures that the net reaction remains forward, preventing reversible reaction which maintains the presence of the OH^- bridge (Equation 2.11).

Oxolation is the final step in condensation process. The oxolation process entirely eliminates H_2O ligands from the coordination sphere which eventually forms the edge and face M-O-M bridges as shown in Equations 2.12-2.13 [44].

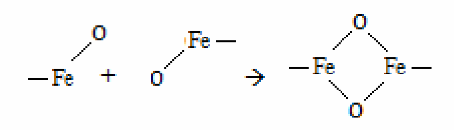

(2.12)

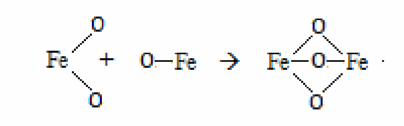

(2.13)

2.5.1.3 Hydrothermal Method

Hydrothermal method is widely used to synthesize magnetite, Fe_3O_4 nanoparticles [34]-[35], [37]. This method begins with hydroxylation as explained in Section 2.5.1.1 [44] and accomplished in an autoclave. Figure 2.13 shows a schematic diagram of a typical laboratory autoclave [45].

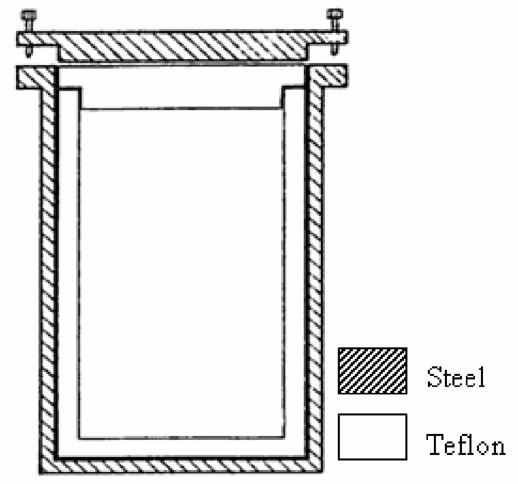

Figure 2.13: Schematic diagram of an autoclave [45].

Water is utilized as a solvent which generates vapor. It also works as the pressure transmitting medium. The hydrothermal method is typically accomplished at certain pressure and temperature above the boiling point of water [44]. Hydrazine hydrate, $N_2H_4.H_2O$ is a common additive used in the hydrothermal method [34]-[35], [37]. It serves as a base that increases the pH of the $[Fe(H_2O)_6]^{3+}$ complex precursor [1], [44]. This induces polymerization and precipitation processes, hence yielding a precipitated polymer, $Fe(OH)_3.nH_2O$ [1]. Equation 2.14 [1] shows the chemical equation for the precipitation process.

$[Fe(H_2O)_6]^{3+}{}_{(aq)} + (3 + n)H_2O \rightarrow Fe(OH)_3.nH_2O + 3H_3O^+{}_{(aq)}$ (2.14)

Besides acting as a precipitant, hydrazine, N_2H_4 also serves as a powerful reducing agent, having a standard reduction potential, E^o of -1.16 V [1], [10], [34]. The standard reduction potential, E^o for reducing Fe^{3+} to Fe^{2+} at 25^oC is 0.771 V [1], [10]. A reducing agent that has more negative standard reduction potential, E^o than that of a metal must be employed to reduce the metal [46]. This explained the selection of N_2H_4 in preparing Fe_3O_4 via the hydrothermal method [34]-[35], [37]. However, the capability of reducing becomes less in an open system and under hot alkaline environment due to the disproportionation reaction as described in Equation 2.15 [47].

$3N_2H_4 \leftrightarrow N_2 + 4NH_3 \quad E_o = -1.16\ V$ (2.15)

Highly negative standard reduction potential, E^o of N_2H_4 shifted the overall process to the right side, enriching N_2 and NH_3 (Equation 2.15). Therefore, the use of an autoclave is to avoid the N_2 and NH_3 from escaping to the atmosphere, thus generating high partial pressures of these two components. Increasing synthesis temperature pressurized the internal part of an autoclave which subsequently raised the partial pressure of nitrogen, N_2 and ammonia, NH_3 to a critical value. As a result, the overall reaction (Equation 2.15) is reversed, maintaining N_2H_4 as the dominant component. Thus, the reducibility of Fe^{3+} to Fe^{2+} can be enhanced [47].

During the hydrothermal process, the $N_2H_4.H_2O$ initially dissociates, forming $N_2H_5^+$ and OH^- ions in the presence of water (Equation 2.16 [34], [37]) at room temperature. The presence of the OH^- anions dissolved the iron (III) hydroxide, $Fe(OH)_3$ precipitate, forming an intermediate phase goethite, FeO(OH) (Equation 2.17 [34], [37]). Finally, N_2H_4 reduces the goethite, FeO(OH) to yield magnetite Fe_3O_4 (Equation 2.17 [34], [37]) that is usually accomplished at 80-160^{o}C, as reported in literature [34], [37]. The proposed chemical equations for these steps are written in Equations 2.16 – 2.18 [34], [37].

$N_2H_4 + H_2O \rightarrow N_2H_5^+ + OH^-$ (2.16)

$Fe(OH)_3 \rightarrow FeO(OH) + H_2O$ (2.17)

$12FeO(OH) + N_2H_4 \rightarrow 4Fe_3O_4 + 6H_2O + N_2$ (2.18)

2.5.1.4 Precipitation Method

Precipitation method is often used to synthesize magnetite, Fe_3O_4 nanocatalyst [31]-[32], [36], [48]-[50]. The synthesis can be carried out either by precipitation of Fe^{2+} or a mixture Fe^{2+} and Fe^{3+} with the molar ratio of 1:2 precursors. After undergoing hydroxylation process (Section 2.5.1.1), the pH of the precursor is increased to above 7 by adding a precipitating agent such as ammonia hydroxide, NH_4OH, and sodium hydroxide, NaOH. This is to remove H_2O and introduce OH ligands to the Fe center. Consequently, a hydrous iron oxide precipitate is formed (Equation 2.13, Section 2.5.1.2). This follows the proposed Charge-pH diagram as illustrated in Figure 2.14 [44].

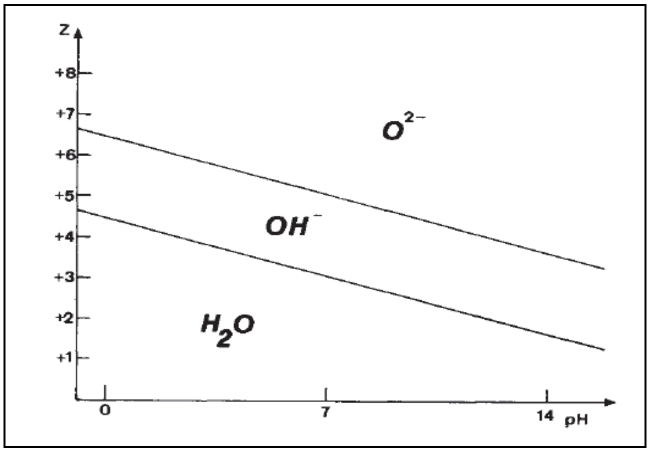

Figure 2.14: Charge-pH diagram for transition metal [44].

For ferrous, Fe^{2+} precursor, the minimum pH to form ferrous hydroxide, $Fe(OH)_2$ precipitate is 7 [20], [32]. This pH has to be increased to accelerate the partial oxidation of ferrous, Fe^{2+} to ferric, Fe^{3+} by the dissolved oxygen molecules in the system, hence yielding a mixture of ferrous hydroxide-ferrihydrite, $Fe(OH)_2$-$Fe_5HO_8.4H_2O$. The electrons mobility between Fe^{2+} and Fe^{3+} finally drives to a spinel arrangement [20], [32].

In the case of using Fe^{3+}/Fe^{2+} mixture, Fe^{3+} ions firstly undergo hydrolysis at pH 3 forming a highly soluble ferrihydrite, $Fe_5HO_8.4H_2O$. The $Fe_5HO_8.4H_2O$ is then combined with the existing Fe^{2+} ions to form Fe_3O_4 at higher pH. The proposed chemical equation for this formation is described in Equation 2.19 [32].

$$2Fe^{3+} + Fe^{2+} + 8OH^- \rightarrow Fe_3O_4 + 8H_2O \qquad (2.19)$$

There are several factors which influence the properties of resultant, Fe_3O_4 nanocatalyst. They comprise rate of pH increment [32], synthesis temperature [32], dropping rate of precipitant [36], and type of precipitant [36]. In the case of Fe^{2+}/Fe^{3+}

precursor, a rise in pH must be sufficiently fast to accelerate the incorporation of the Fe^{2+} ions into $Fe_5HO_8.4H_2O$ yielding Fe_3O_4. This avoids the oxidation of Fe^{2+} to Fe^{3+}, which easily occurs at higher pH [32]. Temperature has to be monitored. Higher temperature accelerates the oxidation of Fe^{2+} to Fe^{3+} by the dissolved oxygen in the system, thus leading to the formation of undesired phases [32]. In addition, dropping rate influences the size of resultant nanoparticles. Slow dropping rate is recommended as it can form a homogenous pH variation that is uniform all over the solution, thus producing much smaller particles with narrow size distribution [36]. The selection of proper precipitating agent is also emphasized in precipitation method. It was reported that the use of NH_4OH produced smaller particle size than that of NaOH. The NH_4OH allows a smooth increase in pH due to gradual increase of OH^- ions. This makes the formation of particles controllable. On the other hand, NaOH contains higher concentration of OH^- even if the concentration is the same as NH_4OH. This leads to the attainment of bigger particles [36].

2.5.2 Comparison between Various Methods of Preparation

There are several methods widely used to prepare unsupported Fe-based nanocatalysts such as sol gel [33], [40], [51], hydrothermal [47], [52]-[55] and co-precipitation [48], [56]. In general, the size and crystallinity of the resultant nanocatalyst is greatly influenced by annealing or calcination process. Elevating the annealing temperature enhances the crystallinity [57]-[58] and enlarges the particles size [57]-[59]. An increase in particle size is a result of the agglomeration of the smaller particles due to their high surface energy [60]-[61]. Particles agglomeration is enhanced by increasing the annealing temperature [57], [59].

The sol gel method promotes simplicity, homogeneity, low cost and high purity [33], [44], [62]. The underlying principles of this method have been elaborated in Section 2.5.1.2. Solvent selection and mechanical agitation are crucial factors for the sol gel method. A solvent must be able to entirely dissolve the metal precursor [43]. Meanwhile, mechanical agitation induces homogeneity of the sol which subsequently leads to the achievement of supersaturating point. The supersaturation point is a condition where the precursor is dissolved completely, hence accelerating the nucleation process [63]-[65].

Several advantages of using hydrothermal method include safe and environmental friendly as it is performed at moderate temperature [66], kinetic of reaction is accelerated with a small increase in temperature and single-phase crystals can be obtained easily [67].

The chemistry of this method has been described in Section 2.5.1.3. The pH, concentration, temperature, aging time and mineralizer are some of the parameters which influence the resultant properties (size, crystallinity and phase) of nanocatalysts [68]. Increasing the pH of the precursor reduces the particle size whereas an enlargement in particle size is observed as an outcome of increasing the concentration of precursor [68]. The particle size increases with extending the aging time of hydrothermal [34], [68]. Moreover, increasing hydrothermal temperature formed bigger particles size with more pure Fe_3O_4 phase [34]. Mineralizer refers to an agent that can precipitate the aqueous precursor. In the case of preparing Fe_3O_4 via hydrothermal method, $N_2H_4.H_2O$ is used frequently due to its ability to reduce Fe^{3+} to Fe^{2+}. The concentration of $N_2H_4.H_2O$ also influences the formation of Fe_3O_4 in the hydrothermal method [34].

2.5.2.1 Unsupported Iron Oxide Nanocatalyst

Formation of Different Phases of Iron Oxide

Previous work employed sol gel method with $Fe(NO_3)_3.9H_2O$ as the main precursor [33], [40]. They found that the use of citric acid as a solvent formed α-Fe_2O_3 whereas γ-Fe_2O_3 was formed as a result of elevating the annealing temperature [40]. Fe_3O_4 phase was attained when ethylene glycol was used as a solvent [33].

The oxidation state of iron precursor and the synthesis pH are crucial for hydrothermal and precipitation routes [34]-[35], [37], [53]-[54]. Using hydrothermal method, Fe^{2+} precursor was merely oxidized to give pure FeOOH and finally yielded α-Fe_2O_3 at pH of 3-5 [54]. Fe_3O_4 was successfully obtained by increasing the pH to 11 and above [54]. Meanwhile, Fe_3O_4 was also attained by reducing Fe^{3+} precursor to Fe^{2+} at pH 11 using hydrothermal method [37]. Fe_3O_4 phase was also obtained through precipitation method at pH 10-13 [31]-[32], [36], [48]. A mixture consisting of Fe^{2+} and Fe^{3+} salts with a ratio of 0.5 (Fe^{3+}/Fe^{2+}) together with NH_4OH is often deployed in precipitation route.

The concentration of reducing agent and synthesis temperature are vital in hydrothermal route. Most literatures obtained highly crystalline Fe_3O_4 and α-Fe_2O_3 nanoparticles at synthesis temperature of 140-180°C [34]-[35], [37], [53]-[55]. The use of 5% concentrated $N_2H_4.H_2O$ at synthesis temperature of 120°C formed α-Fe_2O_3 while at 20% concentration; it led to formation of Fe_3O_4 phase [32]. Other attempts mostly employed 50-85% concentrated $N_2H_4.H_2O$ in synthesizing Fe_3O_4 nanoparticles [34]-[36], [54].

Particle Size Alteration

The concentration of solvent influences the size of resultant nanoparticles. Raising citric acid, $C_6H_8O_7$ concentration from 0.05M to 0.2 M reduced the size of α-Fe_2O_3 nanoparicles from 56 nm to 22 nm [40]. Increasing annealing temperature from 200^oC to 400^oC enhanced crystallinity of Fe_3O_4 nanoparticles that were synthesized via sol gel method using ethylene glycol, $HOCH_2CH_2OH$ as the solvent. The particle size also increased from 8.5 nm to 15.5 nm [33]. Similar effect was also observed in the preparation of magnetoelectric $BiFeO_3$ system via the precipitation method [60].

The synthesis temperature and aging time influence the size of the resultant nanoparticles in hydrothermal method. The average particle size of Fe_3O_4 was reported to be enlarged from 7 nm to 30 nm when synthesis temperature elevated from 80^oC to 160^oC [34]. Similar trend was also observed in the preparation of TiO_2 thin films. Increasing synthesis temperature from 350^oC to 600^oC increased the particle size from 15 nm to 30 nm [61]. Others observed that the particle size of $FeNi_3$ nanoparticles was enlarged from 20 nm to 70 nm when the synthesis duration increased from 2 h to 15 h [47].

Magnetic Behavior

Magnetic behavior of iron oxide is greatly influenced by the particle size and its composition. Previous works claimed that an increment in particle size increased the magnetization saturation, M_s value [31]-[33]. The magnetization saturation, M_s value for Fe_3O_4 nanoparticles increased from 11.2 emu/g to 14.5 emu/g when particle size increased from 7 nm to 30 nm [34]. The superparamagnetic behavior is often observed for nanoparticles with size less than 10 nm [31], [33].

α-Fe_2O_3 behaves as a weak ferromagnetic material while γ-Fe_2O_3 reveals strong ferromagnetic character at room temperature. The M_s value for α-Fe_2O_3 nanoparticles was enhanced from 3.7 emu/g to 24.9 emu/g when annealing temperature increased from 210^oC to 400^oC [40]. These particles were synthesized through sol gel method deploying citric acid, $C_6H_8O_7$ as a solvent. The enlarged particles may be due to the enrichment of γ-Fe_2O_3 as a result of elevating annealing temperature [40]. In the case of precipitation method, the M_s value for Fe_3O_4 nanoparticles decreased from 58.7 emu/g to 17.4 emu/g as the pH was further extended from 4.7 to 6.7 [32]. Enrichment of FeOOH composition was claimed to be the major factor for the increase in particle size. FeOOH exhibits antiferromagnetic behavior which is difficult to be magnetized by the exerted magnetic field [32].

2.5.2.2 Supported Iron Oxide Nanocatalyst

Incorporating iron metal crystallites onto the support such as alumina, γ-Al_2O_3, silica oxide, SiO_2, manganese oxide, MgO; can be accomplished through several methods such as impregnation, precipitation and sol gel [69]. To be a good catalyst, it must hold a few criteria such as highly dispersed, easy to be reduced and unpoisoned [9]. Figure 2.15 shows the schematic visualization of particles agglomeration and supported metal particles [70].

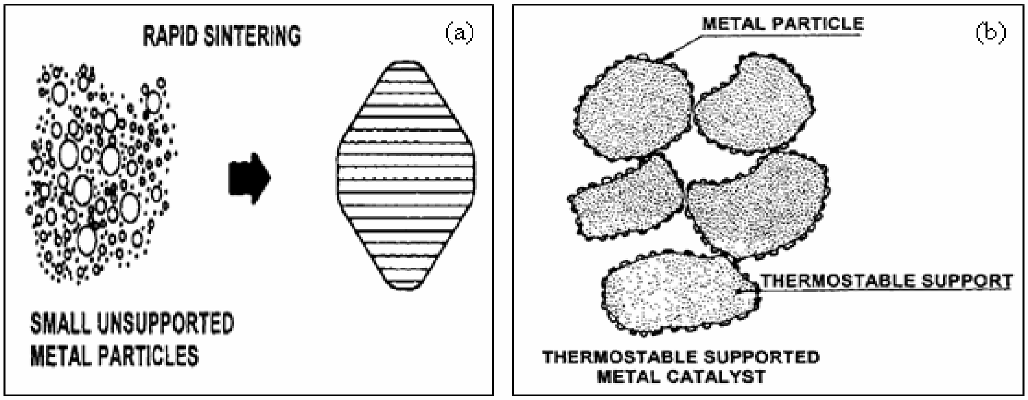

Figure 2.15: Schematic visualizations of (a) agglomerated and (b) supported metal particles [70].

Impregnation is a common method to prepare iron supported on alumina, α-Fe_2O_3/Al_2O_3 catalyst. The procedures are based on heterogeneous interaction between γ-Al_2O_3 support and iron precursor solution. Generally, the precursor is allowed to fill up the pores of the support. The system will then undergo aging, drying and annealing processes [51], [69]. Previous studies have used Fe $(NO_3)_3.9H_2O$ precursor solution which was impregnated onto commercial γ- Al_2O_3 solid system. The surface area of bulk α-Fe_2O_3 was 42 m^2/g while α-Fe_2O_3 supported on alumina, α-Fe_2O_3/Al_2O_3 resulted in surface area of 166 m^2/g [51]. Introduction of support influences the temperature of reduction. The first reduction temperature for the α-Fe_2O_3/Al_2O_3 (705 K) was slightly higher than that of unsupported α-Fe_2O_3 (644K) catalysts due to the formation of a strong spinel-hercynite,

$FeAl_2O_4$. However, temperature for second reduction stage shifted from 850 K to 800 K, comparing unsupported α-Fe_2O_3, and α-Fe_2O_3/Al_2O_3 catalysts [71]

Feasibility of performing impregnation is actively investigated recently. It was claimed that this approach is able to control the size of Fe particles on the γ-Al_2O_3 support. The preparation started by synthesizing iron oxide nanoparticles through hydrothermal route that was performed at synthesis temperature of 130 – 250°C. The size of the produced nanoparticles was in the range of 2 – 12 nm. These particles were then attached onto γ-Al_2O_3 via impregnation. The size of Fe nanoparticles for the supported and unsupported did not change, which indicates that agglomeration effect is minimized. It was also reported that reduction became easier and accomplished at slightly lower temperature for those catalysts with bigger size of iron particles. Conversely, small particles showed difficulty in completing reduction process. This was claimed to be due to the strong interaction between smaller Fe particles with the γ-Al_2O_3 surface, which eventually retards the accomplishment of complete reduction [72].

The properties of supported Fe catalyst can also be influenced by the type of the catalyst support. Complete reduction of iron oxide particles to zero valence state occurred at much lower temperature when γ-Al_2O_3 was replaced with activated C. TPR characterization revealed that the first reduction for Fe/C and Fe/Al_2O_3 catalysts occurred at 227°C and 391°C, respectively. Meanwhile, complete reduction was accomplished at approximately 900°C for Fe/C while Fe/Al_2O_3 was reduced completely at temperature above 1000°C [71].

2.6 Catalyst Activation

Reduction Process

Reduction is the first process that must be carried out before the catalytic reaction takes place. The purpose of reduction is mainly to convert metal oxide to pure metal for active sites to exist. Hydrogen, H_2 and carbon monoxide, CO gases are two typical reducing agents. They must be of high purity since O_2, S_2 and H_2O could contaminate the catalyst which can retard the catalytic steps [9]. H_2 gas is preferred as it generates H_2O as the bi-product. The use of CO produces CO_2 which can contribute to green house effect [73]. Reduction is heterogeneous and controlled by nucleation process. It is highly sensitive to several kinds of defects such as point defects, grain boundaries and mechanical with inclusion of promoter and iron [8]. Figure 2.16 illustrates a typical reduction profile of Fe_2O_3 [74].

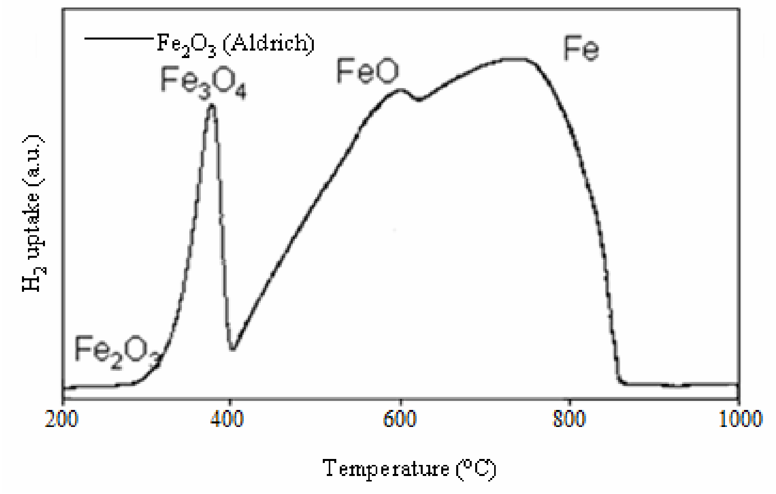

Figure 2.16: Typical reduction profile of α-Fe_2O_3 [74].

Reduction of Fe_2O_3 to Fe_3O_4 usually occurred at 150^oC to 400^oC while temperature above 500^oC is required to completely reduce Fe_3O_4 to α-Fe [22], [75]-[78]. Reduction of Fe_3O_4 involves two nucleation steps. It begins with nucleation of $Fe_{1-x}O$ within Fe_3O_4 intermediate phase framework and subsequently nucleation of α-Fe within $Fe_{1-x}O$ intermediate phase [8]. Figure 2.17 illustrates the nucleation process of Fe_3O_4 during reduction process.

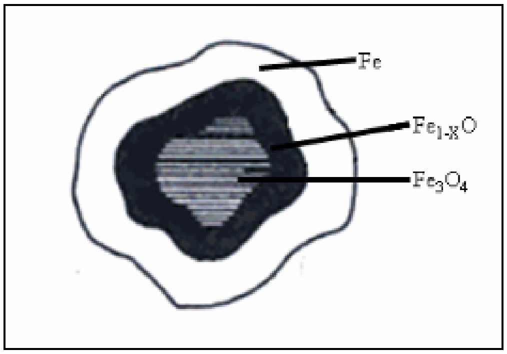

Figure 2.17: Core and shell structure for Fe_3O_4 during reduction process [8].

The structure consists of unreduced core of Fe_3O_4 which is surrounded by a dense layer of $Fe_{1-x}O$. The reduced α-Fe metallic becomes outermost layer (Figure 2.17) [8].

The mechanism of reduction involving iron oxides is quite complex. In the case of Fe_3O_4, direct access of H_2 onto reaction interface is prevented. This is due to dense and rigid properties of Fe_3O_4. Thereby, the requirement for producing the electrons is vital in this case. These electrons are formed by reacting H_2 with interface oxide, O^{2-} anions originated from nonstoichiometry $Fe_{1-x}O$. Equation 2.20 describes the chemical equation for this reaction [8], [22]. Once generated, the electrons will reduce Fe^{3+} to Fe^{2+}, yielding $Fe_{1-x}O$ as an intermediate phase as described by Equation 2.21. The reduction process is continued with direct interaction between $Fe_{1-x}O$ and H_2, resulting in iron, α-Fe metallic. Equation 2.22 [1], [8], [73], [76], [78] shows the proposed chemical equation for this process.

$$O^{2-} + H_2 \rightarrow H_2O + 2 \text{ electrons} \tag{2.20}$$

$$Fe_3O_4 + Fe^{2+} + 2 \text{ electrons} \rightarrow 4Fe_{1-x}O \tag{2.21}$$

$$Fe_{1-x}O + H_2 \rightarrow Fe + H_2O \tag{2.22}$$

Previous study examined the fraction composition of iron oxides during reduction by “in situ” XRD. It was found that at temperature up to 400^oC, α-Fe_2O_3 was almost fully converted to Fe_3O_4 with 97% composition. However, composition of Fe_3O_4 consistently decreased with elevating temperature to 560^oC. Three phases of iron oxide which consists of Fe_3O_4 (53%), $Fe_{1-X}O$ (7%) and Fe (40%) appeared as the temperature was increased to 580^oC. At 600^oC, Fe_3O_4 phase disappeared while two-phase system comprising $Fe_{1-X}O$ (41%) and Fe (59%) emerged. The $Fe_{1-x}O$ phase was found to be thermodynamically stable. Consequently, a complete reduction of $Fe_{1-x}O$ to Fe was entirely accomplished at 680^oC. These results suggested that the reduction of Fe_3O_4 involves disproportionation reaction as written by Equation 2.23 [22].

$$4Fe_{1-x}O \leftrightarrow Fe_3O_4 + Fe \tag{2.23}$$

This equation can be further expanded into two reactions as shown by Equation 2.24 and Equation 2.22 [22], [73], [75]-[76], [78].

$$Fe_3O_4 + H_2 \rightarrow 3Fe_{1-x}O + H_2O \tag{2.24}$$

Based on the findings, it can be deduced that reduction of α-Fe_2O_3 can occur via either two or three stages as stated in Equation 2.25 and Equation 2.26 [22], respectively.

$$3Fe_2O_3 \rightarrow 2Fe_3O_4 \rightarrow 6Fe \tag{2.25}$$

$$Fe_2O_3 \rightarrow Fe_3O_4 \rightarrow Fe_{1-x}O \rightarrow Fe \tag{2.26}$$

Reduction of α-Fe_2O_3 can occur in two stages at temperature less than 450^oC (Equation 2.25) by applying low heating rate [22], [75]-[76]. Theoretically, lowering the heating rate prolongs the contact time between the hydrogen and specimen, thus permitting complete reduction to occur at lower temperatures [22]. In this case, reaction 2.24 (Equation 2.24) is decelerated while reaction 2.22 (Equation 2.22) becomes faster, inhibiting the appearance of metastable $Fe_{1-x}O$ [22]. Complete reduction has been achieved at 450-480°C with the heating rate of 0.58°C/min [21]. On the other hand, the use of higher heating rate can lead to three-stage reduction process (Equation 2.26) which requires higher temperature to accomplish [22], [75]-[76]. Herein, reaction 2.22 (Equation 2.22) is inhibited and at the same time accelerates reaction 2.24 (Equation 2.24). This consequently enriches $Fe_{1-x}O$ composition [22]. The $Fe_{1-x}O$ phase is stable at temperature above 570°C. Thus, much higher temperature is needed to completely transform it to Fe metallic [22], [73]. Figure 2.18 deduces the steps involve in the reduction of α-Fe_2O_3.

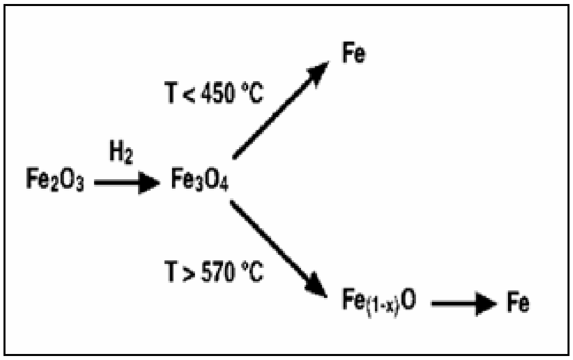

Figure 2.18: Reduction steps of α-Fe_2O_3 [22], [73], [79].

Low heating rate could enhance the reducibility. Unfortunately, longer period is required to achieve complete reduction. Conversely, the reduction can be performed faster by increasing the heating rate. However, this will shift reduction temperatures to higher temperature with larger hydrogen consumption. These drawbacks can possibly be overcome by dispersing iron particles on a support.

Degree of dispersion greatly influences reducibility of metal-supported catalyst. Well dispersion is desirable to enhance the activity-selectivity patterns of catalyst [79]. It also could bring down the reduction temperature. It was reported that the reduction temperature of α-Fe_2O_3 to Fe_3O_4 on alumina (Fe/γ-Al_2O_3) is found to be slightly lower than that of unsupported α-Fe_2O_3. This is due to well dispersed α-Fe_2O_3 particles on the support which makes them easier to be reduced [80]. Unfortunately, supported catalyst has some disadvantages. The formation of strong metal-support interaction is a well known drawback which will elevate the reduction temperature. It was claimed that reduction temperature for supported Fe_3O_4 was increased by 100-200°C as compared to those of unsupported samples [80]-[81]. This is mainly due to the existence of highly stable $Fe_{1-x}O$ phase on γ-Al_2O_3 at temperature 570^oC and above [81].

Higher annealing temperature during sample preparation will induce the agglomeration of the particles, thus reducing the surface area of the active phase [78]-[79]. Moreover, it also increases the strength of spinel phase which makes catalyst harder to be reduced. As investigated using $FeAl_{3.5}$ catalyst, the temperatures to reduce α-Fe_2O_3 to Fe_3O_4 and Fe_3O_4 to α-Fe were 430-460^oC and 780-810^oC, respectively. However, the reduction temperatures shifted to 550-560^oC and 840-860^oC when the $FeAl_{3.5}$ catalyst annealed at 1100^oC was characterized due to the enhancement in the strength of spinel phase [80].

The amount of iron oxide loading particles also influences the reduction behavior. Previous work found that catalysts loaded with 60-70% α-Fe_2O_3 particles gave broader reduction peaks and larger hydrogen consumption in TPR measurement compared to those of 40-43% α-Fe_2O_3 particles [80]. The reduction temperatures for the ones with 60-70% α-Fe_2O_3 particles loading were also shifted toward higher region which may be due to strong metal-support interaction. In addition, the catalyst containing 41.8 % α-Fe_2O_3 on γ-Al_2O_3 revealed lowest reduction temperature than that of the catalyst with 72.4% α-Fe_2O_3. This might be related to the fact that excess γ-Al_2O_3 offers more sites for iron oxide particles to be attached which aids in attaining a well dispersed catalyst [80].

2.7 Steps in Catalytic Reaction

There are three steps in catalytic reaction which are adsorption, surface reaction and desorption.

2.7.1 Adsorption

The interaction of gas-catalyst surface involves several steps. In ammonia synthesis, the collision between nitrogen and hydrogen molecules with pure metal surface is firstly undertaken. It creates an attraction potential which binds these molecules together. This binding is called adsorption [11]. In adsorption, molecules will firstly adsorp by physical adsorption (physisorption) and chemical adsorption (chemisorption) afterwards.

Physical adsorption (physisorption) involves Van der Waal's force. The enthalpy change of adsorption (ΔH_{ads}) does not exceed 80 kJ/mol [82]. This energy is insufficient to overcome the activation energy for H_2 and N_2 molecules dissociation which is about 436 kJ/mol and 945 kJ/mol, respectively. This prevents the dissociation process [10]; hence the molecules remain undissociated and eventually form multilayer adsorption.

In order to initiate the reaction, the molecules have to be adsorbed and dissociated. This is achieved by chemical adsorption (chemisorption). Chemisorption produces a strong bonding between reactant molecules and iron metal via electron sharing. The enthalpy change (ΔH_{ads}) for chemisorption is around 50-500 kJ/mol, which is sufficient to induce the cleavage of the molecules [83].

H_2 and N_2 molecules are evolved by the overlapping of the orbitals. Figure 2.19 illustrates the orbital diagram for nitrogen and hydrogen molecules [10], [84].

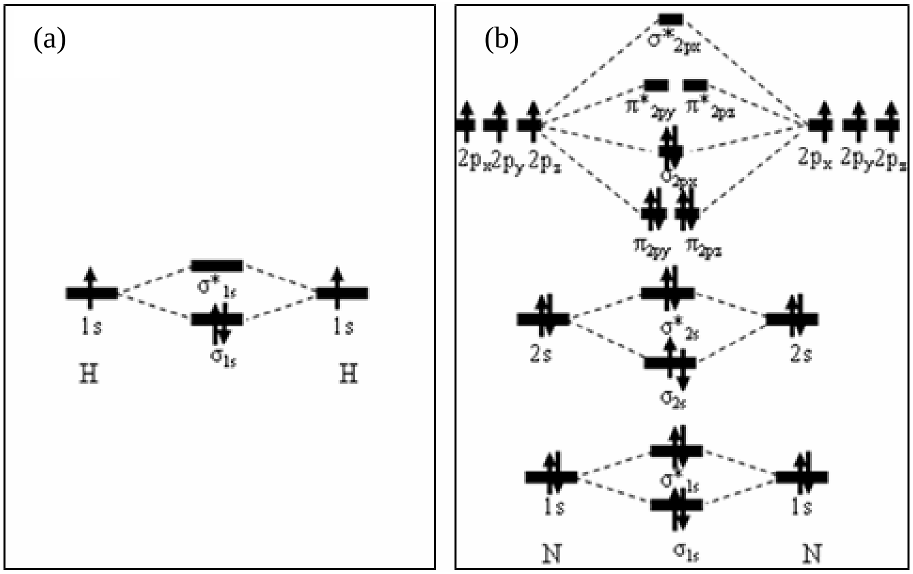

Figure 2.19: Molecular orbital diagram for (a) H_2 and (b) N_2 molecules [10], [84].

H_2 and N_2 molecules are also known as ligands. They tend to behave as electron donors by donating the electrons to the unoccupied d-orbital of iron. Due to the existence of a single bond, H_2 immediately dissociated forming H monoatomics [12], [85].

The rate of ammonia synthesis is determined by the N_2 dissociation [1], [13], [86]. However, the triple bond within N_2 is not easy to break even at high temperature. This is due to high bonding strength which is about 941.6 kJ/mol. The use of Fe as a catalyst can lower this energy to about ≈ 10 kJ/mol [12]. N_2 is also known as a π acceptor ligand. The direct electrons donation from high electron density within nitrogen triple bond (N≡N) to the unoccupied d-orbital of Fe produces a strong metal-ligand bond (M-H). However, the donation of excess electrons will also disturb the iron stabilization. This drawback can be overcome by π back donation process. Figure 2.20 demonstrates the π back donation process. The good π acceptor character of N_2 favors it to receive these electrons and place them in π antibonding orbitals (π*) (Figure 2.19). This process is called π back donation. The occupation of antibonding orbitals with electrons destabilizes the bonding within N≡N molecule, thus weakening as well as lengthening this bond. This consequently promotes the cleavage of N_2 [1], [10], [13], [82], [87]-[88].

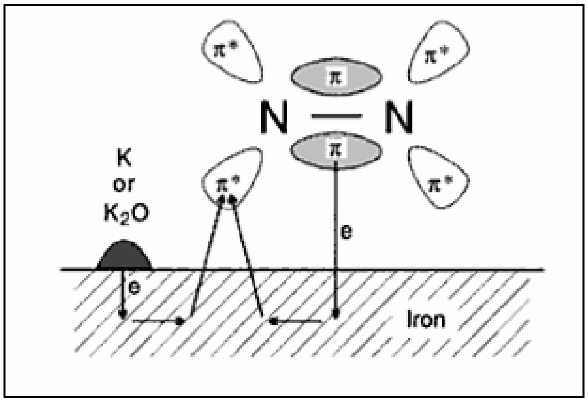

Figure 2.20: Steps involved during chemisorption of N_2 molecule on free Fe surface [87].

In addition, the dissociation of molecules can also be accelerated by the aid from a promoter. Potassium oxide, K_2O is a common promoter for ammonia synthesis catalyst. It provides additional electrons that could enhance the π back donation process (Figure 2.20) [87].

2.7.2 Surface Reaction

Migration takes place when hydrogen and nitrogen monoatomics are attached onto iron, Fe surface. Once nitrogen is attached, it will immediately pick up the hydrogen atoms to produce ammonia, NH_3 (Figure 2.20) [1], [85].

2.7.3 Desorption

Desorption is the final step in ammonia synthesis reaction. It involves the detachment of ammonia, NH_3 from the active sites once it is formed. This process leaves free sites so that the adsorption and migration of incoming molecules can occur continuously (Figure 2.21)

[1], [13], [85]. The proposed overall mechanisms in ammonia synthesis reaction are summarized in Figure 2.21 [89]-[90]. In addition, the energy profile for producing ammonia is revealed in Figure 2.22.

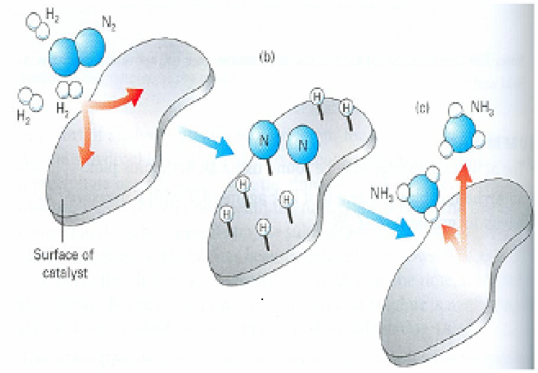

$N_2 \rightleftharpoons N_{2ads} \rightleftharpoons 2N_{ads}$ (1)

$H_2 \rightleftharpoons 2H_{ads}$ (2)

$N_{ads} + H_{ads} \rightleftharpoons NH_{ads}$ (3)

$NH_{ads} + H_{ads} \rightleftharpoons NH_{2,ads}$ (4)

$NH_{2,ads} + H_{ads} \rightleftharpoons NH_{3,ads} \rightleftharpoons NH_3$ (5)

Figure 2.21: Overall steps involved in ammonia synthesis reaction [89]-[90].

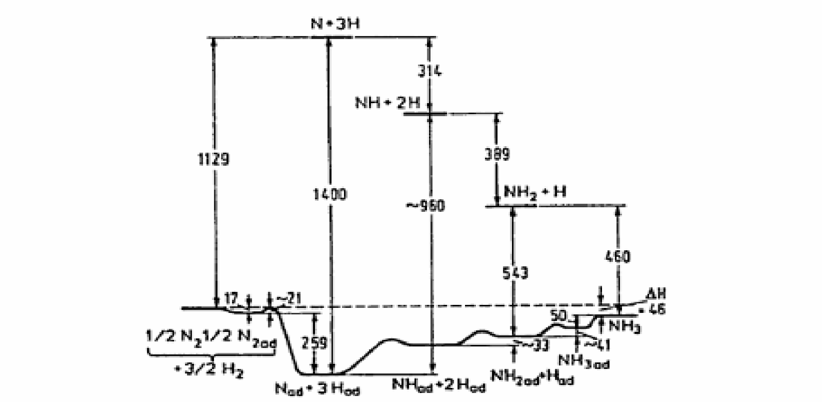

Figure 2.22: Energy profile of each steps involved in ammonia synthesis [8], [88].

2.8 Ammonia Synthesis

2.8.1 Overview of Ammonia Synthesis

Ammonia synthesis is an exothermic reaction. Therefore, the process is usually carried out at low temperature and high pressure environment. The overall chemical reaction for this process can be described in Equation 2.27 [1], [4], [9]-[10]:

$$N_2\ (g) + 3H_2\ (g) \leftrightarrow NH_3\ (g) \quad \Delta H = -92\ kJ \tag{2.27}$$

Le Chatelier's principle can be used to elucidate the role of temperature and pressure in this reaction. The participation of temperature is vital to increase the collision frequency between nitrogen and hydrogen molecules. This will increase the reaction rate and eventually accelerate the process. Unfortunately, higher temperature may disrupt the reaction equilibrium and decomposition of ammonia is favored. Herein, the reverse reaction is favored to re-establish the equilibrium. The temperature has to be lowered thereby shifting the equilibrium to the right side and enriching ammonia composition. However, this will lower the reaction rate and extends the time for reaction completion which is impractical at the plant-scale production.

The application of high pressure can enhance the production of ammonia. Equation 2.28 shows the expression of ideal gas law where P the partial pressure (atm), n is the number of mol, V is the volume (L), R is the gas constant (L.atm/mol.K) and T is temperature (K) [10].

$$PV = nRT \tag{2.28}$$

According to this formula, an increase in pressure causes the concentration of N_2, H_2 and NH_3 (Equation 2.27) to increase as a result of decreasing the volume. Equation 2.29 shows the expression to determine equilibrium constant, K_c for ammonia synthesis where [ ] signifies the concentration [10].

$$K_c = [NH_3]^2/[N_2][H_2]^3 \tag{2.29}$$

However, utilization of pressure does not affect the value of K_c due to nature of the reaction which involves a change in the total number of mole of gases. Pressure only does affect the value of reaction quotient, Q. Equation 2.30 describes the expression of Q for ammonia synthesis reaction [10].

$$Q = [NH_3]^2/[N_2][H_2]^3 \tag{2.30}$$

Based on this equation, it can be projected even though an increase in pressure enhances the concentration of N_2, H_2 and NH_3 gases (Equation 2.28), denominator of Q will maintain higher that that of numerator as the pressure is increased (Equation 2.30). This results in $Q<K_c$, bringing equilibrium reaction to forward direction to enrich composition of ammonia [9], [91]-[92]. Figure 2.23 reveals the dependency of reaction rates on various temperatures and pressures [93].

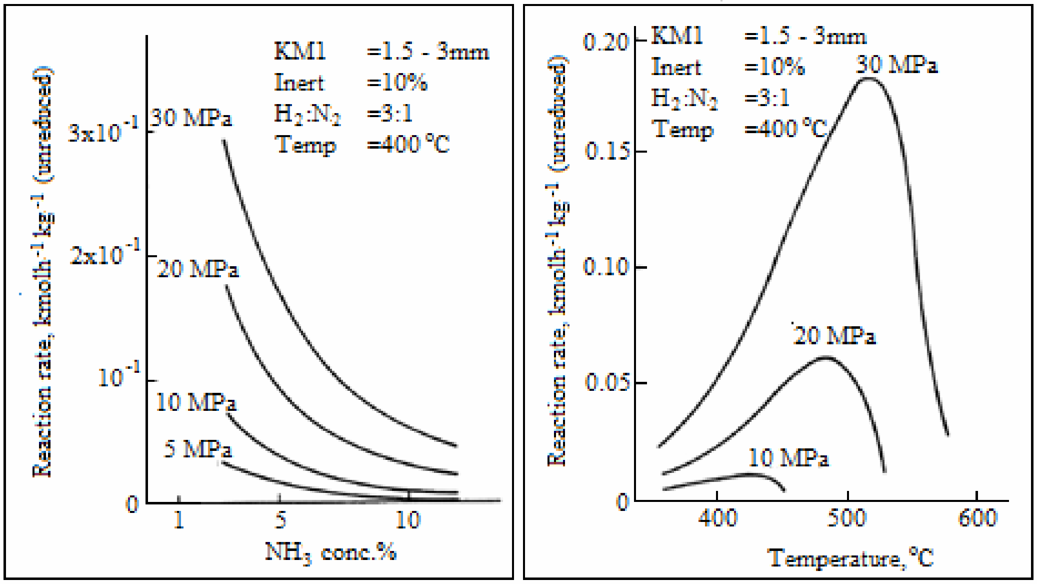

Figure 2.23: Dependency of ammonia synthesis rates at various temperatures and pressures [93].

2.8.2 Typical Industrial Practices

The earliest step in producing ammonia is the generation of synthesis gas. The syngas must be free from any poisoning elements such as sulfur and oxygen which retard the synthesis efficiency. Therefore, gas purification stage is required to ensure the composition of synthesis gas obeys the standard specification. The feedstocks containing light hydrocarbons such as natural gas, liquid petroleum gas or naphtha undergo steam reforming process, whereas partial oxidation route is recommended for heavy hydrocarbon such as heavy fuel oil, crude oil, asphalt and tar [8]. Figure 2.24 illustrates the schematic diagram of the ammonia synthesis process which involved steam reforming step.

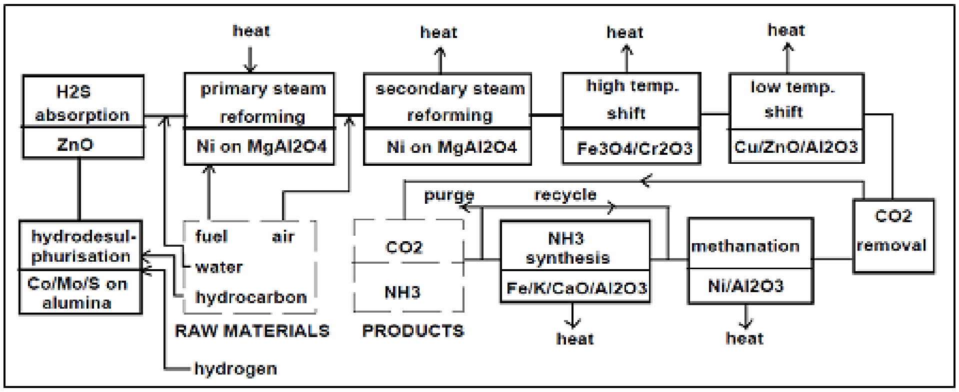

Figure 2.24: Schematic illustration of steps involved in plant scale ammonia synthesis [88].

Natural gas (CH_4) is an example of a typical feedstock. It will firstly undergo the desulfurization process. Next, the desulfurized natural gas enters the primary steam reformer which is operated at temperature and pressure of 750-850^oC and 35-40 bars, respectively. The steam reforming used NiO as a catalyst. The primary reformer involves two processes. The first one is the methane reaction with steam to produce CO and H_2 gases (Equation 2.31) [8]. In order to maximize the H_2 formation, the second reaction, which is called CO shift, takes place yielding CO_2 and H_2 gases (Equation 2.32) [8].

Methane-steam reaction $CH_4 + H_2O \leftrightarrow CO + H_2$ (2.31)

CO-shift reaction $CO + H_2O \leftrightarrow CO_2 + H_2$ (2.32)

In the next step, the gas will pass through secondary steam reforming process. Its purpose is to introduce nitrogen molecules, N_2 to the process gas and provides high temperature which is sufficient to reduce the methane content to an acceptable value. It is usually accomplished at 1000^oC, yielding approximately 0.3% (dry basis) of methane concentration [8].

Carbon monoxide, CO-shift conversion continuously occurred to convert the remaining CO from the previous reforming steps. It involves two stages. The first stage is at temperature of 350-500^oC in the presence of iron oxide/chromium oxide catalyst. It results in 3% (dry basis) of CO concentration. The second stage is undertaken to reduce the concentration of CO to 0.2 and 0.4% (dry basis). This second stage process is accomplished at 200-250^oC with the aid by $CuO/ZnO/Al_2O_3$ catalyst [8].

Carbon dioxide, CO_2 removal step is performed after the reaction in secondary reforming is completed. The concentration of CO_2 is further declined to about 0.1% (dry basis) by employing solvent scrubbing. After completing all the steps, the synthesis gas composition must reach the acceptable values as summarized in Table 2.4 [8].

Table 2.4: Recommended gas composition [8]

Type of gas	Mol%
H_2	74.6
N_2	24.4
CH_4	0.3
CO	0.3
CO_2	0.1
Ar	0.3

The final stage in synthesis gas preparation is methanation. The objective of methanation is to completely eliminate the remaining carbon oxides (CO_2 and CO). This stage is accomplished at 250-350^{o}C over reduced NiO catalyst, reducing carbon oxides concentration to less than 5 ppm [8], [88], [93].

The type of ammonia converter plays a significant role in ammonia synthesis. Figure 2.25 shows three reactors for ammonia synthesis commonly used by industries [92].

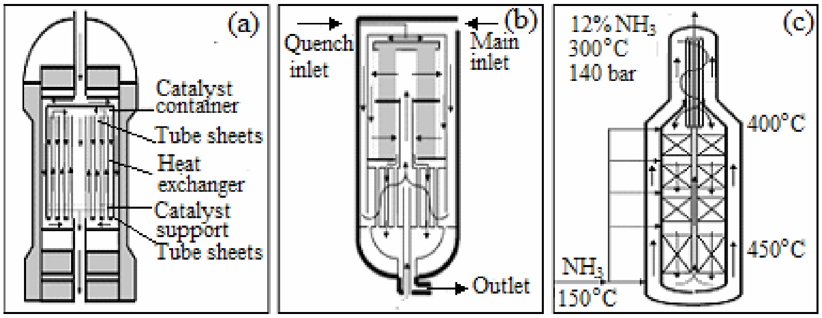

Figure 2.25: Ammonia synthesis reactors (a) Haber-Bosch (b) Haldor-Topsoe with radial flow and (c) Four-beds cold with axial flow [88].

There are two types of reactant flows namely axial (Figure 2.25 (a) and Figure 2.25 (b)) and radial (Figure 2.25 (c)). Radial flow design is commonly employed in the plant scale of ammonia synthesis. The utilization of the radial flow reduces the pressure drop effect caused by bed geometry and size of the catalyst. The bed geometry provides larger flow area and shorter flow path with catalyst size of 1.5 -.3 mm [8]-[9] is adequate for pressure drop to be minimized, hence reducing the volume of catalyst needed. Pressure drop is inversely proportional to the catalyst size [8]-[9]. These factors enhance the conversion performance due to the absence of diffusional limitation [9].

2.8.3 Ammonia Yield Collection and Quantification

Kjedahl or back titration method is used to quantify ammonia [6], [94]-[95]. This method captures ammonia gas using known concentration of acidic solution e.g. hydrochloric acid, HCl. The mixture will be titrated with known concentration of alkaline e.g. sodium hydroxide, NaOH to neutralize the excess acidic solution. The amount (mole) of ammonia produced which is also equal to reacted acidic solution can be calculated [96]-[97]. The overall chemical reaction is expressed in Equation 2.33 and Equation 2.34.

$$NH_3 + HCl \rightarrow NH_4Cl \tag{2.33}$$

The excess HCl is then back titrated using NaOH as described in Equation 2.31.

$$HCl_{excess} + NaOH \rightarrow NaCl + H_2O \tag{2.34}$$

Gas Chromatography (GC) is another method of quantifying the ammonia yield [94], [98]. Figure 2.26 shows the basic set up of the GC [99].

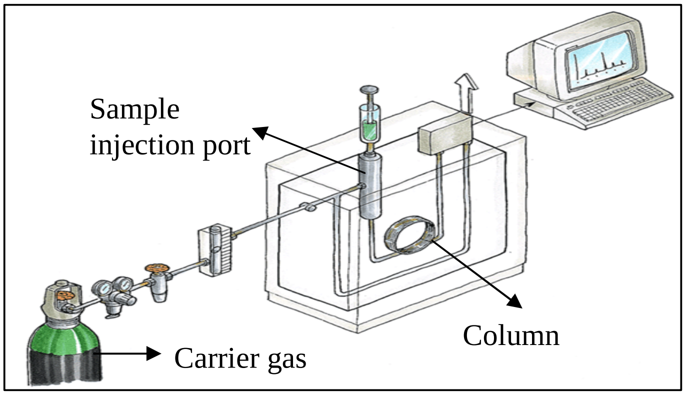

Figure 2.26: Set up of Gas Chromatography [99].

The set up consists of a gas carrier (Ar, He or N_2), detector, sample injection port, column (capillary or packed) and chromatograph displayer (Figure 2.26) [97]. The sample is firstly heated in the injection port at temperature relatively $50^{o}C$ above its boiling point, obtaining a vapor phase with the pressure of at least 10 torr. The carrier gas will then bring the vapor to enter the column for separation process. The chromatogram is then emerged on the displayer. The ammonia is identified by comparing the retention time, T_R between the standard and the analyzed sample. T_R is described as the minutes between the times of sample are injected and chromatograph is recorded. The area under chromatograph peak symbolizes the concentration of the produced ammonia [97].

In GC, the crucial factors include temperature during analysis and type of column [75]. Previous study performed analysis at 333 K using helium, He as a carrier gas. A packed column consisting of 5% KOH + 20% Carbowex 1500 on Chromosorb W-AW 80-100 mesh (5 m x 5 mm I.D) was utilized. Another alternative to detect ammonia is by using non-dispersive infrared detector (BINOS detector) [14], [18].

2.9 Ammonia Synthesis Reaction Study

The catalyst used for ammonia synthesis in industries is mostly iron oxides (95 wt %) together with small amount of promoters such as alumina, γ-Al_2O_3, calcium oxide, CaO, potassium oxide, K_2O and magnesium oxide, MgO. The catalyst is deployed under severe conditions of high temperature and pressure. Several studies were recently performed which focussed on several aspects of the catalytic system.

Fusion (melting) and high-energy ball milling methods are commonly used in altering the catalyst features. It has been reported that the activity of fused catalyst was about 1.3-1.9 times faster than conventional one [100]. This was recorded at temperature and pressure of 325-425^{o}C and 5-20MPa, respectively. The improvement was claimed to be related to the composition of the fused catalyst which contained 2.5 times more FeO than the conventional catalyst. In addition, the reducibility of this catalyst was also found to be 3.3 times faster than that of conventional one [18].

High-energy ball milling process revealed only 4% increment in ammonia production rate. This was showed by the catalyst which was milled for 110 hours with particles size approximately 100 times smaller than the one unmilled. This observation was deemed to be caused by the replacement of magnetite phase with promoter atoms, hence stabilizing the iron particles during reduction step. Consequently, the role of promoter that acts as the electron donor is retarded [18].

2.9.1 Performance evaluation between Fe_3O_4 and $Fe_{1-X}O$ based catalysts

$Fe_{1-x}O$ has been proposed to replace Fe_3O_4-based catalyst that may overcome the standing issue of low ammonia yield. The activity of $Fe_{1-x}O$ -based catalyst was 30-90% higher than the one consisting of Fe_3O_4 phase. Moreover, the reaction temperature was slightly reduced to about 25-40^{o}C lower than that of conventional one [100]. Other researcher [101] reported that $Fe_{1-x}O$ -based catalyst exhibited 70% higher reaction rate as compared to magnetite-based catalyst. The activation energy for $Fe_{1-x}O$-based catalyst was also reduced by 5.8% when the ammonia synthesis was performed at 460^oC and 100 – 400 bars. The improvement in reaction rate was due to surface area of the catalyst particles. A reduction in surface area was observed for $Fe_{1-x}O$ and Fe_3O_4 where both values were 16.6 m^2/g and 12.6 m^2/g, respectively. This reduction was claimed to be caused by the evolvement of H_2O during reduction process. Fe_3O_4 produces 20% more water than that of $Fe_{1-x}O$, which increased the rate of iron, Fe particles sintering [101]. Moreover, $Fe_{1-x}O$-based catalyst also displayed 14 % enhancement in catalytic activity per volume (moles of ammonia produced per hour per cubic meter catalyst). Higher bulk density of $Fe_{1-x}O$ compared to Fe_3O_4 due to compact ionic arrangement, was suggested as the major reason for this observation [101].

2.9.2 Effect of Catalyst Support

One of the ways to improve the catalytic activity is by dispersing the active phase onto a catalyst support. Previous study reported that iron supported on activated carbon in presence of small amount of potassium (Fe-AC-K); resulted in 10 ml NH_3/hr/g cat, catalytic activity at temperature of 250-400^oC and under atmospheric pressure [6]. Only 0.5 % mole of ammonia was produced using iron supported on activated carbon at 470^oC and atmospheric pressure in the absence of a chemical promoter.

2.9.3 Synergism between Iron and Ruthenium Based-Catalysts

Previous study [6] reported on the ability of ruthenium-based catalyst in improving the yield of ammonia synthesis. However, the synergism between iron and ruthenium is yet to be understood. It was reported that [6] pure ruthenium catalyst (Ru-AC-K) resulted in about 80% equilibrium conversion at 250-400^oC and atmospheric pressure. Meanwhile, the activity dropped by 50% when iron (Fe-AC-K) was used. Catalyst comprising equal ratio of both metallics (Ru50-Fe50-AC-K) resulted in a decline in the activity by 30% [6].

2.9.4 Effect of Reaction Temperature

One of the most crucial reaction parameters is temperature. Sufficient temperature is required to achieve equilibrium conversion while too high favors the decomposition of ammonia to nitrogen and hydrogen [18], [94], [100]-[101]. In the case of Ru/Al_2O_3-KOH derived from $Ru_3(CO)_{12}$ catalyst, the equilibrium conversion was attained at 390^oC under atmospheric pressure with the ammonia production rate of approximately 250 mg/g(Ru). However, the product subsequently declined with increase in temperature [94]. Similar trend was also revealed on iron and ruthenium catalyst. The equilibrium conversion was attained at 350°C under atmospheric pressure for all catalysts [6].

2.9.5 Effect of Pressure

Previous investigation [14] proved that an increase in pressure does not lead to a significant increase in conversion at low temperature. The ammonia was not detected for the synthesis performed at 580K under pressure of 1-50 bars with H_2:N_2 ratio of 3:1 and flow feed rate of 40 cm^3/min [14]. However most of equilibrium conversions were achieved at temperature higher than 700 K. Pressure of 50 bars exhibited maximum conversion (3.5% NH_3 mole fraction) that was obtained at H_2:N_2 ratio, flow feed rate and temperature of 3:1, 40 cm^3/min and 770 K, respectively [14].

2.9.6 Effect of Hydrogen and Nitrogen (H_2:N_2) Gases Ratio

The effect of varying hydrogen and nitrogen gases, (H_2:N_2) on the ammonia production have been studied [14]. In the case of $CsNO_3$-Ru/Al_2O_3 catalyst, it was observed that the ratio of 1:3 (H_2:N_2) resulted in improved ammonia yield effect where optimum activity was attained at 610 K with the ammonia effluent approximately 2700 ppm. Inhibiting effect appeared when the H_2:N_2 was increased to 3:1. The ratio of H_2:N_2 was further varied from 5:95 to 75:25 and pressure applied was also elevated to 50 bars. The catalytic activity evaluation showed that the ratio of 5:95 (H_2:N_2) revealed significant rate of NH_3 formation at temperature as low as 520K. However, the decomposition of ammonia was favored as a result of increasing temperature due to the disturbance in reaction equilibrium. Maximum ammonia yield was achieved at 720 K using 60:40 (H_2:N_2) ratio [14].

CHAPTER 3

METHODOLOGY

3.1 Introduction

This chapter consists of three major sections namely the preparation of nanocatalysts, characterization of nanocatalysts and evaluation of catalytic activity. Three types of nanocatalysts prepared were unsupported α-Fe_2O_3, Fe_3O_4 and 5% α-Fe_2O_3/γ-Al_2O_3. Several methods were utilized which include sol gel, self combustion, self assembly, precipitation, hydrothermal and a hybrid sol gel-hydrothermal. The parameters studied include synthesis methods, synthesis temperature, period of stirring, annealing temperature and inclusion of surfactant. The prepared nanocatalysts were characterized using x-ray diffraction (XRD), raman spectroscopy, field emission scanning electron microscopy (FESEM), energy dispersed x-ray (EDX), temperature programmed reduction (TPR), vibration sample magnetometer (VSM) and N_2 adsorption. Catalytic evaluation was evaluated in a fix bed microreactor at 30^oC to 200^oC under atmospheric pressure at various total feed flow rates and H_2/N_2 volumetric ratios. The effect of magnetic field on the catalytic activity was also examined.

3.2 List of Chemicals and Gases

Chemicals and gases used in this study including their source and purity are summarized in Table 3.1.

Table 3.1: Chemicals and gases employed in this study.

Name	Chemical Formula	Supplier	Purity	Usage
Iron (III) nitrate nonahydrate	$Fe(NO_3)_3.9H_2O$	Hamburg Chemicals	99.99%	Catalyst Precursor
Iron (II) chloride	$FeCl_2$	Hamburg Chemicals	99.99%	Catalyst Precursor
Sodium bis(2-ethylhexyl) sulfosuccinate	$C_{20}H_{37}NaO_7S$	Acros Organic	96%	Catalyst Surfactant
Tetrapropylammonium hydroxide	$C1_2H_{29}NO$	Fluka Chemika	-	Catalyst Surfactant
Nitric acid	HNO_3	R & M Chemicals	65%	Synthesis Solvent
Ethylene glycol	$HOCH_2CH_2OH$	R & M Chemicals	99.95%	Synthesis Solvent
Hydrazine hydrate	$N_2H_4.H_2O$	Across Organics	55%	Reducing agent
Ammonia hydroxide	NH_4OH	Across Organics	55.00%	Precipitant
Methanol	CH_3CH_2OH	Hamburg Chemicals	99.98%	Catalyst Washer
Sodium hydroxide	NaOH	System	99.00%	Product Quantifier
Hydrochloric acid	HCl	System	99.00%	Product Quantifier
Hydrogen gas	H_2	MOX	99.99%	Reactant
Nitrogen gas	N_2	MOX	99.99%	Reactant
5% hydrogen in 95% nitrogen gas	$5\%H_2$-$95\%N_2$	MOX	96.99%	TPR

3.3 Preparation of Nanocatalyst

Three types of nanocatalysts were prepared namely α-Fe_2O_3, Fe_3O_4, and α-Fe_2O_3/ γ-Al_2O_3.

3.3.1 Unsupported Hematite, α-Fe_2O_3 Nanocatalyst

Parameters studied were synthesis method, stirring period and annealing temperature.

3.3.1.1 Effect of Synthesis Method

The sol-gel [40], [51], self-combustion [102] and self-assembly [103] methods were employed. The procedures for the sol gel method are shown in Figure 3.1.

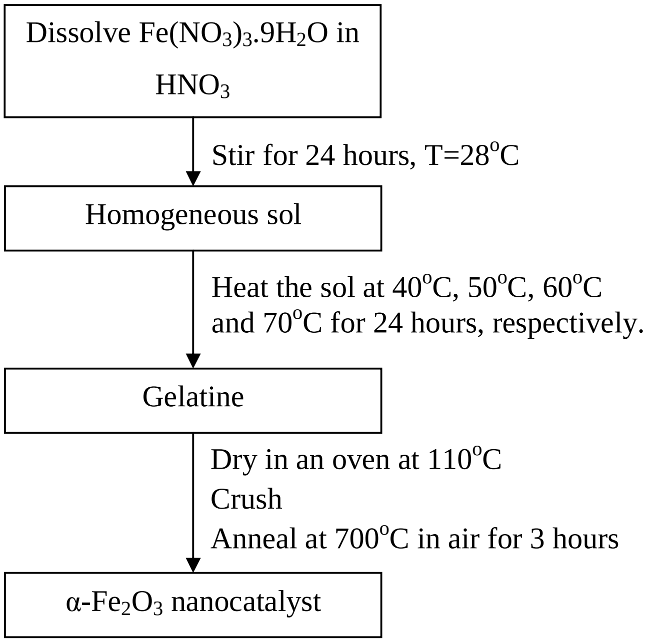

Figure 3.1: Procedures to prepare α-Fe_2O_3 nanocatalyst using sol-gel method.

20 g of iron (III) nitrate nonahydrate, $Fe(NO_3)_3.9H_2O$ was weighed and dissolved in 100 mL of 65% nitric acid, HNO_3. The mixture was stirred vigorously on a magnetic stirrer for 24 hours to obtain a homogeneous sol. The homogeneous sol was then heated at 40°C, 50°C, 60°C and 70°C, respectively for 24 hours forming a gelatine. The gelatine was dried in an oven at 110°C overnight. The dried sample was crushed using mortar and pestle, followed by annealing at 700°C in air for three hours.

The procedures in self-combustion and self-assembly methods are similar to the sol-gel method but differ in certain steps. In the self-combustion method, the homogeneous sol was gradually heated until it combusted at 110°C. In self-assembly method, the homogeneous sol was placed in a fume cupboard for three months without stirring.

Figure 3.2 illustrates the steps involved in the self-combustion method. The synthesis started by weighing 20 g of iron (III) nitrate nonahydrate, $Fe(NO_3)_3.9H_2O$ and dissolving it into 100 mL of 65% nitric acid, HNO_3.

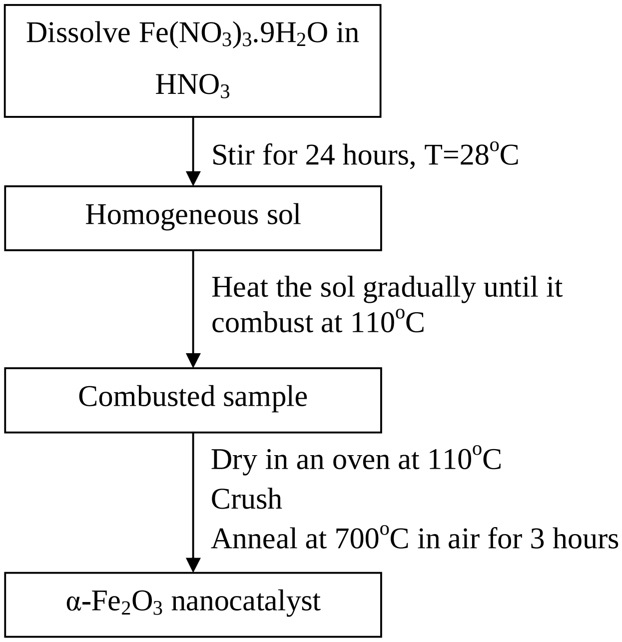

Figure 3.2: Procedures to prepare α-Fe_2O_3 nanocatalyst using self-combustion method.

The mixture was stirred vigorously on a magnetic stirrer for 24 hours to obtain a homogeneous sol. The sol was then gradually heated until it combusted at temperature of 110°C. The sample was dried in an oven at 110°C overnight. It was followed by crushing and annealing at 700°C in air for three hours.

The procedures for the self-assembly method are shown in Figure 3.3. It began with weighing 20 g of iron (III) nitrate nonahydrate, $Fe(NO_3)_3$. $9H_2O$. The weighed $Fe(NO_3)_3$ was then dissolved into 100 mL of 65% nitric acid, HNO_3. The mixture was stirred on a magnetic stirrer for 24 hours to form a homogeneous sol. The sol was then stored in a sealed beaker and placed inside a fume cupboard for 3 months. The sol was then heated at 40°C, 50°C, 60°C and 70°C for 24 hours, respectively forming a gelatine. The gelatine was then dried in an oven at 110°C overnight. The dried sample was crushed using mortar and pestle, followed by annealing at 700°C in air for three hours.

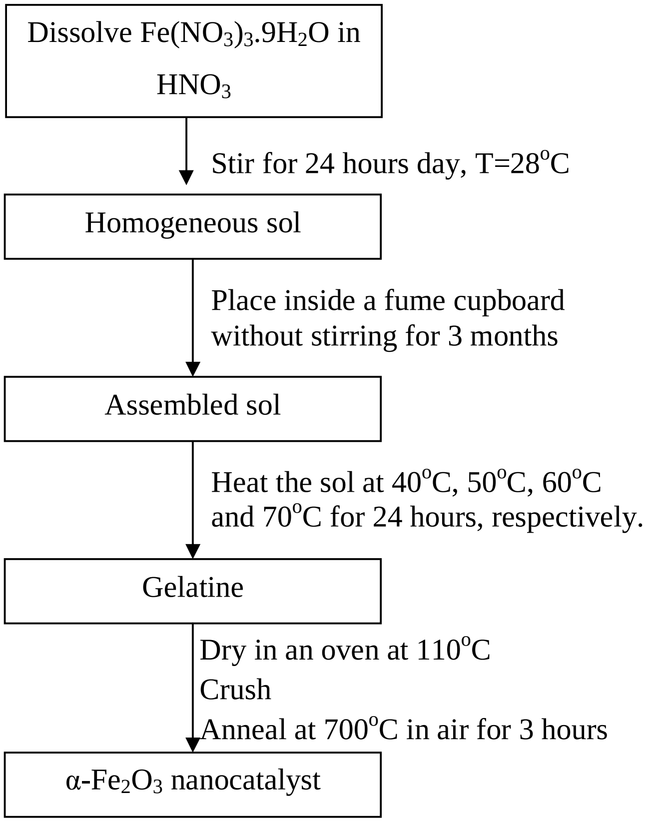

Figure 3.3: Procedures to prepare α-Fe_2O_3 nanocatalyst using self-assembly method.

3.3.1.2 Effects of Period of Stirring and Annealing Temperature

The effect of stirring was studied for α-Fe_2O_3 nanocatalyst prepared using the sol-gel method (Section 3.3.1.1). The stirring period was prolonged to 1 week and 1 month. The resultant catalysts were annealed at 300^{o}C in air for three hours. The effect of annealing temperature was studied using the catalyst stirred for 1 day. The sample was separated into few portions and each portion was then annealed at 400^{o}C, 500^{o}C, 600^{o}C and 700^{o}C, respectively in air for three hours.

3.3.2 Unsupported Magnetite, Fe_3O_4 Nanocatalyst

Preliminary study involving several typical methods such as sol-gel, precipitation and hydrothermal were firstly conducted. The outcome of the preliminary study led to development of a hybrid method namely sol gel-hydrothermal.

3.3.2.1 Effects of Preparation Methods

A preliminary study on synthesizing Fe_3O_4 via various methods was conducted. It comprised sol-gel [33], precipitation [36] and hydrothermal [37] methods.

Preparation via sol-gel method began by dissolving 10 g of iron (III) nitrate, Fe $(NO_3)_3.9H_2O$ in 50 mL of ethylene glycol, $HOCH_2CH_2OH$ and stirred for 24 hours to obtain a homogeneous solution. This homogenized solution was then heated until gelatine was formed. The gelatine was then dried in a vacuum oven at 110°C overnight. These procedures are summarized in Figure 3.4.

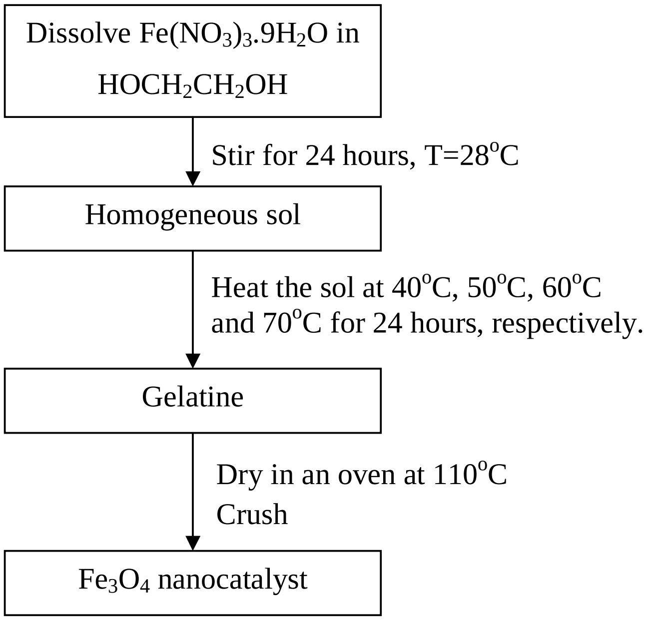

Figure 3.4: Procedures to prepare Fe_3O_4 nanocatalyst using sol-gel method

Figure 3.5 shows the procedures for precipitation method. The method started by preparing a homogeneous sol. It was accomplished by dissolving 3 g of iron (II) chloride, $FeCl_2$ salt in 50 mL distilled water and stirred for 24 hours. This homogenized solution was then titrated with ammonium hydroxide, NH_4OH solution forming a black precipitate at pH~10-11. The precipitate was filtered and washed with deionized water as well as absolute ethanol for several times. The wet precipitate was then dried in a vacuum oven at 110°C overnight.

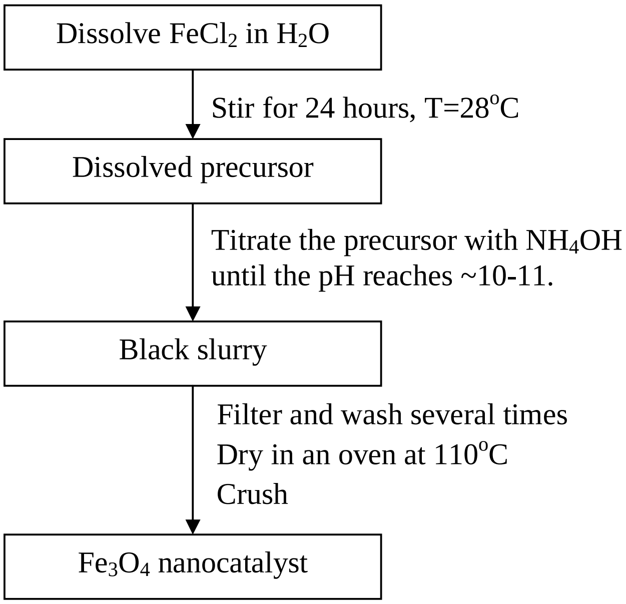

Figure 3.5: Procedures to prepare Fe_3O_4 nanocatalyst using precipitation method.

The hydrothermal method employed 50 µL of tetrapropylammoniumhydroxide, $C_{12}H_{29}NO$ surfactant and 0.4 g of iron (III) nitrate, $Fe(NO_3)_3.9H_2O$ as the precursors. These chemicals were dissolved in 10 mL of distilled water and stirred for 24 hours to obtain a homogeneous solution. The homogenized solution was transferred into an autoclave, then 1.8 mL of 55% hydrazine hydrate, $N_2H_4.H_2O$ aqueous solution was added to the autoclave. The autoclave was sealed tightly and heated in an oven at 160°C for 10 hours. The slurry formed was then filtered and washed with deionized water followed by absolute ethanol several times. The wet precipitate was then dried in a vacuum oven at 110°C overnight. Figure 3.6 summarizes the procedures for the hydrothermal method.

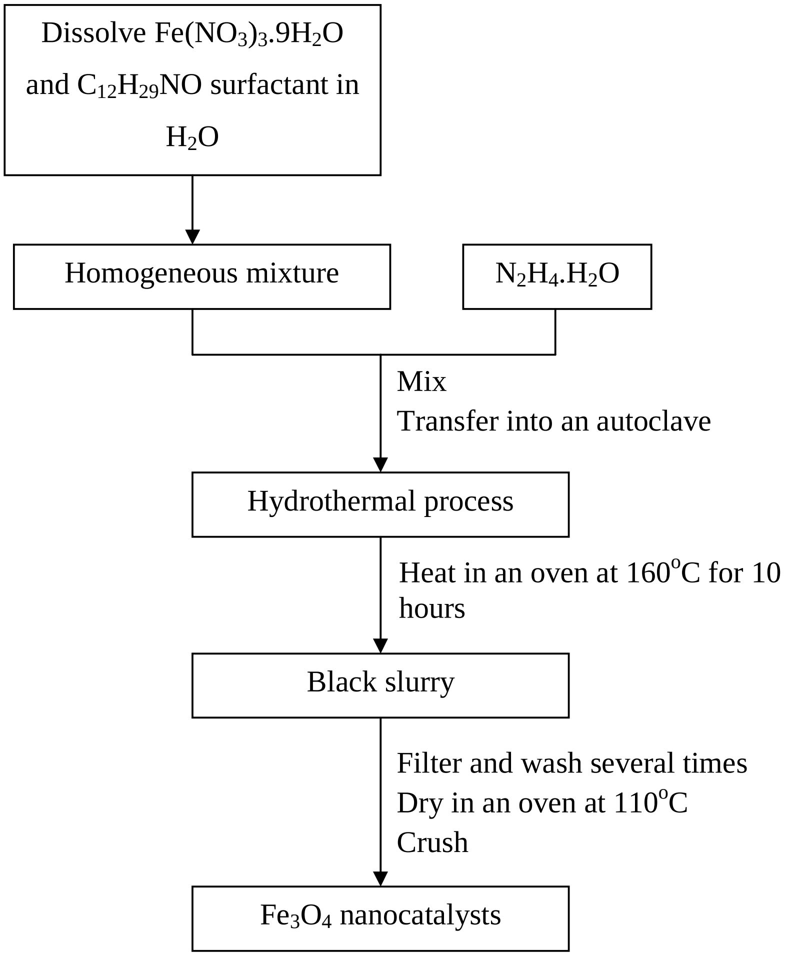

Figure 3.6: Procedures to prepare Fe_3O_4 nanocatalyst using hydrothermal method.

3.3.2.2 Hybrid Sol Gel-Hydrothermal Method

Interpretation of the results obtained from the preliminary study led to the development of a new combined approach which was named as sol gel-hydrothermal method. This approach comprised two major sections which were formation of gelatine and consequently followed by hydrothermal treatment. Figure 3.7 shows the steps involved in the sol gel-hydrothermal method.

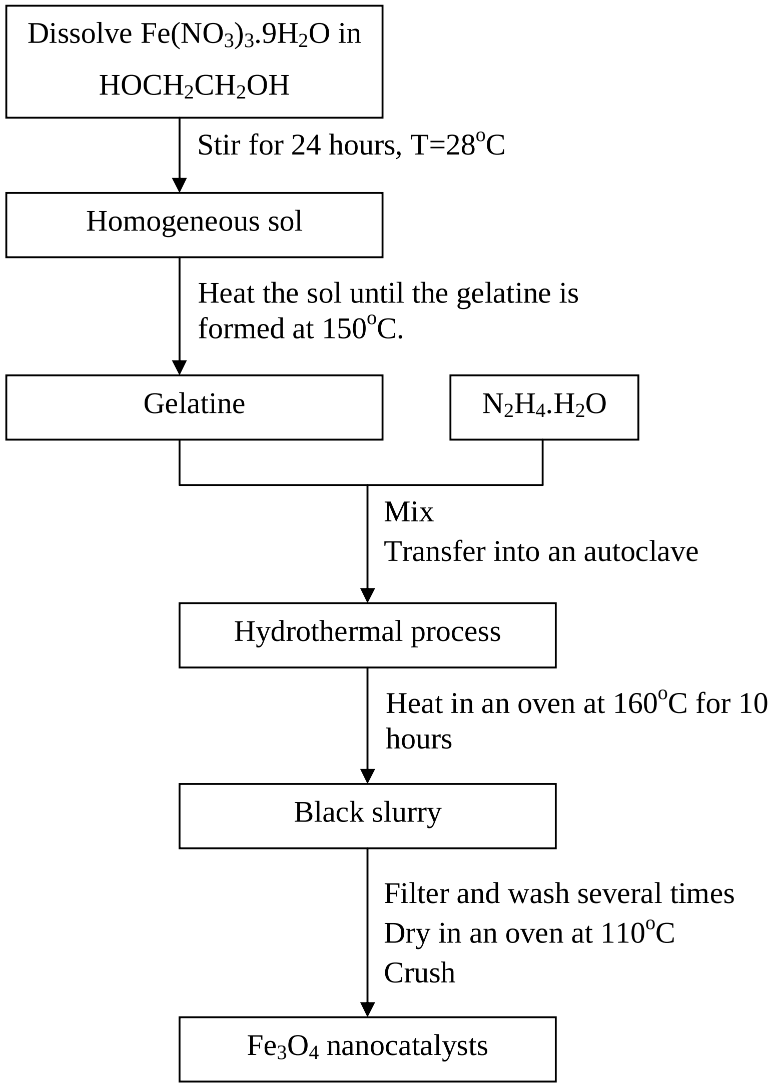

Figure 3.7: Procedures to prepare Fe_3O_4 nanocatalysts using sol gel-hydrothermal method.

Typically, 1 g of iron (III) nitrate, $Fe(NO_3)_3.9H_2O$ salt was dissolved in 10 mL of ethylene glycol and stirred for 24 hours to obtain a homogeneous solution. This homogenized solution was then heated until the gelatine was formed at 150^oC. Then the gelatine was rapidly transferred into an autoclave followed by addition of 5 mL of 55% hydrazine hydrate, NH_4OH aqueous solution and 25 mL of distilled water. The autoclave was sealed tightly and heated in an oven at 160^oC for 10 hours. The slurry formed was then filtered and washed with deionized water and absolute ethanol several times. The wet precipitate was then dried in a vacuum oven at 110^oC overnight.

Further investigations regarding this approach were also conducted. The synthesis temperature was varied to 28^oC, 50^oC, 80^oC and 120^oC for 10 hours respectively.

Furthermore, the effect of annealing temperature was studied using catalyst synthesized at 160°C. This catalyst was annealed at 300°C, 400°C and 500°C in vacuum furnace for three hours, respectively.

3.3.3 Supported Hematite on Alumina (5% α-Fe_2O_3/γ-Al_2O_3) Nanocatalyst

α-Fe_2O_3 was synthesized using sol gel-hydrothermal method on alumina, γ-Al_2O_3 support. Two parameters studied were the synthesis periods and iron (III) nitrate to sodium bis(2-ethylhexyl) sulfucinnate surfactant ($Fe(NO_3)_3$:SBS) ratios.

3.3.3.1 Effect of Synthesis Period

The overall procedures are illustrated in Figure 3.8. Typically, 0.7 g of iron (III) nitrate, $Fe(NO_3)_3.9H_2O$ was dissolved in 10 mL of ethylene glycol, $C_2H_6O_2$ and the mixture was stirred for 1 day to obtain a homogeneous sol. The homogeneous sol was then heated at 160°C under vigorous stirring to obtain gelatine. The gelatine was then transferred into an autoclave containing 1.90 g of commercial alumina oxide, γ-Al_2O_3 and 18 ml distilled water. Then, 3.5 mL of 55% hydrazine hydrate, NH_4OH was added to the mixture. The autoclave was then tightly sealed and placed in an oil bath at 160°C for 1 hour. The resultant catalyst was filtered, washed and dried at 50°C in an oven. Then, it was annealed at 400°C in nitrogen flow at 10 ccm/min for three hours. The synthesis periods for the hydrothermal part were then varied to 10 hours and 1 day. The calculations are shown in Appendix C.

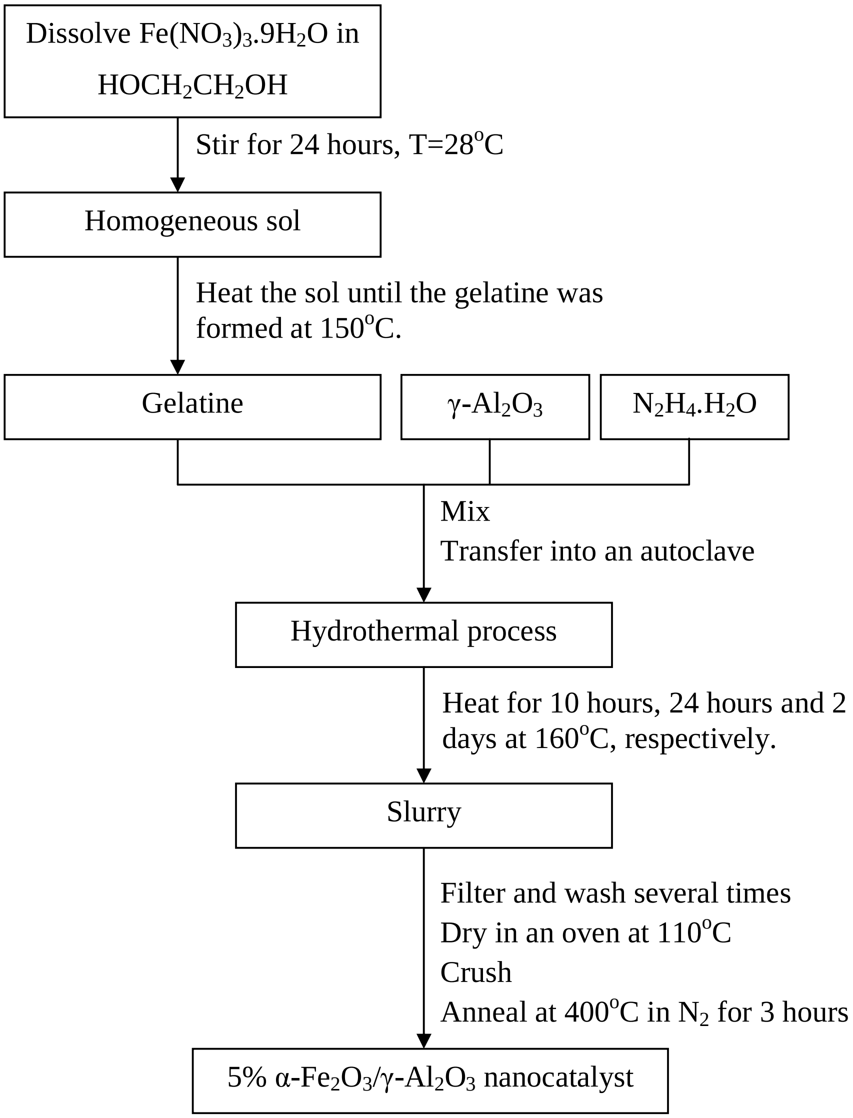

Figure 3.8: Procedures to prepare supported 5% α-Fe_2O_3/γ-Al_2O_3 nanocatalysts using sol gel-hydrothermal method at different synthesis periods

3.3.3.2 Effect of Surfactant

Iron (III) nitrate, $Fe(NO_3)_3.9H_2O$ and sodium bis(2-ethylhexyl) sulfucinnate (SBS) surfactant were weighed according to 2:1 w/w ratio. Figure 3.9 summarizes the steps in this synthesis.

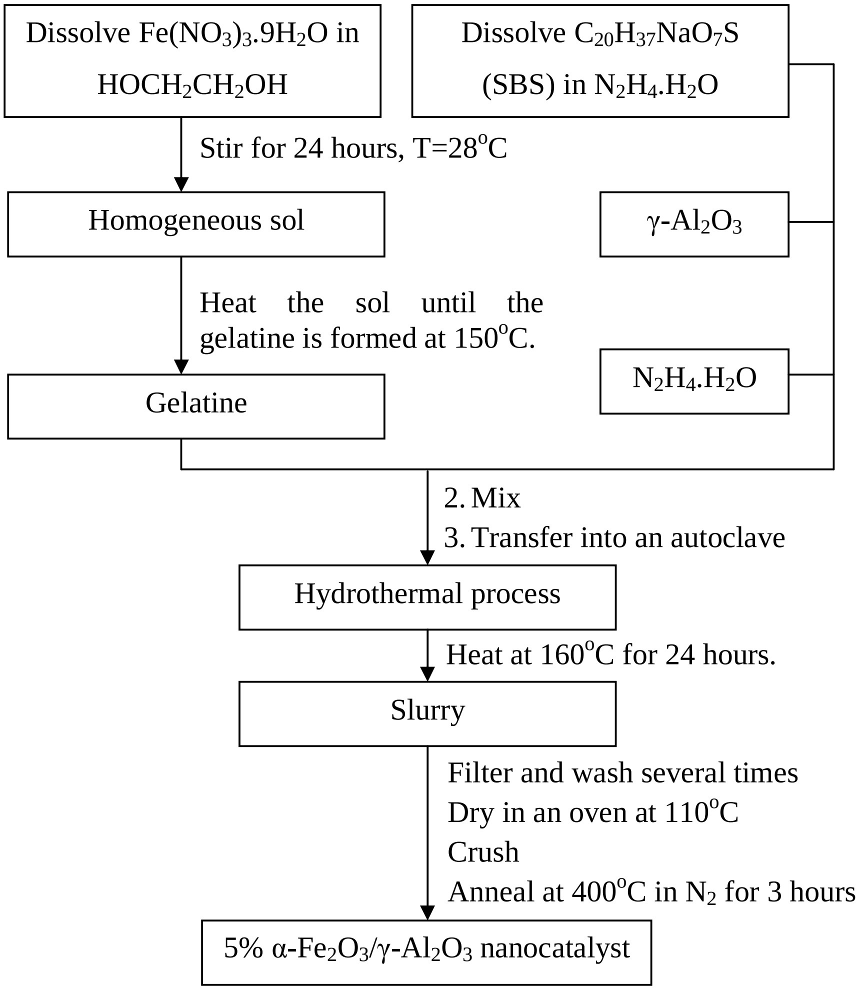

Figure 3.9: Procedures to prepare supported 5% α-Fe_2O_3/γ-Al_2O_3 nanocatalysts using sol gel-hydrothermal method at different iron (III) nitrate to SBS surfactant ($Fe(NO_3)_3$:Surf) ratios.

The precursor and surfactant were separately dissolved in 10 mL of ethylene glycol solution, $HOCH_2CH_2OH$ and 5 mL of 55% hydrazine hydrate, NH_4OH solution, respectively. Both mixtures were stirred for 24 hours. The dissolved iron (III) precursor was heated at 160°C under vigorous stirring to form the gelatine. The gelatine and the dissolved surfactant were then quickly poured into an autoclave containing 1.90 g of alumina, γ-Al_2O_3. The autoclave was tightly sealed and consequently heated in an oil bath at 160°C for 1 day. The resultant catalyst was filtered, washed and dried at 50°C in an oven. It was annealed at 400°C in nitrogen flow at 10 ccm/min for three hours. The procedures were repeated and the iron (III) nitrate to SBS surfactant, ($Fe(NO_3)_3$: Surf) ratio was then varied to 2:1 and 2:3.

3.4 Characterization of Nanocatalyst

Several analytical methods were used to obtain the physicochemical information of the prepared nanocatalysts. They include x-ray diffraction (XRD), raman spectroscopy, field emission scanning electron microscopy (FESEM), energy dispersed x-ray (EDX), temperature programmed reduction, (TPR), vibration sample magnetometer (VSM), N_2 adsorption and transmission electron microscopy (TEM).

3.4.1 X-Ray Diffraction (XRD)

X-ray powder diffraction (XRD) is one of the most versatile characterizations tools used for identifying the types of phases present in the specimen. The underlying principle of this tool is based on Brag's Law ($2d \sin \theta = n\lambda$) which describes the relation between the angle (θ) and wavelength (λ) of focussed x-ray with the distance between atomics, d-spacing (d) in the crystal. The average particle size can be measured using Scherer's equation as described by Equation 3.1, where k is the shape factor with typical value of 0.9, λ is the x-ray wavelength (Å), β is the line broadening at half the maximum intensity (FWHM) in radians, and θ is the Bragg angle [63], [104].

$$d = \frac{k\lambda}{\beta\cos\theta} \tag{3.1}$$

XRD measurements were conducted using a Bruker A&S D8 Advanced Diffractometer instrument equipped with a CuK_α radiation source, at 40 kV and 30 mA. The scanning angle (2θ) used was in the range of range of 2–80° at scanning speed and step size of 1.2°/min and 0.02^o/min, respectively. By using Bruker Eva software, the resultant spectra were compared with the standard library to confirm the phase of tested specimen. Information such as Bragg angle (2θ), full width half maximum (FWHM), d-spacing and lattice parameter were also determined using this software.

3.4.2 Raman Spectroscopy

Raman spectroscopy is used to study the internal structure of the molecules. It also provides useful information on molecular patterns, spacing and bonding. The working principle is based on the inelastic scattering of the molecules. This phenomenon is called Raman Effect [63].

The Raman spectroscopy analysis was carried out using Horiba Jobin HR800 Raman Spectroscope instrument. The calibration was initially made by targeting the ultraviolet (UV) ray to a blank sample slide placed on the microscope platform. Then, a small amount of catalyst sample was spread on the sample slide. Sample was illuminated by a 20mW He-Ne lesser at 514 nm wavelength. The lenses were adjusted for zooming on the targeted area and the scanning range was set from 100 cm^{-1} to 1800 cm^{-1}.

3.4.3 Field Emission Scanning Electron Microscopy (FESEM)

FESEM is a microscopy tool which provides information on the topography, morphology, and elemental composition of sample. Figure 3.10 shows the schematic diagram of FESEM.

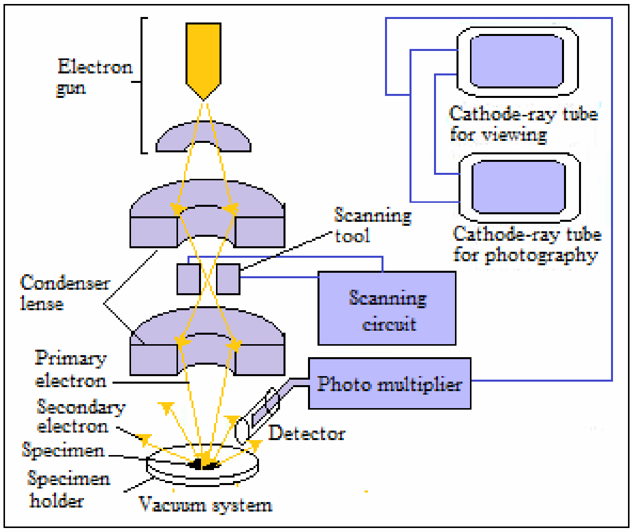

Figure 3.10: Schematic illustration on working principle of FESEM.

Electrons are produced by heating the tungsten filament. The resultant electrons are attracted to anode which accelerates their movements. The electrons are then converted to a monochromatic beam by focusing them directly to the magnetic lenses in the column and the apertures filtered out scattered electrons. Depending on the types of electrons scope, this beam will target the specimen and consequently produces signals which include secondary, backscattered, auger electrons as well as x-ray. These signals are detected and represented as an image by a photo multiplier.

The FESEM model Zeiss Supra 55/55 VP, was used for characterizing nanocatalysts. It was operated at 0.1kV to 30kV and magnification of 20X to 900KX. Small amount of sample was spread on a carbon tape pasted on a sample holder. The chamber was vacuumed using a vacuum pump operated at pressure of 2Pa to 133Pa.

3.4.4 Energy Dispersed X-ray (EDX)

Energy Dispersed X-Ray (EDX) is linked to the FESEM. It identifies type of atoms present within the sample and quantifies its composition. This information is presented as a spectrum.

3.4.5 Temperature Programmed Reduction (TPR)

Temperature Programmed Reduction (TPR) was used to estimate the temperatures required to reduce a metal oxide to a metallic state. Additional information that can also be evaluated from the TPR profiles is metal-support interaction, number of active sites and dispersion [9]. The typical reducing agents employed are hydrogen, H_2 and carbon monoxide, CO gases [9], [73].

TPR studies were conducted using a Thermo Finnigan TPDRO 1100 instrument equipped with a TCD detector. The process consists of two stages namely a pre-treatment step and the analysis step. About 0.12 g of catalyst was weighed and placed in between two layers of glass wool in the quartz sample cell. The quartz cell was then placed in the holder of the electrical furnace. The catalyst was pre-treated in a stream of nitrogen, N_2 at a flow rate of 20 cc/min and heating rate of 40^{o}C/min. The temperature was set to 200^{o}C and held at 200^{o}C for 10 minutes. The sample was analyzed in a stream of 5% H_2-N_2 gas at heating rate of 10 ^{o}C /min. TPR profiles were obtained from room temperature until 800^{o}C. The sample was held at 800^{o}C for 10 min. This analysis gas passed through a thermal conductivity detector (TCD) which detected the change in hydrogen concentration in the gas stream. Distinct reducible species in the catalyst were shown as peaks in the TPR spectra.

3.4.6 Vibration Sample Magnetometer (VSM)

VSM examines the magnetic behavior of samples particularly for magnetic materials. The working principle is based on recording the magnetization behavior of vibrating sample in a uniform magnetic field. The measurement can be performed as a function of temperature and magnetic field strength. Figure 3.11 reveals the schematic diagram of VSM [105].

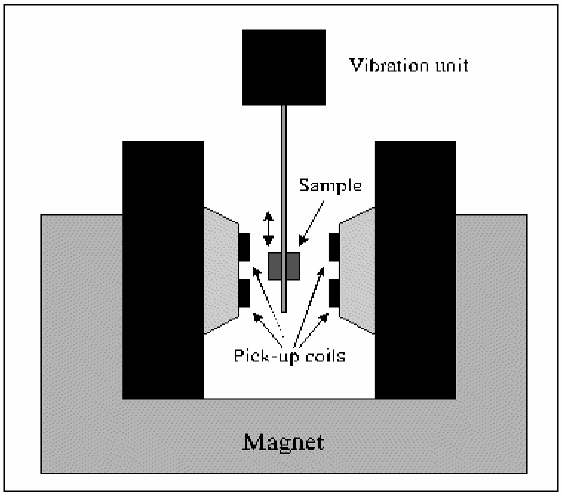

Figure 3.11: Vibration Sample Magnetometer [105].

The nanocatalysts were characterized using the VSM model DMS 8810. The sample was weighed and placed into a sample holder of 3 mm I.D. A rod was inserted into the sample holder and then attached to a vibration exciter. Water-cooled electromagnet and power supply were turned on, generating a constant magnetic field to magnetize the sample. The magnetic field strength was set to -15k to 15k Oe. The sample holder was moved up and down by the vibration exciter at a set frequency of usually 85 Hz to ensure that the sample was entirely magnetized. The magnetization values were then recorded.

3.4.7 N_2 Adsorption

The surface area, pore volume, average pore size and pore size distribution of the nanocatalysts was determined using N_2 adsorption method. This method is based on multipoint nitrogen adsorption-desorption principle. Generally, a sample contained in an evacuated sample tube is cooled to cryogenic temperature (-196°C) and exposed to analysis gas at a series of precisely controlled pressures. The number of gas molecules adsorbed on the surface increases with each incremental pressure. The pressure at which adsorption equilibrium occurs is measured and the universal gas law is applied to determine the quantity of gas adsorbed. The N_2 adsorption experiments were performed on a Micromeritics ASAP 2020 instrument.

A blank sample tube was weighed and subsequently loaded with 0.3 gram of nanocatalyst. The sample was degassed at 130°C overnight to remove impurities and moisture. The cold trap dewar that was filled with liquid nitrogen was installed to trap impurities in the manifold. After degassing, the sample was cooled to ambient temperature and the tube was removed from the degassing port. Since the sample was under vacuum, the tube was backfilled with nitrogen gas before it can be removed safely. The sample tube was reweighed to determine the actual sample mass which was keyed into the software. Subsequently, it was placed into the analysis port. The sample cell was immersed in liquid nitrogen in a dewar flask on an elevator. The sample information was then fed into the software to start the analysis. The nitrogen adsorption-desorption measurements were conducted for 56 points.

The surface area was calculated using the Brunauer-Emmett-Teller (BET) method, while the pore size distribution was determined from the desorption branch of the adsorption isotherm by the Barrett-Joyner-Halenda (BJH) method.

3.5 Procedure for Catalytic Evaluation

Typically, 0.2 g of powdered catalyst sample was placed on the glass wool and packed in the reactor tube. Thermocouple was attached to the reactor tube and the packed reactor tube was placed in the middle of the north and south poles of magnets. Heater, thermocouple and temperature indicator wire were then correctly positioned. The system was purged with 10 cm^3/min of purified nitrogen gas for about 20 minutes. Reduction process was performed by flowing 30 cm^3/min of purified hydrogen at 200^oC for four hours. After the reduction process was completed, the controller was set to the desired reaction temperatures. The reactant gas comprised a mixture of nitrogen and hydrogen, was fed into the reactor at total flow rates of 40 cm^3/min and H_2:N_2 ratio of 3:1. Typical reaction duration was four hours. A tube made from polyvinyl chrolide (PVC) was connected to the exhaust of microreactor. Its end was then dipped into 0.001 M hydrochloric acid, HCl, enabling the outlet gas to be bubbled. Ammonia was quantified by titrating 0.001 M hydrochloric acid, HCl, containing the bubled ammonia, NH_3 with 0.001 M sodium hydroxide, NaOH solution.

The procedures were repeated for examining the effects of various synthesis temperatures (30^oC, 70^oC, 110^oC, 150^oC and 190^oC), total feed gas flow rates (28 cm^3/min, 40 cm^3/min and 100 cm^3/min), H_2:N_2 (1:3, 3:1 and 5:1) ratios and magnetic field strength on the ammonia yield. Figure 3.12 shows the schematic diagram of microreactor system.

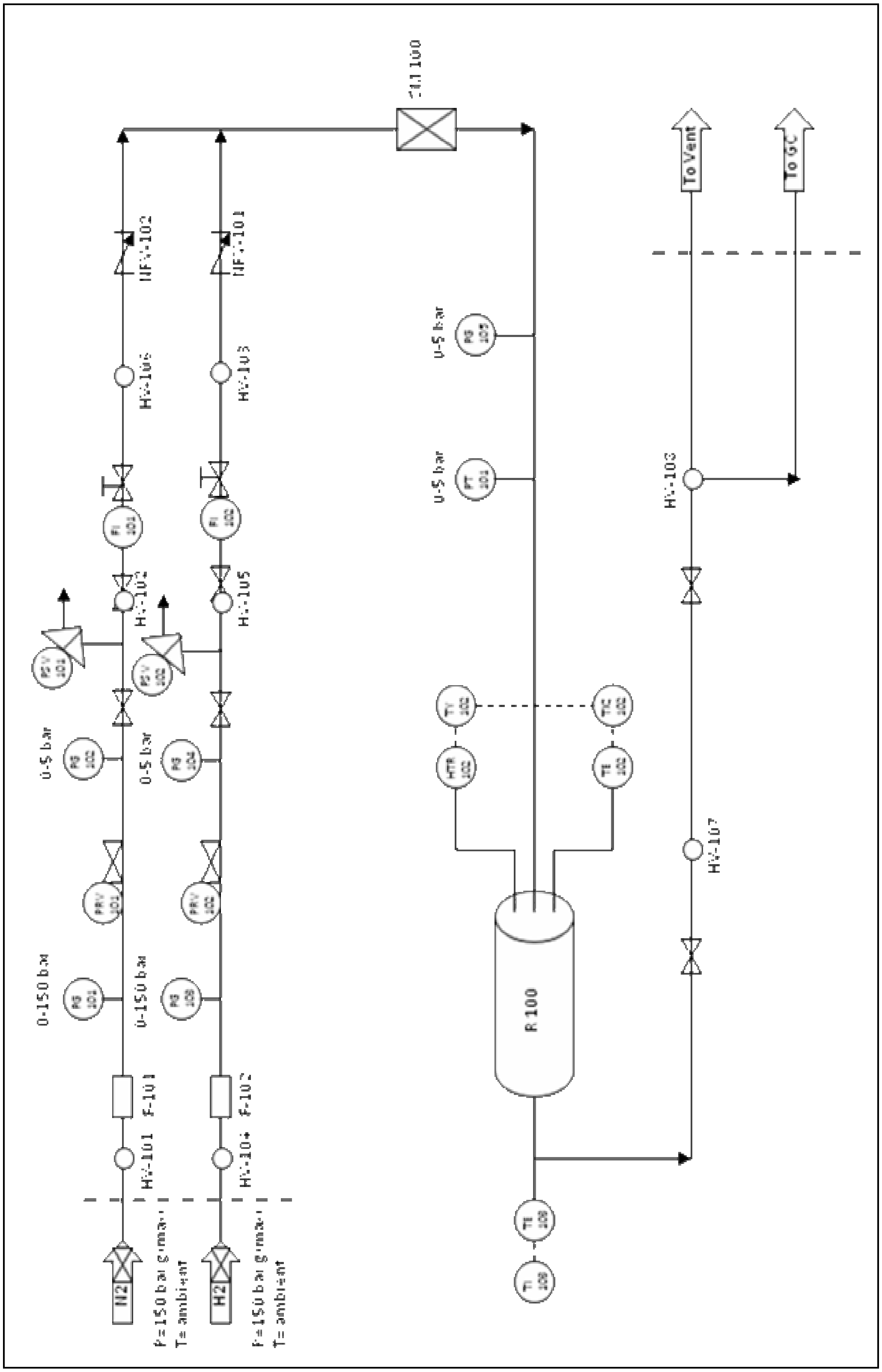

Figure 3.12: Schematic diagram of microreactor system

CHAPTER 4

RESULTS AND DISCUSSION

4.1 Characterization of Nanocatalyst

The prepared nanocatalysts were characterized using XRD, Raman, FESEM, H_2-TPR, VSM, N_2 adsorption and TEM.

4.1.1 Unsupported Hematite (α-Fe_2O_3) Nanocatalyst

4.1.1.1 Effect of Preparation Methods

This study aimed to select the best synthesis method which can produce a well-crystallined nanocatalyst at desired particle size of 20 nm to 30 nm. The sol-gel, self-combustion, and self-assembly methods were tested. The resultant nanocatalysts were annealed in air at 700^oC for 3 hours.

XRD analysis was performed to determine the phase of the prepared α-Fe_2O_3 nanocatalysts and the XRD spectra are shown in Figure 4.1. All diffracted peaks are for hematite (α-Fe_2O_3) phase as these peaks matched with those in the standard card (SS-NNNN 89-0599) and the values reported in literature [20], [40]. This can be further confirmed by the existence of (104) major peak, which is typically diffracted at 2θ approximately 33.0-34.0^o (Figure 4.1) [20], [40].

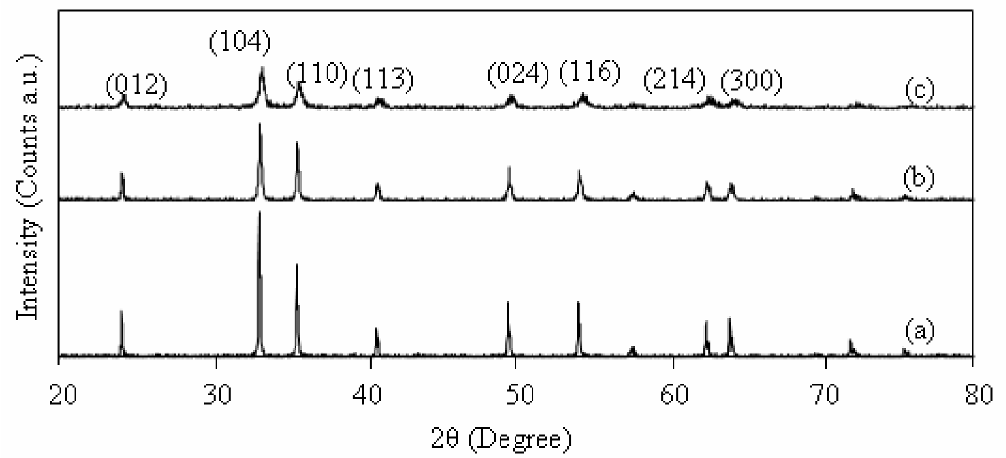

Figure 4.1: XRD spectra of α-Fe_2O_3 nanocatalysts prepared via (a) sol-gel (b) self-combustion and (c) self-assembly methods annealed at 700^oC.

The XRD data (Table 4.1) were interpreted using the Bruker Eva software. All the α-Fe_2O_3 nanocatalysts have rhombohedral structure with hexagonal close packed (hcp) crystal lattice, as confirmed by the lattice constants, where a=b≠c (Table 4.1), symbolizing hexagonal unit cell [10], [20], [40]. The XRD data are summarized in Table 4.1.

Table 4.1: XRD data of α-Fe_2O_3 nanocatalysts prepared via different methods annealed at 700^oC. The interpretation was based on (104) major plane.

Method		Sol-Gel	Self-Combustion	Self-Assembly	Literature
2θ (Degree)		33.17	33.22	33.3	33.2 [40]
Intensity (a.u)		240.00	130.00	60.80	-
D-spacing (Å)		2.698	2.694	2.682	2.690 [20]
FWHM		0.139	0.152	0.302	-
Lattice Constant (Å)	a	5.032	5.028	5.028	5.034 [20]
	b	5.032	5.028	5.028	5.035 [20]
	c	13.733	13.733	13.733	13.752 [20]
Average crystallite Size (nm)		60.67	55.50	27.90	-

All values in Table 4.1 are based on the (104) major plane. The average crystallite size was calculated using Scherer's equation (Equation 3.1) and the calculations are described in Appendix D. The highest peak intensity was achieved by the α-Fe_2O_3 nanocatalyst prepared via the sol-gel method. The sol-gel method resulted in bigger particles and larger d-spacing (Table 4.1) compared to those of other methods. The particle size of α-Fe_2O_3 prepared via sol-gel method (Table 4.1) is also smaller than the one obtained through hydrothermal method, as reported in literature [54]. The Raman spectra of α-Fe_2O_3 nanocatalysts prepared via different methods are displayed in Figure 4.2.

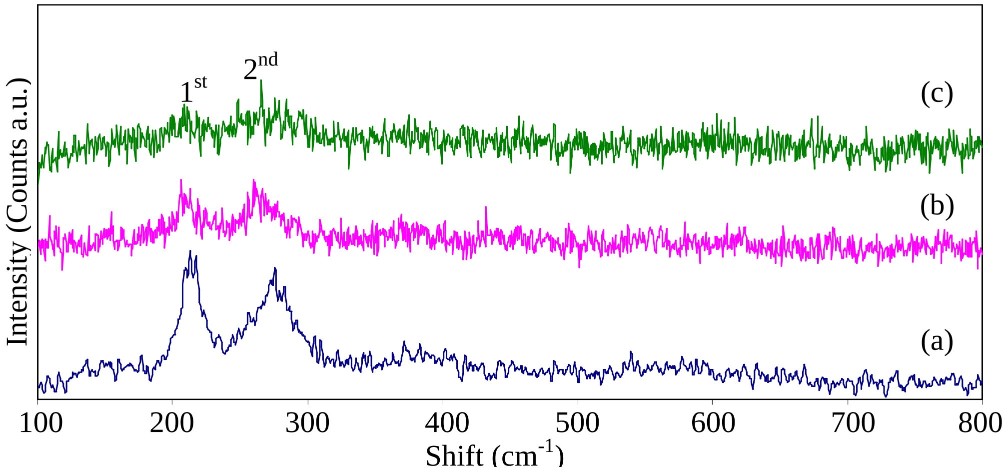

Figure 4.2: Raman spectra of α-Fe_2O_3 nanocatalysts prepared via (a) sol-gel (b) self-combustion and (c) self-assembly methods annealed at 700°C.

The spectra show two separated peaks which are positioned in the range of 200-300 cm^{-1} (Figure 4.2). These values are consistent with the shifts for α-Fe_2O_3 phase as reported in literature [106]-[107]. The data of Raman analysis are summarized in Table 4.2.

Table 4.2: Raman data of α-Fe_2O_3 nanocatalysts prepared via different methods annealed at 700°C.

Method		Sol-Gel	Self-Combustion	Self-Assembly	Literature
1st Peak	Shift (cm^{-1})	213.91	210.87	214.93	200-230 [65], [106]
	Intensity (Counts a.u)	38.29	7.94	5.74	-
2nd Peak	Shift (cm^{-1})	277.69	277.69	280.49	270-300 [65], [106]
	Intensity (Counts a.u)	22.51	6.59	5.79	-
Ratio I_{1st} / I_{2nd}		1.70	1.20	0.99	-

According to the literatures [65], [106], the peaks at 225-230 cm^{-1} and 290-300 cm^{-1} are attributed to A_{1g} Fe-O symmetry stretching and E_{1g} Fe-O symmetry bending, respectively. The α-Fe_2O_3 phase has the point symmetry group of D^6_{3d}. Highest ratio of peak intensity (I_{1st}/I_{2nd}) was displayed by α-Fe_2O_3 nanocatalyst synthesized through the sol-gel method, demonstrating that well-crystallized phase has been formed (Figure 4.2). The Raman spectrum for the sample synthesized via self-assembly revealed noisy pattern (Figure 4.2) which might due to poor crystallinity, which was also shown by XRD analysis (Figure 4.1).

The effects of different synthesis methods on the surface morphology of α-Fe_2O_3 nanocatalysts were examined by FESEM and the images are illustrated in Figure 4.3. The α-Fe_2O_3 nanocatalyst synthesized via self-assembly method exhibited spherical-shape of agglomerated particles. The average grain size was about 24 – 36 nm (Figure 4.3 (a)). Hexagonal-shape particles with average grain size around 70 – 250 nm can be seen for the sample obtained via self-combustion method (Figure 4.3 (b)). The sol-gel method resulted in α-Fe_2O_3 nanocatalyst with average grain size of 160 nm.

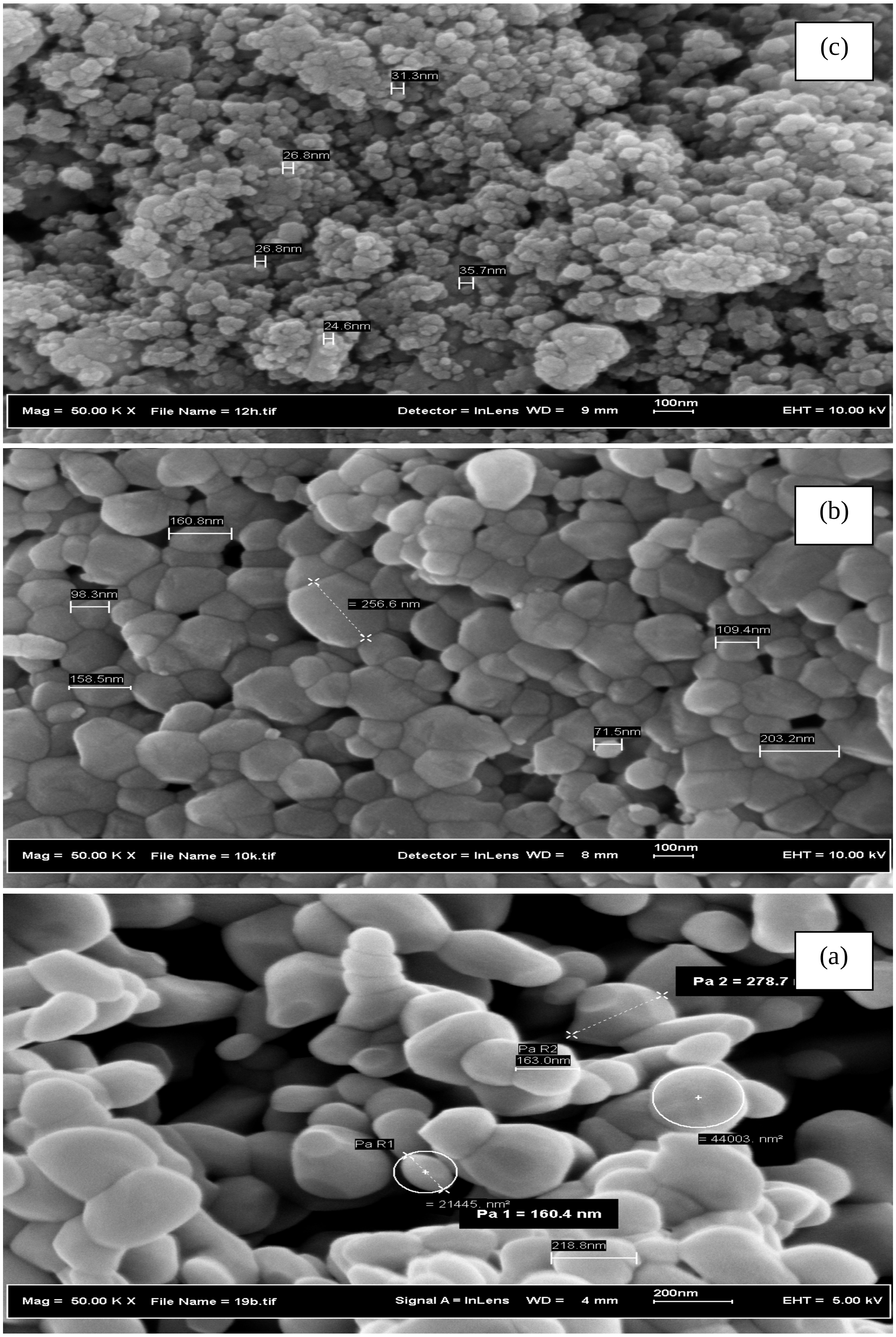

Figure 4.3: FESEM images α-Fe_2O_3 nanocatalysts prepared via (a) sol-gel (b) self-combustion and (c) self-assembly methods annealed at 700^oC.

In order to determine the elemental constituents within the synthesized α-Fe_2O_3 nanocatalysts, EDX analysis was carried out and the resultant spectra are illustrated in Figure 4.4.

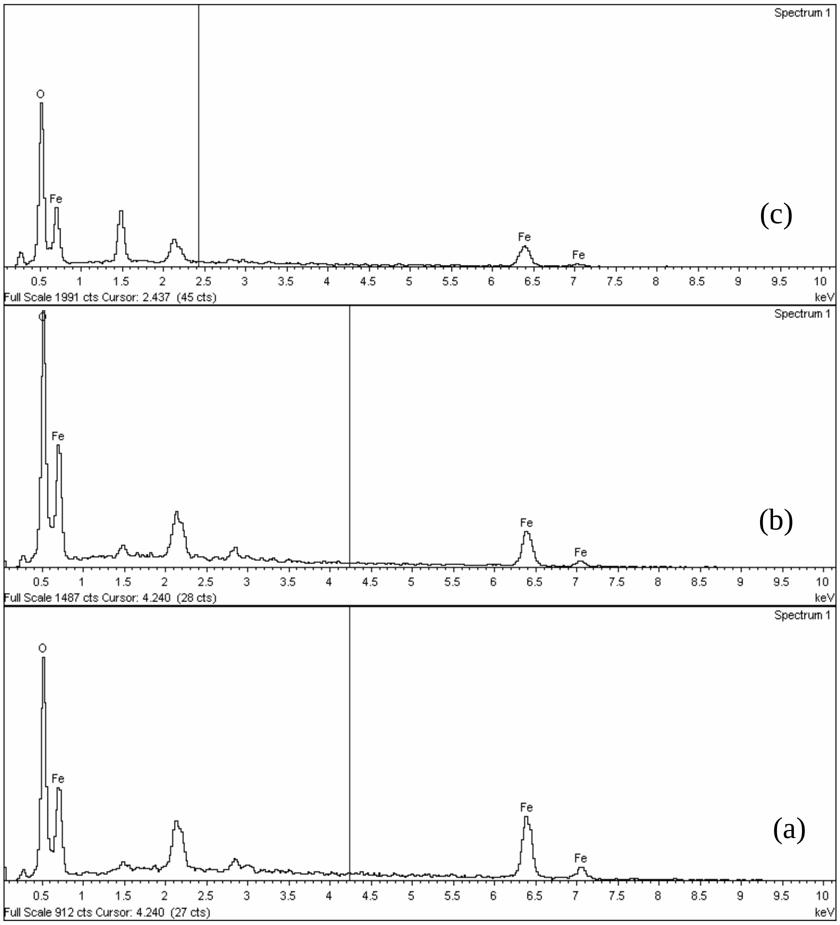

Figure 4.4: EDX spectra of α-Fe_2O_3 nanocatalysts prepared via (a) sol-gel (b) self-combustion and (c) self-assembly methods annealed at 700°C.

Iron (Fe) and (O) were detected in all catalysts. The unlabelled peaks are assigned to coating material that was used to coat the specimens during characterization (Figure 4.4). The EDX data are tabulated in Table 4.3. The calculations are shown in Appendix F.

Table 4.3: EDX data of α-Fe_2O_3 nanocatalysts prepared via different methods annealed at 700^{o}C.

Method			Sol-Gel	Self-Combustion	Self-Assembly
Atomic %	Fe	Exp.	37.90	33.77	28.12
		Dev.	5.25	16.58	29.70
	O	Exp.	56.50	58.24	55.08
		Dev.	5.83	2.93	8.20
Weight %	Fe	Exp.	64.90	50.56	48.96
		Dev.	7.26	27.70	29.97
	O	Exp.	28.0	24.94	27.53
		Dev.	6.82	17.00	8.38

The calculated theoretical atomic percentages for Fe and O are 40% and 60%, respectively. As shown in Table 4.3, nanocatalyst synthesized by sol-gel showed the highest Fe elemental composition compared to those of the other two methods. The percentage deviations were also less than 10% which suggest that the hexagonal lattice sites have been entirely occupied by Fe and O atoms. Meanwhile, the samples processed through self-combustion and self-assembly exhibited incomplete atoms occupation as indicated by large deviation of Fe atomic composition (Table 4.3). Therefore, these α-Fe_2O_3 nanocatalysts have to be annealed at much high temperature to improve their crsytallinity.

The reducibility of α-Fe_2O_3 nanocatalysts was studied using H_2-TPR. Figure 4.5 reveals the H_2-TPR profiles for Fe_2O_3 nanocatalysts prepared by different methods.

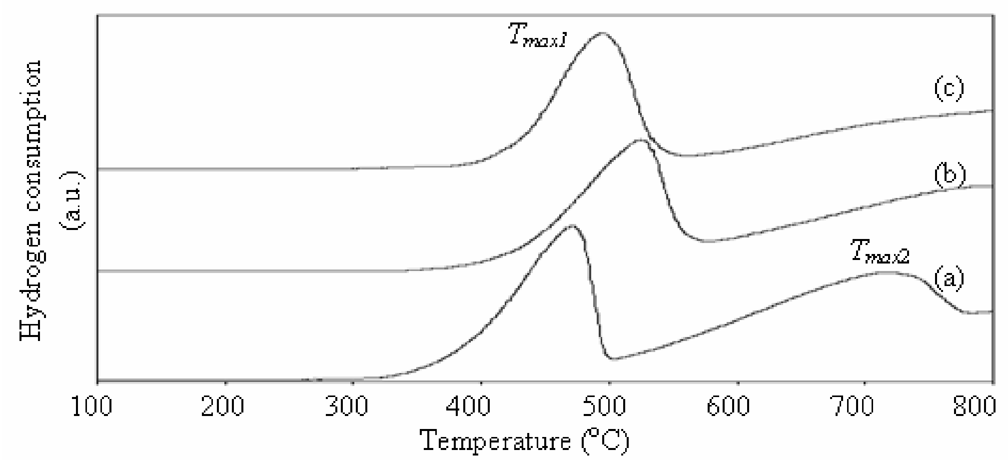

Figure 4.5: H_2-TPR profiles of α-Fe_2O_3 nanocatalysts prepared via (a) sol-gel (b) self-combustion and (c) self-assembly methods annealed at 700^{o}C.

The first peak, T_{max1} which is located in temperature range of 470–530°C, is for the reduction of α-Fe_2O_3 to Fe_3O_4. Transformation of Fe_3O_4 to α-Fe occurred at the peak, T_{max2}, at temperature of 700-800°C (Figure 4.5). Similar observation was reported in literature [22], [75]-[76]. Table 4.4 summarizes the H_2-TPR data for α-Fe_2O_3 nanocatalysts prepared by different methods.

Table 4.4: H_2-TPR profiles of α-Fe_2O_3 nanocatalysts prepared via different methods annealed at 700°C.

	Method		Sol-Gel	Self-Combustion	Self-Assembly	Literature
TPR	Path A (T_{max1}) (°C)	$Fe_2O_3 \rightarrow Fe_3O_4$	472	525	495	500-530 [80]
	Path B (T_{max2}) (°C)	$Fe_2O_3 \rightarrow Fe$	715	784	807	880-900 [80]

The reduction temperatures for all nanocatalysts were slightly lower than the results obtained by R. Brown and co-workers (Table 4.4) [80]. Difference in particle size and the use of higher flow rate (20 ccm/min) compared to literature (10 ccm/min) [80] might be the reason for this decrement even though the heating rate used in this experiment (10°C/min) was the same as that in literature [80].

Different methods yielded different particle sizes (Table 4.1) which influenced the reducibility behavior (Table 4.4). Second-stage reduction (Path B) for nanocatalyst synthesized by sol-gel method occurred at slightly lower temperature (Table 4.4) than those of nanocatalysts prepared by the other two methods (Table 4.4). An increase in temperature for the second stage reduction, T_{max2} (Table 4.4) might be due to the enrichment of $Fe_{1-x}O$ phase as well as enhancement in its stability. As described in Section 2.6, $Fe_{1-x}O$ is thermodynamically stable above 570°C [22]. The presence of $Fe_{1-x}O$ stable phase caused the second reduction stage (Path B) for all nanocatalysts to be accomplished at temperature above 700°C (Table 4.4). The reduction for all α-Fe_2O_3 nanocatalysts in this work was suggested in the following sequence: $Fe_2O_3 \rightarrow Fe_3O_4 \rightarrow Fe_{1-x}O \rightarrow Fe$ [22], [73]. Figure 4.6 shows the hydrogen consumption for reducing the nanocatalysts.

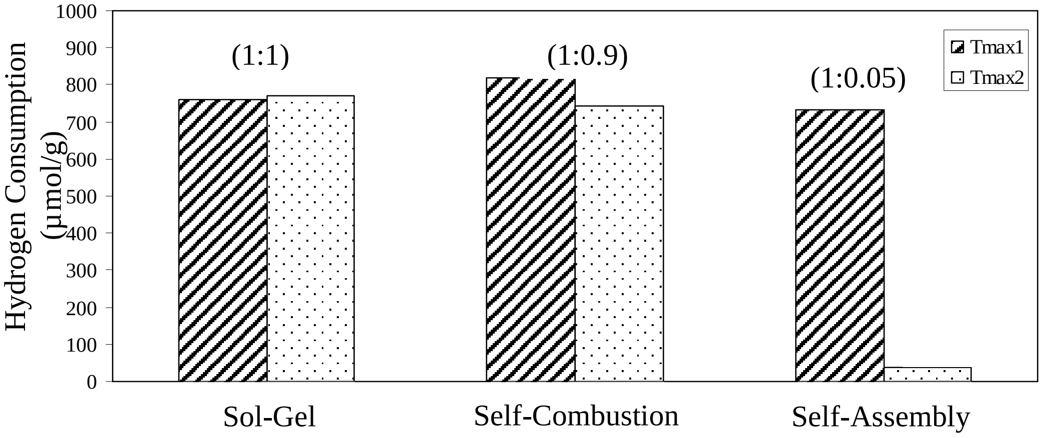

Figure 4.6: Hydrogen consumption to reduce of α-Fe_2O_3 nanocatalysts prepared via different methods annealed at 700°C.

Transformation of $Fe_2O_3 \rightarrow Fe_3O_4 \rightarrow$ α-Fe typically consumed hydrogen at T_{max1}/T_{max2} ratio of 1:8 for reduction to be entirely completed [76]. However in this study, the consumption ratios are approximately 1:1, 1:0.9, 1:0.05 for sol gel, self combustion and self assembly methods, respectively (Figure 4.6), indicating incomplete reduction process. This may due to the temperature range exerted is insufficient to overcome the higher activation energy of reduction involving smaller particles.

Based on results of XRD, FESEM and H_2-TPR, the sol gel was chosen as the best synthesis method amongst the methods tested for this work. This method successfully produced well-crystallized, larger size and irregular shape of particles which were easily reducible. Samples synthesized via the sol-gel method have been used for further investigations.

4.1.1.2 Effect of Periods of Stirring

This part focused on how to vary the size of nanocatalyst particles. The targeted size of nanoparticles is 20-30 nm. It is expected that an increase in stirring duration of the sol can produce smaller particles using the sol gel method. The period of stirring was prolonged to 1 day, 1 week and 1 month, respectively. The resultant nanocatalysts were annealed in air at 300°C for three hours.

The phase of the α-Fe_2O_3 nanocatalysts was identified by XRD and the recorded spectra are displayed in Figure 4.7.

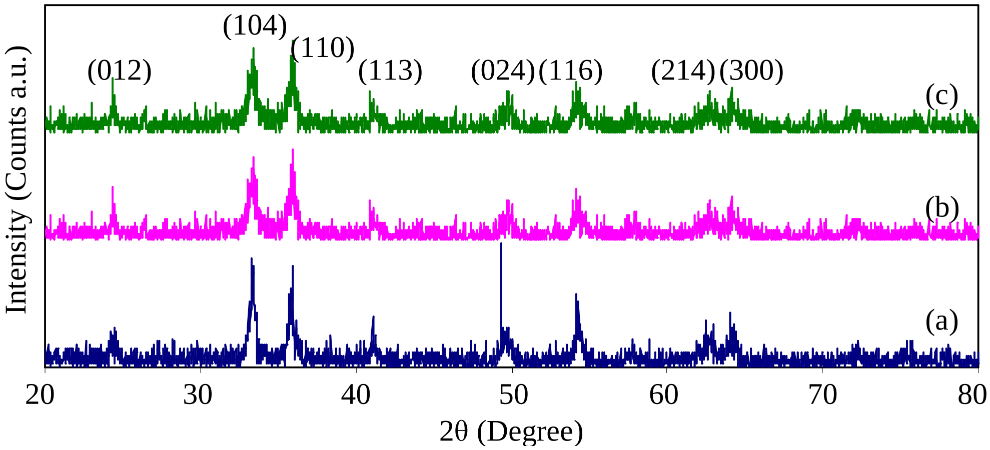

Figure 4.7: XRD spectra of α-Fe_2O_3 nanocatalysts prepared via sol-gel method stirred for (a) 1 day (b) week (c) 1 month, annealed at 300°C.

The diffraction peak at about 2θ of 33.405° was assigned to (104) major plane for hematite, α-Fe_2O_3 (Figure 4.7) as it matched with the standard card (SS-NNNN 89-0599) and reported values [40]-[41], [54]. In addition, the absence of other diffraction peaks for ferrite nitrite or other iron oxides, such as Fe_3O_4 and γ-Fe_2O_3 confirmed that the resultant particles were purely hematite (α-Fe_2O_3). Table 4.5 reviews the XRD data analysis of prepared nanocatalysts obtained at various stirring periods.

Table 4.5: XRD data of α-Fe_2O_3 nanocatalysts prepared via sol-gel method at different periods of stirring, annealed at 300°C. The interpretation was based on (104) major plane.

Method		1 day	1 week	1 month	Literature
2θ (Degree)		33.44	33.46	33.47	33.2 [40]
Intensity (a.u)		63.40	43.50	29.10	-
D-spacing (Å)		2.699	2.681	2.701	2.690 [20]
FWHM		0.329	0.364	0.448	-
Lattice constant (Å)	a	5.032	5.035	5.028	5.034 [20]
	b	5.032	5.035	5.028	5.034 [20]
	c	13.733	13.748	13.730	13.752 [20]
Average crystallite size(nm)		25.60	23.20	18.80	-

The data (Table 4.5) were obtained using Bruker Eva software which was based on (104) major plane. The crystallite size was calculated using Scherer's Equation (Equation 3.1, Section 3.4.1). Period of stirring influenced the particle size of resultant nanocatalyst (Table 4.5). Prolonging stirring period from 1 day to 1 month reduced the average crystallite size by 26.65%. Furthermore, the distance between atomic planes (D-spacing) increased with increasing stirring period (Table 4.5). Stirring process is essential to promote the formation of homogeneous sol and achieve “supersaturation” point. Prolonging the stirring period enriched the nucleation points and caused nucleation process to occur more rapidly. Consequently, smaller particles were attained (Table 4.5) [63]-[65].

The structure of α-Fe_2O_3 nanocatalysts prepared via sol-gel method was examined by Raman spectroscopy and the recorded spectra are displayed in Figure 4.8.

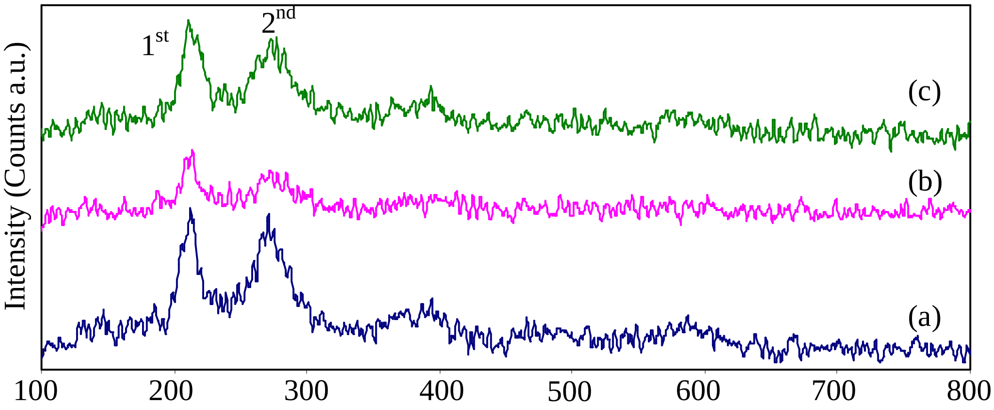

Figure 4.8: Raman spectra of α-Fe_2O_3 nanocatalysts prepared via sol-gel method at stirring periods of (a) 1 day (b) 1 week and (c) 1 month, annealed at 300^oC.

The spectra show two strong Raman bands located at 200 – 300 cm^{-1}. These bands show α-Fe_2O_3 characteristic and matched with literature data [106]-[107]. The data for these spectra are tabulated in Table 4.6.

Table 4.6: Raman data of α-Fe_2O_3 nanocatalysts prepared via sol-gel method at different stirring periods, annealed at 300^oC.

Temperature (^oC)		1 day	1 weak	1 month	Literature
1^{st} Peak	Shift (cm^{-1})	212.89	213.90	211.37	200-230 [65], [106]
	Intensity (Counts a.u)	9.58	5.02	7.61	-
2^{nd} Peak	Shift (cm^{-1})	271.62	272.63	273.64	200-300 [65], [106]
	Intensity (Counts a.u)	9.17	3.68	6.55	-
I_{1st}/I_{2nd}		1.04	1.16	1.36	-

Intensity of the Raman peak decreased with increasing stirring period (Table 4.6). Sample stirred at 1 day revealed the highest intensity of Raman peaks, indicating a well crystallized structure. However, 1 month stirring resulted in poorly crystallized sample as the Raman peaks were not too intense. This analysis was substantiated by the interpretation of XRD results (Figure 4.7, Table 4.5).

The surface morphology of resultant α-Fe_2O_3 nanoparticles was examined using FESEM and the images are shown in Figure 4.9. Irregular-shape particles were observed for nanoparticles obtained at 1 day stirring. Meanwhile, samples stirred at 1 week and 1 month illustrated well-defined spherical shape nanoparticles (Figure 4.9).

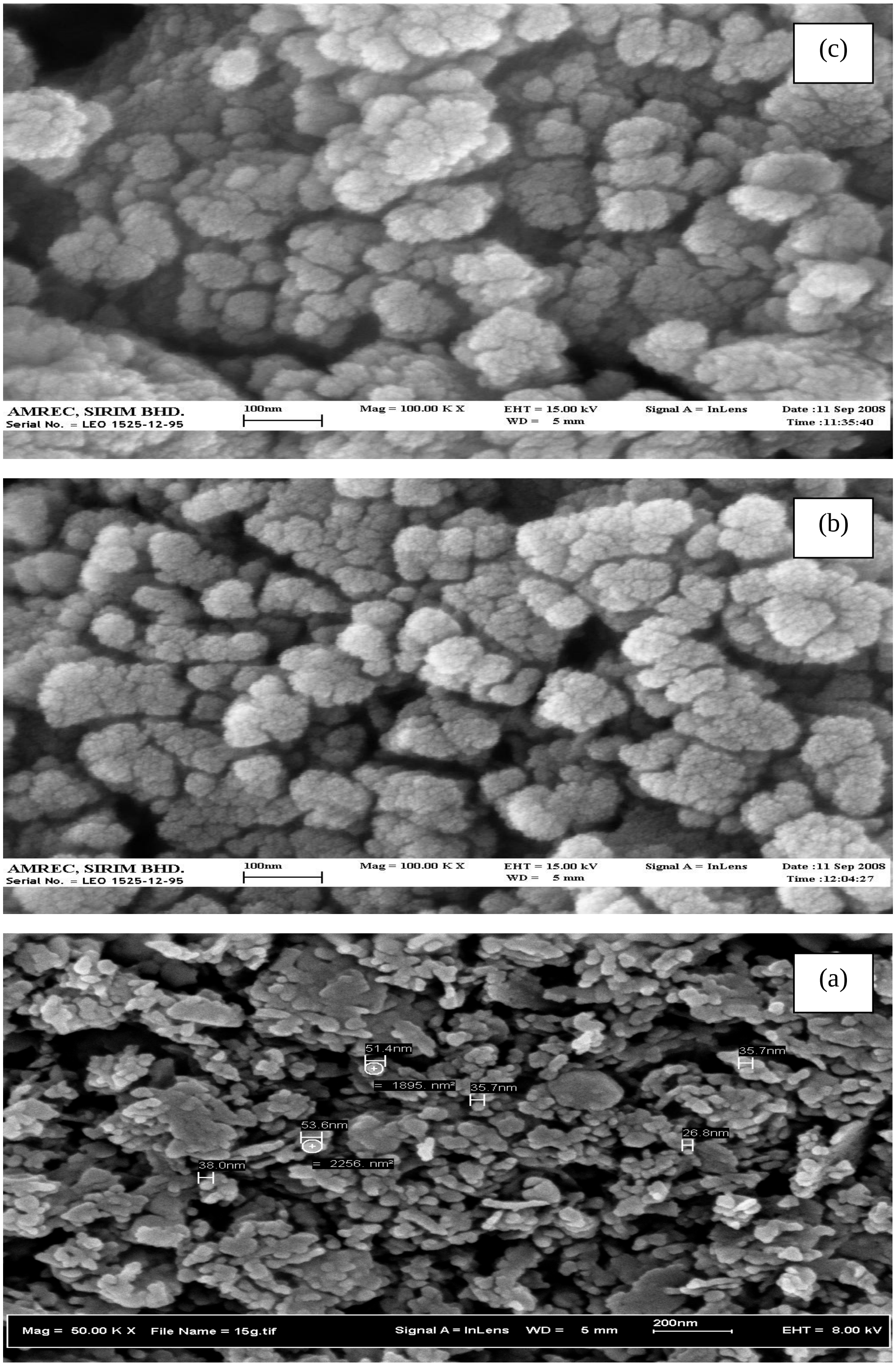

Figure 4.9: FESEM images α-Fe_2O_3 nanocatalysts prepared via sol-gel stirred at (a) 1 day (b) 1 week and (c) 1 month, annealed at 300°C.

The EDX spectra for α-Fe_2O_3 nanocatalysts prepared via sol-gel method at different stirring periods are shown in Figure 4.10.

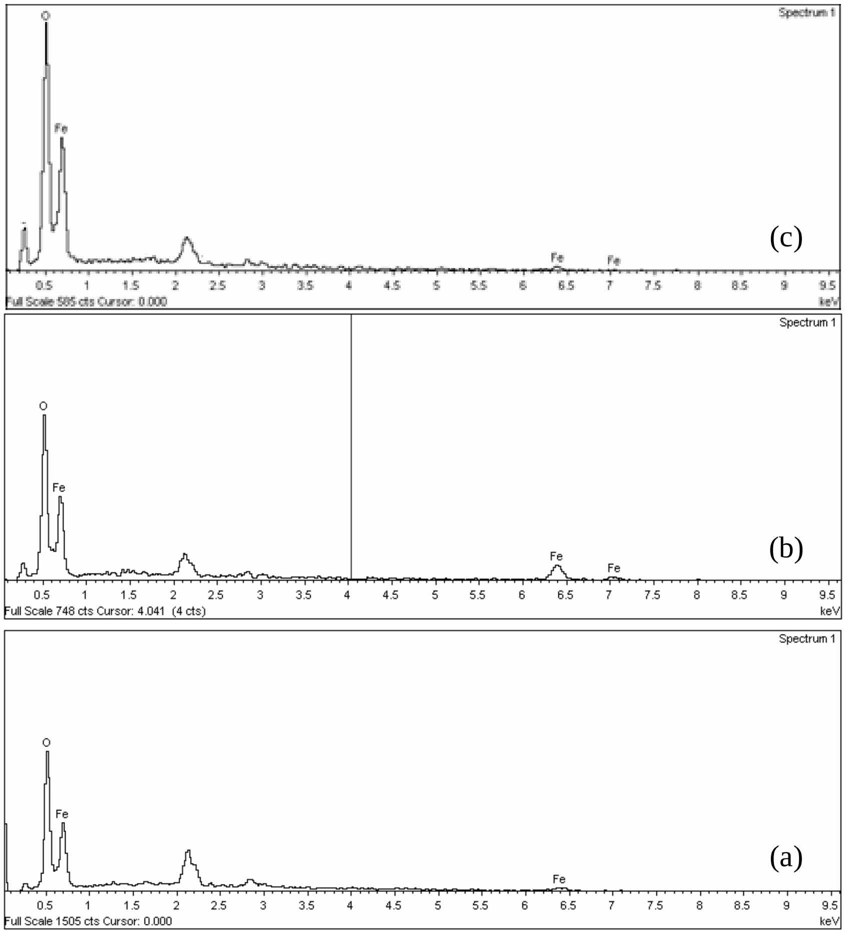

Figure 4.10: EDX spectra of α-Fe_2O_3 nanocatalysts prepared via sol-gel method at stirring periods of (a) 1 day (b) 1 week and (c) 1 month, annealed at 300^oC.

Iron and oxygen elements were detected in all nanocatalysts, confirming the presence of iron oxide, α-Fe_2O_3 as the major phase. The amount of detected elements is summarized in Table 4.7. The details of calculation are revealed in Appendix G. The theoretical atomic percentage for iron and oxygen are 40% and 60%, respectively. The 1-month stirring period resulted in nanocatalyst having 5% deviation for both elements while the ones stirred for 1 day and 1 week showed more than 10% deviation from the theoretical values (Table 4.7). This concludes that stirring period also has significant influence on the composition of resultant nanocatalysts.

Table 4.7: EDX data of α-Fe_2O_3 nanocatalysts prepared via sol-gel method at different stirring periods, annealed at 300°C.

Method			1 day	1 week	1 month
Atomic (%)	Fe	Exp.	22.56	28.84	41.74
		Dev.	77.30	38.69	-4.16
	O	Exp.	31.358	71.16	58.26
		Dev.	89.99	-15.68	2.98
Weight (%)	Fe	Exp.	54.40	58.89	71.43
		Dev.	28.67	18.86	-2.00
	O	Exp.	31.58	41.40	28.57
		Dev.	-5.00	-27.53	5.00

Figure 4.11 shows the H_2-TPR profiles for the α-Fe_2O_3 nanocatalysts synthesized at different stirring periods.

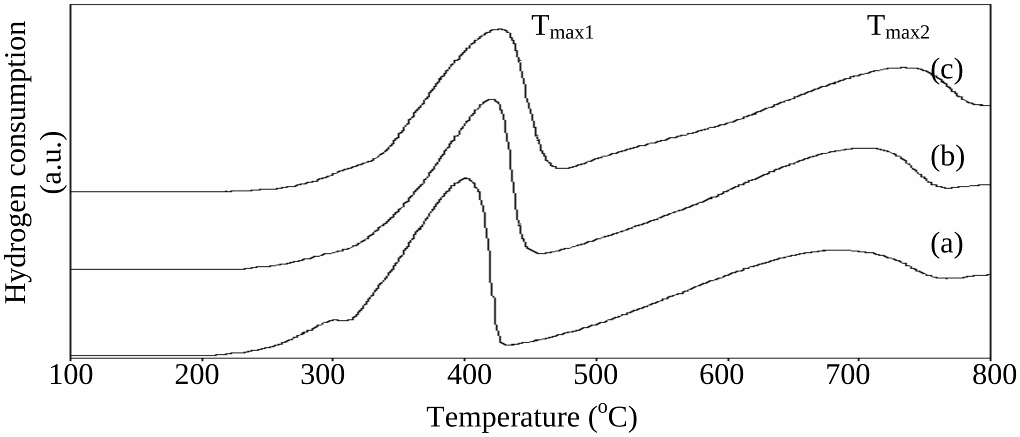

Figure 4.11: H_2-TPR profiles of α-Fe_2O_3 nanocatalysts prepared via sol gel-method at stirring periods of (a) 1 day, (b) 1 week and (c) 1 month, annealed at 300°C.

The first intense peak, T_{max1} which was situated at temperature 300°C to 500°C was assigned to reduction of α-Fe_2O_3 to Fe_3O_4. Meanwhile, the second reduction step, T_{max2}, involving transformation Fe_3O_4 to α-Fe was accomplished at much higher temperature (Figure 4.11). Both reduction temperatures are still in the range of reported values [22], [76]. Table 4.8 shows the data for the H_2-TPR spectra.

Table 4.8: H_2-TPR data of α-Fe_2O_3 nanocatalysts prepared via sol-gel method at different stirring periods, annealed at 300°C.

	Method		1 day	1 week	1 month	1 month
TPR	Path A (T_{max1})	$Fe_2O_3 \rightarrow Fe_3O_4$	400	420	426	500-530 [79]
	Path B (T_{max2})	$Fe_2O_3 \rightarrow Fe$	681	697	732	880-900 [79]

Increasing stirring period resulted in smaller particle size which was more difficult to reduce, as exhibited by the shift to higher temperature. Particles synthesized at 1 month have smaller particle size (Table 4.5), and required much higher temperatures for complete reduction compared to those stirred at 1 day and 1 week (Table 4.8). The hydrogen consumption during reduction of α-Fe_2O_3 nanocatalysts is revealed in Figure 4.12.

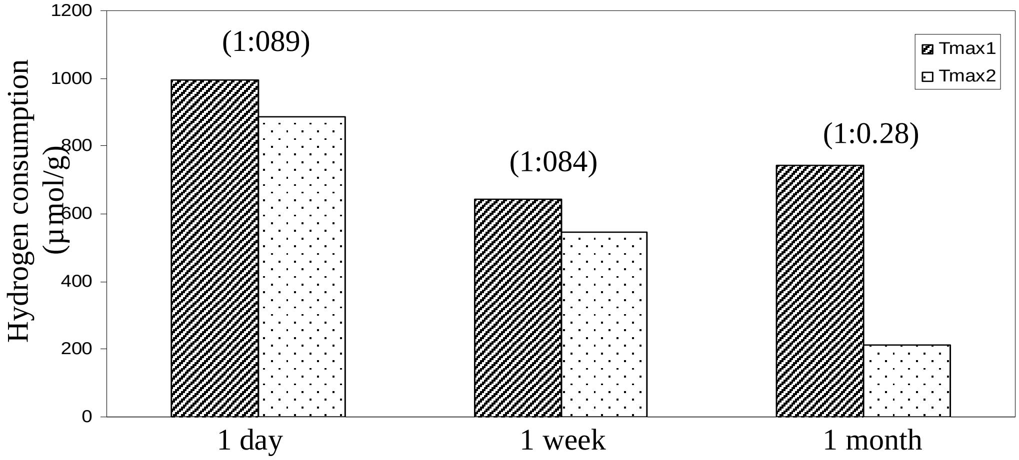

Figure 4.12: Hydrogen consumption to reduce α-Fe_2O_3 nanocatalysts prepared via sol-gel method at different stirring periods, annealed at 300°C.

The calculated hydrogen consumption ratios for T_{max1}/T_{max2} were 1:0.89, 1:0.84, and 1:0.28 for stirring period of 1 day, 1 week and 1 month, respectively (Figure 4.12). According to the literature, complete reduction of α-Fe_2O_3 to Fe is generally achieved with the hydrogen consumption ratio of 1:8 [76]. Reduction became less complete with increasing stirring period, possibly due to decrease in size of α-Fe_2O_3 nanoparticles.

4.1.1.3 Effect of Annealing Temperature

This section focused on improving the crystallinity of nanocatalyst. The nanocatalyst that was synthesized via sol gel method and stirred for 1 day was utilized. It was annealed in air at different temperatures for 3 hours. XRD spectra for the α-Fe_2O_3 nanocatalysts prepared via sol-gel method and annealed at different temperatures are shown in Figure 4.13.

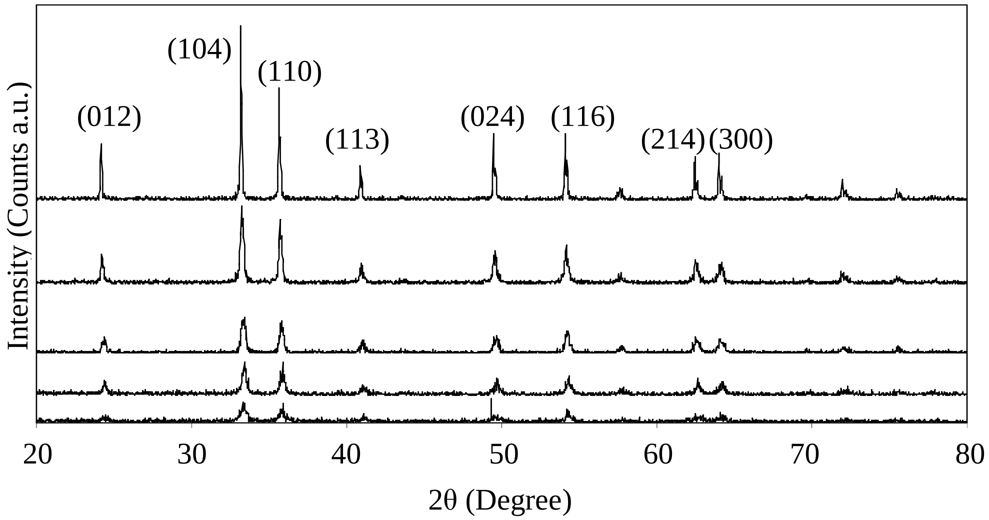

Figure 4.13: XRD spectra of α-Fe_2O_3 nanocatalysts prepared via sol-gel method stirred for 1 day, annealed at (a) 300°C, (b) 400°C, (c) 500°C, (d) 600°C and (e) 700°C.

All diffracted peaks matched with the data for standard card of SS-NNNN 89-0599, confirming the presence of hematite, α-Fe_2O_3 as the major phase. The emergence of (104) plane as a major peak which was recorded at 2θ of 33.24° (Figure 4.13) further confirmed the characteristic of α-Fe_2O_3 phase [40], [52], [54]. The intensity of diffracted peaks increased with increasing annealing temperature from 300°C to 700°C. This trend concurred with the observation reported in the literature [58], [60]. The data of XRD analysis are tabulated in Table 4.9.

Table 4.9: XRD data of α-Fe_2O_3 nanocatalysts prepared via sol-gel method stirred for 1 day, annealed at different temperatures. The interpretation was based on (104) major plane.

Temperature (°C)		300	400	500	600	700	Literature
2θ (Degree)		33.36	33.40	33.40	33.24	33.16	33.2 [39]
Intensity (a.u)		24.20	40.80	46.60	109.00	240.00	-
D-spacing(Å)		2.683	2.680	2.680	2.679	2.670	2.69 [19]
FWHM		0.388	0.315	0.369	0.268	0.139	-
Lattice Constant (Å)	a	5.031	5.031	5.031	5.032	5.031	5.034 [19]
	b	5.031	5.031	5.031	5.032	5.031	5.034 [19]
	c	13.737	13.737	13.737	13.733	13.737	13.752 [19]
Average Crystallite size (nm)		21.74	26.78	22.86	31.47	60.67	-

Increasing annealing temperature enhanced the crystallinity of the α-Fe_2O_3 nanocatalysts as indicated by an increase in intensity of diffracted peaks (Figure 4.13 and Table 4.9). The particle size increased when the annealing temperature was elevated from 300°C to 700°C (Table 4.9). Similar trend was also reported by previous works [33], [60] as described in Section 2.5.2.1. This could be due to higher tendency of small particles to agglomerate when exposed to high temperature environment. This agglomeration reduced the surface energy of the particles which subsequently led to the formation of bigger particles [60], [108].

The structure of nanocatalysts prepared via sol-gel method at different annealing temperatures was examined by Raman spectroscopy and the spectra are shown in Figure 4.14.

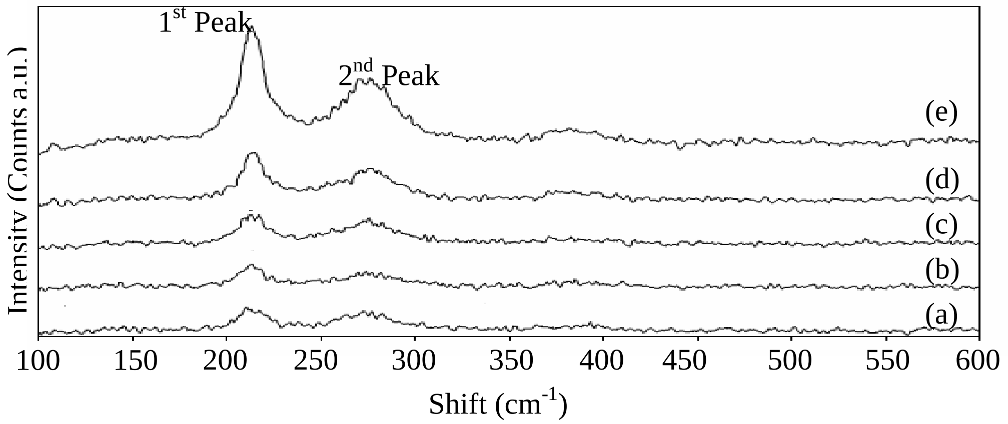

Figure 4.14: Raman spectra of α-Fe_2O_3 nanocatalysts prepared via sol-gel method stirred for 1 day, annealed at (a) 300°C (b) 400°C (c) 500°C (d) 600°C and (e) 700°C.

All spectra exhibit two peaks in the range of 200-300 cm^{-1} (Figure 4.14). According to the literature, these values corresponded to hematite, α-Fe_2O_3 characteristics [106]-[107]. Elevating annealing temperature increased the intensity of the Raman peaks (Figure 4.14), denoting an enhancement in crystallinity. The highest intensity for Raman peak was obtained for catalyst annealed at 700^{o}C. The Raman data for prepared nanocatalysts are summarized in Table 4.10.

Table 4.10: Raman data of α-Fe_2O_3 nanocatalysts prepared via sol-gel method stirred at 1 day, annealed at different temperatures.

Temperature (^{o}C)		300	400	500	600	700	Literature
1st Peak	Shift (cm^{-1})	213.91	214.41	241.41	215.93	213.40	200-230 [65], [106]
	Intensity (Counts a.u)	7.99	7.501	10.03	16.23	36.33	-
2nd Peak	Shift (cm^{-1})	278.71	278.20	277.18	280.73	277.69	270-300 [65], [106]
	Intensity (Counts a.u)	6.65	4.92	9.29	10.82	20.55	-
I_{1st}/I_{2nd}		1.20	1.52	1.10	1.50	1.76	-

Figure 4.15 shows the FESEM images of α-Fe_2O_3 nanocatalysts prepared via sol-gel method and annealed at various temperatures. The agglomeration of particles was more pronounced with increasing annealing temperature. Smaller particles favor to agglomerate to reduce its surface energy which consequently resulted in bigger particles [57], [60], [108]. Therefore, the temperature that can result in nanoparticles with the size of 20-30 nm is in the range of 300 – 600^{o}C (Table 4.9).

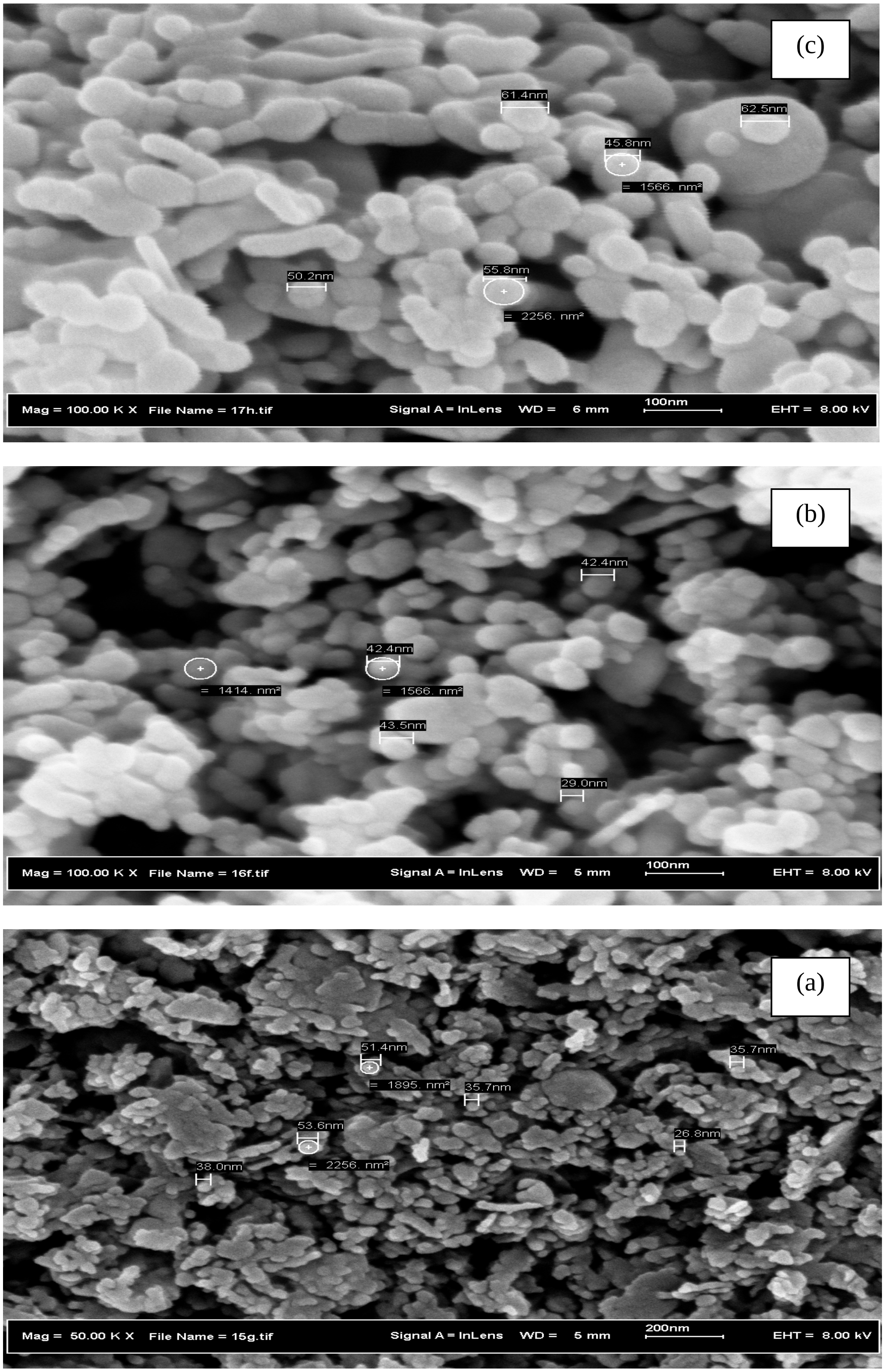

Figure 4.15: FESEM images of α-Fe_2O_3 nanocatalysts prepared via sol-gel method stirred for 1 day, annealed at (a) 300^{o}C (b) 400^{o}C (c) 500 (d) 600^{o}C and (e) 700^{o}C.

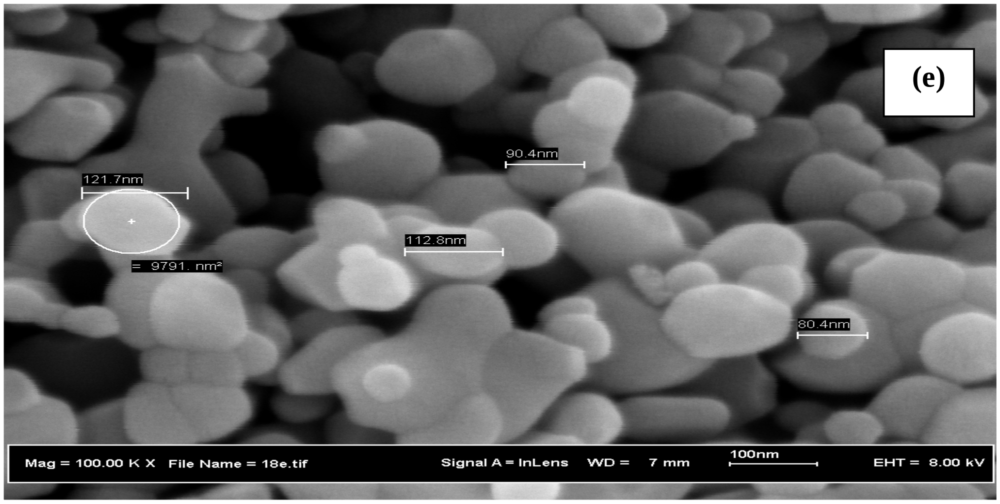
(e)
121.7nm
= 9791. nm²
90.4nm
112.8nm
80.4nm
Mag = 100.00 K X File Name = 18e.tif
Signal A = InLens WD = 7 mm
100nm
EHT = 8.00 kV

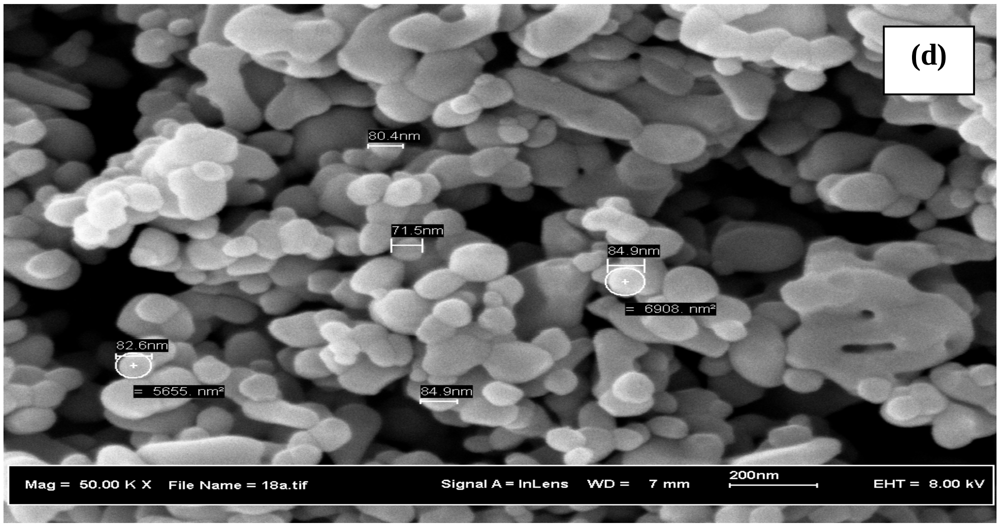
(d)
80.4nm
71.5nm
84.9nm
= 6908. nm²
82.6nm
= 5655. nm²
84.9nm
Mag = 50.00 K X File Name = 18a.tif
Signal A = InLens WD = 7 mm
200nm
EHT = 8.00 kV

Figure 4.16 displays EDX spectra of α-Fe_2O_3 nanocatalysts prepared via sol-gel method and annealed at different temperatures.

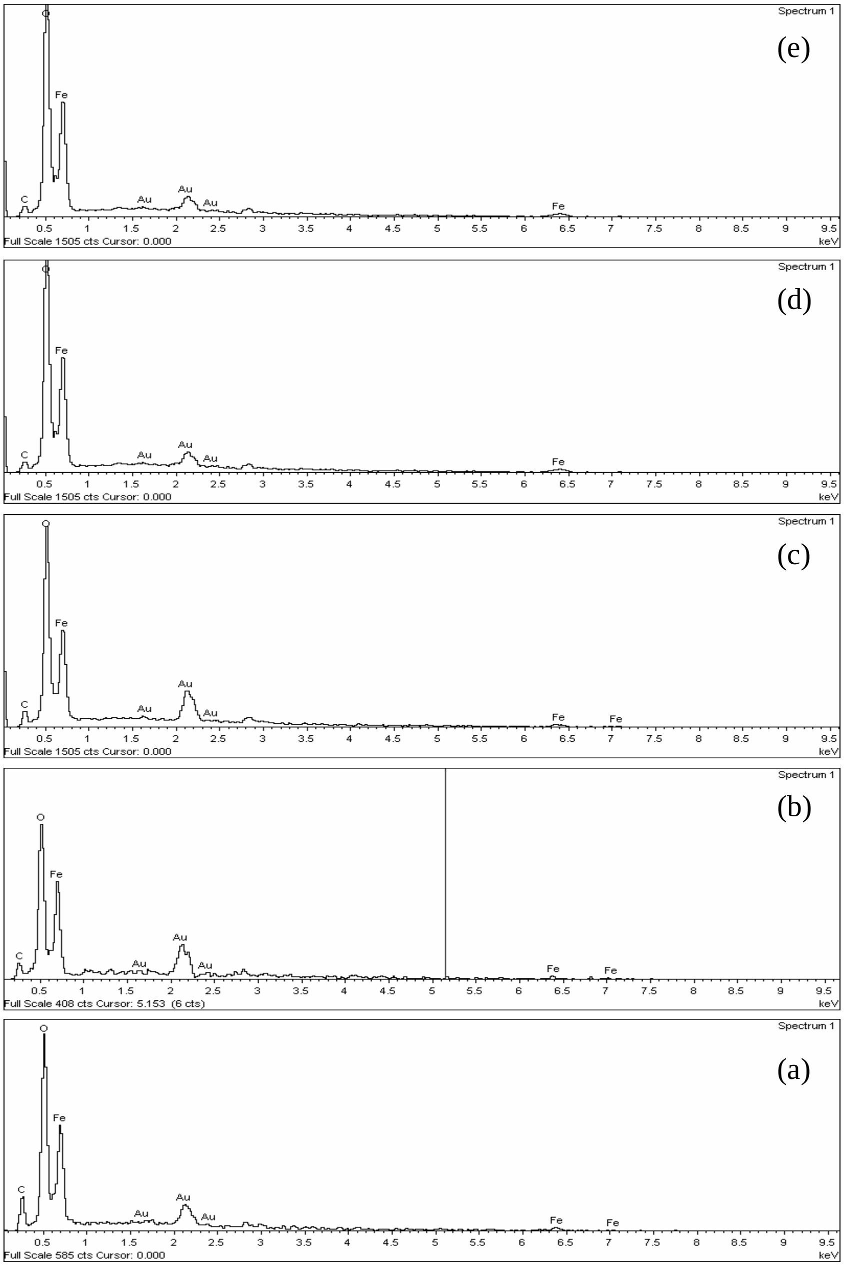

Figure 4.16: EDX spectra of α-Fe_2O_3 nanocatalysts prepared via sol-gel method stirred for 1 day, annealed at (a) 300^{o}C (b) 400^{o}C (c) 500^{o}C (d) 600^{o}C and (e) 700^{o}C.

Elements of Fe and O were detected in all iron oxide nanocatalysts (Figure 4.16). Theoretically, both Fe and O have weight percentages of 69.8% and 30.1%, respectively while the atomic percentages are 40% and 60%, respectively. The complete data for EDX are shown in Table 4.11.

EDX data reveal that both weight and atomic percentages of Fe and O increased with increasing annealing temperature (Table 4.11). The α-Fe_2O_3 nanocatalyst which was annealed at 700°C had less than 10% deviation for both Fe and O. However, the sample annealed at 300°C had more than 10% deviation, indicating incomplete occupancy of Fe and O atoms.

Table 4.11: EDX data of α-Fe_2O_3 nanocatalysts prepared via sol-gel method stirred for 1 day, annealed at different temperatures.

Annealing Temperature (°C)			300	400	500	600	700
Atomic %	Fe	Exp.	32.30	37.38	34.51	37.83	37.90
		Dev.	19.20	3.70	13.70	5.50	5.20
	O	Exp.	48.50	49.14	53.53	55.92	56.5
		Dev.	19.10	18.10	10.80	6.80	5.80
Weight %	Fe	Exp.	56.50	55.57	53.66	63.01	64.90
		Dev.	19.10	20.40	23.20	9.59	7.02
	O	Exp.	24.30	20.71	23.85	26.69	28.05
		Dev.	19.20	31.20	20.90	11.60	6.97

The reducibility investigation involving α-Fe_2O_3 nanocatalysts prepared via sol- gel method was carried out and the profiles are recorded in Figure 4.17.

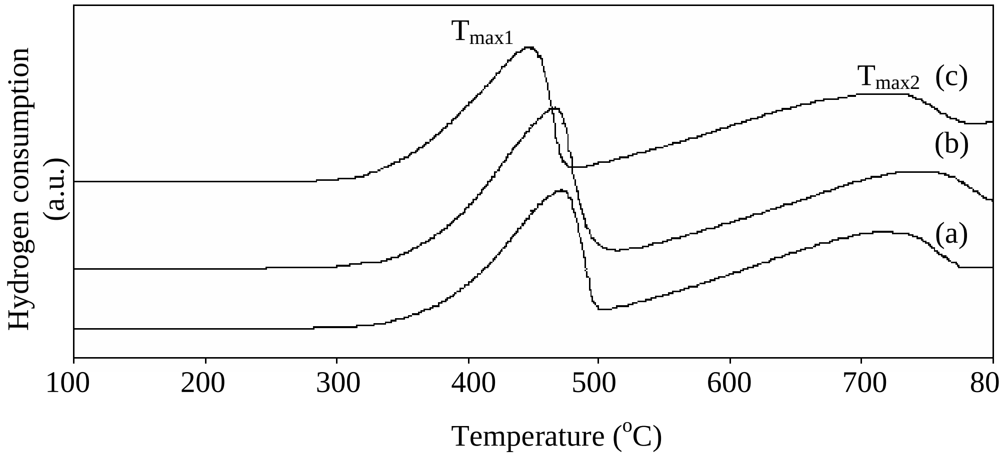

Figure 4.17: H_2-TPR profiles of α-Fe_2O_3 nanocatalysts prepared via sol-gel method stirred for 1 day, annealed at (a) 500°C (b) 600°C and (c) 700°C.

The reduction temperatures for nanocatalyst annealed at 500°C was slightly higher than those annealed at 600°C and 700°C which could be due to its smaller particle size. Table 4.12 summarizes the TPR data.

Table 4.12: H_2-TPR data of α-Fe_2O_3 nanocatalysts prepared via sol-gel method stirred for 1 day, annealed at different temperatures.

Annealing Temperature (^{o}C)			500	600	700	Literature
TPR	Path A (T_{max1})	$\alpha Fe_2O_3 \rightarrow Fe_3O_4$	474	464	448	500-530 [80]
	Path B (T_{max2})	$Fe_3O_4 \rightarrow Fe$	719	746	723	880-900 [80]

These results show that increasing annealing temperature promotes the formation of well crystallized but larger nanoparticles.

4.1.2 Unsupported Magnetite (Fe_3O_4) Nanocatalyst

4.1.2.1 Effect of Preparation Methods

A preliminary study in synthesizing magnetite Fe_3O_4 nanocatalysts was conducted by repeating various reported methods. These methods are sol gel [25], hydrothermal [35] and precipitation [31]. Subsequently, a hybrid method namely sol gel-hydrothermal was investigated in preparing the Fe_3O_4 nanocatalyst.

The phase of Fe_3O_4 nanocatalysts prepared via various methods was identified using XRD and the recorded spectra are displayed in Figure 4.18. All diffracted peaks with their miller planes matched with reported values for Fe_3O_4 from standard card (SS-NNNN-86-1345(A)) and literature [33], [35]-[36]. The Fe_3O_4 phase was further confirmed by existence of (311) major plane at 2θ of 35.14^{o} and (111) minor peak located at 2θ of 18.52^{o}. The minor peak of (104) that is usually located at 2θ of $10\text{-}20^{o}$ was not detected which indicates the absence of maghemite, γ-Fe_2O_3 phase (Figure 4.18) [33], [35]-[36].

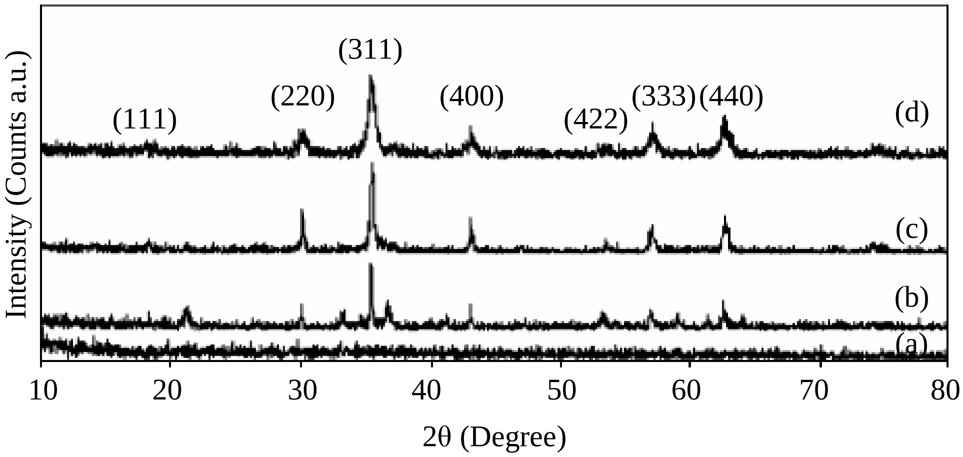

Figure 4.18: XRD spectra of Fe_3O_4 nanocatalysts prepared via (a) sol-gel (b) hydrothermal (c) precipitation and (d) sol gel-hydrothermal methods.

Diffraction peaks were absent for nanocatalyst synthesized via sol-gel, indicating poor crystallinity (Figure 4.18(a)). A combination between sol-gel and hydrothermal enhanced the crystallinity of the sample and resulted in smaller nanoparticles (Figure 4.18 (d)). Table 4.13 summarizes the data analysis of XRD. The atomics within nanocatalysts are anticipated to arrange in a cubic structure manner. The values of lattice constants matched with the literature [53]-[54] (Table 4.13) and obeyed a sequence of a=b=c, verifying that the structure of Fe_3O_4 nanocatalysts is cubic [10], [53]-[54]. The sol gel-hydrothermal method produced well-crystallined nanoparticles with smallest average crystallite size compared to those of other methods (Figure 4.18 and Table 4.13). The average crystallite size was 32.14 nm for sample synthesized by precipitation method. Precipitation method often faces several difficulties. Higher tendency of particles to agglomerate during the preparation is a well known problem. Thus, continuous stirring is necessary. Furthermore, the rate in dropping precipitant must also be controlled. Precipitation at fast rate will generate bigger particles [36]. In addition, the presence of counter ion, Cl in the synthesis system could also influence the stability of Fe_3O_4 phase.

Table 4.13: XRD data of Fe_3O_4 nanocatalysts prepared via sol-gel (SG), hydrothermal (HO), precipitation (PC) and sol gel-hydrothermal (SG-H) methods. The interpretation was based on (311) major plane.

Sample		SG	HO	PC	SG-H	Literature
2θ (Degree)		-	35.43	35.51	35.40	35.48 [33]
Intensity (Counts a.u)		-	56.50	71.43	70.60	-
FWHM		-	0.16	0.26	0.28	-
d-spacing (Å)		-	2.53	2.52	2.53	2.532 [20]
Lattice Constant (Å)	a	-	8.396	8.397	8.374	8.390 [20], 8.405 [54]
	b	-	8.396	8.397	8.374	8.390 [20], 8.405 [54]
	c	-	8.396	8.397	8.374	8.390 [20], 8.405 [54]
Av. crystallite size (nm)		-	53.36	32.14	29.97	-

The hydrothermal method resulted in larger particles compared to those of other preparation methods. The existence of pressure in hydrothermal method was beneficial for crystallinity enhancement which may accelerate the occupation of atoms into lattice sites. However, this method also suffers from Oswald ripening phenomenon which formed bigger particles [109]. The Oswald ripening may be the reason for the biggest average crystallite size obtained via hydrothermal in this study (Table 4.13). In addition, the use of organic surfactant during preparation can contribute to existence of impurity.

The sol gel-hydrothermal method resulted in smallest nanoparticles. Ethylene glycol not only behaved as the solvent, but also served as a stabilizing agent [110], reducing agent [111], and surfactant [112]. It possesses strong nucleophilic character originated from the two hydroxyl groups, (OH); attached at two ends of molecule chain [113]. When $Fe(NO_3)_3$ salt was dissolved in ethylene glycol, NO_3^- counter ions were favored to dissociate due to weak chelating property. Several vacant positions were created which then became deactivated by occupation of OH^- ions [113]. The possible structure of Fe ions in ethylene glycol environment is displayed in Figure 4.19 [114]. The NO_3^- ions were released from the system by heating process to form gelatine. This consequently minimized the oxidation effect carriers by NO_3^- ions to Fe^{2+}. The formation of gelatine in the earlier step could also reduce the Oswald ripening effect, thus resulting in smaller particles. Application of pressure also continuously improved the sample’s crystallinity.

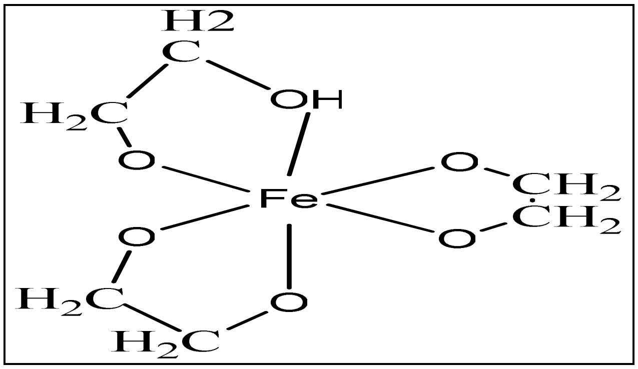

Figure 4.19: Proposed structure of iron-ethylene glycol complex [114].

The surface morphology of Fe_3O_4 nanocatalyst prepared via sol gel-hydrothermal method was examined by FESEM and the image is shown in Figure 4.20. The FESEM image shows cubic-shaped nanoparticles with irregular size.

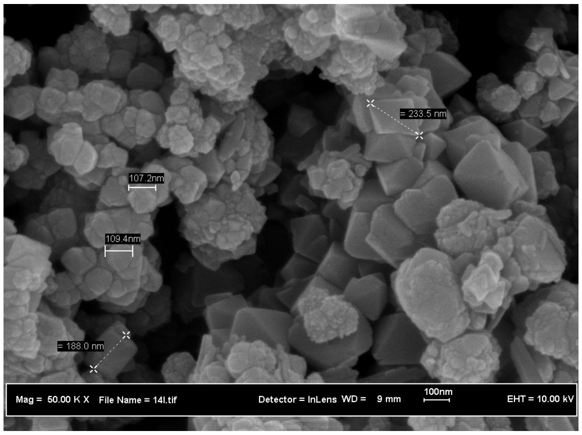

Figure 4.20: FESEM image of Fe_3O_4 nanocatalyst prepared via sol gel-hydrothermal method at 160^{o}C.

EDX spectrum of Fe_3O_4 nanocatalyst prepared via sol gel-hydrothermal method is displayed in Figure 4.21.

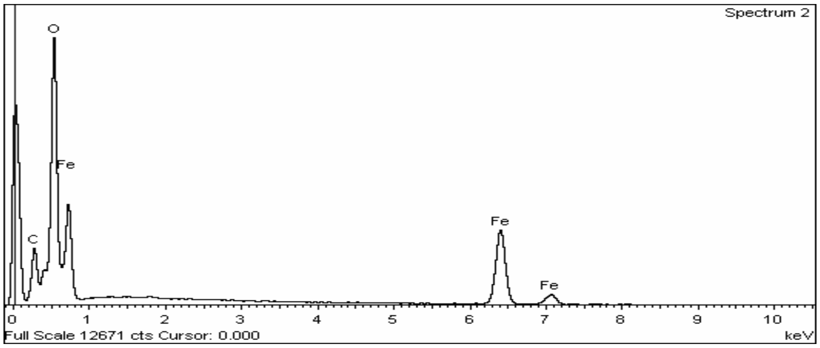

Figure 4.21: EDX spectrum of Fe_3O_4 nanocatalyst prepared via sol gel-hydrothermal method at 160^{o}C.

EDX spectrum shows the presence of Fe, O and C. Carbon was the impurity which could be originated from the solvent.

The magnetization effect of Fe_3O_4 nanocatalysts prepared via different methods was tested using VSM and the curves are presented in Figure 4.22.

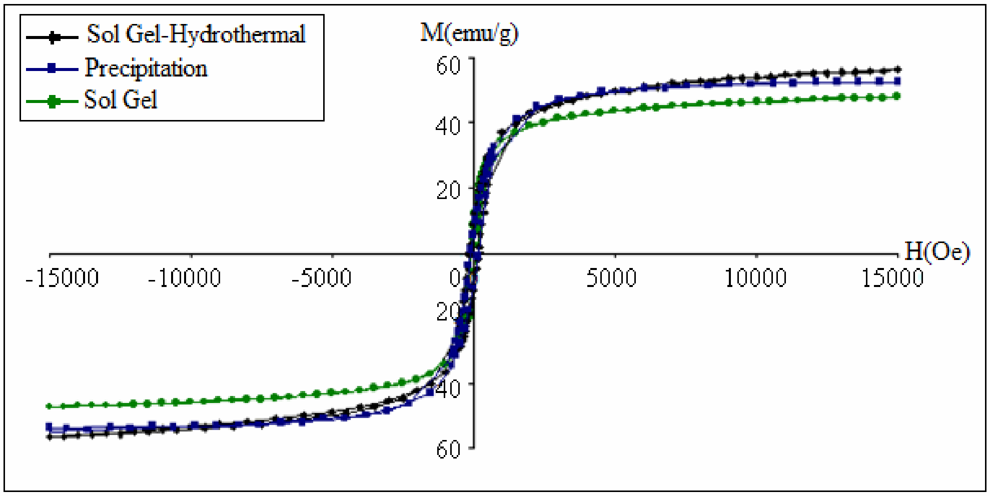

Figure 4.22: Hysteresis curves of Fe_3O_4 nanocatalysts prepared via different methods

All curves reveal remanance magnetization, M_r and coercivity force, H_c values. S-shaped curves were obtained for all samples. These features indicate the absence of superparamagnetic character in all of the nanocatalysts synthesized using these three methods [31]. VSM data are summarized in Table 4.14.

Table 4.14: Hysteresis data of Fe_3O_4 nanocatalysts prepared via different methods.

	Sol Gel-Hydrothermal	Precipitation	Sol Gel
MagnetizationSaturation, M_s (emu/g)	56.1	53.46	47.70
Remanance Magnetization, M_r (emu/g)	9.89	7.30	9.83
Coercivity Force, H_c (Oe)	148.85	79.2	108.1

Fe_3O_4 nanocatalyst obtained via the sol gel hydrothermal method, in the absence of surfactant, had the highest value of M_s, in comparison with the ones synthesized by precipitation and sol gel methods (Table 4.14). It was reported that Fe_3O_4 nanoparticles with the size of 27 nm prepared via the hydrothermal method using the $Fe(NO_3)_3.9H_2O$ precursor exhibited the M_s value of ~3.69 emu/g [37]. The M_s value obtained in this work via the sol gel-hydrothermal method in the absence of surfactant was 15 times higher

(Table 4.14) than the reported value. Y. H. Zheng et al. [37] reported that the use of organic surfactant, sodium bis(2-ethylhexyl) sulfosccinate; was claimed to be a major factor for reduction of M_s value. The presence of surfactant in the system covered the surface of the nanoparticles which was difficult to remove entirely during drying or annealing process [37]. Consequently, this reduced the response of the nanoparticles towards exerted field [35]. On the other hand, preparation of Fe_3O_4 using ferric acethylacetonate, $Fe(ACAC)_3$ via the hydrothermal method produced 30 nm particles with Ms value of 14.5 emu/g [34].

Nanocatalyst synthesized via precipitation method had weaker magnetization behavior (Table 4.14). The M_r and H_c values were reduced to about 35.47% and 87.94%, respectively as compared to those obtained via sol gel-hydrothermal method. This may suggest that Fe_3O_4 composition was enriched in nanocatalyst obtained via the sol gel hydrothermal method but not in the case of precipitation. Previous investigation concluded that the magnetization saturation linearly increased with increasing magnetite content [32]. Precipitation method was believed to enhance the formation of the goethite phase due to presence of hydroxyl groups, OH^- originated from the use of water and precipitating agent. The OH^- replaced Fe ions and created vacant sites, thus retarding the magnetic interaction between Fe and O. As a consequence, the population of magnetite phase was no longer balanced and exhibited a bad respond to the exerted field [35]. Goethite displays antiferromagnetic with Curie temperature, Tc of 390 K [20], [35]. Therefore, it was deduced that the weak magnetization behavior displayed by the nanocatalyst obtained via precipitation method might be due to the formation of the goethite phase.

The sol gel-hydrothermal method resulted in well-crystallined Fe_3O_4 nanocatalys having smallest crystallite size and highest M_s value amongst the tested methods. Therefore, the sol gel-hydrothermal method was selected to prepare more samples for further characterizations.

4.1.2.2 Hybrid Sol Gel-Hydrothermal Method

This part investigated the effect of synthesis temperature on the sol gel-hydrothermal method. Finding an optimum temperature is important to obtain highly crystallined nanocatalyst.

The recorded XRD spectra for Fe_3O_4 nanocatalysts synthesized via sol gel-hydrothermal method at various synthesis temperatures are shown in Figure 4.23.

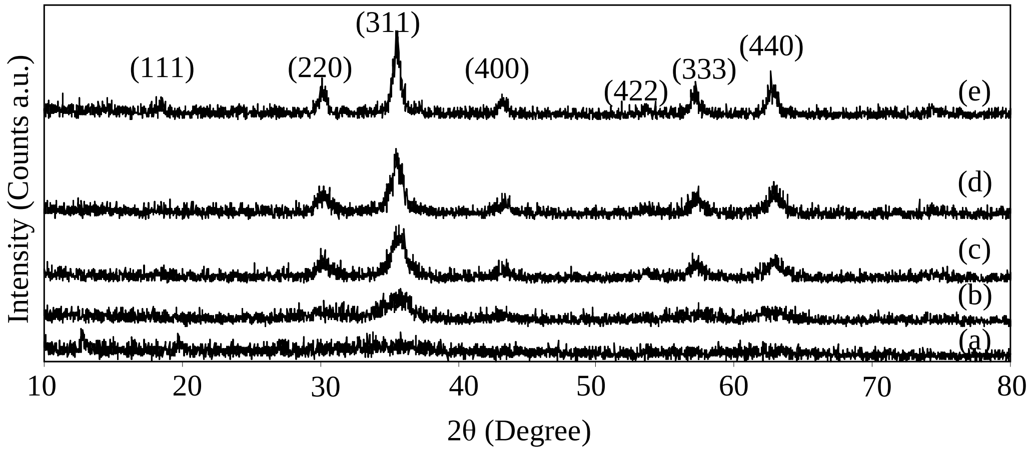

Figure 4.23: XRD spectra of Fe_3O_4 nanocatalysts prepared via sol gel-hydrothermal method at synthesis temperatures of (a) 28°C (b) 50°C (c) 80°C (d) 120°C and (e) 160°C.

All diffracted peaks were for magnetite (Fe_3O_4) phase with the appearance of (311) as a major plane at 2θ of 35.40° (Figure 4.23). The appearance of a (111) minor plane at 2θ of 10-20°, indicating the maghemite (γ-Fe_2O_3) phase [20], [48] was not detected. The crystallinity of Fe_3O_4 nanocatalysts was enhanced with increasing the synthesis temperature. The synthesis temperature at 160°C produced well crystallined Fe_3O_4 nanocatalyst (Figure 4.23). This temperature was also employed in synthesizing Fe_3O_4 nanocatalyst using the hydrothermal method by other workers [34], [37].

Synthesis temperature plays a vital role in the hydrothermal method [115]. Lower synthesis temperature decreases the solubility of the precursor and decelerates the crystallization step. This is due to inability of low temperature in supplying sufficient energy for the precursor to completely break up. This explains poor crystallinity for nanocatalyst synthesized at 28°C (Figure 4.23). However, the crystallinity can be enhanced by increasing the synthesis temperature. The growth velocity of the crystals is written in Equation 4.1 [115] where V is the growth velocity, C is constant, R is gas constant and T is temperature.

$$\frac{d\ln V}{dT} = \frac{C}{RT^2} \tag{4.1}$$

Equation 4.1 [115] shows that high synthesis temperature is beneficial for crystal growth. However, if the temperature is too high, the crystals may grow in random manner, thus preventing the formation of single particles [115].

Figure 4.24 illustrates the H_2-TPR profiles of Fe_3O_4 nanocatalyst prepared via sol gel-hydrothermal method at 160°C for 10 hours.

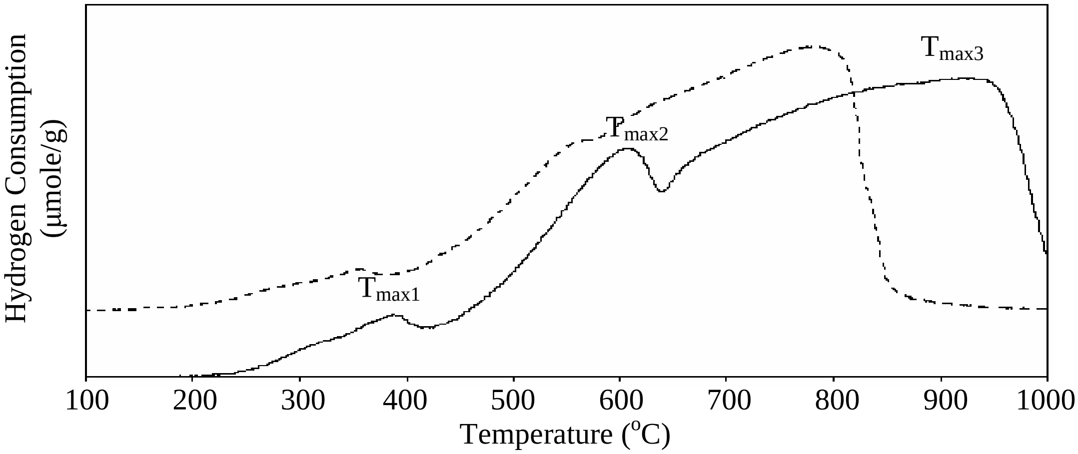

Figure 4.24: H_2-TPR profiles Fe_3O_4 nanocatalyst prepared via sol gel-hydrothermal method at synthesis temperature of 160°C. These profiles were recorded at the heating rate, β of 10°C/min (solid line) and 5°C/min (dotted line).

An intense peak, T_{max2}; at 500-600°C in both profiles corresponded to the reduction of $Fe_3O_4 \rightarrow FeO$. Meanwhile, the reduction of $FeO \rightarrow Fe$ happened at about 700-1000°C, indicated by a broad peak, T_{max3}; (Figure 4.24). The reduction was accomplished at much lower temperature as the heating rate, β; was reduced to 5°C/min (dotted line). As discussed in Section 2.6, lowering heating rate increased the contact time between the sample and hydrogen. This retards the formation of metastable $Fe_{1-x}O$ (Equation 2.24, Section 2.6) and at the same time accelerates direct reduction from Fe_3O_4 to α-Fe (Equation 2.22, Section 2.6). Hence, high temperature is not required due to decrease the amount of intermediate $Fe_{1-x}O$ which is difficult to reduce [22], [75]. A small reduction peak located at temperature 350-400°C was due to α-Fe_2O_3 residual resulted from oxidation of small portion of magnetite during annealing process [73]. The data for the reduction are summarized in Table 4.15.

Table 4.15: H_2-TPR data of Fe_3O_4 nanocatalyst prepared via sol gel-hydrothermal method at synthesis temperature of 160°C using different heating rates

Heating rate, β (°C/min)			5	10	Literature
TPR peak (T_{max})	Peak (T_{max1})	$Fe_2O_3 \rightarrow Fe_3O_4$	357	387	-
	Peak (T_{max2})	$Fe_3O_4 \rightarrow FeO$	575	606	800-820 [80]
	Peak (T_{max3})	$FeO \rightarrow Fe$	782	921	

Reduction at β of 10 °C/min was accomplished at much higher temperature compared to values reported in literature (Table 4.15) which used commercial Fe_3O_4 [80]. The Fe_3O_4 nanocatalysts were then annealed at different annealing temperatures and characterized using XRD. Their spectra were recorded and revealed in Figure 4.25.

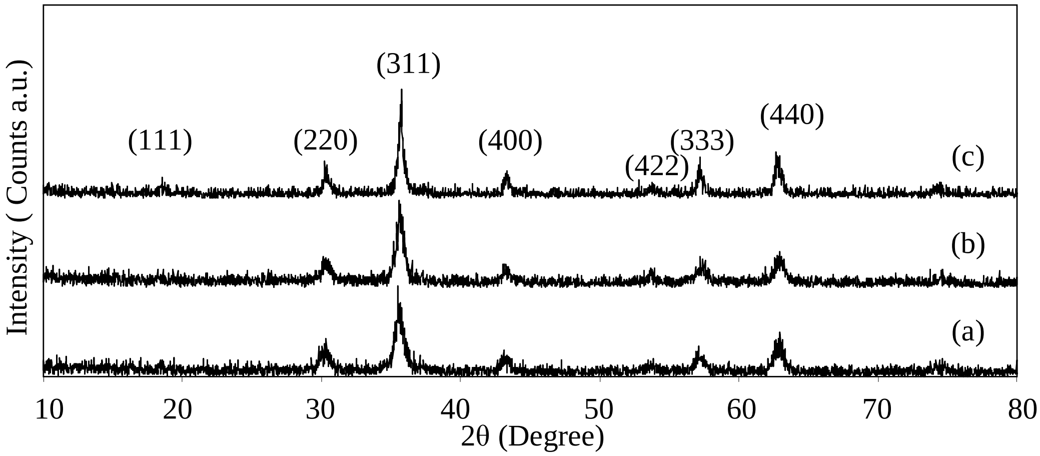

Figure 4.25: XRD spectra of Fe_3O_4 nanocatalysts prepared via sol gel-hydrothermal method at synthesis temperature of 160°C, annealed at (a) 200°C (b) 300°C and (c) 400°C.

The crystallinity of Fe_3O_4 nanocatalysts improved with increasing annealing temperature (Figure 4.25). The XRD data of samples are summarized in Table 4.16.

Table 4.16: XRD data of Fe_3O_4 nanocatalyst prepared via sol gel-hydrothermal method at synthesis temperature of 160^{o}C annealed at different temperatures. The interpretation was based on (311) major plane.

Annealing temperature (^{o}C)		200	300	400	Literature
2θ (Degree)		35.46	35.61	35.78	35.48 [33]
Intensity (a.u)		61.00	52.60	73.00	-
FWHM		0.447	0.451	0.268	-
D-spacing (Å)		2.5294	2.5189	2.5076	2.532 [20]
Lattice constant (Å)	a	8.374	8.333	8.330	8.390 [20], 8.405 [54]
	b	8.374	8.333	8.330	8.390 [20], 8.405 [54]
	c	8.374	8.333	8.330	8.390 [20], 8.405 [54]
Average crystallite size(nm)		19.00	18.84	31.72	-

The average crystallite size increased with increasing annealing temperature. This is due to high surface energy effect which promotes agglomeration at high temperature. An increase in intensity as a result of increasing annealing temperature signifies the enhancement of crystallinity (Table 4.16) [57]-[58], [60], [108].

4.1.3 Supported Hematite on Alumina (5% α-Fe_2O_3/γ-Al_2O_3) Nanocatalyst

The synthesis was accomplished by utilizing the sol gel-hydrothermal method. The effects of synthesis period and iron to surfactant ratio were studied. The supported nanocatalysts were annealed at 400^{o}C in nitrogen at flow of 10 cm^3/min for four hours.

4.1.3.1 Effect of Synthesis Period

Figure 4.26 compares the XRD spectra of pure γ-Al_2O_3, unsupported α-Fe_2O_3 and supported 5% α-Fe_2O_3/γ-Al_2O_3 samples.

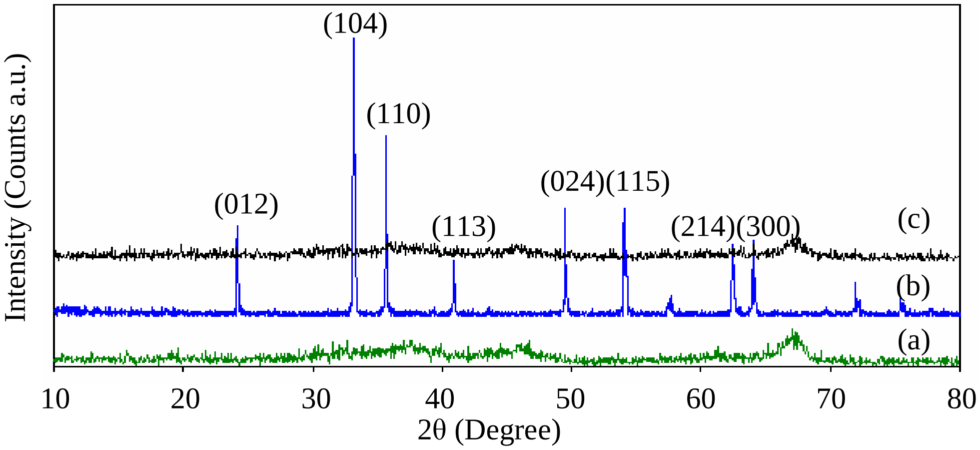

Figure 4.26: XRD spectra of (a) γ-Al_2O_3 support (b) unsupported α-Fe_2O_3 and (c) supported 5% α-Fe_2O_3/γ-Al_2O_3 nanocatalyst prepared via sol gel-hydrothermal method at 160°C for 1 day.

The XRD pattern for supported 5% α-Fe_2O_3/γ-Al_2O_3 resembled the XRD pattern of γ-Al_2O_3 (Figure 4.26). The α-Fe_2O_3 phase was not detected due to small amount of α-Fe_2O_3 on the γ-Al_2O_3 support which was below the detection limit of XRD. Raman spectra are revealed in Figure 4.27.

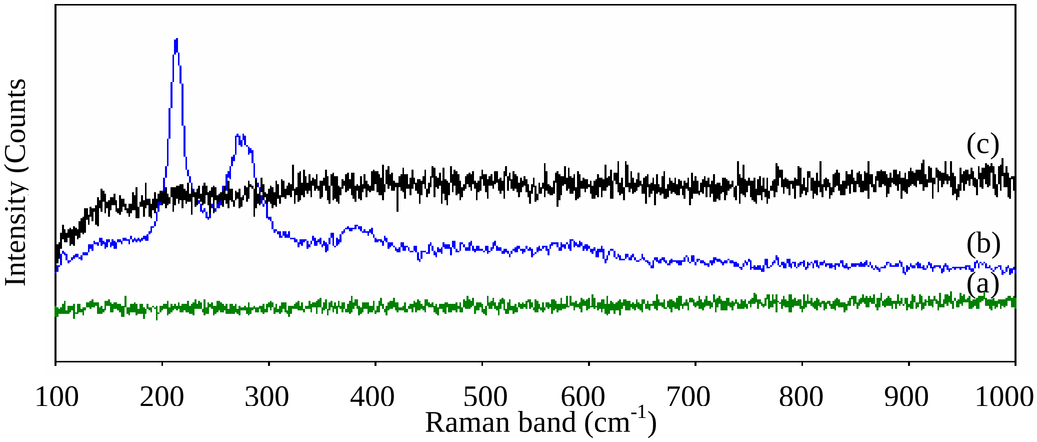

Figure 4.27: Raman spectra of (a) γ-Al_2O_3 support (b) α-Fe_2O_3 unsupported nanocatalyst and (c) supported 5% α-Fe_2O_3/γ-Al_2O_3 nanocatalyst prepared via sol gel-hydrothermal method at 160°C for 1 day.

Raman peaks were absent for 5% α-Fe_2O_3/γ-Al_2O_3 nanocatalyst (Figure 4.27 (c)). Major α-Fe_2O_3 peaks were not detected for the supported α-Fe_2O_3 possibly due to low amount of α-Fe_2O_3 in the sample. The surface morphology of supported 5% α-Fe_2O_3/γ-Al_2O_3 was examined by FESEM and the FESEM image is shown in Figure 4.28.

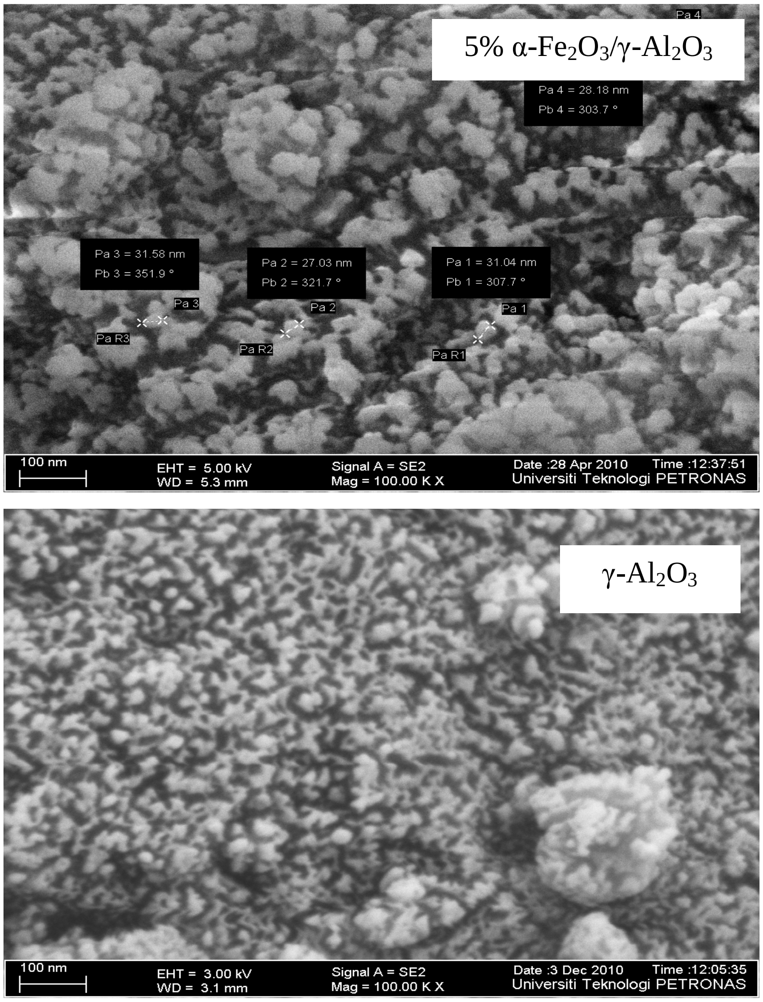

Figure 4.28: FESEM images of commercial γ-Al_2O_3 support and supported 5% α-Fe_2O_3/γ-Al_2O_3 nanocatalyst prepared via sol gel-hydrothermal method at 160^{o}C for 1 day.

The slight morphological change could be due agglomerated γ-Al_2O_3 particles (Figure 4.28). EDX was used to determine the elements in the 5% α-Fe_2O_3/γ-Al_2O_3 nanocatalyst and the result is revealed in Figure 4.29.

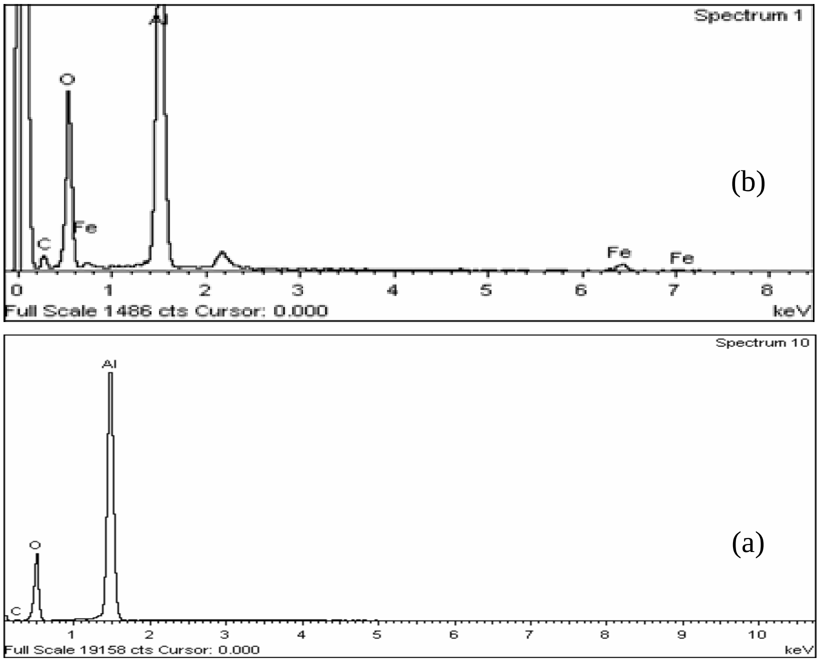

Figure 4.29: EDX spectrum of (a) γ-Al_2O_3 support and supported 5% α-Fe_2O_3/γ-Al_2O_3 nanocatalyst prepared via sol gel-hydrothermal method at 160^{o}C for 1 day.

Fe, O and Al were detected by EDX. In addition, carbon was also detected as an impurity which could be attained during preparation steps.

The influence of synthesis periods on the elemental distribution was investigated using EDX mapping. Figure 4.30 shows the images of Fe particles distribution as a function of synthesis temperature. The images for the other elements are shown in Appendix G.

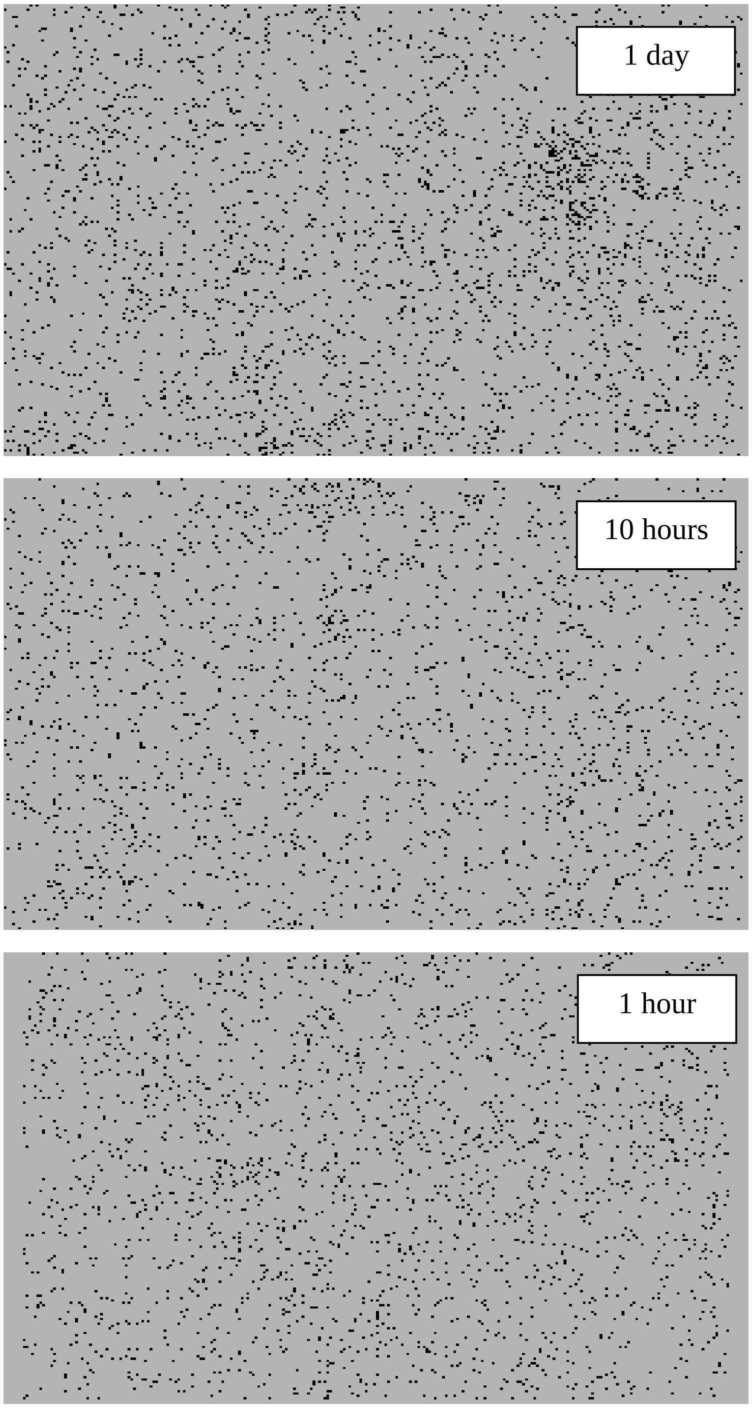

Figure 4.30: Fe particles distribution of supported 5% α-Fe_2O_3/γ-Al_2O_3 nanocatalysts prepared via sol gel hydrothermal method in the absence of surfactant at 160^{o}C and different synthesis periods. The scale of measurement applied was 10 μm.

Better dispersion of Fe particles was revealed by nanocatalyst synthesized at 1 hour compared to those obtained at 10 hour and 1 day synthesis periods (Figure 4.30).

Reducibility study was conducted using H_2-TPR to determine the influence of various synthesis periods on the reducibility of supported 5% α-Fe_2O_3/γ-Al_2O_3 nanocatalysts. The H_2-TPR profiles are presented in Figure 4.31.

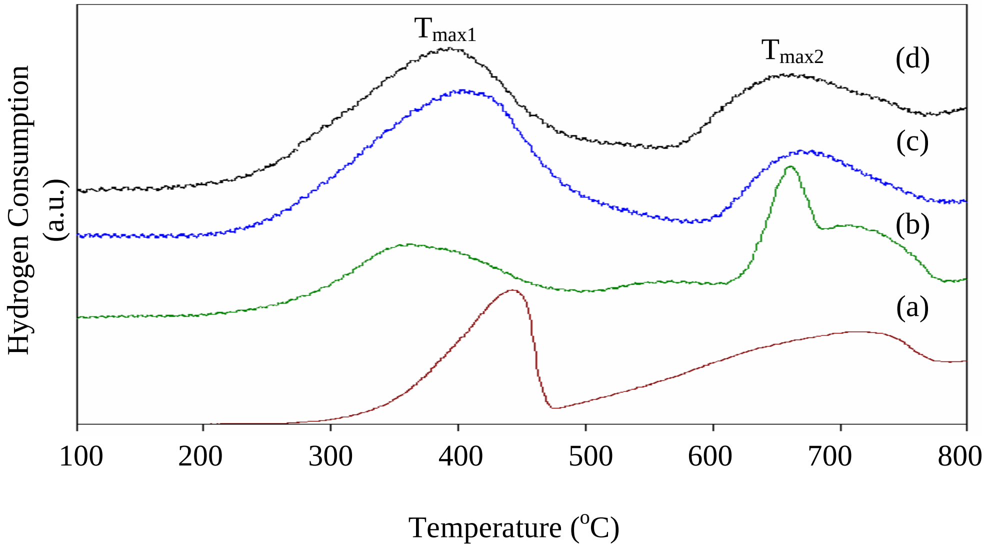

Figure 4.31: H_2-TPR profiles of (a) unsupported α-Fe_2O_3 and supported 5% α-Fe_2O_3/γ-Al_2O_3 nanocatalysts prepared via sol gel hydrothermal at 160°C for (b) 1 hour (c) 10 hours and (d) 1 day.

Two reduction peaks were obtained for reduction of α-Fe_2O_3 to Fe_3O_4 and Fe_3O_4 to Fe. The reduction temperatures for both peaks are consistent with previous reports [115]-[116]. The reducibility was improved in presence of γ-Al_2O_3 support. Reduction of 5% α-Fe_2O_3/γ-Al_2O_3 nanocatalysts occurred at much lower temperature as compared with that of the unsupported α-Fe_2O_3 (Figure 4.31). The data for reduction of 5% α-Fe_2O_3/γ-Al_2O_3 catalysts at different synthesis periods are summarized in Table 4.17.

Table 4.17: H_2-TPR data for supported 5% α-Fe_2O_3/γ-Al_2O_3 nanocatalysts prepared via sol gel-hydrothermal method at different synthesis periods.

Sample		1 hour	10 hours	1 day	Literature
TPR peak (T_{max})	T_{max1}(^oC)	363	403	395	430-460 [116], 400-450 [117]
	T_{max2}(^oC)	662	671	657	650-690 [116], 600-800 [117]

The reduction process for the 5% α-Fe_2O_3/γ-Al_2O_3 nanocatalysts occurred at much lower temperature in comparison with literature values (Table 4.17) [116]-[117]. Figure 4.32 summarizes the Fe particles dispersion and hydrogen consumption for 5% α-Fe_2O_3/γ-Al_2O_3 nanocatalysts based on TPR data interpretation. The example of calculation for Fe particles dispersion (%) is described in Appendix E.

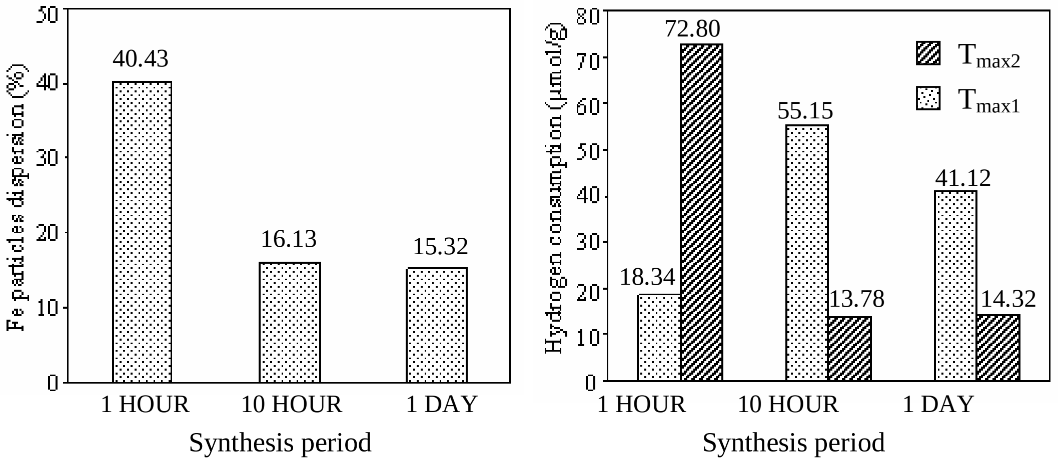

Figure 4.32: Summary for (a) Fe particles dispersion and (b) hydrogen consumption of supported 5% α-Fe_2O_3/γ-Al_2O_3 nanocatalysts prepared via sol gel-hydrothermal at 160^oC for different synthesis periods.

As shown in Table 4.17, reduction for nanocatalyst synthesized at 1 hour was accomplished at much lower temperature compared to the ones prepared at 10 hours and 1 day. This may be due to good dispersion of Fe particles as shown in Figure 4.32 (a). As described in Section 2.6, catalyst with highly dispersed particles improves reducibility, hence lowering the reduction temperatures [78]-[79]. The degree of dispersion for iron particles decreased as the synthesis period was extended from 1 hour to 1 day (Figure 4.32 (a)). This suggests that prolonging the synthesis period promotes the agglomeration of particles.

Incomplete reduction was observed for nanocatalysts synthesized at 10 hour and 1 day (Figure 4.32 (b)). They consumed 5 times lesser hydrogen than the one synthesized at 1 hour in completing second stage of reduction, T_{max2} (Figure 4.32 (b)). This is an indicative for the formation of a strong spinel interaction between $Fe_{1-x}O$ and γ-Al_2O_3, eventually forming hercynite ($FeAl_2O_4$) as explained by other researchers [80]-[81]. The formation of stable $FeAl_2O_4$ inhibits the continuation of the reduction, hence preventing the reaction between hydrogen molecules and $Fe_{1-x}O$ phase (Figure 4.32). This may justify for the observation in Figure 4.33 (c). It is understood that $Fe_{1-x}O$ phase can only be stable at temperature above 570^{o}C [22], [79], [81], [117]. However, highly stable $Fe_{1-x}O$ phase can also be attained below this temperature when $Fe_{1-x}O$ particles are supported on γ-Al_2O_3 (Section 2.6) [80], [118]-[121]. This may also explain an increase in reduction temperature as a result of extending the synthesis period (Figure 4.32 (b)).

4.1.3.2 Effect of Iron (III) Nitrate to SBS Surfactant Ratio

The effect of sodium bis(2-ethylhexyl) sulfosuccinate (SBS) surfactant on the properties of supported 5% α-Fe_2O_3/γ-Al_2O_3 was studied. The one-day period was chosen and the $Fe(NO_3)_3$:SBS surfactant was varied to 2:1, 2:2 and 2:3. The resultant nanocatalysts were annealed at 400^{o}C in nitrogen at flow 10 cm^3/min for four hours.

Figure 4.33 displays the FESEM image of supported 5% α-Fe_2O_3/γ-Al_2O_3 nanocatalyst prepared using the sol gel-hydrothermal method at $Fe(NO_3)_3$:SBS surfactant ratio of 2:3. The FESEM images for the catalyst synthesized at 2:1 and 2:2 were similar as that of 2:3 ratios. The appearance of iron nanoparticles is difficult to distinguish because the loading of α-Fe_2O_3 particles was only 5% on γ-Al_2O_3. Thus FESEM image is likely representing only γ-Al_2O_3 particles.

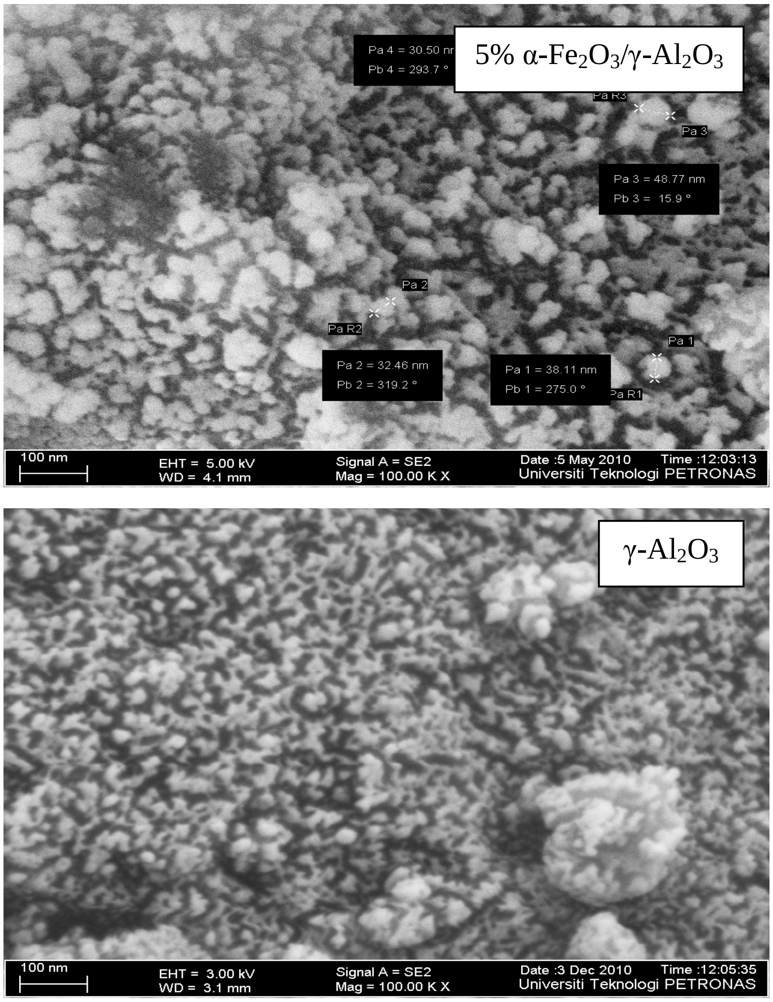

Figure 4.33: FESEM images of commercial γ-Al_2O_3 support and supported 5% α-Fe_2O_3/γ-Al_2O_3 nanocatalyst prepared via sol gel-hydrothermal method at $Fe(NO_3)_3$:SBS surfactant ratio of 2:3.

EDX characterization was performed to determine the elemental composition of supported 5% α-Fe_2O_3/γ-Al_2O_3 nanocatalyst and the spectra are revealed in Figure 4.34. The nanocatalysts contained Fe, O and Al elements as well as carbon impurity (Figure 4.34) which originated from the surfactant used in sol gel-hydrothermal method and the preparation steps.

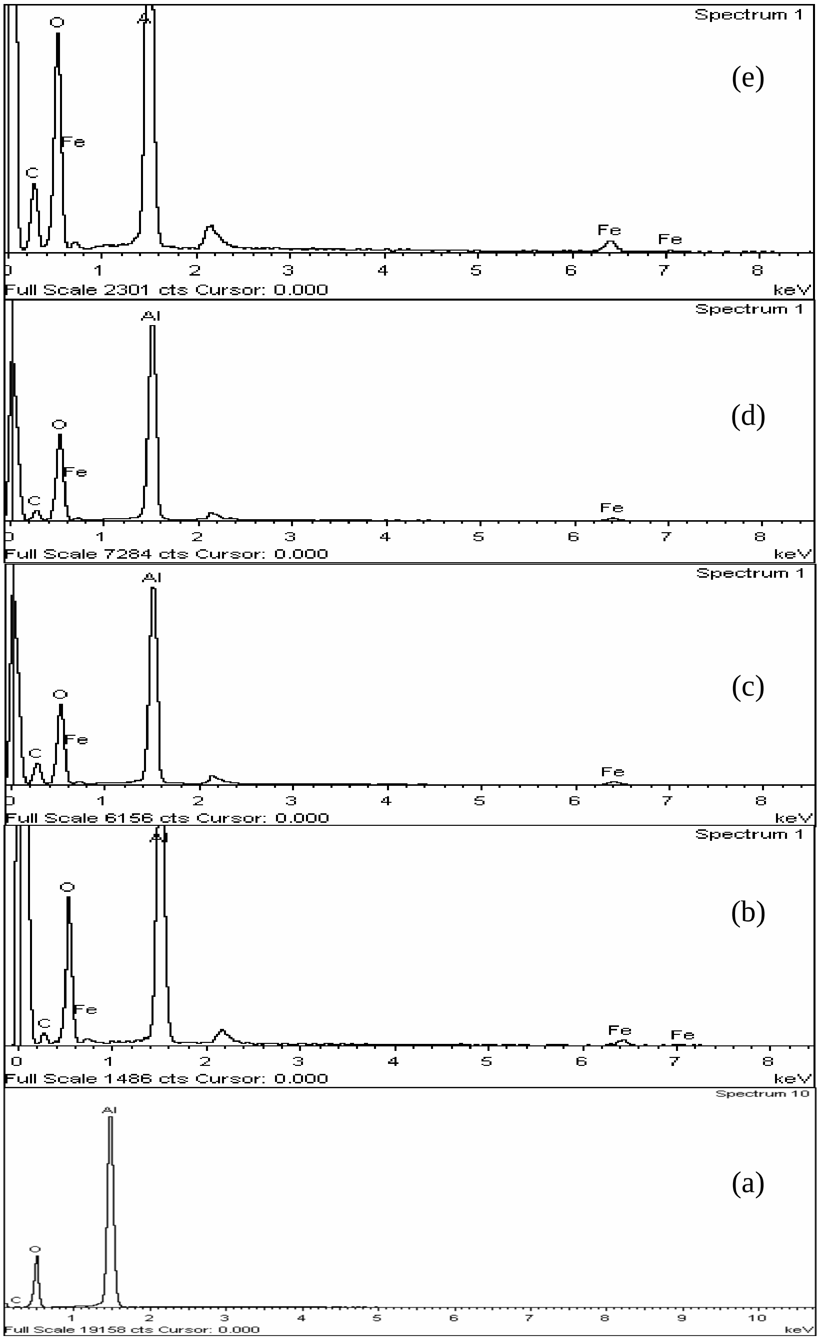

Figure 4.34: EDX spectra for supported 5% α-Fe_2O_3/γ-Al_2O_3 nanocatalysts prepared via sol gel-hydrothermal method at 160°C $Fe(NO_3)_3$:SBS surfactant ratios of (a) 2:0 (b) 2:1 (c) 2:2 and (d) 2:3.

The EDX data are summarized in Table 4.18. Amount of carbon presence increased with increasing $Fe(NO_3)_3$:SBS surfactant ratio (Table 4.18) which was difficult to remove entirely during annealing process. The percentages of atomic and weight for carbon, oxygen and aluminium did not exhibit a specific trend. This could be due to the analysis technique which only targeted on several spots but not on the whole surface, thus resulting in an uneven surface scanning. The elemental mapping images of Fe are shown in Figure 4.35 while for the other elements are shown in Appendix I.

Table 4.18: EDX data for supported 5% α-Fe_2O_3/γ-Al_2O_3 nanocatalysts prepared via sol gel-hydrothermal method at 160°C using different $Fe(NO_3)_3$:SBS surfactant ratios.

Method		2:0	2:1	2:2	2:3
Atomic (%) Experiment	Fe	1.54	1.25	1.36	1.37
	Al	22.00	17.88	21.80	17.46
	O	53.56	43.25	50.05	41.40
	C	22.90	37.62	26.79	39.75
Weight (%) Experiment	Fe	4.75	4.12	4.26	4.55
	Al	32.77	28.44	32.91	27.91
	O	47.30	40.80	44.82	39.25
	C	15.18	26.64	18.01	28.29

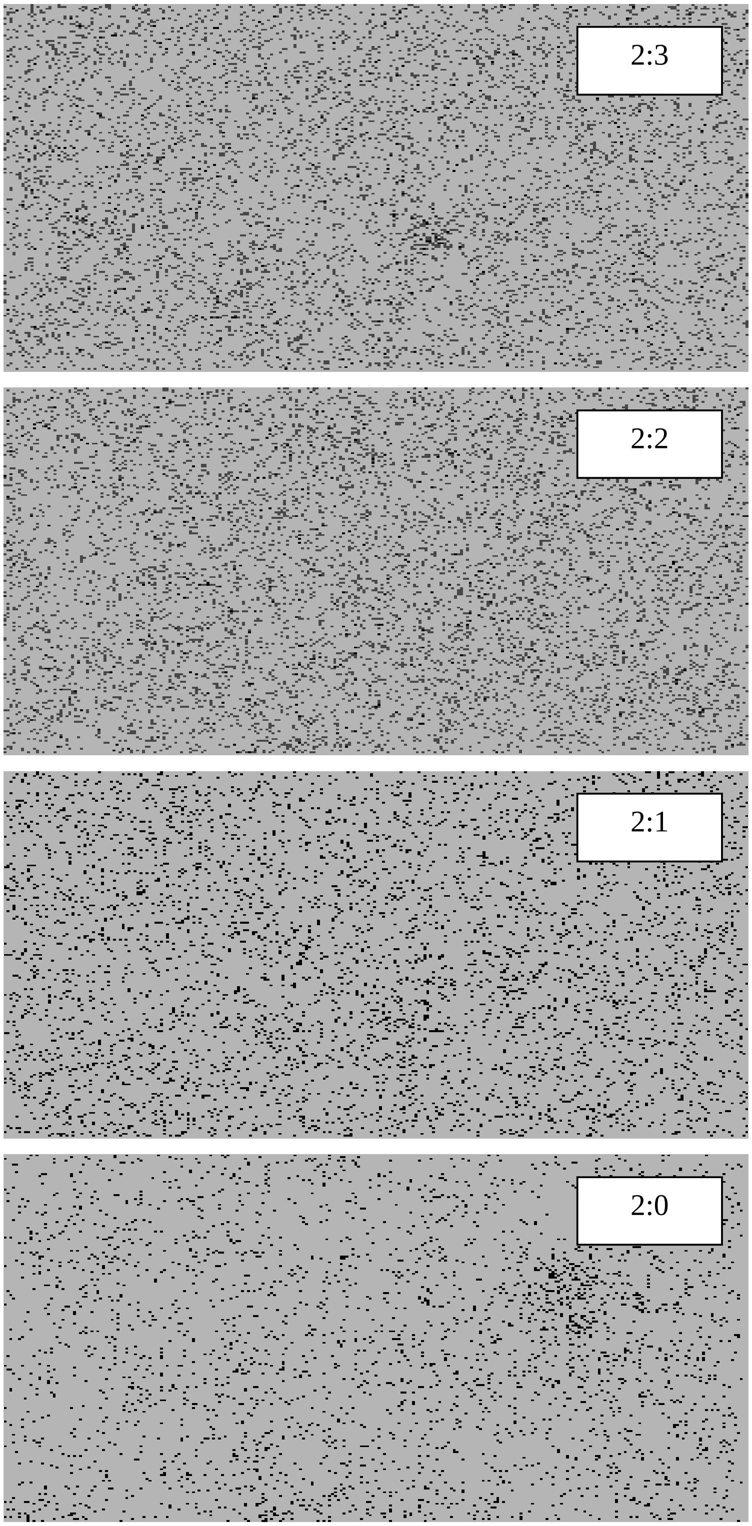

Figure 4.35: Fe particles distribution of supported 5% α-Fe_2O_3/γ-Al_2O_3 nanocatalysts prepared via sol gel hydrothermal method at different $Fe(NO_3)_3$:SBS surfactant ratios. The scale of measurement applied was 10 μm.

Increasing the amount of surfactant resulted in an enhancement in Fe particles distribution. Poor distribution of Fe particles was observed for nanocatalyst synthesized in absence of surfactant. Fe particles distribution improved when the ratios were increased from 2:1 to 2:3. However, excessive amount of surfactant led to particles agglomeration as shown by FESEM image of 2:3 ratio (Figure 4.35).

Figure 4.36 illustrates the reduction profiles of supported 5% α-Fe_2O_3/γ-Al_2O_3 nanocatalysts synthesized using the sol gel-hydrothermal method at different iron (III) nitrate to SBS surfactant ($Fe(NO_3)_3$:SBS) ratios.

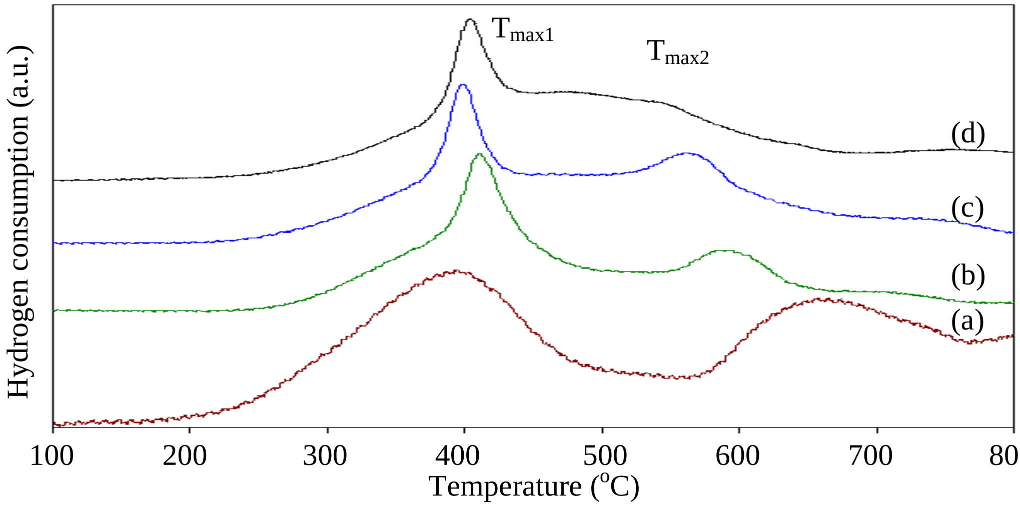

Figure 4.36: H_2-TPR profiles of supported 5%Fe_2O_3/γ-Al_2O_3 nanocatalysts prepared via sol gel-hydrothermal method at $Fe(NO_3)_3$:SBS surfactant ratios of (a) 2:0 (b) 2:1 (c) 2:2 and (d) 2:3.

Varying iron to surfactant ratios changed the H_2-TPR profiles. Two reduction peaks were obtained for each sample (Figure 4.36). The temperatures for accomplishing second reduction step, T_{max2} decreased consistently to slightly lower temperature with increasing surfactant. Table 4.19 summarizes the data for H_2-TPR.

Table 4.19: H_2-TPR data of supported 5% α-Fe_2O_3/γ-Al_2O_3 nanocatalysts prepared via sol gel-hydrothermal method at different $Fe(NO_3)_3$:SBS surfactant ratios.

Sample		2:0	2:1	2:2	2:3	Literature
TPR peak (T_{max})	T_{max1}(°C)	395	411	399	404	430-460 [116], 400-450 [117]
	T_{max2}(°C)	657	587	564	440	650-690 [116], 600-800 [117]

As the surfactant increased, the second reduction stage became easier to accomplish (Table 4.19). This suggested that the strength of iron-support interaction may be reduced and subsequently inhibited the formation of $Fe_{1-x}O$ by varying the amount of surfactant. Figure 4.37 summarizes the Fe particles dispersion and hydrogen consumption for supported 5% α-Fe_2O_3/γ-Al_2O_3 nanocatalysts based on H_2-TPR data interpretation.

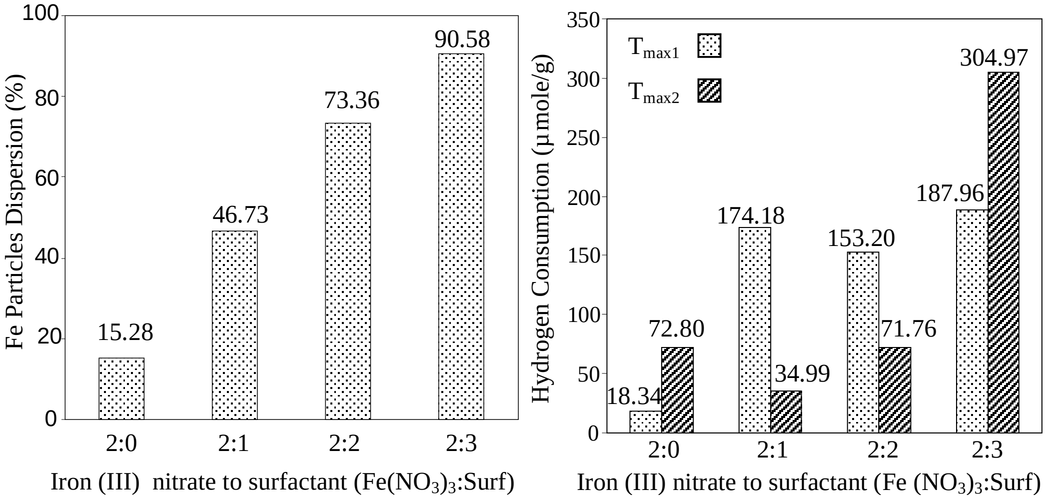

Figure 4.37: Summary for (a) Fe particles dispersion and (b) hydrogen consumption of supported 5% α-Fe_2O_3/ γ-Al_2O_3 nanocatalysts prepared via sol gel-hydrothermal method at 160°C using different $Fe(NO_3)_3$:SBS surfactant ratios

Example of the calculation for Fe particles dispersion is shown in Appendix E.3.1. The degree of Fe particles dispersion was enhanced by a factor of seven when iron nitrate to surfactant ratios increased from 2:0 to 2:3 (Figure 4.37 (a)). This was supported by an enhancement in Fe particle distribution as shown by EDX mapping (Figure 4.35). Higher dispersion of particles caused the reduction to occur more easily (Section 2.6) [79]-[81], justifying for the decrease in reduction temperature (Table 4.19). Table 4.20 summarizes the hydrogen consumption ratio to reduce supported 5% α-Fe_2O_3/ γ-Al_2O_3 nanocatalysts prepared at different $Fe(NO_3)_3$:SBS surfactant ratios.

Table 4.20: Hydrogen consumption ratio, T_{max1}/T_{max2} in reducing supported 5% α-Fe_2O_3/ γ-Al_2O_3 nanocatalysts prepared at different $Fe(NO_3)_3$: SBS surfactant ratios.

$Fe(NO_3)_3$: SBS ratio	T_{max1}:T_{max2}
2:0	1:4
2:1	1:0.20
2:2	1:0.46
2:3	1:1.62

Complete transformation of unsupported α-Fe_2O_3 to Fe typically consumed hydrogen with T_{max1}/T_{max2} ratio of 1:8 [76]. The nanocatalyst synthesized in the absence of surfactant consumed hydrogen with the T_{max1}/T_{max2} ratio of 1:4 (Table 4.20), denoting incomplete reduction of Fe_3O_4 to Fe. Meanwhile, adding surfactant at ratio 2:1 ($Fe(NO_3)_3$: SBS) enhanced the dispersion of Fe particles (Figure 4.37 (a)), but decreased the extent of reduction (Table 4.20). Enhanced dispersion increases the interaction between Fe particles and γ-Al_2O_3 support, thus could induce the formation of a stable spinel interaction hercynite ($FeAl_2O_4$) phase. The existence of the stable $FeAl_2O_4$ prevented the reduction of $Fe_{1-x}O$ to Fe (Section 2.6). The reducibility performance improved further when $Fe(NO_3)_3$:SBS ratios were increased to 2:2 and 2:3. The dispersion of Fe particles was enhanced with increasing surfactant as exhibited by Figure 4.35 and Figure 4.37. The temperature, T_{max2} slighlty shifted to lower region (Figure 4.36, Table 4.20) while hydrogen consumption of T_{max2} increased (Figure 4.37 (b)) for these catalysts. Moreover, T_{max1}/T_{max2} ratio was also increased (Table 4.20). These suggest that raising the amount of surfactant destabilized the intermediate $Fe_{1-x}O$ phase on γ-Al_2O_3. The $FeAl_2O_4$ interaction strength was minimized, thus overcoming the disproportination reaction (Equation 2.23, Section 2.6). Consequently, direct transformation of $Fe_{1-x}O$ to Fe was favored.

Figure 4.38 illustrates the nitrogen adsorption isotherms for supported 5%α-Fe_2O_3/γ-Al_2O_3 nanocatalysts synthesized at different $Fe(NO_3)_3$:SBS surfactant ratios.

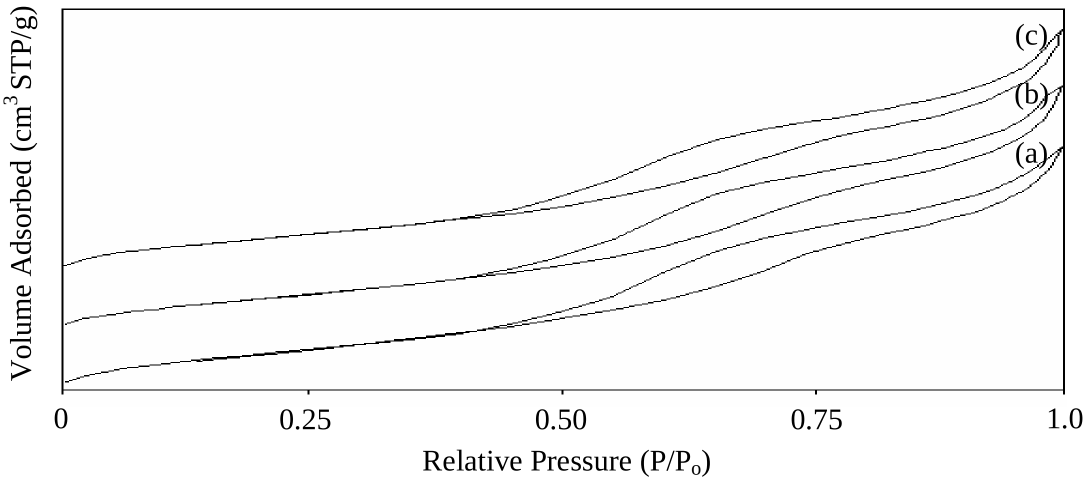

Figure 4.38: Nitrogen adsorption isotherms on supported 5%α-Fe_2O_3/γ-Al_2O_3 nanocatalysts prepared via sol gel-hydrothermal method at $Fe(NO_3)_3$:SBS surfactant ratios of (a) 2:1 (b) 2:2 and (c) 2:3.

The BET data for supported 5%α-Fe_2O_3/γ-Al_2O_3 nanocatalysts synthesized at iron nitrate to surfactant ratios are tabulated in Table 4.21.

Table 4.21: BET data for supported 5%α-Fe_2O_3/γ-Al_2O_3 nanocatalysts synthesized at different $Fe(NO_3)_3$:SBS surfactant ratios.

Fe:Surf	BET Surface Area (m^2/g)	Pore Volume (cm^3/g)	Pore Size (Å)
γ-Al_2O_3	190	0.10	98.0
2:1	151.4217	0.261474	69.0718
2:2	135.3409	0.244584	72.2869
2:3	140.3443	0.242378	69.0811

Increasing $Fe(NO_3)_3$:SBS surfactant ratio from 2:1 to 2:3 reduced the surface area of the nanocatalysts (Table 4.21). This reduction could be caused by the filling of γ-Al_2O_3 pores up by Fe particles. The formation of agglomerated Fe particles with increasing iron (III) nitrate to SBS surfactant ratio as exhibited by EDX-mapping images (Figure 4.35), also contributed to a decrease in surface area of the nanocatalysts. A summary of the physicochemical properties of the prepared nanocatalysts is shown in Table 4.22.

Table 4.22: Summary of the physicochemical properties of the prepared nanocatalysts.

Catalyst		A. C. Size (nm)	Raman I_{st}/I_{2nd} ratio	EDX				H_2-TPR		VSM			BET Surface Area (m^2/g)
				% Atomic		% Deviation		T_{max1} α-$Fe_2O_3 \rightarrow Fe_3O_4$ (^oC)	T_{max2} $Fe_3O_4 \rightarrow Fe$ (^oC)	M_s (emu/g)	M_r (emu/g)	H_c (O_e)	
				Fe	O	Fe	O						
α-Fe_2O_3	S. Combustion	55.50	1.20	33.77	58.24	16.58	2.93	525	784	-	-	-	-
α-Fe_2O_3	S. Assembly	27.90	0.99	28.12	55.08	29.70	8.20	495	807	-	-	-	-
α-Fe_2O_3	S. Gel, 1 month	18.80	1.16	41.74	58.26	-4.16	2.98	426	732	-	-	-	-
α-Fe_2O_3	S. Gel, 1 week,	23.20	1.36	28.84	71.16	38.69	-15.68	420	697	-	-	-	-
α-Fe_2O_3	S. Gel, 1 day, 300^{o}C	21.74	1.20	32.30	48.50	19.20	19.10	-	-	-	-	-	-
α-Fe_2O_3	S. Gel, 1 day, 400^{o}C	26.78	1.52	37.38	49.14	3.70	18.10	-	-	-	-	-	-
α-Fe_2O_3	S. Gel, 1 day, 500^{o}C	22.86	1.10	34.51	53.53	13.70	10.80	474	719	-	-	-	-
α-Fe_2O_3	S. Gel, 1 day, 600^{o}C	31.47	1.50	37.83	55.92	5.50	6.80	464	746	-	-	-	-
α-Fe_2O_3	S. Gel, 1 day, 700^{o}C	60.67	1.76	37.90	56.5	5.20	5.80	448	723	-	-	-	2.15
Fe_3O_4	Sol Gel	-	-	-	-	-	-	-	-	47.70	9.83	108.10	-
Fe_3O_4	Hydrothermal	53.36	-	-	-	-	-	-	-	-	-	-	-
Fe_3O_4	Precipitation	32.14	-	-	-	-	-			53.46	7.30	79.20	-
Fe_3O_4	Sol Gel-Hydrothermal	29.97	-	35.93	64.07	19.25	-10.81	-	606-921	56.10	9.89	148.85	3.79

5%α-Fe_2O_3/γ-Al_2O_3	Sol Gel-Hydrothermal, 1hour	-	-	-	-	-	-	363	662	-	-	-	-
5%α-Fe_2O_3/γ Al_2O_3	Sol Gel-Hydrothermal, 10 hours	-	-	-	-	-	-	403	671	-	-	-	-
5% α-Fe_2O_3/γ-Al_2O_3	Sol Gel-Hydrothermal, 1 day	-	-	-	-	-	-	395	657	-	-	-	-
5% α-Fe_2O_3/γ-Al_2O_3	Sol Gel-Hydrothermal, 1 day, 2:1 (Fe:Surf)	-	-	-	-	-	-	411	587	-	-	-	151.42
5% α-Fe_2O_3/γ-Al_2O_3	Sol Gel-Hydrothermal, 1 day, 2:2 (Fe:Surf)	-	-	-	-	-	-	399	564	-	-	-	135.34
5% α-Fe_2O_3/γ-Al_2O_3	Sol Gel-Hydrothermal, 1 day, 2:3 (Fe:Surf)	-	-	-	-	-	-	404	440	-	-	-	140.34

4.2 Catalytic Reaction Study

4.2.1 Unsupported Iron Oxide Nanocatalyst

The catalytic reaction was studied using 0.2 g of α-Fe_2O_3 at flow rate of 40 cm^3/min, H_2:N_2 ratio of 3:1, space velocity of 12000 cm^3/g_{cat}. h, atmospheric pressure and reaction period of 3 hours. Effect of magnetic field was studied by applying magnetic field at 1 Tesla to the catalyst system. Figure 4.39 summarizes the effect of magnetic field and various reaction temperatures on the ammonia synthesis deploying α-Fe_2O_3 nanocatalyst. The calculations of ammonia yield are shown in Appendix A.

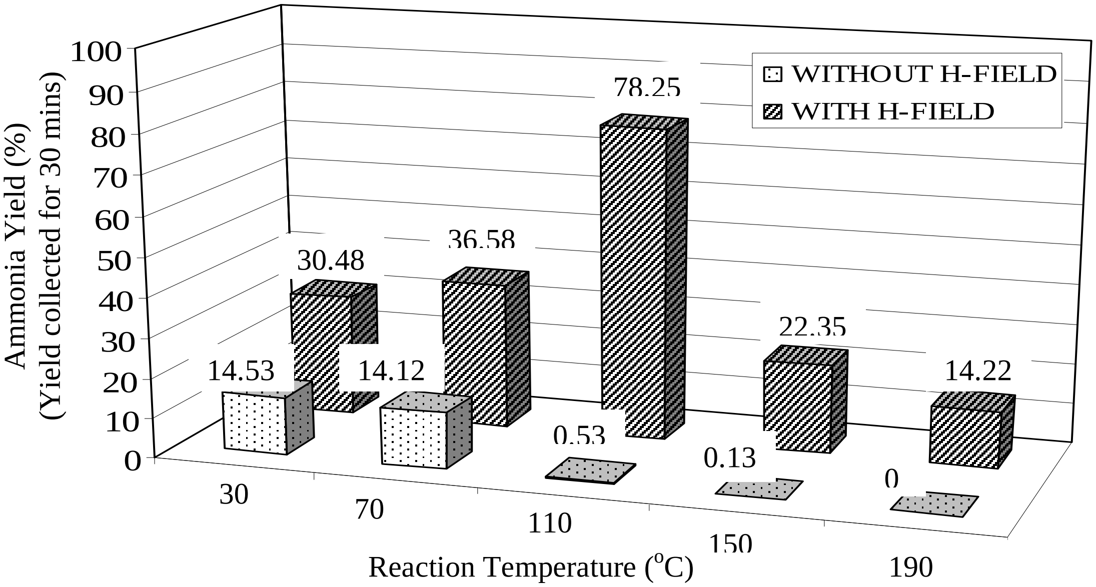

Figure 4.39: Effect of magnetic field and various reaction temperatures on ammonia yield produced in presence of α-Fe_2O_3 nanocatalyst. T = 30°C-190°C, P = 1 atm, H-F = 1 T, Cat. = 0.2 g, GHSV = 12000 cm^3/g_{cat}.h, F = 40 cm^3/min, H_2:N_2 = 3:1. The ammonia yield was collected for 30 mins at each temperature.

The ammonia yield consistently decreased when reaction temperature was increased from 28°C to 188°C (Figure 4.39). This trend concurs with observation in previous studies [6], [14], [94]. According to Le'Chatelier principle, due to exothermic type of ammonia synthesis, an increase in temperature favors the reaction system to shift to the left side for equilibrium to be established, resulting in the decomposition of ammonia, hence enriching the reactant molecules, N_2 and H_2 (Section 2.8.1) [1], [10]-[11]. Enhancement in the ammonia yield by about two orders of magnitude was attained by introducing magnetic field to the reactor. The reaction produced optimum ammonia yield at temperature 110°C and the ammonia yield was 145 times higher than the one obtained in the absence of magnetic field (Figure 4.39). However, the yield progressively declined when temperature was increased to 190^{o}C (Figure 4.39). At room temperature, α-Fe_2O_3 revealed weak ferromagnetic character with the spins magnetic moments randomly oriented within the multidomains (Section 2.4.1 and Section 2.4.4) [10]. However, exerting magnetic field diminished the domain walls, thus assembling all magnetic moments in a large single domain causing the magnetic moments to be aligned parallel to the exerted magnetic field direction (Section 2.4.3) [12]. Interaction of reactant molecules with the magnetized catalyst overcame the difficulty for the electrons to be transferred, pairing and exchange among d-orbital of catalyst and π-orbital of reactant molecules. However, when the synthesis temperature was increased above 110^{o}C, the yield reduced by about a factor of 3 (Figure 4.39). As elaborated by Le Chaterlier's principle (Section 2.8.1), increasing reaction temperature encourages the decomposition of ammonia to N_2 and H_2 due to exothermic and reversible properties of ammonia synthesis reaction [1], [10]-[11].

Figure 4.40 shows the effect of different forms of iron oxide catalysts on the ammonia yield at various reaction temperatures. The magnetic field was also applied during the catalytic reaction study.

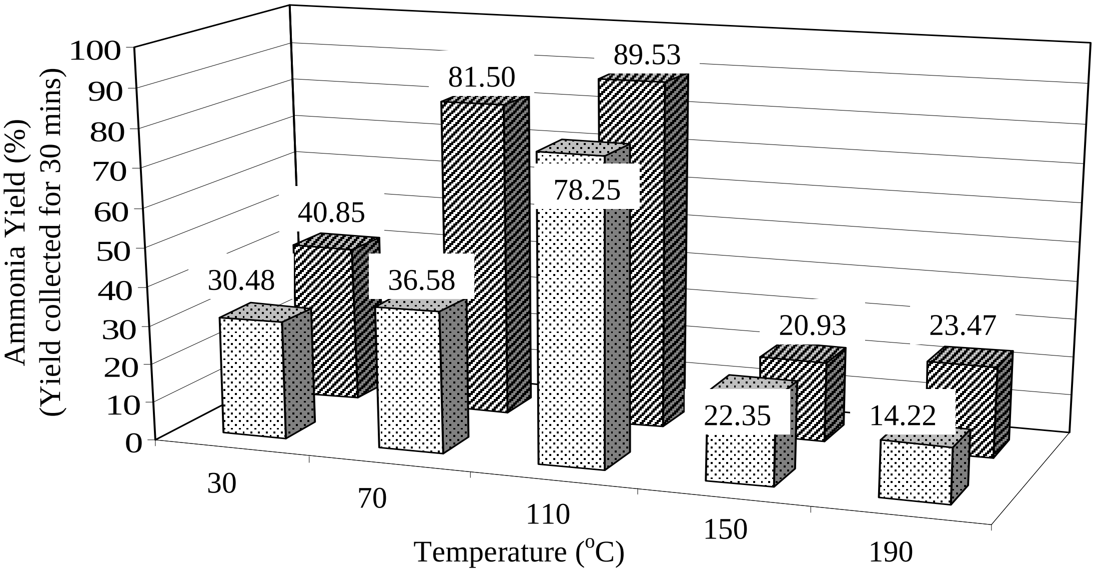

Figure 4.40: Effect of various reaction temperatures and different catalyst phases on ammonia yield produced. T = 30^{o}C-190^{o}C, P = 1 atm, H-F = 1 T, Cat. = 0.2 g, GHSV = 12000 $cm^3/g_{cat}.h$, F = 40 cm^3/min, H_2:N_2 = 3:1. The ammonia yield was collected for 30 mins at each temperature.

The use of Fe_3O_4 catalyst resulted in 15% higher ammonia yield than that of α-Fe_2O_3 at 110°C (Figure 4.40). The increase in ammonia yield might be due to magnetic character of the Fe_3O_4 catalyst. At room temperature, α-Fe_2O_3 was a weak ferromagnetic while Fe_3O_4 exhibited good ferrimagnetic properties (Table 4.14) [20]. The strength of exerted field might not be adequate to overcome the energy barrier for magnetic moments rotation in α-Fe_2O_3 structure, thus confining the catalytic steps. Higher ammonia yield was obtained when Fe_3O_4 was used as a catalyst due to stronger magnetic character compared to α-Fe_2O_3 which enhanced electrons sharing and exchanging processes between the catalyst and the reactants.

The activation energy was determined using a well know equation for ammonia synthesis namely Temkin-Phyzev and the calculations are shown in Appendix B. The expression is described in Equation 4.2 [90],[101] where k_A is the rate constant for forward reaction, k_B is the rate constant for reverse reaction, P_A is the partial pressure of substance and α is the reaction order.

$$\text{Rate}_{NH3}\,(\text{mole}_{NH3}/\text{gcat.h}) = k_A P_{N2}\,[(P^3_{H2})/(P^2_{NH3})]^{\alpha} - k_B\,[(P^2_{NH3})/(P^3_{H2})]^{1-\alpha} \qquad (4.2)$$

The equation assumed that nitrogen dissociative adsorption is the rate-determining step and the surface coverage by atomic nitrogen is high [90]. The value of reaction order, α used in this study was 0.75, similar to that of value employed by Pernicone et al. [101]. Previous study also reported that the value of reaction order, α was found to be in between 0.5 to 0.8 [90]. As explained by Aparicio et al. [90], if α equals to 0, the change in the heat of nitrogen adsorption with coverage does affect only the activation energy of desorption whereas α equals to 1 causes the activation energy for adsorption to get affected. It was found in this study that the Temkin-Phyzev equation did work for temperature up to 110°C. Conversely, the results became insignificant for the calculation involving data obtained at temperature above 110°C. The values of rate, equilibrium constant, K_{eq}, mole fraction, X_A, partial pressure, P_A, and rate constant, k_A are shown in Table 4.23.

Table 4.23: Data to determine the activation energy of α-Fe_2O_3 and Fe_3O_4 nanocatalysts in the presence of magnetic field.

Catalyst	T (°C)	K_{eq}	X_A			P_A (atm)			Rate ($mol_{NH3}/g_{cat}.h$)	k_A ($g_{cat}.^{-1}h^{-1}$)	ln k_A	E_a
			N_2	H_2	NH_3	N_2	H_2	NH_3				
α-Fe_2O_3	30	1.853×10^5	0.216	0.650	0.130	0.216	0.650	0.130	3.0×10^{-3}	1.724×10^{-3}	-6.363	34.18 kJ/mol
	70	2.617×10^3	0.211	0.635	0.154	0.211	0.635	0.154	3.6×10^{-3}	2.866×10^{-3}	-5.854	
	110	90	0.179	0.539	0.281	0.179	0.539	0.281	7.7×10^{-3}	2.650×10^{-2}	-3.627	
Fe_3O_4	30	1.853×10^5	0.208	0.623	0.170	0.208	0.623	0.170	4.020×10^{-3}	3.930×10^{-3}	-5.539	30.57 kJ/mol
	70	2.617×10^3	0.178	0.533	0.290	0.178	0.533	0.290	8.020×10^{-3}	2.860×10^{-2}	-3.555	
	110	90	0.173	0.518	0.309	0.173	0.518	0.309	8.810×10^{-3}	4.020×10^{-02}	-3.213	

Arrhenius plot was plotted using the data tabulated in Table 4.23 so as to obtain the activation energy of the nanocatalysts as shown in Figure 4.41.

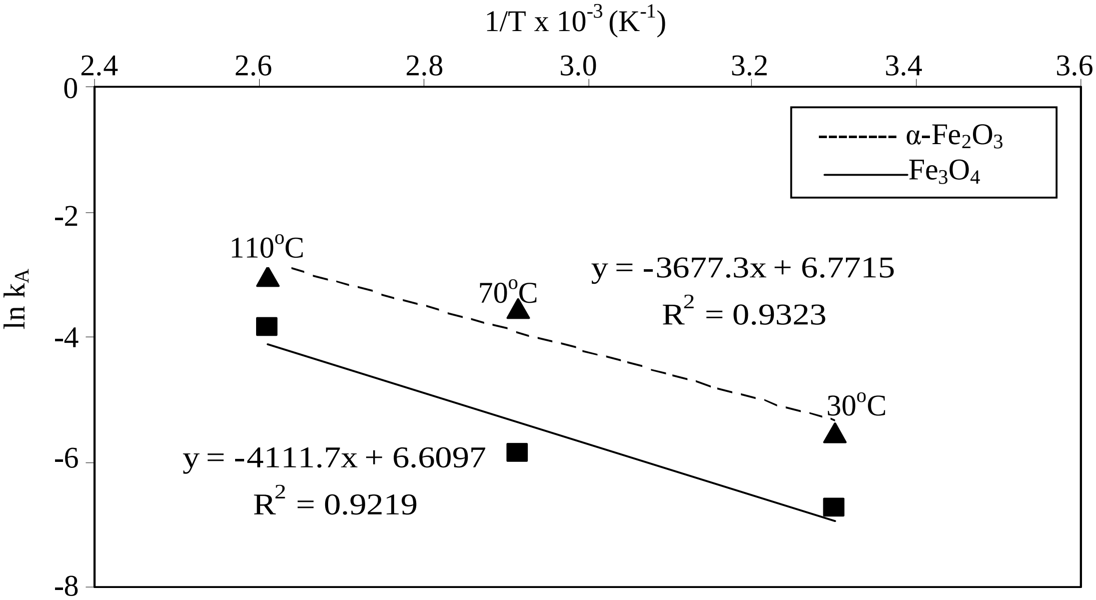

Figure 4.41: Arrhenius plot of ammonia production for α-Fe_2O_3 (■) and Fe_3O_4 (▲) nanocatalysts. T = 30^{o}C-190^{o}C, P = 1 atm, H-F = 1 T, Cat. = 0.2 g, GHSV = 12000 cm^3/g$_{cat}$.h, F = 40 cm^3/min, H_2:N_2 = 3:1

Both plots of α-Fe_2O_3 and Fe_3O_4 have R-square values of 0.9219 and 0.9323, respectively. These values are closed to 1 with the percentage error in between 6.5% to 8.0% (Figure 4.41). The activation energy, E_a was determined by calculating the gradient of the linear lines (Figure 4.41). In the absence of magnetic field, the α-Fe_2O_3 nanocatalyst had the activation energy of 96.49 kJ/mol. In the presence of magnetic field, the E_a of α-Fe_2O_3 catalyst was 34.18 kJ/mol whereas for Fe_3O_4 catalyst was 30.57 kJ/mol. The E_a values in this investigation were found to be slightly lower than those of results reported in literature [122]. Strongin et al. [122] examined that the E_a values for Fe and K/Fe catalysts were 65.73 kJ/mol and 66.57 kJ/mole, respectively. This was measured at reaction temperature and pressure of 365 – 450^{o}C and 20 atm, respectively [122]. Pernicone and co-workers [101] compared the performance of Fe_3O_4 and $Fe_{1-x}O$-based catalysts to produce ammonia at 400 – 460^{o}C and 100 bars. They found that the E_a for Fe_3O_4 and $Fe_{1-x}O$-based catalysts were 44.9 kJ/mol and 47.5 kJ/mol, respectively, which was slightly higher than those values obtained in this study by a factor of 1.3 – 1.6. This deduces that magnetizing the catalyst minimized the difficulty in electrons exchanging and pairing processes between the catalyst and reactant, thus permitting the catalytic steps to occur easily.

4.2.2 Supported Iron Oxide Nanocatalyst

Three factors were studied which encompass effects of properties of supported 5% α-Fe_2O_3/γ-Al_2O_3 nanocatalyst, H_2:N_2 ratio and total feed gas flow rate.

4.2.2.1 Effect of Properties of 5% α-Fe_2O_3/γ-Al_2O_3 Nanocatalyst

The results for ammonia synthesis involving 5% α-Fe_2O_3/γ-Al_2O_3 catalyst prepared at different $Fe(NO_3)_3$:SBS surfactant ratios are shown in Figure 4.42. The reaction utilized total H_2 and N_2 gases flow of 40 cm^3/min, H_2:N_2 ratio of 3:1, space velocity of 12000 cm^3/g_{cat}.h and under atmospheric pressure.

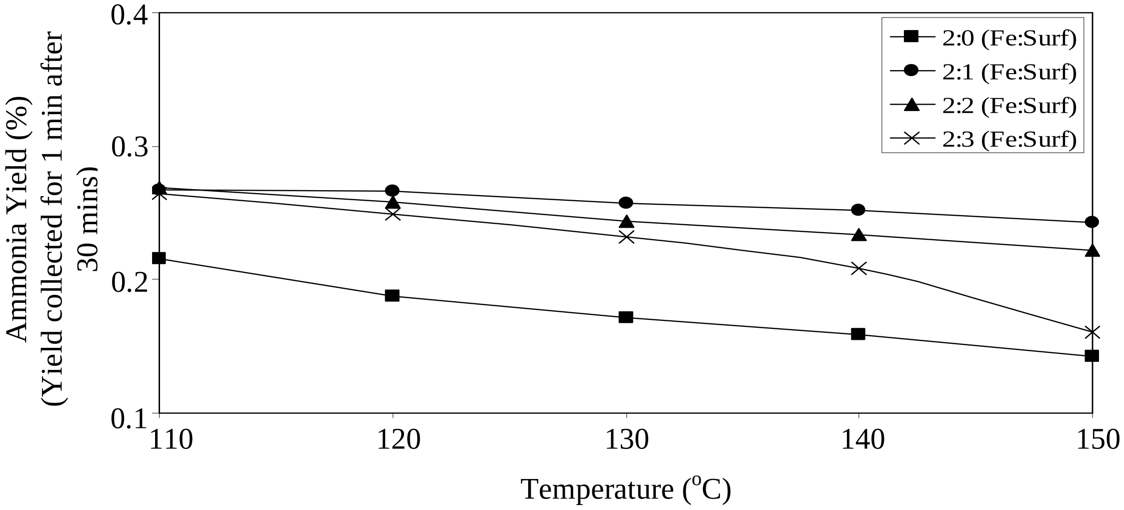

Figure 4.42: Effect of various reaction temperatures and different $Fe(NO_3)_3$:SBS surfactant ratios of supported 5% α-Fe_2O_3/γ-Al_2O_3 catalysts on ammonia yield. T = 110°C – 150°C, P = 1 atm, H-F = Absence, Cat. = 0.2 g, GHSV = 12000 cm^3/g_{cat}.h, F = 40 cm^3/min, H_2:N_2 = 3:1. The ammonia yield was collected for 1 minute after 30 mins at each temperature.

Ammonia yield produced in the presence of these catalysts decreased with increasing reaction temperature (Figure 4.42), consistent with Le Chatelier's principle (Section 2.8.1) and previous observations [1], [6], [10]-[11], [14], [94]. At 150°C, ammonia yield dropped by about 50% for the catalyst prepared using 2:3 $Fe(NO_3)_3$:SBS surfactant compared to that of catalyst synthesized at 2:1 $Fe(NO_3)_3$:SBS surfactant ratios. The major role of surfactant is to enhance the dispersion of particles as well as to avoid agglomeration phenomenon. However, increasing amount of surfactant increased amount of carbon impurity as interpreted by EDX analysis (Figure 4.34 and Table 4.18). Excess surfactant can cover the surface of Fe particles, thus preventing H_2 and N_2 molecules to be adsorbed on the surface of Fe particles. Section 4.1.3.2 revealed that adding more surfactant enhanced the Fe particles dispersion (Figure 4.37 (a)). However, few agglomerated particles were observed for nanocatalysts prepared at 2:2 and 2:3 $Fe(NO_3)_3$:SBS surfactant ratios (Figure 4.35) which caused reduction in surface area of Fe particles (Table 4.21). Consequently, the ammonia yield reduced due to decrease in surface area of Fe particles (Figure 4.42).

The supported 5% α-Fe_2O_3/γ-Al_2O_3 nanocatalyst synthesized using 2:1 $Fe(NO_3)_3$: SBS Surf ratio revealed highest ammonia yield that was attained at 110^oC. This nanocatalyst showed good improvement on physicochemical properties. Therefore, this nanocatalyst and temperature of 110^oC were chosen in further catalytic studies.

4.2.2.2 Effect of H_2:N_2 ratio

It is known that the ideal gas ratio (H_2:N_2) applies in ammonia synthesis is 3:1. This investigation utilized supported 5% α-Fe_2O_3/γ-Al_2O_3 nanocatalyst obtained using iron to surfactant ratio of 2:1. This study was conducted at total feed flow rate gas (H_2:N_2) of 40 cm^3/min, space velocity of 12000 cm^3/g_{cat}.h, reaction temperature of 110^oC and under atmospheric pressure. The H_2:N_2 volume ratios were varied to 1:3, 3:1 and 5:1. Figure 4.43 illustrates the influence of various reactant gas ratios (H_2:N_2) on the ammonia yield.

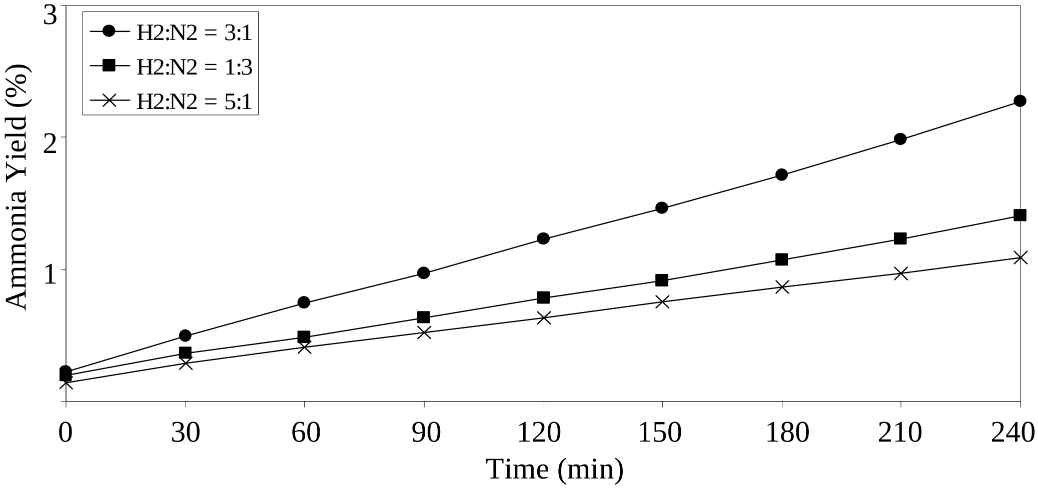

Figure 4.43: Effect of various volume ratios of reactants gas (H_2:N_2) on ammonia yield produced using 5% α-Fe_2O_3/γ-Al_2O_3 nanocatalyst (2:1). T = 110^oC, P = 1 atm, H-F = absence, Cat. = 0.2 g, GHSV = 12000 cm^3/g_{cat}.h, F = 40 cm^3/min, H_2:N_2 = 3:1, 1:3 and 5:1. The ammonia yield was collected for 1 minute at each 30 minutes interval.

The 3:1 H_2:N_2 ratio resulted in highest ammonia yield as compared to others (Figure 4.43). This ratio agrees with the general chemical equation for producing ammonia [20]. The 1:3 ratio resulted in lower yield than that of 3:1 ratio. This trend was also reported in literature [14] which might be due to insufficient hydrogen to react with surplus nitrogen molecules. Furthermore, the lowest ammonia yield was attained using the 5:1 ratio (Figure 4.43) which could be due to inhibiting effect of increasing the fraction of H_2 adsorbed.

The 3:1 is the optimum ratio of H_2:N_2 as it produced highest ammonia yield. This ratio was applied in examining the effect of different feed gas flow rates.

4.2.2.3 Effect of Feed Gas Flow Rate

This study used the supported 5% α-Fe_2O_3/γ-Al_2O_3 nanocatalyst obtained at $Fe(NO_3)_3$:SBS ratio of 2:1. The reaction was conducted at H_2:N_2 of 3:1, space velocity of 12000 cm^3/g_{cat}.h, reaction temperature of 110^{o}C and under atmospheric pressure. The feed gas flow rates were varied at 28 cm^3/min, 40 cm^3/min and 100 cm^3/min. The result is shown in Figure 4.44.

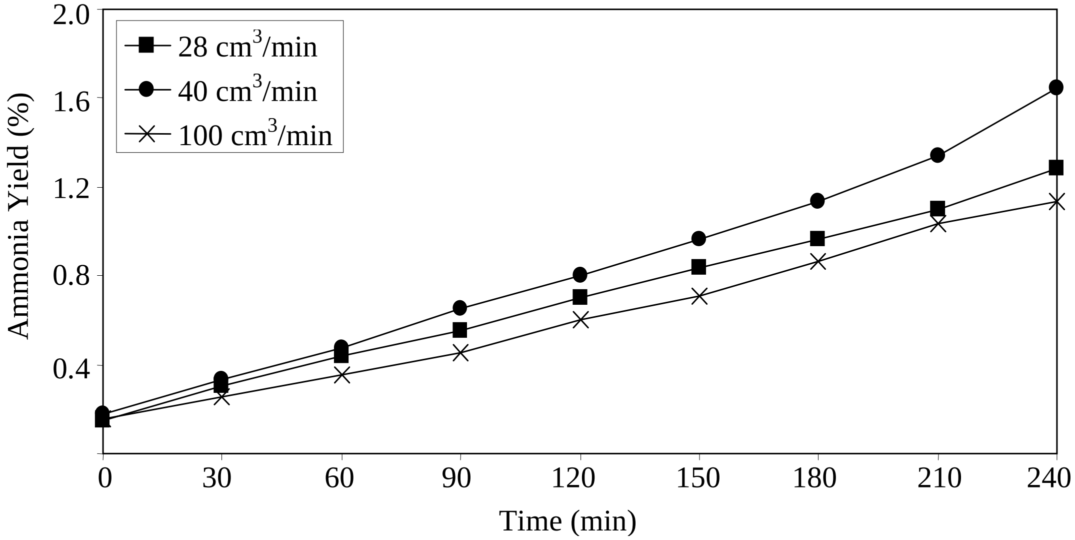

Figure 4.44: Effect of various total feed gas flow rates on ammonia yield produced over supported 5% α-Fe_2O_3/γ-Al_2O_3 nanocatalyst (2:3). T = 110^{o}C, P = 1 atm, H-F = Absence, Cat. = 0.2 g, GHSV = 8400 cm^3/g_{cat}.h – 30000 cm^3/g_{cat}.h - , F = 28 cm^3/min – 100 cm^3/min, H_2:N_2 = 3:1. The ammonia yield was collected for 1 minute at each 30 minutes interval.

Higher ammonia yield was obtained at total feed flow rate of 40 cm^3/min (Figure 4.44) compared to those at 28 cm^3/min and 100 cm^3/min. Decreasing the gas flow rate to 28

cm^3/min reduced the ammonia yield due to increase in the time of travelling for reactant gas to arrive at the catalyst surface, thus decelerating the catalytic processes. However, excessive feeding rate will speed up the movement of the molecules but reduce the contact time which might not provide sufficient chance for the incoming molecules to undergo surface reaction process. Figure 4.45 describes the relation between the ammonia yield recorded at t= 240 mins (Figure 4.44) and the space velocity.

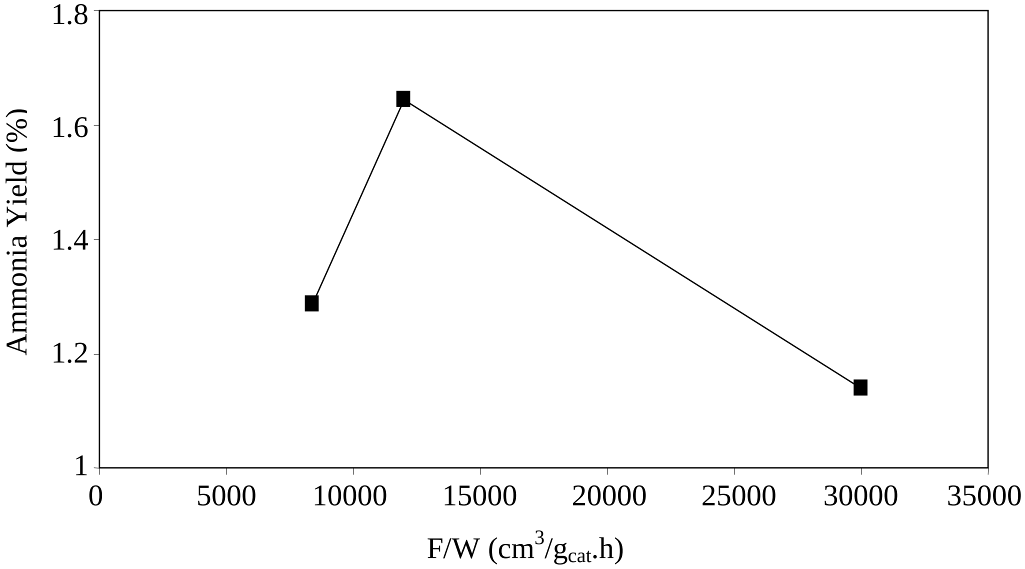

Figure 4.45: Effect of various space velocities on ammonia yield produced using 5% α-Fe_2O_3/γ-Al_2O_3 nanocatalyst (2:3). T = 110^oC, P = 1 atm, H-F = Absence, Cat. = 0.2 g, GHSV = 8400 cm^3/g_{cat}.h – 30000 cm^3/g_{cat}.h, F = 28 cm^3/min – 100 cm^3/min, H_2:N_2 = 3:1.

According to Figure 4.45, 12000 cm^3/g_{cat}.h (40 cm^3/min) was found to be an optimum space velocity as it produced highest yield than that of at 28 cm^3/min and 100 cm^3/min. As reported by L. Xiaonian et al. [123], the catalytic activity performed at 400^oC and 150 atm, reduced by a factor of two when the space velocity was increased from 5000 h^{-1} to 50000 h^{-1}.

A comparison on the ammonia yield obtained between unsupported and supported nanocatalysts was made and the result is illustrated in Figure 4.46. It is proven that the presence of metal-support interaction enhanced the catalytic activity as obtained by 5% α-Fe_2O_3/γ-Al_2O_3 nanocatalyst. The 5% α-Fe_2O_3/γ-Al_2O_3 resulted in the ammonia yield about 10 times higher than that of unsupported α-Fe_2O_3 nanocatalyst (Figure 4.46). This enhancement is due to the presence of support which prevents the agglomeration of particles (Section 2.9.2)

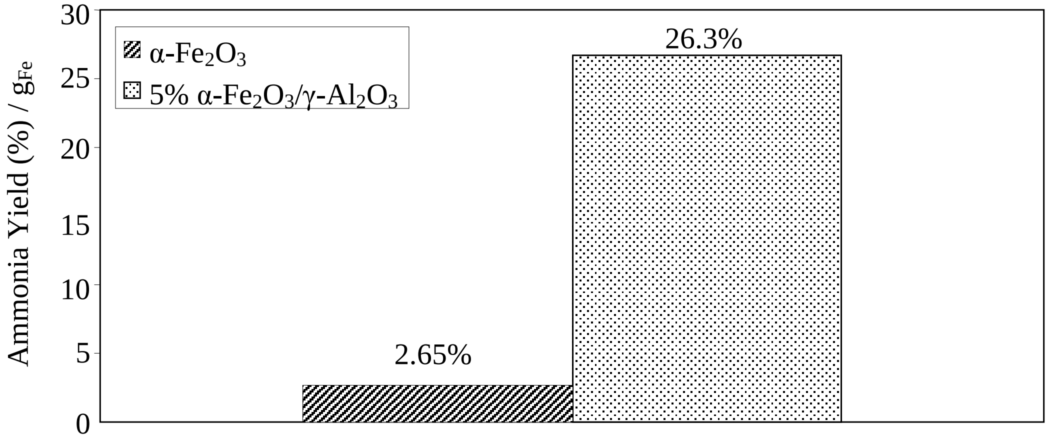

Figure 4.46: Ammonia yield comparison between unsupported α-Fe_2O_3 and supported 5% α-Fe_2O_3/γ-Al_2O_3 nanocatalysts. T = 110°C, P = 1 atm, H-F = Absence, Cat. = 0.2 g, GHSV = 12000 $cm^3/g_{cat}.h$, F = 40 cm^3/min, $H_2:N_2$ = 3:1. The ammonia yield was collected 1 minute for 30 mins.

The ammonia yield produced per gram of catalyst for all prepared nanocatalysts is summarized in Figure 4.47.

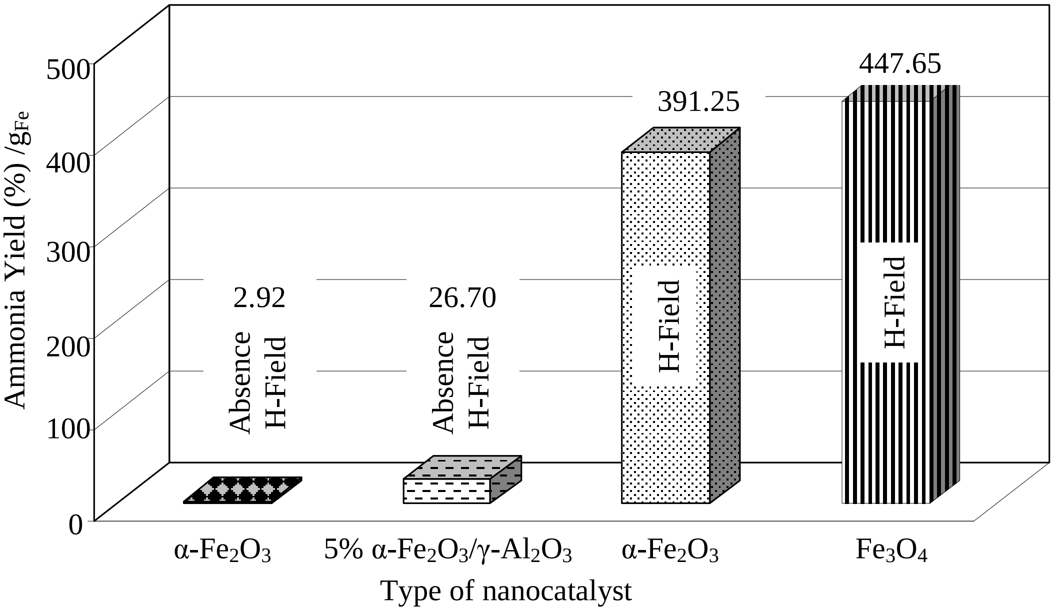

Figure 4.47: Summary on ammonia yield produced per gram of catalyst for all prepared nanocatalyst. T = 110°C, P = 1 atm, Cat. = 0.2 g, GHSV = 12000 $cm^3/g_{cat}.h$, F = 40 cm^3/min, $H_2:N_2$ = 3:1. The ammonia yield was collected for 30 mins.

In the absence of magnetic field, the supported 5% α-Fe_2O_3/ γ-Al_2O_3 catalyst showed activity 10 times higher than that of unsupported α-Fe_2O_3 catalyst (Figure 4.47). Dispersing α-Fe_2O_3 particles on a γ-Al_2O_3 minimized the agglomeration of iron nanoparticles, which increased the surface area of the nanocatalyst, thus more active sites were created for H_2 and N_2 to react, hence enriching the catalytic activity. A combination between nanotechnology and magnetism improved the catalytic activity. As shown in Figure 4.47, the activity was enhanced by about 145 times as a result of applying magnetic field to the reaction in the presence of α-Fe_2O_3 catalyst. Exerting magnetic field reduced the difficulty in pairing or exchanging the electrons between Fe and H_2 and N_2 molecules, thus enhanced the catalytic activity. Therefore, the hypothesis made in Section 1.3 is proven.

A summary on catalytic performance observed in this work and from previous investigations is summarized in Table 4.24. The ammonia yield, under influence of magnetic field, in the presence of α-Fe_2O_3 and Fe_3O_4 nanocatalysts in this investigation was approximately 18-20 times more active than those of K-Fe/C and K-Fe-Ru/C, which was conducted at 350^oC and 1 atm [6] (Table 4.24). Activity involving K-Ru/C catalyst conducted at 350^oC and 1 atm, performed by H. Mahapatra et al. [6] was about 12-14 times less active than those of α-Fe_2O_3 and Fe_3O_4 nanocatalysts in the presence of magnetic field (Table 4.24). Supported 5% α-Fe_2O_3/γ-Al_2O_3 showed better performance compared to those of K-Fe/C and K-Fe-Ru/C catalysts. However, the activity of 5% α-Fe_2O_3/γ-Al_2O_3 was about 1.2 less active than that of K-Ru/C which could be due to the use of Ru as the active metal. As elucidated in Section 2.1, dissociation of N_2 is extremely active using Ru which enhanced the catalytic activity [12], [20]. Catalytic activity of $Fe_{1-x}O$ and Fe_3O_4 catalysts with the particle size of 0.2-0.3 and 1.0-1.4 mm at high pressure was much higher [123]-[124] than those of results obtained in this investigation (Table 4.24).

Table 4.24: Comparison of ammonia yields.

Reference	Catalyst	Particle size	Metal Loading (wt.%)	Ammonia Synthesis Conditions				
				T (^{o}C)	P (atm)	H_2:N_2 ratio	Other	Rate
This work	α-Fe_2O_3	31.47 nm	-	110	1	3:1	With H-Field	7.70×10^{-3} mole.$g_{cat}^{-1}h^{-1}$
This work	Fe_3O_4	31.72 nm	-	110	1	3:1	With H-Field	8.81×10^{-3} mole.$g_{cat}^{-1}h^{-1}$
This work	α-Fe_2O_3	31.47 nm	-	110	1	3:1	Without H-Field	5.30×10^{-5} mole.$g_{cat}^{-1}h^{-1}$
This work	α-Fe_2O_3/γ-Al_2O_3	-	5 Fe_2O_3	110	1	3:1	Without H-Field	5.26×10^{-4} mole.$g_{Fe}^{-1}h^{-1}$
[6]	K-Fe/C	-	1.2 Fe	350	1	3:1	Without H-Field	~4.27×10^{-4} mole.$g_{Fe}^{-1}h^{-1}$
[6]	K-Fe-Ru/C	-	0.6 Fe and 0.6 Ru	350	1	3:1	Without H-Field	~4.85×10^{-4} mole.$g_{FeRu}^{-1}h^{-1}$
[6]	K-Ru/C	-	1.2 Ru	350	1	3:1	Without H-Field	~6.30×10^{-4} mole.$g_{Ru-}^{1}h^{-1}$
[122]	$Fe_{1-x}O$	0.2-0.3 mm	-	475	150	3:1	Without H-Field	9.00×10^{-2} mole.$g_{cat}^{-1}h^{-1}$
[123]	Fe_3O_4	1.0-1.4 mm	-	400	150	3:1	Without H-Field	6.00×10^{-2} mole.$g_{cat}^{-1}h^{-1}$
[125]	Fe/γ-Al_2O_3	-	2.3 Fe	310	40	3:1	Without H-Field	1.87×10^{-3} mole.$g_{Fe}^{-1}h^{-1}$

CHAPTER 5

CONCLUSION

5.1 Conclusion

Three different types of iron based-nanocatalysts consisting of α-Fe_2O_3, Fe_3O_4 and 5% α-Fe_2O_3 supported on γ-Al_2O_3 were successfully synthesized via so-gel and sol gel-hydrothermal methods.

Effects of period of stirring, annealing temperature, synthesis temperature and inclusion of surfactant were tested in nanocatalyst preparation. For sol-gel method, extending period of stirring from 1 day to 1 month reduced the particle size of α-Fe_2O_3 nanocatalyst from 60 nm to 27 nm while increasing annealing temperature from 300^{o}C to 700^{o}C enlarged the particle size by a factor of three as shown by XRD interpretation. The H_2-TPR examination exhibited that a decrease in iron particle size caused the reduction process to be accomplished at much higher temperature. A hybrid method namely sol gel-hydrothermal was found to be the best synthesis method in producing a highly crystallined Fe_3O_4 nanocatalyst at synthesis temperature of 160^{o}C and exhibited the highest magnetization value compared to those of other methods. Introducing surfactant in preparing 5% α-Fe_2O_3/γ-Al_2O_3 improved the physicochemical features of this catalyst model. The iron (III) nitrate to surfactant ratio of 2:3 enhanced the Fe particles dispersion by approximately 90% as indicated by H_2-TPR and EDX-mapping.

Catalytic evaluation studies proved that introduction of magnetic field to the reaction enhanced the ammonia yield by 145 times using α-Fe_2O_3 nanocatalyst at reaction conditions of 110^{o}C and 1 atm. The ammonia yield was further increased by 15% using Fe_3O_4 compared to that of α-Fe_2O_3 nanocatalysts at the same reaction conditions. The 5% α-Fe_2O_3/γ-Al_2O_3 produced ammonia yield 10 times higher than that of unsupported α-Fe_2O_3, recorded in absence of magnetic field. This study successfully discovered that a combination of nanotechnology and magnetism concept could lead to higher ammonia yield production. The severity of the reaction was also successfully minimized. The catalytic activity was accelerated by utilizing supported α-Fe_2O_3 nanocatalyst.

5.2 Recommendations

The recommendations to improve this study are as follow:

1. The microreactor should be able to work at much higher temperature and pressure to ensure that the activation process can occur completely.

2. Reaction at high pressure should be conducted in the absence and presence of magnetic field to get a clear examination on the effect of magnetic field.

3. The magnetic field strength should be varied to determine the effect of magnetic field strength to the ammonia synthesis reaction.

4. The reactor should be equipped with an online gas chromatograph (GC) in order to improve detection and quantification of ammonia.

5. Effect of applying magnetic field to α-Fe_2O_3/γ-Al_2O_3 nanocatalyst on the ammonia yield should be investigated.

REFERENCES

[1] D. F. Shriver and P. W. Atkins, *Inorganic Chemistry*, 3rd ed. Oxford, United Kingdom: Oxford University Press, 1999.

[2] N. Kumar, “Structure Sensitive Adsorption of Hydrogen on Ruthenium and Ruthenium-silver Catalysts Supported on Silica,” Ph.D. dissertation, Ames Lab., Iowa State Univ., Ames, Iowa, 1999.

[3] *Ammonia: Physical and Chemical Information* [Online]. Availabe: http://www.atsdr.cdc.gov/ToxProfiles

[4] C. M. Roebuck, *Excel HSC Chemistry*, 1st ed. New South Wales, Australia: Pascal Press, 2004.

[5] United States Geological Survey Mineral Resources Program. (2008, June 13). *Ammonia: World Production by Country* [Online]. Available: http://www.indexmundi.com.

[6] H. Mahapatra, E. S. Kalyuzhnaya, S.M. Yunusov and V.B. Shur, “Synergism of iron and ruthenium in ammonia synthesis catalyst at low temperature,” *Stud. Surface Sci. and Catalysis*, vol.113, pp. 267-270, 1998.

[7] C. Liang, Z. Wei, Q. Xin and C. Li, “Ammonia synthesis over Ru/C catalysts with different carbon supports by barium and potassium compounds,” *Appl. Catalysis A: General*, vol. 208, issue 1-2, pp. 193-201, Feb. 2001.

[8] J. R. Rennings, *Catalytic Ammonia Synthesis: Fundamental and Practice*, 2nd ed. Spring Street, New York: Plenum Press, 1994.

[9] C. H. Bartholomew and R. J. Farrauto, *Fundamental of Industrial Catalytic Process*, 2nd ed. Hoboken, New Jersey: Wiley Interscience, 2006.

[10] K. M. Whitten, R. E. Dais, M. L. Peck and G. G. Stanley, *General Chemistry*, 7th ed. Belmont, CA: Thomson Brooks/Cole , 2004.

[11] G. A. Samorjai, *Introduction to Surface Chemistry and Catalysis*, 1st ed. Hoboken, New Jersey: Wiley Interscience, 1994.

[12] D. A. McQuarrie and J. D. Simon, *Physical Chemistry: A Molecular Approach*, 1st ed. Sausalito, CA: University Science Books, 1997.

[13] S. Bencic. (2001, April). *Literature Report: Ammonia Synthesis Promoted by Iron Catalysts* [Online]. Available: http://www.cem.msu.edu/~cem924sg/SandraBencic.pdf.

[14] F. Rosowski, A. Hornung, O. Hinrichsen, D. Herein, M. Muhler and G. Ertl, "Ruthenium catalysts for ammonia synthesis at high pressures: Preparation, characterization, and power-law kinetics," *Appl. Catalysis A: General,* vol. 151, pp. 443-460, 1997.

[15] Oxford Laboratory. (2010). *Price List* [Online]. Available: http://www.oxfordlabchem.com/price_c.html.

[16] J. M. Köhler and W. Fritzsche, *Nanotechnology: An Introduction to Nanostructuring Techniques,* 2nd ed. Weinheim, Germany: Villey-VCH Publication, 2007.

[17] F. J. Owens and C. P. Poole, *The Physics and Chemistry of Nanosolids,* 2nd ed. Hoboken, New Jersey: John Wiley & Sons Inc., 2008.

[18] C. J. H. Jacobsen, J. Jiang, S. Morup, B. S. Clausen and H. Topsoe, "Ammonia synthesis over multi-promoted iron catalysts obtained by high-energy ball-milling," *Catalysis Lett.*, vol. 61, no. 3-4, pp. 115-120, June 1999.

[19] A. Jedynak, D. Szmigiel, W. Rarog, J. Zielinski, J. Pielaszek, P. Dluzweski and Z. Kowalczyk, "Potassium-promoted carbon-based iron catalyst for ammonia synthesis: Effect of Fe dispersion," Catalysis Letts., vol. 81, no. 3-4, pp. 213-218, August 2002.

[20] R. M. Cornell and U. Schwertmann, *The Iron Oxides: Structures, Properties, Reactions, Occurrence and Uses,* 1st ed. Weinheim, Germany: VCH Publisher, 1996.

[21] D. Wagner, O. Devisme, F. Pattison and Denis Ablitzer, "A laboratory study of the reduction iron oxides by hydrogen," in *Proc. Sohn International Symp.*, vol. 2. San Diego, 2006, pp. 111-120.

[22] W. K. Jozwiak, E. Kaczmarek, T.P. Maniecki, W. Ignaczak and W. Maniukiewicz, "Reduction behaviour of iron oxides in hydrogen and carbon monoxide atmospheres," *Appl. Catalysis A: General*, vol. 326, issue 1, pp. 17-27, June 2007.

[23] Laboratory of Ohba. (2010, March 12). *Crystal Structures* [Online]. Available: http://www.geocities.jp/ohba_lab_ob_page.

[24] B. Larson. (2009). *Similarities and Different Between the FCC and HCP Structures* [Online]. Available: http://www.ndt-ed.org.

[25] S. O. Pillai, *Solid State Physics*, 5th ed. New Delhi, India: New Age International Publishers, 2003.

[26] J. P. Jakubovics, *Magnetism and Magnetic Materials*, 2nd ed. London, United Kingdom: The Institute of Materials, 1994.

[27] Wikipedia The Free Encylopedia. (2008, November). *Magnetic Domain* [Online]. Available: http://www.wikipedia.org.

[28] Institute for Rock and Magnetism, University of Minnesota. (2008). *Classes of Magnetic Materials* [Online]. Available: http://www.irm.umn.edu.

[29] R. C. Dorf, *The electrical engineering handbook*, 2nd ed., CA: CRC Press, 1997.

[30] Z. L. Wang, Y. Liu and Z. Zhang, *Handbook of Nanophase and Nanostructured Materials: Materials systems and applications*, 2nd Ed. Tsinghua University, Beijing, China: Kluwer Academic/Plenum Publishers, 2003.

[31] R. Vanezuela, M. C. Fuentes, C. Parra, J. Baeza, N. Duran, S.K. Sharma, M. Knobel and J. Freer, "Influence of stirring velocity on the synthesis of magnetite nanoparticles (Fe_3O_4) by co-precipitation method," *J. Alloys and Compounds*, vol. 488, issue 1, pp. 227-231, Nov. 2009.

[32] G. Gnanaprakash, D. Mahadevan, T. Jayakumar, P. Kalyanasundaram, J. Philip and B. Raj, "Effect of initial pH and temperature of ion salt solutions on formation of magnetite nanoparticles," *Materials Chemistry and Physics*, vol. 103, issue 1, pp.168-175, May 2007.

[33] J. Xu, H. Yang, W. Fu, K. Du, Y. Sui, J. Chen, Y. Zeng, M. Li and G. Zuo, "Preparation and magnetic properties of magnetite nanoparticles by sol gel method," *J. Magnetism and Magnetic Materials*, vol. 309, issue 2, pp. 307-311, Feb. 2007.

[34] X. Wu, J. Tang, Y. Zhang and H. Wang, "Low temperature synthesis of Fe_3O_4 nanocrystals by hydrothermal decomposition of a metallorganic molecular precursor," *Materials Sci. Eng. B*, vol. 157, issues 1-3, pp. 81-86, Feb. 2009.

[35] H. Zhu, D. Yang and L. Zhu, "Hydrothermal growth and characterization of magnetite (Fe_3O_4) thin films," *Surface and Coatings Technology*, vol. 201, issue 12, pp. 5870-5874, March 2007.

[36] Z. Yuanbi, Q. Zumin and H. Jiaying, "Preparation and analysis of Fe_3O_4 magnetic nanoparticles used as targeted-drug carriers," *Chinese J. Chemical Eng.*, vol. 16, issue 3, pp. 451-455, June 2008

[37] Y. H. Zheng, Y. Cheng, F. Bao and Y. S. Wang, "Synthesis and magnetic properties of Fe_3O_4 nanoparticles," *Materials Research Bulletin*, vol. 41, issue 3, pp. 525-529, March 2006.

[38] J. H. Wu, S. P. Ko, H. L. Liu, M. H. Jung, J. H. Lee, J. S. Ju and Y. K. Kim, "Sub 5 nm Fe_3O_4 nanocrystals via coprecipitation method," *Colloids and Surfaces A: Physicochemical and Eng. Aspects*, vol. 313-314, issue1, pp. 268-272, Feb. 2008.

[39] A. H. Lu, E. L. Salabas and F. Schuth, "Magnetic Nanoparticles: Synthesis, Protection, Functionalization, and Application," *Angewantde Chemie Int.*, volume 46, issue 8, pp. 1222–1244, Feb. 2007.

[40] S. Akbar, S. K. Hasanain, N. Azmat and M. Nadeem. (2004). *Synthesis of Fe_2O_3 nanoparticles by sol gel method and their structural and magnetic characterizations* [Online]. Available: http://arxiv.org/ftp/cond-mat/papers/0408/0408480.pdf.

[41] C. Chen, O. Kitakami and Y. Shimada, "Particle size effects and surface anisotropy in Fe-based granular films," *J. Appl. Physics*, vol. 84, issue 4, pp. 2184-2188, Aug. 1998.

[42] A. R. West, *Solid State Chemistry and Its Applications*, 1st ed. Aberdeen, UK: John Wiley and Sons, 1987

[43] F. Szabadváry, *History of Analytical Chemistry,* 2nd ed. Langhome, Pennsylvania: Grodon and Breach Science Publisher, 1992.

[44] J. Livage and M. Henry, C. Sanchez, "Sol-Gel Chemistry of Transition Metal Oxides," *Progress in Solid State Chemistry*, vol. 18, issue 4, pp. 259-341, 1988.

[45] R. Szostak, *Molecular Sieves: Principles of Synthesis and Identification*, 2nd ed. London, United Kingdom: Blackie Academic & Professional, 1998.

[46] C. Liu, X. Wu, T. Klemmer, N. Shukla, X. Yang, D. Weller, A.G. Roy, M. Tanase and D. Laughlin, "Polyol process synthesis of monodispersed FePt nanoparticles," *J. Physical Chemistry: B*, vol. 108 (20) pp. 6121-6123, April 2004.

[47] Q. Liao, R. Tannenbaum and Z. L. Wang, "Synthesis of $FeNi_3$ nanoparticles by hydrothermal reduction," *J. Physical Chemistry B*, vol. 110, no. 29, pp. 14262-14265, June. 2006.

[48] I. Nedkov, T. Merodiiska, L. Slavov, R. E. Vandenberghe, Y. Kusano and J. Takada, "Surface Oxidation, size and shape of nano-sized magnetite obtained by co-precipitation," *J. Magnetism and Magnetic Materials*, vol. 300, issue 2, pp. 358-367, May 2006.

[49] D. Thapa, V. R. Palkar, M. B. Kurup and S. K. Malik, “Properties of magnetite nanoparticles synthesised through a novel chemical route,” *Materials Lett.*, vol. 58, issue 21, pp. 2692-2694, Aug. 2004.

[50] Y. Sun and H. Zeng, “Size-Controlled Synthesis of Magnetite Nanoparticles,” *J. American Chemical Soc.*, vol. 124, issue 28, pp. 8204-8205, June. 2002.

[51] G. Pecchi, P. Reyes and J. Villasenor, “Fe Supported Catalysts Prepared by The Sol Gel Method. Characterization and Evaluation in Phenol Abatement,” *J. Sol-Gel Sci. and Technology,* vol. 26, no. 1-3, pp. 865–867, Jan. 2003.

[52] W. W. Wang, Y. J. Zhu and M. L. Ruan, “Microwave-assisted synthesis and magnetic property of magnetite and hematite nanoparticles,” *J. Nanoparticle Research*, vol. 9, no. 3, pp. 419-426, June 2007.

[53] R. Fan, X. H. Chen, Z. Gui, L. Liu and Z.Y. Chen, “A new simple hydrothermal preparation of polycrystalline magnetite Fe_3O_4,” *Materials Research Bulletin*, vol. 36, issues 3-4, pp. 497-502, March 2001.

[54] Y. Li, H. Liao and Y. Qian, “Hydrothermal synthesis of ultrafine α-Fe_2O_3 and Fe_3O_4 powders,”*Materials Research Bulletin*, vol. 33, issue 6, pp. 841-844, June 1998.

[55] A. A. Burukhin, B. R. Churagulov, N. N. Oleynikov and A. V. Knot’ko, “Hydrothermal synthesis of mesoporous iron oxide powders,” in *Proc. Joint Sixth Int. Symp. Hydrothermal Reactions and Fourth Conf. on Solvo-Thermal Reactions*, Kochi, Japan, 2000, pp. 561-564.

[56] K. D. Kim, S. S. Kim, Y. H. Choa and H. T. Kim, “Formation and surface modification of Fe_3O_4 nanoparticles by co-precipitation and sol gel method,” *J. Ind. and Eng. Chemistry*, vol. 13, no. 7, pp. 1137-1141, Nov. 2007.

[57] S. Kim, U. Paik and J. Park, “Effect of calcination time on the physical properties of synthesized ceria particles for the shallow trench isolation chemical mechanical planarization process,” *J. Ceramic Process. Research,* vol. 7, no. 1, pp. 53-57, June 2006.

[58] K. P. Sanosh, M. C. Chu, A. Balakrishnan, T.N. Kim and S. J. Ho, “Preparation and characterization of nano-hydroxypatite powder using sol-gel technique,” *Bulletin Materials of Sci.*, vol. 32, no. 5, pp. 465-470, Oct. 2009.

[59] S. R. Janasi, D. Rodrigues and F. J. G. Landgraf, “Effect of Calcination Conditions on the Magnetic Properties of MnZn Ferrites Powders Produced by Co-precipitation,” *Materials Sci. Forum*, vol. 498-499, pp. 119-124, Nov. 2005.

[60] S. Shetty, V. R. Palkar and R. Pinto, "Size effect study in magnetoelectric $BiFeO_3$ system," *PRAMANA- J. Physics*, vol. 58, no. 5-6, pp.1027-1030, May 2002.

[61] C. H. Lu, W. H. Wu and R. B. Kale, "Synthesis of photocatalytic TiO_2 thin films via the high-pressure crystallization process at low temperatures," *J. Hazardous Materials*, vol. 147, issue 1-2, pp. 213-218, Aug. 2007.

[62] J. D. Wright and N. A. J. M. Sommerdik, *Sol-Gel Materials Chemistry and Applications*, 4th ed. Boca Raton, Florida: CRC Press, 2001.

[63] R. Balasubramaniam, A. V. Ramesh Kumar and P. Dillmann, "Characterization of rust on ancient Indian iron," *Current Sci.*, vol. 85, no. 11, pp. 200-204, Dec. 2003.

[64] M. Kucher, D. Babic and M. Kind, "Precipitation of barium sulfate: Experimental investigation about the influence of supersaturation and free lattice ion ratio on particle formation," *Chemical Eng. and Process.*, vol. 45, issue 10, pp. 900–907, Oct. 2006.

[65] M. A. Legodi and D.Wall, "The preparation of magnetite, goethite, hematite and maghemite of pigment quality from mill scale iron waste," *J. Dye and Pigments*, vol. 74, issue 1, pp. 167-168, Sept. 2007.

[66] R. A. Zarate, F. Hevia, S. Fuentes, V. M. Fuenzalida and A. Zuniga, "Novel Route to Synthesize CuO nanoplates," *J. Solid State Chemistry*, vol. 180, pp. 1464-1469, Jan. 2007.

[67] S. Komarneni, "Nanophase Materials by Hydrothermal, Microwave-Hydrothermal and Microwave-Solvothermal Methods," *Current Sci.*, vol. 85, no. 12, pp. 1730-1734, Dec. 2000.

[68] Y. Hakuta, H. Ura, H. Hayashi and K. Arai, "Effets of Hydrothermal Conditions on The Particles Size of γ-AlO(OH) in sub and supercritical water using a flow reaction system," *Materials Chemistry and Physics*, vol. 93, issues 2-3, pp. 466-472, Oct. 2005.

[69] G. J. K. Acres, A. J. Bird, J. W. Jenkins and F. King, "The Design and Preparation of Supported Catalysts," *Roy. Soc. Chemistry*, vol. 4, pp.1-30, Jan. 1981.

[70] R. A. Santen, "Catalysis: An integrated approach," *Stud. Surface Sci. and Catalysis*, vol. 2, p. 459-485, Sep. 1999.

[71] P. Michorczyka, P. Kustrowski, L. Chmielarzb and J. Ogonowskia, "Influence of redox properties on the activity of iron oxide catalysts in dehydrogenation of propane with CO_2," *Reaction Kinetics and Catalysis Lett.*, vol. 82, no.1, pp. 121-130, Dec. 2003.

[72] J. Y. Park, Y. J. Lee, P. K. Khanna, K. W. Jun, J. W. Bae and Y. H. Kim, “Alumina-supported iron oxide nanoparticles as Fischer–Tropsch catalysts: Effect of particle size of iron oxide,” *J. Molecular Catalysis A: Chemical*, vol. 323, issue 1-2, pp. 84–90, May 2010.

[73] A. Pineau, N. Kanari and I. Gaballah, “Kinetics of reduction of iron oxides by H_2 Part I: Low temperature reduction of hematite,” *Thermochimica Acta*, vol. 447, issue 1 pp. 89–100, Aug. 2006.

[74] E. V. Steen and C. Claeys, *Recent advances in the science and technology of zeolites and related materials*, Houston, Texas: Gulf Professional Publishing – Technology and Engineering, pp. 2387-2394, 2004.

[75] H. Y. Lin, Y.W. Chen and C. Li, “The mechanism of reduction of iron oxide by hydrogen,” *Thermochimica Acta*, vol. 400, issues 1-2, pp. 61-67, April 2003.

[76] M. Liang, W. Kang and K. Xie, “Comparison of reduction behaviour of Fe_2O_3, ZnO and $ZnFe_2O_4$ by TPR Technique,” *J. Natural Gas Chemistry*, vol. 18, issue 1, pp. 110-113, March 2009.

[77] G. Giecko, T. Borowiecki, W. Gac and J. Kruk, “Fe_2O_3/Al_2O_3 catalysts for the N_2O decomposition in the nitric acid industry,” *Catalysis Today*, vol. 137, issues 2-4, pp. 403-409, Sept. 2008.

[78] C. Messi, P. Carniti and A. Gervasini, “Kinetics of reduction of supported nanoparticles iron oxide,” *J. Thermal Analysis and Calorimetry*, vol. 91, no. 1, pp. 93–100, Jan. 2008.

[79] A. Pineau, N. Kanari and I. Gaballah, “Kinetics of reduction of iron oxides by H_2 Part II: Low temperature reduction of magnetite,” *Thermochimica Acta*, vol. 456, issue 2, pp. 75-88, May 2007.

[80] R. Brown, M. E. Cooper and D. A. Whan, “Temperature Programmed Reduction of Alumina-Supported Iron, Cobalt and Nickel bimetallic catalysts,” *Appl. Catalysis*, vol. 3, issue 2, pp.177-186, July 1982.

[81] H. J. Wan, B. S. Wu , C. H. Zhang, H. W. Xiang ,Y. W. Li, B. F. Xu and F. Yi, “Study on Fe–Al_2O_3 interaction over precipitated iron catalyst for Fischer–Tropsch synthesis,” *Catalysis Commun.*, vol. 8, issue 10, pp.1538–1545, Oct. 2007.

[82] K. W. Kolasinski, *Surface Science: Foundation of Catalysis and Nanoscience*, 2nd ed. West Sussex, United Kingdom: Wiley-Interscience, 2008, pp. 452-454.

[83] *Adsorption of gases on solid* [Online]. Available: http://www.ece.eng.wayne.edu/~jchoi/Adsorption%20of%20gases%20on%20solids.pdf.

[84] K. Tock. (1999). *The Crossover* [Online]. Available: http://www.web.tock.com.

[85] R. S. Swathi and K. L. Sebastian, "Molecular Mechanism of Heterogeneous Catalysis, General Article: The 2007 Nobel Prize in chemistry," *Humanities, Social Sci. and Law*, vol.13, no. 6, pp. 548-560, June 2008.

[86] L. M. Falicov and G. A. Somorjai, "Correlation between catalytic activity and bonding and coordination number of atoms and molecules on transition metal surfaces: Theory and experimental evidence," in *Proc. Of the National Academy Sciences*, USA, vol.82, no. 8, 1985, pp. 2207-2211.

[87] J. Hagen, *Industrial catalysis: a practical approach*, 2nd ed. Weinheim, Germany: Wiley-Interscience, 2006, pp. 189-192.

[88] P. C. J. Kamer, G. Rothenberg, E. K. Poels and D. S. Brands. (2002, Jan). The Synthesis of Ammonia, Supplementary information for the course: Catalysis, Theory and Applications [Online]. Available: http://www.science.uva.nl/~gadi/pdf_files/Ammonia _synthesis.pdf.

[89] *Collision Theory* [Online]. Available: http://chemicalparadigms.wikispaces.com.

[90] L. M. Aparicio and J. A. Dumesic, "Ammonia synthesis kinetics: Surface chemistry, rate expressions, and kinetic analysis," *Topics in Catalysis*, vol. 1, no. 3-4, pp. 233-252, Sept. 1994.

[91] *Uses and Production of Ammonia (Haber Process)* [Online]. Available: http://www.ausetute.com.au.

[92] J. M. Modak. (2002). *9.4 Chemical Monitoring and Management: 2. Maximize Production* [Online]. Available: http://www.hsc.csu.edu.au.

[93] G. R. Maxwell, *Synthetic Nitrogen Products: A Practical Guide to Products and Processes*, 1st ed. Spring Street, New York: Kluwer Academic/Plenum Publishers, 2005.

[94] P. Moggi, G. Albanesi, G. Predieri and G. Spoto, "Ruthenium cluster-derived catalysts for ammonia synthesis," *Appl. Catalysis A: General*, vol. 123, issue 1, pp. 149-159, March 1995.

[95] J. Iwamoto, M. Itoh, Y. Kajita, M. Saito and K. Machida, "Ammonia synthesis on magnesia supported ruthenium catalysts with mesoporous structure," *Catalysis Commun.*, vol. 8, issue 6, pp. 941-944, June 2007.

[96] Laboratory of Ohba. (2010, March 12). *Crystal Structures* [Online]. Available: http://www.geocities.jp/ohba_lab_ob_page.

[97] G. D. Christian, *Analytical Chemistry*, 6th ed. Washington: John Willey & Sons Incorporation, 2003.

[98] A. C. Oliveira, A. Valentini, P. S. S. Nobre and M. C. Rangel, “Influence of The Starting Materials on The Catalytic Properties of Iron Oxides,” *Reaction Kinetics Catalysis Lett.*, vol. 75, no. 1, pp. 135-140, Aug. 2002.

[99] The Linde Group. (2008). *Gas Chromatography* [Online]. Available: http://www.hiq.lind-gas.com.

[100] H. Z. Liu, X. N. Li and Z. N. Hu, “Development of novel low temperature and low pressure ammonia synthesis catalyst,” *Appl. Catalysis A: General*, vol. 142, issue 2, pp. 209-222, Aug. 1996.

[101] N. Pernicone, F. Ferrero, I. Rosetti, L. Forni, P. Canton, P. Riello, G. Fagherazzi, M. Signoretto and F. Pinna, “Wustite as a new precursor of industrial ammonia synthesis catalysts,” *Appl. Catalysis A: General* vol. 251, issue 1, pp. 121-129, Sept. 2003.

[102] N. Yahya, S. M. S. N. S. Zahari, A. Ramli, N. M. Mohamad, P. Puspitasari and N. L. C. Zul, “Synthesis And Characterization Of Zinc Oxide Nanoparticles Prepared Via Precipitation And Self-Combustion Methods,” in *2009 AIP Conf. Proc.*, vol. 1136, pp. 401-405.

[103] J. C. Huie, “Guided molecular self-assembly: a review of recent efforts,” *Smart Mater. Struct.*, vol. 12, issue 2, pp. 264, Apr. 2003.

[104] D. Brandon and W. D. Kaplan, *Microstructural Characterization of Materials*, 1st ed. Michigan: Johns Willey & Sons Publication, 1999.

[105] T. Bolhuis (1997, September 9). *Vector Vibrating Sample Magnetometer* [Online]. Available: http://www.el.utwente.nl.

[106] F. J. Owens and J. Orosz, “Effect of nanosizing on lattice and magnon modes of hematite,” *Solid State Commun.*, vol. 138, issue 2, pp. 95-98, Apr. 2006.

[107] C. J. Sartoretti, M. Ulmann and B. Alexander, “La photolyse de l’eau et la production et d’oxygene au moyen de l’energie solaire,” Univ. de Geneva, Geneva, Switzerland, Rep. JB06_152152-101747, Nov. 2006.

[108] G. Wang, X. Y. Chen, R. Huang and L. Zhang, “Nano-$CaCO_3$/polypropylene composites made with ultra-high-speed mixer,” *J. Material Sci. Lett.*, vol. 21, no. 13, pp. 985-986, July 2002.

[109] T. Adschiri, Y. Hakuta, K. Sue and K. Arai, “Hydrothermal synthesis of metal oxide nanoparticles at supercritical conditions,” *J. Nanoparticle Research*, vol. 3, no. 2-3, pp. 227-235, June 2001.

[110] C. Livage, A. Safari and L. C. Klein, “Glycol based sol-gel process for the fabrication of ferroelectric PZT thin films,” *J. Sol-Gel Sci. and Technology*, vol. 2, no. 1-3, pp. 605-609, Jan. 2004.

[111] C. Luo, Y. Zhang, X. Zeng, Y. Zeng and Y. Wang, “The role of poly(ethylene glycol) in the formation of silver nanoparticles,” *J. Colloid and Interface Sci.*, vol. 288, issue 2, pp. 444-448, Aug. 2005.

[112] J. C. Yang and Y. G. Shul, “Effects of ethylene glycol addition on the properties of Ru/Al_2O_3 catalyst prepared by solo-gel method,” *Catalysis Lett.*, vol. 36, issues 1-2, pp. 41-49, Aug. 1996.

[113] F. Mizukami, “Design of solid catalysts by sol-gel method using organic polydentate ligands and their catalytic performance,” *J. Japan Petroleum Inst*, vol. 51, no. 6, pp. 332-347, June 2008.

[114] N. Takahashi, N. Kakuta, A. Ueno, K. Yamaguchi, T. Fujii, “Characterization of iron oxide thin film prepared by the sol gel method,” *J. Materials Sci.*, vol. 26, no. 2, pp. 497-504, Feb. 1991.

[115] Z. Jiang, Q. Niu and W. Deng, “Hydrothermal synthesis of CuO nanostructures with novel shapes,” *Nanoscience*, vol. 12, no. 1, pp. 40-44, May 2007.

[116] N. R. E. Radwan, E. A. El-Sharkawy and A. M. Youssef, “Influence of gold and manganese as promoters on surface and catalytic performance of Fe_2O_3/Al_2O_3 system,” *Appl. Catalysis A: General*, vol. 281, issues 1-2, pp. 93-106, March 2005.

[117] M. J. Tiernan, P. A. Barnes and G. M. B. Parkes, “Reduction of Iron Oxide Catalysts: The Investigation of Kinetic Parameters Using Rate Perturbation and Linear Heating Thermoanalytical Techniques,” *J. Physical Chemistry. B*, vol. 105, no. 1, pp. 220-228, Dec. 2001.

[118] M. Boudart, A. Delbouille, J.A. Dumesic, S. Khammouma and H. Topsøe, “Surface, catalytic and magnetic properties of small iron particles : I. Preparation and characterization of samples,” *J. Catalysis,* vol. 37, issue 3, pp. 486-502, June 1975.

[119] A. J. H. M. Kock, H. M. Fortuin and J. W. Geus, “The reduction behavior of supported iron catalysts in hydrogen or carbon monoxide atmospheres,” *J. Catalysis.,* vol. 96, issue 1, pp. 261-275, Nov. 1985

[120] A. F. H. Wielers, A. J. H. M. Kock, C. E. C.A. Hop, J. W. Geus and A. M. van der Kraan, “The reduction behavior of silica-supported and alumina-supported iron catalysts: A Mössbauer and infrared spectroscopic study,” *J. Catal*ysis, vol. 117, issue 1, pp. 1-18, May 1989.

[121] C. H. Zhang, Y. Yang, B. T. Teng, T. Z. Li, H. Y. Zheng, H. W. Xiang and Y. W. Li, “Study of an iron-manganese Fischer–Tropsch synthesis catalyst promoted with copper,” *J. Catalysis*, vol. 237, issue 2, pp. 405, Jan. 2006.

[122] D. R. Strongin and G. A. Somorjai, “The effects of potassium on an ammonia synthesis over iron single-crystal surfaces,” *J. Catalysis*, vol. 109, pp. 51-60, 1998.

[123] L. Xiaonian, L. Huazhang, C. Yaqing and H. Zhangneng, “Analysis on Ammonia Synthesis Over Wustite-Based Iron Catalyst,” *Chinese J. Chem. Eng*, vol. 11, no. 1, pp. 19-26, Jan. 2003.

[124] L. Huazhang and L. Xiaonian, “Precursor of Iron Catalyst for Ammonia Syntheses: Fe_3O_4, Fe1-xO, Fe_2O_3 or Their Mixture,” *Studies in Surface Science and Catalysis*, vol. 130, pp. 2207-2212, July 2000.

[125] N. Homs, P. R. D. L. Piscina, “Iron-Based Ammonia Synthesis Catalysts Prepared via Non-Oxidic Precursors”, *Applied Catalysis*, vol. 59, pp. 249-265, March 1990.

APPENDIX A

AMMONIA YIELD QUANTIFICATION

A.1 5% α-Fe_2O_3/γ-Al_2O_3

Table A1 : Effect of magnetic field and various reaction temperatures on ammonia yield produced in presence of α-Fe_2O_3 nanocatalyst. T=30^oC-190^oC, P = 1 am, H-F = 1 T, Cat. = 0.2 g, GHSV = 12000 $cm^3/g_{cat}.h$, F = 40 cm^3/min, $H_2:N_2$ = 3:1. The ammonia yield was collected for 30 mins at each temperature.

Table A1.1: Ammonia yield produced in the presence of 5% α-Fe_2O_3/γ-Al_2O_3 nanocatalyst synthesized at $Fe(NO_3)_3$:Surf ratio of 2:1

Time (min)	V_{NaOH} (mL)	$Mole_{NH3}$ (mole)	NH_3 Yield (%)
0	22.75	2.25×10^{-6}	0.23
30	20.17	4.83×10^{-6}	0.49
60	17.68	7.32×10^{-6}	0.74
90	15.48	9.52×10^{-6}	0.97
120	12.94	1.21×10^{-5}	1.23
150	10.61	1.44×10^{-5}	1.46
180	8.11	1.69×10^{-5}	1.72
210	5.46	1.95×10^{-5}	1.99
240	2.66	2.23×10^{-5}	2.27

Chemicals used:

Hydrochloric acid, HCl : Volume = 25 mL , [HCl] = 0.001 M

Sodium hydroxide, NaOH : [NaOH] = 0.001

A.1.Quantification of Ammonia

A.1.1 Chemical equations:

$NH_3 + HCl \rightarrow NH_4Cl$ (A.1.1)

The excess HCl was back titrated using NaOH:

$HCl_{Excess} + NaOH \rightarrow NaCl + H_2O$(A.1.2)

A.1.2 Calculations:

1. Mole of HCl_{Excess} = Mole of $NaOH_{Titrated}$ (Equation A.1.1)

   = 0.01M x volume of $NaOH_{Titrated}$

2. Mole of $HCl_{Reacted}$ = Mole (HCl_{Total} –HCl_{Excess})

   = Mole of NH_3

A.2. Ammonia Yield (%)

A.2.1. Chemical equation:

$N_2 + 3H_2 \leftrightarrow 2NH_3$ (A.2.1)

A.2.2. Calculations:

1. Mole of N_2 used = 4.92×10^{-4} mol (Limiting reactant)
2. Mole of H_2 used = 1.47×10^{-3} mol
3. Theoretical mole of NH3 based on Equation A.2.1

   = 2 x mole of N_2

   = 9.84×10^{-4} mol

5. Ammonia yield (%) = (mole actual/mole theoretical) x 100%

Table A1.2: Example of calculation to quantify ammonia yield produced in the presence of 5% α-Fe_2O_3/γ-Al_2O_3 nanocatalyst synthesized at $Fe(NO_3)_3$:Surf ratio of 2:1.

Time (min)	V_{NaOH} (mL)	Mole of NaOH (μmol) = Mole of HCl_{excess} (μmol)	Mole of $HCl_{Reacted}$ (μmol) = Mole of NH_3 (μmol)	Ammonia Yield (%)
0	22.75	= 0.001M x (22.75 mL/1000L) = 2.275 x 10^{-5} mol	= 2.5 x 10^{-5} – 2.275 x10^{-5} = 2.25 x 10^{-6}	= (2.25 x 10^{-6} /9.84 x 10^{-4}) x 100% = 0.23%
30	20.17	= 0.001M x (20.17 mL/1000L) = 2.017 x 10^{-5} mol	= 2.5 x 10^{-5} – 2.017 x10^{-5} = 4.83 x 10^{-6}	= (4.835 x 10^{-6} /9.84 x 10^{-4}) x 100% = 0.49%
60	17.68	= 0.001M x (17.68 mL/1000L) = 1.768 x 10^{-5} mol	= 2.5 x 10^{-5} – 1.768 x10^{-5} = 7.32 x 10^{-6}	= (7.32 x 10^{-6} /9.84 x 10^{-4}) x 100% = 0.74%
90	15.48	= 0.001M x (15.48 mL/1000L) = 1.548 x 10^{-5}	= 2.5 x 10^{-5} – 1.548 x10^{-5} = 9.52 x 10^{-6}	= (9.52 x 10^{-6} /9.84 x 10^{-4}) x 100% = 0.97%
120	12.94	= 0.001M x (12.94 mL/1000L) = 1.294 x 10^{-5}	= 2.5 x 10^{-5} – 1.294 x10^{-5} = 1.21 x 10^{-6}	= (1.21 x 10^{-6} /9.84 x 10^{-4}) x 100% = 1.23%
150	10.61	= 0.001M x (10.61 mL/1000L) = 1.061 x 10^{-5}	= 2.5 x 10^{-5} – 1.061 x10^{-5} = 1.439 x 10^{-6}	= (1.439 x 10^{-6} /9.84 x 10^{-4}) x 100% = 1.46%

180	8.11	= 0.001M x (8.11 mL/1000L) = 0.811 x 10^{-5}	= 2.5 x 10^{-5} – 0.811 x10^{-5} = 1.689 x 10^{-6}	= (1.689 x 10^{-6} /9.84 x 10^{-4}) x 100% = 1.72%
210	5.46	= 0.001M x (5.46mL/1000L) = 0.546 x 10^{-5}	= 2.5 x 10^{-5} – 0.546 x10^{-5} = 1.954 x 10^{-6}	= (1.954 x 10^{-6} /9.84 x 10^{-4}) x 100% = 1.99%
240	2.66	= 0.001M x (2.66 mL/1000L) = 0.266 x 10^{-5}	= 2.5 x 10^{-5} – 0.266 x10^{-5} = 2.234 x 10^{-6}	= (2.234 x 10^{-6} /9.84 x 10^{-4}) x 100% = 2.27%

APPENDIX B

CALCULATION OF ACTIVATION ENERGY

Formula

B.1. Rate of Ammonia Production

Rate = mole of ammonia produced / (mass of catalyst (g) x duration of reaction (t))

= $\text{mole}_{NH3}/g_{cat}.h$

B.2. K_A and K_B [89]

Based on equations proposed by Aparicio et al. [90] at T = 251 ^{o}C and P = 1 atm

$k_A = 3.289 \exp [(50690 \text{ J/mol})/RT]$

$k_B = 7.35 \times 10^{12} \exp [(-59040 \text{ J/mol})/RT]$

Where,

k_A = Rate constant for the formation of ammonia

k_B = Rate constant for the decomposition of ammonia

B.3. Von't Hoff's Equation [10]

$\ln (K_{T1}/K_{T2}) = \Delta H/R\ (1/T_1 - 1/T_2)$

Where,

T = Temperature (K)

K = Equilibrium constant

ΔH = Heat of ammonia production = -92 kJ/mole

R = Gas constant (J/mol.K) = 8.314 J/mole.K

B.4. Ideal Gas Law [10]

PV = nRT

Where,

P= Pressure (atm)

V = Volume (L)

R = Gas constant = 0.0821 L.atm/mol. K

n = Number of mole

T = Temperature (K)

B.5. Mole fraction of component [10]

X_A = no. mol A / (∑ mol of all components)

B.6. Partial pressure of reactant/product [9]

$P_A = X_A \times P_{Total}$

Where,

P_A = Partial pressure of component A

X_A = Mole fraction of A

P_T = Total pressure

B.7. Temkin-Phyzev Equation [90], [101]

Rate ($mole_{NH3}/g_{cat}.h$) = $k_A P_{N2}[(P^3_{H2})/(P^2_{NH3})]^{\alpha} - k_B\,[(P^2_{NH3})/(P^3_{H2})]^{1-\alpha}$

Where,

α is assumed = 0.75 [90], [101]

B.8. Arrhenius equation [10]

$k = Ae^{-Ea/RT}$

$\ln k = \ln A - E_a/RT$

Where,

k = Rate constant

A = Exponential factor

E_a = Activation energy

T = Temperature (K)

Calculation

Determination of reference k_A, k_B and K_{eq}.

Based on work done by Aparicio et al. [90] at T = 251 °C and P = 1 atm, using Equation B.2:

k_A = 3.289 exp [(50690 J/mol)/8.314 x (251+273)]

$= 3.717 \times 10^5$

$k_B = 7.35 \times 10^{12}$ exp [(-59.04kJ/mol)/8.314 x (251+273)]

$= 9.568 \times 10^6$

$K_{eq} = K_R = k_A/k_B = 0.038$

Hematite, α-Fe_2O_3 nanocatalyst in the presence of magnetic field.

T = 30^oC [$T_1 = 30^oC$ $T_2 = 251^oC$ (R)]

A. Rate of Ammonia Production

Using Equation B.1:

Rate = (300 µmole x $1x10^{-6}$) / (0.2 g x 0.5 h)

= 3.0×10^{-3} $mol_{NH3}/g_{cat}.h$

B. Determination of K_{30}

Using Equation B.3:

ln (K_{30}/0.038) = (92000 / 8.314) x (1.391×10^{-3})

ln K_{30}/0.038 = 15.40

$e^{\ln KT1/0.038} = e^{15.40}$

K_{30}/0.038 = 4.876×10^6

K_{30} = 1.853×10^5

C. Determination of P_A

Mole of fed N_2 and H_2

Using Equation B.4:

n_{N2} = PV/RT

= (1.2 atm x 0.01 L)/(0.0821 L.atm/mol. K x 301 K)

= 4.920×10^{-4} mol

n_{H2} = (1.2 atm x 0.03 L)/(0.0821 L.atm/mol. K x 301 K)

= 1.476×10^{-3} mol

n_{NH3} obtained = 300µmol= 3×10^{-4} mol

Using equation B.5:

X_{N2} = (4.920×10^{-4} mol) / [(4.920×10^{-4} + 1.476×10^{-3} + 3×10^{-4}) mol]

= 0.216

X_{H2} = (1.476×10^{-3} mol) / [(4.920×10^{-4} + 1.476×10^{-3} + 3×10^{-4}) mol]

= 0.650

X_{NH3} = (3×10^{-4}mol) / [(4.920×10^{-4} + 1.476×10^{-3} + 3×10^{-4}) mol]

= 0.130

Using equation B.6:

P_{N2} = 0.216 x 1atm = 0.216 atm

P_{H2} = 0.650 x 1 atm = 0.650 atm

P_{NH3} = 0.130 x 1 atm = 0.130 atm

D. Determination of k_A

Using Equation B.7:

$3 \times 10^{-3} = k_A(0.216)[(0.65)^3/(0.13)^2]^{0.75} - k_B[(0.13)^2/(0.65)^3]^{1-0.75}$

$3 \times 10^{-3} = 1.74\ k_A – 0.49\ k_B$

$= 1.74\ k_A – 0.49\ (k_A/K_{30})$

$k_A = 1.724 \times 10^{-3}\ g_{cat}^{-1}.h^{-1}$

APPENDIX C

CALCULATION OF IRON LOADING

C.1 Preparation of 5% α-Fe_2O_3/γ-Al_2O_3 Catalyst in Absence of Sodium Bis(2-ethylhexyl) Sulfosuccinate

Total weight of 5% α-Fe_2O_3/γ-Al_2O_3 catalyst = 2.0 g

5% α-Fe_2O_3 = 5/ 100 x 2.0 g

= 0.1 g

From the chemical equation:

$2Fe(NO_3)_3 + HNO_3 \rightarrow \alpha\text{-}Fe_2O_3$(Equation C.1)

Mole of α-Fe_2O_3 = Mass of α-Fe_2O_3 (g) / MRM of α-Fe_2O_3 ($gmole^{-1}$)

= 0.1 g/159.69 $gmole^{-1}$

= 6.262×10^{-4} moles

Based on Equation C.1:

Mole of $Fe(NO_3)_3$ = 2 mol $Fe(NO_3)_3$: 1 mole α-Fe_2O_3

= ½ x mole of α-Fe_2O_3

= 3.131×10^{-4} moles

Mass of $Fe(NO_3)_3$ = Mole of $Fe(NO_3)_3$ / MMR of $Fe(NO_3)_3$ ($gmole^{-1}$)

= 3.131×10^{-4} moles x 241.86 $gmole^{-1}$

= 0.075 g

Mass of $Fe(NO_3)_3.9H_2O$ required = MRM [($Fe(NO_3)_3.9H_2O$/$Fe(NO_3)_3$)]x Mass of $Fe(NO_3)_3$

= [404.2 $gmole^{-1}$/241.86 $gmole^{-1}$] x 0.075 g

= 0.125 g

C.2 Calculation of Iron (III) Nitrate to Sodium Bis(2-ethylhexyl) Sulfosuccinate (SBS) Ratio

A. Iron (III) nitrate to sodium bis(2-ethylhexyl) sulfosuccinate ratio of 2:1

Mole of $Fe(NO_3)_3$ = 0.075 g / 241.86 $gmole^{-1}$
= 3.131×10^{-4} moles

The mole ratio of $Fe(NO_3)_3$:SBS is 2:1
Mole of SBS surfactant = 1/2 x 3.131×10^{-4} moles
= 1.565×10^{-4} moles
Mass of SBS surfactant = 1.565×10^{-4} moles x 444.56 $gmole^{-1}$
= 0.069 g

B. Iron (III) nitrate to sodium bis(2-ethylhexyl) sulfosuccinate ratio of 2:2

Mole of $Fe(NO_3)_3$ = 0.075 g / 241.86 $gmole^{-1}$
= 3.131×10^{-4} moles

The mole ratio of $Fe(NO_3)_3$:SBS is 2:2
Mole of SBS surfactant = 3.131×10^{-4} moles
Mass of SBS surfactant = 3.131×10^{-4} moles x 444.56 $gmole^{-1}$
= 0.139 g

C. Iron (III) nitrate to sodium bis(2-ethylhexyl) sulfosuccinate ratio of 2:3

Mole of $Fe(NO_3)_3$ = 0.075 g / 241.86 $gmole^{-1}$
= 3.131×10^{-4} moles

The mole ratio of $Fe(NO_3)_3$:SBS is 2:3
Mole of SBS surfactant = 3/2 x 3.131×10^{-4} moles
= 4.696×10^{-4} moles
Mass of SBS surfactant = 4.696×10^{-4} moles x 444.56 $gmole^{-1}$
= 0.208 g

APPENDIX D

X-RAY DIFFRACTION

D.1 X-Ray diffraction spectra

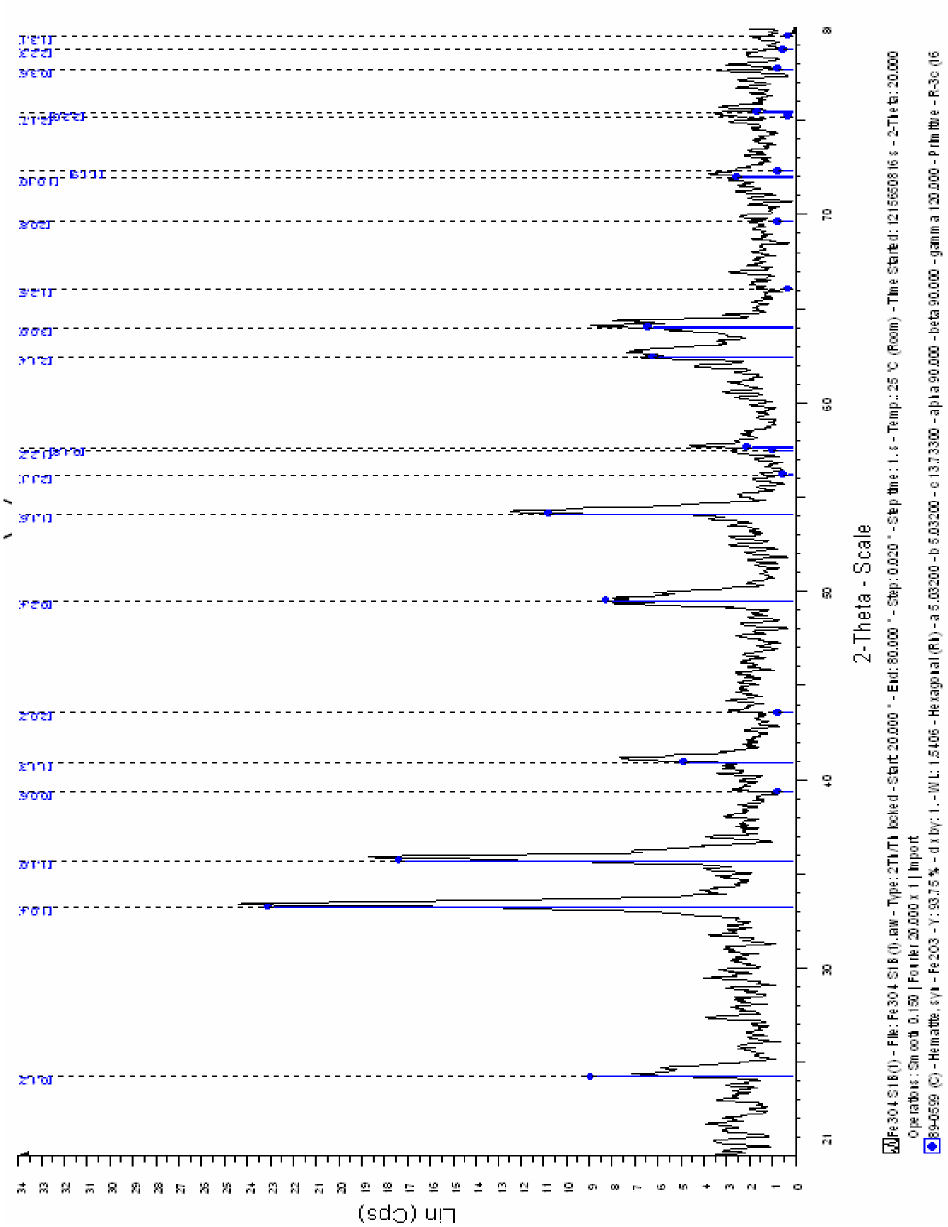

Figure D.1.1 : XRD spectrum of α-Fe_2O_3 nanocatalyst prepared via sol gel method, stirred at 1 day and annealed at 300°C in atmospheric environment.

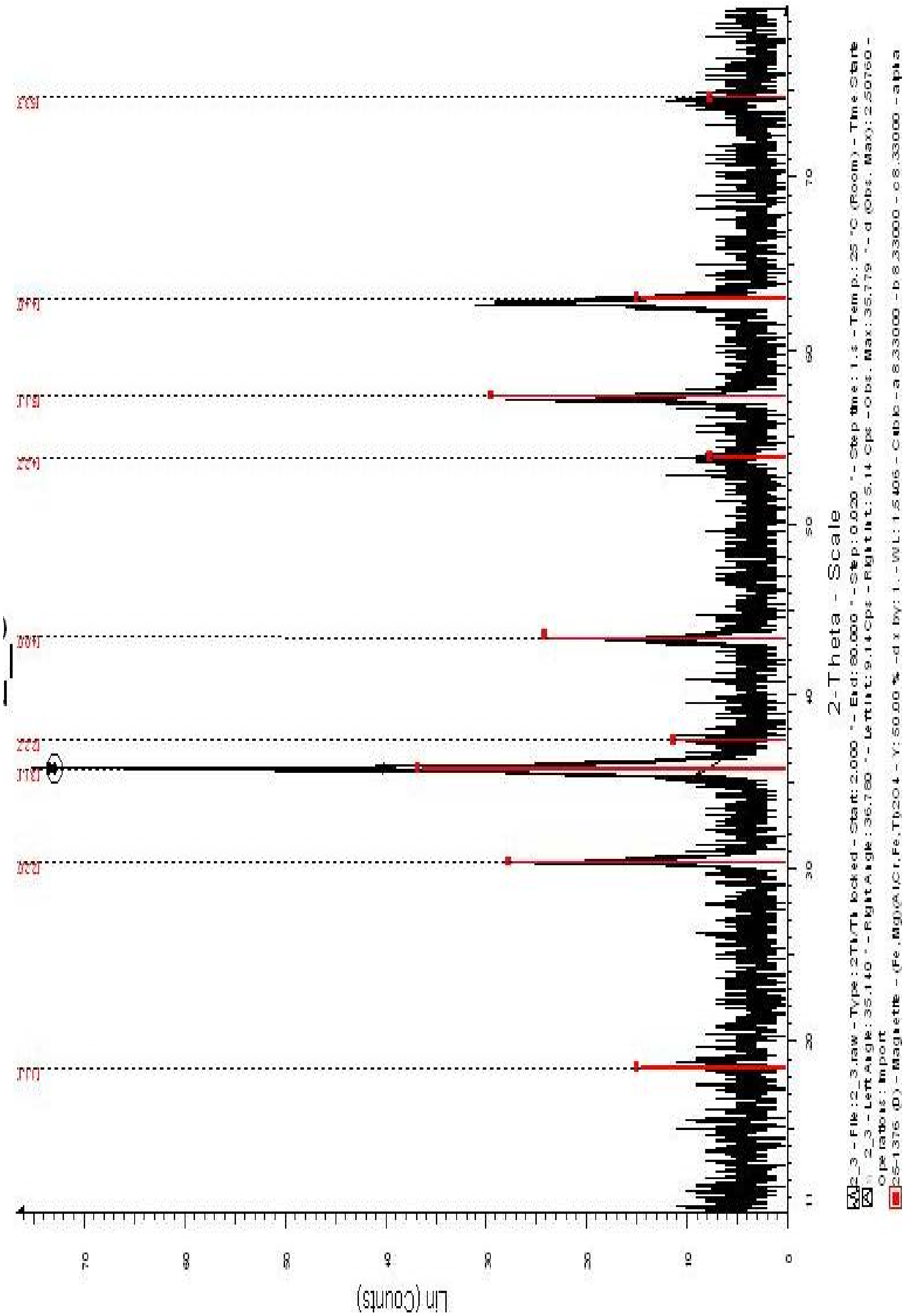

Figure D.1.2 : XRD spectrum of Fe_3O_4 nanocatalyst prepared via sol gel-hydrothermal method 160^{o}C for 10 hours day and annealed at 400^{o}C in vacuum flow.

D.2 Average crystallite size calculation

Table 4.22: XRD data of Fe_3O_4 nanocatalysts prepared via sol gel-hydrothermal method at different annealing temperatures. The interpretation was based on (311) major plane.

Annealing temperature (^oC)	200	300	400
2θ (Degree)	35.46	35.61	35.78
Intensity (a.u)	61.00	52.60	73.00
D-spacing (Å)	2.5294	2.5189	2.5076
FWHM	0.447	0.451	0.268
Average crystallite size(nm)	19.00	18.84	31.73

D.2.1. Formula:

A. Average Crystallite Size, d (nm) = $k\lambda / \beta \cos\theta$ [39]

Where,

k= Shape factor

λ= Wavelength of x-ray

θ= Diffracted angle

β= Full width half maximum of the major peak

B. β (FWHM) = $(\beta \times 2\pi) / 360^o$

C. Values

k= 0.916 [39]

λ_{Cu} = 1.54178×10^{-10} m

1 nm = 1×10^{-9} m

D.2.2. Calculation

(^{o}C)	k λ	$\beta = (\beta x2\pi)/360^{o}$	β cos θ	*d* (nm)
200	$=0.916$ x $1.54178x10^{-10}$ $=1.4122x10^{-10}$	$=(0.447x2\pi)/360^{o}$ $=7.801x10^{-3}$	$=(7.801x10^{-3})\cos 17.73^{o}$ $=7.430x10^{-3}$	19.00
300	$=0.916$ x $1.54178x10^{-10}$ $=1.4122x10^{-10}$	$=(0.451x2\pi)/360^{o}$ $=7.871x10^{-3}$	$=(7.871x10^{-3})\cos 17.80$ $=7.494x10^{-3}$	18.84
400	$=0.916$ x $1.54178x10^{-10}$ $=1.4122x10^{-10}$	$=(0.268x2\pi)/360^{o}$ $=4.677x10^{-3}$	$=(4.677x10^{-3})\cos 17.89$ $=4.450x10^{-3}$	31.73

APPENDIX E

TEMPERATURE PROGRAMMED REDUCTION

E.1 TPR Data of α-Fe_2O_3 Nanocatalyst Prepared via Sol Gel Method, Stirred at 1 day and Annealed at 300°C

TPD/R/O 1100 **Thermo** Electron

Standard Data Report

1.1 Run Nr.: 1203

File:D:\Data 2\shahrul\unsupported Fe2O3\ANNEALED EFFECT\a-Fe2O3- S1-1-300oC annelaed.110
Info:
Operator: Shahrul Room Temperature 28°C Atmospheric Pressure 1000hPa

1.2 Sample

Producer:	shahrul	Sample-Code:	0
Name:	a-Fe2O3	Customer-Code:	0
Mass:	0.1313 g	Support:	
Info:		Metals:	1
Preparation:	Sol gel-annealed at 300oC	0%	Iron

1.3 Pretreatment

Method Name: not defined or external pretreatment Info:
On Instrument: with Ser.Nr. on ,
Started at finished
Gas Port when Ready: (a) Nitrogen
Gas Port when End: (a) Nitrogen
Sample rate: 1 s
Gain: 10
Polarity: +

Phase	With Gas	Flow [ccm/min]	Start at T [°C]	Ramp [°/min]	Stop at T [°C]	Hold for [min]
Cleaning		0		Off		0
1:	Off					
2:	Off					
3:	Off					
4:	Off					
End Pretreatment with Oven Off						

1.4 TPD/R/O

Method Name: a-Fe2O3 Info:
On Instrument: TPDRO1100 MS with Ser.Nr.20022897 on Right Oven
Started 7/13/2009 at 2:24:35 PM finished 4:12:01 PM

With gas: Hydrogen 5.1% in Nitrogen and flow of 20 ccm/min
Start at 40 °C, heating rate 10 °/min, stop at 800 °C, hold for 30 min
Temperature at end of experiment 40 °C

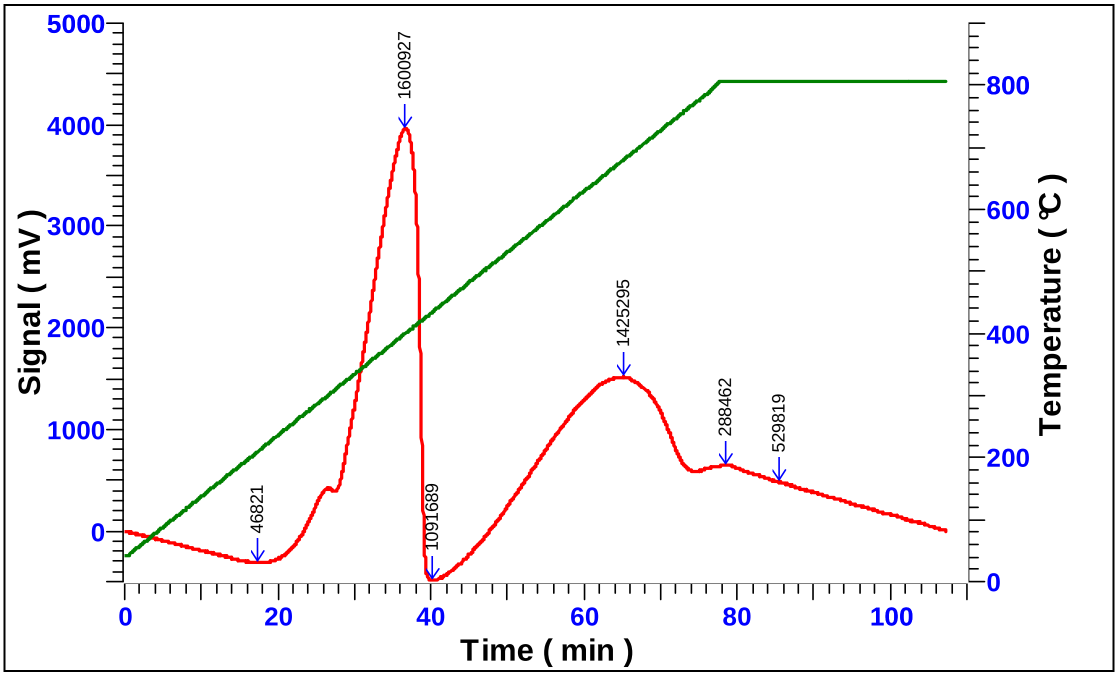

Results

Amount gas adsorbed :0.00000 µmol/g
Stoichiometric factor :0
Amount of metal reacted :0.00000 µmol/g (sample)
Total metal surface :0.000 m^2
Metal surface :0.000 m^2/g (sample)
0.0 m^2/g (metal)
0.000 m^2/g (support)
Dispersion degree :0.000%
Mean particle diameter :0.000 nm (spheres)
Total Metal :0.000 %

1.5 Baseline

Start at 0.0167 min -0.61035 mV, Stop at 107.2667 min 2102.96631 mV

1.6 Calibration

Use Calibration Factor: $0.000000 \cdot 10^{-9}$ mmol/mVs

1.7 Peaks

#	Start[min]	Stop[min]	Maximum[min]	T[°C]	Integral[mVs]	[%]	[µmol/g]
1	16.9500	26.4833	17.3167	209	46820.81	0.94	0.00000
2	27.6333	40.1000	36.6667	400	1600927.49	32.13	0.00000
3	36.9167	64.6167	40.1500	434	1091688.88	21.91	0.00000
4	40.6833	74.0667	65.2333	681	1425294.58	28.60	0.00000
5	77.1500	85.4333	78.5000	806	288461.52	5.79	0.00000
6	79.0500	106.9167	85.4667	806	529819.46	10.63	0.00000

E.2 TPR Data of Fe_3O_4 Nanocatalyst Prepared via Sol Gel-Hydrothermal Method at 160^{o}C

TPD/R/O 1100 **Thermo** Electron

Standard Data Report

1.8 Run Nr.: 688

File:C:\SHAHRUL_MSC\DEC 2009\Fe3O4\160\Fe3O4_160_200 IN AR_3.110
Info:
Operator: SHAHRUL Room Temperature 28°C Atmospheric Pressure 1000hPa

1.9 Sample

Producer:	SHAHRUL	Sample-Code:	0
Name:	Fe3O4_160_200 IN AR_3	Customer-Code:	0
Mass:	0.0507 g		
		Support:	
Info:		Metals:	1
Preparation:	SOL GEL-HYDROTHERMAL	0%	Iron

1.10 Pretreatment

Method Name: Pre Jan 2010 Info:
On Instrument: TPDRO 1100 with Ser.Nr.20033057 on Left Oven,
Started 1/20/2010 at 8:54:06 AM finished 10:22:02 AM
Gas Port when Ready: (a) Nitrogen
Gas Port when End: (a) Nitrogen

Sample rate:	1	s
Gain:	10	
Polarity:	+	

Phase	With Gas	Flow [ccm/min]	Start at T [°C]	Ramp [°/min]	Stop at T [°C]	Hold for [min]
Cleaning	Nitrogen	20	Off			10
1:	Nitrogen	20	Off	10	300	30
2:	Off					
3:	Off					
4:	Off					
End Pretreatment with Oven Off						

1.11 TPD/R/O

Method Name: SHAHRUL_NEW Info:
On Instrument: TPDRO 1100 with Ser.Nr.20033057 on Left Oven
Started 1/20/2010 at 11:05:16 AM finished 12:52:54 PM

With gas: Hydrogen 5% in Nitrogen and flow of 20 ccm/min
Start at 40 °C, heating rate 10 °/min, stop at 1000 °C, hold for 10 min
Temperature at end of experiment Oven Off

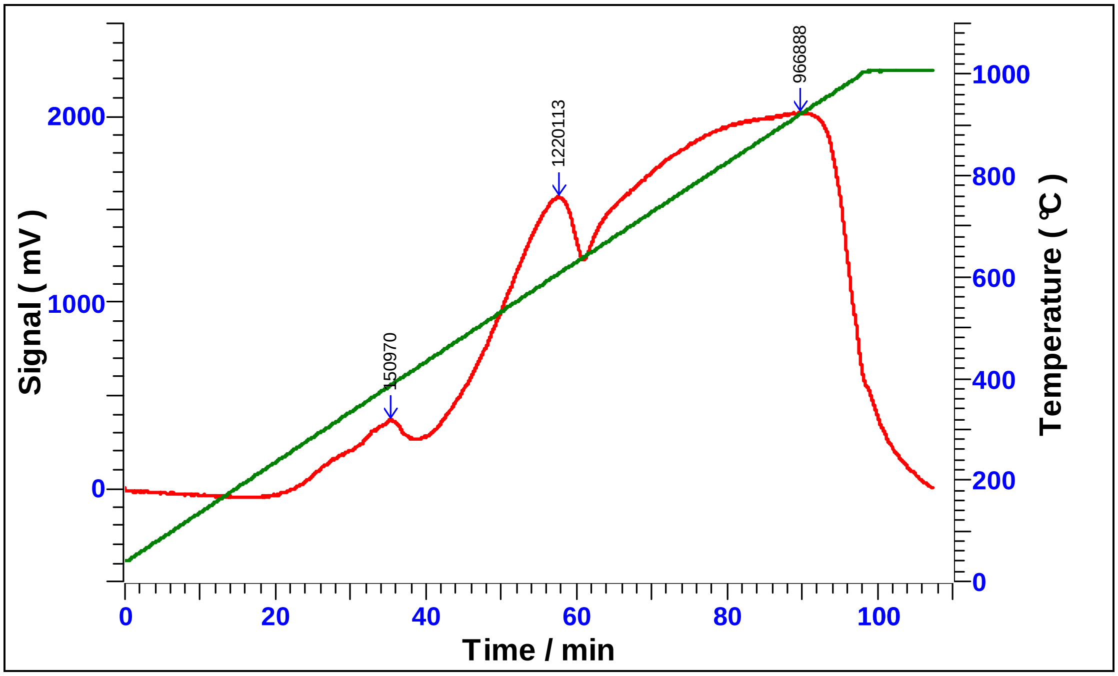

Results

Amount gas adsorbed : 3768.30600 µmol/g
Stoichiometric factor : 0
Amount of metal reacted : 0.00000 µmol/g (sample)
Total metal surface : 0.000 m^2
Metal surface : 0.000 m^2/g (sample)
0.0 m^2/g (metal)
0.000 m^2/g (support)
Dispersion degree : 0.000%
Mean particle diameter : 0.000 nm (spheres)
Total Metal : 0.000 %

1.12 Baseline

Start at 0.0167 min 11.85099 mV, Stop at 107.4667 min 267.28312 mV

1.13 Calibration

Use Calibration Factor: 81.717476 $\cdot 10^{-9}$ mmol/mVs

1.14 Peaks

#	Start[min]	Stop[min]	Maximum[min]	T[°C]	Integral[mVs]	[%]	[µmol/g]
1	29.3167	37.9667	35.3500	387	150969.53	6.46	243.33035
2	39.3833	60.8333	57.5833	606	1220113.36	52.19	1966.55980
3	89.4333	107.1167	89.8000	921	966888.42	41.36	1558.41580

E.3 TPR Data of 5% α-Fe_2O_3/γ-Al_2O_3 Nanocatalyst Prepared via Sol Gel-Hydrothermal Method, Stirred at 1 day and Annealed at 300^{o}C

TPD/R/O 1100 **Thermo** Electron

Standard Data Report

1.15 Run Nr.: 892

File:C:\SHAHRUL_MSC\2010\APRIL\5%FeAl2O3\H2O BATCH\SURFACTANT\2_1\5%FeAl2O3_1 DAY_2_1_400 IN N2.110
Info:
Operator: SHAHRUL Room Temperature 28°C Atmospheric Pressure 1000hPa

1.16 Sample

Producer:	SHAHRUL	Sample-Code:	0
Name:	5%FeAl2O3_1 DAY_2_1_400 IN N2	Customer-Code:	0
Mass:	0.1208 g		
		Support:	alumina
Info:		Metals:	1
Preparation:	SOL GEL-HYDROTHERMAL	5%	Iron

1.17 Pretreatment

Method Name: Pre-shahrul Info:
On Instrument: TPDRO 1100 with Ser.Nr.20033057 on Left Oven,
Started 5/4/2010 at 10:23:38 AM finished 11:09:33 AM
Gas Port when Ready: (a) Nitrogen
Gas Port when End: (a) Nitrogen
Sample rate: 1 s
Gain: 10
Polarity: +

Phase	With Gas	Flow [ccm/min]	Start at T [°C]	Ramp [°/min]	Stop at T [°C]	Hold for [min]
Cleaning	Nitrogen	20	40 °C			5
1:	Nitrogen	20	40	10	200	10
2:	Off					
3:	Off					
4:	Off					
End Pretreatment with Oven at 40°C						

1.18 PD/R/O

Method Name: TPR_SHAHRUL_800 Info:
On Instrument: TPDRO 1100 with Ser.Nr.20033057 on Left Oven
Started 5/4/2010 at 12:09:14 PM finished 1:36:18 PM

With gas: Hydrogen 5% in Nitrogen and flow of 20 ccm/min
Start at 40 °C, heating rate 10 °/min, stop at 800 °C, hold for 10 min
Temperature at end of experiment Oven Off

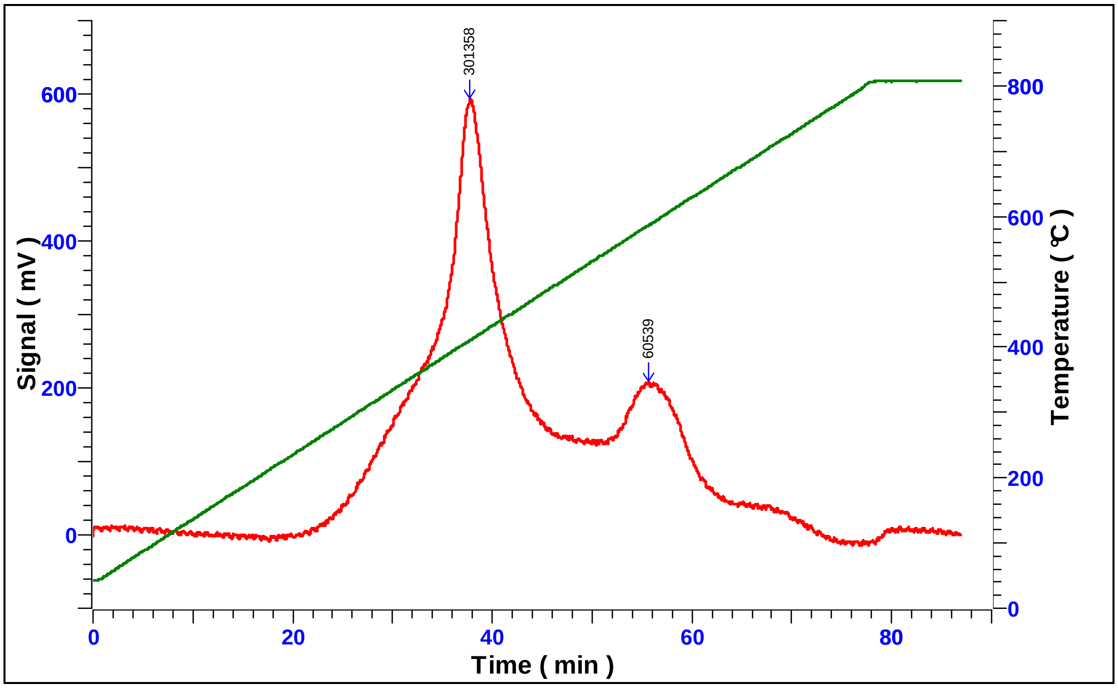

Results

Amount gas adsorbed : 209.16721 µmol/g
Stoichiometric factor : 2
Amount of metal reacted : 418.33441 µmol/g (sample)
Total metal surface :1.978 m^2
Metal surface :16.375 m^2/g (sample)
327.5 m^2/g (metal)
17.237 m^2/g (support)
Dispersion degree : 46.728%
Mean particle diameter : 2.331 nm (spheres)
Total Metal : 2.336 %

1.19 Baseline

Start at 0.0167 min -9.96908 mV, Stop at 86.9167 min 46.23413 mV

1.20 Calibration

Use Calibration Factor: 69.819292 $\cdot 10^{-9}$ mmol/mVs

1.21 Peaks

#	Start[min]	Stop[min]	Maximum[min]	T[°C]	Integral[mVs]	[%]	[µmol/g]
1	24.8500	45.3833	37.7667	411	301358.14	83.27	174.17725
2	55.2833	62.7667	55.6833	587	60538.94	16.73	34.98995

E.3.1 Example of Calculation

Percentage of Dispersion (%D) and Mean Particle Diameter (*d*)

E.3.1.1. Formula

Percentage of dispersion, % D = C_2X/fw [8]

Where,

C_2 = Constant

X = Chemisorptive H_2 uptake (μmol/g)

f = Fraction of active element present in metallic state

w = Weight percentage of the catalytic element present as either metal or oxide

E.3.1.2 Values

C_2 = 1.12 (Fe)

f = 100% (Assuming Fe particles reduced completely)

E.3.1.3 Calculation

% D = [1.12 x 209.16721 μmol/g] / [100(1) x (0.05)]

= 46.85 %

APPENDIX F

EDX ANALYSIS CALCULATION

Table F: EDX Data of α-Fe_2O_3 Nanocatalysts Prepared via Sol Gel Method at Different Stirring Periods Annealed at 300^{o}C.

Method			1 day	1 week	1 month
Atomic (%)	Fe	Exp.	22.56	28.84	41.74
		Dev.	77.30	38.69	-4.16
	O	Exp.	31.35	71.16	58.26
		Dev.	91.38	-15.68	2.98
Weight (%)	Fe	Exp.	54.40	58.89	71.43
		Dev.	28.57	18.86	-2.08
	O	Exp.	31.58	41.40	28.57
		Dev.	-5.09	-37.80	4.92

A. Theoretical calculation based on α-Fe_2O_3

Atomic %

Fe = 2 Fe / (2 Fe + 3O)
= 2/5 x 100%
= 40%

O = 3O / (2 Fe + 3O)
= 3/5 x 100%
= 60%

Weight %

Fe = 2 x MRM for Fe (gmole^{-1}) / MRM (gmole^{-1})[2Fe + 3O]
= 2(55.847) / [2(55.747)+3(15.994)]
= 0.70 x 100%
= 70%

O = 3 x MRM for O (gmole^{-1}) / MRM (gmole^{-1}) [2 Fe + 3O]

= 3(15.994) / [2(55.747)+3(15.994)]

= 30%

Atomic Percentage

Stirring period	Deviation (%) = (Theory – Experiment)/Experiment x 100%	
	Fe	O
1 day	= (40-22.56)/22.56 x 100% = 77.30%	=(60-31.35)/31.35x100% = 91.38%
1 week	= (40-28.84)/28.84 x 100% = 38.69%	=(60-71.16)/71.16x100% = -15.68%
1 month	= (40-41.74)/41.74 x 100% = -4.16%	=(60-58.26)/58.26x100% =2.98

Weight Percentage

Stirring period	Deviation (%) = (Theory – Experiment)/Experiment x 100%	
	Fe	O
1 day	=(70-54.40)/54.40x100% =28.67%	=(30-31.58)/31.58x100% =-5.00%
1 week	=(70-58.89)/58.89x100% =18.86%	=(30-41.40)/41.40x100% =-27.53%
1 month	=(70-71.43)/71.43x100% =-2%	=(30-28.57)/28.57x100% =5%

APPENDIX G

EDX-Elemental Mapping of Supported 5% α-Fe_2O_3/γ-Al_2O_3 Nanocatalysts

G.1.Supported 5% α-Fe_2O_3/γ-Al_2O_3 Nanocatalysts – Effect of Synthesis Period

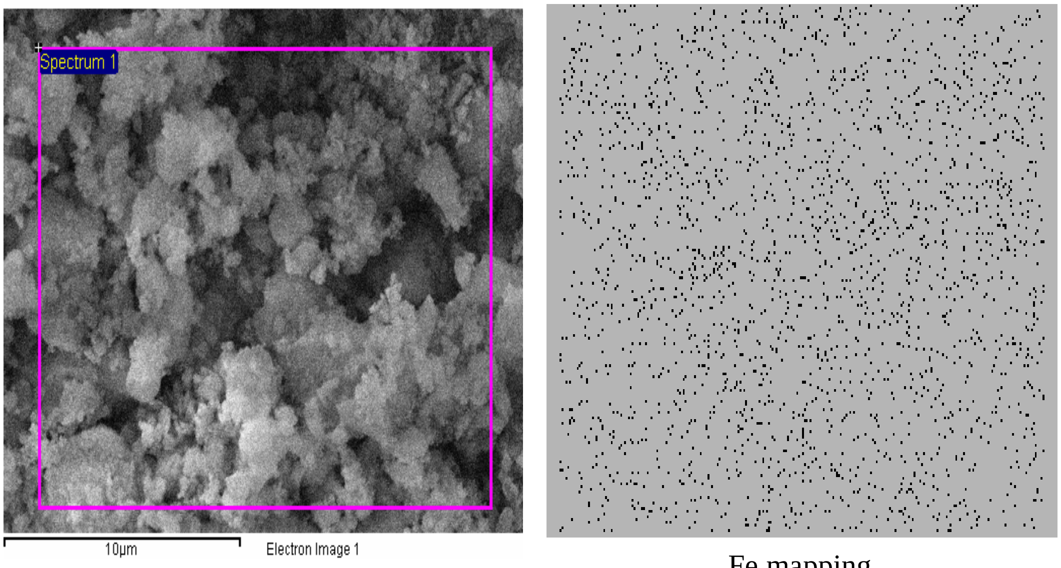

5% α-Fe_2O_3/γ-Al_2O_3

Fe mapping

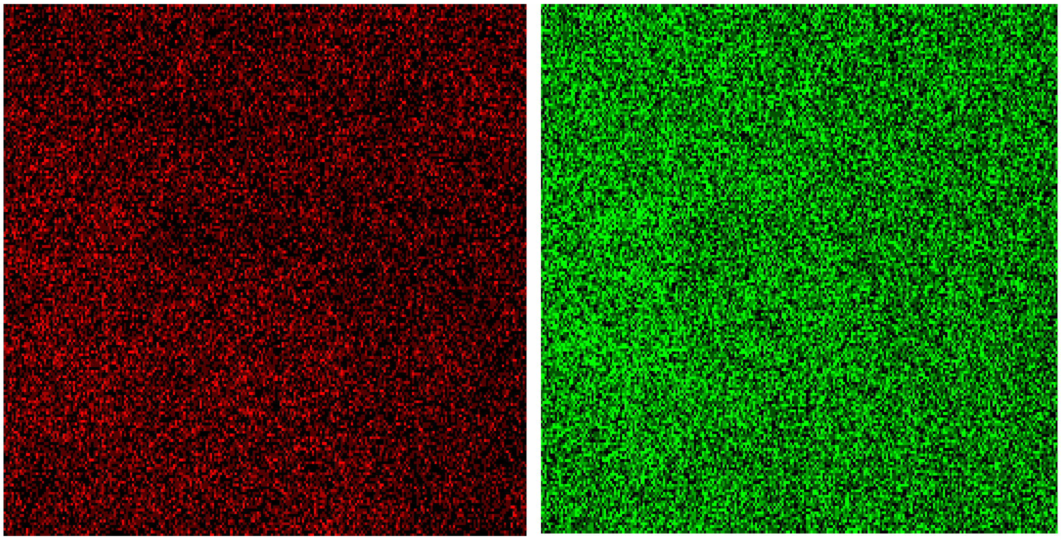

O mapping

Al mapping

Figure G.1.1: EDX mapping of 5% α-Fe_2O_3/γ-Al_2O_3 nanocatalyst prepared via sol gel-hydrothermal method in the absence of surfactant at 160°C for 1 hour.

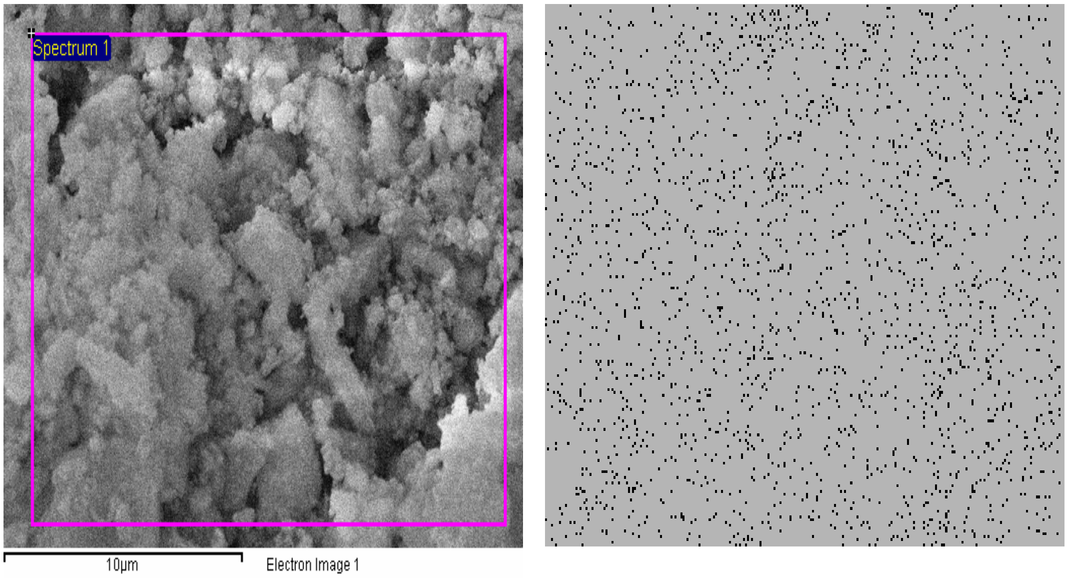

5% α-Fe_2O_3/γ-Al_2O_3 Fe mapping

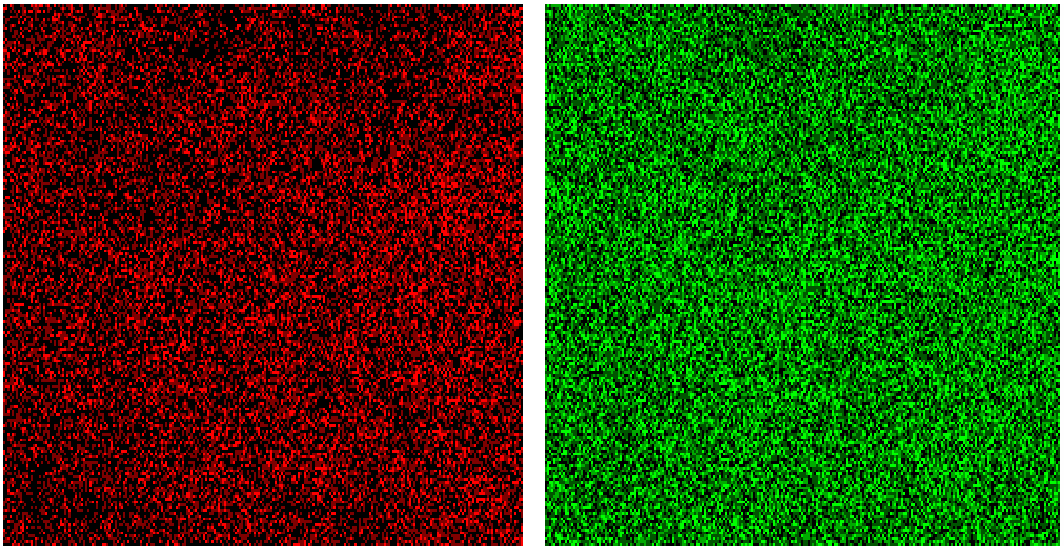

O mapping Al mapping

Figure G.1.2: EDX mapping of 5% α-Fe_2O_3/γ-Al_2O_3 nanocatalyst prepared via sol gel-hydrothermal method in the absence of surfactant at 160°C for 10 hours.

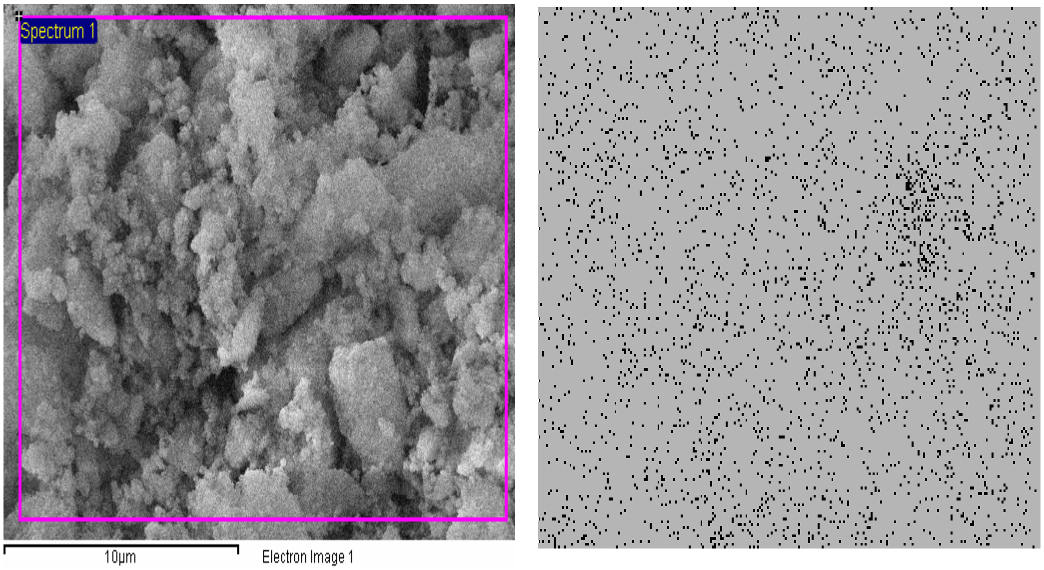

5% α-Fe_2O_3/γ-Al_2O_3 Fe mapping

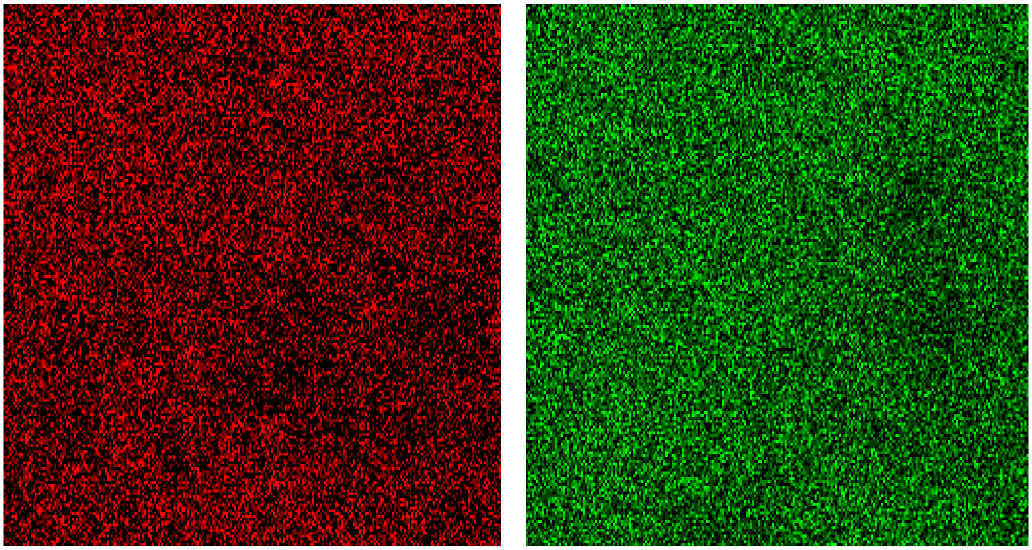

O mapping Al mapping

Figure G.1.3: EDX mapping of 5% α-Fe_2O_3/γ-Al_2O_3 nanocatalyst prepared via sol gel-hydrothermal method in the absence of surfactant at 160°C for 1 day.

G.2. Supported 5% α-Fe_2O_3/γ-Al_2O_3 Nanocatalysts – Effect of Iron (III) Nitrate to Sodium Bis(2-ethylhexyl) Sulfosuccinate (SBS) Surfactant Ratio.

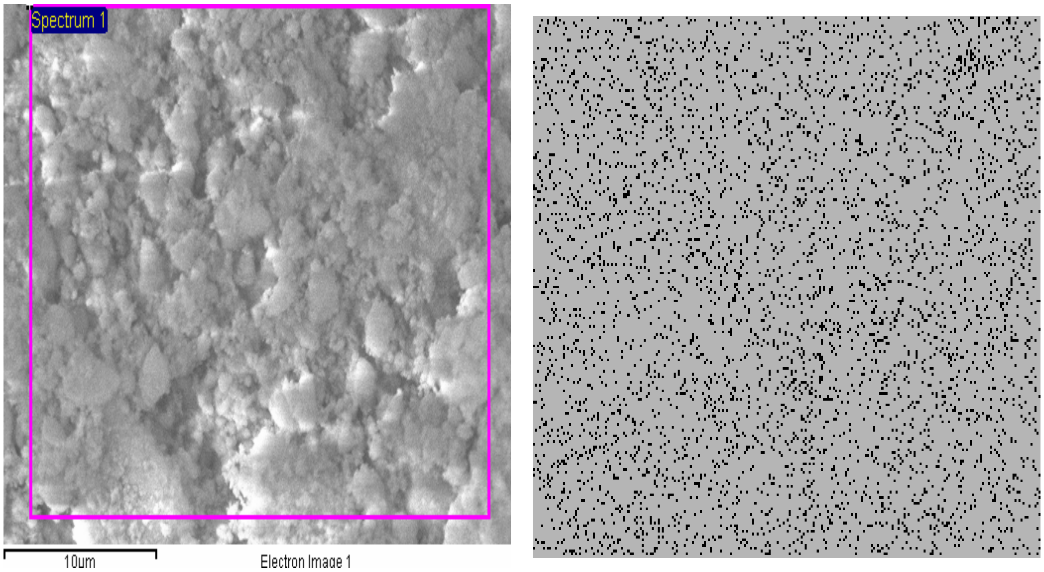

5% α-Fe_2O_3/γ-Al_2O_3 Fe mapping

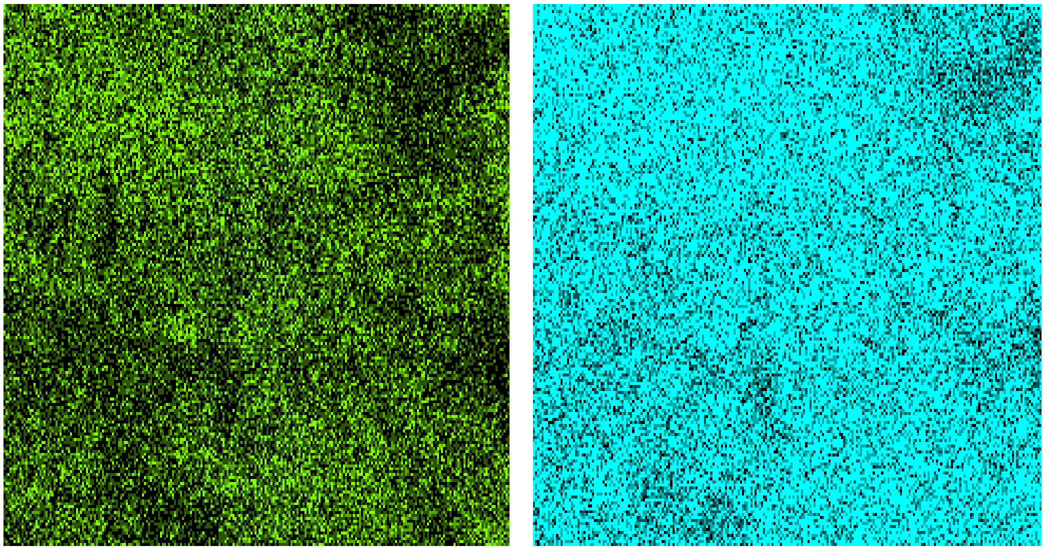

O mapping Al mapping

Figure G.2.1: EDX mapping for 5% α-Fe_2O_3/γ-Al_2O_3 nanocatalyst prepared via sol gel hydrothermal method at iron (III) nitrate to surfactant ($Fe(NO_3)_3$:Surf) ratios of 2:1

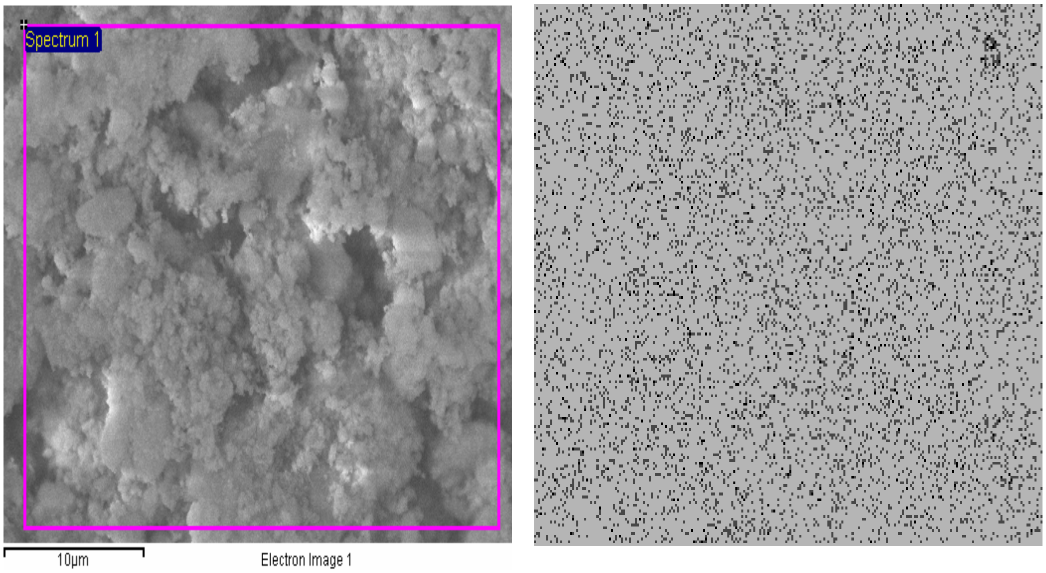

5% α-Fe_2O_3/γ-Al_2O_3 Fe mapping

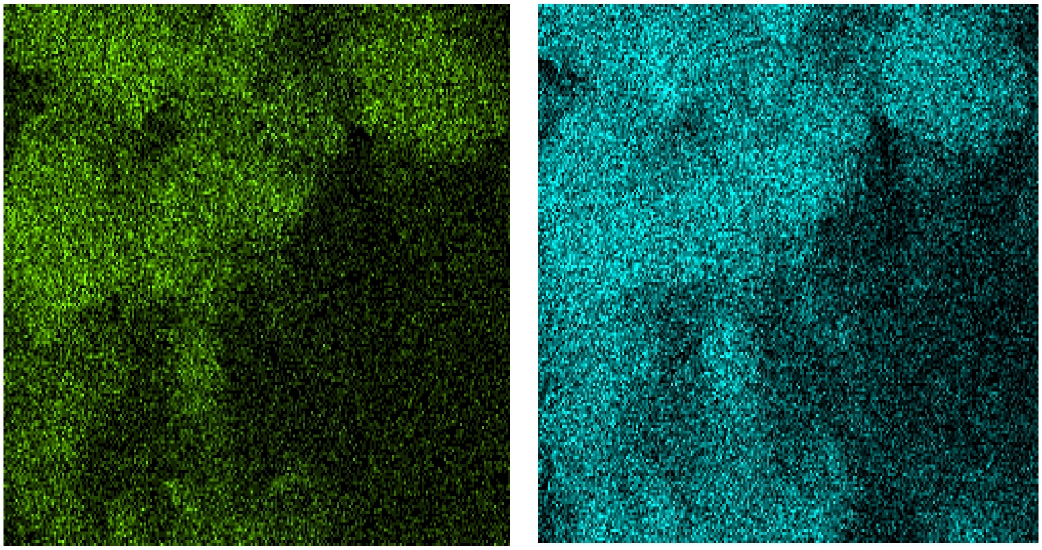

O mapping Al mapping

Figure G.2.2: EDX mapping for 5% α-Fe_2O_3/γ-Al_2O_3 nanocatalyst prepared via sol gel hydrothermal method at iron (III) nitrate to surfactant ($Fe(NO_3)_3$:Surf) ratios of 2:2.

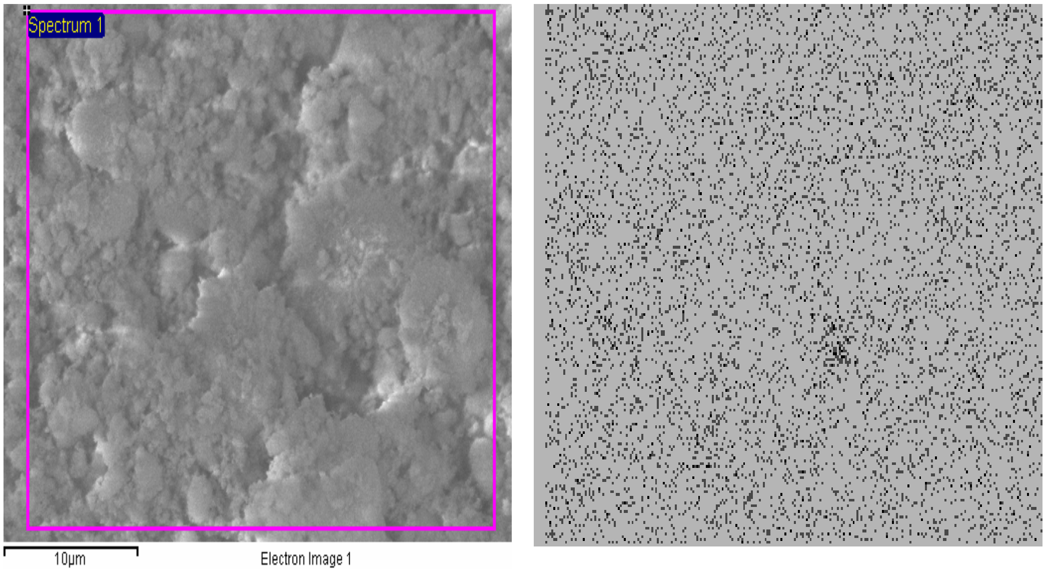

5% α-Fe_2O_3/γ-Al_2O_3 Fe mapping

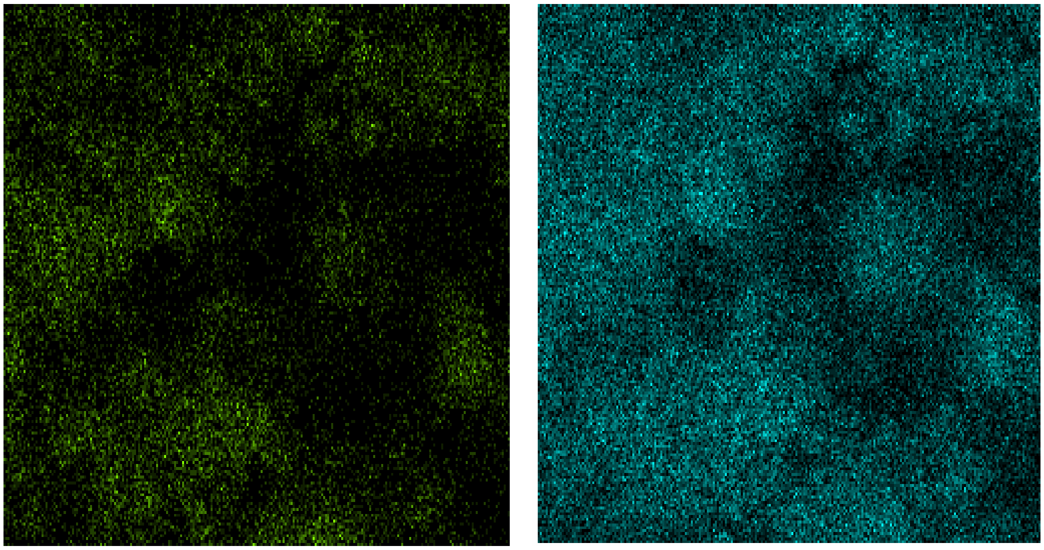

O mapping Al mapping

Figure G.2.3: EDX mapping for 5% α-Fe_2O_3/γ-Al_2O_3 nanocatalyst prepared via sol gel hydrothermal method at iron (III) nitrate to surfactant ($Fe(NO_3)_3$:Surf) ratios of 2:3.

APPENDIX H

Physical Adsorption

H.1 BET Surface Area

H.1.1. 5% α-Fe_2O_3/γ-Al_2O_3 Nanocatalyst (2:1)

Table H.1.1: BET surface area data of 5% α-Fe_2O_3/γ-Al_2O_3 nanocatalyst (2:1)

Relative Pressure (P/Po)	1/[Q(Po/P - 1)]
0.066343242	0.002188554
0.079519995	0.002574848
0.100211227	0.003172701
0.119876366	0.00373073
0.140146372	0.004302564
0.160100759	0.004864737
0.180142444	0.005431878
0.200136641	0.005996395
0.248925859	0.007395424

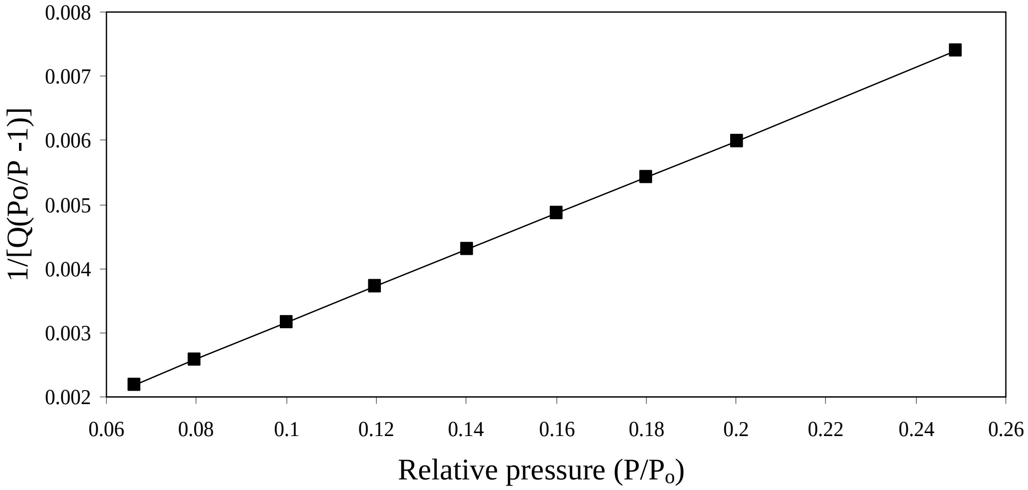

Figure H.1.1: BET surface area plot of 5% α-Fe_2O_3/γ-Al_2O_3 nanocatalyst (2:1).

H.1.2. 5% α-Fe_2O_3/γ-Al_2O_3 Nanocatalyst (2:2)

Table H.1.1: BET surface area data of 5% α-Fe_2O_3/γ-Al_2O_3 nanocatalyst (2:2)

Relative Pressure (P/Po)	1/[Q(Po/P - 1)]
0.065012	0.002418
0.07932	0.002888
0.099854	0.003552
0.119856	0.004189
0.139824	0.004821
0.16017	0.005464
0.179849	0.006086
0.200101	0.006723
0.248952	0.008279

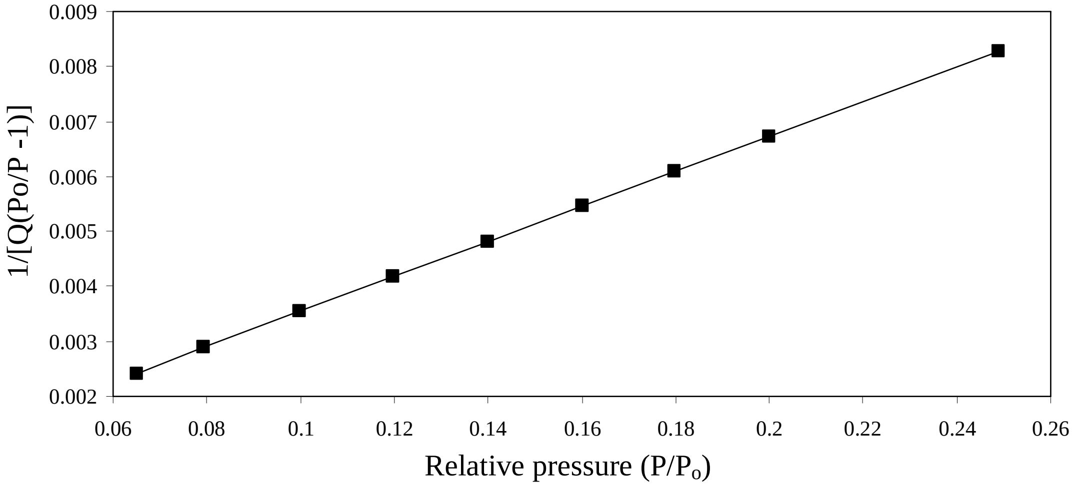

Figure H.1.2: BET surface area plot of 5% α-Fe_2O_3/γ-Al_2O_3 nanocatalyst (2:2)

H.1.3. 5% α-Fe_2O_3/γ-Al_2O_3 Nanocatalyst (2:3)

Table H.1.1: BET surface area data of 5% α-Fe_2O_3/γ-Al_2O_3 nanocatalyst (2:3)

Relative Pressure (P/Po)	1/[Q(Po/P - 1)]
0.064463	0.002281
0.079008	0.002739
0.100124	0.003393
0.119822	0.003998
0.140042	0.004615
0.15979	0.005214
0.179797	0.005823
0.199878	0.006438
0.248448	0.007948

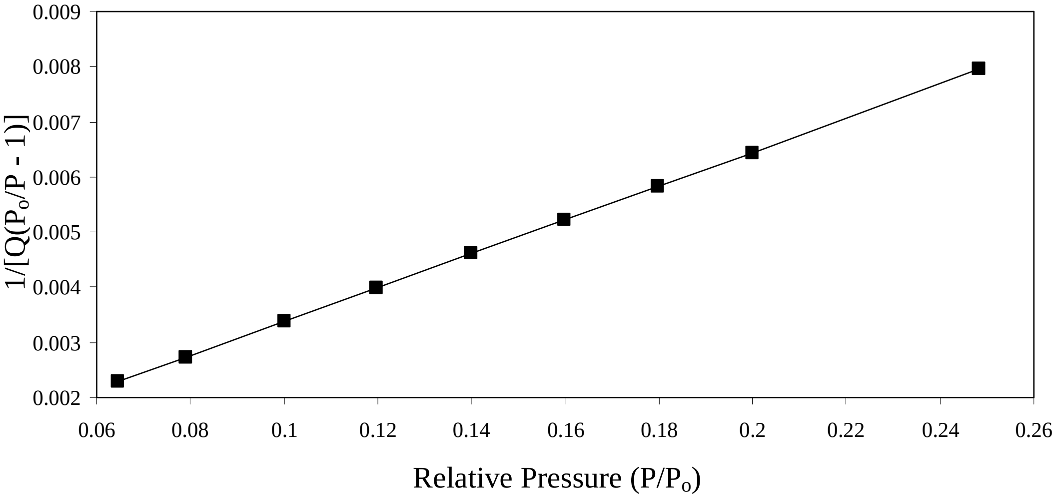

Figure H.1.3: BET surface area plot of 5% α-Fe_2O_3/γ-Al_2O_3 nanocatalyst (2:3)

APPENDIX I

Standard Operating Procedure of Microreactor

Loading the Catalyst

1. Load the catalyst between two layers of glass wool inside the tubular tube.
2. Couple the tubular tube with a pair of heating block. This forms a system namely tubular reactor system.
3. Loosen the screws of a pair of tube holder ring. Than, place the tubular reactor system into the rings and tighten up the screws.
4. Place a magnet block consisting of north and south poles. The location of the magnetic block and chamber is then adjusted so that both of them are in parallel position.
5. Connect two ends of the loaded tubular tube with inlet and out let gas tubes. Then, tighten the screws.
6. Place the thermocouple, heating rods and temperature indicator wire into the right channels at tubular reactor system.

A. Starting The Reactor

1. Connect regulator terminals of reactant gas (H_2 and N_2) to the gas ports of microreactor. Open the control valves of gas tanks as well needle valves of regulator.
2. Open the needle valves to flow the H_2 and N_2 into the system.
3. Adjust the control valves (H_2 and N_2) until the pressure gauge (H_2:N_2) indicators reach 1.2 barg.

4. Open the needle valves of flow meter. Then, set the flow rate of the feed gas (H_2 and N_2) according to the desired ratio using fine controller. The reactant gas is now flowed into the tubular reactor system.
5. Switch on the main control panel switch and set the temperature from 0^o to a desired value using temperature controller.
6. Turn on the magnetizer.
7. Turn the needle valve of gas outlet to “outlet” selection to bubble the outlet gas into hydrochloric acid.

B. Turn off the Reactor

1. Reduce the temperature of reaction to 25^oC using the temperature controller and then switch off the main switch of control panel.
2. Reduce the flow rate of the feed gas to zero and than turn off the fine controllers.
3. Reduce the pressure gauge reading (H_2 and N_2) to zero by adjusting the control valves. Then, close the needle valves.
4. Close the control vales of gas tanks as well needle valves of regulator.

STATUS OF THESIS

Title of thesis	SYNTHESIS, CHARACTERIZATION AND ACTIVITY OF IRON OXIDE NANOCATALYSTS FOR AMMONIA PRODUCTION

I SHIKH MOHD SHAHRUL NIZAN SHIKH ZAHARI
(CAPITAL LETTERS)

hereby allow my thesis to be placed at the Information Resource Center (IRC) of Universiti Teknologi PETRONAS (UTP) with the following conditions:

1. The thesis becomes the property of UTP
2. The IRC of UTP may make copies of the thesis for academic purposes only.
3. This thesis is classified as

☑ Confidential

☐ Non-confidential

If this thesis is confidential, please state the reason:
____

The contents of the thesis will remain confidential for 6 years.

Remarks on disclosure:

Effect of magnetic field on the ammonia synthesis reaction is a new innovation in heterogeneous catalysis field. Enhancement in the ammonia yield and minimization in reaction condition were successfully achieved in this study.

Endorsed by

______________________________	______________________________
Signature of Author	Signature of Supervisor
Permanent address:	Name of Supervisor
No 8, Lorong 29, R.R.M Balok Baru,	Assoc. Prof. Dr. Noor Asmawati
26100 Kuantan, Pahang Darul Makmur.	Mohd Zabidi
Date: ________________________	Date: ________________________

UNIVERSITI TEKNOLOGI PETRONAS

SYNTHESIS, CHARACTERIZATION AND ACTVITY OF IRON OXIDE NANOCATALYSTS FOR AMMONIA PRODUCTION

by

SHIKH MOHD SHAHRUL NIZAN SHIKH ZAHARI

The undersigned certify that they have read, and recommend to the Postgraduate Studies Programme for acceptance this thesis for the fulfilment of the requirements for the degree stated.

Signature:	________________________
Main Supervisor:	ASSOC. PROF. DR. NOOR ASMAWATI MOHD ZABIDI
Signature:	________________________
Co-Supervisor:	PROF. DR. NOORHANA YAHYA
Signature:	________________________
Head of Department:	ASSOC. PROF. DR. SUHAIMI MAHADZIR
Date:	________________________

SYNTHESIS, CHARACTERIZATION AND ACTIVITY OF IRON OXIDE NANOCATALYST FOR AMMONIA PRODUCTION

by

SHIKH MOHD SHAHRUL NIZAN SHIKH ZAHARI

A Thesis
Submitted to the Postgraduate Studies Programme
as a Requirement for the Degree of

MASTER OF SCIENCE
CHEMICAL ENGINEERING DEPARTMENT
UNIVERSITI TEKNOLOGI PETRONAS
BANDAR SERI ISKANDAR,
PERAK

MAY 2011

DECLARATION OF THESIS

Title of thesis	SYNTHESIS, CHARACTERIZATION AND ACTIVITY OF IRON OXIDE NANOCATALYSTS FOR AMMONIA PRODUCTION

I SHIKH MOHD SHAHRUL NIZAN SHIKH ZAHARI

(CAPITAL LETTERS)

hereby declare that the thesis is based on my original work except for quotations and citations which have been duly acknowledged. I also declare that it has not been previously or concurrently submitted for any other degree at UTP or other institutions.

	Witnessed by
____________________________	____________________________
Signature of Author	Signature of Supervisor
Permanent address:	Name of Supervisor
No 8, Lorong 29, R.R.M Balok Baru, 26100 Kuantan, Pahang Darul Makmur.	Assoc. Prof. Dr. Noor Asmawati Mohd Zabidi
Date : ________________________	Date : ________________________

ACKNOWLEDGEMENT

Bismillahirrahmanirrahim…

Alhamdulillah and thanks to ALLAH S.W.T for giving me such a huge blessing in completing this master research successfully. This thesis symbolizes hard work and dedication that have been paid to this project accompanied with the support from family and friends.

Highly appreciation is firstly dedicated to my supervisor, Assoc. Prof. Dr. Noor Asmawati Mohd Zabidi and co-supervisor, Prof. Dr. Noorhana Yahya for their willingness and kindness in guiding me throughout this project. Great support and encouragement from both of them are priceless and will not be forgotten. To my research partner, Poppy Puspitasari, her good cooperation and assistant are also appreciated.

I would also like to acknowledge The Ministry of Science, Technology and Innovation of Malaysia and Universiti Teknologi PETRONAS for the funding (E-Science Fund Code: 03-02-02-SF0031) and facilities provided. Also not to be missed staffs and technicians from Chemical Engineering Department, Fundamental & Applied Sciences Department, Mechanical Engineering Department, Nanotechnology Laboratory and Centralized Laboratory who had given me opinion, suggestion and technical knowledge.

Finally, for those who had threw out constructive comments and ideas as well as assisted directly or indirectly, thank you very much.

ABSTRACT

Ammonia synthesis was evaluated in the presence of α-Fe_2O_3, Fe_3O_4 and 5% α-Fe_2O_3/γ-Al_2O_3 nanocatalysts. The nanocatalysts were prepared via sol-gel and sol gel-hydrothermal methods. The variables studied for synthesis using sol gel method were stirring period and annealing temperature. Samples were characterized using x-ray diffraction (XRD), raman spectroscopy, field emission scanning electron microscopy (FESEM), energy dispersed x-ray (EDX), temperature programmed reduction (TPR), vibration sample magnetometer (VSM) and N_2 adsorption. Extending synthesis period from 1 day to 1 month in the sol gel method reduced the size of α-Fe_2O_3 nanocatalyst particles from 60 nm to 27 nm. Particle size increased from 21 nm to 60 nm when the annealing temperature was increased from 300^oC to 700^oC. The sol gel-hydrothermal produced a well crystallined Fe_3O_4 nanocatalyst at synthesis temperature of 160^oC. The 5% α-Fe_2O_3/γ-Al_2O_3 prepared using sol gel-hydrothermal method at iron nitrate to sodium bis(2-ethylhexyl) sulfucinnate surfactant ratio of 2:3 exhibited better particles dispersion compared to those prepared at other ratios. The TPR profiles for the nanocatalysts exhibited two reduction stages for the transformations of α-Fe_2O_3 to Fe_3O_4 and Fe_3O_4 to α-Fe. For the unsupported α-Fe_2O_3, reduction peaks were observed at 400^oC to 460^oC and 680^oC to 780^oC regions whereas for the γ-Al_2O_3-supported α-Fe_2O_3, the reduction peaks shifted to 350^oC to 400^oC and 550^oC to 650^oC. The catalytic study was conducted in a fixed bed microreactor at 30^oC to 200^oC under atmospheric pressure with a total feed flow rate of 40 cm^3/min and H_2/N_2 volume ratio of 3:1. The amount of ammonia was determined using an acid-base titration method. The ammonia yield over α-Fe_2O_3 and 5% α-Fe_2O_3/γ-Al_2O_3 catalysts at 110^oC measured in the absence of magnetic field was 2.65 %/g_{Fe} and 26.3 %/g_{Fe}, respectively. Applying magnetic field at 1 Tesla to the α-Fe_2O_3 catalyst resulted in two orders of magnitude increase in the ammonia yield while using Fe_3O_4 nanocatalyst further enhanced the ammonia yield by about 14% greater than that of α-Fe_2O_3. The performance of nanocatalysts for the ammonia synthesis in the absence and presence of magnetic field can be ranked as 5% α-Fe_2O_3/γ-Al_2O_3> α-Fe_2O_3 and Fe_3O_4> α-Fe_2O_3, respectively.

ABSTRAK

Sintesis ammonia telah dinilai dengan kehadiran pemangkin-pemangkin nano α-Fe_2O_3, Fe_3O_4 dan 5% α-Fe_2O_3/γ-Al_2O_3. Pemangkin-pemangkin nano ini telah dihasilkan menggunakan kaedah-kaedah sol gel dan sol gel-hidrotermal. Pembolehubah-pembolehubah yang telah diuji bagi sintesis menggunakan kaedah sol- gel adalah tempoh pengacauan dan suhu pemanasan haba. Sifat-sifat bagi sampel-sampel telah diuji menggunakan pembelauan x-ray (XRD), spektroskopi raman, mikroskopi pengesanan medan pemancaran elektron (FESEM), tenaga penaburan x-ray (EDX), program suhu penurunan (TPR), magnetometer sampel bergetar (VSM) dan penjerapan N_2. Pemanjangan tempoh pengacauan dari 1 hari ke 1 bulan bagi kaedah sol gel telah mengecilkan saiz zarah-zarah pemangkin nano α-Fe_2O_3 daripada 60 nm ke 27 nm. Saiz zarah-zarah juga turut meningkat dari 21 nm kepada 60 nm apabila suhu pemanasan haba telah ditingkatkan daripada 300^{o}C ke 700^{o}C. Kaedah sol gel-hidrotermal telah menghasilkan pemangkin nano Fe_3O_4 dengan tahap pengkristalan yang bagus pada suhu 160^{o}C. Bagi pemangkin nano 5% α-Fe_2O_3/γ-Al_2O_3 yang telah dihasilkan melalui kaedah sol gel-hidrotermal pada nisbah 2:3 bagi ferum nitrate kepada natrium bis(2-etilhexil) sulfucinnate, ianya telah menunjukkan penyerakan zarah-zarah yang bagus jika dibandingkan dengan sampel-sampel yang telah dihasilkan menggunakan nisbah-nisbah yang lain. Profil-profil TPR untuk kesemua pemangkin-pemangkin nano telah menunjukkan dua peringkat proses penurunan bagi transformasi α-Fe_2O_3 kepada Fe_3O_4 dan Fe_3O_4 kepada α-Fe. Bagi pemangkin nano α-Fe_2O_3 yang tidak disokong, puncak-puncak penurunan telah dilihat pada 400^{o}C ke 460^{o}C dan 680^{o}C ke 780^{o}C manakala bagi γ-Al_2O_3 yang menyokong α-Fe_2O_3, puncak-puncak penurunan telah teranjak kepada 350^{o}C ke 400^{o}C and 550^{o}C ke 650^{o}C. Penilaian pemangkinan telah dijalankan dalam satu lapisan tetap mikroreaktor pada suhu 30^{o}C ke 200^{o}C pada tekanan atmosferik dengan jumlah kadar aliran suapan gas pada 40 cm^3/min dan nisbah isipadu H_2/N_2 adalah 3:1. Kuantitit ammonia yang terhasil diperolehi menggunakan kaedah pentitratan asid-bes. Penghasilan ammonia bagi pemangkin-pemangkin α-Fe_2O_3 dan 5% α-Fe_2O_3/γ-Al_2O_3 pada 110^{o}C

diukur dalam ketidakhadiran medan magnet adalah masing-masing 2.65 $\%/g_{Fe}$ and 26.3 $\%/g_{Fe}$. Pengenalan medan magnet pada 1 Tesla kepada pemangkin α-Fe_2O_3 telah meningkatkan penghasilan ammonia dengan urutan dua magnitud manakala penggunaan Fe_3O_4 turut meningkatkan penghasilan ammonia 14% lebih banyak berbanding α-Fe_2O_3. Prestasi pemangkin-pemangkin nano dalam ketidakhadiran dan kehadiran medan magnet masing-masing boleh didisusun seperti berikut $5\%\alpha$-Fe_2O_3/γ-Al_2O_3> α-Fe_2O_3 dan Fe_3O_4>α-Fe_2O_3.

In compliance with the terms of the Copyright Act 1987 and the IP Policy of the university, the copyright of this thesis has been reassigned by the author to the legal entity of the university,

Institute of Technology PETRONAS Sdn Bhd.

Due acknowledgement shall always be made of the use of any material contained in, or derived from, this thesis.

© Shikh Mohd Shahrul Nizan Shikh Zahari, January 2011
Institute of Technology PETRONAS Sdn Bhd
All rights reserved.

TABLE OF CONTENTS

CHAPTER 1: INTRODUCTION

CHAPTER 2: THEORY AND LITERATURE REVIEW

CHAPTER 3: METHODOLOGY

CHAPTER 4: RESULTS AND DISCUSSION

CHAPTER 5 CONCLUSION

LIST OF TABLES

LIST OF FIGURES

LIST OF ABBREVIATIONS

GNP	-	Gross national product
PASB	-	PETRONAS Ammonia Sdn. Bhd.
PFK	-	PETRONAS Fertilizer Kedah
KAAP	-	Kellog Advanced Ammonia Process
TCD	-	Thermal conductivity detector
PPM	-	Part per million
XRD	-	X-ray diffraction
H_2-TPR	-	Temperature-programmed reduction (Hydrogen)
FESEM	-	Field emission scanning electron microscopy
EDX	-	Energy dispersed x-ray
TEM	-	Transmission electron microscopy
BET	-	Brunauer-Emmett-Teller Method
VSM	-	Vibration sample magnetometer
GC	-	Gas chromatography
H_2	-	Hydrogen gas
CO	-	Carbon monoxide
N_2	-	Nitrogen gas
SYN	-	Synthesis
CHARAC	-	Characterization
ACT	-	Activity
FE	-	Iron
NANOCAT	-	Nanocatalyst
PROD	-	Production

LIST OF SYMBOLS

^{o}C - Degree Celsius
φ - Work function
π - Pie orbital
π^* - Pie antibonding orbital
M_s - Saturation magnetization
M_r - Remanence magnetization
H_c - Coercivity force
T_c - Curie temperature
ΔE - Energy barrier
K_s - Anisotropy constant
S - Surface area
δ - Charge
$\bar{\chi}$ - Electronegativity
p - Proton released
Z - Formal charge
N - Coordination number
E^{o} - Standard reduction potential
H_{ads} - Heat of adsorption
θ - Bragg angle
k - Shape factor
λ - Wavelength
β - Full width half maximum
I.D - Internal diameter
O.D - Outer diameter
I - Intensity
T_{max} - Maximum temperature
R - Gas constant
X_A - Mole fraction of component A
K_{eq} - Equilibrium constant

CHAPTER 1

INTRODUCTION

1.1 Background

Catalysis is an important discipline in reaction engineering and its application covers many areas such as natural gas conversion, chemical synthesis and refining. Catalysis can be divided into two categories namely homogeneous and heterogeneous catalysis. Heterogeneous catalysis refers to a chemical reaction between two phases such as solid (catalyst) and gas (reactant) phases. Heterogeneous catalysts offer several advantages to industrial syntheses such as higher resistivity to severe reaction conditions and no extra steps required for product separation [1]. In terms of economy aspect, the role of heterogeneous catalysis in generating nation income cannot be discounted. The involvement of this field contributes about $ 5 trillion per year of world's GNP [2].

Ammonia or NH_3 is a useful chemical substance particularly for agriculture activities. It has a boiling point and a melting point of -33.35^{o}C and -77.7^{o}C, respectively. Ammonia exists as a colourless gas at room temperature having sharp and intensely irritating odours [3].

Many industrial products contain ammonia as one of the raw ingredients. Figure 1.1 summarizes the use of ammonia in several applications [4].

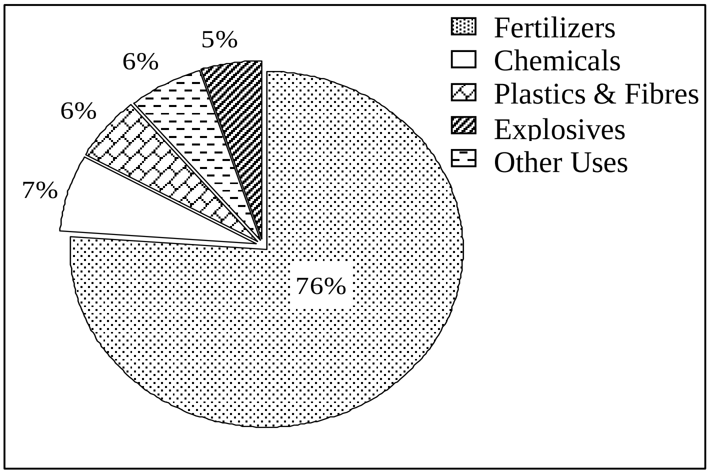

Figure 1.1: Industrial ammonia applications [4]

Ammonia production in Asia has been extensively growing every year. Table 1.1 describes the ammonia production involving some Asian countries in the year of 2003 until 2007 [5].

Table 1.1: Ammonia production in Asia [5].

Country	Thousand metric tons of contained nitrogen				
	2003	**2004**	**2005**	**2006**	**2007**
Malaysia	910	843	920	950	960
India	10048	10718	10800	10900	11000
Indonesia	4250	4120	4400	4300	4400
Iran	1115	1088	1020	1020	2000
Japan	1061	1101	1083	1091	1090
Pakistan	2357	2114	2114	2200	2250
Saudi Arabia	1743	1726	1780	2000	2600

Malaysia has two ammonia production plants namely PETRONAS Ammonia (PASB), located in Kerteh, Terengganu and PETRONAS Fertilizer (PFK) in Gurun, Kedah.

Haber Bosch is a well known process for synthesis of ammonia. A huge appreciation has to be paid to Fritz Haber and Carl Bosch who discovered and introduced this remarkable process at the beginning of 19th century. Generally, ammonia is attained by reacting a mixture of hydrogen and nitrogen gases at a ratio of 3:1 (H_2:N_2) over magnetite (Fe_3O_4) fused-catalyst, at 300-500^oC and 100-200 atm [4], [6]-[7].

1.2 Problem Statement

The well known drawbacks in the ammonia synthesis using Haber Bosch process are the low ammonia yield as well as capital and energy intensive of production operations [4], [6]-[7]. Due to thermodynamic factor, the Haber Bosch process is commonly performed under high temperature (300-500^oC) and pressure (100-200atm) environments. Under this condition, yield of ammonia was only 10-20%. Unfortunately, these facts remain unsolved and controversial until today, thus overcoming steps are highly desirable [4], [6]-[7].

The application of nanotechnology has potential to overcome the drawbacks on ammonia synthesis. Using nanoscale particles in the presence of magnetic field is expected to reduce severity of ammonia synthesis process condition and improve the ammonia yield.

1.3 Hypothesis

Nanosize catalyst provides high surface area which will enhance the chance of reactant molecules to interact with the surface of the catalyst. Employing magnetic field throughout the reaction could minimize the difficulty of interaction between the electrons within the catalyst particles and reactant molecules. The enhanced interaction could lead to higher ammonia yield as well as reduce the severity of the reaction condition.

1.4 Objective

The objectives of this study are:

1. To synthesize unsupported and supported iron oxide nanocatalysts for ammonia production.
2. To characterize the physicochemical properties of the prepared iron oxide nanocatalysts.
3. To evaluate the performance in terms of the rate and ammonia yield of the prepared nanocatalysts in ammonia production in the absence and presence of magnetic field.

1.5 Scope of Work

The scope of work included synthesis, characterization and catalytic study of unsupported and supported iron oxide nanocatalysts in ammonia synthesis. Iron nanocatalysts have been synthesized using sol gel, self assembly, self combustion, hydrothermal, precipitation and sol gel-hydrothermal methods. Three groups of nanocatalysts were prepared, namely hematite (α-Fe_2O_3), magnetite (Fe_3O_4) and hematite supported on alumina, (α-Fe_2O_3/γ-Al_2O_3). Nanocatalysts were characterized using x-ray diffraction (XRD), raman spectroscopy, field emission scanning electron microscopy (FESEM), energy dispersed x-ray (EDX), temperature programmed reduction (TPR), vibration sample magnetometer (VSM) and N_2 adsorption.

The performance of iron nanocatalysts was studied in a microreactor at temperature 30^oC to 200^oC, feed flow rate 28 cm^3/min to 120 cm^3/min, space velocity 8400 $cm^3/g_{cat}.h$ to 30000 $cm^3/g_{cat}.h$, H_2/N_2 volume ratio 3:1 to 5:1 and under atmospheric pressure. The effect of magnetic field on the ammonia yield was also investigated.

1.6 Overview of Thesis

This thesis consists of five main chapters. Chapter 1 provides an overview about ammonia synthesis industries. Chapter 2 elaborates on theories and reviews several works that have been carried out previously. Methodology used in carrying out the research is covered in Chapter 3. Chapter 4 presents the results and discussion of the work. The work is summarized in Chapter 5.

CHAPTER 2

REVIEW OF LITERATURE

2.1 The Role of Transition Metal in Catalysis

Transition metals are important in catalysis. Certain chemical syntheses use transition metals to catalyze the reaction such as Haber Bosch and Fischer-Tropsch reactions [8]-[9]. In general, elements which have d-orbital as the outermost orbital are categorized as transition metals [1], [10].

Iron, Fe is a part of transition metal elements. It possesses 26 electrons with electronic configuration of $1s^2$ $2s^2$ $2p^6$ $3s^2$ $3p^6$ $4s^2$ $3d^6$ or [Ar] $4s^2$ $3d^6$ [1], [10]. The use of iron as a catalyst especially in ammonia synthesis is crucial. Ammonia may not be formed or reaction has to be carried out in severe conditions if iron catalyst is not used.

In ammonia synthesis reaction, atomization is an initial step which has to be experienced by nitrogen and hydrogen molecules before proceeding to the next steps. It allows molecules to dissociate, eventually forming nitrogen and hydrogen monoatomics. This step occurs once reactant molecules are bonded onto metal surface. This bonding is called surface bond. Moreover, the strength of this bonding determines the energy that is required to accomplish the overall mechanism. This energy is recognized as a thermodynamic driving force. The strength of the surface bond and the thermodynamic driving force are greatly influenced by the number electrons in the d-orbital of the transition metals. These factors could predict how fast the atomization, subsequently influencing the ammonia production process as elaborated in [8], [11]. A diagram called “Volcano Curve” can be cited which explains the dependency of ammonia produced on the number of electrons in d orbital as illustrated in Figure 2.1.

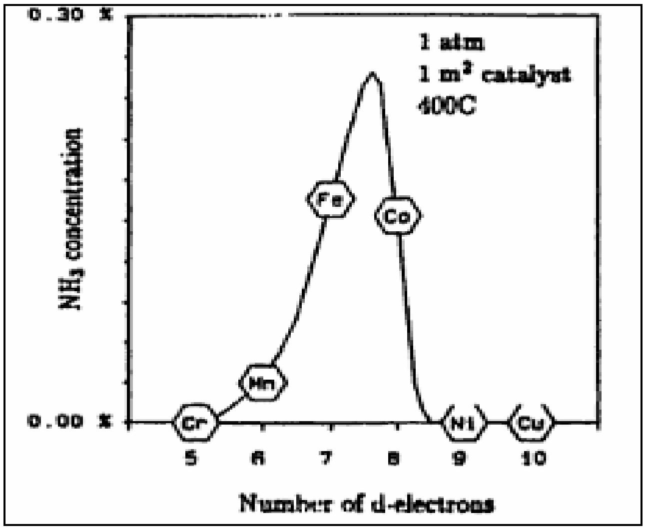

Figure 2.1: Dependency of ammonia yield on transition metals [8], [11].

The curve in Figure 2.1 clearly emphasizes that ammonia concentration depends on the number of electrons in the d-orbital of transition metals. Interestingly, the highest concentration is achieved using iron as a catalyst (Figure 2.1) which has six valence electrons in the d-orbital [8], [11].

Theoretically, metals with fewer d-electrons will create a strong surface bond. It will prolong the residence time of adsorbed nitrogen and hydrogen molecules on the metal surfaces, thus blocking the adsorption of incoming molecules during reaction intermediates. As a consequence, the reaction may stop early and low ammonia concentration might be attained. These explained the trend observed for Cr and Mn (Figure 2.1). Conversely, the necessary surface bond may not be present for Ni and Cu due to full occupancy of the d-orbital forbidding the catalytic activity of the metals (Figure 2.1). Iron gives highest ammonia yield as compared to other elements (Figure 2.1) due to partial occupancy of the d-orbital. Therefore, intermediate-strength surface bond is formed which is sufficient to induce the dissociation steps especially for nitrogen molecules. Herein, residence time for the intermediate process is shortened, hence accelerating the desorption of ammonia [8], [12].

Surface property is an important aspect in catalysis. Ammonia synthesis is a structural sensitive reaction. Figure 2.2 shows the rate of ammonia synthesis over different iron surfaces. Fe (111) and Fe (211) are active surfaces for the ammonia synthesis. Both of them reveal higher ammonia production rate as compared to those other surfaces (Figure 2.2). Few possible factors were suggested to account for this trend which includes surface roughness, work function, φ and C_7 active site.

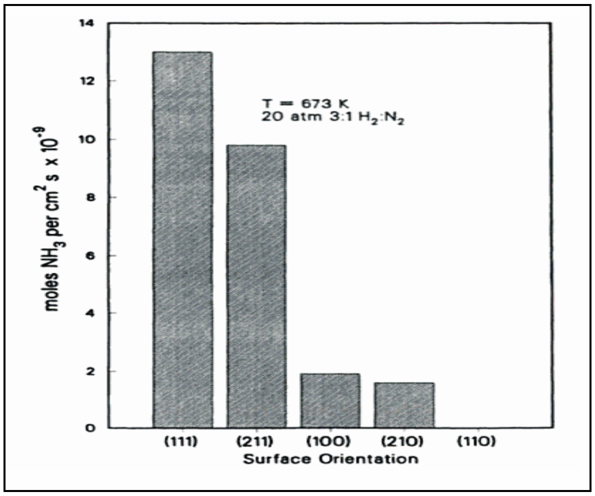

Figure 2.2: Rate of ammonia synthesis over different iron surfaces [8], [11].

Figure 2.3 illustrates the schematic orientation for different iron surfaces which are Fe(111), Fe(210), Fe(100), Fe(211) and Fe(110).

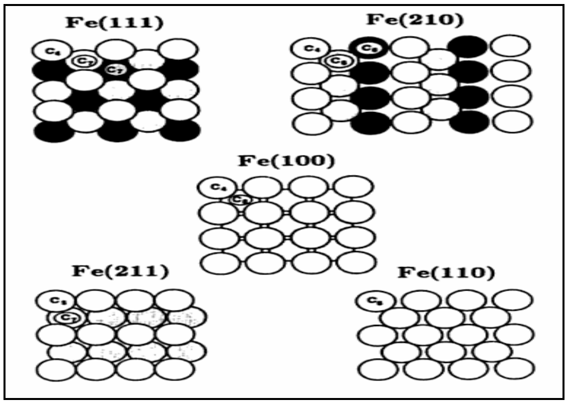

Figure 2.3: Iron (Fe) surfaces [8], [11].

Fe (111) surface has high roughness as it has open face structure which exposes the second and third layers of atoms. Meanwhile, low surface roughness is anticipated for Fe (110) surface. The atoms for the Fe(110) are arranged in close packing manner and only first layer of atoms are exposed (Figure 2.3). Surface roughness is inversely proportional to work function, φ. Low work function is required for inducing electrons transfer process from d-orbital of iron to 2π* antibonding orbital in nitrogen molecules. This process is called "π back donation". The triple bond within nitrogen molecules becomes weaker, thus encouraging the dissociation process. Highest activity for Fe (111) surface (Figure 2.2) is possibly due to high surface roughness and low work function, φ. The same deduction can also be applied to Fe (110) surface [8], [11].

Fe (210) should exhibit higher activity than Fe (211) as it also exposes second and third layers of atoms. However, that is not the case here which suggests that the presence of C_7 active site is important. The C_7 site exists when the central atom is surrounded by seven nearest atoms. The existence of this site in Fe (211) surface increases the catalytic activity due to low energy fluctuations of highly coordinated surface atoms (Figure 2.3) [8], [13].

The importance of iron-based catalyst in ammonia synthesis has been elaborated previously. However, the performance of conventional catalyst remains questionable. It was reported that, current industries are only capable of generating approximately 10-20% ammonia yield under severe synthesis conditions [4]. Recent studies showed that ruthenium is a good catalyst for ammonia synthesis. The activity increased by 10-fold when Ru was promoted with alkali metal and supported on carbon catalyst [7]. Kellogg Advanced Ammonia Process (KAAP) applied Ru- based catalyst and produced about 600 t NH_3/day. This yield was attained under slightly lower pressure (70-105 bar) compared to 150 – 300 bar for iron based catalyst system [7], [14].

Figure 2.4 shows the activity of various transition metals for synthesizing ammonia as a function of the degree of d-band electron filling.

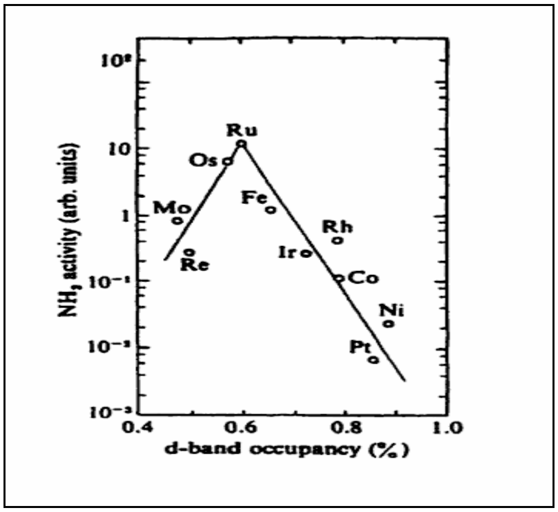

Figure 2.4: Activity of various transition metals on ammonia synthesis [8], [11].

The highest activity is given by Ru catalyst (Figure 2.4). One of the factors contributing to this trend is the presence of small number of the so-called B-5 sites in the ruthenium structure. The B-5 site is found to be extremely active for nitrogen dissociation in rate determining-step, which eventually controls the overall reaction rate. However turning to ruthenium is uneconomical due to its high price compared to other elements, as summarized in Table 2.1 [14]. Plant-scale ammonia synthesis usually involves high cost of productions and the use ruthenium-based catalyst as investigated by Liang [7] and Rosowski [14], could escalate the operational cost as well.

Table 2.1: Transition metal prices in 2010 [15].

Element	Purity (%)	Price (USD)/gram
Iron (Fe)	99.97	0.06
Ruthenium (Ru)	99.95	53.3
Nickel (Ni)	99.90	0.26
Cobalt (Co)	99.90	0.44

2.2 Nanocatalyst

Nanotechnology is a study of controlling the matter so that the size of its structure lies at 100 nm and below. Nanocatalyst is a part of these technology applications [16]. The most essential property of a nanocatalyst is the large surface area than those of bulky materials [17]. These features could enhance the catalytic activity. Study on performance of iron-based nanocatalysts over ammonia synthesis has been actively conducted nowadays. Fe_3O_4 catalyst with the size 8.0 nm was utilized by Jacobsen et al. [18] in ammonia synthesis. Other investigation [19] synthesized ammonia using 31 nm of iron particles supported on an activated carbon.

2.3 Ammonia Synthesis Catalyst

Typical ammonia synthesis catalyst is developed by combining metal crystallite (active phase), textural and electronic promoters [9], [20].

2.3.1 Active phase

Metal that can catalyze the reaction is called the active phase. Intermediate surface bond strength, low work function and high roughness are desired characteristics for active phase which usually exists as oxide compounds. This oxide will initially undergo reduction process to form metallic phase. The reduction can be performed using reducing agents such as hydrogen, H_2 or carbon monoxide, CO gases at specific conditions [8], [21]-[22]. Hematite, α-Fe_2O_3 and magnetite, Fe_3O_4 are two typical oxides for ammonia synthesis catalyst.

α-Fe_2O_3 is evolved by the arrangement of Fe^{3+} and O^{2-} ions in hexagonal unit cell (Figure 2.5 (a)). These ions are arrayed as hexagonal close-packed where every Fe^{3+} cation is surrounded by six O^{2-} anions, forming an octahedral site (Figure 2.5 (b)). The unit cell has lattice parameters of a = 0.5034 nm and c = 1.3572 nm. Moreover, each octahedron shares edges with three neighbouring octahedral in the same plane and also one face with an octahedron in the adjacent plane (Figure 2.5 (c)).

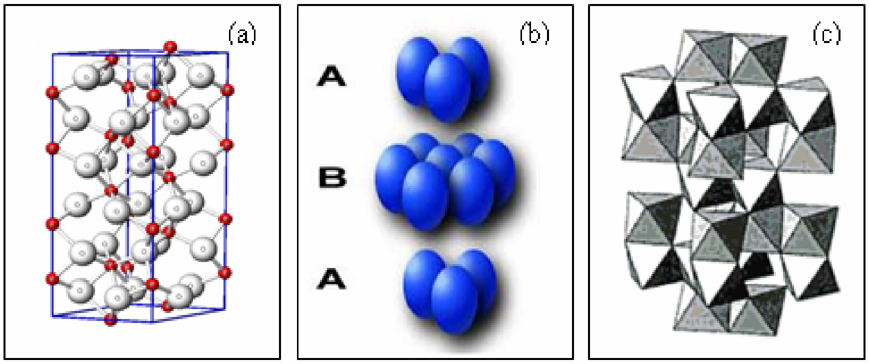

Figure 2.5: Structure of hematite, α-Fe_2O_3 (a) ball and stick model of ions arrangement in unit cell [23] (b) hexagonal close-packed system of ionic arrangement [24] and (c) arrangement of octahedron [20].

On the other hand, Fe_3O_4 encompasses a mixture of α-Fe_2O_3, and $Fe_{1-x}O$. The structure consists of two sites namely octahedral and tetrahedral. Octahedral is occupied by Fe^{3+} and Fe^{2+}, while tetrahedral is filled by Fe^{2+} ions (Figure 2.6 (a)). The presence of these sites gives inverse spinel behavior to Fe_3O_4. Furthermore, all ions are arrayed as cubic closed packed in cubic unit cell with edge length, α of 0.839 nm [20].

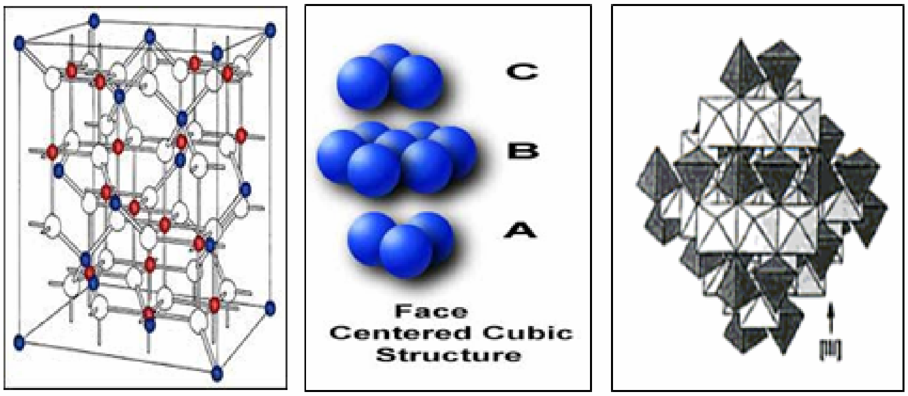

Figure 2.6: Structure of magnetite, Fe_3O_4 (a) ball and stick model of ions arrangement in unit cell [20] (b) face centred-cubic close-packed system of ionic arrangement [24] and (c) arrangement of octahedron [20].

2.3.2 Textural Promoter

Active phase or pure metal will not be stable by itself. It tends to agglomerate with neighbouring particles especially at high temperature due to high surface energy. As a consequence, bulky particles are formed hence reducing the surface area. Thus, fewer sites are available for the catalytic reaction to take place. Therefore, a component that can hold the particles and prevent agglomeration is needed. This component is known as a textural promoter. Textural promoter should have few interesting characteristics such as highly porous, high surface area and significant pore volumes which can improve dispersion of the active phase. A typical textural promoter in ammonia synthesis catalyst is alumina, γ-Al_2O_3. It offers several benefits such as excellent thermal stability and wide range of chemical, physical and catalytic properties. Table 2.2 summarizes some physical properties of γ-Al_2O_3 [9].

Table 2.2: Common physical properties of alumina, γ-Al_2O_3 [9].

BET surface area (m^2/g)	Pore Volume (cm^3/g)	Pore Diameter (nm)
100-300	0.4-0.5	6-40

2.3.3 Electronic Promoter

The main reason of including promoter is to provide excess electron to the catalyst system. This could enhance and accelerate the dissociation of reactant molecules. Electronic promoter is usually included with relatively small quantities (e.g. 1-5%). Excess amount will inhibit the catalytic activity as it can cover the surface area of active phase, hence blocking the adsorption of incoming molecules. Potassium oxide, K_2O is a typical electronic promoter for ammonia synthesis catalyst [9]

2.4 Magnetic Material

Magnetic material refers to any material that exhibits magnetic behavior. Three facts must be considered when discussing this topic. Firstly, some materials may have natural magnetic behavior and become more magnetic with introduction of magnetic field. Secondly, materials will lose its magnetic behavior when the temperature is above their critical temperature. Thirdly, an opposite behavior towards external magnetic field can also be observed for some materials [25].

2.4.1 Magnetic Domain

Magnetic domain can be described as the region within the magnetic material. Their existence can minimize the magnetic free energy. In addition, magnetic materials could possess a single or multi domains. Each domain is separated by domain walls and has a uniform magnetization which is equal to saturation magnetization, Ms. Different domains show diverse magnetization directions [26]. Figure 2.7 illustrates the alignment of magnetic moments in multi domains without magnetic field influence [27].

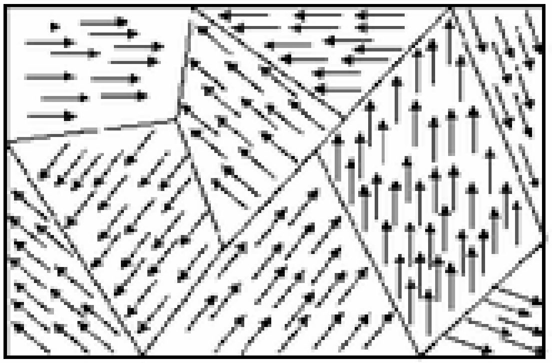

Figure 2.7: Schematic illustration of magnetic moments alignments in multi domains [27].

2.4.2 Classification of Magnetic Materials

Magnetic materials can be divided into several classes which depend on the way of moments alignment in the domain. Few typical classes include ferromagnetic, antiferromagnetic, ferrimagnetic and paramagnetic [20]. Figure 2.8 illustrates the alignments of magnetic moments in the domain.

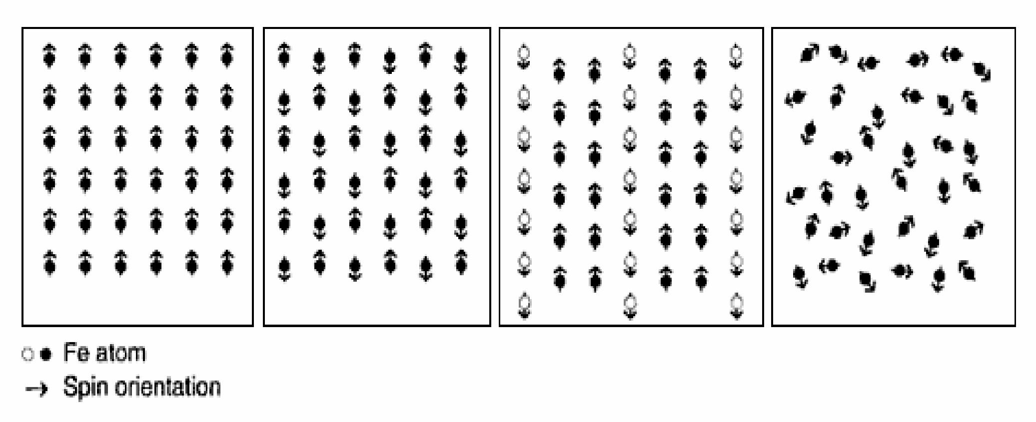

Figure 2.8: Schematic illustration of magnetic moments alignments in (a) ferromagnetic, (b) antiferromagnetic, (c) ferrimagnetic and (d) paramagnetic materials [20].

For some iron oxides, the moments are aligned either in parallel or antiparallel manners (Figure 2.8). It is due to the super exchange interaction which exists when unpaired electrons in e_g orbital of Fe^{3+} and p orbital of O^{2-} are magnetically interacted. Consequently, the Fe-O bond distance becomes shorter, thus enhancing the electron-coupling process [20], [26].

2.4.3 Magnetic Field Strength

The magnetic behavior becomes more pronounced even in weak magnetic field strength. This is due to the existence of a “torque” experienced by the moments as a result of introducing external magnetic field, hence permitting the moments to be aligned in the direction of exerted field. The degree of alignment can be computed as the total of magnetic moments per unit volume or commonly refers to magnetization (M) [25]. In addition, magnetization is also found to be related to the strength of the applied field (H) as expressed in Equation 2.1 [25] where χ refers to the magnetic susceptibility of the materials.

$$M = \chi H \tag{2.1}$$

Under a weak field, the moments begun to orient in the direction of exerted field. The movement of domain walls is also initiated at this point. Meanwhile, increasing the strength of exerted field can speed up the walls movement; eventually constructing a single large domain. At present, all moments are thought to align in a parallel manner. This occurrence designates that the saturation magnetization has been attained. Figure 2.9

demonstrates the effect of magnetic field strength on the magnetic behavior of materials [28].

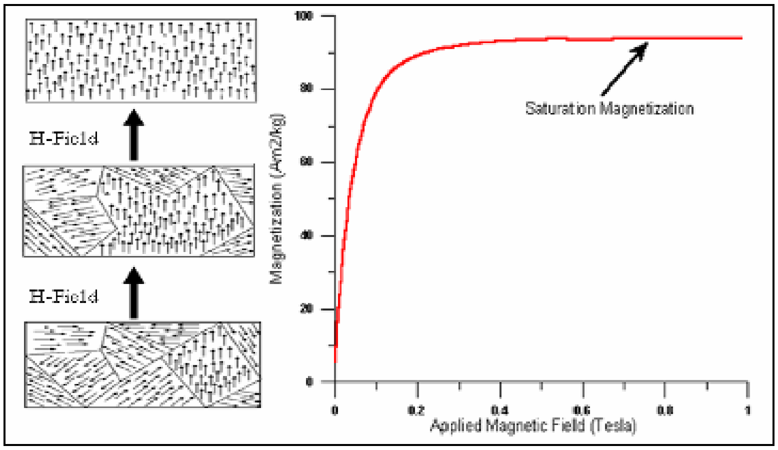

Figure 2.9: Orientation of magnetic moments in the domains with increasing magnetic field strength [28].

A loop called “Hysteresis” is commonly used to study the response of material with a change in the applied field using the vibration sample magnetometer (VSM) equipment. The curve patterns are varied depending on the type of magnetism [25]-[26]. Figure 2.10 demonstrates the typical hysteresis loops for magnetic materials [29].

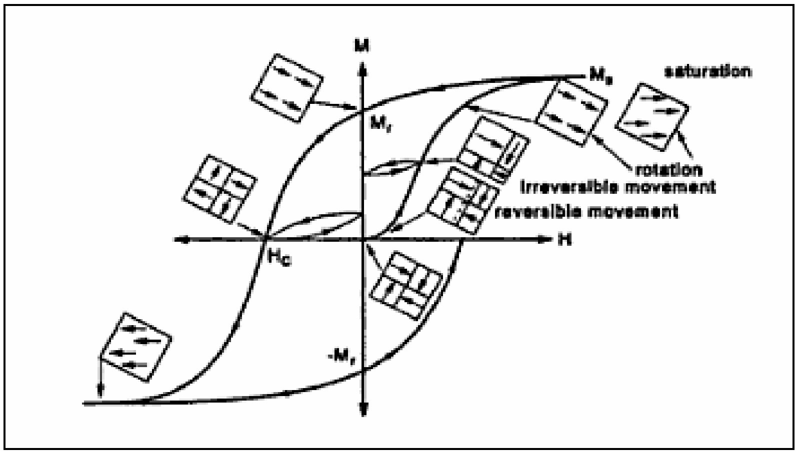

Figure 2.10: Typical hysteresis loop for magnetic material [29].

As illustrated in Figure 2.10, the moments are aligned antiparallel in the absence of external field. However, increasing the strength of the magnetic field will provide sufficient energy for the moments to overcome the randomizing effect. Consequently, all moments can be eventually aligned in parallel manner and the material has achieved saturation magnetization which is labelled as M_s (Figure 2.10). On the other hand, some moments remain aligned when reducing the exerted field strength to zero. This point is called remanence magnetization, M_r. Therefore; further reduction of exerted field strength to negative values is required to restore the moments to be aligned equally as their initial position. Herein, the measured strength is named as coercivity force, H_c [25]-[30].

2.4.4 Effect of Environmental Temperature

Material can reveal various magnetic characters in different temperature environments. It will exhibit superparamagnetic character when the temperature is increased beyond the critical point. This point is called Curie temperature or T_c [31]. At this point, the alignment of moments is no longer in a parallel manner but randomly oriented. Thus an opposite respond towards applied field is obtained. Figure 2.11 reveals the dependency of magnetic character on the temperature of the environment [28].

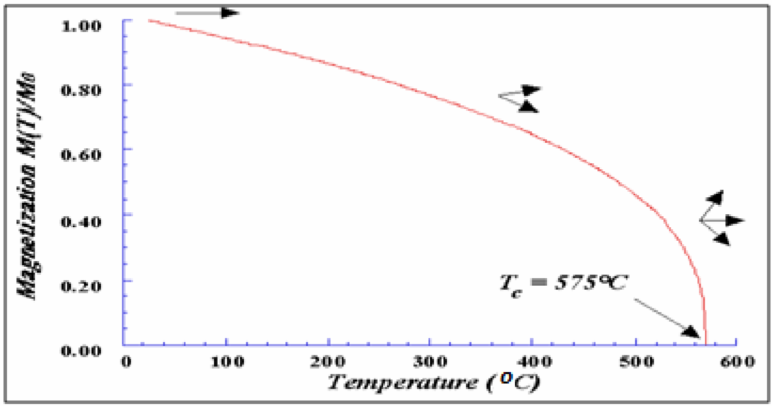

Figure 2.11: Effect of temperature on magnetic characters [28].

α-Fe_2O_3 exhibits weak ferromagnetic at room temperature and transforms to antiferromagnetic at the Morin temperature, T_m of 260 K. The Morin temperature, T_m is defined as a point where the magnetic character of a material turns to be antiferromagnetic. Furthermore, it also reveals paramagnetic above the Curie temperature, T_c of 950 K. On the other hand, ferrimagnetic character is displayed by magnetite at room temperature with Curie temperature, T_c of 850 K [20]. The existence of ferrimagnetic behavior is related to the unique alignment of magnetic moments in the internal structure. Fe_3O_4 contains Fe^{2+} and Fe^{3+} ions. The Fe^{2+} ions occupy tetrahedral site while Fe^{3+} ions are partially distributed to octahedral and tetrahedral sites. The electron spins for Fe^{3+} in both sites are aligned antiparallel, thus giving no net magnetic moments. The appearance of Fe^{2+} ions in octahedral site gives parallel spins alignment with neighbouring Fe^{3+} spins, hence revealing a net magnetic moment [32]. The spins arrangement in magnetite structure can be written as $Fe^{3+}\downarrow [Fe^{3+}\uparrow Fe^{2+}\uparrow] O_4$ [20].

2.4.5 Effect of Particle Size

Magnetic character is found to vary with particles size. Several works examined a consistent increase in magnetization saturation value, M_s; as a result of enlarging the size of particle [32]-[36]. Increasing particle size will increase the fraction of magnetism phase, thus growing the domain from a single to multidomains. Therefore, more magnetic moments are available to respond to the exerted field. In addition, large coercivity force, H_c may be required to completely demagnetize the remaining aligned moments [31]-[32]. The synthesized particles ought to come with the size beyond finite point. Particles with or below than finite point often exhibit superparamagnetic phase. Previous studies investigated that the critical size for most of iron oxides was approximately 10 nm [20], [31], [33], [37]-[39]. These particles displayed small saturation magnetization, M_s and large coercivity, H_c as reported elsewhere [31], [40]-[41]. Theoretically, materials with fewer or no domains will exhibit higher coercivity than those of multidomains [42]. This trend is related to the energy barrier (ΔE) for the rotation of magnetic moments, as elaborated in literatures [40]-[41]. It was discovered that there is a significant relation between surface area, S and energy barrier for the moments rotation, ΔE (J) as described by Equation 2.2 where K_s is the anisotropy constant (J/m^2) [40]-[41].

$$\Delta E = K_s S \tag{2.2}$$

Large surface area particles may possess greater energy barrier for the moment's rotation. However when particles having size equal or less than critical point, domain which is smaller than the single domain can be evolved. As investigated previously, single domain existed for those spherical particles with the size of ~15 – 100 nm [37], [39]. Herein, the available space may be insufficient to allow moments orientation, thus requiring stronger magnetic force to accomplish complete demagnetization. Consequently, higher coercivity value can also be expected. The relation between particles size with coercivity force is expressed in Equation 2.3 [40]-[41] where H_c corresponds to coercivity force (Oe) and *d* is the particle size.

$$H_c \sim 1/d \tag{2.3}$$

2.5 Nanocatalyst Preparation Method

The typical methods to synthesize iron oxide nanocatalysts are sol gel, precipitation and hydrothermal.

2.5.1 Theory of Preparation Method

2.5.1.1 Hydroxylation Step

Hydroxylation is the earliest step in many synthesis methods such as sol gel, precipitation and hydrothermal. The hydroxylation or hydrolysis is defined as a process to introduce hydroxyl ligand, OH^- in the structure of metal complex [43].

The hydroxylation step depends on two factors. Firstly is the formation of a soluble precursor. Iron (III) nitrate nonahydarates, $Fe\ (NO_3)_3.9H_2O$ salt is highly soluble in many solvents such as water, ethylene glycol, as well as nitric acid [43]. Secondly is the dissociation of undesired counter ions. Figure 2.12 illustrates the chemical structure of $Fe(NO_3)_3.9H_2O$ in an aqueous state [44].

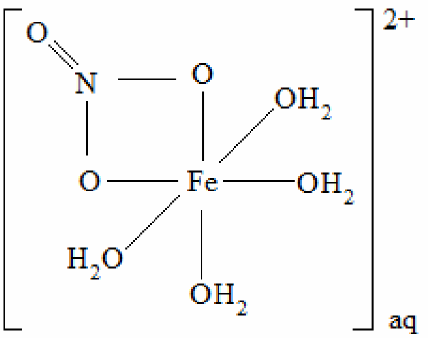

Figure 2.12: Chemical structure of the $Fe(NO_3)_3.9H_2O$ in aqueous state [44].

Nitrate, NO_3^- is a bidentate ligand [1], [44] which is able to replace two H_2O ligands [44]. On the other hand, NO_3^- is also a π donor ligand while H_2O behaves as a donor ligand and a good nucleophile. When NO_3^- and H_2O are coordinated around the Fe center, the electrons within these ligands are transferred to the Fe center, thus enriching the electron density of Fe. However, both NO_3^- and H_2O tend to compete so as to remain coordinated at the Fe center. Hence, electronegativity factor is taken into account which determines the ability of these ligands to remain coordinated or dissociated at the Fe center. The electronegativity, $\bar{\chi}$ for H_2O and NO_3^- is 2.49 and 2.76, respectively. Because NO_3^- has a slightly higher electronegativity, it favors to attract the electrons from the high electron density of the Fe center. This increases the negative charge of NO_3^- to a value of -0.84. The π back donation process increases, hence raising the electron density of NO_3^-. The Fe-ONO_2^- bonds become weaker which subsequently reduces the ability of the NO_3^- to complex with the Fe center. The NO_3^- is finally dissociated, leaving two vacant sites which are then filled by the H_2O ligands. The ionic dissociation process shifts to the right side, eliminating the NO_3^- from the Fe-complex structure as described in Equation 2.4 [44].

$$[Fe(NO_3)(OH_2)_4]^{2+}_{(aq)} \leftrightarrow Fe(OH_2)_6]^{3+}_{(aq)} + NO_3^-{}_{(aq)} \qquad (2.4)$$

Equation 2.5 [44] describes the general chemical equation for the hydroxylation process, where p is the number of acidic proton released, Z is the formal charge and N is the coordination number.

$$[MO_NH_{2N}]^{z+} + pH_2O \leftrightarrow [MO_NH_{2N-p}]^{(z-p)+} + pH_3O^+ \qquad (2.5)$$

Water is amphiprotic which means that the process of transferring a proton, H_3O^+ happened even in the absence of acid or base. The H^+ is transferred from one water molecule to another and this occurrence is named as autoionization. Equation 2.6 [1], [10] describes the autoionization process.

$$2H_2O_{(aq)} \leftrightarrow H_3O^+{}_{(aq)} + OH^-{}_{(aq)} \qquad (2.6)$$

2.5.1.2 Sol Gel Method

The sol gel method is based on hydroxylation and condensation processes. The hydroxylation process has been elaborated in Section 2.5.1.1. The $[Fe(H_2O)_6]^{3+}$ complex must be entirely converted to zero valence charge complex, $[Fe(OH)_3(OH_2)_3]^o$ for the condensation process to take place. This can be accomplished by adding oxidizing agent such as the HNO_3 or hydrogen peroxide, H_2O_2 [44]. Nitric acid, HNO_3 is a strong oxidizing agent [1], [10] that can dissolve most metal precursors [43]. The mixture must be heated to initiate the condensation due to enthalpy change, ΔH is positive [44].

Condensation process comprises olation, gelation and oxolation steps. The olation is a process where the hydroxo or “ol” bridge, Fe-OH-Fe is formed via nucleophilic substitution (SN). This step is initiated when the $[Fe(OH)_3(OH_2)_3]^o$ has been successfully formed. In this step, iron-hydroxyl, Fe-OH acts as the nucleophile while water, H_2O

operates as the leaving group. The "ol" bridges can be formed via several ways as demonstrated in Equations 2.7-2.10 [44].

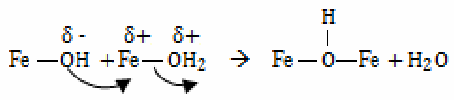
(2.7)

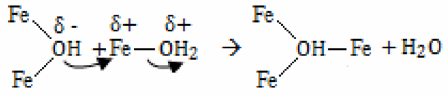
(2.8)

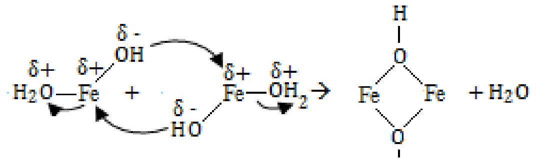
(2.9)

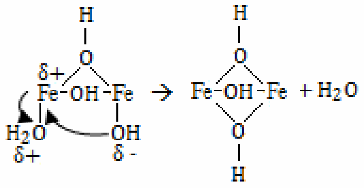
(2.10)

The olation step is ended when all H_2O ligands are entirely removed from the coordination sphere. The next step is the gelation which involves prototropic reaction whereby a proton jumps in between two adjacent OH^- ligands as illustrated in Equation 2.11.

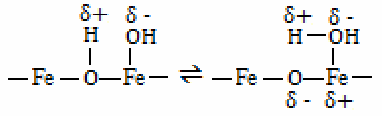
(2.11)

The occurrence of protonic reaction mainly depends on electronegativity of the H_2O ligand, $\delta(H_2O)$ and type of transition metal. The electronegativity of H_2O, $\delta(H_2O)$ value for the Fe complexes is tabulated in Table 2.3.

Table 2.3: Stability of hydroxide $M(OH)_z$ for Fe complexes calculated from Partial Charge Model [44].

Soluble precursor	$\delta(H_2O)$	Solid hydroxide formed by pure olation	$\delta(H_2O)$
$[Fe(OH)_3(H_2O)_3]^o$	+ 0.03	$Fe(OH)_3$	+ 0.07

As shown in Table 2.3, the electronegativity of $\delta(H_2O)$ for the Fe complexes is greater than zero, ($\delta(H_2O)>0$), resulting in a net repulsion force between the Fe (δ+) and H_2O ligand (δ+). This ensures that the net reaction remains forward, preventing reversible reaction which maintains the presence of the OH^- bridge (Equation 2.11).

Oxolation is the final step in condensation process. The oxolation process entirely eliminates H_2O ligands from the coordination sphere which eventually forms the edge and face M-O-M bridges as shown in Equations 2.12-2.13 [44].

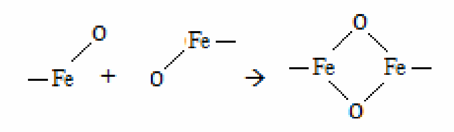

(2.12)

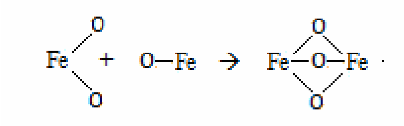

(2.13)

2.5.1.3 Hydrothermal Method

Hydrothermal method is widely used to synthesize magnetite, Fe_3O_4 nanoparticles [34]-[35], [37]. This method begins with hydroxylation as explained in Section 2.5.1.1 [44] and accomplished in an autoclave. Figure 2.13 shows a schematic diagram of a typical laboratory autoclave [45].

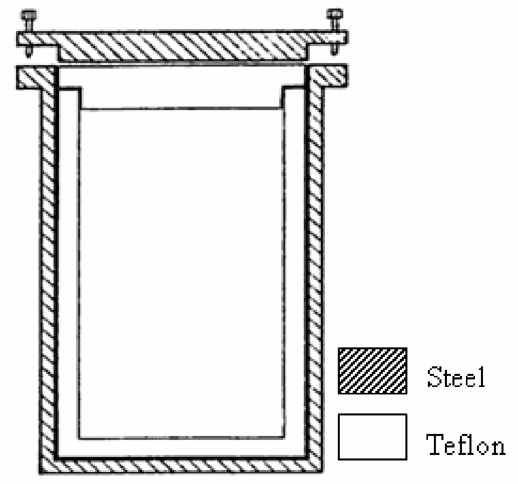

Figure 2.13: Schematic diagram of an autoclave [45].

Water is utilized as a solvent which generates vapor. It also works as the pressure transmitting medium. The hydrothermal method is typically accomplished at certain pressure and temperature above the boiling point of water [44]. Hydrazine hydrate, $N_2H_4.H_2O$ is a common additive used in the hydrothermal method [34]-[35], [37]. It serves as a base that increases the pH of the $[Fe(H_2O)_6]^{3+}$ complex precursor [1], [44]. This induces polymerization and precipitation processes, hence yielding a precipitated polymer, $Fe(OH)_3.nH_2O$ [1]. Equation 2.14 [1] shows the chemical equation for the precipitation process.

$[Fe(H_2O)_6]^{3+}{}_{(aq)} + (3 + n)H_2O \rightarrow Fe(OH)_3.nH_2O + 3H_3O^+{}_{(aq)}$ (2.14)

Besides acting as a precipitant, hydrazine, N_2H_4 also serves as a powerful reducing agent, having a standard reduction potential, E^o of -1.16 V [1], [10], [34]. The standard reduction potential, E^o for reducing Fe^{3+} to Fe^{2+} at 25°C is 0.771 V [1], [10]. A reducing agent that has more negative standard reduction potential, E^o than that of a metal must be employed to reduce the metal [46]. This explained the selection of N_2H_4 in preparing Fe_3O_4 via the hydrothermal method [34]-[35], [37]. However, the capability of reducing becomes less in an open system and under hot alkaline environment due to the disproportionation reaction as described in Equation 2.15 [47].

$3N_2H_4 \leftrightarrow N_2 + 4NH_3 \quad E_o = -1.16\ V$ (2.15)

Highly negative standard reduction potential, E^o of N_2H_4 shifted the overall process to the right side, enriching N_2 and NH_3 (Equation 2.15). Therefore, the use of an autoclave is to avoid the N_2 and NH_3 from escaping to the atmosphere, thus generating high partial pressures of these two components. Increasing synthesis temperature pressurized the internal part of an autoclave which subsequently raised the partial pressure of nitrogen, N_2 and ammonia, NH_3 to a critical value. As a result, the overall reaction (Equation 2.15) is reversed, maintaining N_2H_4 as the dominant component. Thus, the reducibility of Fe^{3+} to Fe^{2+} can be enhanced [47].

During the hydrothermal process, the $N_2H_4.H_2O$ initially dissociates, forming $N_2H_5^+$ and OH^- ions in the presence of water (Equation 2.16 [34], [37]) at room temperature. The presence of the OH^- anions dissolved the iron (III) hydroxide, $Fe(OH)_3$ precipitate, forming an intermediate phase goethite, FeO(OH) (Equation 2.17 [34], [37]). Finally, N_2H_4 reduces the goethite, FeO(OH) to yield magnetite Fe_3O_4 (Equation 2.17 [34], [37]) that is usually accomplished at 80-160°C, as reported in literature [34], [37]. The proposed chemical equations for these steps are written in Equations 2.16 – 2.18 [34], [37].

$N_2H_4 + H_2O \rightarrow N_2H_5^+ + OH^-$ (2.16)

$Fe(OH)_3 \rightarrow FeO(OH) + H_2O$ (2.17)

$12FeO(OH) + N_2H_4 \rightarrow 4Fe_3O_4 + 6H_2O + N_2$ (2.18)

2.5.1.4 Precipitation Method

Precipitation method is often used to synthesize magnetite, Fe_3O_4 nanocatalyst [31]-[32], [36], [48]-[50]. The synthesis can be carried out either by precipitation of Fe^{2+} or a mixture Fe^{2+} and Fe^{3+} with the molar ratio of 1:2 precursors. After undergoing hydroxylation process (Section 2.5.1.1), the pH of the precursor is increased to above 7 by adding a precipitating agent such as ammonia hydroxide, NH_4OH, and sodium hydroxide, NaOH. This is to remove H_2O and introduce OH ligands to the Fe center. Consequently, a hydrous iron oxide precipitate is formed (Equation 2.13, Section 2.5.1.2). This follows the proposed Charge-pH diagram as illustrated in Figure 2.14 [44].

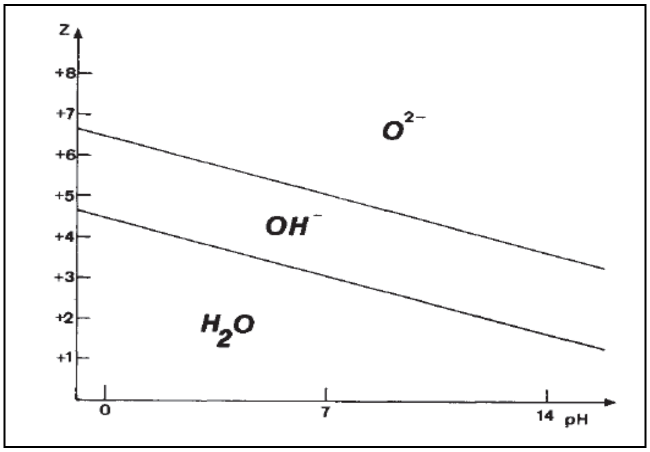

Figure 2.14: Charge-pH diagram for transition metal [44].

For ferrous, Fe^{2+} precursor, the minimum pH to form ferrous hydroxide, $Fe(OH)_2$ precipitate is 7 [20], [32]. This pH has to be increased to accelerate the partial oxidation of ferrous, Fe^{2+} to ferric, Fe^{3+} by the dissolved oxygen molecules in the system, hence yielding a mixture of ferrous hydroxide-ferrihydrite, $Fe(OH)_2$-$Fe_5HO_8.4H_2O$. The electrons mobility between Fe^{2+} and Fe^{3+} finally drives to a spinel arrangement [20], [32].

In the case of using Fe^{3+}/Fe^{2+} mixture, Fe^{3+} ions firstly undergo hydrolysis at pH 3 forming a highly soluble ferrihydrite, $Fe_5HO_8.4H_2O$. The $Fe_5HO_8.4H_2O$ is then combined with the existing Fe^{2+} ions to form Fe_3O_4 at higher pH. The proposed chemical equation for this formation is described in Equation 2.19 [32].

$$2Fe^{3+} + Fe^{2+} + 8OH^- \rightarrow Fe_3O_4 + 8H_2O \qquad (2.19)$$

There are several factors which influence the properties of resultant, Fe_3O_4 nanocatalyst. They comprise rate of pH increment [32], synthesis temperature [32], dropping rate of precipitant [36], and type of precipitant [36]. In the case of Fe^{2+}/Fe^{3+}

precursor, a rise in pH must be sufficiently fast to accelerate the incorporation of the Fe^{2+} ions into $Fe_5HO_8.4H_2O$ yielding Fe_3O_4. This avoids the oxidation of Fe^{2+} to Fe^{3+}, which easily occurs at higher pH [32]. Temperature has to be monitored. Higher temperature accelerates the oxidation of Fe^{2+} to Fe^{3+} by the dissolved oxygen in the system, thus leading to the formation of undesired phases [32]. In addition, dropping rate influences the size of resultant nanoparticles. Slow dropping rate is recommended as it can form a homogenous pH variation that is uniform all over the solution, thus producing much smaller particles with narrow size distribution [36]. The selection of proper precipitating agent is also emphasized in precipitation method. It was reported that the use of NH_4OH produced smaller particle size than that of NaOH. The NH_4OH allows a smooth increase in pH due to gradual increase of OH^- ions. This makes the formation of particles controllable. On the other hand, NaOH contains higher concentration of OH^- even if the concentration is the same as NH_4OH. This leads to the attainment of bigger particles [36].

2.5.2 Comparison between Various Methods of Preparation

There are several methods widely used to prepare unsupported Fe-based nanocatalysts such as sol gel [33], [40], [51], hydrothermal [47], [52]-[55] and co-precipitation [48], [56]. In general, the size and crystallinity of the resultant nanocatalyst is greatly influenced by annealing or calcination process. Elevating the annealing temperature enhances the crystallinity [57]-[58] and enlarges the particles size [57]-[59]. An increase in particle size is a result of the agglomeration of the smaller particles due to their high surface energy [60]-[61]. Particles agglomeration is enhanced by increasing the annealing temperature [57], [59].

The sol gel method promotes simplicity, homogeneity, low cost and high purity [33], [44], [62]. The underlying principles of this method have been elaborated in Section 2.5.1.2. Solvent selection and mechanical agitation are crucial factors for the sol gel method. A solvent must be able to entirely dissolve the metal precursor [43]. Meanwhile, mechanical agitation induces homogeneity of the sol which subsequently leads to the achievement of supersaturating point. The supersaturation point is a condition where the precursor is dissolved completely, hence accelerating the nucleation process [63]-[65].

Several advantages of using hydrothermal method include safe and environmental friendly as it is performed at moderate temperature [66], kinetic of reaction is accelerated with a small increase in temperature and single-phase crystals can be obtained easily [67].

The chemistry of this method has been described in Section 2.5.1.3. The pH, concentration, temperature, aging time and mineralizer are some of the parameters which influence the resultant properties (size, crystallinity and phase) of nanocatalysts [68]. Increasing the pH of the precursor reduces the particle size whereas an enlargement in particle size is observed as an outcome of increasing the concentration of precursor [68]. The particle size increases with extending the aging time of hydrothermal [34], [68]. Moreover, increasing hydrothermal temperature formed bigger particles size with more pure Fe_3O_4 phase [34]. Mineralizer refers to an agent that can precipitate the aqueous precursor. In the case of preparing Fe_3O_4 via hydrothermal method, $N_2H_4.H_2O$ is used frequently due to its ability to reduce Fe^{3+} to Fe^{2+}. The concentration of $N_2H_4.H_2O$ also influences the formation of Fe_3O_4 in the hydrothermal method [34].

2.5.2.1 Unsupported Iron Oxide Nanocatalyst

Formation of Different Phases of Iron Oxide

Previous work employed sol gel method with $Fe(NO_3)_3.9H_2O$ as the main precursor [33], [40]. They found that the use of citric acid as a solvent formed α-Fe_2O_3 whereas γ-Fe_2O_3 was formed as a result of elevating the annealing temperature [40]. Fe_3O_4 phase was attained when ethylene glycol was used as a solvent [33].

The oxidation state of iron precursor and the synthesis pH are crucial for hydrothermal and precipitation routes [34]-[35], [37], [53]-[54]. Using hydrothermal method, Fe^{2+} precursor was merely oxidized to give pure FeOOH and finally yielded α-Fe_2O_3 at pH of 3-5 [54]. Fe_3O_4 was successfully obtained by increasing the pH to 11 and above [54]. Meanwhile, Fe_3O_4 was also attained by reducing Fe^{3+} precursor to Fe^{2+} at pH 11 using hydrothermal method [37]. Fe_3O_4 phase was also obtained through precipitation method at pH 10-13 [31]-[32], [36], [48]. A mixture consisting of Fe^{2+} and Fe^{3+} salts with a ratio of 0.5 (Fe^{3+}/Fe^{2+}) together with NH_4OH is often deployed in precipitation route.

The concentration of reducing agent and synthesis temperature are vital in hydrothermal route. Most literatures obtained highly crystalline Fe_3O_4 and α-Fe_2O_3 nanoparticles at synthesis temperature of 140-180^oC [34]-[35], [37], [53]-[55]. The use of 5% concentrated $N_2H_4.H_2O$ at synthesis temperature of 120^oC formed α-Fe_2O_3 while at 20% concentration; it led to formation of Fe_3O_4 phase [32]. Other attempts mostly employed 50-85% concentrated $N_2H_4.H_2O$ in synthesizing Fe_3O_4 nanoparticles [34]-[36], [54].

Particle Size Alteration

The concentration of solvent influences the size of resultant nanoparticles. Raising citric acid, $C_6H_8O_7$ concentration from 0.05M to 0.2 M reduced the size of α-Fe_2O_3 nanoparicles from 56 nm to 22 nm [40]. Increasing annealing temperature from 200°C to 400°C enhanced crystallinity of Fe_3O_4 nanoparticles that were synthesized via sol gel method using ethylene glycol, $HOCH_2CH_2OH$ as the solvent. The particle size also increased from 8.5 nm to 15.5 nm [33]. Similar effect was also observed in the preparation of magnetoelectric $BiFeO_3$ system via the precipitation method [60].

The synthesis temperature and aging time influence the size of the resultant nanoparticles in hydrothermal method. The average particle size of Fe_3O_4 was reported to be enlarged from 7 nm to 30 nm when synthesis temperature elevated from 80°C to 160°C [34]. Similar trend was also observed in the preparation of TiO_2 thin films. Increasing synthesis temperature from 350°C to 600°C increased the particle size from 15 nm to 30 nm [61]. Others observed that the particle size of $FeNi_3$ nanoparticles was enlarged from 20 nm to 70 nm when the synthesis duration increased from 2 h to 15 h [47].

Magnetic Behavior

Magnetic behavior of iron oxide is greatly influenced by the particle size and its composition. Previous works claimed that an increment in particle size increased the magnetization saturation, M_s value [31]-[33]. The magnetization saturation, M_s value for Fe_3O_4 nanoparticles increased from 11.2 emu/g to 14.5 emu/g when particle size increased from 7 nm to 30 nm [34]. The superparamagnetic behavior is often observed for nanoparticles with size less than 10 nm [31], [33].

α-Fe_2O_3 behaves as a weak ferromagnetic material while γ-Fe_2O_3 reveals strong ferromagnetic character at room temperature. The M_s value for α-Fe_2O_3 nanoparticles was enhanced from 3.7 emu/g to 24.9 emu/g when annealing temperature increased from 210°C to 400°C [40]. These particles were synthesized through sol gel method deploying citric acid, $C_6H_8O_7$ as a solvent. The enlarged particles may be due to the enrichment of γ-Fe_2O_3 as a result of elevating annealing temperature [40]. In the case of precipitation method, the M_s value for Fe_3O_4 nanoparticles decreased from 58.7 emu/g to 17.4 emu/g as the pH was further extended from 4.7 to 6.7 [32]. Enrichment of FeOOH composition was claimed to be the major factor for the increase in particle size. FeOOH exhibits antiferromagnetic behavior which is difficult to be magnetized by the exerted magnetic field [32].

2.5.2.2 Supported Iron Oxide Nanocatalyst

Incorporating iron metal crystallites onto the support such as alumina, γ-Al_2O_3, silica oxide, SiO_2, manganese oxide, MgO; can be accomplished through several methods such as impregnation, precipitation and sol gel [69]. To be a good catalyst, it must hold a few criteria such as highly dispersed, easy to be reduced and unpoisoned [9]. Figure 2.15 shows the schematic visualization of particles agglomeration and supported metal particles [70].

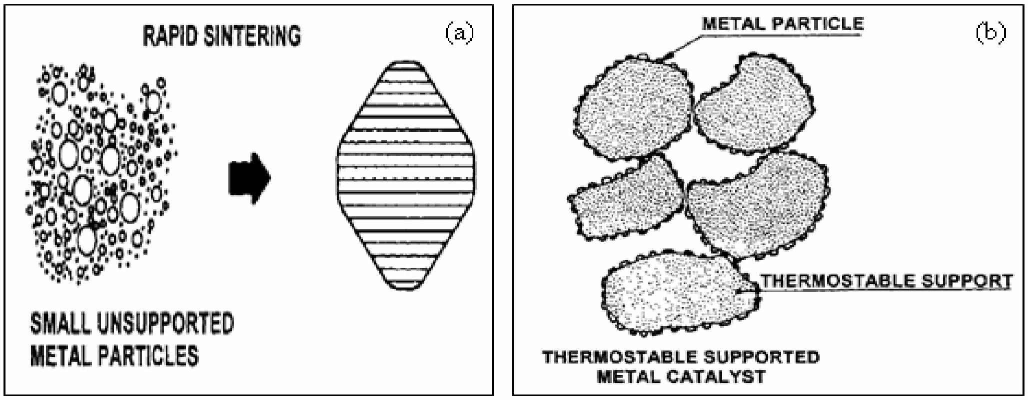

Figure 2.15: Schematic visualizations of (a) agglomerated and (b) supported metal particles [70].

Impregnation is a common method to prepare iron supported on alumina, α-Fe_2O_3/Al_2O_3 catalyst. The procedures are based on heterogeneous interaction between γ-Al_2O_3 support and iron precursor solution. Generally, the precursor is allowed to fill up the pores of the support. The system will then undergo aging, drying and annealing processes [51], [69]. Previous studies have used Fe $(NO_3)_3.9H_2O$ precursor solution which was impregnated onto commercial γ- Al_2O_3 solid system. The surface area of bulk α-Fe_2O_3 was 42 m^2/g while α-Fe_2O_3 supported on alumina, α-Fe_2O_3/Al_2O_3 resulted in surface area of 166 m^2/g [51]. Introduction of support influences the temperature of reduction. The first reduction temperature for the α-Fe_2O_3/Al_2O_3 (705 K) was slightly higher than that of unsupported α-Fe_2O_3 (644K) catalysts due to the formation of a strong spinel-hercynite,

$FeAl_2O_4$. However, temperature for second reduction stage shifted from 850 K to 800 K, comparing unsupported α-Fe_2O_3, and α-Fe_2O_3/Al_2O_3 catalysts [71]

Feasibility of performing impregnation is actively investigated recently. It was claimed that this approach is able to control the size of Fe particles on the γ-Al_2O_3 support. The preparation started by synthesizing iron oxide nanoparticles through hydrothermal route that was performed at synthesis temperature of 130 – 250^{o}C. The size of the produced nanoparticles was in the range of 2 – 12 nm. These particles were then attached onto γ-Al_2O_3 via impregnation. The size of Fe nanoparticles for the supported and unsupported did not change, which indicates that agglomeration effect is minimized. It was also reported that reduction became easier and accomplished at slightly lower temperature for those catalysts with bigger size of iron particles. Conversely, small particles showed difficulty in completing reduction process. This was claimed to be due to the strong interaction between smaller Fe particles with the γ-Al_2O_3 surface, which eventually retards the accomplishment of complete reduction [72].

The properties of supported Fe catalyst can also be influenced by the type of the catalyst support. Complete reduction of iron oxide particles to zero valence state occurred at much lower temperature when γ-Al_2O_3 was replaced with activated C. TPR characterization revealed that the first reduction for Fe/C and Fe/Al_2O_3 catalysts occurred at 227^{o}C and 391^{o}C, respectively. Meanwhile, complete reduction was accomplished at approximately 900^{o}C for Fe/C while Fe/Al_2O_3 was reduced completely at temperature above 1000^{o}C [71].

2.6 Catalyst Activation

Reduction Process

Reduction is the first process that must be carried out before the catalytic reaction takes place. The purpose of reduction is mainly to convert metal oxide to pure metal for active sites to exist. Hydrogen, H_2 and carbon monoxide, CO gases are two typical reducing agents. They must be of high purity since O_2, S_2 and H_2O could contaminate the catalyst which can retard the catalytic steps [9]. H_2 gas is preferred as it generates H_2O as the bi-product. The use of CO produces CO_2 which can contribute to green house effect [73]. Reduction is heterogeneous and controlled by nucleation process. It is highly sensitive to several kinds of defects such as point defects, grain boundaries and mechanical with inclusion of promoter and iron [8]. Figure 2.16 illustrates a typical reduction profile of Fe_2O_3 [74].

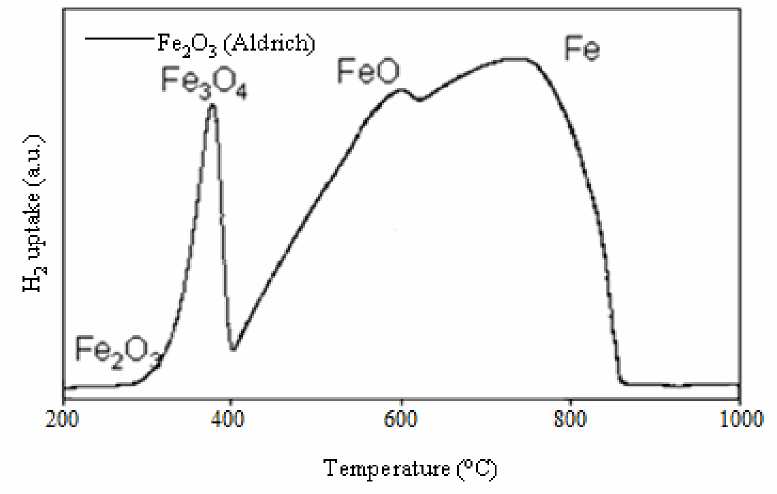

Figure 2.16: Typical reduction profile of α-Fe_2O_3 [74].

Reduction of Fe_2O_3 to Fe_3O_4 usually occurred at 150^oC to 400^oC while temperature above 500^oC is required to completely reduce Fe_3O_4 to α-Fe [22], [75]-[78]. Reduction of Fe_3O_4 involves two nucleation steps. It begins with nucleation of $Fe_{1-x}O$ within Fe_3O_4 intermediate phase framework and subsequently nucleation of α-Fe within $Fe_{1-x}O$ intermediate phase [8]. Figure 2.17 illustrates the nucleation process of Fe_3O_4 during reduction process.

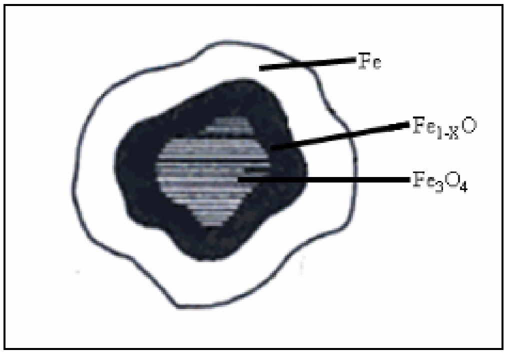

Figure 2.17: Core and shell structure for Fe_3O_4 during reduction process [8].

The structure consists of unreduced core of Fe_3O_4 which is surrounded by a dense layer of $Fe_{1-x}O$. The reduced α-Fe metallic becomes outermost layer (Figure 2.17) [8].

The mechanism of reduction involving iron oxides is quite complex. In the case of Fe_3O_4, direct access of H_2 onto reaction interface is prevented. This is due to dense and rigid properties of Fe_3O_4. Thereby, the requirement for producing the electrons is vital in this case. These electrons are formed by reacting H_2 with interface oxide, O^{2-} anions originated from nonstoichiometry $Fe_{1-x}O$. Equation 2.20 describes the chemical equation for this reaction [8], [22]. Once generated, the electrons will reduce Fe^{3+} to Fe^{2+}, yielding $Fe_{1-x}O$ as an intermediate phase as described by Equation 2.21. The reduction process is continued with direct interaction between $Fe_{1-x}O$ and H_2, resulting in iron, α-Fe metallic. Equation 2.22 [1], [8], [73], [76], [78] shows the proposed chemical equation for this process.

$$O^{2-} + H_2 \rightarrow H_2O + 2\text{ electrons} \tag{2.20}$$

$$Fe_3O_4 + Fe^{2+} + 2\text{ electrons} \rightarrow 4Fe_{1-x}O \tag{2.21}$$

$$Fe_{1-x}O + H_2 \rightarrow Fe + H_2O \tag{2.22}$$

Previous study examined the fraction composition of iron oxides during reduction by "in situ" XRD. It was found that at temperature up to 400^{o}C, α-Fe_2O_3 was almost fully converted to Fe_3O_4 with 97% composition. However, composition of Fe_3O_4 consistently decreased with elevating temperature to 560^{o}C. Three phases of iron oxide which consists of Fe_3O_4 (53%), $Fe_{1-X}O$ (7%) and Fe (40%) appeared as the temperature was increased to 580^{o}C. At 600^{o}C, Fe_3O_4 phase disappeared while two-phase system comprising $Fe_{1-X}O$ (41%) and Fe (59%) emerged. The $Fe_{1-x}O$ phase was found to be thermodynamically stable. Consequently, a complete reduction of $Fe_{1-x}O$ to Fe was entirely accomplished at 680^{o}C. These results suggested that the reduction of Fe_3O_4 involves disproportionation reaction as written by Equation 2.23 [22].

$$4Fe_{1-x}O \leftrightarrow Fe_3O_4 + Fe \tag{2.23}$$

This equation can be further expanded into two reactions as shown by Equation 2.24 and Equation 2.22 [22], [73], [75]-[76], [78].

$$Fe_3O_4 + H_2 \rightarrow 3Fe_{1-x}O + H_2O \tag{2.24}$$

Based on the findings, it can be deduced that reduction of α-Fe_2O_3 can occur via either two or three stages as stated in Equation 2.25 and Equation 2.26 [22], respectively.

$$3Fe_2O_3 \rightarrow 2Fe_3O_4 \rightarrow 6Fe \tag{2.25}$$

$$Fe_2O_3 \rightarrow Fe_3O_4 \rightarrow Fe_{1-x}O \rightarrow Fe \tag{2.26}$$

Reduction of α-Fe_2O_3 can occur in two stages at temperature less than 450^{o}C (Equation 2.25) by applying low heating rate [22], [75]-[76]. Theoretically, lowering the heating rate prolongs the contact time between the hydrogen and specimen, thus permitting complete reduction to occur at lower temperatures [22]. In this case, reaction 2.24 (Equation 2.24) is decelerated while reaction 2.22 (Equation 2.22) becomes faster, inhibiting the appearance of metastable $Fe_{1-x}O$ [22]. Complete reduction has been achieved at 450-480°C with the heating rate of 0.58°C/min [21]. On the other hand, the use of higher heating rate can lead to three-stage reduction process (Equation 2.26) which requires higher temperature to accomplish [22], [75]-[76]. Herein, reaction 2.22 (Equation 2.22) is inhibited and at the same time accelerates reaction 2.24 (Equation 2.24). This consequently enriches $Fe_{1-x}O$ composition [22]. The $Fe_{1-x}O$ phase is stable at temperature above 570°C. Thus, much higher temperature is needed to completely transform it to Fe metallic [22], [73]. Figure 2.18 deduces the steps involve in the reduction of α-Fe_2O_3.

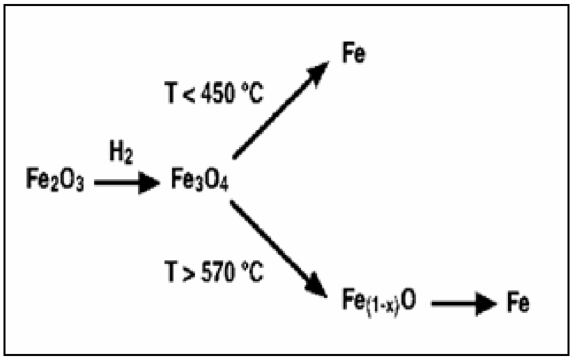

Figure 2.18: Reduction steps of α-Fe_2O_3 [22], [73], [79].

Low heating rate could enhance the reducibility. Unfortunately, longer period is required to achieve complete reduction. Conversely, the reduction can be performed faster by increasing the heating rate. However, this will shift reduction temperatures to higher temperature with larger hydrogen consumption. These drawbacks can possibly be overcome by dispersing iron particles on a support.

Degree of dispersion greatly influences reducibility of metal-supported catalyst. Well dispersion is desirable to enhance the activity-selectivity patterns of catalyst [79]. It also could bring down the reduction temperature. It was reported that the reduction temperature of α-Fe_2O_3 to Fe_3O_4 on alumina (Fe/γ-Al_2O_3) is found to be slightly lower than that of unsupported α-Fe_2O_3. This is due to well dispersed α-Fe_2O_3 particles on the support which makes them easier to be reduced [80]. Unfortunately, supported catalyst has some disadvantages. The formation of strong metal-support interaction is a well known drawback which will elevate the reduction temperature. It was claimed that reduction temperature for supported Fe_3O_4 was increased by 100-200°C as compared to those of unsupported samples [80]-[81]. This is mainly due to the existence of highly stable $Fe_{1-x}O$ phase on γ-Al_2O_3 at temperature 570°C and above [81].

Higher annealing temperature during sample preparation will induce the agglomeration of the particles, thus reducing the surface area of the active phase [78]-[79]. Moreover, it also increases the strength of spinel phase which makes catalyst harder to be reduced. As investigated using $FeAl_{3.5}$ catalyst, the temperatures to reduce α-Fe_2O_3 to Fe_3O_4 and Fe_3O_4 to α-Fe were 430-460°C and 780-810°C, respectively. However, the reduction temperatures shifted to 550-560°C and 840-860°C when the $FeAl_{3.5}$ catalyst annealed at 1100°C was characterized due to the enhancement in the strength of spinel phase [80].

The amount of iron oxide loading particles also influences the reduction behavior. Previous work found that catalysts loaded with 60-70% α-Fe_2O_3 particles gave broader reduction peaks and larger hydrogen consumption in TPR measurement compared to those of 40-43% α-Fe_2O_3 particles [80]. The reduction temperatures for the ones with 60-70% α-Fe_2O_3 particles loading were also shifted toward higher region which may be due to strong metal-support interaction. In addition, the catalyst containing 41.8 % α-Fe_2O_3 on γ-Al_2O_3 revealed lowest reduction temperature than that of the catalyst with 72.4% α-Fe_2O_3. This might be related to the fact that excess γ-Al_2O_3 offers more sites for iron oxide particles to be attached which aids in attaining a well dispersed catalyst [80].

2.7 Steps in Catalytic Reaction

There are three steps in catalytic reaction which are adsorption, surface reaction and desorption.

2.7.1 Adsorption

The interaction of gas-catalyst surface involves several steps. In ammonia synthesis, the collision between nitrogen and hydrogen molecules with pure metal surface is firstly undertaken. It creates an attraction potential which binds these molecules together. This binding is called adsorption [11]. In adsorption, molecules will firstly adsorp by physical adsorption (physisorption) and chemical adsorption (chemisorption) afterwards.

Physical adsorption (physisorption) involves Van der Waal’s force. The enthalpy change of adsorption (ΔH_{ads}) does not exceed 80 kJ/mol [82]. This energy is insufficient to overcome the activation energy for H_2 and N_2 molecules dissociation which is about 436 kJ/mol and 945 kJ/mol, respectively. This prevents the dissociation process [10]; hence the molecules remain undissociated and eventually form multilayer adsorption.

In order to initiate the reaction, the molecules have to be adsorbed and dissociated. This is achieved by chemical adsorption (chemisorption). Chemisorption produces a strong bonding between reactant molecules and iron metal via electron sharing. The enthalpy change (ΔH_{ads}) for chemisorption is around 50-500 kJ/mol, which is sufficient to induce the cleavage of the molecules [83].

H_2 and N_2 molecules are evolved by the overlapping of the orbitals. Figure 2.19 illustrates the orbital diagram for nitrogen and hydrogen molecules [10], [84].

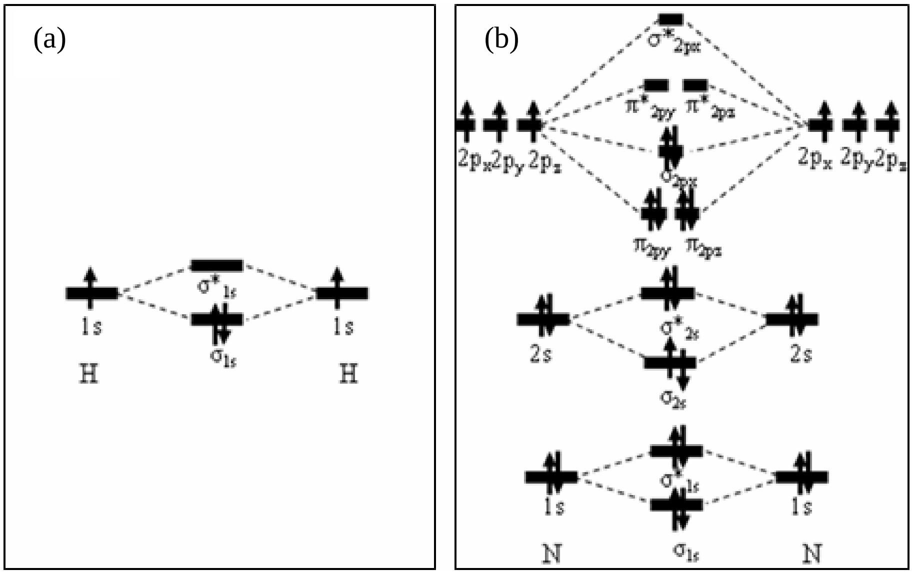

Figure 2.19: Molecular orbital diagram for (a) H_2 and (b) N_2 molecules [10], [84].

H_2 and N_2 molecules are also known as ligands. They tend to behave as electron donors by donating the electrons to the unoccupied d-orbital of iron. Due to the existence of a single bond, H_2 immediately dissociated forming H monoatomics [12], [85].

The rate of ammonia synthesis is determined by the N_2 dissociation [1], [13], [86]. However, the triple bond within N_2 is not easy to break even at high temperature. This is due to high bonding strength which is about 941.6 kJ/mol. The use of Fe as a catalyst can lower this energy to about ≈ 10 kJ/mol [12]. N_2 is also known as a π acceptor ligand. The direct electrons donation from high electron density within nitrogen triple bond (N≡N) to the unoccupied d-orbital of Fe produces a strong metal-ligand bond (M-H). However, the donation of excess electrons will also disturb the iron stabilization. This drawback can be overcome by π back donation process. Figure 2.20 demonstrates the π back donation process. The good π acceptor character of N_2 favors it to receive these electrons and place them in π antibonding orbitals (π*) (Figure 2.19). This process is called π back donation. The occupation of antibonding orbitals with electrons destabilizes the bonding within N≡N molecule, thus weakening as well as lengthening this bond. This consequently promotes the cleavage of N_2 [1], [10], [13], [82], [87]-[88].

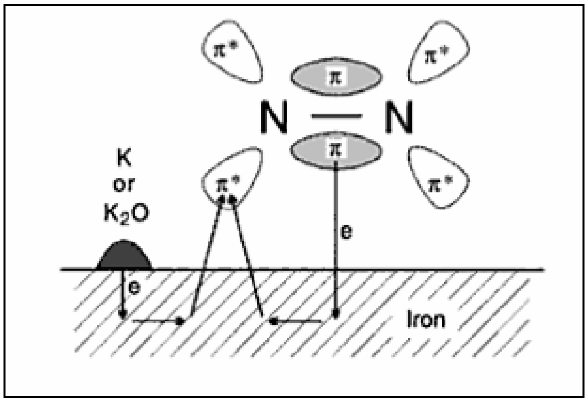

Figure 2.20: Steps involved during chemisorption of N_2 molecule on free Fe surface [87].

In addition, the dissociation of molecules can also be accelerated by the aid from a promoter. Potassium oxide, K_2O is a common promoter for ammonia synthesis catalyst. It provides additional electrons that could enhance the π back donation process (Figure 2.20) [87].

2.7.2 Surface Reaction

Migration takes place when hydrogen and nitrogen monoatomics are attached onto iron, Fe surface. Once nitrogen is attached, it will immediately pick up the hydrogen atoms to produce ammonia, NH_3 (Figure 2.20) [1], [85].

2.7.3 Desorption

Desorption is the final step in ammonia synthesis reaction. It involves the detachment of ammonia, NH_3 from the active sites once it is formed. This process leaves free sites so that the adsorption and migration of incoming molecules can occur continuously (Figure 2.21)

[1], [13], [85]. The proposed overall mechanisms in ammonia synthesis reaction are summarized in Figure 2.21 [89]-[90]. In addition, the energy profile for producing ammonia is revealed in Figure 2.22.

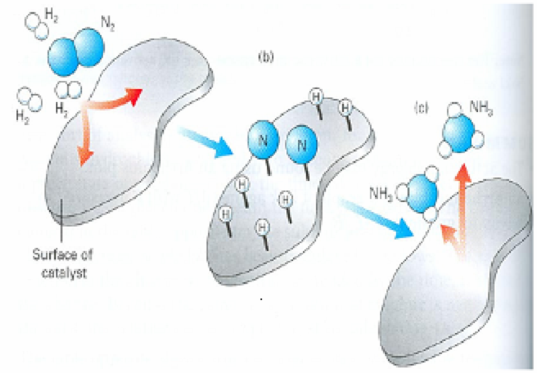

$$N_2 \rightleftharpoons N_{2ads} \rightleftharpoons 2N_{ads} \quad (1)$$

$$H_2 \rightleftharpoons 2H_{ads} \quad (2)$$

$$N_{ads} + H_{ads} \rightleftharpoons NH_{ads} \quad (3)$$

$$NH_{ads} + H_{ads} \rightleftharpoons NH_{2,ads} \quad (4)$$

$$NH_{2,ads} + H_{ads} \rightleftharpoons NH_{3,ads} \rightleftharpoons NH_3 \quad (5)$$

Figure 2.21: Overall steps involved in ammonia synthesis reaction [89]-[90].

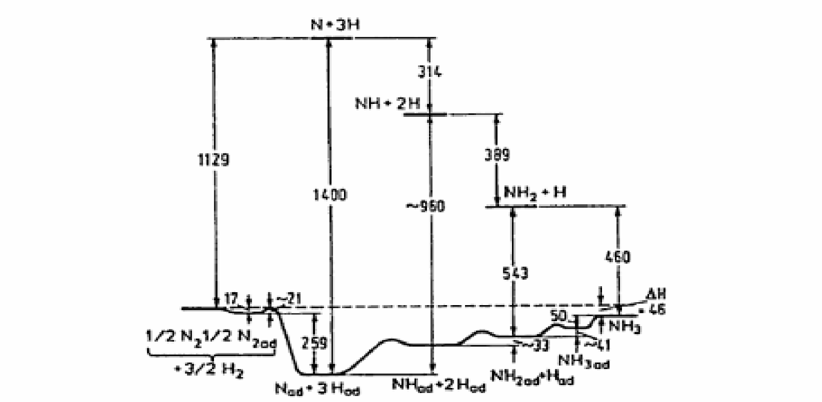

Figure 2.22: Energy profile of each steps involved in ammonia synthesis [8], [88].

2.8 Ammonia Synthesis

2.8.1 Overview of Ammonia Synthesis

Ammonia synthesis is an exothermic reaction. Therefore, the process is usually carried out at low temperature and high pressure environment. The overall chemical reaction for this process can be described in Equation 2.27 [1], [4], [9]-[10]:

$$N_2\ (g) + 3H_2\ (g) \leftrightarrow NH_3\ (g) \quad \Delta H = -92\ kJ \qquad (2.27)$$

Le Chatelier's principle can be used to elucidate the role of temperature and pressure in this reaction. The participation of temperature is vital to increase the collision frequency between nitrogen and hydrogen molecules. This will increase the reaction rate and eventually accelerate the process. Unfortunately, higher temperature may disrupt the reaction equilibrium and decomposition of ammonia is favored. Herein, the reverse reaction is favored to re-establish the equilibrium. The temperature has to be lowered thereby shifting the equilibrium to the right side and enriching ammonia composition. However, this will lower the reaction rate and extends the time for reaction completion which is impractical at the plant-scale production.

The application of high pressure can enhance the production of ammonia. Equation 2.28 shows the expression of ideal gas law where *P* the partial pressure (atm), *n* is the number of mol, *V* is the volume (L), *R* is the gas constant (L.atm/mol.K) and *T* is temperature (K) [10].

$$PV = nRT \tag{2.28}$$

According to this formula, an increase in pressure causes the concentration of N_2, H_2 and NH_3 (Equation 2.27) to increase as a result of decreasing the volume. Equation 2.29 shows the expression to determine equilibrium constant, K_c for ammonia synthesis where [ ] signifies the concentration [10].

$$K_c = [NH_3]^2/[N_2][H_2]^3 \tag{2.29}$$

However, utilization of pressure does not affect the value of K_c due to nature of the reaction which involves a change in the total number of mole of gases. Pressure only does affect the value of reaction quotient, Q. Equation 2.30 describes the expression of Q for ammonia synthesis reaction [10].

$$Q = [NH_3]^2/[N_2][H_2]^3 \tag{2.30}$$

Based on this equation, it can be projected even though an increase in pressure enhances the concentration of N_2, H_2 and NH_3 gases (Equation 2.28), denominator of Q will maintain higher that that of numerator as the pressure is increased (Equation 2.30). This results in $Q<K_c$, bringing equilibrium reaction to forward direction to enrich composition of ammonia [9], [91]-[92]. Figure 2.23 reveals the dependency of reaction rates on various temperatures and pressures [93].

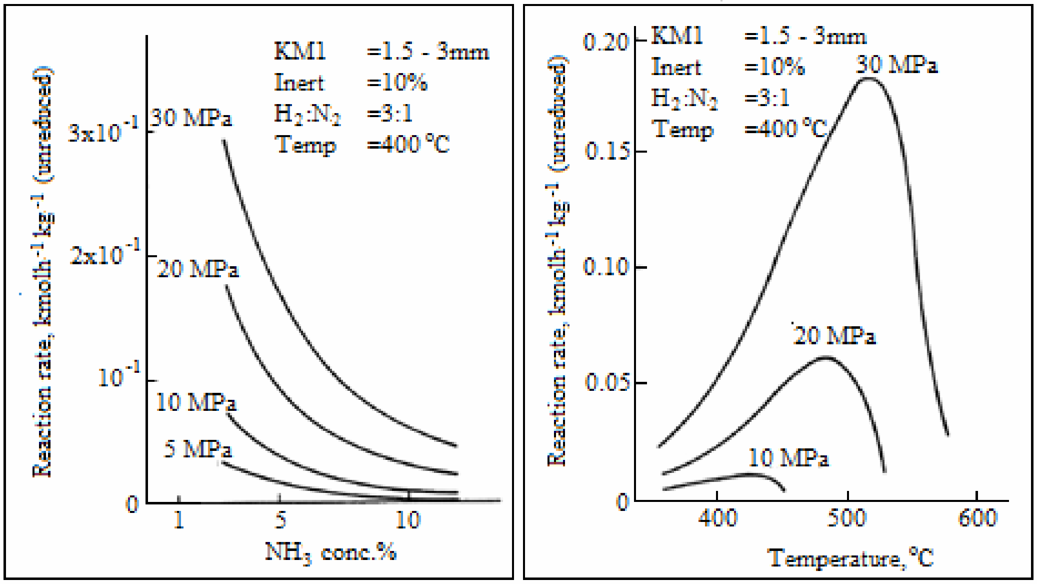

Figure 2.23: Dependency of ammonia synthesis rates at various temperatures and pressures [93].

2.8.2 Typical Industrial Practices

The earliest step in producing ammonia is the generation of synthesis gas. The syngas must be free from any poisoning elements such as sulfur and oxygen which retard the synthesis efficiency. Therefore, gas purification stage is required to ensure the composition of synthesis gas obeys the standard specification. The feedstocks containing light hydrocarbons such as natural gas, liquid petroleum gas or naphtha undergo steam reforming process, whereas partial oxidation route is recommended for heavy hydrocarbon such as heavy fuel oil, crude oil, asphalt and tar [8]. Figure 2.24 illustrates the schematic diagram of the ammonia synthesis process which involved steam reforming step.

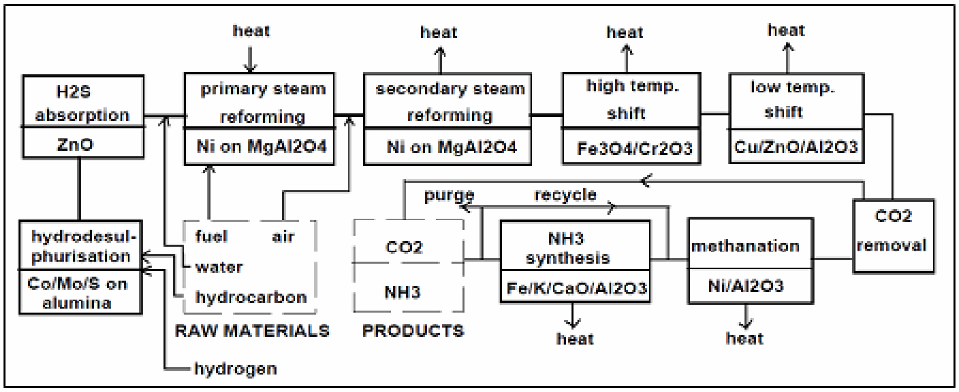

Figure 2.24: Schematic illustration of steps involved in plant scale ammonia synthesis [88].

Natural gas (CH_4) is an example of a typical feedstock. It will firstly undergo the desulfurization process. Next, the desulfurized natural gas enters the primary steam reformer which is operated at temperature and pressure of 750-850^oC and 35-40 bars, respectively. The steam reforming used NiO as a catalyst. The primary reformer involves two processes. The first one is the methane reaction with steam to produce CO and H_2 gases (Equation 2.31) [8]. In order to maximize the H_2 formation, the second reaction, which is called CO shift, takes place yielding CO_2 and H_2 gases (Equation 2.32) [8].

Methane-steam reaction $CH_4 + H_2O \leftrightarrow CO + H_2$ (2.31)

CO-shift reaction $CO + H_2O \leftrightarrow CO_2 + H_2$ (2.32)

In the next step, the gas will pass through secondary steam reforming process. Its purpose is to introduce nitrogen molecules, N_2 to the process gas and provides high temperature which is sufficient to reduce the methane content to an acceptable value. It is usually accomplished at 1000^oC, yielding approximately 0.3% (dry basis) of methane concentration [8].

Carbon monoxide, CO-shift conversion continuously occurred to convert the remaining CO from the previous reforming steps. It involves two stages. The first stage is at temperature of 350-500^oC in the presence of iron oxide/chromium oxide catalyst. It results in 3% (dry basis) of CO concentration. The second stage is undertaken to reduce the concentration of CO to 0.2 and 0.4% (dry basis). This second stage process is accomplished at 200-250^oC with the aid by $CuO/ZnO/Al_2O_3$ catalyst [8].

Carbon dioxide, CO_2 removal step is performed after the reaction in secondary reforming is completed. The concentration of CO_2 is further declined to about 0.1% (dry basis) by employing solvent scrubbing. After completing all the steps, the synthesis gas composition must reach the acceptable values as summarized in Table 2.4 [8].

Table 2.4: Recommended gas composition [8]

Type of gas	Mol%
H_2	74.6
N_2	24.4
CH_4	0.3
CO	0.3
CO_2	0.1
Ar	0.3

The final stage in synthesis gas preparation is methanation. The objective of methanation is to completely eliminate the remaining carbon oxides (CO_2 and CO). This stage is accomplished at 250-350^oC over reduced NiO catalyst, reducing carbon oxides concentration to less than 5 ppm [8], [88], [93].

The type of ammonia converter plays a significant role in ammonia synthesis. Figure 2.25 shows three reactors for ammonia synthesis commonly used by industries [92].

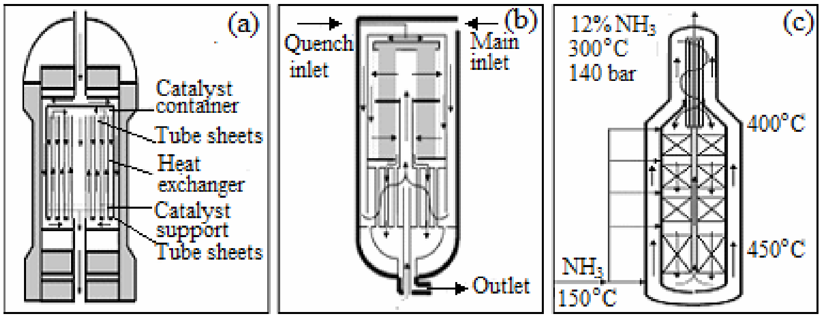

Figure 2.25: Ammonia synthesis reactors (a) Haber-Bosch (b) Haldor-Topsoe with radial flow and (c) Four-beds cold with axial flow [88].

There are two types of reactant flows namely axial (Figure 2.25 (a) and Figure 2.25 (b)) and radial (Figure 2.25 (c)). Radial flow design is commonly employed in the plant scale of ammonia synthesis. The utilization of the radial flow reduces the pressure drop effect caused by bed geometry and size of the catalyst. The bed geometry provides larger flow area and shorter flow path with catalyst size of 1.5 -.3 mm [8]-[9] is adequate for pressure drop to be minimized, hence reducing the volume of catalyst needed. Pressure drop is inversely proportional to the catalyst size [8]-[9]. These factors enhance the conversion performance due to the absence of diffusional limitation [9].

2.8.3 Ammonia Yield Collection and Quantification

Kjedahl or back titration method is used to quantify ammonia [6], [94]-[95]. This method captures ammonia gas using known concentration of acidic solution e.g. hydrochloric acid, HCl. The mixture will be titrated with known concentration of alkaline e.g. sodium hydroxide, NaOH to neutralize the excess acidic solution. The amount (mole) of ammonia produced which is also equal to reacted acidic solution can be calculated [96]-[97]. The overall chemical reaction is expressed in Equation 2.33 and Equation 2.34.

$$NH_3 + HCl \rightarrow NH_4Cl \qquad (2.33)$$

The excess HCl is then back titrated using NaOH as described in Equation 2.31.

$$HCl_{excess} + NaOH \rightarrow NaCl + H_2O \qquad (2.34)$$

Gas Chromatography (GC) is another method of quantifying the ammonia yield [94], [98]. Figure 2.26 shows the basic set up of the GC [99].

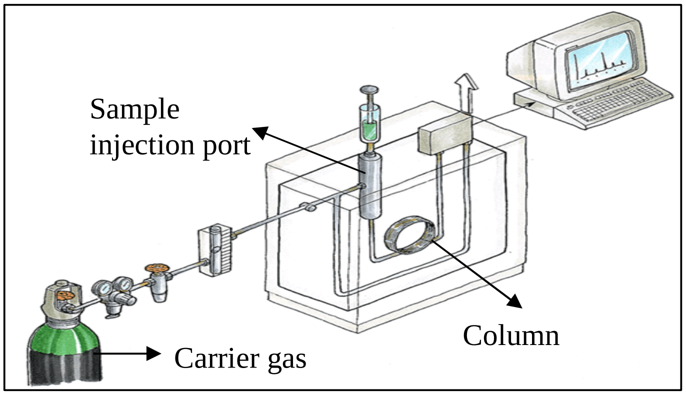

Figure 2.26: Set up of Gas Chromatography [99].

The set up consists of a gas carrier (Ar, He or N_2), detector, sample injection port, column (capillary or packed) and chromatograph displayer (Figure 2.26) [97]. The sample is firstly heated in the injection port at temperature relatively $50^{o}C$ above its boiling point, obtaining a vapor phase with the pressure of at least 10 torr. The carrier gas will then bring the vapor to enter the column for separation process. The chromatogram is then emerged on the displayer. The ammonia is identified by comparing the retention time, T_R between the standard and the analyzed sample. T_R is described as the minutes between the times of sample are injected and chromatograph is recorded. The area under chromatograph peak symbolizes the concentration of the produced ammonia [97].

In GC, the crucial factors include temperature during analysis and type of column [75]. Previous study performed analysis at 333 K using helium, He as a carrier gas. A packed column consisting of 5% KOH + 20% Carbowex 1500 on Chromosorb W-AW 80-100 mesh (5 m x 5 mm I.D) was utilized. Another alternative to detect ammonia is by using non-dispersive infrared detector (BINOS detector) [14], [18].

2.9 Ammonia Synthesis Reaction Study

The catalyst used for ammonia synthesis in industries is mostly iron oxides (95 wt %) together with small amount of promoters such as alumina, γ-Al_2O_3, calcium oxide, CaO, potassium oxide, K_2O and magnesium oxide, MgO. The catalyst is deployed under severe conditions of high temperature and pressure. Several studies were recently performed which focussed on several aspects of the catalytic system.

Fusion (melting) and high-energy ball milling methods are commonly used in altering the catalyst features. It has been reported that the activity of fused catalyst was about 1.3-1.9 times faster than conventional one [100]. This was recorded at temperature and pressure of 325-425^{o}C and 5-20MPa, respectively. The improvement was claimed to be related to the composition of the fused catalyst which contained 2.5 times more FeO than the conventional catalyst. In addition, the reducibility of this catalyst was also found to be 3.3 times faster than that of conventional one [18].

High-energy ball milling process revealed only 4% increment in ammonia production rate. This was showed by the catalyst which was milled for 110 hours with particles size approximately 100 times smaller than the one unmilled. This observation was deemed to be caused by the replacement of magnetite phase with promoter atoms, hence stabilizing the iron particles during reduction step. Consequently, the role of promoter that acts as the electron donor is retarded [18].

2.9.1 Performance evaluation between Fe_3O_4 and $Fe_{1-X}O$ based catalysts

$Fe_{1-x}O$ has been proposed to replace Fe_3O_4-based catalyst that may overcome the standing issue of low ammonia yield. The activity of $Fe_{1-x}O$ -based catalyst was 30-90% higher than the one consisting of Fe_3O_4 phase. Moreover, the reaction temperature was slightly reduced to about 25-40^{o}C lower than that of conventional one [100]. Other researcher [101] reported that $Fe_{1-x}O$ -based catalyst exhibited 70% higher reaction rate as compared to magnetite-based catalyst. The activation energy for $Fe_{1-x}O$-based catalyst was also reduced by 5.8% when the ammonia synthesis was performed at 460^oC and 100 – 400 bars. The improvement in reaction rate was due to surface area of the catalyst particles. A reduction in surface area was observed for $Fe_{1-x}O$ and Fe_3O_4 where both values were 16.6 m^2/g and 12.6 m^2/g, respectively. This reduction was claimed to be caused by the evolvement of H_2O during reduction process. Fe_3O_4 produces 20% more water than that of $Fe_{1-x}O$, which increased the rate of iron, Fe particles sintering [101]. Moreover, $Fe_{1-x}O$-based catalyst also displayed 14 % enhancement in catalytic activity per volume (moles of ammonia produced per hour per cubic meter catalyst). Higher bulk density of $Fe_{1-x}O$ compared to Fe_3O_4 due to compact ionic arrangement, was suggested as the major reason for this observation [101].

2.9.2 Effect of Catalyst Support

One of the ways to improve the catalytic activity is by dispersing the active phase onto a catalyst support. Previous study reported that iron supported on activated carbon in presence of small amount of potassium (Fe-AC-K); resulted in 10 ml NH_3/hr/g cat, catalytic activity at temperature of 250-400^oC and under atmospheric pressure [6]. Only 0.5 % mole of ammonia was produced using iron supported on activated carbon at 470^oC and atmospheric pressure in the absence of a chemical promoter.

2.9.3 Synergism between Iron and Ruthenium Based-Catalysts

Previous study [6] reported on the ability of ruthenium-based catalyst in improving the yield of ammonia synthesis. However, the synergism between iron and ruthenium is yet to be understood. It was reported that [6] pure ruthenium catalyst (Ru-AC-K) resulted in about 80% equilibrium conversion at 250-400^oC and atmospheric pressure. Meanwhile, the activity dropped by 50% when iron (Fe-AC-K) was used. Catalyst comprising equal ratio of both metallics (Ru50-Fe50-AC-K) resulted in a decline in the activity by 30% [6].

2.9.4 Effect of Reaction Temperature

One of the most crucial reaction parameters is temperature. Sufficient temperature is required to achieve equilibrium conversion while too high favors the decomposition of ammonia to nitrogen and hydrogen [18], [94], [100]-[101]. In the case of Ru/Al_2O_3-KOH derived from $Ru_3(CO)_{12}$ catalyst, the equilibrium conversion was attained at 390^oC under atmospheric pressure with the ammonia production rate of approximately 250 mg/g(Ru). However, the product subsequently declined with increase in temperature [94]. Similar trend was also revealed on iron and ruthenium catalyst. The equilibrium conversion was attained at 350°C under atmospheric pressure for all catalysts [6].

2.9.5 Effect of Pressure

Previous investigation [14] proved that an increase in pressure does not lead to a significant increase in conversion at low temperature. The ammonia was not detected for the synthesis performed at 580K under pressure of 1-50 bars with H_2:N_2 ratio of 3:1 and flow feed rate of 40 cm^3/min [14]. However most of equilibrium conversions were achieved at temperature higher than 700 K. Pressure of 50 bars exhibited maximum conversion (3.5% NH_3 mole fraction) that was obtained at H_2:N_2 ratio, flow feed rate and temperature of 3:1, 40 cm^3/min and 770 K, respectively [14].

2.9.6 Effect of Hydrogen and Nitrogen (H_2:N_2) Gases Ratio

The effect of varying hydrogen and nitrogen gases, (H_2:N_2) on the ammonia production have been studied [14]. In the case of $CsNO_3$-Ru/Al_2O_3 catalyst, it was observed that the ratio of 1:3 (H_2:N_2) resulted in improved ammonia yield effect where optimum activity was attained at 610 K with the ammonia effluent approximately 2700 ppm. Inhibiting effect appeared when the H_2:N_2 was increased to 3:1. The ratio of H_2:N_2 was further varied from 5:95 to 75:25 and pressure applied was also elevated to 50 bars. The catalytic activity evaluation showed that the ratio of 5:95 (H_2:N_2) revealed significant rate of NH_3 formation at temperature as low as 520K. However, the decomposition of ammonia was favored as a result of increasing temperature due to the disturbance in reaction equilibrium. Maximum ammonia yield was achieved at 720 K using 60:40 (H_2:N_2) ratio [14].

CHAPTER 3

METHODOLOGY

3.1 Introduction

This chapter consists of three major sections namely the preparation of nanocatalysts, characterization of nanocatalysts and evaluation of catalytic activity. Three types of nanocatalysts prepared were unsupported α-Fe_2O_3, Fe_3O_4 and 5% α-Fe_2O_3/γ-Al_2O_3. Several methods were utilized which include sol gel, self combustion, self assembly, precipitation, hydrothermal and a hybrid sol gel-hydrothermal. The parameters studied include synthesis methods, synthesis temperature, period of stirring, annealing temperature and inclusion of surfactant. The prepared nanocatalysts were characterized using x-ray diffraction (XRD), raman spectroscopy, field emission scanning electron microscopy (FESEM), energy dispersed x-ray (EDX), temperature programmed reduction (TPR), vibration sample magnetometer (VSM) and N_2 adsorption. Catalytic evaluation was evaluated in a fix bed microreactor at 30^oC to 200^oC under atmospheric pressure at various total feed flow rates and H_2/N_2 volumetric ratios. The effect of magnetic field on the catalytic activity was also examined.

3.2 List of Chemicals and Gases

Chemicals and gases used in this study including their source and purity are summarized in Table 3.1.

Table 3.1: Chemicals and gases employed in this study.

Name	Chemical Formula	Supplier	Purity	Usage
Iron (III) nitrate nonahydrate	$Fe(NO_3)_3.9H_2O$	Hamburg Chemicals	99.99%	Catalyst Precursor
Iron (II) chloride	$FeCl_2$	Hamburg Chemicals	99.99%	Catalyst Precursor
Sodium bis(2-ethylhexyl) sulfosuccinate	$C_{20}H_{37}NaO_7S$	Acros Organic	96%	Catalyst Surfactant
Tetrapropylammonium hydroxide	$C1_2H_{29}NO$	Fluka Chemika	-	Catalyst Surfactant
Nitric acid	HNO_3	R & M Chemicals	65%	Synthesis Solvent
Ethylene glycol	$HOCH_2CH_2OH$	R & M Chemicals	99.95%	Synthesis Solvent
Hydrazine hydrate	$N_2H_4.H_2O$	Across Organics	55%	Reducing agent
Ammonia hydroxide	NH_4OH	Across Organics	55.00%	Precipitant
Methanol	CH_3CH_2OH	Hamburg Chemicals	99.98%	Catalyst Washer
Sodium hydroxide	NaOH	System	99.00%	Product Quantifier
Hydrochloric acid	HCl	System	99.00%	Product Quantifier
Hydrogen gas	H_2	MOX	99.99%	Reactant
Nitrogen gas	N_2	MOX	99.99%	Reactant
5% hydrogen in 95% nitrogen gas	$5\%H_2$-$95\%N_2$	MOX	96.99%	TPR

3.3 Preparation of Nanocatalyst

Three types of nanocatalysts were prepared namely α-Fe_2O_3, Fe_3O_4, and α-Fe_2O_3/ γ-Al_2O_3.

3.3.1 Unsupported Hematite, α-Fe_2O_3 Nanocatalyst

Parameters studied were synthesis method, stirring period and annealing temperature.

3.3.1.1 Effect of Synthesis Method

The sol-gel [40], [51], self-combustion [102] and self-assembly [103] methods were employed. The procedures for the sol gel method are shown in Figure 3.1.

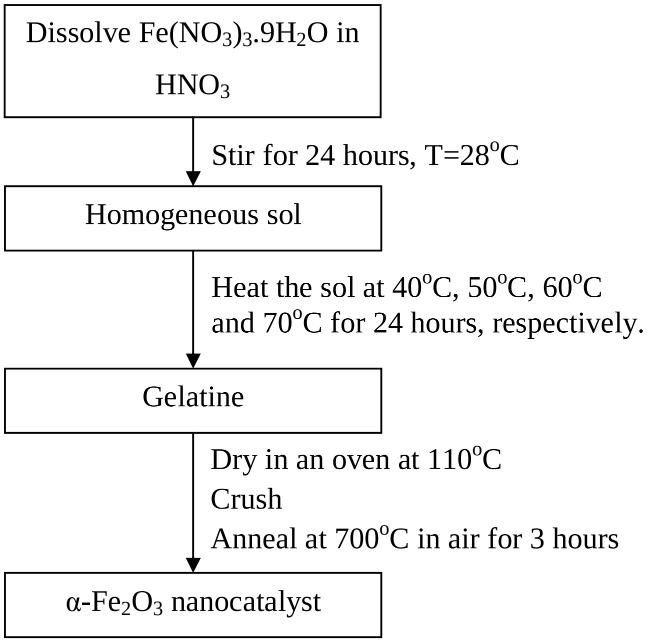

Figure 3.1: Procedures to prepare α-Fe_2O_3 nanocatalyst using sol-gel method.

20 g of iron (III) nitrate nonahydrate, $Fe(NO_3)_3.9H_2O$ was weighed and dissolved in 100 mL of 65% nitric acid, HNO_3. The mixture was stirred vigorously on a magnetic stirrer for 24 hours to obtain a homogeneous sol. The homogeneous sol was then heated at 40°C, 50°C, 60°C and 70°C, respectively for 24 hours forming a gelatine. The gelatine was dried in an oven at 110°C overnight. The dried sample was crushed using mortar and pestle, followed by annealing at 700°C in air for three hours.

The procedures in self-combustion and self-assembly methods are similar to the sol-gel method but differ in certain steps. In the self-combustion method, the homogeneous sol was gradually heated until it combusted at 110°C. In self-assembly method, the homogeneous sol was placed in a fume cupboard for three months without stirring.

Figure 3.2 illustrates the steps involved in the self-combustion method. The synthesis started by weighing 20 g of iron (III) nitrate nonahydrate, $Fe(NO_3)_3.9H_2O$ and dissolving it into 100 mL of 65% nitric acid, HNO_3.

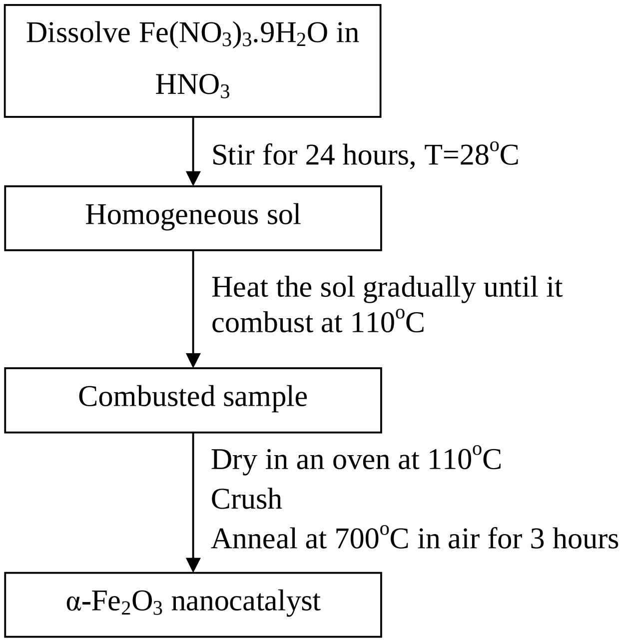

Figure 3.2: Procedures to prepare α-Fe_2O_3 nanocatalyst using self-combustion method.

The mixture was stirred vigorously on a magnetic stirrer for 24 hours to obtain a homogeneous sol. The sol was then gradually heated until it combusted at temperature of 110°C. The sample was dried in an oven at 110°C overnight. It was followed by crushing and annealing at 700°C in air for three hours.

The procedures for the self-assembly method are shown in Figure 3.3. It began with weighing 20 g of iron (III) nitrate nonahydrate, $Fe(NO_3)_3$. $9H_2O$. The weighed $Fe(NO_3)_3$ was then dissolved into 100 mL of 65% nitric acid, HNO_3. The mixture was stirred on a magnetic stirrer for 24 hours to form a homogeneous sol. The sol was then stored in a sealed beaker and placed inside a fume cupboard for 3 months. The sol was then heated at 40°C, 50°C, 60°C and 70°C for 24 hours, respectively forming a gelatine. The gelatine was then dried in an oven at 110°C overnight. The dried sample was crushed using mortar and pestle, followed by annealing at 700°C in air for three hours.

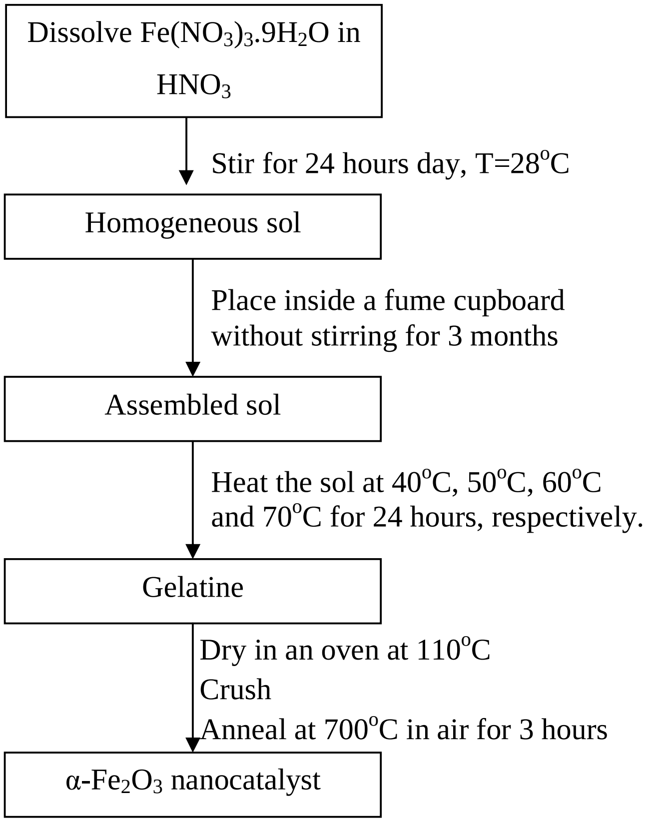

Figure 3.3: Procedures to prepare α-Fe_2O_3 nanocatalyst using self-assembly method.

3.3.1.2 Effects of Period of Stirring and Annealing Temperature

The effect of stirring was studied for α-Fe_2O_3 nanocatalyst prepared using the sol-gel method (Section 3.3.1.1). The stirring period was prolonged to 1 week and 1 month. The resultant catalysts were annealed at 300°C in air for three hours. The effect of annealing temperature was studied using the catalyst stirred for 1 day. The sample was separated into few portions and each portion was then annealed at 400°C, 500°C, 600°C and 700°C, respectively in air for three hours.

3.3.2 Unsupported Magnetite, Fe_3O_4 Nanocatalyst

Preliminary study involving several typical methods such as sol-gel, precipitation and hydrothermal were firstly conducted. The outcome of the preliminary study led to development of a hybrid method namely sol gel-hydrothermal.

3.3.2.1 Effects of Preparation Methods

A preliminary study on synthesizing Fe_3O_4 via various methods was conducted. It comprised sol-gel [33], precipitation [36] and hydrothermal [37] methods.

Preparation via sol-gel method began by dissolving 10 g of iron (III) nitrate, Fe $(NO_3)_3.9H_2O$ in 50 mL of ethylene glycol, $HOCH_2CH_2OH$ and stirred for 24 hours to obtain a homogeneous solution. This homogenized solution was then heated until gelatine was formed. The gelatine was then dried in a vacuum oven at 110°C overnight. These procedures are summarized in Figure 3.4.

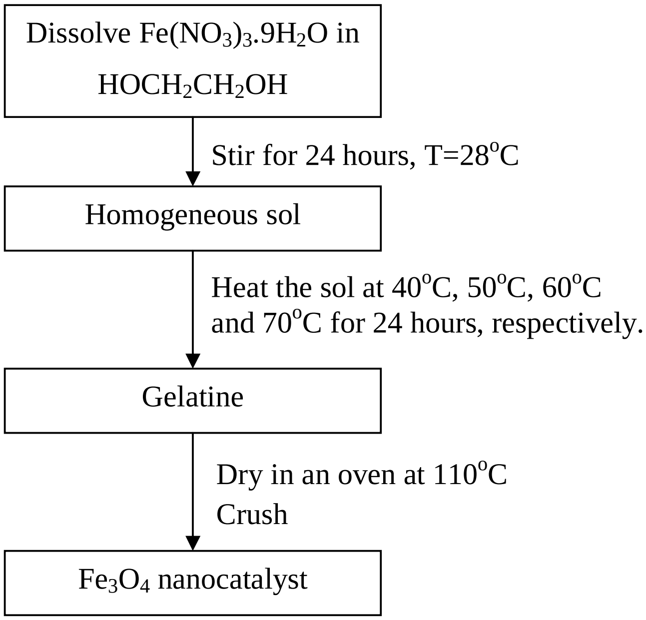

Figure 3.4: Procedures to prepare Fe_3O_4 nanocatalyst using sol-gel method

Figure 3.5 shows the procedures for precipitation method. The method started by preparing a homogeneous sol. It was accomplished by dissolving 3 g of iron (II) chloride, $FeCl_2$ salt in 50 mL distilled water and stirred for 24 hours. This homogenized solution was then titrated with ammonium hydroxide, NH_4OH solution forming a black precipitate at pH~10-11. The precipitate was filtered and washed with deionized water as well as absolute ethanol for several times. The wet precipitate was then dried in a vacuum oven at 110°C overnight.

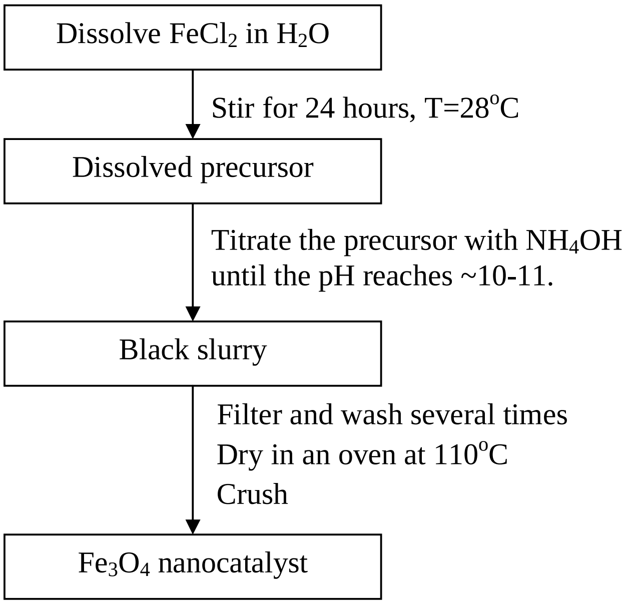

Figure 3.5: Procedures to prepare Fe_3O_4 nanocatalyst using precipitation method.

The hydrothermal method employed 50 µL of tetrapropylammoniumhydroxide, $C_{12}H_{29}NO$ surfactant and 0.4 g of iron (III) nitrate, $Fe(NO_3)_3.9H_2O$ as the precursors. These chemicals were dissolved in 10 mL of distilled water and stirred for 24 hours to obtain a homogeneous solution. The homogenized solution was transferred into an autoclave, then 1.8 mL of 55% hydrazine hydrate, $N_2H_4.H_2O$ aqueous solution was added to the autoclave. The autoclave was sealed tightly and heated in an oven at 160°C for 10 hours. The slurry formed was then filtered and washed with deionized water followed by absolute ethanol several times. The wet precipitate was then dried in a vacuum oven at 110°C overnight. Figure 3.6 summarizes the procedures for the hydrothermal method.

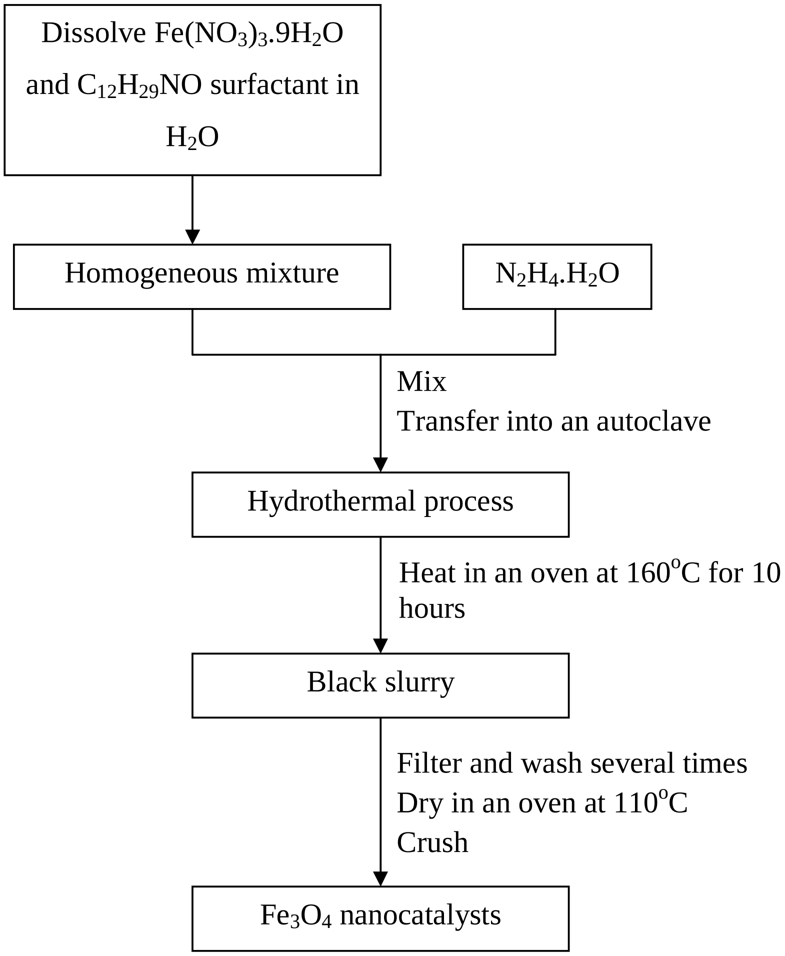

Figure 3.6: Procedures to prepare Fe_3O_4 nanocatalyst using hydrothermal method.

3.3.2.2 Hybrid Sol Gel-Hydrothermal Method

Interpretation of the results obtained from the preliminary study led to the development of a new combined approach which was named as sol gel-hydrothermal method. This approach comprised two major sections which were formation of gelatine and consequently followed by hydrothermal treatment. Figure 3.7 shows the steps involved in the sol gel-hydrothermal method.

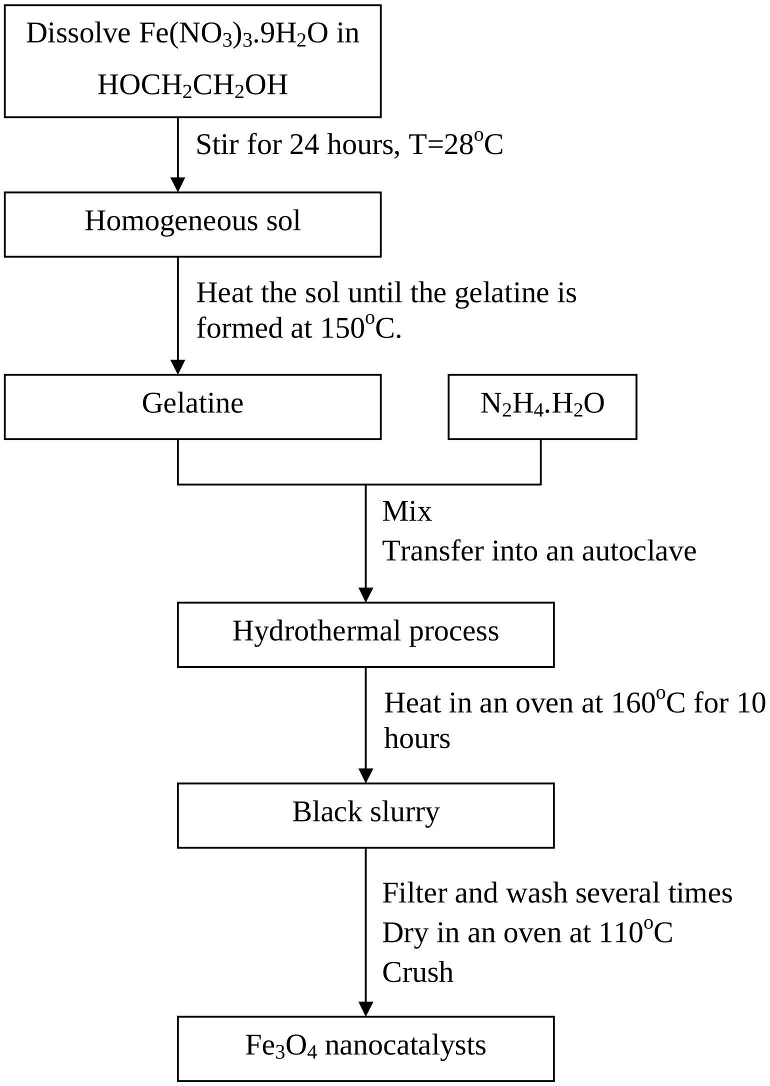

Figure 3.7: Procedures to prepare Fe_3O_4 nanocatalysts using sol gel-hydrothermal method.

Typically, 1 g of iron (III) nitrate, $Fe(NO_3)_3.9H_2O$ salt was dissolved in 10 mL of ethylene glycol and stirred for 24 hours to obtain a homogeneous solution. This homogenized solution was then heated until the gelatine was formed at 150°C. Then the gelatine was rapidly transferred into an autoclave followed by addition of 5 mL of 55% hydrazine hydrate, NH_4OH aqueous solution and 25 mL of distilled water. The autoclave was sealed tightly and heated in an oven at 160°C for 10 hours. The slurry formed was then filtered and washed with deionized water and absolute ethanol several times. The wet precipitate was then dried in a vacuum oven at 110°C overnight.

Further investigations regarding this approach were also conducted. The synthesis temperature was varied to 28°C, 50°C, 80°C and 120°C for 10 hours respectively.

Furthermore, the effect of annealing temperature was studied using catalyst synthesized at 160^oC. This catalyst was annealed at 300^oC, 400^oC and 500^oC in vacuum furnace for three hours, respectively.

3.3.3 Supported Hematite on Alumina (5% α-Fe_2O_3/γ-Al_2O_3) Nanocatalyst

α-Fe_2O_3 was synthesized using sol gel-hydrothermal method on alumina, γ-Al_2O_3 support. Two parameters studied were the synthesis periods and iron (III) nitrate to sodium bis(2-ethylhexyl) sulfucinnate surfactant ($Fe(NO_3)_3$:SBS) ratios.

3.3.3.1 Effect of Synthesis Period

The overall procedures are illustrated in Figure 3.8. Typically, 0.7 g of iron (III) nitrate, $Fe(NO_3)_3.9H_2O$ was dissolved in 10 mL of ethylene glycol, $C_2H_6O_2$ and the mixture was stirred for 1 day to obtain a homogeneous sol. The homogeneous sol was then heated at 160^oC under vigorous stirring to obtain gelatine. The gelatine was then transferred into an autoclave containing 1.90 g of commercial alumina oxide, γ-Al_2O_3 and 18 ml distilled water. Then, 3.5 mL of 55% hydrazine hydrate, NH_4OH was added to the mixture. The autoclave was then tightly sealed and placed in an oil bath at 160^oC for 1 hour. The resultant catalyst was filtered, washed and dried at 50^oC in an oven. Then, it was annealed at 400^oC in nitrogen flow at 10 ccm/min for three hours. The synthesis periods for the hydrothermal part were then varied to 10 hours and 1 day. The calculations are shown in Appendix C.

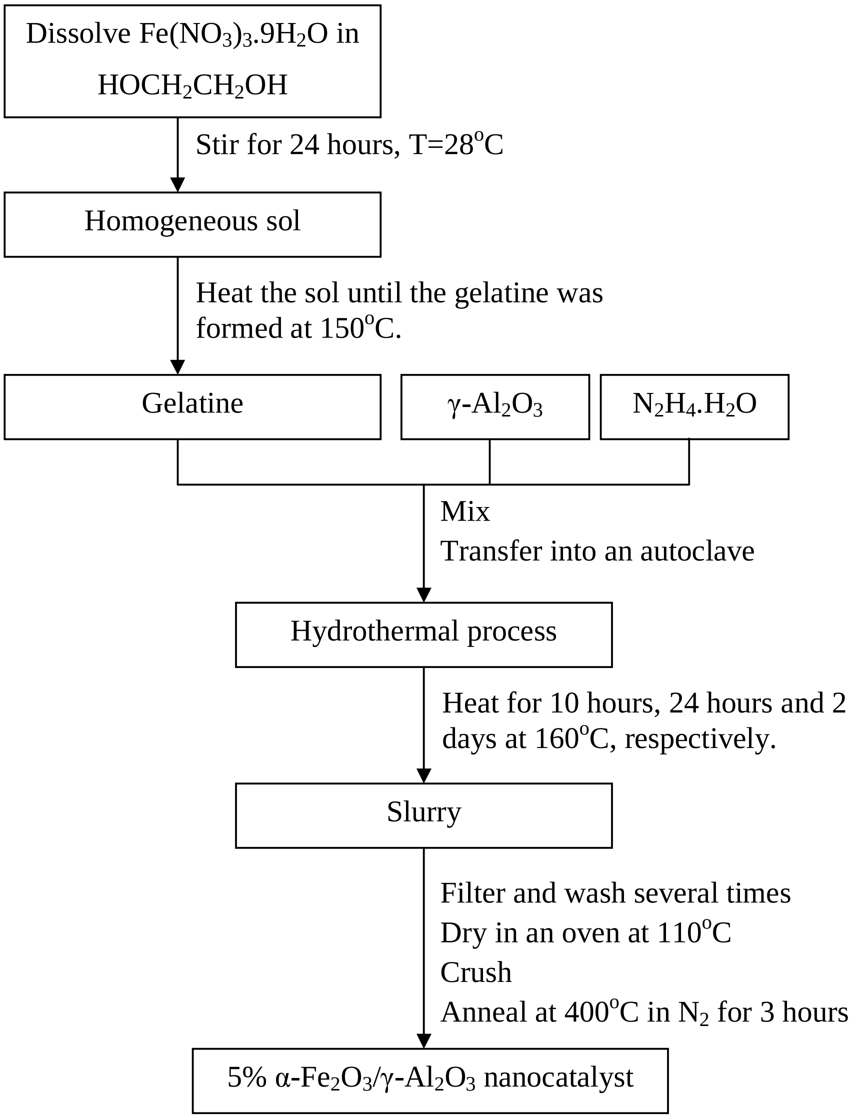

Figure 3.8: Procedures to prepare supported 5% α-Fe_2O_3/γ-Al_2O_3 nanocatalysts using sol gel-hydrothermal method at different synthesis periods

3.3.3.2 Effect of Surfactant

Iron (III) nitrate, $Fe(NO_3)_3.9H_2O$ and sodium bis(2-ethylhexyl) sulfucinnate (SBS) surfactant were weighed according to 2:1 w/w ratio. Figure 3.9 summarizes the steps in this synthesis.

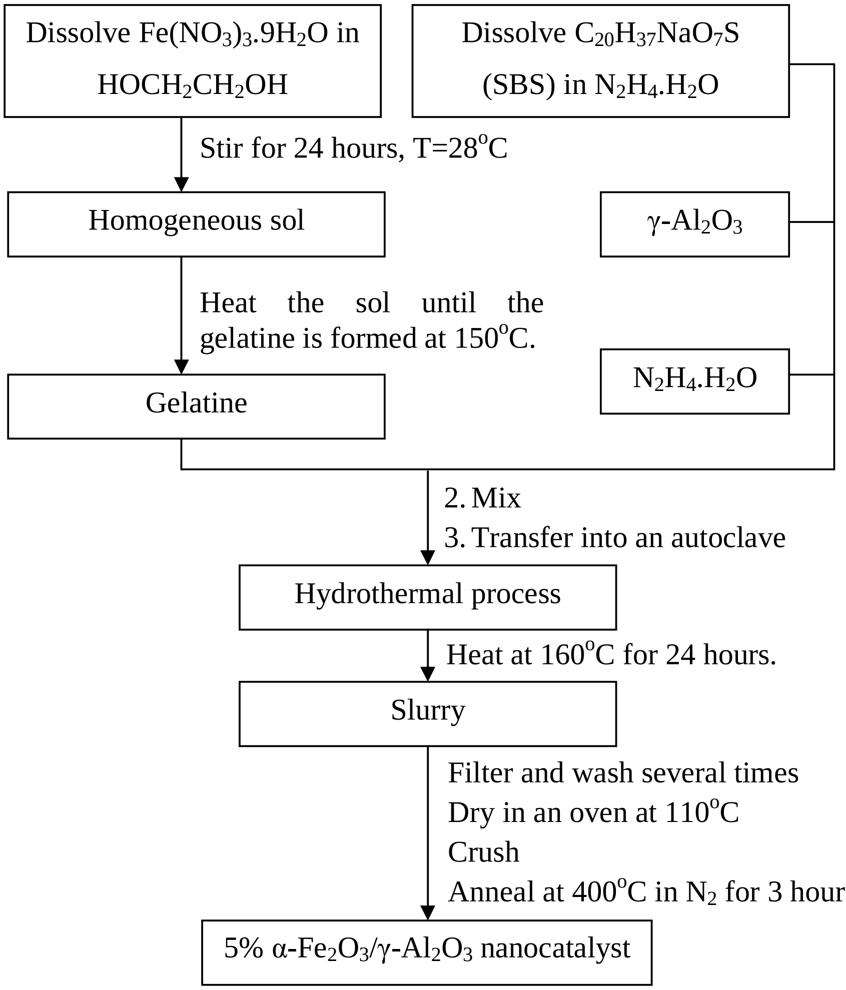

Figure 3.9: Procedures to prepare supported 5% α-Fe_2O_3/γ-Al_2O_3 nanocatalysts using sol gel-hydrothermal method at different iron (III) nitrate to SBS surfactant ($Fe(NO_3)_3$:Surf) ratios.

The precursor and surfactant were separately dissolved in 10 mL of ethylene glycol solution, $HOCH_2CH_2OH$ and 5 mL of 55% hydrazine hydrate, NH_4OH solution, respectively. Both mixtures were stirred for 24 hours. The dissolved iron (III) precursor was heated at 160^oC under vigorous stirring to form the gelatine. The gelatine and the dissolved surfactant were then quickly poured into an autoclave containing 1.90 g of alumina, γ-Al_2O_3. The autoclave was tightly sealed and consequently heated in an oil bath at 160^oC for 1 day. The resultant catalyst was filtered, washed and dried at 50^oC in an oven. It was annealed at 400^oC in nitrogen flow at 10 ccm/min for three hours. The procedures were repeated and the iron (III) nitrate to SBS surfactant, ($Fe(NO_3)_3$: Surf) ratio was then varied to 2:1 and 2:3.

3.4 Characterization of Nanocatalyst

Several analytical methods were used to obtain the physicochemical information of the prepared nanocatalysts. They include x-ray diffraction (XRD), raman spectroscopy, field emission scanning electron microscopy (FESEM), energy dispersed x-ray (EDX), temperature programmed reduction, (TPR), vibration sample magnetometer (VSM), N_2 adsorption and transmission electron microscopy (TEM).

3.4.1 X-Ray Diffraction (XRD)

X-ray powder diffraction (XRD) is one of the most versatile characterizations tools used for identifying the types of phases present in the specimen. The underlying principle of this tool is based on Brag's Law ($2d \sin \theta = n\lambda$) which describes the relation between the angle (θ) and wavelength (λ) of focussed x-ray with the distance between atomics, d-spacing (d) in the crystal. The average particle size can be measured using Scherer's equation as described by Equation 3.1, where k is the shape factor with typical value of 0.9, λ is the x-ray wavelength (Å), β is the line broadening at half the maximum intensity (FWHM) in radians, and θ is the Bragg angle [63], [104].

$$d = \frac{k\lambda}{\beta \cos\theta} \tag{3.1}$$

XRD measurements were conducted using a Bruker A&S D8 Advanced Diffractometer instrument equipped with a CuK_α radiation source, at 40 kV and 30 mA. The scanning angle (2θ) used was in the range of range of 2–80° at scanning speed and step size of 1.2°/min and 0.02^{o}/min, respectively. By using Bruker Eva software, the resultant spectra were compared with the standard library to confirm the phase of tested specimen. Information such as Bragg angle (2θ), full width half maximum (FWHM), d-spacing and lattice parameter were also determined using this software.

3.4.2 Raman Spectroscopy

Raman spectroscopy is used to study the internal structure of the molecules. It also provides useful information on molecular patterns, spacing and bonding. The working principle is based on the inelastic scattering of the molecules. This phenomenon is called Raman Effect [63].

The Raman spectroscopy analysis was carried out using Horiba Jobin HR800 Raman Spectroscope instrument. The calibration was initially made by targeting the ultraviolet (UV) ray to a blank sample slide placed on the microscope platform. Then, a small amount of catalyst sample was spread on the sample slide. Sample was illuminated by a 20mW He-Ne lesser at 514 nm wavelength. The lenses were adjusted for zooming on the targeted area and the scanning range was set from 100 cm^{-1} to 1800 cm^{-1}.

3.4.3 Field Emission Scanning Electron Microscopy (FESEM)

FESEM is a microscopy tool which provides information on the topography, morphology, and elemental composition of sample. Figure 3.10 shows the schematic diagram of FESEM.

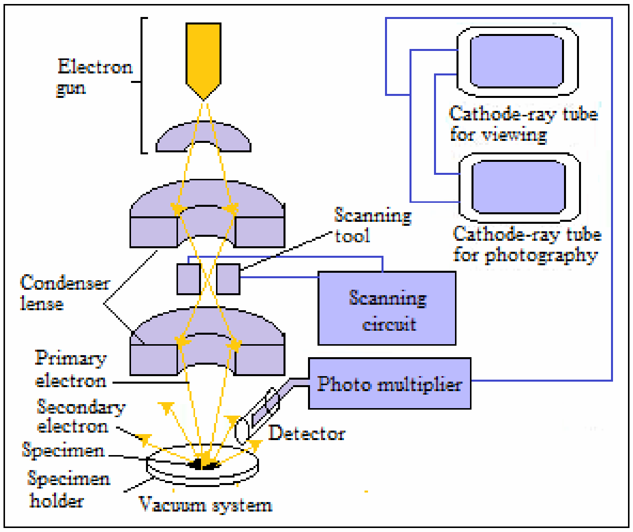

Figure 3.10: Schematic illustration on working principle of FESEM.

Electrons are produced by heating the tungsten filament. The resultant electrons are attracted to anode which accelerates their movements. The electrons are then converted to a monochromatic beam by focusing them directly to the magnetic lenses in the column and the apertures filtered out scattered electrons. Depending on the types of electrons scope, this beam will target the specimen and consequently produces signals which include secondary, backscattered, auger electrons as well as x-ray. These signals are detected and represented as an image by a photo multiplier.

The FESEM model Zeiss Supra 55/55 VP, was used for characterizing nanocatalysts. It was operated at 0.1kV to 30kV and magnification of 20X to 900KX. Small amount of sample was spread on a carbon tape pasted on a sample holder. The chamber was vacuumed using a vacuum pump operated at pressure of 2Pa to 133Pa.

3.4.4 Energy Dispersed X-ray (EDX)

Energy Dispersed X-Ray (EDX) is linked to the FESEM. It identifies type of atoms present within the sample and quantifies its composition. This information is presented as a spectrum.

3.4.5 Temperature Programmed Reduction (TPR)

Temperature Programmed Reduction (TPR) was used to estimate the temperatures required to reduce a metal oxide to a metallic state. Additional information that can also be evaluated from the TPR profiles is metal-support interaction, number of active sites and dispersion [9]. The typical reducing agents employed are hydrogen, H_2 and carbon monoxide, CO gases [9], [73].

TPR studies were conducted using a Thermo Finnigan TPDRO 1100 instrument equipped with a TCD detector. The process consists of two stages namely a pre-treatment step and the analysis step. About 0.12 g of catalyst was weighed and placed in between two layers of glass wool in the quartz sample cell. The quartz cell was then placed in the holder of the electrical furnace. The catalyst was pre-treated in a stream of nitrogen, N_2 at a flow rate of 20 cc/min and heating rate of 40^{o}C/min. The temperature was set to 200^{o}C and held at 200^{o}C for 10 minutes. The sample was analyzed in a stream of 5% H_2-N_2 gas at heating rate of 10 ^{o}C /min. TPR profiles were obtained from room temperature until 800^{o}C. The sample was held at 800^{o}C for 10 min. This analysis gas passed through a thermal conductivity detector (TCD) which detected the change in hydrogen concentration in the gas stream. Distinct reducible species in the catalyst were shown as peaks in the TPR spectra.

3.4.6 Vibration Sample Magnetometer (VSM)

VSM examines the magnetic behavior of samples particularly for magnetic materials. The working principle is based on recording the magnetization behavior of vibrating sample in a uniform magnetic field. The measurement can be performed as a function of temperature and magnetic field strength. Figure 3.11 reveals the schematic diagram of VSM [105].

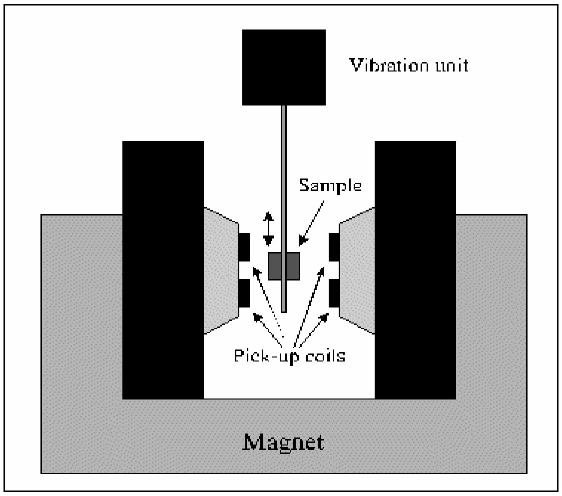

Figure 3.11: Vibration Sample Magnetometer [105].

The nanocatalysts were characterized using the VSM model DMS 8810. The sample was weighed and placed into a sample holder of 3 mm I.D. A rod was inserted into the sample holder and then attached to a vibration exciter. Water-cooled electromagnet and power supply were turned on, generating a constant magnetic field to magnetize the sample. The magnetic field strength was set to -15k to 15k Oe. The sample holder was moved up and down by the vibration exciter at a set frequency of usually 85 Hz to ensure that the sample was entirely magnetized. The magnetization values were then recorded.

3.4.7 N_2 Adsorption

The surface area, pore volume, average pore size and pore size distribution of the nanocatalysts was determined using N_2 adsorption method. This method is based on multipoint nitrogen adsorption-desorption principle. Generally, a sample contained in an evacuated sample tube is cooled to cryogenic temperature (-196°C) and exposed to analysis gas at a series of precisely controlled pressures. The number of gas molecules adsorbed on the surface increases with each incremental pressure. The pressure at which adsorption equilibrium occurs is measured and the universal gas law is applied to determine the quantity of gas adsorbed. The N_2 adsorption experiments were performed on a Micromeritics ASAP 2020 instrument.

A blank sample tube was weighed and subsequently loaded with 0.3 gram of nanocatalyst. The sample was degassed at 130°C overnight to remove impurities and moisture. The cold trap dewar that was filled with liquid nitrogen was installed to trap impurities in the manifold. After degassing, the sample was cooled to ambient temperature and the tube was removed from the degassing port. Since the sample was under vacuum, the tube was backfilled with nitrogen gas before it can be removed safely. The sample tube was reweighed to determine the actual sample mass which was keyed into the software. Subsequently, it was placed into the analysis port. The sample cell was immersed in liquid nitrogen in a dewar flask on an elevator. The sample information was then fed into the software to start the analysis. The nitrogen adsorption-desorption measurements were conducted for 56 points.

The surface area was calculated using the Brunauer-Emmett-Teller (BET) method, while the pore size distribution was determined from the desorption branch of the adsorption isotherm by the Barrett-Joyner-Halenda (BJH) method.

3.5 Procedure for Catalytic Evaluation

Typically, 0.2 g of powdered catalyst sample was placed on the glass wool and packed in the reactor tube. Thermocouple was attached to the reactor tube and the packed reactor tube was placed in the middle of the north and south poles of magnets. Heater, thermocouple and temperature indicator wire were then correctly positioned. The system was purged with 10 cm^3/min of purified nitrogen gas for about 20 minutes. Reduction process was performed by flowing 30 cm^3/min of purified hydrogen at 200^oC for four hours. After the reduction process was completed, the controller was set to the desired reaction temperatures. The reactant gas comprised a mixture of nitrogen and hydrogen, was fed into the reactor at total flow rates of 40 cm^3/min and H_2:N_2 ratio of 3:1. Typical reaction duration was four hours. A tube made from polyvinyl chrolide (PVC) was connected to the exhaust of microreactor. Its end was then dipped into 0.001 M hydrochloric acid, HCl, enabling the outlet gas to be bubbled. Ammonia was quantified by titrating 0.001 M hydrochloric acid, HCl, containing the bubled ammonia, NH_3 with 0.001 M sodium hydroxide, NaOH solution.

The procedures were repeated for examining the effects of various synthesis temperatures (30^oC, 70^oC, 110^oC, 150^oC and 190^oC), total feed gas flow rates (28 cm^3/min, 40 cm^3/min and 100 cm^3/min), H_2:N_2 (1:3, 3:1 and 5:1) ratios and magnetic field strength on the ammonia yield. Figure 3.12 shows the schematic diagram of microreactor system.

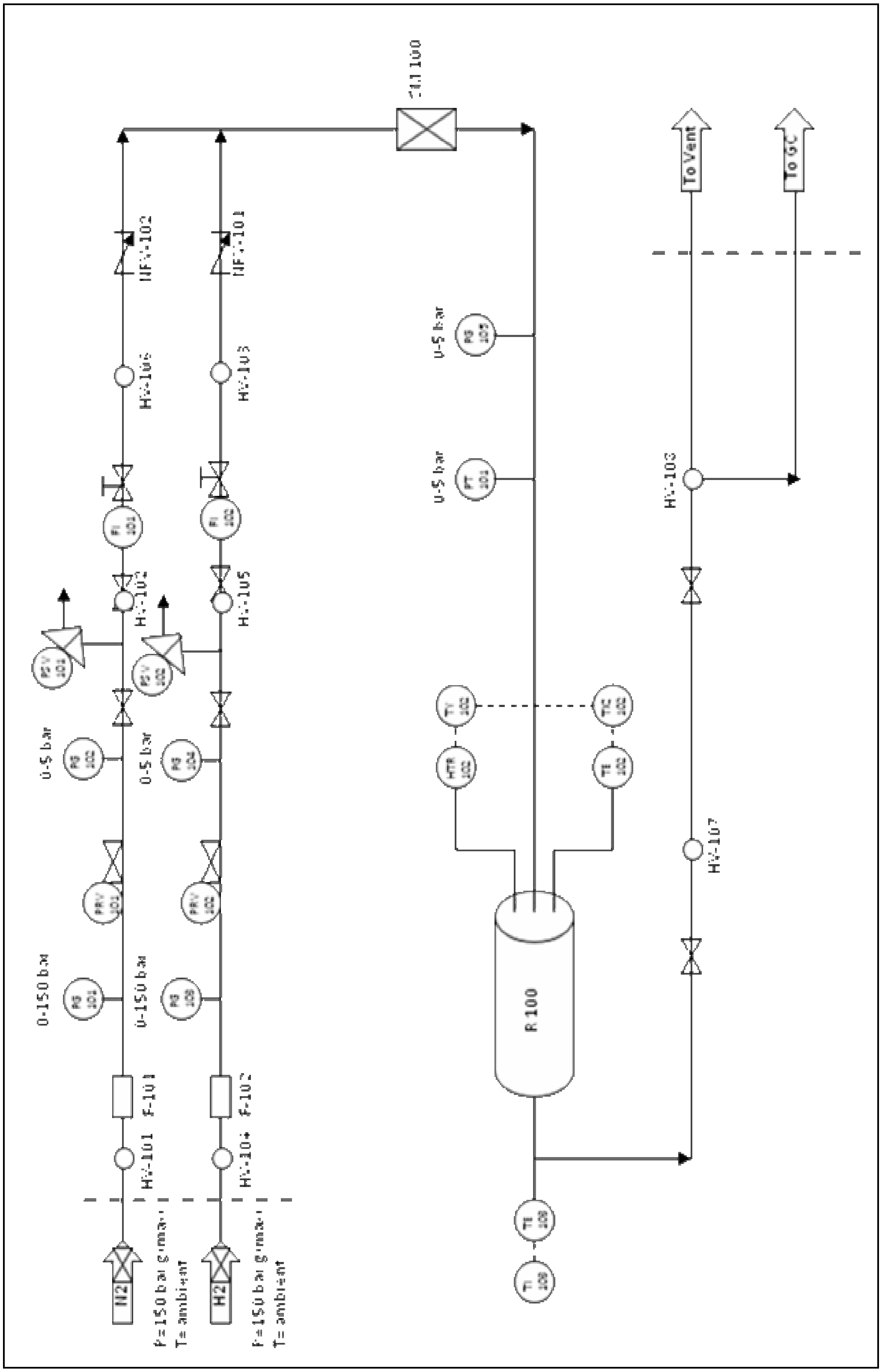

Figure 3.12: Schematic diagram of microreactor system

CHAPTER 4

RESULTS AND DISCUSSION

4.1 Characterization of Nanocatalyst

The prepared nanocatalysts were characterized using XRD, Raman, FESEM, H_2-TPR, VSM, N_2 adsorption and TEM.

4.1.1 Unsupported Hematite (α-Fe_2O_3) Nanocatalyst

4.1.1.1 Effect of Preparation Methods

This study aimed to select the best synthesis method which can produce a well-crystallined nanocatalyst at desired particle size of 20 nm to 30 nm. The sol-gel, self-combustion, and self-assembly methods were tested. The resultant nanocatalysts were annealed in air at 700^{o}C for 3 hours.

XRD analysis was performed to determine the phase of the prepared α-Fe_2O_3 nanocatalysts and the XRD spectra are shown in Figure 4.1. All diffracted peaks are for hematite (α-Fe_2O_3) phase as these peaks matched with those in the standard card (SS-NNNN 89-0599) and the values reported in literature [20], [40]. This can be further confirmed by the existence of (104) major peak, which is typically diffracted at 2θ approximately 33.0-34.0^{o} (Figure 4.1) [20], [40].

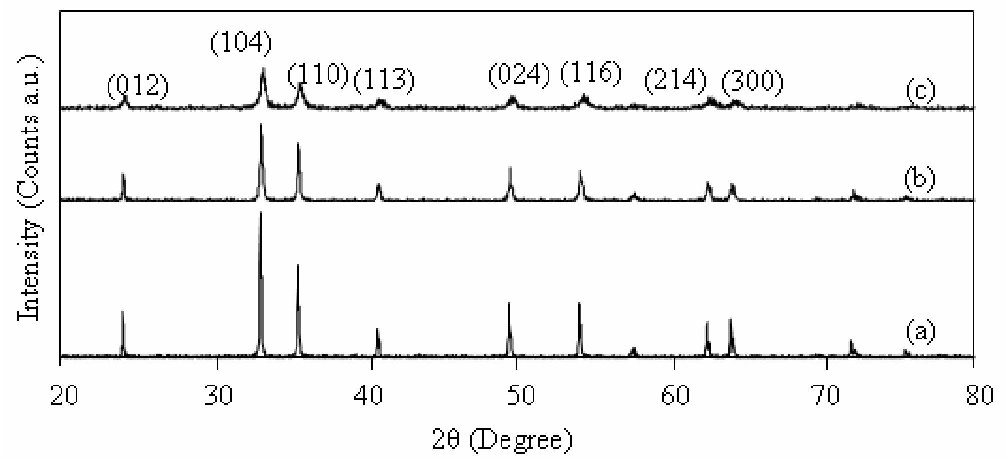

Figure 4.1: XRD spectra of α-Fe_2O_3 nanocatalysts prepared via (a) sol-gel (b) self-combustion and (c) self-assembly methods annealed at 700^{o}C.

The XRD data (Table 4.1) were interpreted using the Bruker Eva software. All the α-Fe_2O_3 nanocatalysts have rhombohedral structure with hexagonal close packed (hcp) crystal lattice, as confirmed by the lattice constants, where $a=b\neq c$ (Table 4.1), symbolizing hexagonal unit cell [10], [20], [40]. The XRD data are summarized in Table 4.1.

Table 4.1: XRD data of α-Fe_2O_3 nanocatalysts prepared via different methods annealed at 700^{o}C. The interpretation was based on (104) major plane.

Method		Sol-Gel	Self-Combustion	Self-Assembly	Literature
2θ (Degree)		33.17	33.22	33.3	33.2 [40]
Intensity (a.u)		240.00	130.00	60.80	-
D-spacing (Å)		2.698	2.694	2.682	2.690 [20]
FWHM		0.139	0.152	0.302	-
Lattice Constant (Å)	a	5.032	5.028	5.028	5.034 [20]
	b	5.032	5.028	5.028	5.035 [20]
	c	13.733	13.733	13.733	13.752 [20]
Average crystallite Size (nm)		60.67	55.50	27.90	-

All values in Table 4.1 are based on the (104) major plane. The average crystallite size was calculated using Scherer's equation (Equation 3.1) and the calculations are described in Appendix D. The highest peak intensity was achieved by the α-Fe_2O_3 nanocatalyst prepared via the sol-gel method. The sol-gel method resulted in bigger particles and larger d-spacing (Table 4.1) compared to those of other methods. The particle size of α-Fe_2O_3 prepared via sol-gel method (Table 4.1) is also smaller than the one obtained through hydrothermal method, as reported in literature [54]. The Raman spectra of α-Fe_2O_3 nanocatalysts prepared via different methods are displayed in Figure 4.2.

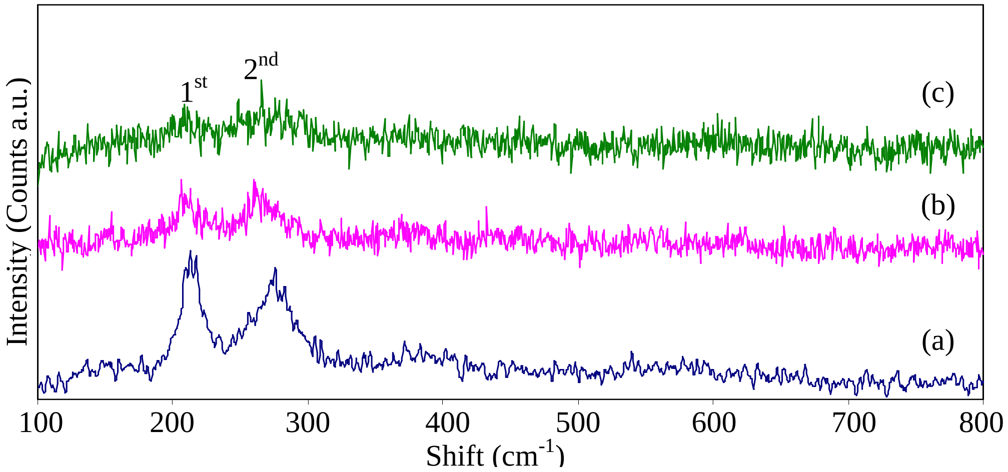

Figure 4.2: Raman spectra of α-Fe_2O_3 nanocatalysts prepared via (a) sol-gel (b) self-combustion and (c) self-assembly methods annealed at 700^oC.

The spectra show two separated peaks which are positioned in the range of 200-300 cm^{-1} (Figure 4.2). These values are consistent with the shifts for α-Fe_2O_3 phase as reported in literature [106]-[107]. The data of Raman analysis are summarized in Table 4.2.

Table 4.2: Raman data of α-Fe_2O_3 nanocatalysts prepared via different methods annealed at 700^oC.

Method		Sol-Gel	Self-Combustion	Self-Assembly	Literature
1st Peak	Shift (cm^{-1})	213.91	210.87	214.93	200-230 [65], [106]
	Intensity (Counts a.u)	38.29	7.94	5.74	-
2nd Peak	Shift (cm^{-1})	277.69	277.69	280.49	270-300 [65], [106]
	Intensity (Counts a.u)	22.51	6.59	5.79	-
Ratio I_{1st} / I_{2nd}		1.70	1.20	0.99	-

According to the literatures [65], [106], the peaks at 225-230 cm^{-1} and 290-300 cm^{-1} are attributed to A_{1g} Fe-O symmetry stretching and E_{1g} Fe-O symmetry bending, respectively. The α-Fe_2O_3 phase has the point symmetry group of D^6_{3d}. Highest ratio of peak intensity (I_{1st}/I_{2nd}) was displayed by α-Fe_2O_3 nanocatalyst synthesized through the sol-gel method, demonstrating that well-crystallized phase has been formed (Figure 4.2). The Raman spectrum for the sample synthesized via self-assembly revealed noisy pattern (Figure 4.2) which might due to poor crystallinity, which was also shown by XRD analysis (Figure 4.1).

The effects of different synthesis methods on the surface morphology of α-Fe_2O_3 nanocatalysts were examined by FESEM and the images are illustrated in Figure 4.3. The α-Fe_2O_3 nanocatalyst synthesized via self-assembly method exhibited spherical-shape of agglomerated particles. The average grain size was about 24 – 36 nm (Figure 4.3 (a)). Hexagonal-shape particles with average grain size around 70 – 250 nm can be seen for the sample obtained via self-combustion method (Figure 4.3 (b)). The sol-gel method resulted in α-Fe_2O_3 nanocatalyst with average grain size of 160 nm.

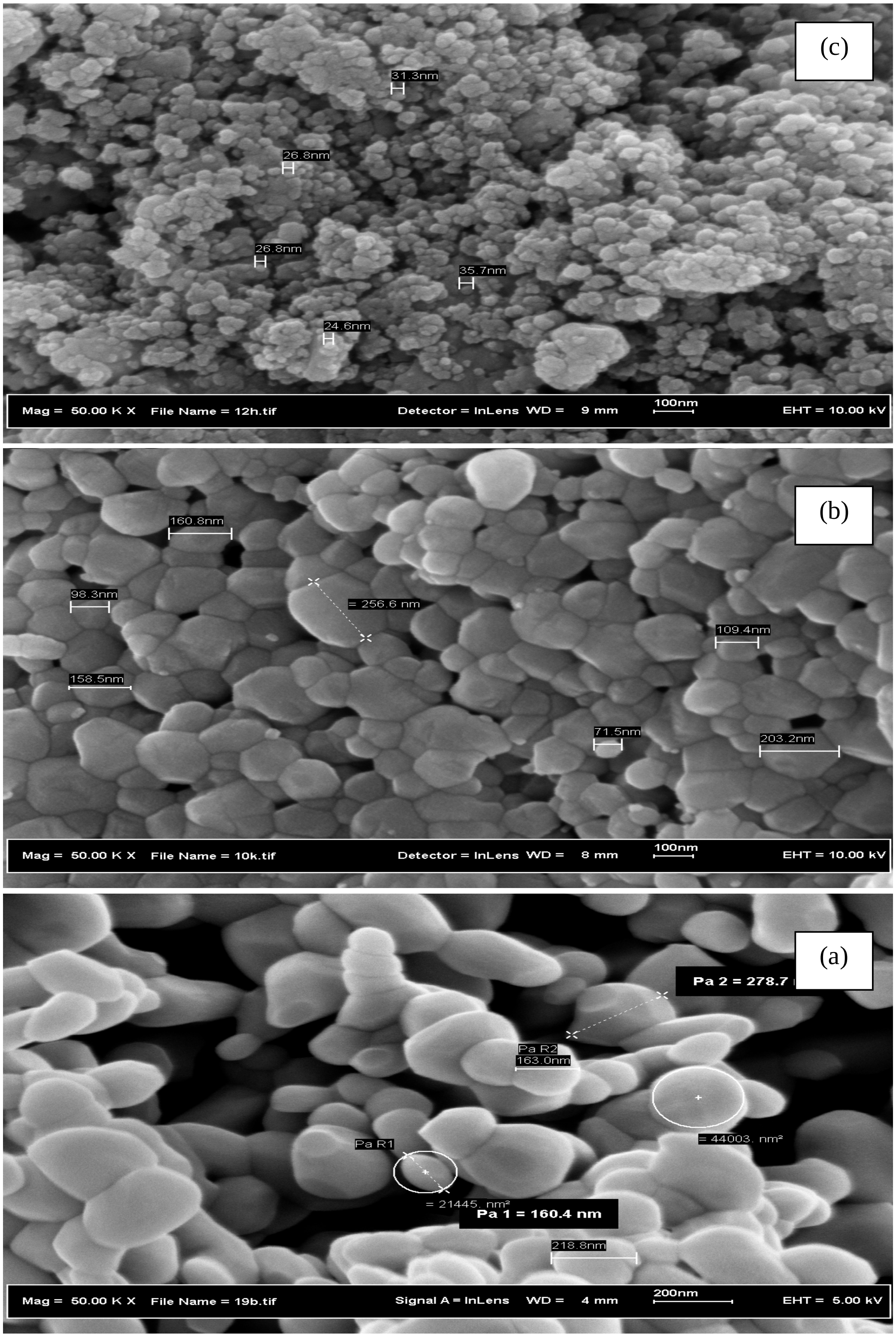

Figure 4.3: FESEM images α-Fe_2O_3 nanocatalysts prepared via (a) sol-gel (b) self-combustion and (c) self-assembly methods annealed at 700^{o}C.

In order to determine the elemental constituents within the synthesized α-Fe_2O_3 nanocatalysts, EDX analysis was carried out and the resultant spectra are illustrated in Figure 4.4.

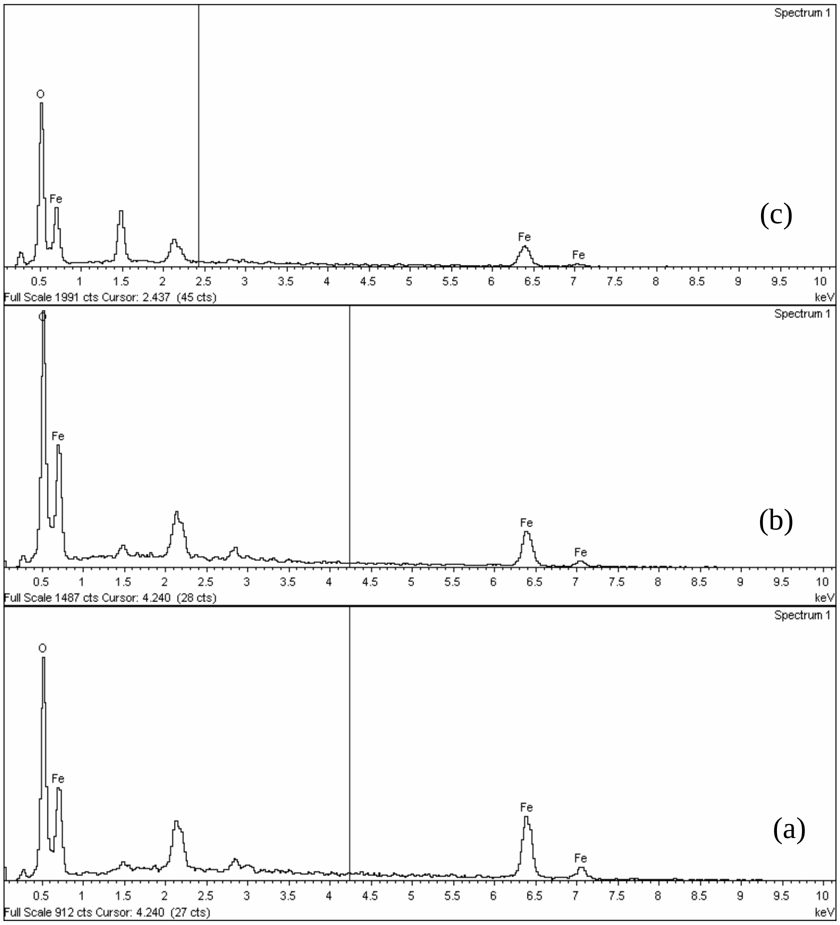

Figure 4.4: EDX spectra of α-Fe_2O_3 nanocatalysts prepared via (a) sol-gel (b) self-combustion and (c) self-assembly methods annealed at 700°C.

Iron (Fe) and (O) were detected in all catalysts. The unlabelled peaks are assigned to coating material that was used to coat the specimens during characterization (Figure 4.4). The EDX data are tabulated in Table 4.3. The calculations are shown in Appendix F.

Table 4.3: EDX data of α-Fe_2O_3 nanocatalysts prepared via different methods annealed at 700°C.

Method			Sol-Gel	Self-Combustion	Self-Assembly
Atomic %	Fe	Exp.	37.90	33.77	28.12
		Dev.	5.25	16.58	29.70
	O	Exp.	56.50	58.24	55.08
		Dev.	5.83	2.93	8.20
Weight %	Fe	Exp.	64.90	50.56	48.96
		Dev.	7.26	27.70	29.97
	O	Exp.	28.0	24.94	27.53
		Dev.	6.82	17.00	8.38

The calculated theoretical atomic percentages for Fe and O are 40% and 60%, respectively. As shown in Table 4.3, nanocatalyst synthesized by sol-gel showed the highest Fe elemental composition compared to those of the other two methods. The percentage deviations were also less than 10% which suggest that the hexagonal lattice sites have been entirely occupied by Fe and O atoms. Meanwhile, the samples processed through self-combustion and self-assembly exhibited incomplete atoms occupation as indicated by large deviation of Fe atomic composition (Table 4.3). Therefore, these α-Fe_2O_3 nanocatalysts have to be annealed at much high temperature to improve their crsytallinity.

The reducibility of α-Fe_2O_3 nanocatalysts was studied using H_2-TPR. Figure 4.5 reveals the H_2-TPR profiles for Fe_2O_3 nanocatalysts prepared by different methods.

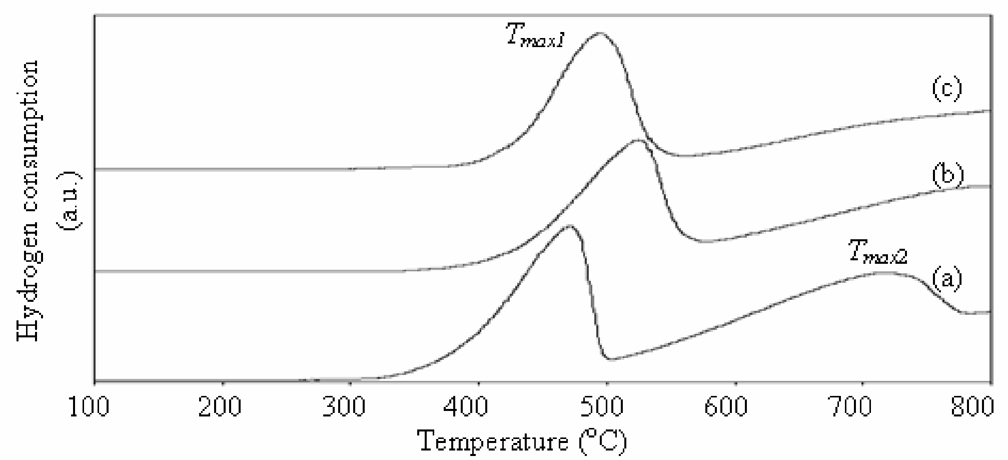

Figure 4.5: H_2-TPR profiles of α-Fe_2O_3 nanocatalysts prepared via (a) sol-gel (b) self-combustion and (c) self-assembly methods annealed at 700°C.

The first peak, T_{max1} which is located in temperature range of 470–530°C, is for the reduction of α-Fe_2O_3 to Fe_3O_4. Transformation of Fe_3O_4 to α-Fe occurred at the peak, T_{max2}, at temperature of 700-800°C (Figure 4.5). Similar observation was reported in literature [22], [75]-[76]. Table 4.4 summarizes the H_2-TPR data for α-Fe_2O_3 nanocatalysts prepared by different methods.

Table 4.4: H_2-TPR profiles of α-Fe_2O_3 nanocatalysts prepared via different methods annealed at 700°C.

	Method		Sol-Gel	Self-Combustion	Self-Assembly	Literature
TPR	Path A (T_{max1}) (°C)	$Fe_2O_3 \rightarrow Fe_3O_4$	472	525	495	500-530 [80]
	Path B (T_{max2}) (°C)	$Fe_2O_3 \rightarrow$ Fe	715	784	807	880-900 [80]

The reduction temperatures for all nanocatalysts were slightly lower than the results obtained by R. Brown and co-workers (Table 4.4) [80]. Difference in particle size and the use of higher flow rate (20 ccm/min) compared to literature (10 ccm/min) [80] might be the reason for this decrement even though the heating rate used in this experiment (10°C/min) was the same as that in literature [80].

Different methods yielded different particle sizes (Table 4.1) which influenced the reducibility behavior (Table 4.4). Second-stage reduction (Path B) for nanocatalyst synthesized by sol-gel method occurred at slightly lower temperature (Table 4.4) than those of nanocatalysts prepared by the other two methods (Table 4.4). An increase in temperature for the second stage reduction, T_{max2} (Table 4.4) might be due to the enrichment of $Fe_{1-x}O$ phase as well as enhancement in its stability. As described in Section 2.6, $Fe_{1-x}O$ is thermodynamically stable above 570°C [22]. The presence of $Fe_{1-x}O$ stable phase caused the second reduction stage (Path B) for all nanocatalysts to be accomplished at temperature above 700°C (Table 4.4). The reduction for all α-Fe_2O_3 nanocatalysts in this work was suggested in the following sequence: $Fe_2O_3 \rightarrow Fe_3O_4 \rightarrow Fe_{1-x}O \rightarrow$ Fe [22], [73]. Figure 4.6 shows the hydrogen consumption for reducing the nanocatalysts.

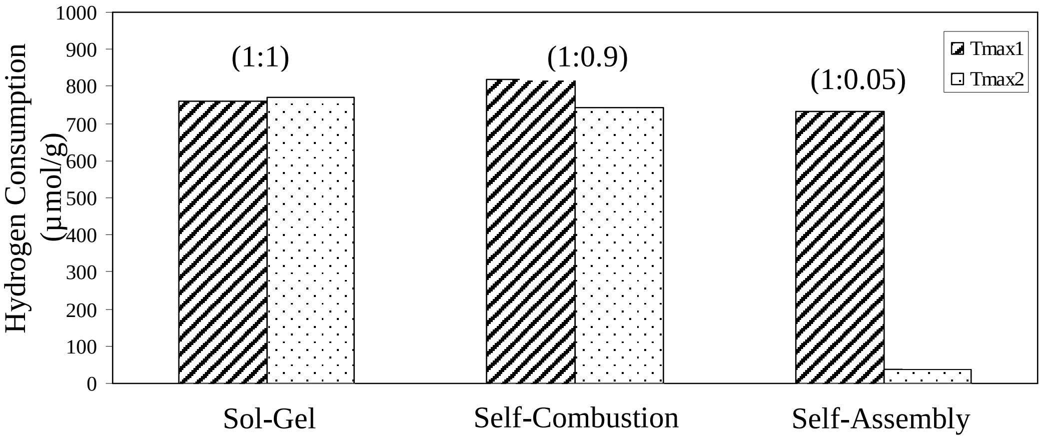

Figure 4.6: Hydrogen consumption to reduce of α-Fe_2O_3 nanocatalysts prepared via different methods annealed at 700°C.

Transformation of $Fe_2O_3 \rightarrow Fe_3O_4 \rightarrow$ α-Fe typically consumed hydrogen at T_{max1}/T_{max2} ratio of 1:8 for reduction to be entirely completed [76]. However in this study, the consumption ratios are approximately 1:1, 1:0.9, 1:0.05 for sol gel, self combustion and self assembly methods, respectively (Figure 4.6), indicating incomplete reduction process. This may due to the temperature range exerted is insufficient to overcome the higher activation energy of reduction involving smaller particles.

Based on results of XRD, FESEM and H_2-TPR, the sol gel was chosen as the best synthesis method amongst the methods tested for this work. This method successfully produced well-crystallized, larger size and irregular shape of particles which were easily reducible. Samples synthesized via the sol-gel method have been used for further investigations.

4.1.1.2 Effect of Periods of Stirring

This part focused on how to vary the size of nanocatalyst particles. The targeted size of nanoparticles is 20-30 nm. It is expected that an increase in stirring duration of the sol can produce smaller particles using the sol gel method. The period of stirring was prolonged to 1 day, 1 week and 1 month, respectively. The resultant nanocatalysts were annealed in air at 300°C for three hours.

The phase of the α-Fe_2O_3 nanocatalysts was identified by XRD and the recorded spectra are displayed in Figure 4.7.

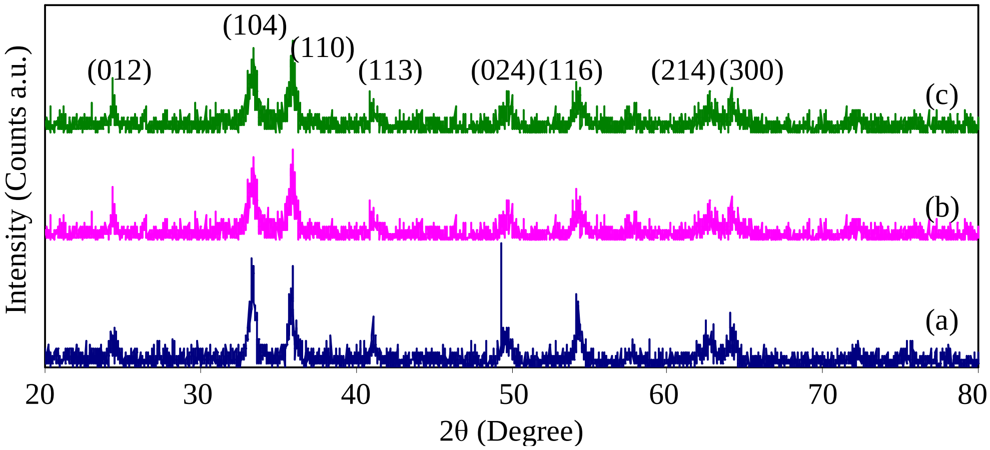

Figure 4.7: XRD spectra of α-Fe_2O_3 nanocatalysts prepared via sol-gel method stirred for (a) 1 day (b) week (c) 1 month, annealed at 300°C.

The diffraction peak at about 2θ of 33.405° was assigned to (104) major plane for hematite, α-Fe_2O_3 (Figure 4.7) as it matched with the standard card (SS-NNNN 89-0599) and reported values [40]-[41], [54]. In addition, the absence of other diffraction peaks for ferrite nitrite or other iron oxides, such as Fe_3O_4 and γ-Fe_2O_3 confirmed that the resultant particles were purely hematite (α-Fe_2O_3). Table 4.5 reviews the XRD data analysis of prepared nanocatalysts obtained at various stirring periods.

Table 4.5: XRD data of α-Fe_2O_3 nanocatalysts prepared via sol-gel method at different periods of stirring, annealed at 300°C. The interpretation was based on (104) major plane.

Method		1 day	1 week	1 month	Literature
2θ (Degree)		33.44	33.46	33.47	33.2 [40]
Intensity (a.u)		63.40	43.50	29.10	-
D-spacing (Å)		2.699	2.681	2.701	2.690 [20]
FWHM		0.329	0.364	0.448	-
Lattice constant (Å)	a	5.032	5.035	5.028	5.034 [20]
	b	5.032	5.035	5.028	5.034 [20]
	c	13.733	13.748	13.730	13.752 [20]
Average crystallite size(nm)		25.60	23.20	18.80	-

The data (Table 4.5) were obtained using Bruker Eva software which was based on (104) major plane. The crystallite size was calculated using Scherer's Equation (Equation 3.1, Section 3.4.1). Period of stirring influenced the particle size of resultant nanocatalyst (Table 4.5). Prolonging stirring period from 1 day to 1 month reduced the average crystallite size by 26.65%. Furthermore, the distance between atomic planes (D-spacing) increased with increasing stirring period (Table 4.5). Stirring process is essential to promote the formation of homogeneous sol and achieve “supersaturation” point. Prolonging the stirring period enriched the nucleation points and caused nucleation process to occur more rapidly. Consequently, smaller particles were attained (Table 4.5) [63]-[65].

The structure of α-Fe_2O_3 nanocatalysts prepared via sol-gel method was examined by Raman spectroscopy and the recorded spectra are displayed in Figure 4.8.

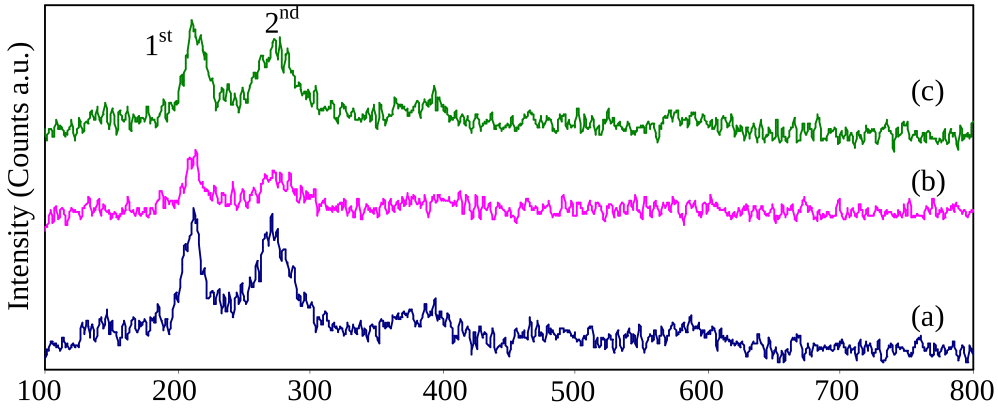

Figure 4.8: Raman spectra of α-Fe_2O_3 nanocatalysts prepared via sol-gel method at stirring periods of (a) 1 day (b) 1 week and (c) 1 month, annealed at 300°C.

The spectra show two strong Raman bands located at 200 – 300 cm^{-1}. These bands show α-Fe_2O_3 characteristic and matched with literature data [106]-[107]. The data for these spectra are tabulated in Table 4.6.

Table 4.6: Raman data of α-Fe_2O_3 nanocatalysts prepared via sol-gel method at different stirring periods, annealed at 300°C.

Temperature (°C)		1 day	1 weak	1 month	Literature
1st Peak	Shift (cm^{-1})	212.89	213.90	211.37	200-230 [65], [106]
	Intensity (Counts a.u)	9.58	5.02	7.61	-
2nd Peak	Shift (cm^{-1})	271.62	272.63	273.64	200-300 [65], [106]
	Intensity (Counts a.u)	9.17	3.68	6.55	-
I_{1st}/I_{2nd}		1.04	1.16	1.36	-

Intensity of the Raman peak decreased with increasing stirring period (Table 4.6). Sample stirred at 1 day revealed the highest intensity of Raman peaks, indicating a well crystallized structure. However, 1 month stirring resulted in poorly crystallized sample as the Raman peaks were not too intense. This analysis was substantiated by the interpretation of XRD results (Figure 4.7, Table 4.5).

The surface morphology of resultant α-Fe_2O_3 nanoparticles was examined using FESEM and the images are shown in Figure 4.9. Irregular-shape particles were observed for nanoparticles obtained at 1 day stirring. Meanwhile, samples stirred at 1 week and 1 month illustrated well-defined spherical shape nanoparticles (Figure 4.9).

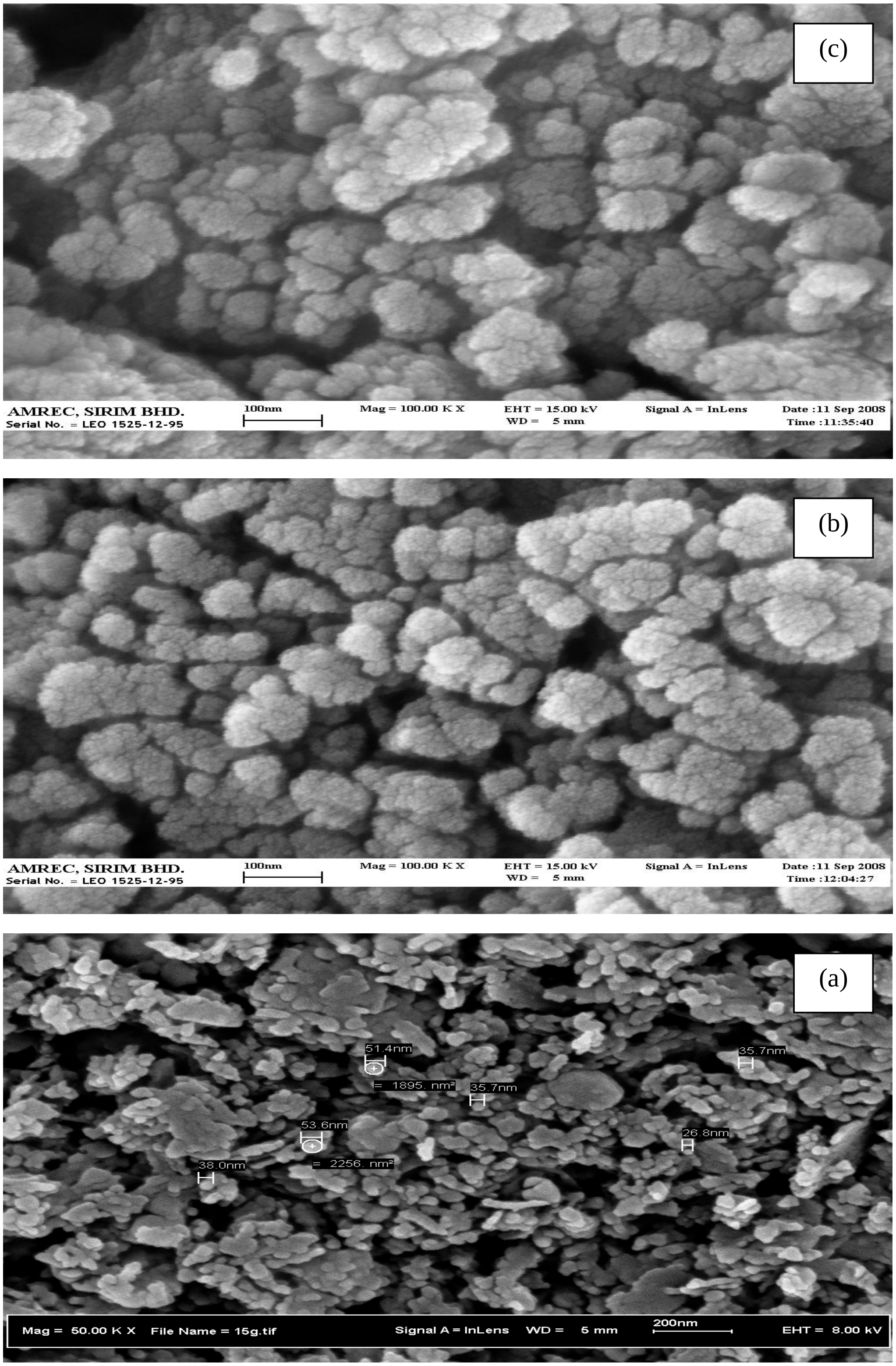

Figure 4.9: FESEM images α-Fe_2O_3 nanocatalysts prepared via sol-gel stirred at (a) 1 day (b) 1 week and (c) 1 month, annealed at 300^{o}C.

The EDX spectra for α-Fe_2O_3 nanocatalysts prepared via sol-gel method at different stirring periods are shown in Figure 4.10.

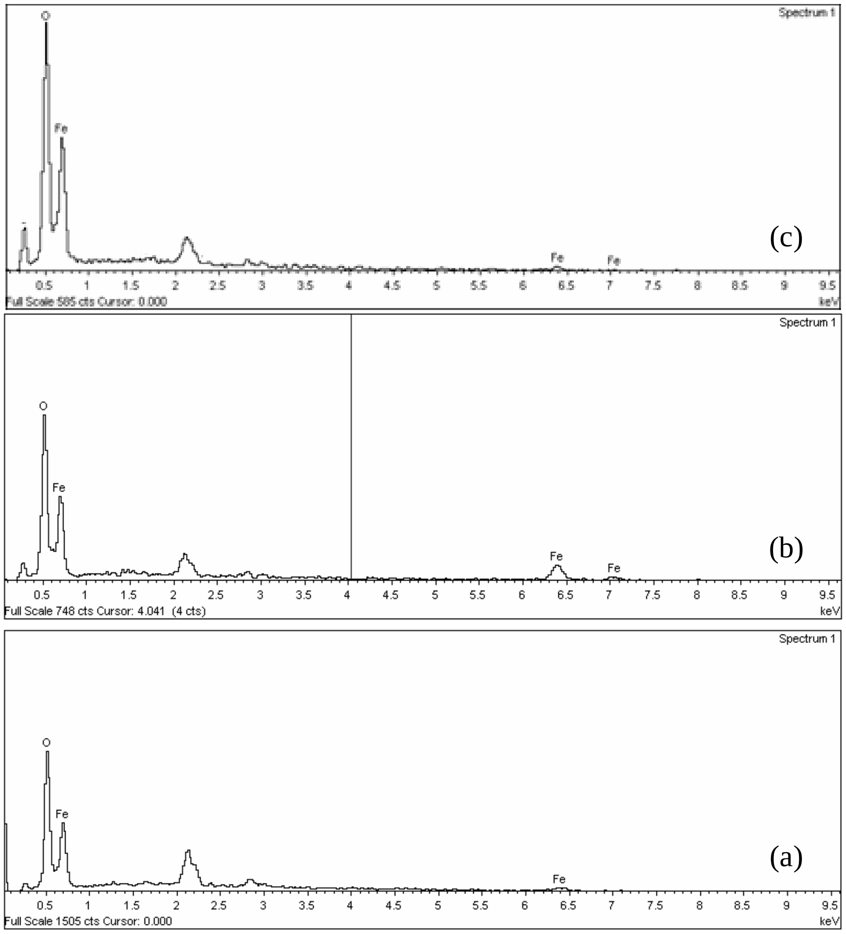

Figure 4.10: EDX spectra of α-Fe_2O_3 nanocatalysts prepared via sol-gel method at stirring periods of (a) 1 day (b) 1 week and (c) 1 month, annealed at 300^oC.

Iron and oxygen elements were detected in all nanocatalysts, confirming the presence of iron oxide, α-Fe_2O_3 as the major phase. The amount of detected elements is summarized in Table 4.7. The details of calculation are revealed in Appendix G. The theoretical atomic percentage for iron and oxygen are 40% and 60%, respectively. The 1-month stirring period resulted in nanocatalyst having 5% deviation for both elements while the ones stirred for 1 day and 1 week showed more than 10% deviation from the theoretical values (Table 4.7). This concludes that stirring period also has significant influence on the composition of resultant nanocatalysts.

Table 4.7: EDX data of α-Fe_2O_3 nanocatalysts prepared via sol-gel method at different stirring periods, annealed at 300°C.

Method			1 day	1 week	1 month
Atomic (%)	Fe	Exp.	22.56	28.84	41.74
		Dev.	77.30	38.69	-4.16
	O	Exp.	31.358	71.16	58.26
		Dev.	89.99	-15.68	2.98
Weight (%)	Fe	Exp.	54.40	58.89	71.43
		Dev.	28.67	18.86	-2.00
	O	Exp.	31.58	41.40	28.57
		Dev.	-5.00	-27.53	5.00

Figure 4.11 shows the H_2-TPR profiles for the α-Fe_2O_3 nanocatalysts synthesized at different stirring periods.

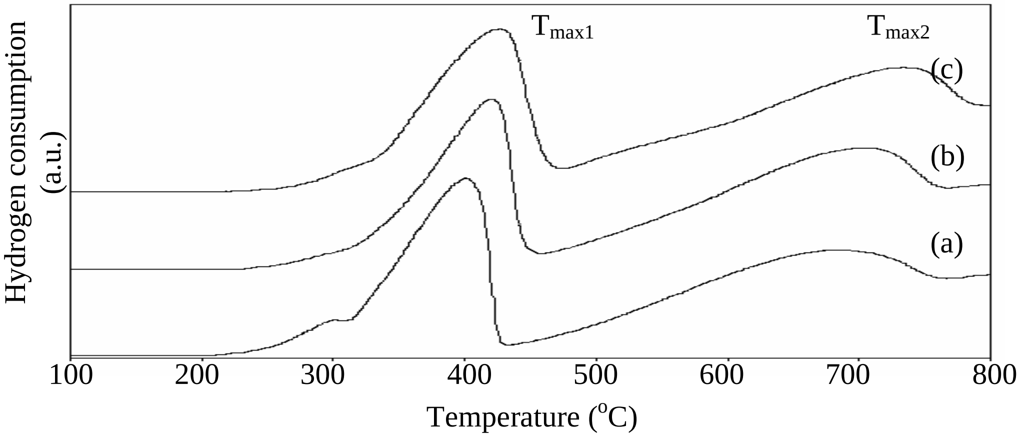

Figure 4.11: H_2-TPR profiles of α-Fe_2O_3 nanocatalysts prepared via sol gel-method at stirring periods of (a) 1 day, (b) 1 week and (c) 1 month, annealed at 300°C.

The first intense peak, T_{max1} which was situated at temperature 300°C to 500°C was assigned to reduction of α-Fe_2O_3 to Fe_3O_4. Meanwhile, the second reduction step, T_{max2}, involving transformation Fe_3O_4 to α-Fe was accomplished at much higher temperature (Figure 4.11). Both reduction temperatures are still in the range of reported values [22], [76]. Table 4.8 shows the data for the H_2-TPR spectra.

Table 4.8: H_2-TPR data of α-Fe_2O_3 nanocatalysts prepared via sol-gel method at different stirring periods, annealed at 300°C.

	Method		1 day	1 week	1 month	1 month
TPR	Path A (T_{max1})	$Fe_2O_3 \rightarrow Fe_3O_4$	400	420	426	500-530 [79]
	Path B (T_{max2})	$Fe_2O_3 \rightarrow Fe$	681	697	732	880-900 [79]

Increasing stirring period resulted in smaller particle size which was more difficult to reduce, as exhibited by the shift to higher temperature. Particles synthesized at 1 month have smaller particle size (Table 4.5), and required much higher temperatures for complete reduction compared to those stirred at 1 day and 1 week (Table 4.8). The hydrogen consumption during reduction of α-Fe_2O_3 nanocatalysts is revealed in Figure 4.12.

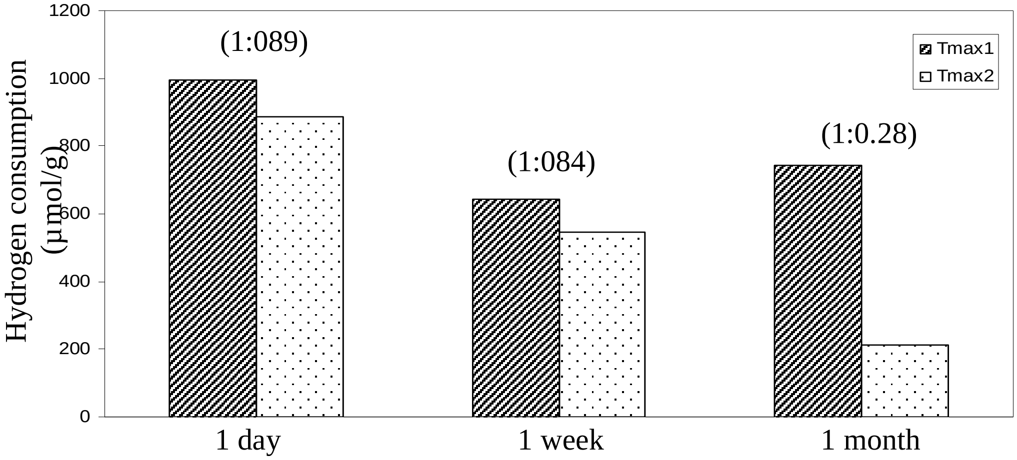

Figure 4.12: Hydrogen consumption to reduce α-Fe_2O_3 nanocatalysts prepared via sol-gel method at different stirring periods, annealed at 300°C.

The calculated hydrogen consumption ratios for T_{max1}/T_{max2} were 1:0.89, 1:0.84, and 1:0.28 for stirring period of 1 day, 1 week and 1 month, respectively (Figure 4.12). According to the literature, complete reduction of α-Fe_2O_3 to Fe is generally achieved with the hydrogen consumption ratio of 1:8 [76]. Reduction became less complete with increasing stirring period, possibly due to decrease in size of α-Fe_2O_3 nanoparticles.

4.1.1.3 Effect of Annealing Temperature

This section focused on improving the crystallinity of nanocatalyst. The nanocatalyst that was synthesized via sol gel method and stirred for 1 day was utilized. It was annealed in air at different temperatures for 3 hours. XRD spectra for the α-Fe_2O_3 nanocatalysts prepared via sol-gel method and annealed at different temperatures are shown in Figure 4.13.

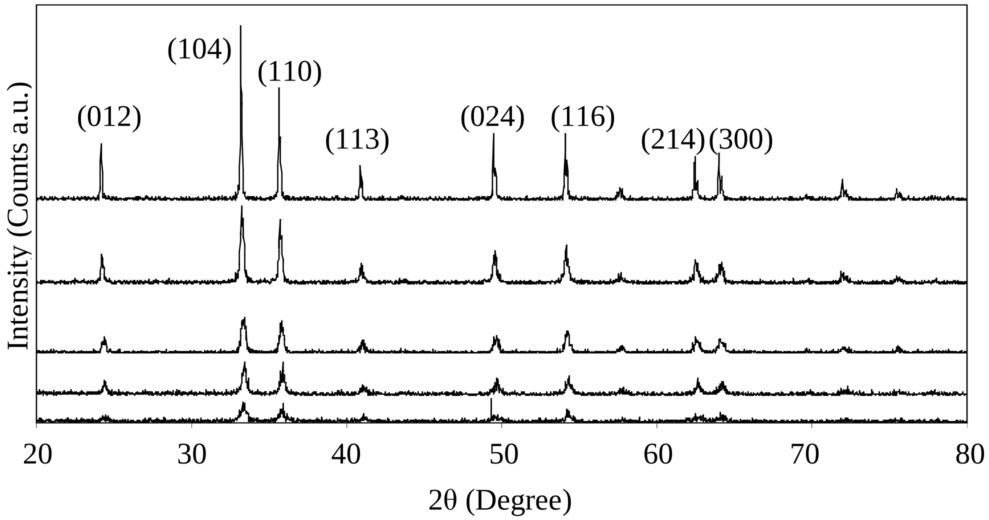

Figure 4.13: XRD spectra of α-Fe_2O_3 nanocatalysts prepared via sol-gel method stirred for 1 day, annealed at (a) 300°C, (b) 400°C, (c) 500°C, (d) 600°C and (e) 700°C.

All diffracted peaks matched with the data for standard card of SS-NNNN 89-0599, confirming the presence of hematite, α-Fe_2O_3 as the major phase. The emergence of (104) plane as a major peak which was recorded at 2θ of 33.24° (Figure 4.13) further confirmed the characteristic of α-Fe_2O_3 phase [40], [52], [54]. The intensity of diffracted peaks increased with increasing annealing temperature from 300°C to 700°C. This trend concurred with the observation reported in the literature [58], [60]. The data of XRD analysis are tabulated in Table 4.9.

Table 4.9: XRD data of α-Fe_2O_3 nanocatalysts prepared via sol-gel method stirred for 1 day, annealed at different temperatures. The interpretation was based on (104) major plane.

Temperature (°C)		300	400	500	600	700	Literature
2θ (Degree)		33.36	33.40	33.40	33.24	33.16	33.2 [39]
Intensity (a.u)		24.20	40.80	46.60	109.00	240.00	-
D-spacing(Å)		2.683	2.680	2.680	2.679	2.670	2.69 [19]
FWHM		0.388	0.315	0.369	0.268	0.139	-
Lattice Constant (Å)	a	5.031	5.031	5.031	5.032	5.031	5.034 [19]
	b	5.031	5.031	5.031	5.032	5.031	5.034 [19]
	c	13.737	13.737	13.737	13.733	13.737	13.752 [19]
Average Crystallite size (nm)		21.74	26.78	22.86	31.47	60.67	-

Increasing annealing temperature enhanced the crystallinity of the α-Fe_2O_3 nanocatalysts as indicated by an increase in intensity of diffracted peaks (Figure 4.13 and Table 4.9). The particle size increased when the annealing temperature was elevated from 300°C to 700°C (Table 4.9). Similar trend was also reported by previous works [33], [60] as described in Section 2.5.2.1. This could be due to higher tendency of small particles to agglomerate when exposed to high temperature environment. This agglomeration reduced the surface energy of the particles which subsequently led to the formation of bigger particles [60], [108].

The structure of nanocatalysts prepared via sol-gel method at different annealing temperatures was examined by Raman spectroscopy and the spectra are shown in Figure 4.14.

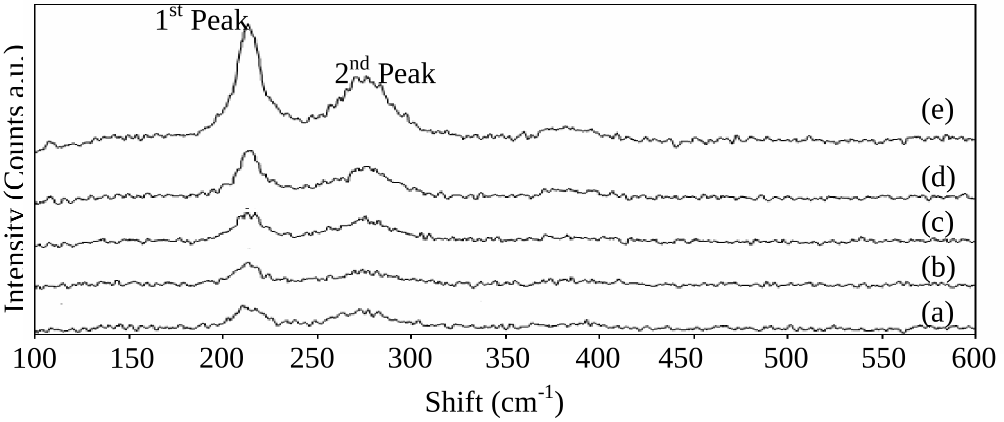

Figure 4.14: Raman spectra of α-Fe_2O_3 nanocatalysts prepared via sol-gel method stirred for 1 day, annealed at (a) 300°C (b) 400°C (c) 500°C (d) 600°C and (e) 700°C.

All spectra exhibit two peaks in the range of 200-300 cm^{-1} (Figure 4.14). According to the literature, these values corresponded to hematite, α-Fe_2O_3 characteristics [106]-[107]. Elevating annealing temperature increased the intensity of the Raman peaks (Figure 4.14), denoting an enhancement in crystallinity. The highest intensity for Raman peak was obtained for catalyst annealed at 700^{o}C. The Raman data for prepared nanocatalysts are summarized in Table 4.10.

Table 4.10: Raman data of α-Fe_2O_3 nanocatalysts prepared via sol-gel method stirred at 1 day, annealed at different temperatures.

Temperature (^{o}C)		300	400	500	600	700	Literature
1st Peak	Shift (cm^{-1})	213.91	214.41	241.41	215.93	213.40	200-230 [65], [106]
	Intensity (Counts a.u)	7.99	7.501	10.03	16.23	36.33	-
2nd Peak	Shift (cm^{-1})	278.71	278.20	277.18	280.73	277.69	270-300 [65], [106]
	Intensity (Counts a.u)	6.65	4.92	9.29	10.82	20.55	-
I_{1st}/I_{2nd}		1.20	1.52	1.10	1.50	1.76	-

Figure 4.15 shows the FESEM images of α-Fe_2O_3 nanocatalysts prepared via sol-gel method and annealed at various temperatures. The agglomeration of particles was more pronounced with increasing annealing temperature. Smaller particles favor to agglomerate to reduce its surface energy which consequently resulted in bigger particles [57], [60], [108]. Therefore, the temperature that can result in nanoparticles with the size of 20-30 nm is in the range of 300 – 600^{o}C (Table 4.9).

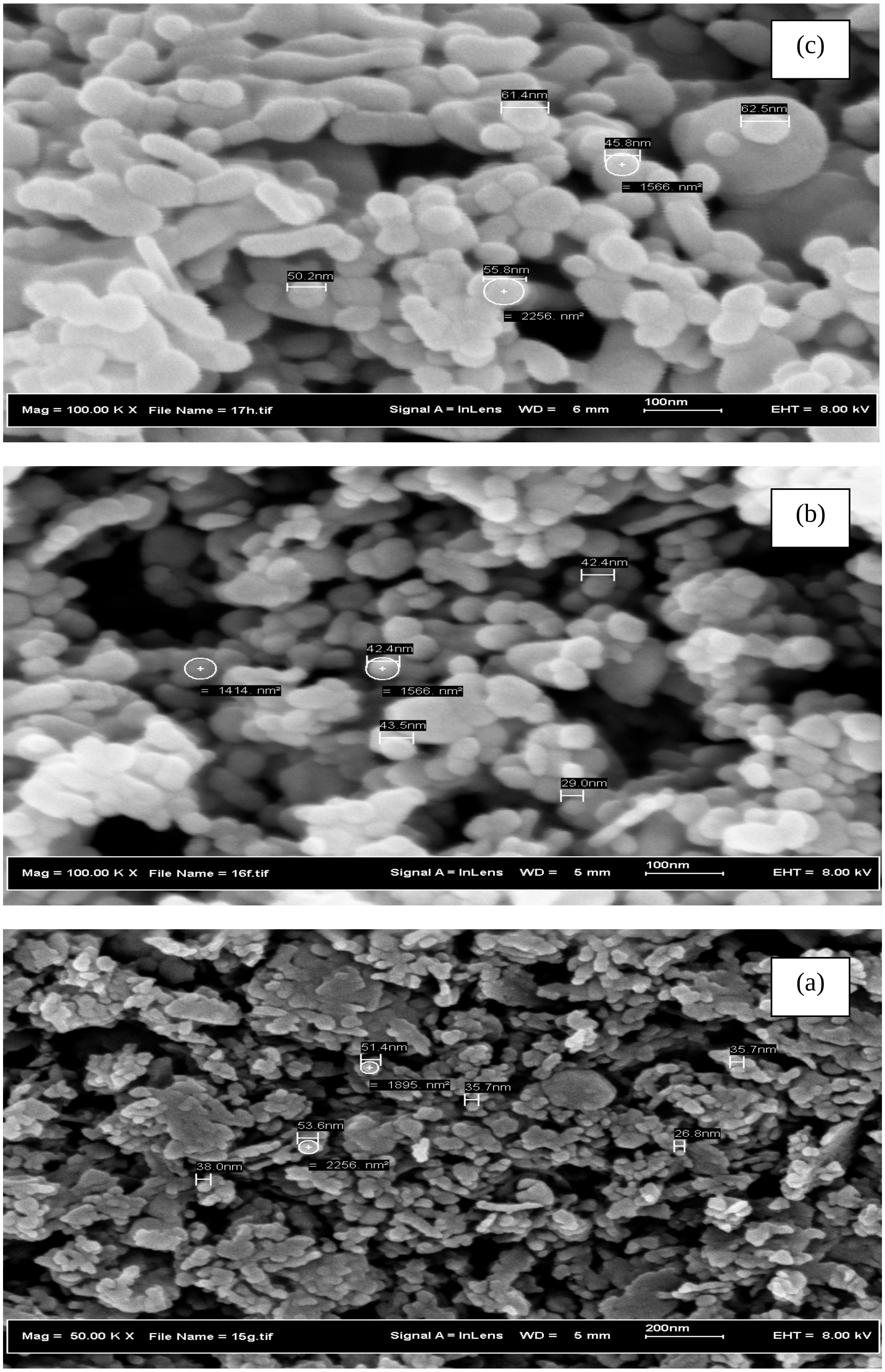

Figure 4.15: FESEM images of α-Fe_2O_3 nanocatalysts prepared via sol-gel method stirred for 1 day, annealed at (a) 300^{o}C (b) 400^{o}C (c) 500 (d) 600^{o}C and (e) 700^{o}C.

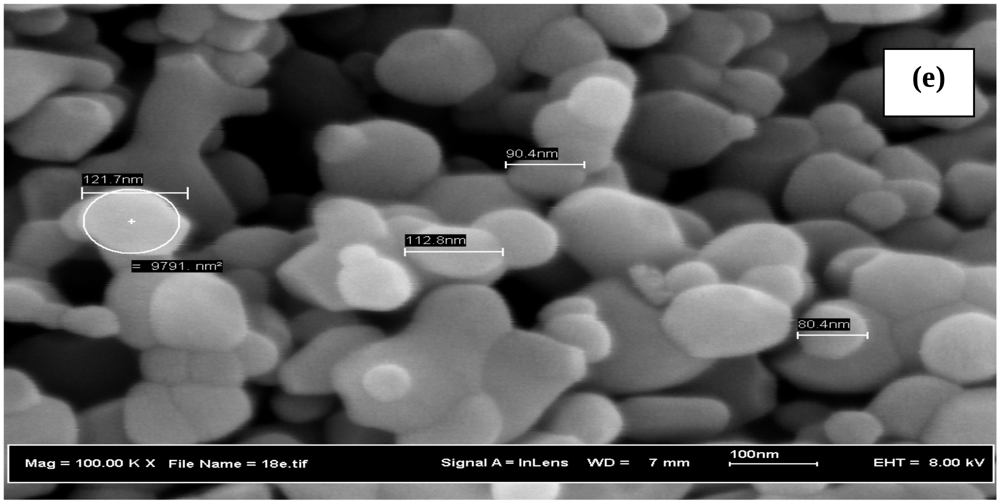
(e)
121.7nm
= 9791. nm²
90.4nm
112.8nm
80.4nm
Mag = 100.00 K X
File Name = 18e.tif
Signal A = InLens
WD = 7 mm
100nm
EHT = 8.00 kV

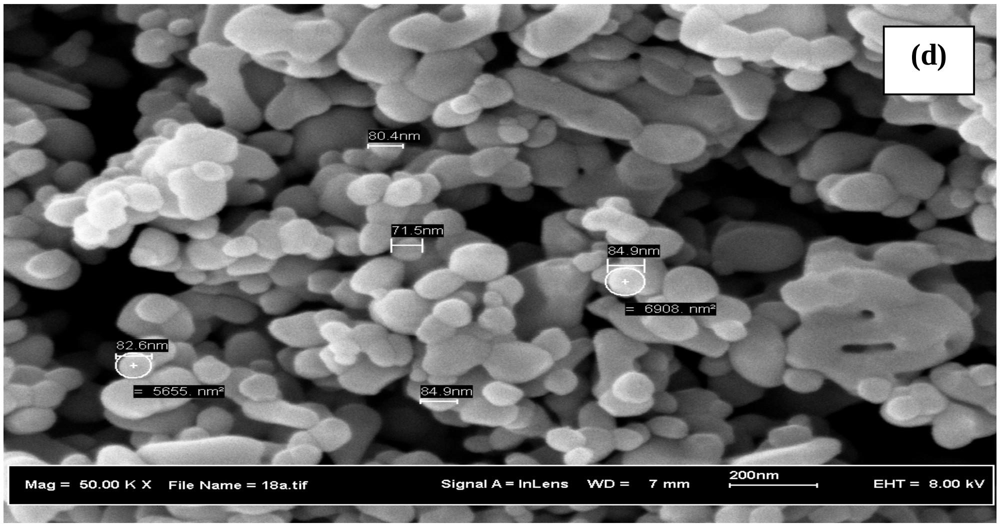
(d)
80.4nm
71.5nm
84.9nm
= 6908. nm²
82.6nm
= 5655. nm²
84.9nm
Mag = 50.00 K X
File Name = 18a.tif
Signal A = InLens
WD = 7 mm
200nm
EHT = 8.00 kV

Figure 4.16 displays EDX spectra of α-Fe_2O_3 nanocatalysts prepared via sol-gel method and annealed at different temperatures.

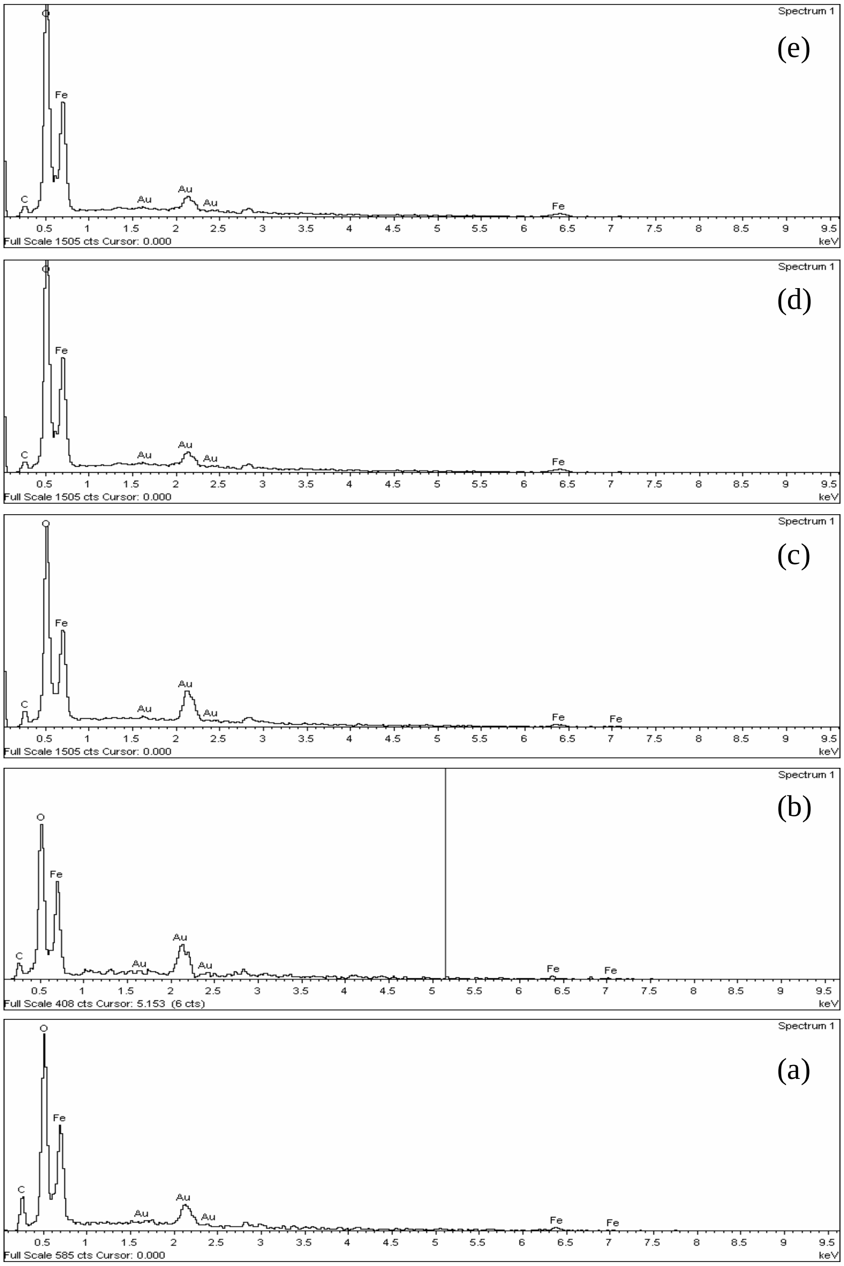

Figure 4.16: EDX spectra of α-Fe_2O_3 nanocatalysts prepared via sol-gel method stirred for 1 day, annealed at (a) 300^{o}C (b) 400^{o}C (c) 500^{o}C (d) 600^{o}C and (e) 700^{o}C.

Elements of Fe and O were detected in all iron oxide nanocatalysts (Figure 4.16). Theoretically, both Fe and O have weight percentages of 69.8% and 30.1%, respectively while the atomic percentages are 40% and 60%, respectively. The complete data for EDX are shown in Table 4.11.

EDX data reveal that both weight and atomic percentages of Fe and O increased with increasing annealing temperature (Table 4.11). The α-Fe_2O_3 nanocatalyst which was annealed at 700°C had less than 10% deviation for both Fe and O. However, the sample annealed at 300°C had more than 10% deviation, indicating incomplete occupancy of Fe and O atoms.

Table 4.11: EDX data of α-Fe_2O_3 nanocatalysts prepared via sol-gel method stirred for 1 day, annealed at different temperatures.

Annealing Temperature (°C)			300	400	500	600	700
Atomic %	Fe	Exp.	32.30	37.38	34.51	37.83	37.90
		Dev.	19.20	3.70	13.70	5.50	5.20
	O	Exp.	48.50	49.14	53.53	55.92	56.5
		Dev.	19.10	18.10	10.80	6.80	5.80
Weight %	Fe	Exp.	56.50	55.57	53.66	63.01	64.90
		Dev.	19.10	20.40	23.20	9.59	7.02
	O	Exp.	24.30	20.71	23.85	26.69	28.05
		Dev.	19.20	31.20	20.90	11.60	6.97

The reducibility investigation involving α-Fe_2O_3 nanocatalysts prepared via sol- gel method was carried out and the profiles are recorded in Figure 4.17.

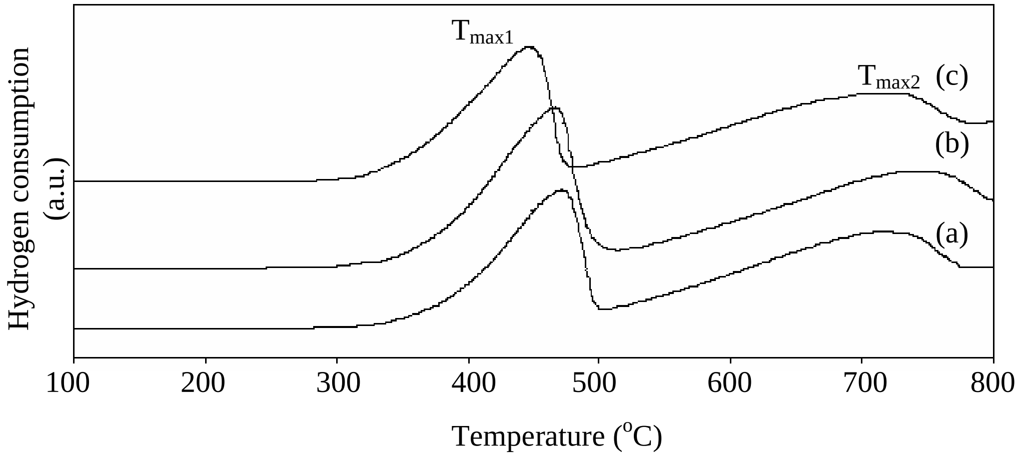

Figure 4.17: H_2-TPR profiles of α-Fe_2O_3 nanocatalysts prepared via sol-gel method stirred for 1 day, annealed at (a) 500°C (b) 600°C and (c) 700°C.

The reduction temperatures for nanocatalyst annealed at 500°C was slightly higher than those annealed at 600°C and 700°C which could be due to its smaller particle size. Table 4.12 summarizes the TPR data.

Table 4.12: H_2-TPR data of α-Fe_2O_3 nanocatalysts prepared via sol-gel method stirred for 1 day, annealed at different temperatures.

Annealing Temperature (^oC)			500	600	700	Literature
TPR	Path A (T_{max1})	$\alpha Fe_2O_3 \rightarrow Fe_3O_4$	474	464	448	500-530 [80]
	Path B (T_{max2})	$Fe_3O_4 \rightarrow Fe$	719	746	723	880-900 [80]

These results show that increasing annealing temperature promotes the formation of well crystallized but larger nanoparticles.

4.1.2 Unsupported Magnetite (Fe_3O_4) Nanocatalyst

4.1.2.1 Effect of Preparation Methods

A preliminary study in synthesizing magnetite Fe_3O_4 nanocatalysts was conducted by repeating various reported methods. These methods are sol gel [25], hydrothermal [35] and precipitation [31]. Subsequently, a hybrid method namely sol gel-hydrothermal was investigated in preparing the Fe_3O_4 nanocatalyst.

The phase of Fe_3O_4 nanocatalysts prepared via various methods was identified using XRD and the recorded spectra are displayed in Figure 4.18. All diffracted peaks with their miller planes matched with reported values for Fe_3O_4 from standard card (SS-NNNN-86-1345(A)) and literature [33], [35]-[36]. The Fe_3O_4 phase was further confirmed by existence of (311) major plane at 2θ of 35.14^o and (111) minor peak located at 2θ of 18.52^o. The minor peak of (104) that is usually located at 2θ of $10\text{-}20^o$ was not detected which indicates the absence of maghemite, γ-Fe_2O_3 phase (Figure 4.18) [33], [35]-[36].

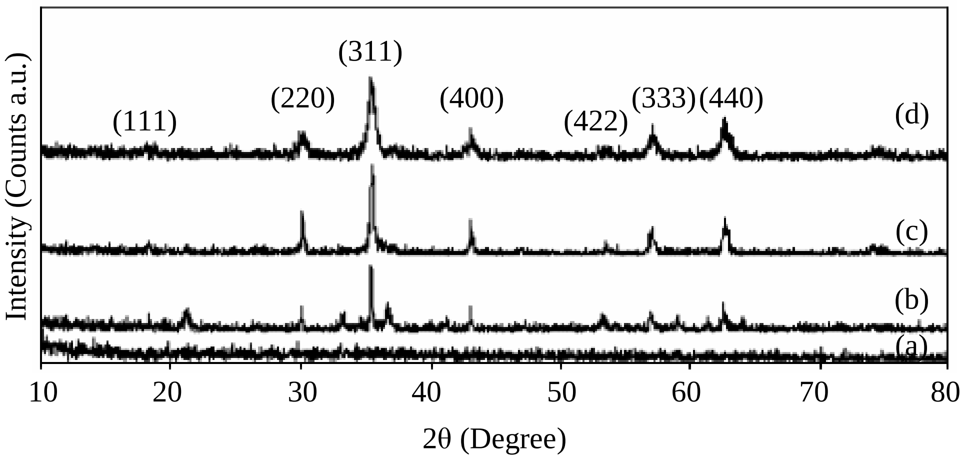

Figure 4.18: XRD spectra of Fe_3O_4 nanocatalysts prepared via (a) sol-gel (b) hydrothermal (c) precipitation and (d) sol gel-hydrothermal methods.

Diffraction peaks were absent for nanocatalyst synthesized via sol-gel, indicating poor crystallinity (Figure 4.18(a)). A combination between sol-gel and hydrothermal enhanced the crystallinity of the sample and resulted in smaller nanoparticles (Figure 4.18 (d)). Table 4.13 summarizes the data analysis of XRD. The atomics within nanocatalysts are anticipated to arrange in a cubic structure manner. The values of lattice constants matched with the literature [53]-[54] (Table 4.13) and obeyed a sequence of a=b=c, verifying that the structure of Fe_3O_4 nanocatalysts is cubic [10], [53]-[54]. The sol gel-hydrothermal method produced well-crystallined nanoparticles with smallest average crystallite size compared to those of other methods (Figure 4.18 and Table 4.13). The average crystallite size was 32.14 nm for sample synthesized by precipitation method. Precipitation method often faces several difficulties. Higher tendency of particles to agglomerate during the preparation is a well known problem. Thus, continuous stirring is necessary. Furthermore, the rate in dropping precipitant must also be controlled. Precipitation at fast rate will generate bigger particles [36]. In addition, the presence of counter ion, Cl in the synthesis system could also influence the stability of Fe_3O_4 phase.

Table 4.13: XRD data of Fe_3O_4 nanocatalysts prepared via sol-gel (SG), hydrothermal (HO), precipitation (PC) and sol gel-hydrothermal (SG-H) methods. The interpretation was based on (311) major plane.

Sample		SG	HO	PC	SG-H	Literature
2θ (Degree)		-	35.43	35.51	35.40	35.48 [33]
Intensity (Counts a.u)		-	56.50	71.43	70.60	-
FWHM		-	0.16	0.26	0.28	-
d-spacing (Å)		-	2.53	2.52	2.53	2.532 [20]
Lattice Constant (Å)	a	-	8.396	8.397	8.374	8.390 [20], 8.405 [54]
	b	-	8.396	8.397	8.374	8.390 [20], 8.405 [54]
	c	-	8.396	8.397	8.374	8.390 [20], 8.405 [54]
Av. crystallite size (nm)		-	53.36	32.14	29.97	-

The hydrothermal method resulted in larger particles compared to those of other preparation methods. The existence of pressure in hydrothermal method was beneficial for crystallinity enhancement which may accelerate the occupation of atoms into lattice sites. However, this method also suffers from Oswald ripening phenomenon which formed bigger particles [109]. The Oswald ripening may be the reason for the biggest average crystallite size obtained via hydrothermal in this study (Table 4.13). In addition, the use of organic surfactant during preparation can contribute to existence of impurity.

The sol gel-hydrothermal method resulted in smallest nanoparticles. Ethylene glycol not only behaved as the solvent, but also served as a stabilizing agent [110], reducing agent [111], and surfactant [112]. It possesses strong nucleophilic character originated from the two hydroxyl groups, (OH); attached at two ends of molecule chain [113]. When $Fe(NO_3)_3$ salt was dissolved in ethylene glycol, NO_3^- counter ions were favored to dissociate due to weak chelating property. Several vacant positions were created which then became deactivated by occupation of OH^- ions [113]. The possible structure of Fe ions in ethylene glycol environment is displayed in Figure 4.19 [114]. The NO_3^- ions were released from the system by heating process to form gelatine. This consequently minimized the oxidation effect carriers by NO_3^- ions to Fe^{2+}. The formation of gelatine in the earlier step could also reduce the Oswald ripening effect, thus resulting in smaller particles. Application of pressure also continuously improved the sample's crystallinity.

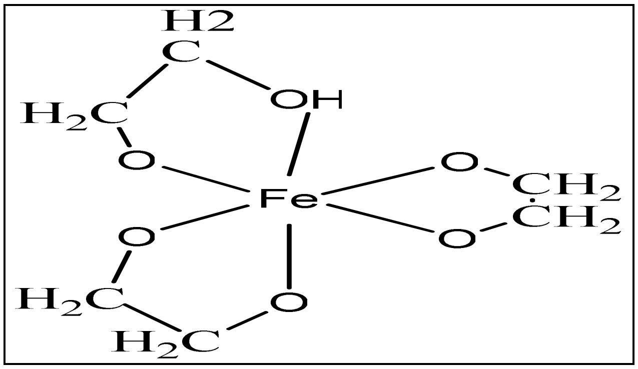

Figure 4.19: Proposed structure of iron-ethylene glycol complex [114].

The surface morphology of Fe_3O_4 nanocatalyst prepared via sol gel-hydrothermal method was examined by FESEM and the image is shown in Figure 4.20. The FESEM image shows cubic-shaped nanoparticles with irregular size.

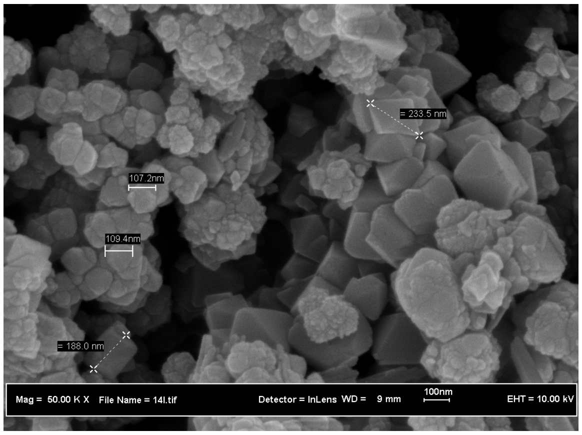

Figure 4.20: FESEM image of Fe_3O_4 nanocatalyst prepared via sol gel-hydrothermal method at 160^{o}C.

EDX spectrum of Fe_3O_4 nanocatalyst prepared via sol gel-hydrothermal method is displayed in Figure 4.21.

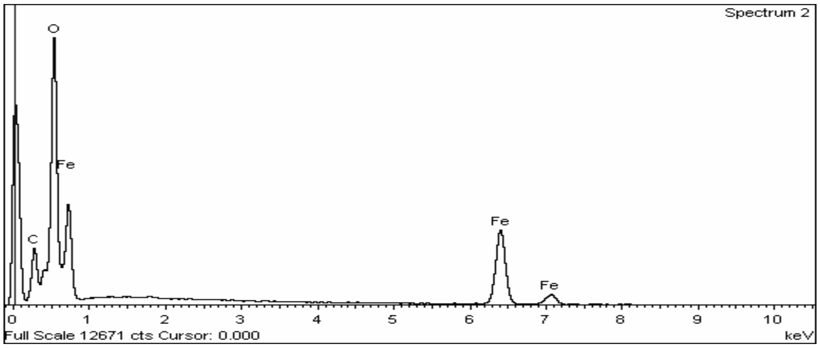

Figure 4.21: EDX spectrum of Fe_3O_4 nanocatalyst prepared via sol gel-hydrothermal method at 160^{o}C.

EDX spectrum shows the presence of Fe, O and C. Carbon was the impurity which could be originated from the solvent.

The magnetization effect of Fe_3O_4 nanocatalysts prepared via different methods was tested using VSM and the curves are presented in Figure 4.22.

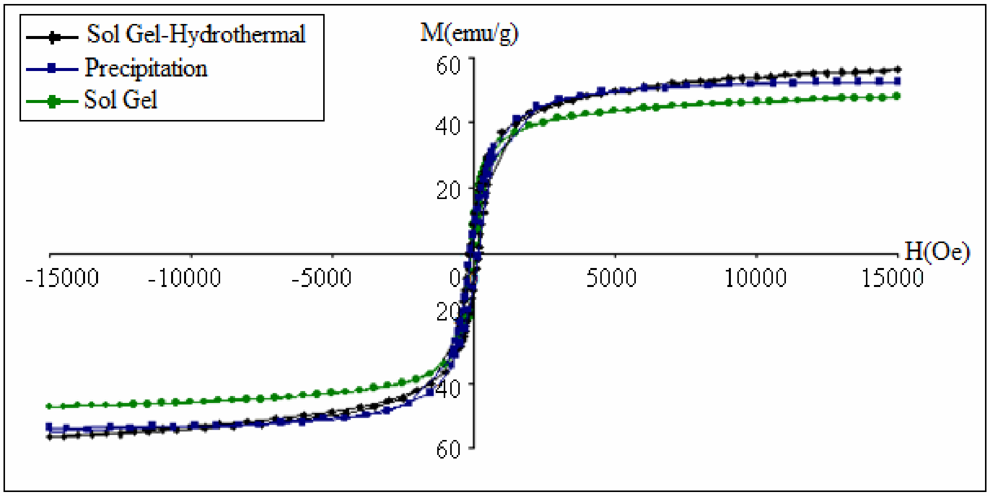

Figure 4.22: Hysteresis curves of Fe_3O_4 nanocatalysts prepared via different methods

All curves reveal remanance magnetization, M_r and coercivity force, H_c values. S-shaped curves were obtained for all samples. These features indicate the absence of superparamagnetic character in all of the nanocatalysts synthesized using these three methods [31]. VSM data are summarized in Table 4.14.

Table 4.14: Hysteresis data of Fe_3O_4 nanocatalysts prepared via different methods.

	Sol Gel-Hydrothermal	Precipitation	Sol Gel
MagnetizationSaturation, M_s (emu/g)	56.1	53.46	47.70
Remanance Magnetization, M_r (emu/g)	9.89	7.30	9.83
Coercivity Force, H_c (Oe)	148.85	79.2	108.1

Fe_3O_4 nanocatalyst obtained via the sol gel hydrothermal method, in the absence of surfactant, had the highest value of M_s, in comparison with the ones synthesized by precipitation and sol gel methods (Table 4.14). It was reported that Fe_3O_4 nanoparticles with the size of 27 nm prepared via the hydrothermal method using the $Fe(NO_3)_3.9H_2O$ precursor exhibited the M_s value of ~3.69 emu/g [37]. The M_s value obtained in this work via the sol gel-hydrothermal method in the absence of surfactant was 15 times higher

(Table 4.14) than the reported value. Y. H. Zheng et al. [37] reported that the use of organic surfactant, sodium bis(2-ethylhexyl) sulfosccinate; was claimed to be a major factor for reduction of M_s value. The presence of surfactant in the system covered the surface of the nanoparticles which was difficult to remove entirely during drying or annealing process [37]. Consequently, this reduced the response of the nanoparticles towards exerted field [35]. On the other hand, preparation of Fe_3O_4 using ferric acethylacetonate, $Fe(ACAC)_3$ via the hydrothermal method produced 30 nm particles with Ms value of 14.5 emu/g [34].

Nanocatalyst synthesized via precipitation method had weaker magnetization behavior (Table 4.14). The M_r and H_c values were reduced to about 35.47% and 87.94%, respectively as compared to those obtained via sol gel-hydrothermal method. This may suggest that Fe_3O_4 composition was enriched in nanocatalyst obtained via the sol gel hydrothermal method but not in the case of precipitation. Previous investigation concluded that the magnetization saturation linearly increased with increasing magnetite content [32]. Precipitation method was believed to enhance the formation of the goethite phase due to presence of hydroxyl groups, OH^- originated from the use of water and precipitating agent. The OH^- replaced Fe ions and created vacant sites, thus retarding the magnetic interaction between Fe and O. As a consequence, the population of magnetite phase was no longer balanced and exhibited a bad respond to the exerted field [35]. Goethite displays antiferromagnetic with Curie temperature, Tc of 390 K [20], [35]. Therefore, it was deduced that the weak magnetization behavior displayed by the nanocatalyst obtained via precipitation method might be due to the formation of the goethite phase.

The sol gel-hydrothermal method resulted in well-crystallined Fe_3O_4 nanocatalys having smallest crystallite size and highest M_s value amongst the tested methods. Therefore, the sol gel-hydrothermal method was selected to prepare more samples for further characterizations.

4.1.2.2 Hybrid Sol Gel-Hydrothermal Method

This part investigated the effect of synthesis temperature on the sol gel-hydrothermal method. Finding an optimum temperature is important to obtain highly crystallined nanocatalyst.

The recorded XRD spectra for Fe_3O_4 nanocatalysts synthesized via sol gel-hydrothermal method at various synthesis temperatures are shown in Figure 4.23.

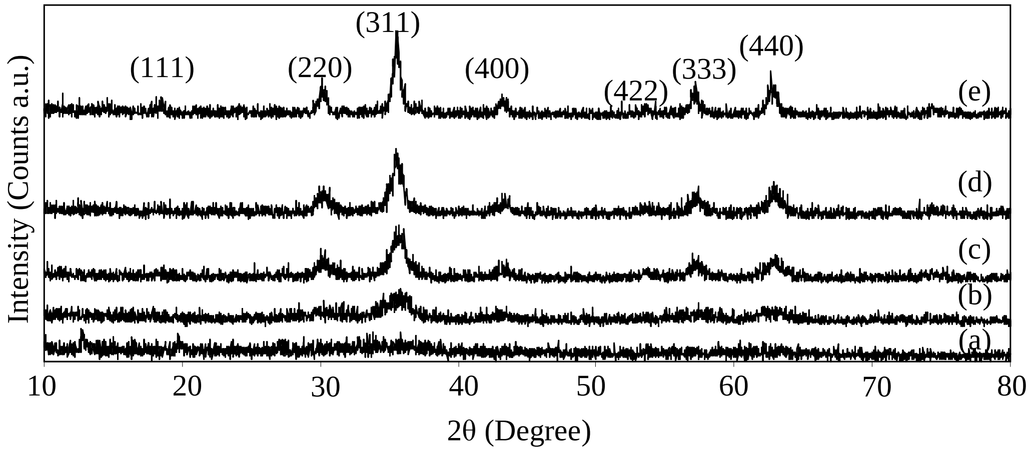

Figure 4.23: XRD spectra of Fe_3O_4 nanocatalysts prepared via sol gel-hydrothermal method at synthesis temperatures of (a) 28°C (b) 50°C (c) 80°C (d) 120°C and (e) 160°C.

All diffracted peaks were for magnetite (Fe_3O_4) phase with the appearance of (311) as a major plane at 2θ of 35.40° (Figure 4.23). The appearance of a (111) minor plane at 2θ of 10-20°, indicating the maghemite (γ-Fe_2O_3) phase [20], [48] was not detected. The crystallinity of Fe_3O_4 nanocatalysts was enhanced with increasing the synthesis temperature. The synthesis temperature at 160°C produced well crystallined Fe_3O_4 nanocatalyst (Figure 4.23). This temperature was also employed in synthesizing Fe_3O_4 nanocatalyst using the hydrothermal method by other workers [34], [37].

Synthesis temperature plays a vital role in the hydrothermal method [115]. Lower synthesis temperature decreases the solubility of the precursor and decelerates the crystallization step. This is due to inability of low temperature in supplying sufficient energy for the precursor to completely break up. This explains poor crystallinity for nanocatalyst synthesized at 28°C (Figure 4.23). However, the crystallinity can be enhanced by increasing the synthesis temperature. The growth velocity of the crystals is written in Equation 4.1 [115] where V is the growth velocity, C is constant, R is gas constant and T is temperature.

$$\frac{d\ln V}{dT} = \frac{C}{RT^2} \tag{4.1}$$

Equation 4.1 [115] shows that high synthesis temperature is beneficial for crystal growth. However, if the temperature is too high, the crystals may grow in random manner, thus preventing the formation of single particles [115].

Figure 4.24 illustrates the H_2-TPR profiles of Fe_3O_4 nanocatalyst prepared via sol gel-hydrothermal method at 160°C for 10 hours.

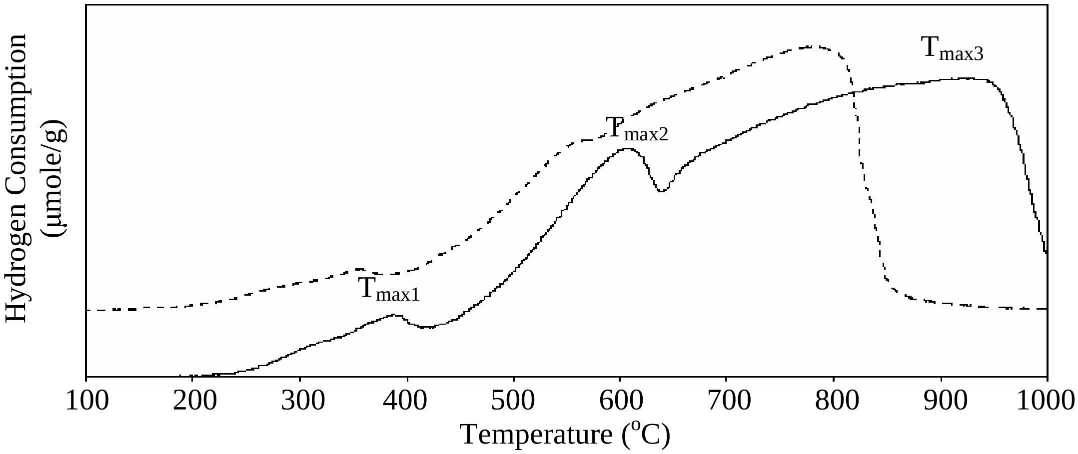

Figure 4.24: H_2-TPR profiles Fe_3O_4 nanocatalyst prepared via sol gel-hydrothermal method at synthesis temperature of 160°C. These profiles were recorded at the heating rate, β of 10°C/min (solid line) and 5°C/min (dotted line).

An intense peak, T_{max2}; at 500-600°C in both profiles corresponded to the reduction of $Fe_3O_4 \rightarrow FeO$. Meanwhile, the reduction of $FeO \rightarrow Fe$ happened at about 700-1000°C, indicated by a broad peak, T_{max3}; (Figure 4.24). The reduction was accomplished at much lower temperature as the heating rate, β; was reduced to 5°C/min (dotted line). As discussed in Section 2.6, lowering heating rate increased the contact time between the sample and hydrogen. This retards the formation of metastable $Fe_{1-x}O$ (Equation 2.24, Section 2.6) and at the same time accelerates direct reduction from Fe_3O_4 to α-Fe (Equation 2.22, Section 2.6). Hence, high temperature is not required due to decrease the amount of intermediate $Fe_{1-x}O$ which is difficult to reduce [22], [75]. A small reduction peak located at temperature 350-400°C was due to α-Fe_2O_3 residual resulted from oxidation of small portion of magnetite during annealing process [73]. The data for the reduction are summarized in Table 4.15.

Table 4.15: H_2-TPR data of Fe_3O_4 nanocatalyst prepared via sol gel-hydrothermal method at synthesis temperature of 160°C using different heating rates

Heating rate, β (°C/min)			5	10	Literature
TPR peak (T_{max})	Peak (T_{max1})	$Fe_2O_3 \rightarrow Fe_3O_4$	357	387	-
	Peak (T_{max2})	$Fe_3O_4 \rightarrow FeO$	575	606	800-820 [80]
	Peak (T_{max3})	$FeO \rightarrow Fe$	782	921	

Reduction at β of 10 °C/min was accomplished at much higher temperature compared to values reported in literature (Table 4.15) which used commercial Fe_3O_4 [80]. The Fe_3O_4 nanocatalysts were then annealed at different annealing temperatures and characterized using XRD. Their spectra were recorded and revealed in Figure 4.25.

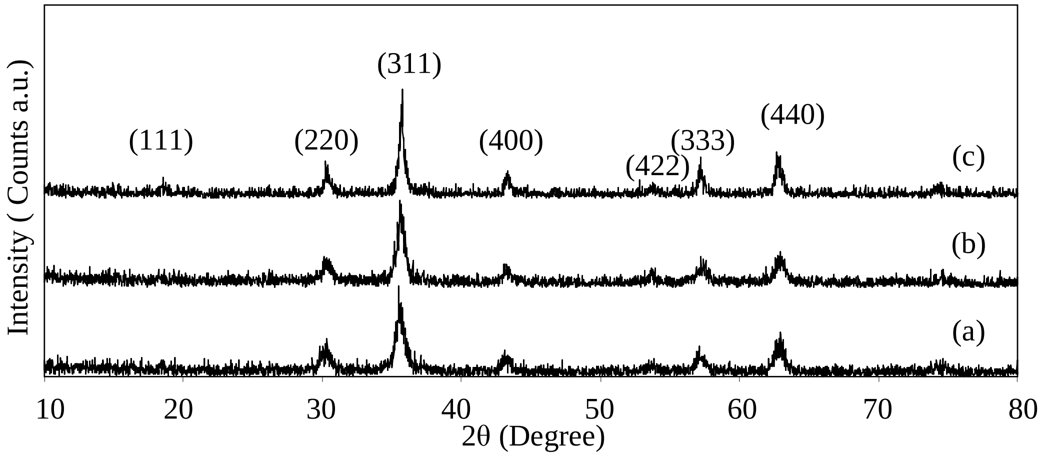

Figure 4.25: XRD spectra of Fe_3O_4 nanocatalysts prepared via sol gel-hydrothermal method at synthesis temperature of 160°C, annealed at (a) 200°C (b) 300°C and (c) 400°C.

The crystallinity of Fe_3O_4 nanocatalysts improved with increasing annealing temperature (Figure 4.25). The XRD data of samples are summarized in Table 4.16.

Table 4.16: XRD data of Fe_3O_4 nanocatalyst prepared via sol gel-hydrothermal method at synthesis temperature of 160^{o}C annealed at different temperatures. The interpretation was based on (311) major plane.

Annealing temperature (^{o}C)		200	300	400	Literature
2θ (Degree)		35.46	35.61	35.78	35.48 [33]
Intensity (a.u)		61.00	52.60	73.00	-
FWHM		0.447	0.451	0.268	-
D-spacing (Å)		2.5294	2.5189	2.5076	2.532 [20]
Lattice constant (Å)	a	8.374	8.333	8.330	8.390 [20], 8.405 [54]
	b	8.374	8.333	8.330	8.390 [20], 8.405 [54]
	c	8.374	8.333	8.330	8.390 [20], 8.405 [54]
Average crystallite size(nm)		19.00	18.84	31.72	-

The average crystallite size increased with increasing annealing temperature. This is due to high surface energy effect which promotes agglomeration at high temperature. An increase in intensity as a result of increasing annealing temperature signifies the enhancement of crystallinity (Table 4.16) [57]-[58], [60], [108].

4.1.3 Supported Hematite on Alumina (5% α-Fe_2O_3/γ-Al_2O_3) Nanocatalyst

The synthesis was accomplished by utilizing the sol gel-hydrothermal method. The effects of synthesis period and iron to surfactant ratio were studied. The supported nanocatalysts were annealed at 400^{o}C in nitrogen at flow of 10 cm^3/min for four hours.

4.1.3.1 Effect of Synthesis Period

Figure 4.26 compares the XRD spectra of pure γ-Al_2O_3, unsupported α-Fe_2O_3 and supported 5% α-Fe_2O_3/γ-Al_2O_3 samples.

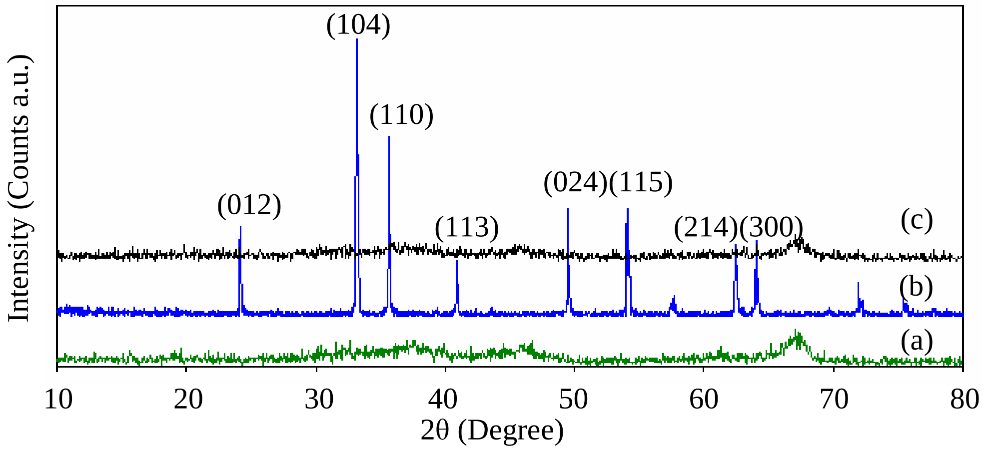

Figure 4.26: XRD spectra of (a) γ-Al_2O_3 support (b) unsupported α-Fe_2O_3 and (c) supported 5% α-Fe_2O_3/γ-Al_2O_3 nanocatalyst prepared via sol gel-hydrothermal method at 160°C for 1 day.

The XRD pattern for supported 5% α-Fe_2O_3/γ-Al_2O_3 resembled the XRD pattern of γ-Al_2O_3 (Figure 4.26). The α-Fe_2O_3 phase was not detected due to small amount of α-Fe_2O_3 on the γ-Al_2O_3 support which was below the detection limit of XRD. Raman spectra are revealed in Figure 4.27.

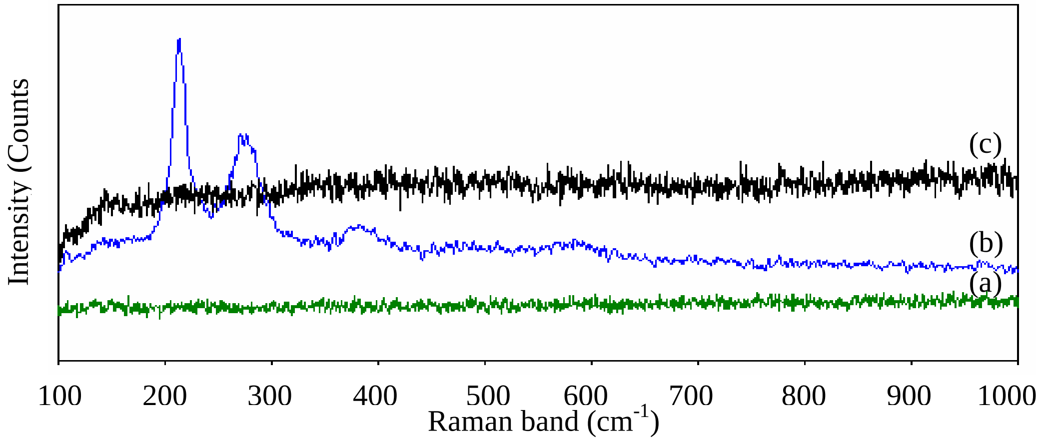

Figure 4.27: Raman spectra of (a) γ-Al_2O_3 support (b) α-Fe_2O_3 unsupported nanocatalyst and (c) supported 5% α-Fe_2O_3/γ-Al_2O_3 nanocatalyst prepared via sol gel-hydrothermal method at 160°C for 1 day.

Raman peaks were absent for 5% α-Fe_2O_3/γ-Al_2O_3 nanocatalyst (Figure 4.27 (c)). Major α-Fe_2O_3 peaks were not detected for the supported α-Fe_2O_3 possibly due to low amount of α-Fe_2O_3 in the sample. The surface morphology of supported 5% α-Fe_2O_3/γ-Al_2O_3 was examined by FESEM and the FESEM image is shown in Figure 4.28.

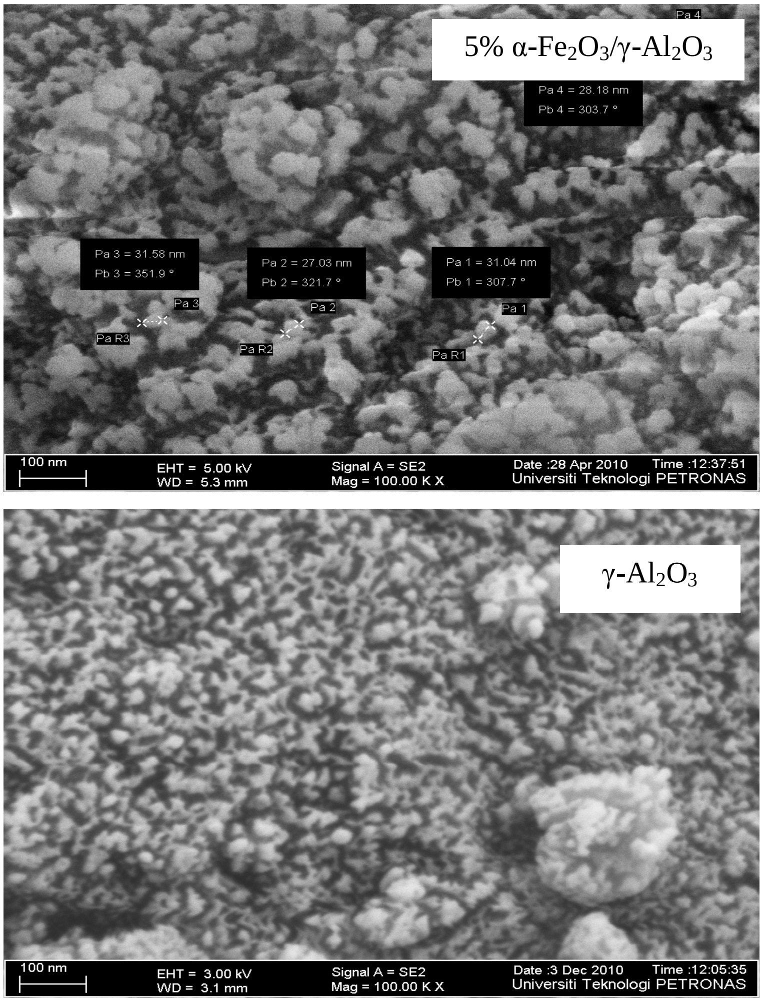

Figure 4.28: FESEM images of commercial γ-Al_2O_3 support and supported 5% α-Fe_2O_3/γ-Al_2O_3 nanocatalyst prepared via sol gel-hydrothermal method at 160^{o}C for 1 day.

The slight morphological change could be due agglomerated γ-Al_2O_3 particles (Figure 4.28). EDX was used to determine the elements in the 5% α-Fe_2O_3/γ-Al_2O_3 nanocatalyst and the result is revealed in Figure 4.29.

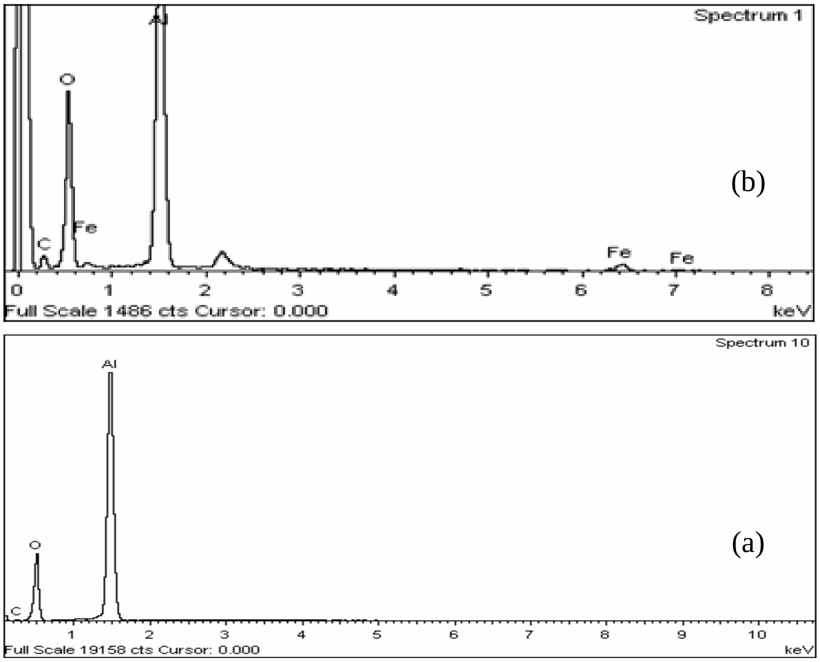

Figure 4.29: EDX spectrum of (a) γ-Al_2O_3 support and supported 5% α-Fe_2O_3/γ-Al_2O_3 nanocatalyst prepared via sol gel-hydrothermal method at 160^{o}C for 1 day.

Fe, O and Al were detected by EDX. In addition, carbon was also detected as an impurity which could be attained during preparation steps.

The influence of synthesis periods on the elemental distribution was investigated using EDX mapping. Figure 4.30 shows the images of Fe particles distribution as a function of synthesis temperature. The images for the other elements are shown in Appendix G.

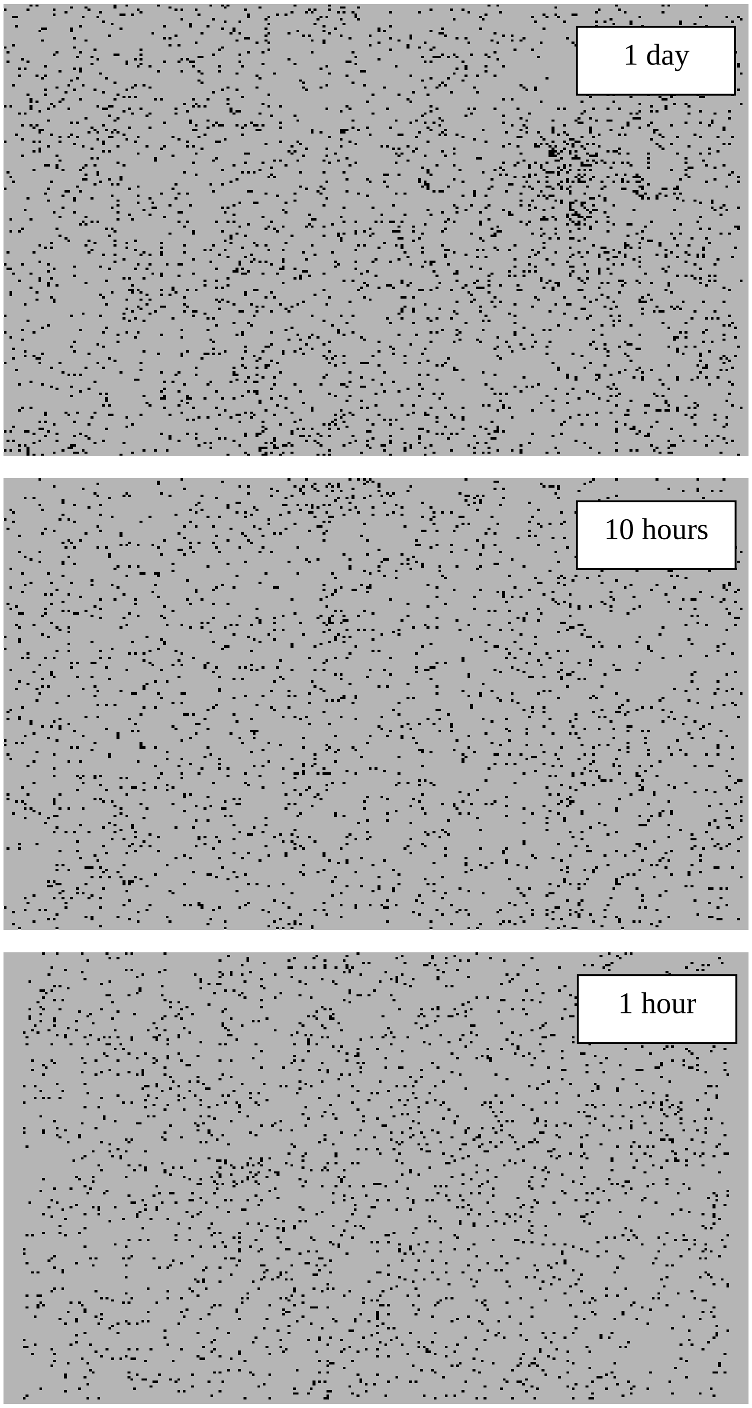

Figure 4.30: Fe particles distribution of supported 5% α-Fe_2O_3/γ-Al_2O_3 nanocatalysts prepared via sol gel hydrothermal method in the absence of surfactant at 160^{o}C and different synthesis periods. The scale of measurement applied was 10 μm.

Better dispersion of Fe particles was revealed by nanocatalyst synthesized at 1 hour compared to those obtained at 10 hour and 1 day synthesis periods (Figure 4.30).

Reducibility study was conducted using H_2-TPR to determine the influence of various synthesis periods on the reducibility of supported 5% α-Fe_2O_3/γ-Al_2O_3 nanocatalysts. The H_2-TPR profiles are presented in Figure 4.31.

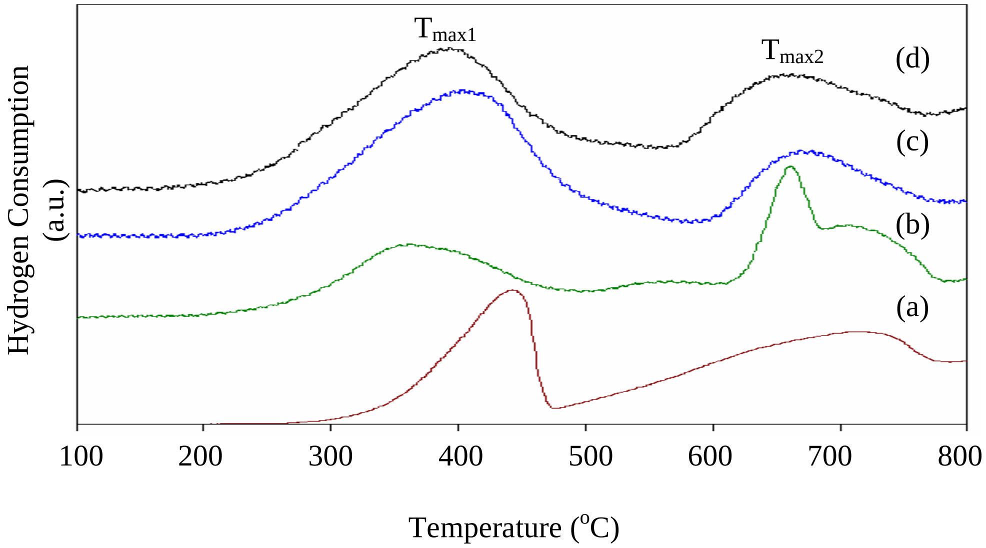

Figure 4.31: H_2-TPR profiles of (a) unsupported α-Fe_2O_3 and supported 5% α-Fe_2O_3/γ-Al_2O_3 nanocatalysts prepared via sol gel hydrothermal at 160^{o}C for (b) 1 hour (c) 10 hours and (d) 1 day.

Two reduction peaks were obtained for reduction of α-Fe_2O_3 to Fe_3O_4 and Fe_3O_4 to Fe. The reduction temperatures for both peaks are consistent with previous reports [115]-[116]. The reducibility was improved in presence of γ-Al_2O_3 support. Reduction of 5% α-Fe_2O_3/γ-Al_2O_3 nanocatalysts occurred at much lower temperature as compared with that of the unsupported α-Fe_2O_3 (Figure 4.31). The data for reduction of 5% α-Fe_2O_3/γ-Al_2O_3 catalysts at different synthesis periods are summarized in Table 4.17.

Table 4.17: H_2-TPR data for supported 5% α-Fe_2O_3/γ-Al_2O_3 nanocatalysts prepared via sol gel-hydrothermal method at different synthesis periods.

Sample		1 hour	10 hours	1 day	Literature
TPR peak (T_{max})	T_{max1}(^oC)	363	403	395	430-460 [116], 400-450 [117]
	T_{max2}(^oC)	662	671	657	650-690 [116], 600-800 [117]

The reduction process for the 5% α-Fe_2O_3/γ-Al_2O_3 nanocatalysts occurred at much lower temperature in comparison with literature values (Table 4.17) [116]-[117]. Figure 4.32 summarizes the Fe particles dispersion and hydrogen consumption for 5% α-Fe_2O_3/γ-Al_2O_3 nanocatalysts based on TPR data interpretation. The example of calculation for Fe particles dispersion (%) is described in Appendix E.

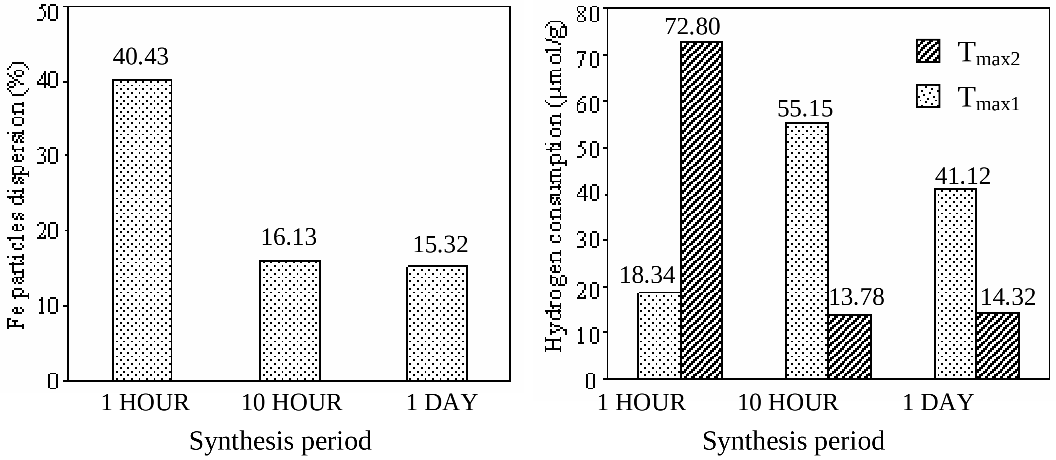

Figure 4.32: Summary for (a) Fe particles dispersion and (b) hydrogen consumption of supported 5% α-Fe_2O_3/γ-Al_2O_3 nanocatalysts prepared via sol gel-hydrothermal at 160^oC for different synthesis periods.

As shown in Table 4.17, reduction for nanocatalyst synthesized at 1 hour was accomplished at much lower temperature compared to the ones prepared at 10 hours and 1 day. This may be due to good dispersion of Fe particles as shown in Figure 4.32 (a). As described in Section 2.6, catalyst with highly dispersed particles improves reducibility, hence lowering the reduction temperatures [78]-[79]. The degree of dispersion for iron particles decreased as the synthesis period was extended from 1 hour to 1 day (Figure 4.32 (a)). This suggests that prolonging the synthesis period promotes the agglomeration of particles.

Incomplete reduction was observed for nanocatalysts synthesized at 10 hour and 1 day (Figure 4.32 (b)). They consumed 5 times lesser hydrogen than the one synthesized at 1 hour in completing second stage of reduction, T_{max2} (Figure 4.32 (b)). This is an indicative for the formation of a strong spinel interaction between $Fe_{1-x}O$ and γ-Al_2O_3, eventually forming hercynite ($FeAl_2O_4$) as explained by other researchers [80]-[81]. The formation of stable $FeAl_2O_4$ inhibits the continuation of the reduction, hence preventing the reaction between hydrogen molecules and $Fe_{1-x}O$ phase (Figure 4.32). This may justify for the observation in Figure 4.33 (c). It is understood that $Fe_{1-x}O$ phase can only be stable at temperature above 570^{o}C [22], [79], [81], [117]. However, highly stable $Fe_{1-x}O$ phase can also be attained below this temperature when $Fe_{1-x}O$ particles are supported on γ-Al_2O_3 (Section 2.6) [80], [118]-[121]. This may also explain an increase in reduction temperature as a result of extending the synthesis period (Figure 4.32 (b)).

4.1.3.2 Effect of Iron (III) Nitrate to SBS Surfactant Ratio

The effect of sodium bis(2-ethylhexyl) sulfosuccinate (SBS) surfactant on the properties of supported 5% α-Fe_2O_3/γ-Al_2O_3 was studied. The one-day period was chosen and the $Fe(NO_3)_3$:SBS surfactant was varied to 2:1, 2:2 and 2:3. The resultant nanocatalysts were annealed at 400^{o}C in nitrogen at flow 10 cm^3/min for four hours.

Figure 4.33 displays the FESEM image of supported 5% α-Fe_2O_3/γ-Al_2O_3 nanocatalyst prepared using the sol gel-hydrothermal method at $Fe(NO_3)_3$:SBS surfactant ratio of 2:3. The FESEM images for the catalyst synthesized at 2:1 and 2:2 were similar as that of 2:3 ratios. The appearance of iron nanoparticles is difficult to distinguish because the loading of α-Fe_2O_3 particles was only 5% on γ-Al_2O_3. Thus FESEM image is likely representing only γ-Al_2O_3 particles.

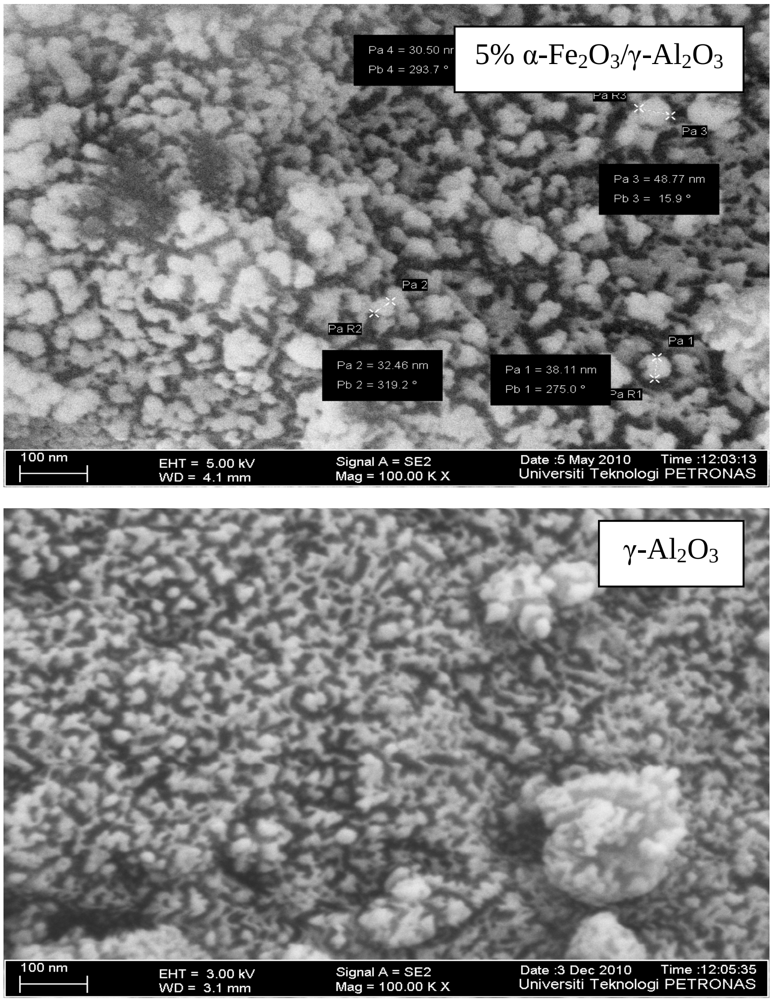

Figure 4.33: FESEM images of commercial γ-Al_2O_3 support and supported 5% α-Fe_2O_3/γ-Al_2O_3 nanocatalyst prepared via sol gel-hydrothermal method at $Fe(NO_3)_3$:SBS surfactant ratio of 2:3.

EDX characterization was performed to determine the elemental composition of supported 5% α-Fe_2O_3/γ-Al_2O_3 nanocatalyst and the spectra are revealed in Figure 4.34. The nanocatalysts contained Fe, O and Al elements as well as carbon impurity (Figure 4.34) which originated from the surfactant used in sol gel-hydrothermal method and the preparation steps.

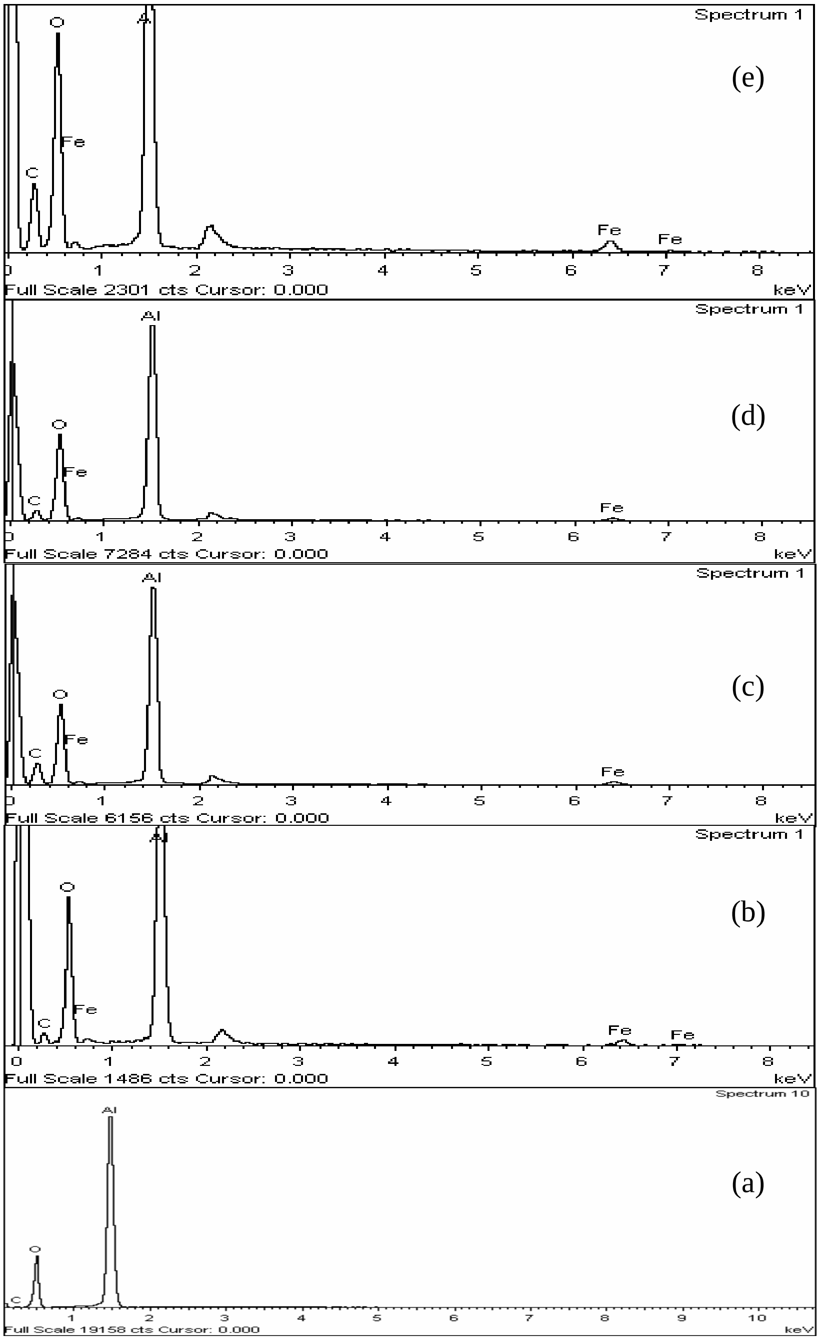

Figure 4.34: EDX spectra for supported 5% α-Fe_2O_3/γ-Al_2O_3 nanocatalysts prepared via sol gel-hydrothermal method at 160^{o}C $Fe(NO_3)_3$:SBS surfactant ratios of (a) 2:0 (b) 2:1 (c) 2:2 and (d) 2:3.

The EDX data are summarized in Table 4.18. Amount of carbon presence increased with increasing $Fe(NO_3)_3$:SBS surfactant ratio (Table 4.18) which was difficult to remove entirely during annealing process. The percentages of atomic and weight for carbon, oxygen and aluminium did not exhibit a specific trend. This could be due to the analysis technique which only targeted on several spots but not on the whole surface, thus resulting in an uneven surface scanning. The elemental mapping images of Fe are shown in Figure 4.35 while for the other elements are shown in Appendix I.

Table 4.18: EDX data for supported 5% α-Fe_2O_3/γ-Al_2O_3 nanocatalysts prepared via sol gel-hydrothermal method at 160°C using different $Fe(NO_3)_3$:SBS surfactant ratios.

Method		2:0	2:1	2:2	2:3
Atomic (%) Experiment	Fe	1.54	1.25	1.36	1.37
	Al	22.00	17.88	21.80	17.46
	O	53.56	43.25	50.05	41.40
	C	22.90	37.62	26.79	39.75
Weight (%) Experiment	Fe	4.75	4.12	4.26	4.55
	Al	32.77	28.44	32.91	27.91
	O	47.30	40.80	44.82	39.25
	C	15.18	26.64	18.01	28.29

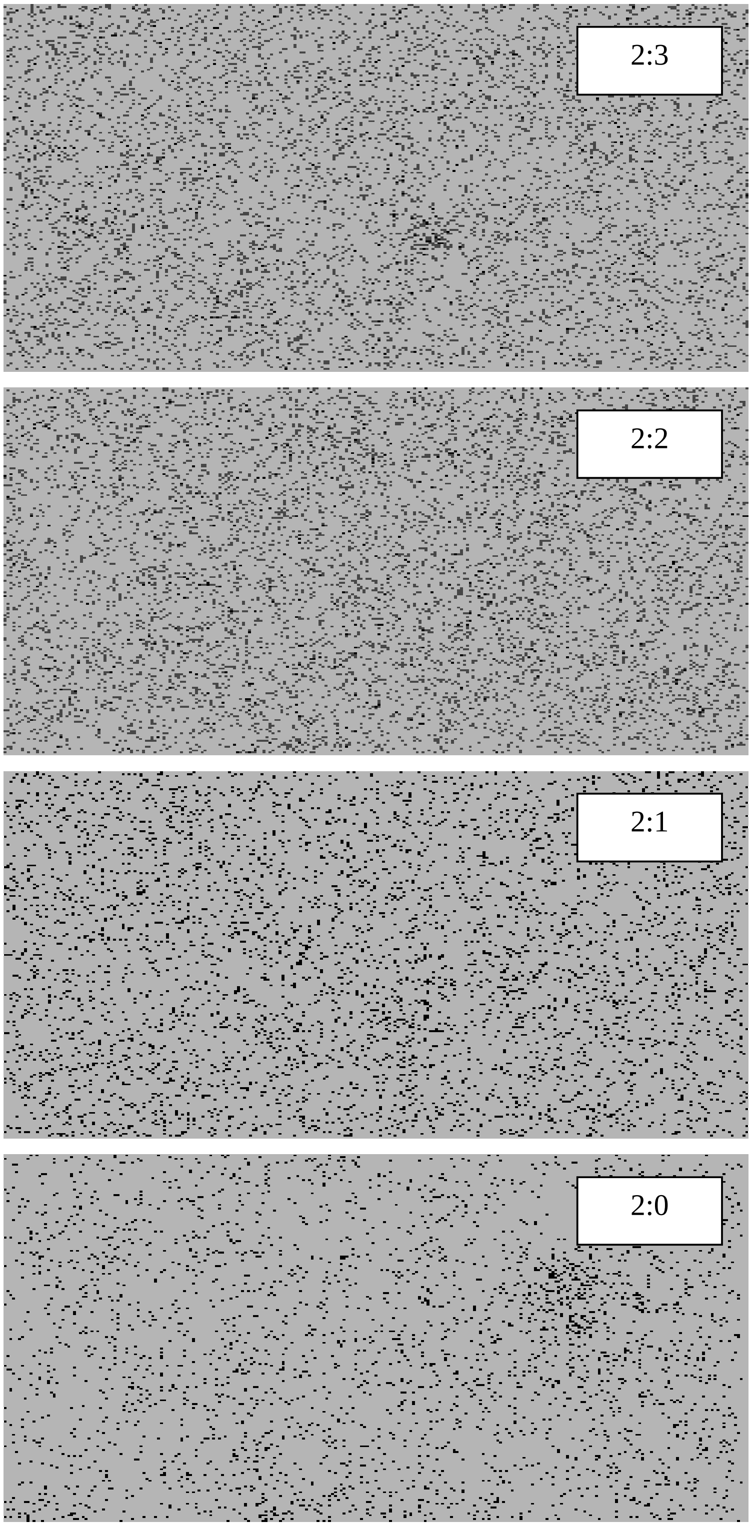

Figure 4.35: Fe particles distribution of supported 5% α-Fe_2O_3/γ-Al_2O_3 nanocatalysts prepared via sol gel hydrothermal method at different $Fe(NO_3)_3$:SBS surfactant ratios. The scale of measurement applied was 10 μm.

Increasing the amount of surfactant resulted in an enhancement in Fe particles distribution. Poor distribution of Fe particles was observed for nanocatalyst synthesized in absence of surfactant. Fe particles distribution improved when the ratios were increased from 2:1 to 2:3. However, excessive amount of surfactant led to particles agglomeration as shown by FESEM image of 2:3 ratio (Figure 4.35).

Figure 4.36 illustrates the reduction profiles of supported 5% α-Fe_2O_3/γ-Al_2O_3 nanocatalysts synthesized using the sol gel-hydrothermal method at different iron (III) nitrate to SBS surfactant ($Fe(NO_3)_3$:SBS) ratios.

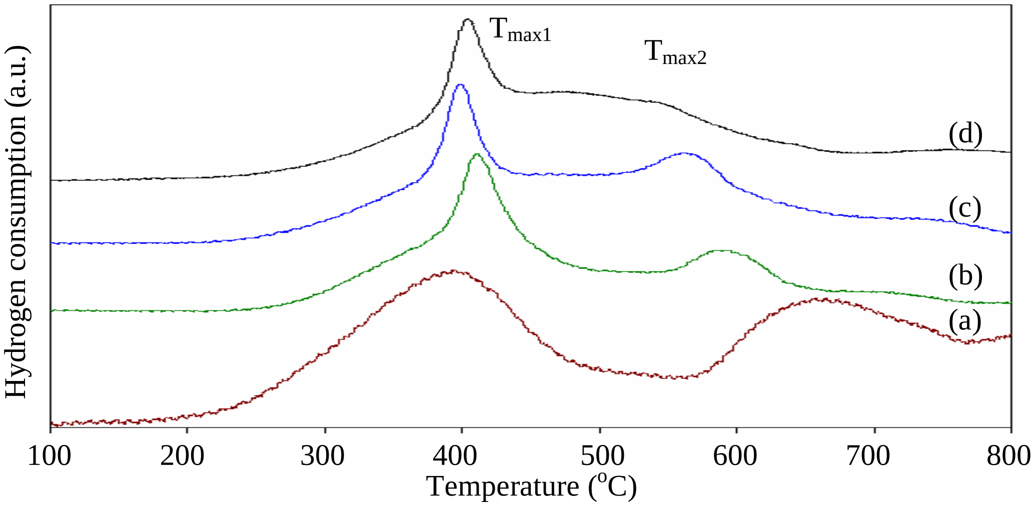

Figure 4.36: H_2-TPR profiles of supported 5%Fe_2O_3/γ-Al_2O_3 nanocatalysts prepared via sol gel-hydrothermal method at $Fe(NO_3)_3$:SBS surfactant ratios of (a) 2:0 (b) 2:1 (c) 2:2 and (d) 2:3.

Varying iron to surfactant ratios changed the H_2-TPR profiles. Two reduction peaks were obtained for each sample (Figure 4.36). The temperatures for accomplishing second reduction step, T_{max2} decreased consistently to slightly lower temperature with increasing surfactant. Table 4.19 summarizes the data for H_2-TPR.

Table 4.19: H_2-TPR data of supported 5% α-Fe_2O_3/γ-Al_2O_3 nanocatalysts prepared via sol gel-hydrothermal method at different $Fe(NO_3)_3$:SBS surfactant ratios.

Sample		2:0	2:1	2:2	2:3	Literature
TPR peak (T_{max})	T_{max1}(°C)	395	411	399	404	430-460 [116], 400-450 [117]
	T_{max2}(°C)	657	587	564	440	650-690 [116], 600-800 [117]

As the surfactant increased, the second reduction stage became easier to accomplish (Table 4.19). This suggested that the strength of iron-support interaction may be reduced and subsequently inhibited the formation of $Fe_{1-x}O$ by varying the amount of surfactant. Figure 4.37 summarizes the Fe particles dispersion and hydrogen consumption for supported 5% α-Fe_2O_3/γ-Al_2O_3 nanocatalysts based on H_2-TPR data interpretation.

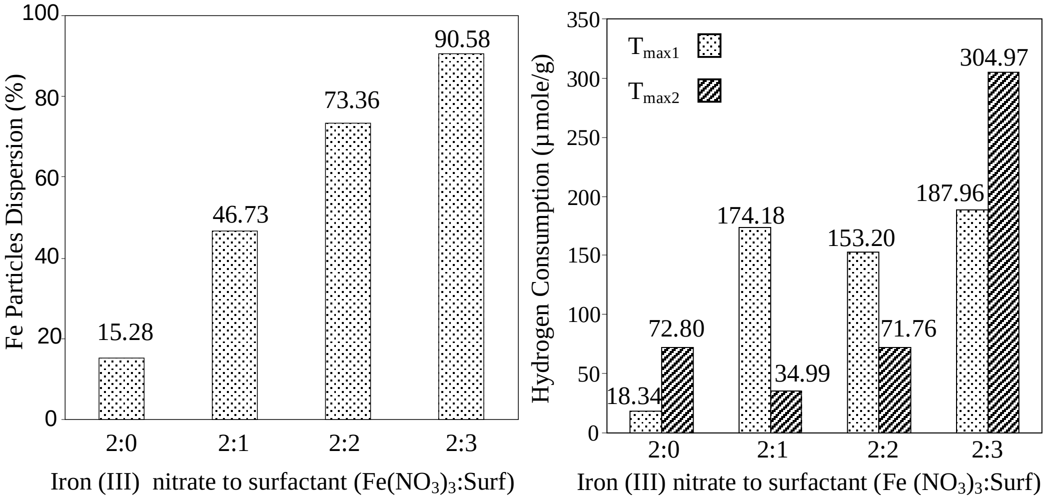

Figure 4.37: Summary for (a) Fe particles dispersion and (b) hydrogen consumption of supported 5% α-Fe_2O_3/ γ-Al_2O_3 nanocatalysts prepared via sol gel-hydrothermal method at 160°C using different $Fe(NO_3)_3$:SBS surfactant ratios

Example of the calculation for Fe particles dispersion is shown in Appendix E.3.1. The degree of Fe particles dispersion was enhanced by a factor of seven when iron nitrate to surfactant ratios increased from 2:0 to 2:3 (Figure 4.37 (a)). This was supported by an enhancement in Fe particle distribution as shown by EDX mapping (Figure 4.35). Higher dispersion of particles caused the reduction to occur more easily (Section 2.6) [79]-[81], justifying for the decrease in reduction temperature (Table 4.19). Table 4.20 summarizes the hydrogen consumption ratio to reduce supported 5% α-Fe_2O_3/ γ-Al_2O_3 nanocatalysts prepared at different $Fe(NO_3)_3$:SBS surfactant ratios.

Table 4.20: Hydrogen consumption ratio, T_{max1}/T_{max2} in reducing supported 5% α-Fe_2O_3/ γ-Al_2O_3 nanocatalysts prepared at different $Fe(NO_3)_3$: SBS surfactant ratios.

$Fe(NO_3)_3$: SBS ratio	T_{max1}:T_{max2}
2:0	1:4
2:1	1:0.20
2:2	1:0.46
2:3	1:1.62

Complete transformation of unsupported α-Fe_2O_3 to Fe typically consumed hydrogen with T_{max1}/T_{max2} ratio of 1:8 [76]. The nanocatalyst synthesized in the absence of surfactant consumed hydrogen with the T_{max1}/T_{max2} ratio of 1:4 (Table 4.20), denoting incomplete reduction of Fe_3O_4 to Fe. Meanwhile, adding surfactant at ratio 2:1 ($Fe(NO_3)_3$: SBS) enhanced the dispersion of Fe particles (Figure 4.37 (a)), but decreased the extent of reduction (Table 4.20). Enhanced dispersion increases the interaction between Fe particles and γ-Al_2O_3 support, thus could induce the formation of a stable spinel interaction hercynite ($FeAl_2O_4$) phase. The existence of the stable $FeAl_2O_4$ prevented the reduction of $Fe_{1-x}O$ to Fe (Section 2.6). The reducibility performance improved further when $Fe(NO_3)_3$:SBS ratios were increased to 2:2 and 2:3. The dispersion of Fe particles was enhanced with increasing surfactant as exhibited by Figure 4.35 and Figure 4.37. The temperature, T_{max2} slighlty shifted to lower region (Figure 4.36, Table 4.20) while hydrogen consumption of T_{max2} increased (Figure 4.37 (b)) for these catalysts. Moreover, T_{max1}/T_{max2} ratio was also increased (Table 4.20). These suggest that raising the amount of surfactant destabilized the intermediate $Fe_{1-x}O$ phase on γ-Al_2O_3. The $FeAl_2O_4$ interaction strength was minimized, thus overcoming the disproportination reaction (Equation 2.23, Section 2.6). Consequently, direct transformation of $Fe_{1-x}O$ to Fe was favored.

Figure 4.38 illustrates the nitrogen adsorption isotherms for supported 5%α-Fe_2O_3/γ-Al_2O_3 nanocatalysts synthesized at different $Fe(NO_3)_3$:SBS surfactant ratios.

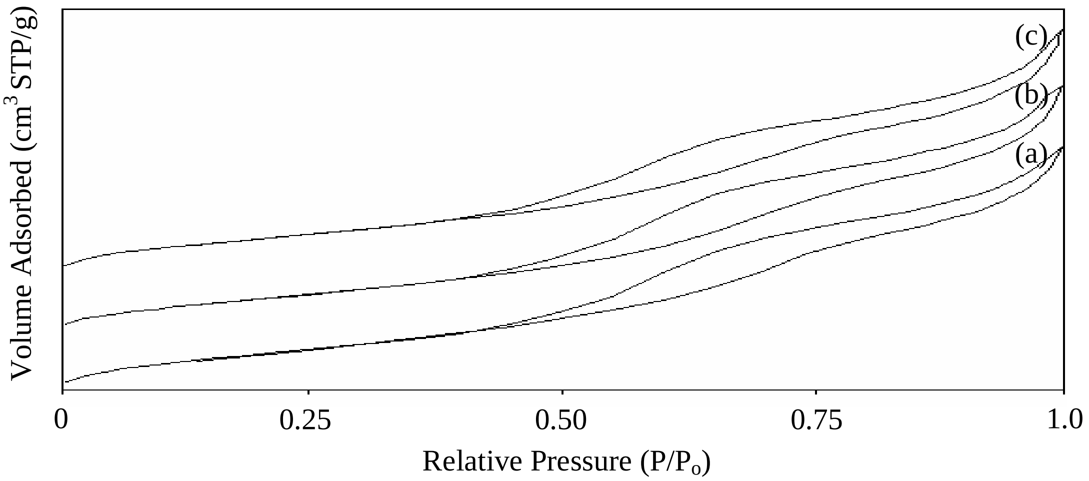

Figure 4.38: Nitrogen adsorption isotherms on supported 5%α-Fe_2O_3/γ-Al_2O_3 nanocatalysts prepared via sol gel-hydrothermal method at $Fe(NO_3)_3$:SBS surfactant ratios of (a) 2:1 (b) 2:2 and (c) 2:3.

The BET data for supported 5%α-Fe_2O_3/γ-Al_2O_3 nanocatalysts synthesized at iron nitrate to surfactant ratios are tabulated in Table 4.21.

Table 4.21: BET data for supported 5%α-Fe_2O_3/γ-Al_2O_3 nanocatalysts synthesized at different $Fe(NO_3)_3$:SBS surfactant ratios.

Fe:Surf	BET Surface Area (m^2/g)	Pore Volume (cm^3/g)	Pore Size (Å)
γ-Al_2O_3	190	0.10	98.0
2:1	151.4217	0.261474	69.0718
2:2	135.3409	0.244584	72.2869
2:3	140.3443	0.242378	69.0811

Increasing $Fe(NO_3)_3$:SBS surfactant ratio from 2:1 to 2:3 reduced the surface area of the nanocatalysts (Table 4.21). This reduction could be caused by the filling of γ-Al_2O_3 pores up by Fe particles. The formation of agglomerated Fe particles with increasing iron (III) nitrate to SBS surfactant ratio as exhibited by EDX-mapping images (Figure 4.35), also contributed to a decrease in surface area of the nanocatalysts. A summary of the physicochemical properties of the prepared nanocatalysts is shown in Table 4.22.

Table 4.22: Summary of the physicochemical properties of the prepared nanocatalysts.

Catalyst		A. C. Size (nm)	Raman I_{st}/I_{2nd} ratio	EDX				H_2-TPR		VSM			BET Surface Area (m^2/g)
				% Atomic		% Deviation		T_{max1} α-Fe_2O_3 → Fe_3O_4 (°C)	T_{max2} Fe_3O_4 → Fe (°C)	M_s (emu/g)	M_r (emu/g)	H_c (O_e)	
				Fe	O	Fe	O						
α-Fe_2O_3	S. Combustion	55.50	1.20	33.77	58.24	16.58	2.93	525	784	-	-	-	-
α-Fe_2O_3	S. Assembly	27.90	0.99	28.12	55.08	29.70	8.20	495	807	-	-	-	-
α-Fe_2O_3	S. Gel, 1 month	18.80	1.16	41.74	58.26	-4.16	2.98	426	732	-	-	-	-
α-Fe_2O_3	S. Gel, 1 week,	23.20	1.36	28.84	71.16	38.69	-15.68	420	697	-	-	-	-
α-Fe_2O_3	S. Gel, 1 day, 300°C	21.74	1.20	32.30	48.50	19.20	19.10	-	-	-	-	-	-
α-Fe_2O_3	S. Gel, 1 day, 400°C	26.78	1.52	37.38	49.14	3.70	18.10	-	-	-	-	-	-
α-Fe_2O_3	S. Gel, 1 day, 500°C	22.86	1.10	34.51	53.53	13.70	10.80	474	719	-	-	-	-
α-Fe_2O_3	S. Gel, 1 day, 600°C	31.47	1.50	37.83	55.92	5.50	6.80	464	746	-	-	-	-
α-Fe_2O_3	S. Gel, 1 day, 700°C	60.67	1.76	37.90	56.5	5.20	5.80	448	723	-	-	-	2.15
Fe_3O_4	Sol Gel	-	-	-	-	-	-	-	-	47.70	9.83	108.10	-
Fe_3O_4	Hydrothermal	53.36	-	-	-	-	-	-	-	-	-	-	-
Fe_3O_4	Precipitation	32.14	-	-	-	-	-			53.46	7.30	79.20	-
Fe_3O_4	Sol Gel-Hydrothermal	29.97	-	35.93	64.07	19.25	-10.81	-	606-921	56.10	9.89	148.85	3.79

5%α-Fe_2O_3/γ-Al_2O_3	Sol Gel-Hydrothermal, 1hour	-	-	-	-	-	-	363	662	-	-	-	-
5%α-Fe_2O_3/γ Al_2O_3	Sol Gel-Hydrothermal, 10 hours	-	-	-	-	-	-	403	671	-	-	-	-
5% α-Fe_2O_3/γ-Al_2O_3	Sol Gel-Hydrothermal, 1 day	-	-	-	-	-	-	395	657	-	-	-	-
5% α-Fe_2O_3/γ-Al_2O_3	Sol Gel-Hydrothermal, 1 day, 2:1 (Fe:Surf)	-	-	-	-	-	-	411	587	-	-	-	151.42
5% α-Fe_2O_3/γ-Al_2O_3	Sol Gel-Hydrothermal, 1 day, 2:2 (Fe:Surf)	-	-	-	-	-	-	399	564	-	-	-	135.34
5% α-Fe_2O_3/γ-Al_2O_3	Sol Gel-Hydrothermal, 1 day, 2:3 (Fe:Surf)	-	-	-	-	-	-	404	440	-	-	-	140.34

4.2 Catalytic Reaction Study

4.2.1 Unsupported Iron Oxide Nanocatalyst

The catalytic reaction was studied using 0.2 g of α-Fe_2O_3 at flow rate of 40 cm^3/min, H_2:N_2 ratio of 3:1, space velocity of 12000 cm^3/g_{cat}. h, atmospheric pressure and reaction period of 3 hours. Effect of magnetic field was studied by applying magnetic field at 1 Tesla to the catalyst system. Figure 4.39 summarizes the effect of magnetic field and various reaction temperatures on the ammonia synthesis deploying α-Fe_2O_3 nanocatalyst. The calculations of ammonia yield are shown in Appendix A.

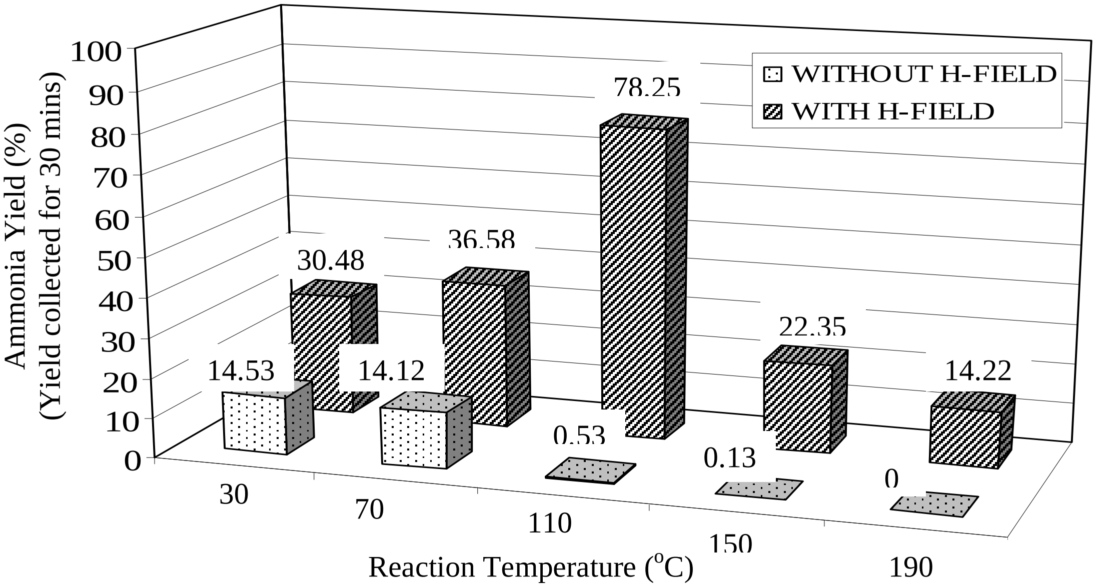

Figure 4.39: Effect of magnetic field and various reaction temperatures on ammonia yield produced in presence of α-Fe_2O_3 nanocatalyst. T = 30°C-190°C, P = 1 atm, H-F = 1 T, Cat. = 0.2 g, GHSV = 12000 cm^3/g_{cat}.h, F = 40 cm^3/min, H_2:N_2 = 3:1. The ammonia yield was collected for 30 mins at each temperature.

The ammonia yield consistently decreased when reaction temperature was increased from 28°C to 188°C (Figure 4.39). This trend concurs with observation in previous studies [6], [14], [94]. According to Le'Chatelier principle, due to exothermic type of ammonia synthesis, an increase in temperature favors the reaction system to shift to the left side for equilibrium to be established, resulting in the decomposition of ammonia, hence enriching the reactant molecules, N_2 and H_2 (Section 2.8.1) [1], [10]-[11]. Enhancement in the ammonia yield by about two orders of magnitude was attained by introducing magnetic field to the reactor. The reaction produced optimum ammonia yield at temperature 110°C and the ammonia yield was 145 times higher than the one obtained in the absence of magnetic field (Figure 4.39). However, the yield progressively declined when temperature was increased to 190°C (Figure 4.39). At room temperature, α-Fe_2O_3 revealed weak ferromagnetic character with the spins magnetic moments randomly oriented within the multidomains (Section 2.4.1 and Section 2.4.4) [10]. However, exerting magnetic field diminished the domain walls, thus assembling all magnetic moments in a large single domain causing the magnetic moments to be aligned parallel to the exerted magnetic field direction (Section 2.4.3) [12]. Interaction of reactant molecules with the magnetized catalyst overcame the difficulty for the electrons to be transferred, pairing and exchange among d-orbital of catalyst and π-orbital of reactant molecules. However, when the synthesis temperature was increased above 110°C, the yield reduced by about a factor of 3 (Figure 4.39). As elaborated by Le Chaterlier's principle (Section 2.8.1), increasing reaction temperature encourages the decomposition of ammonia to N_2 and H_2 due to exothermic and reversible properties of ammonia synthesis reaction [1], [10]-[11].

Figure 4.40 shows the effect of different forms of iron oxide catalysts on the ammonia yield at various reaction temperatures. The magnetic field was also applied during the catalytic reaction study.

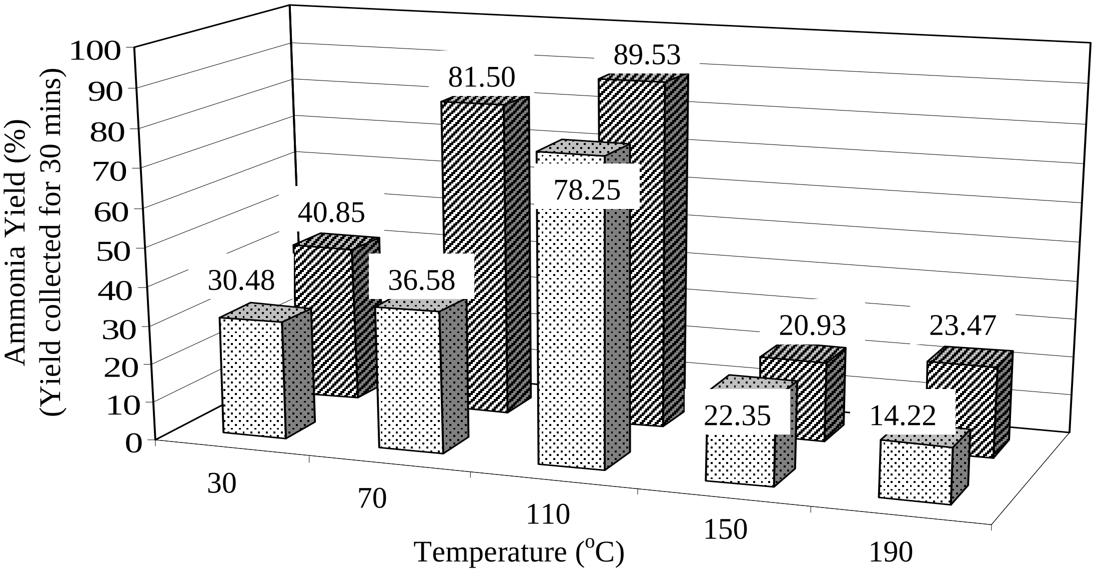

Figure 4.40: Effect of various reaction temperatures and different catalyst phases on ammonia yield produced. T = 30°C-190°C, P = 1 atm, H-F = 1 T, Cat. = 0.2 g, GHSV = 12000 $cm^3/g_{cat}.h$, F = 40 cm^3/min, $H_2:N_2$ = 3:1. The ammonia yield was collected for 30 mins at each temperature.

The use of Fe_3O_4 catalyst resulted in 15% higher ammonia yield than that of α-Fe_2O_3 at 110°C (Figure 4.40). The increase in ammonia yield might be due to magnetic character of the Fe_3O_4 catalyst. At room temperature, α-Fe_2O_3 was a weak ferromagnetic while Fe_3O_4 exhibited good ferrimagnetic properties (Table 4.14) [20]. The strength of exerted field might not be adequate to overcome the energy barrier for magnetic moments rotation in α-Fe_2O_3 structure, thus confining the catalytic steps. Higher ammonia yield was obtained when Fe_3O_4 was used as a catalyst due to stronger magnetic character compared to α-Fe_2O_3 which enhanced electrons sharing and exchanging processes between the catalyst and the reactants.

The activation energy was determined using a well know equation for ammonia synthesis namely Temkin-Phyzev and the calculations are shown in Appendix B. The expression is described in Equation 4.2 [90],[101] where k_A is the rate constant for forward reaction, k_B is the rate constant for reverse reaction, P_A is the partial pressure of substance and α is the reaction order.

$$\mathrm{Rate}_{NH3}\,(\mathrm{mole}_{NH3}/\mathrm{gcat.h}) = k_A P_{N2}\,[(P^3_{H2})/(P^2_{NH3})]^{\alpha} - k_B\,[(P^2_{NH3})/(P^3_{H2})]^{1-\alpha} \qquad (4.2)$$

The equation assumed that nitrogen dissociative adsorption is the rate-determining step and the surface coverage by atomic nitrogen is high [90]. The value of reaction order, α used in this study was 0.75, similar to that of value employed by Pernicone et al. [101]. Previous study also reported that the value of reaction order, α was found to be in between 0.5 to 0.8 [90]. As explained by Aparicio et al. [90], if α equals to 0, the change in the heat of nitrogen adsorption with coverage does affect only the activation energy of desorption whereas α equals to 1 causes the activation energy for adsorption to get affected. It was found in this study that the Temkin-Phyzev equation did work for temperature up to 110°C. Conversely, the results became insignificant for the calculation involving data obtained at temperature above 110°C. The values of rate, equilibrium constant, K_{eq}, mole fraction, X_A, partial pressure, P_A, and rate constant, k_A are shown in Table 4.23.

Table 4.23: Data to determine the activation energy of α-Fe_2O_3 and Fe_3O_4 nanocatalysts in the presence of magnetic field.

Catalyst	T (^oC)	K_{eq}	X_A			P_A (atm)			Rate ($mol_{NH3}/g_{cat}.h$)	k_A ($g_{cat}.^{-1}h^{-1}$)	ln k_A	E_a
			N_2	H_2	NH_3	N_2	H_2	NH_3				
α-Fe_2O_3	30	1.853 x 10^5	0.216	0.650	0.130	0.216	0.650	0.130	3.0 x 10^{-3}	1.724 x 10^{-3}	-6.363	34.18 kJ/mol
	70	2.617 x 10^3	0.211	0.635	0.154	0.211	0.635	0.154	3.6 x 10^{-3}	2.866 x 10^{-3}	-5.854	
	110	90	0.179	0.539	0.281	0.179	0.539	0.281	7.7 x 10^{-3}	2.650 x 10^{-2}	-3.627	
Fe_3O_4	30	1.853 x 10^5	0.208	0.623	0.170	0.208	0.623	0.170	4.020 x 10^{-3}	3.930 x 10^{-3}	-5.539	30.57 kJ/mol
	70	2.617 x 10^3	0.178	0.533	0.290	0.178	0.533	0.290	8.020 x 10^{-3}	2.860 x 10^{-2}	-3.555	
	110	90	0.173	0.518	0.309	0.173	0.518	0.309	8.810 x 10^{-3}	4.020 x 10^{-02}	-3.213	

Arrhenius plot was plotted using the data tabulated in Table 4.23 so as to obtain the activation energy of the nanocatalysts as shown in Figure 4.41.

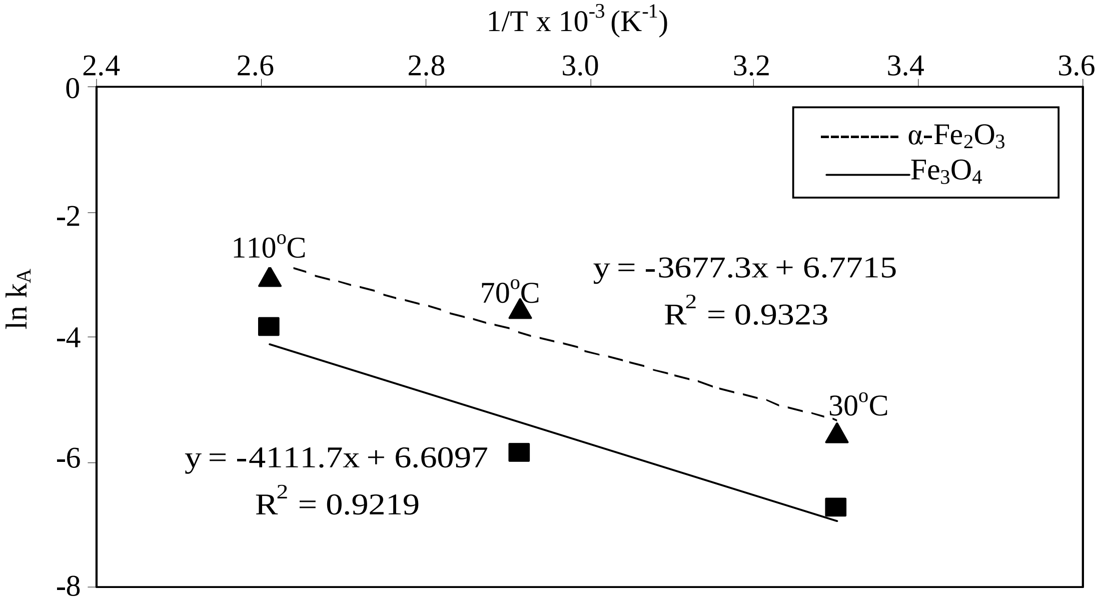

Figure 4.41: Arrhenius plot of ammonia production for α-Fe_2O_3 (■) and Fe_3O_4 (▲) nanocatalysts. T = 30°C-190°C, P = 1 atm, H-F = 1 T, Cat. = 0.2 g, GHSV = 12000 cm^3/g_{cat}.h, F = 40 cm^3/min, $H_2:N_2$ = 3:1

Both plots of α-Fe_2O_3 and Fe_3O_4 have R-square values of 0.9219 and 0.9323, respectively. These values are closed to 1 with the percentage error in between 6.5% to 8.0% (Figure 4.41). The activation energy, E_a was determined by calculating the gradient of the linear lines (Figure 4.41). In the absence of magnetic field, the α-Fe_2O_3 nanocatalyst had the activation energy of 96.49 kJ/mol. In the presence of magnetic field, the E_a of α-Fe_2O_3 catalyst was 34.18 kJ/mol whereas for Fe_3O_4 catalyst was 30.57 kJ/mol. The E_a values in this investigation were found to be slightly lower than those of results reported in literature [122]. Strongin et al. [122] examined that the E_a values for Fe and K/Fe catalysts were 65.73 kJ/mol and 66.57 kJ/mole, respectively. This was measured at reaction temperature and pressure of 365 – 450°C and 20 atm, respectively [122]. Pernicone and co-workers [101] compared the performance of Fe_3O_4 and $Fe_{1-x}O$-based catalysts to produce ammonia at 400 – 460°C and 100 bars. They found that the E_a for Fe_3O_4 and $Fe_{1-x}O$-based catalysts were 44.9 kJ/mol and 47.5 kJ/mol, respectively, which was slightly higher than those values obtained in this study by a factor of 1.3 – 1.6. This deduces that magnetizing the catalyst minimized the difficulty in electrons exchanging and pairing processes between the catalyst and reactant, thus permitting the catalytic steps to occur easily.

4.2.2 Supported Iron Oxide Nanocatalyst

Three factors were studied which encompass effects of properties of supported 5% α-Fe_2O_3/γ-Al_2O_3 nanocatalyst, H_2:N_2 ratio and total feed gas flow rate.

4.2.2.1 Effect of Properties of 5% α-Fe_2O_3/γ-Al_2O_3 Nanocatalyst

The results for ammonia synthesis involving 5% α-Fe_2O_3/γ-Al_2O_3 catalyst prepared at different $Fe(NO_3)_3$:SBS surfactant ratios are shown in Figure 4.42. The reaction utilized total H_2 and N_2 gases flow of 40 cm^3/min, H_2:N_2 ratio of 3:1, space velocity of 12000 cm^3/g_{cat}.h and under atmospheric pressure.

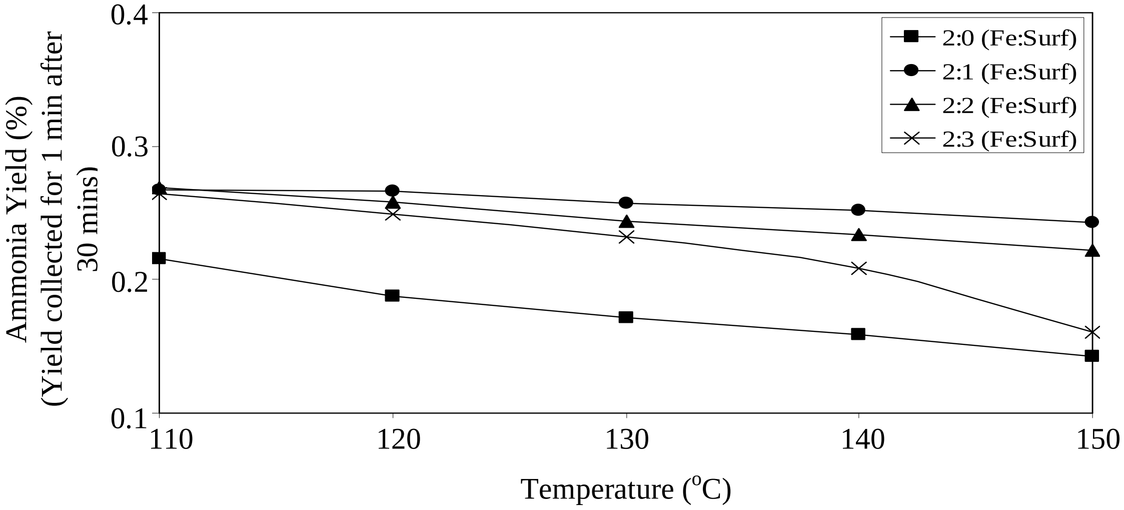

Figure 4.42: Effect of various reaction temperatures and different $Fe(NO_3)_3$:SBS surfactant ratios of supported 5% α-Fe_2O_3/γ-Al_2O_3 catalysts on ammonia yield. T = 110°C – 150°C, P = 1 atm, H-F = Absence, Cat. = 0.2 g, GHSV = 12000 cm^3/g_{cat}.h, F = 40 cm^3/min, H_2:N_2 = 3:1. The ammonia yield was collected for 1 minute after 30 mins at each temperature.

Ammonia yield produced in the presence of these catalysts decreased with increasing reaction temperature (Figure 4.42), consistent with Le Chatelier's principle (Section 2.8.1) and previous observations [1], [6], [10]-[11], [14], [94]. At 150°C, ammonia yield dropped by about 50% for the catalyst prepared using 2:3 $Fe(NO_3)_3$:SBS surfactant compared to that of catalyst synthesized at 2:1 $Fe(NO_3)_3$:SBS surfactant ratios. The major role of surfactant is to enhance the dispersion of particles as well as to avoid agglomeration phenomenon. However, increasing amount of surfactant increased amount of carbon impurity as interpreted by EDX analysis (Figure 4.34 and Table 4.18). Excess surfactant can cover the surface of Fe particles, thus preventing H_2 and N_2 molecules to be adsorbed on the surface of Fe particles. Section 4.1.3.2 revealed that adding more surfactant enhanced the Fe particles dispersion (Figure 4.37 (a)). However, few agglomerated particles were observed for nanocatalysts prepared at 2:2 and 2:3 $Fe(NO_3)_3$:SBS surfactant ratios (Figure 4.35) which caused reduction in surface area of Fe particles (Table 4.21). Consequently, the ammonia yield reduced due to decrease in surface area of Fe particles (Figure 4.42).

The supported 5% α-Fe_2O_3/γ-Al_2O_3 nanocatalyst synthesized using 2:1 $Fe(NO_3)_3$: SBS Surf ratio revealed highest ammonia yield that was attained at 110°C. This nanocatalyst showed good improvement on physicochemical properties. Therefore, this nanocatalyst and temperature of 110°C were chosen in further catalytic studies.

4.2.2.2 Effect of H_2:N_2 ratio

It is known that the ideal gas ratio (H_2:N_2) applies in ammonia synthesis is 3:1. This investigation utilized supported 5% α-Fe_2O_3/γ-Al_2O_3 nanocatalyst obtained using iron to surfactant ratio of 2:1. This study was conducted at total feed flow rate gas (H_2:N_2) of 40 cm^3/min, space velocity of 12000 cm^3/g_{cat}.h, reaction temperature of 110°C and under atmospheric pressure. The H_2:N_2 volume ratios were varied to 1:3, 3:1 and 5:1. Figure 4.43 illustrates the influence of various reactant gas ratios (H_2:N_2) on the ammonia yield.

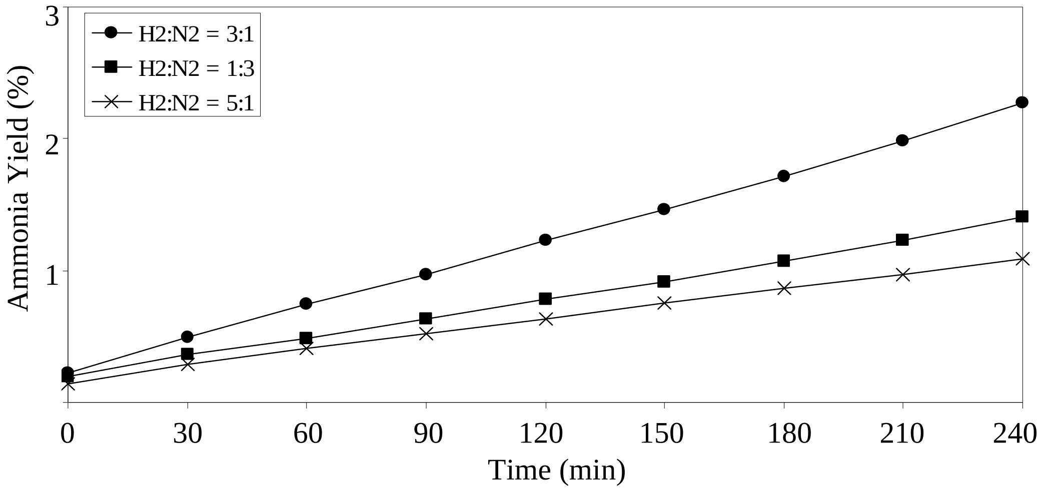

Figure 4.43: Effect of various volume ratios of reactants gas (H_2:N_2) on ammonia yield produced using 5% α-Fe_2O_3/γ-Al_2O_3 nanocatalyst (2:1). T = 110°C, P = 1 atm, H-F = absence, Cat. = 0.2 g, GHSV = 12000 cm^3/g_{cat}.h, F = 40 cm^3/min, H_2:N_2 = 3:1, 1:3 and 5:1. The ammonia yield was collected for 1 minute at each 30 minutes interval.

The 3:1 H_2:N_2 ratio resulted in highest ammonia yield as compared to others (Figure 4.43). This ratio agrees with the general chemical equation for producing ammonia [20]. The 1:3 ratio resulted in lower yield than that of 3:1 ratio. This trend was also reported in literature [14] which might be due to insufficient hydrogen to react with surplus nitrogen molecules. Furthermore, the lowest ammonia yield was attained using the 5:1 ratio (Figure 4.43) which could be due to inhibiting effect of increasing the fraction of H_2 adsorbed.

The 3:1 is the optimum ratio of H_2:N_2 as it produced highest ammonia yield. This ratio was applied in examining the effect of different feed gas flow rates.

4.2.2.3 Effect of Feed Gas Flow Rate

This study used the supported 5% α-Fe_2O_3/γ-Al_2O_3 nanocatalyst obtained at $Fe(NO_3)_3$:SBS ratio of 2:1. The reaction was conducted at H_2:N_2 of 3:1, space velocity of 12000 $cm^3/g_{cat}.h$, reaction temperature of 110^oC and under atmospheric pressure. The feed gas flow rates were varied at 28 cm^3/min, 40 cm^3/min and 100 cm^3/min. The result is shown in Figure 4.44.

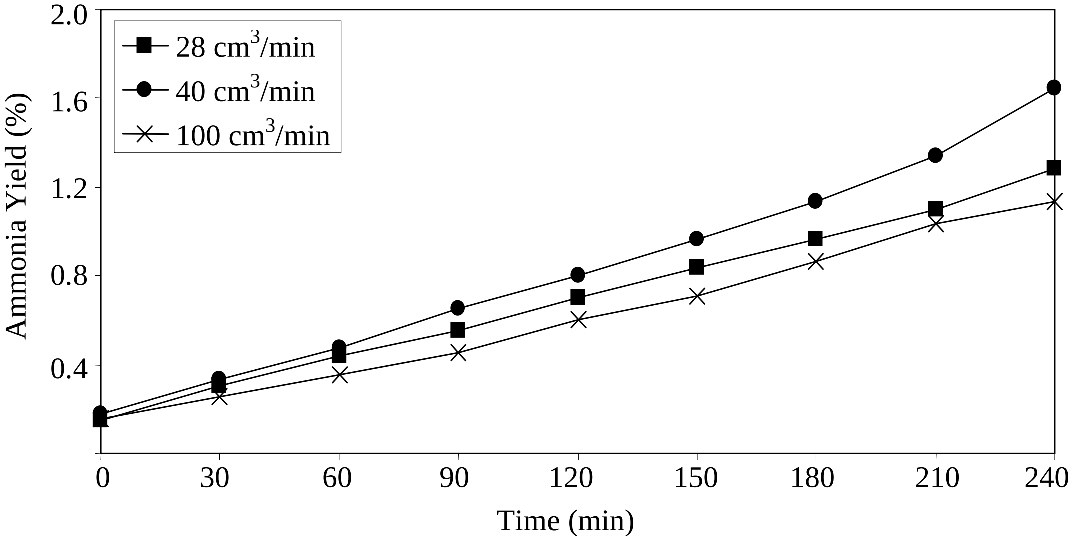

Figure 4.44: Effect of various total feed gas flow rates on ammonia yield produced over supported 5% α-Fe_2O_3/γ-Al_2O_3 nanocatalyst (2:3). T = 110^oC, P = 1 atm, H-F = Absence, Cat. = 0.2 g, GHSV = 8400 $cm^3/g_{cat}.h$ – 30000 $cm^3/g_{cat}.h$ - , F = 28 cm^3/min – 100 cm^3/min, H_2:N_2 = 3:1. The ammonia yield was collected for 1 minute at each 30 minutes interval.

Higher ammonia yield was obtained at total feed flow rate of 40 cm^3/min (Figure 4.44) compared to those at 28 cm^3/min and 100 cm^3/min. Decreasing the gas flow rate to 28

cm^3/min reduced the ammonia yield due to increase in the time of travelling for reactant gas to arrive at the catalyst surface, thus decelerating the catalytic processes. However, excessive feeding rate will speed up the movement of the molecules but reduce the contact time which might not provide sufficient chance for the incoming molecules to undergo surface reaction process. Figure 4.45 describes the relation between the ammonia yield recorded at t= 240 mins (Figure 4.44) and the space velocity.

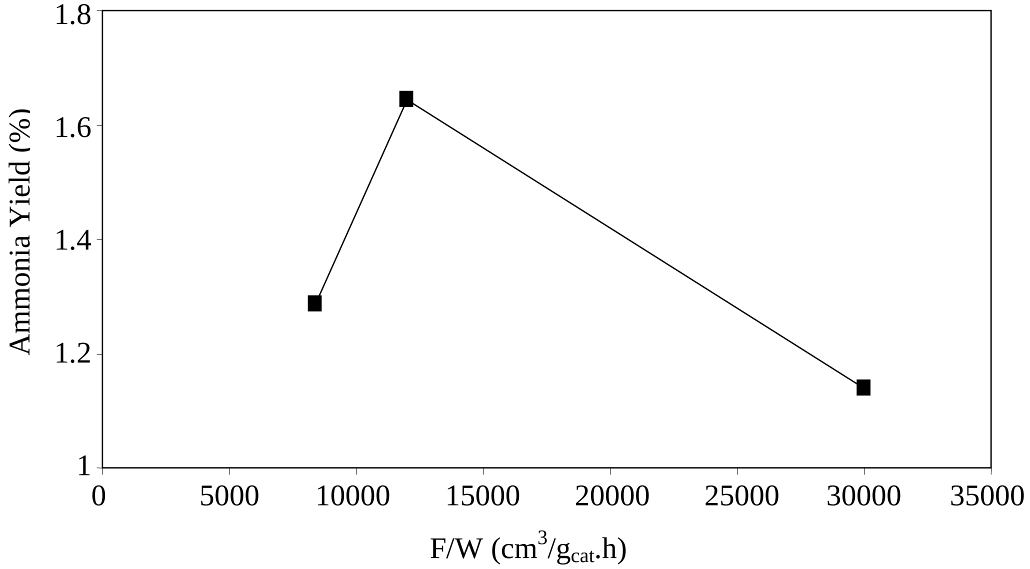

Figure 4.45: Effect of various space velocities on ammonia yield produced using 5% α-Fe_2O_3/γ-Al_2O_3 nanocatalyst (2:3). T = 110°C, P = 1 atm, H-F = Absence, Cat. = 0.2 g, GHSV = 8400 cm^3/g_{cat}.h – 30000 cm^3/g_{cat}.h, F = 28 cm^3/min – 100 cm^3/min, $H_2:N_2$ = 3:1.

According to Figure 4.45, 12000 cm^3/g_{cat}.h (40 cm^3/min) was found to be an optimum space velocity as it produced highest yield than that of at 28 cm^3/min and 100 cm^3/min. As reported by L. Xiaonian et al. [123], the catalytic activity performed at 400°C and 150 atm, reduced by a factor of two when the space velocity was increased from 5000 h^{-1} to 50000 h^{-1}.

A comparison on the ammonia yield obtained between unsupported and supported nanocatalysts was made and the result is illustrated in Figure 4.46. It is proven that the presence of metal-support interaction enhanced the catalytic activity as obtained by 5% α-Fe_2O_3/γ-Al_2O_3 nanocatalyst. The 5% α-Fe_2O_3/γ-Al_2O_3 resulted in the ammonia yield about 10 times higher than that of unsupported α-Fe_2O_3 nanocatalyst (Figure 4.46). This enhancement is due to the presence of support which prevents the agglomeration of particles (Section 2.9.2)

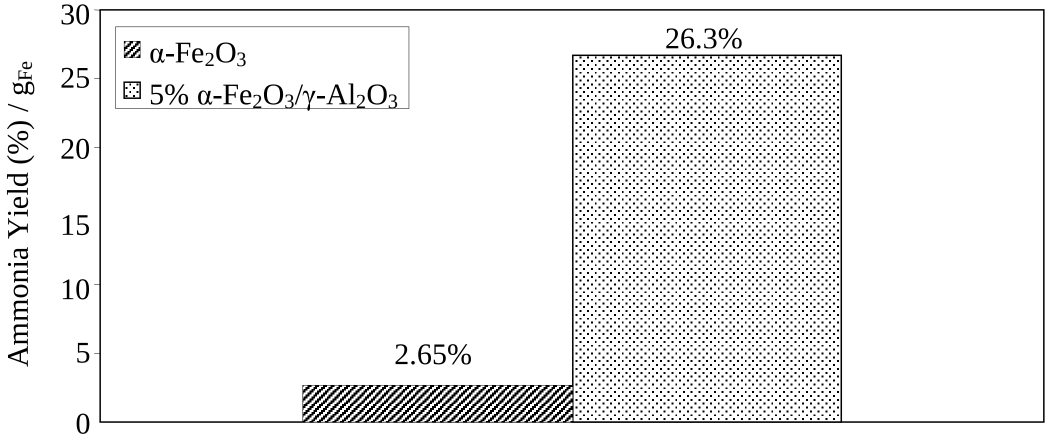

Figure 4.46: Ammonia yield comparison between unsupported α-Fe_2O_3 and supported 5% α-Fe_2O_3/γ-Al_2O_3 nanocatalysts. T = 110°C, P = 1 atm, H-F = Absence, Cat. = 0.2 g, GHSV = 12000 cm^3/g_{cat}.h, F = 40 cm^3/min, H_2:N_2 = 3:1. The ammonia yield was collected 1 minute for 30 mins.

The ammonia yield produced per gram of catalyst for all prepared nanocatalysts is summarized in Figure 4.47.

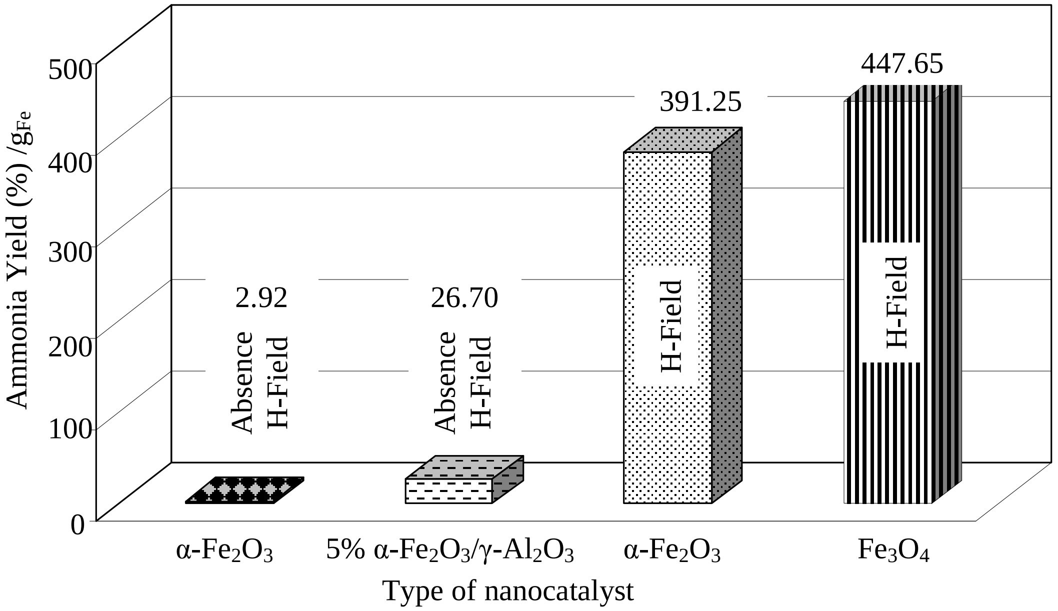

Figure 4.47: Summary on ammonia yield produced per gram of catalyst for all prepared nanocatalyst. T = 110°C, P = 1 atm, Cat. = 0.2 g, GHSV = 12000 cm^3/g_{cat}.h, F = 40 cm^3/min, H_2:N_2 = 3:1. The ammonia yield was collected for 30 mins.

In the absence of magnetic field, the supported 5% α-Fe_2O_3/ γ-Al_2O_3 catalyst showed activity 10 times higher than that of unsupported α-Fe_2O_3 catalyst (Figure 4.47). Dispersing α-Fe_2O_3 particles on a γ-Al_2O_3 minimized the agglomeration of iron nanoparticles, which increased the surface area of the nanocatalyst, thus more active sites were created for H_2 and N_2 to react, hence enriching the catalytic activity. A combination between nanotechnology and magnetism improved the catalytic activity. As shown in Figure 4.47, the activity was enhanced by about 145 times as a result of applying magnetic field to the reaction in the presence of α-Fe_2O_3 catalyst. Exerting magnetic field reduced the difficulty in pairing or exchanging the electrons between Fe and H_2 and N_2 molecules, thus enhanced the catalytic activity. Therefore, the hypothesis made in Section 1.3 is proven.

A summary on catalytic performance observed in this work and from previous investigations is summarized in Table 4.24. The ammonia yield, under influence of magnetic field, in the presence of α-Fe_2O_3 and Fe_3O_4 nanocatalysts in this investigation was approximately 18-20 times more active than those of K-Fe/C and K-Fe-Ru/C, which was conducted at 350^oC and 1 atm [6] (Table 4.24). Activity involving K-Ru/C catalyst conducted at 350^oC and 1 atm, performed by H. Mahapatra et al. [6] was about 12-14 times less active than those of α-Fe_2O_3 and Fe_3O_4 nanocatalysts in the presence of magnetic field (Table 4.24). Supported 5% α-Fe_2O_3/γ-Al_2O_3 showed better performance compared to those of K-Fe/C and K-Fe-Ru/C catalysts. However, the activity of 5% α-Fe_2O_3/γ-Al_2O_3 was about 1.2 less active than that of K-Ru/C which could be due to the use of Ru as the active metal. As elucidated in Section 2.1, dissociation of N_2 is extremely active using Ru which enhanced the catalytic activity [12], [20]. Catalytic activity of $Fe_{1-x}O$ and Fe_3O_4 catalysts with the particle size of 0.2-0.3 and 1.0-1.4 mm at high pressure was much higher [123]-[124] than those of results obtained in this investigation (Table 4.24).

Table 4.24: Comparison of ammonia yields.

Reference	Catalyst	Particle size	Metal Loading (wt.%)	Ammonia Synthesis Conditions				
				T (^oC)	P (atm)	H_2:N_2 ratio	Other	Rate
This work	α-Fe_2O_3	31.47 nm	-	110	1	3:1	With H-Field	$7.70x10^{-3}$ mole.$g_{cat}{}^{-1}h^{-1}$
This work	Fe_3O_4	31.72 nm	-	110	1	3:1	With H-Field	$8.81x10^{-3}$ mole.$g_{cat}{}^{-1}h^{-1}$
This work	α-Fe_2O_3	31.47 nm	-	110	1	3:1	Without H-Field	$5.30x10^{-5}$ mole.$g_{cat}{}^{-1}h^{-1}$
This work	α-Fe_2O_3/γ-Al_2O_3	-	5 Fe_2O_3	110	1	3:1	Without H-Field	$5.26x10^{-4}$ mole.$g_{Fe}{}^{-1}h^{-1}$
[6]	K-Fe/C	-	1.2 Fe	350	1	3:1	Without H-Field	~$4.27x10^{-4}$ mole.$g_{Fe}{}^{-1}h^{-1}$
[6]	K-Fe-Ru/C	-	0.6 Fe and 0.6 Ru	350	1	3:1	Without H-Field	~$4.85x10^{-4}$ mole.$g_{FeRu}{}^{-1}h^{-1}$
[6]	K-Ru/C	-	1.2 Ru	350	1	3:1	Without H-Field	~$6.30x10^{-4}$ mole.$g_{Ru-}{}^{1}h^{-1}$
[122]	$Fe_{1-x}O$	0.2-0.3 mm	-	475	150	3:1	Without H-Field	$9.00x10^{-2}$ mole.$g_{cat}{}^{-1}h^{-1}$
[123]	Fe_3O_4	1.0-1.4 mm	-	400	150	3:1	Without H-Field	$6.00x10^{-2}$ mole.$g_{cat}{}^{-1}h^{-1}$
[125]	Fe/γ-Al_2O_3	-	2.3 Fe	310	40	3:1	Without H-Field	$1.87x10^{-3}$ mole.$g_{Fe}{}^{-1}h^{-1}$

CHAPTER 5

CONCLUSION

5.1 Conclusion

Three different types of iron based-nanocatalysts consisting of α-Fe_2O_3, Fe_3O_4 and 5% α-Fe_2O_3 supported on γ-Al_2O_3 were successfully synthesized via so-gel and sol gel-hydrothermal methods.

Effects of period of stirring, annealing temperature, synthesis temperature and inclusion of surfactant were tested in nanocatalyst preparation. For sol-gel method, extending period of stirring from 1 day to 1 month reduced the particle size of α-Fe_2O_3 nanocatalyst from 60 nm to 27 nm while increasing annealing temperature from 300^{o}C to 700^{o}C enlarged the particle size by a factor of three as shown by XRD interpretation. The H_2-TPR examination exhibited that a decrease in iron particle size caused the reduction process to be accomplished at much higher temperature. A hybrid method namely sol gel-hydrothermal was found to be the best synthesis method in producing a highly crystallined Fe_3O_4 nanocatalyst at synthesis temperature of 160^{o}C and exhibited the highest magnetization value compared to those of other methods. Introducing surfactant in preparing 5% α-Fe_2O_3/γ-Al_2O_3 improved the physicochemical features of this catalyst model. The iron (III) nitrate to surfactant ratio of 2:3 enhanced the Fe particles dispersion by approximately 90% as indicated by H_2-TPR and EDX-mapping.

Catalytic evaluation studies proved that introduction of magnetic field to the reaction enhanced the ammonia yield by 145 times using α-Fe_2O_3 nanocatalyst at reaction conditions of 110^{o}C and 1 atm. The ammonia yield was further increased by 15% using Fe_3O_4 compared to that of α-Fe_2O_3 nanocatalysts at the same reaction conditions. The 5% α-Fe_2O_3/γ-Al_2O_3 produced ammonia yield 10 times higher than that of unsupported α-Fe_2O_3, recorded in absence of magnetic field. This study successfully discovered that a combination of nanotechnology and magnetism concept could lead to higher ammonia yield production. The severity of the reaction was also successfully minimized. The catalytic activity was accelerated by utilizing supported α-Fe_2O_3 nanocatalyst.

5.2 Recommendations

The recommendations to improve this study are as follow:

1. The microreactor should be able to work at much higher temperature and pressure to ensure that the activation process can occur completely.

2. Reaction at high pressure should be conducted in the absence and presence of magnetic field to get a clear examination on the effect of magnetic field.

3. The magnetic field strength should be varied to determine the effect of magnetic field strength to the ammonia synthesis reaction.

4. The reactor should be equipped with an online gas chromatograph (GC) in order to improve detection and quantification of ammonia.

5. Effect of applying magnetic field to α-Fe_2O_3/γ-Al_2O_3 nanocatalyst on the ammonia yield should be investigated.

REFERENCES

[1] D. F. Shriver and P. W. Atkins, *Inorganic Chemistry*, 3rd ed. Oxford, United Kingdom: Oxford University Press, 1999.

[2] N. Kumar, "Structure Sensitive Adsorption of Hydrogen on Ruthenium and Ruthenium-silver Catalysts Supported on Silica," Ph.D. dissertation, Ames Lab., Iowa State Univ., Ames, Iowa, 1999.

[3] *Ammonia: Physical and Chemical Information* [Online]. Availabe: http://www.atsdr.cdc.gov/ToxProfiles

[4] C. M. Roebuck, *Excel HSC Chemistry*, 1st ed. New South Wales, Australia: Pascal Press, 2004.

[5] United States Geological Survey Mineral Resources Program. (2008, June 13). *Ammonia: World Production by Country* [Online]. Available: http://www.indexmundi.com.

[6] H. Mahapatra, E. S. Kalyuzhnaya, S.M. Yunusov and V.B. Shur, "Synergism of iron and ruthenium in ammonia synthesis catalyst at low temperature," *Stud. Surface Sci. and Catalysis*, vol.113, pp. 267-270, 1998.

[7] C. Liang, Z. Wei, Q. Xin and C. Li, "Ammonia synthesis over Ru/C catalysts with different carbon supports by barium and potassium compounds," *Appl. Catalysis A: General*, vol. 208, issue 1-2, pp. 193-201, Feb. 2001.

[8] J. R. Rennings, *Catalytic Ammonia Synthesis: Fundamental and Practice*, 2nd ed. Spring Street, New York: Plenum Press, 1994.

[9] C. H. Bartholomew and R. J. Farrauto, *Fundamental of Industrial Catalytic Process*, 2nd ed. Hoboken, New Jersey: Wiley Interscience, 2006.

[10] K. M. Whitten, R. E. Dais, M. L. Peck and G. G. Stanley, *General Chemistry*, 7th ed. Belmont, CA: Thomson Brooks/Cole , 2004.

[11] G. A. Samorjai, *Introduction to Surface Chemistry and Catalysis*, 1st ed. Hoboken, New Jersey: Wiley Interscience, 1994.

[12] D. A. McQuarrie and J. D. Simon, *Physical Chemistry: A Molecular Approach*, 1st ed. Sausalito, CA: University Science Books, 1997.

[13] S. Bencic. (2001, April). *Literature Report: Ammonia Synthesis Promoted by Iron Catalysts* [Online]. Available: http://www.cem.msu.edu/~cem924sg/SandraBencic.pdf.

[14] F. Rosowski, A. Hornung, O. Hinrichsen, D. Herein, M. Muhler and G. Ertl, "Ruthenium catalysts for ammonia synthesis at high pressures: Preparation, characterization, and power-law kinetics," *Appl. Catalysis A: General,* vol. 151, pp. 443-460, 1997.

[15] Oxford Laboratory. (2010). *Price List* [Online]. Available: http://www.oxfordlabchem.com/price_c.html.

[16] J. M. Köhler and W. Fritzsche, *Nanotechnology: An Introduction to Nanostructuring Techniques,* 2nd ed. Weinheim, Germany: Villey-VCH Publication, 2007.

[17] F. J. Owens and C. P. Poole, *The Physics and Chemistry of Nanosolids,* 2nd ed. Hoboken, New Jersey: John Wiley & Sons Inc., 2008.

[18] C. J. H. Jacobsen, J. Jiang, S. Morup, B. S. Clausen and H. Topsoe, "Ammonia synthesis over multi-promoted iron catalysts obtained by high-energy ball-milling," *Catalysis Lett.*, vol. 61, no. 3-4, pp. 115-120, June 1999.

[19] A. Jedynak, D. Szmigiel, W. Rarog, J. Zielinski, J. Pielaszek, P. Dluzweski and Z. Kowalczyk, "Potassium-promoted carbon-based iron catalyst for ammonia synthesis: Effect of Fe dispersion," Catalysis Letts., vol. 81, no. 3-4, pp. 213-218, August 2002.

[20] R. M. Cornell and U. Schwertmann, *The Iron Oxides: Structures, Properties, Reactions, Occurrence and Uses,* 1st ed. Weinheim, Germany: VCH Publisher, 1996.

[21] D. Wagner, O. Devisme, F. Pattison and Denis Ablitzer, "A laboratory study of the reduction iron oxides by hydrogen," in *Proc. Sohn International Symp.*, vol. 2. San Diego, 2006, pp. 111-120.

[22] W. K. Jozwiak, E. Kaczmarek, T.P. Maniecki, W. Ignaczak and W. Maniukiewicz, "Reduction behaviour of iron oxides in hydrogen and carbon monoxide atmospheres," *Appl. Catalysis A: General,* vol. 326, issue 1, pp. 17-27, June 2007.

[23] Laboratory of Ohba. (2010, March 12). *Crystal Structures* [Online]. Available: http://www.geocities.jp/ohba_lab_ob_page.

[24] B. Larson. (2009). *Similarities and Different Between the FCC and HCP Structures* [Online]. Available: http://www.ndt-ed.org.

[25] S. O. Pillai, *Solid State Physics*, 5th ed. New Delhi, India: New Age International Publishers, 2003.

[26] J. P. Jakubovics, *Magnetism and Magnetic Materials*, 2nd ed. London, United Kingdom: The Institute of Materials, 1994.

[27] Wikipedia The Free Encylopedia. (2008, November). *Magnetic Domain* [Online]. Available: http://www.wikipedia.org.

[28] Institute for Rock and Magnetism, University of Minnesota. (2008). *Classes of Magnetic Materials* [Online]. Available: http://www.irm.umn.edu.

[29] R. C. Dorf, *The electrical engineering handbook*, 2nd ed., CA: CRC Press, 1997.

[30] Z. L. Wang, Y. Liu and Z. Zhang, *Handbook of Nanophase and Nanostructured Materials: Materials systems and applications*, 2nd Ed. Tsinghua University, Beijing, China: Kluwer Academic/Plenum Publishers, 2003.

[31] R. Vanezuela, M. C. Fuentes, C. Parra, J. Baeza, N. Duran, S.K. Sharma, M. Knobel and J. Freer, “Influence of stirring velocity on the synthesis of magnetite nanoparticles (Fe_3O_4) by co-precipitation method,” *J. Alloys and Compounds*, vol. 488, issue 1, pp. 227-231, Nov. 2009.

[32] G. Gnanaprakash, D. Mahadevan, T. Jayakumar, P. Kalyanasundaram, J. Philip and B. Raj, “Effect of initial pH and temperature of ion salt solutions on formation of magnetite nanoparticles,” *Materials Chemistry and Physics*, vol. 103, issue 1, pp.168-175, May 2007.

[33] J. Xu, H. Yang, W. Fu, K. Du, Y. Sui, J. Chen, Y. Zeng, M. Li and G. Zuo, “Preparation and magnetic properties of magnetite nanoparticles by sol gel method,” *J. Magnetism and Magnetic Materials*, vol. 309, issue 2, pp. 307-311, Feb. 2007.

[34] X. Wu, J. Tang, Y. Zhang and H. Wang, “Low temperature synthesis of Fe_3O_4 nanocrystals by hydrothermal decomposition of a metallorganic molecular precursor,” *Materials Sci. Eng. B*, vol. 157, issues 1-3, pp. 81-86, Feb. 2009.

[35] H. Zhu, D. Yang and L. Zhu, “Hydrothermal growth and characterization of magnetite (Fe_3O_4) thin films,” *Surface and Coatings Technology*, vol. 201, issue 12, pp. 5870-5874, March 2007.

[36] Z. Yuanbi, Q. Zumin and H. Jiaying, “Preparation and analysis of Fe_3O_4 magnetic nanoparticles used as targeted-drug carriers,” *Chinese J. Chemical Eng.*, vol. 16, issue 3, pp. 451-455, June 2008

[37] Y. H. Zheng, Y. Cheng, F. Bao and Y. S. Wang, “Synthesis and magnetic properties of Fe_3O_4 nanoparticles,” *Materials Research Bulletin*, vol. 41, issue 3, pp. 525-529, March 2006.

[38] J. H. Wu, S. P. Ko, H. L. Liu, M. H. Jung, J. H. Lee, J. S. Ju and Y. K. Kim, “Sub 5 nm Fe_3O_4 nanocrystals via coprecipitation method,” *Colloids and Surfaces A: Physicochemical and Eng. Aspects*, vol. 313-314, issue1, pp. 268-272, Feb. 2008.

[39] A. H. Lu, E. L. Salabas and F. Schuth, “Magnetic Nanoparticles: Synthesis, Protection, Functionalization, and Application,” *Angewantde Chemie Int.*, volume 46, issue 8, pp. 1222–1244, Feb. 2007.

[40] S. Akbar, S. K. Hasanain, N. Azmat and M. Nadeem. (2004). *Synthesis of Fe_2O_3 nanoparticles by sol gel method and their structural and magnetic characterizations* [Online]. Available: http://arxiv.org/ftp/cond-mat/papers/0408/0408480.pdf.

[41] C. Chen, O. Kitakami and Y. Shimada, “Particle size effects and surface anisotropy in Fe-based granular films,” *J. Appl. Physics*, vol. 84, issue 4, pp. 2184-2188, Aug. 1998.

[42] A. R. West, *Solid State Chemistry and Its Applications*, 1st ed. Aberdeen, UK: John Wiley and Sons, 1987

[43] F. Szabadváry, *History of Analytical Chemistry*, 2nd ed. Langhome, Pennsylvania: Grodon and Breach Science Publisher, 1992.

[44] J. Livage and M. Henry, C. Sanchez, “Sol-Gel Chemistry of Transition Metal Oxides,” *Progress in Solid State Chemistry*, vol. 18, issue 4, pp. 259-341, 1988.

[45] R. Szostak, *Molecular Sieves: Principles of Synthesis and Identification*, 2nd ed. London, United Kingdom: Blackie Academic & Professional, 1998.

[46] C. Liu, X. Wu, T. Klemmer, N. Shukla, X. Yang, D. Weller, A.G. Roy, M. Tanase and D. Laughlin, “Polyol process synthesis of monodispersed FePt nanoparticles,” *J. Physical Chemistry: B*, vol. 108 (20) pp. 6121-6123, April 2004.

[47] Q. Liao, R. Tannenbaum and Z. L. Wang, “Synthesis of $FeNi_3$ nanoparticles by hydrothermal reduction,” *J. Physical Chemistry B*, vol. 110, no. 29, pp. 14262-14265, June. 2006.

[48] I. Nedkov, T. Merodiiska, L. Slavov, R. E. Vandenberghe, Y. Kusano and J. Takada, “Surface Oxidation, size and shape of nano-sized magnetite obtained by co-precipitation,” *J. Magnetism and Magnetic Materials*, vol. 300, issue 2, pp. 358-367, May 2006.

[49] D. Thapa, V. R. Palkar, M. B. Kurup and S. K. Malik, “Properties of magnetite nanoparticles synthesised through a novel chemical route,” *Materials Lett.*, vol. 58, issue 21, pp. 2692-2694, Aug. 2004.

[50] Y. Sun and H. Zeng, “Size-Controlled Synthesis of Magnetite Nanoparticles,” *J. American Chemical Soc.*, vol. 124, issue 28, pp. 8204-8205, June. 2002.

[51] G. Pecchi, P. Reyes and J. Villasenor, “Fe Supported Catalysts Prepared by The Sol Gel Method. Characterization and Evaluation in Phenol Abatement,” *J. Sol-Gel Sci. and Technology,* vol. 26, no. 1-3, pp. 865–867, Jan. 2003.

[52] W. W. Wang, Y. J. Zhu and M. L. Ruan, “Microwave-assisted synthesis and magnetic property of magnetite and hematite nanoparticles,” *J. Nanoparticle Research*, vol. 9, no. 3, pp. 419-426, June 2007.

[53] R. Fan, X. H. Chen, Z. Gui, L. Liu and Z.Y. Chen, “A new simple hydrothermal preparation of polycrystalline magnetite Fe_3O_4,” *Materials Research Bulletin*, vol. 36, issues 3-4, pp. 497-502, March 2001.

[54] Y. Li, H. Liao and Y. Qian, “Hydrothermal synthesis of ultrafine α-Fe_2O_3 and Fe_3O_4 powders,”*Materials Research Bulletin*, vol. 33, issue 6, pp. 841-844, June 1998.

[55] A. A. Burukhin, B. R. Churagulov, N. N. Oleynikov and A. V. Knot’ko, “Hydrothermal synthesis of mesoporous iron oxide powders,” in *Proc. Joint Sixth Int. Symp. Hydrothermal Reactions and Fourth Conf. on Solvo-Thermal Reactions*, Kochi, Japan, 2000, pp. 561-564.

[56] K. D. Kim, S. S. Kim, Y. H. Choa and H. T. Kim, “Formation and surface modification of Fe_3O_4 nanoparticles by co-precipitation and sol gel method,” *J. Ind. and Eng. Chemistry*, vol. 13, no. 7, pp. 1137-1141, Nov. 2007.

[57] S. Kim, U. Paik and J. Park, “Effect of calcination time on the physical properties of synthesized ceria particles for the shallow trench isolation chemical mechanical planarization process,” *J. Ceramic Process. Research,* vol. 7, no. 1, pp. 53-57, June 2006.

[58] K. P. Sanosh, M. C. Chu, A. Balakrishnan, T.N. Kim and S. J. Ho, “Preparation and characterization of nano-hydroxypatite powder using sol-gel technique,” *Bulletin Materials of Sci.*, vol. 32, no. 5, pp. 465-470, Oct. 2009.

[59] S. R. Janasi, D. Rodrigues and F. J. G. Landgraf, “Effect of Calcination Conditions on the Magnetic Properties of MnZn Ferrites Powders Produced by Co-precipitation,” *Materials Sci. Forum*, vol. 498-499, pp. 119-124, Nov. 2005.

[60] S. Shetty, V. R. Palkar and R. Pinto, “Size effect study in magnetoelectric $BiFeO_3$ system,” *PRAMANA- J. Physics*, vol. 58, no. 5-6, pp.1027-1030, May 2002.

[61] C. H. Lu, W. H. Wu and R. B. Kale, “Synthesis of photocatalytic TiO_2 thin films via the high-pressure crystallization process at low temperatures,” *J. Hazardous Materials*, vol. 147, issue 1-2, pp. 213-218, Aug. 2007.

[62] J. D. Wright and N. A. J. M. Sommerdik, *Sol-Gel Materials Chemistry and Applications*, 4th ed. Boca Raton, Florida: CRC Press, 2001.

[63] R. Balasubramaniam, A. V. Ramesh Kumar and P. Dillmann, “Characterization of rust on ancient Indian iron,” *Current Sci.*, vol. 85, no. 11, pp. 200-204, Dec. 2003.

[64] M. Kucher, D. Babic and M. Kind, “Precipitation of barium sulfate: Experimental investigation about the influence of supersaturation and free lattice ion ratio on particle formation,” *Chemical Eng. and Process.*, vol. 45, issue 10, pp. 900–907, Oct. 2006.

[65] M. A. Legodi and D.Wall, “The preparation of magnetite, goethite, hematite and maghemite of pigment quality from mill scale iron waste,” *J. Dye and Pigments*, vol. 74, issue 1, pp. 167-168, Sept. 2007.

[66] R. A. Zarate, F. Hevia, S. Fuentes, V. M. Fuenzalida and A. Zuniga, “Novel Route to Synthesize CuO nanoplates,” *J. Solid State Chemistry*, vol. 180, pp. 1464-1469, Jan. 2007.

[67] S. Komarneni, “Nanophase Materials by Hydrothermal, Microwave-Hydrothermal and Microwave-Solvothermal Methods,” *Current Sci.*, vol. 85, no. 12, pp. 1730-1734, Dec. 2000.

[68] Y. Hakuta, H. Ura, H. Hayashi and K. Arai, “Effets of Hydrothermal Conditions on The Particles Size of γ-AlO(OH) in sub and supercritical water using a flow reaction system,” *Materials Chemistry and Physics*, vol. 93, issues 2-3, pp. 466-472, Oct. 2005.

[69] G. J. K. Acres, A. J. Bird, J. W. Jenkins and F. King, “The Design and Preparation of Supported Catalysts,” *Roy. Soc. Chemistry*, vol. 4, pp.1-30, Jan. 1981.

[70] R. A. Santen, “Catalysis: An integrated approach,” *Stud. Surface Sci. and Catalysis*, vol. 2, p. 459-485, Sep. 1999.

[71] P. Michorczyka, P. Kustrowski, L. Chmielarzb and J. Ogonowskia, “Influence of redox properties on the activity of iron oxide catalysts in dehydrogenation of propane with CO_2,” *Reaction Kinetics and Catalysis Lett.*, vol. 82, no.1, pp. 121-130, Dec. 2003.

[72] J. Y. Park, Y. J. Lee, P. K. Khanna, K. W. Jun, J. W. Bae and Y. H. Kim, “Alumina-supported iron oxide nanoparticles as Fischer–Tropsch catalysts: Effect of particle size of iron oxide,” *J. Molecular Catalysis A: Chemical*, vol. 323, issue 1-2, pp. 84–90, May 2010.

[73] A. Pineau, N. Kanari and I. Gaballah, “Kinetics of reduction of iron oxides by H_2 Part I: Low temperature reduction of hematite,” *Thermochimica Acta*, vol. 447, issue 1 pp. 89–100, Aug. 2006.

[74] E. V. Steen and C. Claeys, *Recent advances in the science and technology of zeolites and related materials*, Houston, Texas: Gulf Professional Publishing – Technology and Engineering, pp. 2387-2394, 2004.

[75] H. Y. Lin, Y.W. Chen and C. Li, “The mechanism of reduction of iron oxide by hydrogen,” *Thermochimica Acta*, vol. 400, issues 1-2, pp. 61-67, April 2003.

[76] M. Liang, W. Kang and K. Xie, “Comparison of reduction behaviour of Fe_2O_3, ZnO and $ZnFe_2O_4$ by TPR Technique,” *J. Natural Gas Chemistry*, vol. 18, issue 1, pp. 110-113, March 2009.

[77] G. Giecko, T. Borowiecki, W. Gac and J. Kruk, “Fe_2O_3/Al_2O_3 catalysts for the N_2O decomposition in the nitric acid industry,” *Catalysis Today*, vol. 137, issues 2-4, pp. 403-409, Sept. 2008.

[78] C. Messi, P. Carniti and A. Gervasini, “Kinetics of reduction of supported nanoparticles iron oxide,” *J. Thermal Analysis and Calorimetry*, vol. 91, no. 1, pp. 93–100, Jan. 2008.

[79] A. Pineau, N. Kanari and I. Gaballah, “Kinetics of reduction of iron oxides by H_2 Part II: Low temperature reduction of magnetite,” *Thermochimica Acta*, vol. 456, issue 2, pp. 75-88, May 2007.

[80] R. Brown, M. E. Cooper and D. A. Whan, “Temperature Programmed Reduction of Alumina-Supported Iron, Cobalt and Nickel bimetallic catalysts,” *Appl. Catalysis*, vol. 3, issue 2, pp.177-186, July 1982.

[81] H. J. Wan, B. S. Wu , C. H. Zhang, H. W. Xiang ,Y. W. Li, B. F. Xu and F. Yi, “Study on Fe–Al_2O_3 interaction over precipitated iron catalyst for Fischer–Tropsch synthesis,” *Catalysis Commun.*, vol. 8, issue 10, pp.1538–1545, Oct. 2007.

[82] K. W. Kolasinski, *Surface Science: Foundation of Catalysis and Nanoscience*, 2nd ed. West Sussex, United Kingdom: Wiley-Interscience, 2008, pp. 452-454.

[83] *Adsorption of gases on solid* [Online]. Available: http://www.ece.eng.wayne.edu/~jchoi/Adsorption%20of%20gases%20on%20solids.pdf.

[84] K. Tock. (1999). *The Crossover* [Online]. Available: http://www.web.tock.com.

[85] R. S. Swathi and K. L. Sebastian, "Molecular Mechanism of Heterogeneous Catalysis, General Article: The 2007 Nobel Prize in chemistry," *Humanities, Social Sci. and Law*, vol.13, no. 6, pp. 548-560, June 2008.

[86] L. M. Falicov and G. A. Somorjai, "Correlation between catalytic activity and bonding and coordination number of atoms and molecules on transition metal surfaces: Theory and experimental evidence," in *Proc. Of the National Academy Sciences*, USA, vol.82, no. 8, 1985, pp. 2207-2211.

[87] J. Hagen, *Industrial catalysis: a practical approach*, 2nd ed. Weinheim, Germany: Wiley-Interscience, 2006, pp. 189-192.

[88] P. C. J. Kamer, G. Rothenberg, E. K. Poels and D. S. Brands. (2002, Jan). The Synthesis of Ammonia, Supplementary information for the course: Catalysis, Theory and Applications [Online]. Available: http://www.science.uva.nl/~gadi/pdf_files/Ammonia _synthesis.pdf.

[89] *Collision Theory* [Online]. Available: http://chemicalparadigms.wikispaces.com.

[90] L. M. Aparicio and J. A. Dumesic, "Ammonia synthesis kinetics: Surface chemistry, rate expressions, and kinetic analysis," *Topics in Catalysis*, vol. 1, no. 3-4, pp. 233-252, Sept. 1994.

[91] *Uses and Production of Ammonia (Haber Process)* [Online]. Available: http://www.ausetute.com.au.

[92] J. M. Modak. (2002). *9.4 Chemical Monitoring and Management: 2. Maximize Production* [Online]. Available: http://www.hsc.csu.edu.au.

[93] G. R. Maxwell, *Synthetic Nitrogen Products: A Practical Guide to Products and Processes*, 1st ed. Spring Street, New York: Kluwer Academic/Plenum Publishers, 2005.

[94] P. Moggi, G. Albanesi, G. Predieri and G. Spoto, "Ruthenium cluster-derived catalysts for ammonia synthesis," *Appl. Catalysis A: General*, vol. 123, issue 1, pp. 149-159, March 1995.

[95] J. Iwamoto, M. Itoh, Y. Kajita, M. Saito and K. Machida, "Ammonia synthesis on magnesia supported ruthenium catalysts with mesoporous structure," *Catalysis Commun.*, vol. 8, issue 6, pp. 941-944, June 2007.

[96] Laboratory of Ohba. (2010, March 12). *Crystal Structures* [Online]. Available: http://www.geocities.jp/ohba_lab_ob_page.

[97] G. D. Christian, *Analytical Chemistry*, 6th ed. Washington: John Willey & Sons Incorporation, 2003.

[98] A. C. Oliveira, A. Valentini, P. S. S. Nobre and M. C. Rangel, “Influence of The Starting Materials on The Catalytic Properties of Iron Oxides,” *Reaction Kinetics Catalysis Lett.*, vol. 75, no. 1, pp. 135-140, Aug. 2002.

[99] The Linde Group. (2008). *Gas Chromatography* [Online]. Available: http://www.hiq.lind-gas.com.

[100] H. Z. Liu, X. N. Li and Z. N. Hu, “Development of novel low temperature and low pressure ammonia synthesis catalyst,” *Appl. Catalysis A: General*, vol. 142, issue 2, pp. 209-222, Aug. 1996.

[101] N. Pernicone, F. Ferrero, I. Rosetti, L. Forni, P. Canton, P. Riello, G. Fagherazzi, M. Signoretto and F. Pinna, “Wustite as a new precursor of industrial ammonia synthesis catalysts,” *Appl. Catalysis A: General* vol. 251, issue 1, pp. 121-129, Sept. 2003.

[102] N. Yahya, S. M. S. N. S. Zahari, A. Ramli, N. M. Mohamad, P. Puspitasari and N. L. C. Zul, “Synthesis And Characterization Of Zinc Oxide Nanoparticles Prepared Via Precipitation And Self-Combustion Methods,” in *2009 AIP Conf. Proc*., vol. 1136, pp. 401-405.

[103] J. C. Huie, “Guided molecular self-assembly: a review of recent efforts,” *Smart Mater. Struct.*, vol. 12, issue 2, pp. 264, Apr. 2003.

[104] D. Brandon and W. D. Kaplan, *Microstructural Characterization of Materials*, 1st ed. Michigan: Johns Willey & Sons Publication, 1999.

[105] T. Bolhuis (1997, September 9). *Vector Vibrating Sample Magnetometer* [Online]. Available: http://www.el.utwente.nl.

[106] F. J. Owens and J. Orosz, “Effect of nanosizing on lattice and magnon modes of hematite,” *Solid State Commun.*, vol. 138, issue 2, pp. 95-98, Apr. 2006.

[107] C. J. Sartoretti, M. Ulmann and B. Alexander, “La photolyse de l’eau et la production et d’oxygene au moyen de l’energie solaire,” Univ. de Geneva, Geneva, Switzerland, Rep. JB06_152152-101747, Nov. 2006.

[108] G. Wang, X. Y. Chen, R. Huang and L. Zhang, “Nano-$CaCO_3$/polypropylene composites made with ultra-high-speed mixer,” *J. Material Sci. Lett.*, vol. 21, no. 13, pp. 985-986, July 2002.

[109] T. Adschiri, Y. Hakuta, K. Sue and K. Arai, “Hydrothermal synthesis of metal oxide nanoparticles at supercritical conditions,” *J. Nanoparticle Research*, vol. 3, no. 2-3, pp. 227-235, June 2001.

[110] C. Livage, A. Safari and L. C. Klein, “Glycol based sol-gel process for the fabrication of ferroelectric PZT thin films,” *J. Sol-Gel Sci. and Technology*, vol. 2, no. 1-3, pp. 605-609, Jan. 2004.

[111] C. Luo, Y. Zhang, X. Zeng, Y. Zeng and Y. Wang, “The role of poly(ethylene glycol) in the formation of silver nanoparticles,” *J. Colloid and Interface Sci.*, vol. 288, issue 2, pp. 444-448, Aug. 2005.

[112] J. C. Yang and Y. G. Shul, “Effects of ethylene glycol addition on the properties of Ru/Al_2O_3 catalyst prepared by solo-gel method,” *Catalysis Lett.*, vol. 36, issues 1-2, pp. 41-49, Aug. 1996.

[113] F. Mizukami, “Design of solid catalysts by sol-gel method using organic polydentate ligands and their catalytic performance,” *J. Japan Petroleum Inst*, vol. 51, no. 6, pp. 332-347, June 2008.

[114] N. Takahashi, N. Kakuta, A. Ueno, K. Yamaguchi, T. Fujii, “Characterization of iron oxide thin film prepared by the sol gel method,” *J. Materials Sci.*, vol. 26, no. 2, pp. 497-504, Feb. 1991.

[115] Z. Jiang, Q. Niu and W. Deng, “Hydrothermal synthesis of CuO nanostructures with novel shapes,” *Nanoscience*, vol. 12, no. 1, pp. 40-44, May 2007.

[116] N. R. E. Radwan, E. A. El-Sharkawy and A. M. Youssef, “Influence of gold and manganese as promoters on surface and catalytic performance of Fe_2O_3/Al_2O_3 system,” *Appl. Catalysis A: General*, vol. 281, issues 1-2, pp. 93-106, March 2005.

[117] M. J. Tiernan, P. A. Barnes and G. M. B. Parkes, “Reduction of Iron Oxide Catalysts: The Investigation of Kinetic Parameters Using Rate Perturbation and Linear Heating Thermoanalytical Techniques,” *J. Physical Chemistry. B***,** vol. 105, no. 1, pp. 220-228, Dec. 2001.

[118] M. Boudart, A. Delbouille, J.A. Dumesic, S. Khammouma and H. Topsøe, “Surface, catalytic and magnetic properties of small iron particles : I. Preparation and characterization of samples,” *J. Catalysis,* vol. 37, issue 3, pp. 486-502, June 1975.

[119] A. J. H. M. Kock, H. M. Fortuin and J. W. Geus, “The reduction behavior of supported iron catalysts in hydrogen or carbon monoxide atmospheres,” *J. Catalysis.,* vol. 96, issue 1, pp. 261-275, Nov. 1985

[120] A. F. H. Wielers, A. J. H. M. Kock, C. E. C.A. Hop, J. W. Geus and A. M. van der Kraan, “The reduction behavior of silica-supported and alumina-supported iron catalysts: A Mössbauer and infrared spectroscopic study,” *J. Catal*ysis, vol. 117, issue 1, pp. 1-18, May 1989.

[121] C. H. Zhang, Y. Yang, B. T. Teng, T. Z. Li, H. Y. Zheng, H. W. Xiang and Y. W. Li, “Study of an iron-manganese Fischer–Tropsch synthesis catalyst promoted with copper,” *J. Catalysis*, vol. 237, issue 2, pp. 405, Jan. 2006.

[122] D. R. Strongin and G. A. Somorjai, “The effects of potassium on an ammonia synthesis over iron single-crystal surfaces,” *J. Catalysis*, vol. 109, pp. 51-60, 1998.

[123] L. Xiaonian, L. Huazhang, C. Yaqing and H. Zhangneng, “Analysis on Ammonia Synthesis Over Wustite-Based Iron Catalyst,” *Chinese J. Chem. Eng*, vol. 11, no. 1, pp. 19-26, Jan. 2003.

[124] L. Huazhang and L. Xiaonian, “Precursor of Iron Catalyst for Ammonia Syntheses: Fe_3O_4, Fe1-xO, Fe_2O_3 or Their Mixture,” *Studies in Surface Science and Catalysis*, vol. 130, pp. 2207-2212, July 2000.

[125] N. Homs, P. R. D. L. Piscina, “Iron-Based Ammonia Synthesis Catalysts Prepared via Non-Oxidic Precursors”, *Applied Catalysis*, vol. 59, pp. 249-265, March 1990.

APPENDIX A

AMMONIA YIELD QUANTIFICATION

A.1 5% α-Fe_2O_3/γ-Al_2O_3

Table A1 : Effect of magnetic field and various reaction temperatures on ammonia yield produced in presence of α-Fe_2O_3 nanocatalyst. T=30°C-190°C, P = 1 am, H-F = 1 T, Cat. = 0.2 g, GHSV = 12000 $cm^3/g_{cat}.h$, F = 40 cm^3/min, $H_2:N_2$ = 3:1. The ammonia yield was collected for 30 mins at each temperature.

Table A1.1: Ammonia yield produced in the presence of 5% α-Fe_2O_3/γ-Al_2O_3 nanocatalyst synthesized at $Fe(NO_3)_3$:Surf ratio of 2:1

Time (min)	V_{NaOH} (mL)	$Mole_{NH3}$ (mole)	NH_3 Yield (%)
0	22.75	2.25×10^{-6}	0.23
30	20.17	4.83×10^{-6}	0.49
60	17.68	7.32×10^{-6}	0.74
90	15.48	9.52×10^{-6}	0.97
120	12.94	1.21×10^{-5}	1.23
150	10.61	1.44×10^{-5}	1.46
180	8.11	1.69×10^{-5}	1.72
210	5.46	1.95×10^{-5}	1.99
240	2.66	2.23×10^{-5}	2.27

Chemicals used:

Hydrochloric acid, HCl : Volume = 25 mL , [HCl] = 0.001 M

Sodium hydroxide, NaOH : [NaOH] = 0.001

A.1. Quantification of Ammonia

A.1.1 Chemical equations:

$NH_3 + HCl \rightarrow NH_4Cl$ (A.1.1)

The excess HCl was back titrated using NaOH:

$HCl_{Excess} + NaOH \rightarrow NaCl + H_2O$(A.1.2)

A.1.2 Calculations:

1. Mole of HCl_{Excess} = Mole of $NaOH_{Titrated}$ (Equation A.1.1)

   = 0.01M x volume of $NaOH_{Titrated}$

2. Mole of $HCl_{Reacted}$ = Mole (HCl_{Total} –HCl_{Excess})

   = Mole of NH_3

<u>A.2. Ammonia Yield (%)</u>

A.2.1. Chemical equation:

$N_2 + 3H_2 \leftrightarrow 2NH_3$ (A.2.1)

A.2.2. Calculations:

1. Mole of N_2 used = 4.92×10^{-4} mol (Limiting reactant)
2. Mole of H_2 used = 1.47×10^{-3} mol
3. Theoretical mole of NH3 based on Equation A.2.1

   = 2 x mole of N_2

   = 9.84×10^{-4} mol

5. Ammonia yield (%) = (mole actual/mole theoretical) x 100%

Table A1.2: Example of calculation to quantify ammonia yield produced in the presence of 5% α-Fe_2O_3/γ-Al_2O_3 nanocatalyst synthesized at $Fe(NO_3)_3$:Surf ratio of 2:1.

Time (min)	V_{NaOH} (mL)	Mole of NaOH (μmol) = Mole of HCl_{excess} (μmol)	Mole of $HCl_{Reacted}$ (μmol) = Mole of NH_3 (μmol)	Ammonia Yield (%)
0	22.75	= 0.001M x (22.75 mL/1000L) = 2.275 x 10^{-5} mol	= 2.5 x 10^{-5} – 2.275 x10^{-5} = 2.25 x 10^{-6}	= (2.25 x 10^{-6} /9.84 x 10^{-4}) x 100% = 0.23%
30	20.17	= 0.001M x (20.17 mL/1000L) = 2.017 x 10^{-5} mol	= 2.5 x 10^{-5} – 2.017 x10^{-5} = 4.83 x 10^{-6}	= (4.835 x 10^{-6} /9.84 x 10^{-4}) x 100% = 0.49%
60	17.68	= 0.001M x (17.68 mL/1000L) = 1.768 x 10^{-5} mol	= 2.5 x 10^{-5} – 1.768 x10^{-5} = 7.32 x 10^{-6}	= (7.32 x 10^{-6} /9.84 x 10^{-4}) x 100% = 0.74%
90	15.48	= 0.001M x (15.48 mL/1000L) = 1.548 x 10^{-5}	= 2.5 x 10^{-5} – 1.548 x10^{-5} = 9.52 x 10^{-6}	= (9.52 x 10^{-6} /9.84 x 10^{-4}) x 100% = 0.97%
120	12.94	= 0.001M x (12.94 mL/1000L) = 1.294 x 10^{-5}	= 2.5 x 10^{-5} – 1.294 x10^{-5} = 1.21 x 10^{-6}	= (1.21 x 10^{-6} /9.84 x 10^{-4}) x 100% = 1.23%
150	10.61	= 0.001M x (10.61 mL/1000L) = 1.061 x 10^{-5}	= 2.5 x 10^{-5} – 1.061 x10^{-5} = 1.439 x 10^{-6}	= (1.439 x 10^{-6} /9.84 x 10^{-4}) x 100% = 1.46%

180	8.11	= 0.001M x (8.11 mL/1000L) $= 0.811 \times 10^{-5}$	$= 2.5 \times 10^{-5} - 0.811 \times 10^{-5}$ $= 1.689 \times 10^{-6}$	$= (1.689 \times 10^{-6} / 9.84 \times 10^{-4}) \times 100\%$ = 1.72%
210	5.46	= 0.001M x (5.46mL/1000L) $= 0.546 \times 10^{-5}$	$= 2.5 \times 10^{-5} - 0.546 \times 10^{-5}$ $= 1.954 \times 10^{-6}$	$= (1.954 \times 10^{-6} / 9.84 \times 10^{-4}) \times 100\%$ = 1.99%
240	2.66	= 0.001M x (2.66 mL/1000L) $= 0.266 \times 10^{-5}$	$= 2.5 \times 10^{-5} - 0.266 \times 10^{-5}$ $= 2.234 \times 10^{-6}$	$= (2.234 \times 10^{-6} / 9.84 \times 10^{-4}) \times 100\%$ = 2.27%

APPENDIX B

CALCULATION OF ACTIVATION ENERGY

Formula

B.1. Rate of Ammonia Production

Rate = mole of ammonia produced / (mass of catalyst (g) x duration of reaction (t))

= $mole_{NH3}/g_{cat}.h$

B.2. K_A and K_B [89]

Based on equations proposed by Aparicio et al. [90] at T = 251 ^oC and P = 1 atm

k_A = 3.289 exp [(50690 J/mol)/RT]

k_B = 7.35 x 10^{12} exp [(-59040 J/mol)/RT]

Where,

k_A = Rate constant for the formation of ammonia

k_B = Rate constant for the decomposition of ammonia

B.3. Von't Hoff's Equation [10]

$\ln (K_{T1}/K_{T2}) = \Delta H/R\ (1/T_1 - 1/T_2)$

Where,

T = Temperature (K)

K = Equilibrium constant

ΔH = Heat of ammonia production = -92 kJ/mole

R = Gas constant (J/mol.K) = 8.314 J/mole.K

B.4. Ideal Gas Law [10]

PV = nRT

Where,

P= Pressure (atm)

V = Volume (L)

R = Gas constant = 0.0821 L.atm/mol. K

n = Number of mole

T = Temperature (K)

B.5. Mole fraction of component [10]

X_A = no. mol A / (∑ mol of all components)

B.6. Partial pressure of reactant/product [9]

$P_A = X_A \times P_{Total}$

Where,

P_A = Partial pressure of component A

X_A = Mole fraction of A

P_T = Total pressure

B.7. Temkin-Phyzev Equation [90], [101]

Rate ($mole_{NH3}/g_{cat}.h$) $= k_A P_{N2}[(P^3_{H2})/(P^2_{NH3})]^{\alpha} - k_B [(P^2_{NH3})/ (P^3_{H2})]^{1-\alpha}$

Where,

α is assumed = 0.75 [90], [101]

B.8. Arrhenius equation [10]

$k = Ae^{-Ea/RT}$

$\ln k = \ln A - E_a/RT$

Where,

k = Rate constant

A = Exponential factor

E_a = Activation energy

T = Temperature (K)

Calculation

Determination of reference k_A, k_B and K_{eq}.

Based on work done by Aparicio et al. [90] at T = 251 ^{o}C and P = 1 atm, using Equation B.2:

k_A = 3.289 exp [(50690 J/mol)/8.314 x (251+273)]

$= 3.717 \times 10^5$

$k_B = 7.35 \times 10^{12}$ exp [(-59.04kJ/mol)/8.314 x (251+273)]

$= 9.568 \times 10^6$

$K_{eq} = K_R = k_A/k_B = 0.038$

Hematite, α-Fe_2O_3 nanocatalyst in the presence of magnetic field.

T = 30^oC [$T_1 = 30^oC$ $T_2 = 251^oC$ (R)]

A. Rate of Ammonia Production

Using Equation B.1:

Rate = (300 µmole x $1x10^{-6}$) / (0.2 g x 0.5 h)

= 3.0×10^{-3} $mol_{NH3}/g_{cat}.h$

B. Determination of K_{30}

Using Equation B.3:

ln (K_{30}/0.038) = (92000 / 8.314) x (1.391 x 10^{-3})

ln K_{30}/0.038 = 15.40

$e^{\ln KT1/0.038} = e^{15.40}$

$K_{30/}$0.038 = 4.876 x10^6

K_{30} = 1.853 x 10^5

C. Determination of P_A

Mole of fed N_2 and H_2

Using Equation B.4:

n_{N2} = PV/RT

= (1.2 atm x 0.01 L)/(0.0821 L.atm/mol. K x 301 K)

= 4.920x10^{-4} mol

n_{H2} = (1.2 atm x 0.03 L)/(0.0821 L.atm/mol. K x 301 K)

= 1.476x10^{-3} mol

n_{NH3} obtained = 300µmol= 3 x 10^{-4} mol

Using equation B.5:

X_{N2} = (4.920x10^{-4} mol) / [(4.920x10^{-4} + 1.476x10^{-3} + 3 x 10^{-4}) mol]

= 0.216

X_{H2} = (1.476x10^{-3} mol) / [(4.920x10^{-4} + 1.476x10^{-3} + 3 x 10^{-4}) mol]

= 0.650

X_{NH3} = (3 x 10^{-4}mol) / [(4.920x10^{-4} + 1.476x10^{-3} + 3 x 10^{-4}) mol]

= 0.130

Using equation B.6:

P_{N2} = 0.216 x 1atm = 0.216 atm

P_{H2} = 0.650 x 1 atm = 0.650 atm

P_{NH3} = 0.130 x 1 atm = 0.130 atm

D. Determination of k_A

Using Equation B.7:

$3 \times 10^{-3} = k_A(0.216)[(0.65)^3/(0.13)^2]^{0.75} - k_B[(0.13)^2/(0.65)^3]^{1-0.75}$

$3 \times 10^{-3} = 1.74\ k_A - 0.49\ k_B$

$= 1.74\ k_A - 0.49\ (k_A/K_{30})$

$k_A = 1.724 \times 10^{-3}\ g_{cat}^{-1}.h^{-1}$

APPENDIX C

CALCULATION OF IRON LOADING

C.1 Preparation of 5% α-Fe_2O_3/γ-Al_2O_3 Catalyst in Absence of Sodium Bis(2-ethylhexyl) Sulfosuccinate

Total weight of 5% α-Fe_2O_3/γ-Al_2O_3 catalyst = 2.0 g

5% α-Fe_2O_3 = 5/ 100 x 2.0 g

= 0.1 g

From the chemical equation:

$2Fe(NO_3)_3 + HNO_3 \rightarrow \alpha\text{-}Fe_2O_3$(Equation C.1)

Mole of α-Fe_2O_3 = Mass of α-Fe_2O_3 (g) / MRM of α-Fe_2O_3 ($gmole^{-1}$)

= 0.1 g/159.69 $gmole^{-1}$

= 6.262×10^{-4} moles

Based on Equation C.1:

Mole of $Fe(NO_3)_3$ = 2 mol $Fe(NO_3)_3$: 1 mole α-Fe_2O_3

= ½ x mole of α-Fe_2O_3

= 3.131×10^{-4} moles

Mass of $Fe(NO_3)_3$ = Mole of $Fe(NO_3)_3$ / MMR of $Fe(NO_3)_3$ ($gmole^{-1}$)

= 3.131×10^{-4} moles x 241.86 $gmole^{-1}$

= 0.075 g

Mass of $Fe(NO_3)_3.9H_2O$ required = MRM [($Fe(NO_3)_3.9H_2O$/$Fe(NO_3)_3$)]x Mass of $Fe(NO_3)_3$

= [404.2 $gmole^{-1}$/241.86 $gmole^{-1}$] x 0.075 g

= 0.125 g

C.2 Calculation of Iron (III) Nitrate to Sodium Bis(2-ethylhexyl) Sulfosuccinate (SBS) Ratio

A. Iron (III) nitrate to sodium bis(2-ethylhexyl) sulfosuccinate ratio of 2:1

Mole of $Fe(NO_3)_3$ = 0.075 g / 241.86 $gmole^{-1}$
= 3.131×10^{-4} moles

The mole ratio of $Fe(NO_3)_3$:SBS is 2:1

Mole of SBS surfactant = 1/2 x 3.131×10^{-4} moles
= 1.565×10^{-4} moles

Mass of SBS surfactant = 1.565×10^{-4} moles x 444.56 $gmole^{-1}$
= 0.069 g

B. Iron (III) nitrate to sodium bis(2-ethylhexyl) sulfosuccinate ratio of 2:2

Mole of $Fe(NO_3)_3$ = 0.075 g / 241.86 $gmole^{-1}$
= 3.131×10^{-4} moles

The mole ratio of $Fe(NO_3)_3$:SBS is 2:2

Mole of SBS surfactant = 3.131×10^{-4} moles

Mass of SBS surfactant = 3.131×10^{-4} moles x 444.56 $gmole^{-1}$
= 0.139 g

C. Iron (III) nitrate to sodium bis(2-ethylhexyl) sulfosuccinate ratio of 2:3

Mole of $Fe(NO_3)_3$ = 0.075 g / 241.86 $gmole^{-1}$
= 3.131×10^{-4} moles

The mole ratio of $Fe(NO_3)_3$:SBS is 2:3

Mole of SBS surfactant = 3/2 x 3.131×10^{-4} moles
= 4.696×10^{-4} moles

Mass of SBS surfactant = 4.696×10^{-4} moles x 444.56 $gmole^{-1}$
= 0.208 g

APPENDIX D

X-RAY DIFFRACTION

D.1 X-Ray diffraction spectra

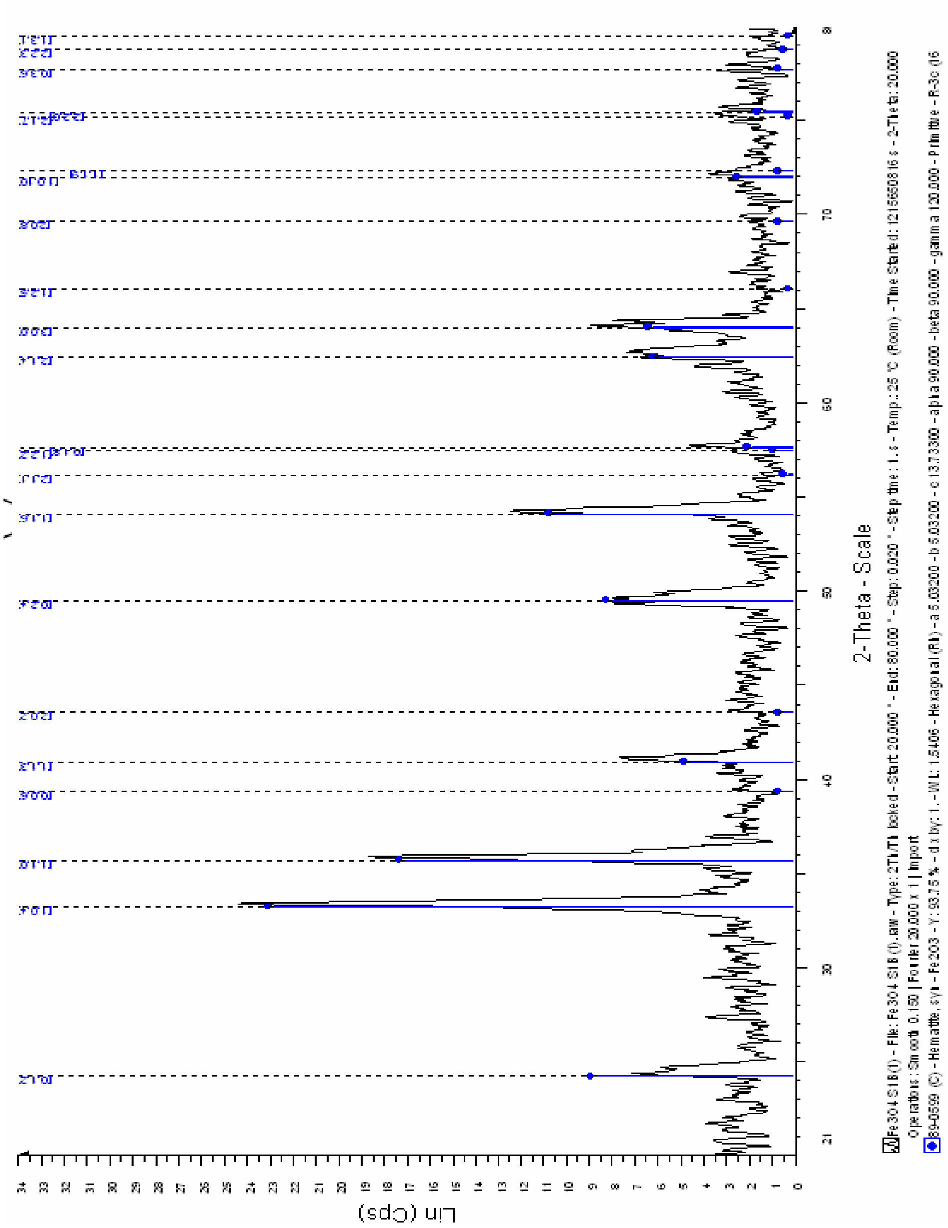

Figure D.1.1 : XRD spectrum of α-Fe_2O_3 nanocatalyst prepared via sol gel method, stirred at 1 day and annealed at 300^oC in atmospheric environment.

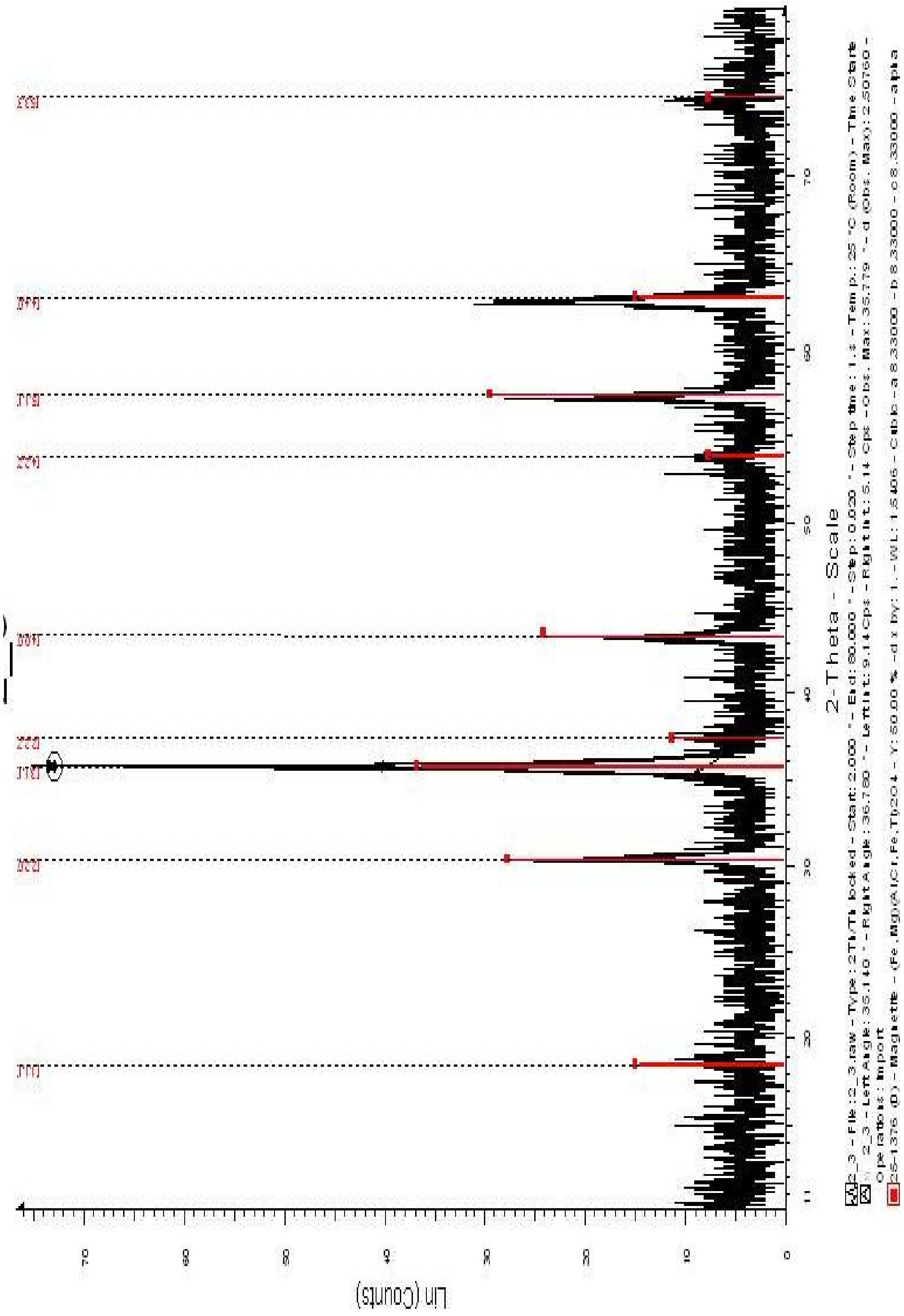

Figure D.1.2 : XRD spectrum of Fe_3O_4 nanocatalyst prepared via sol gel-hydrothermal method 160°C for 10 hours day and annealed at 400°C in vacuum flow.

D.2 Average crystallite size calculation

Table 4.22: XRD data of Fe_3O_4 nanocatalysts prepared via sol gel-hydrothermal method at different annealing temperatures. The interpretation was based on (311) major plane.

Annealing temperature (^oC)	200	300	400
2θ (Degree)	35.46	35.61	35.78
Intensity (a.u)	61.00	52.60	73.00
D-spacing (Å)	2.5294	2.5189	2.5076
FWHM	0.447	0.451	0.268
Average crystallite size(nm)	19.00	18.84	31.73

D.2.1. Formula:

A. Average Crystallite Size, d (nm) = $k\lambda / \beta \cos\theta$ [39]

Where,

k = Shape factor

λ = Wavelength of x-ray

θ = Diffracted angle

β = Full width half maximum of the major peak

B. β (FWHM) = (β x 2π) / 360^o

C. Values

k = 0.916 [39]

λ_{Cu} = 1.54178×10^{-10} m

1 nm = 1×10^{-9} m

D.2.2. Calculation

(^{o}C)	k λ	$\beta = (\beta x 2\pi)/360^{o}$	β cos θ	*d* (nm)
200	$=0.916 \text{ x } 1.54178\text{x}10^{-10}$ $=1.4122\text{x}10^{-10}$	$=(0.447\text{x}2\pi)/360^{o}$ $=7.801\text{x}10^{-3}$	$=(7.801\text{x}10^{-3})\cos 17.73^{o}$ $=7.430\text{x}10^{-3}$	19.00
300	$=0.916 \text{ x } 1.54178\text{x}10^{-10}$ $=1.4122\text{x}10^{-10}$	$=(0.451\text{x}2\pi)/360^{o}$ $=7.871\text{x}10^{-3}$	$=(7.871\text{x}10^{-3}) \cos 17.80$ $=7.494\text{x}10^{-3}$	18.84
400	$=0.916 \text{ x } 1.54178\text{x}10^{-10}$ $=1.4122\text{x}10^{-10}$	$=(0.268\text{x}2\pi)/360^{o}$ $=4.677\text{x}10^{-3}$	$=(4.677\text{x}10^{-3}) \cos 17.89$ $=4.450\text{x}10^{-3}$	31.73

APPENDIX E

TEMPERATURE PROGRAMMED REDUCTION

E.1 TPR Data of α-Fe_2O_3 Nanocatalyst Prepared via Sol Gel Method, Stirred at 1 day and Annealed at 300^oC

TPD/R/O 1100 Thermo Electron

Standard Data Report

1.1 Run Nr.: 1203

File:D:\Data 2\shahrul\unsupported Fe2O3\ANNEALED EFFECT\a-Fe2O3- S1-1-300oC annelaed.110
Info:
Operator: Shahrul Room Temperature 28°C Atmospheric Pressure 1000hPa

1.2 Sample

Producer:	shahrul	Sample-Code:	0
Name:	a-Fe2O3	Customer-Code:	0
Mass:	0.1313 g	Support:	
Info:		Metals:	1
Preparation:	Sol gel-annealed at 300oC	0%	Iron

1.3 Pretreatment

Method Name: not defined or external pretreatment Info:
On Instrument: with Ser.Nr. on ,
Started at finished
Gas Port when Ready: (a) Nitrogen
Gas Port when End: (a) Nitrogen
Sample rate: 1 s
Gain: 10
Polarity: +

Phase	With Gas	Flow [ccm/min]	Start at T [°C]	Ramp [°/min]	Stop at T [°C]	Hold for [min]
Cleaning		0	Off			0
1:	Off					
2:	Off					
3:	Off					
4:	Off					
End Pretreatment with Oven Off						

1.4 TPD/R/O

Method Name: a-Fe2O3 Info:

On Instrument: TPDRO1100 MS with Ser.Nr.20022897 on Right Oven
Started 7/13/2009 at 2:24:35 PM finished 4:12:01 PM

With gas: Hydrogen 5.1% in Nitrogen and flow of 20 ccm/min
Start at 40 °C, heating rate 10 °/min, stop at 800 °C, hold for 30 min
Temperature at end of experiment 40 °C

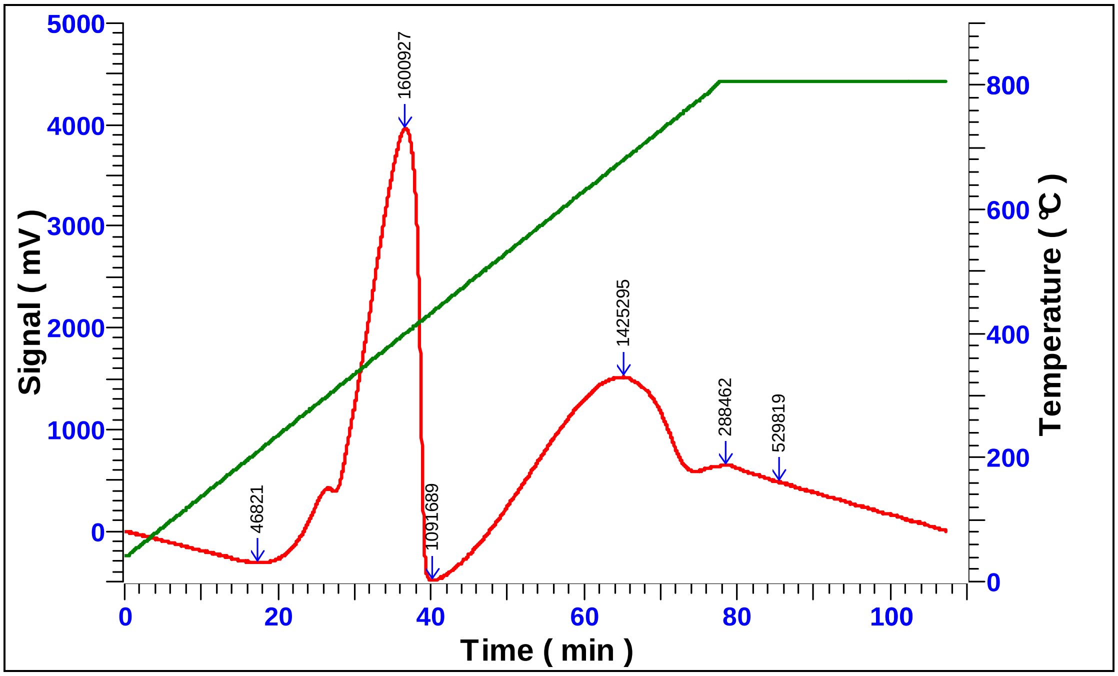

Results

Amount gas adsorbed :0.00000 µmol/g
Stoichiometric factor :0
Amount of metal reacted :0.00000 µmol/g (sample)
Total metal surface :0.000 m^2
Metal surface :0.000 m^2/g (sample)
0.0 m^2/g (metal)
0.000 m^2/g (support)
Dispersion degree :0.000%
Mean particle diameter :0.000 nm (spheres)
Total Metal :0.000 %

1.5 Baseline

Start at 0.0167 min -0.61035 mV, Stop at 107.2667 min 2102.96631 mV

1.6 Calibration

Use Calibration Factor: 0.000000 $\cdot 10^{-9}$ mmol/mVs

1.7 Peaks

#	Start[min]	Stop[min]	Maximum[min]	T[°C]	Integral[mVs]	[%]	[µmol/g]
1	16.9500	26.4833	17.3167	209	46820.81	0.94	0.00000
2	27.6333	40.1000	36.6667	400	1600927.49	32.13	0.00000
3	36.9167	64.6167	40.1500	434	1091688.88	21.91	0.00000
4	40.6833	74.0667	65.2333	681	1425294.58	28.60	0.00000
5	77.1500	85.4333	78.5000	806	288461.52	5.79	0.00000
6	79.0500	106.9167	85.4667	806	529819.46	10.63	0.00000

E.2 TPR Data of Fe_3O_4 Nanocatalyst Prepared via Sol Gel-Hydrothermal Method at 160°C

TPD/R/O 1100 **Thermo** Electron

Standard Data Report

1.8 Run Nr.: 688

File:C:\SHAHRUL_MSC\DEC 2009\Fe3O4\160\Fe3O4_160_200 IN AR_3.110
Info:
Operator: SHAHRUL Room Temperature 28°C Atmospheric Pressure 1000hPa

1.9 Sample

Producer:	SHAHRUL	Sample-Code:	0
Name:	Fe3O4_160_200 IN AR_3	Customer-Code:	0
Mass:	0.0507 g		
		Support:	
Info:		Metals:	1
Preparation:	SOL GEL-HYDROTHERMAL	0%	Iron

1.10 Pretreatment

Method Name: Pre Jan 2010 Info:
On Instrument: TPDRO 1100 with Ser.Nr.20033057 on Left Oven,
Started 1/20/2010 at 8:54:06 AM finished 10:22:02 AM
Gas Port when Ready: (a) Nitrogen
Gas Port when End: (a) Nitrogen
Sample rate: 1 s
Gain: 10
Polarity: +

Phase	With Gas	Flow [ccm/min]	Start at T [°C]	Ramp [°/min]	Stop at T [°C]	Hold for [min]
Cleaning	Nitrogen	20		Off		10
1:	Nitrogen	20	Off	10	300	30
2:	Off					
3:	Off					
4:	Off					
End Pretreatment with Oven Off						

1.11 TPD/R/O

Method Name: SHAHRUL_NEW Info:
On Instrument: TPDRO 1100 with Ser.Nr.20033057 on Left Oven
Started 1/20/2010 at 11:05:16 AM finished 12:52:54 PM

With gas: Hydrogen 5% in Nitrogen and flow of 20 ccm/min
Start at 40 °C, heating rate 10 °/min, stop at 1000 °C, hold for 10 min
Temperature at end of experiment Oven Off

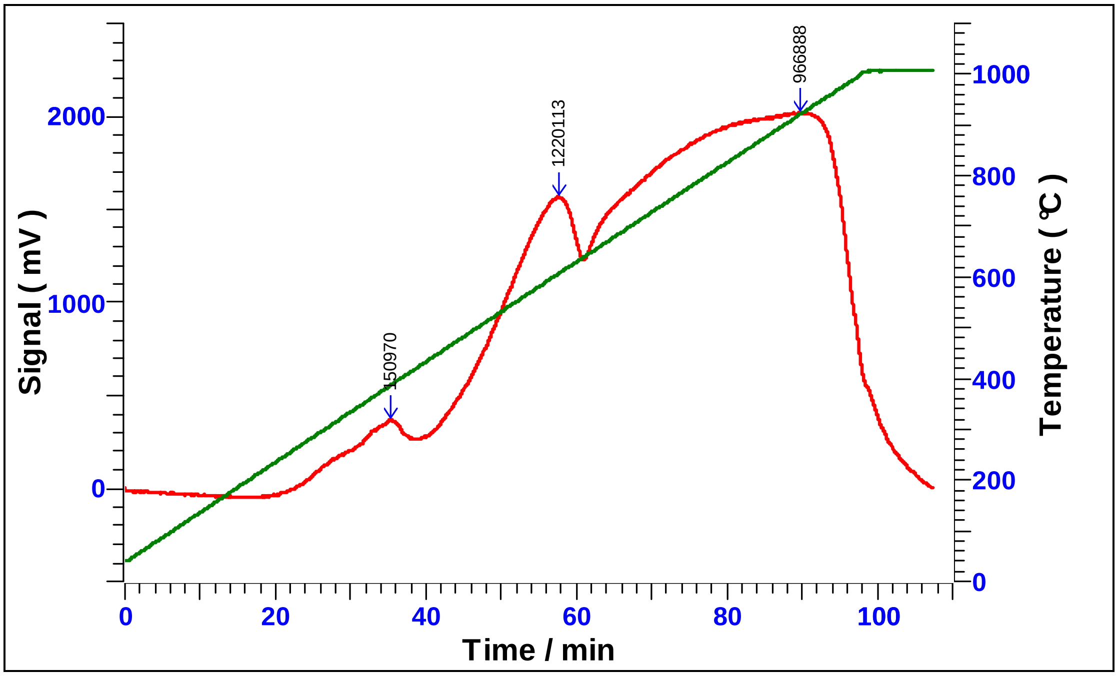

Results

Amount gas adsorbed : 3768.30600 µmol/g
Stoichiometric factor : 0
Amount of metal reacted : 0.00000 µmol/g (sample)
Total metal surface : 0.000 m^2
Metal surface : 0.000 m^2/g (sample)
0.0 m^2/g (metal)
0.000 m^2/g (support)
Dispersion degree : 0.000%
Mean particle diameter : 0.000 nm (spheres)
Total Metal : 0.000 %

1.12 Baseline

Start at 0.0167 min 11.85099 mV, Stop at 107.4667 min 267.28312 mV

1.13 Calibration

Use Calibration Factor: 81.717476 $\cdot 10^{-9}$ mmol/mVs

1.14 Peaks

#	Start[min]	Stop[min]	Maximum[min]	T[°C]	Integral[mVs]	[%]	[µmol/g]
1	29.3167	37.9667	35.3500	387	150969.53	6.46	243.33035
2	39.3833	60.8333	57.5833	606	1220113.36	52.19	1966.55980
3	89.4333	107.1167	89.8000	921	966888.42	41.36	1558.41580

E.3 TPR Data of 5% α-Fe_2O_3/γ-Al_2O_3 Nanocatalyst Prepared via Sol Gel-Hydrothermal Method, Stirred at 1 day and Annealed at 300°C

TPD/R/O 1100 **Thermo** Electron

Standard Data Report

1.15 Run Nr.: 892

File:C:\SHAHRUL_MSC\2010\APRIL\5%FeAl2O3\H2O BATCH\SURFACTANT\2_1\5%FeAl2O3_1 DAY_2_1_400 IN N2.110
Info:
Operator: SHAHRUL Room Temperature 28°C Atmospheric Pressure 1000hPa

1.16 Sample

Producer:	SHAHRUL	Sample-Code:	0
Name:	5%FeAl2O3_1 DAY_2_1_400 IN N2	Customer-Code:	0
Mass:	0.1208 g		
		Support:	alumina
Info:		Metals:	1
Preparation:	SOL GEL-HYDROTHERMAL	5%	Iron

1.17 Pretreatment

Method Name: Pre-shahrul Info:
On Instrument: TPDRO 1100 with Ser.Nr.20033057 on Left Oven,
Started 5/4/2010 at 10:23:38 AM finished 11:09:33 AM
Gas Port when Ready: (a) Nitrogen
Gas Port when End: (a) Nitrogen

Sample rate:	1	s
Gain:	10	
Polarity:	+	

Phase	With Gas	Flow [ccm/min]	Start at T [°C]	Ramp [°/min]	Stop at T [°C]	Hold for [min]
Cleaning	Nitrogen	20	40 °C			5
1:	Nitrogen	20	40	10	200	10
2:	Off					
3:	Off					
4:	Off					
End Pretreatment with Oven at 40°C						

1.18 PD/R/O

Method Name: TPR_SHAHRUL_800 Info:
On Instrument: TPDRO 1100 with Ser.Nr.20033057 on Left Oven
Started 5/4/2010 at 12:09:14 PM finished 1:36:18 PM

With gas: Hydrogen 5% in Nitrogen and flow of 20 ccm/min
Start at 40 °C, heating rate 10 °/min, stop at 800 °C, hold for 10 min
Temperature at end of experiment Oven Off

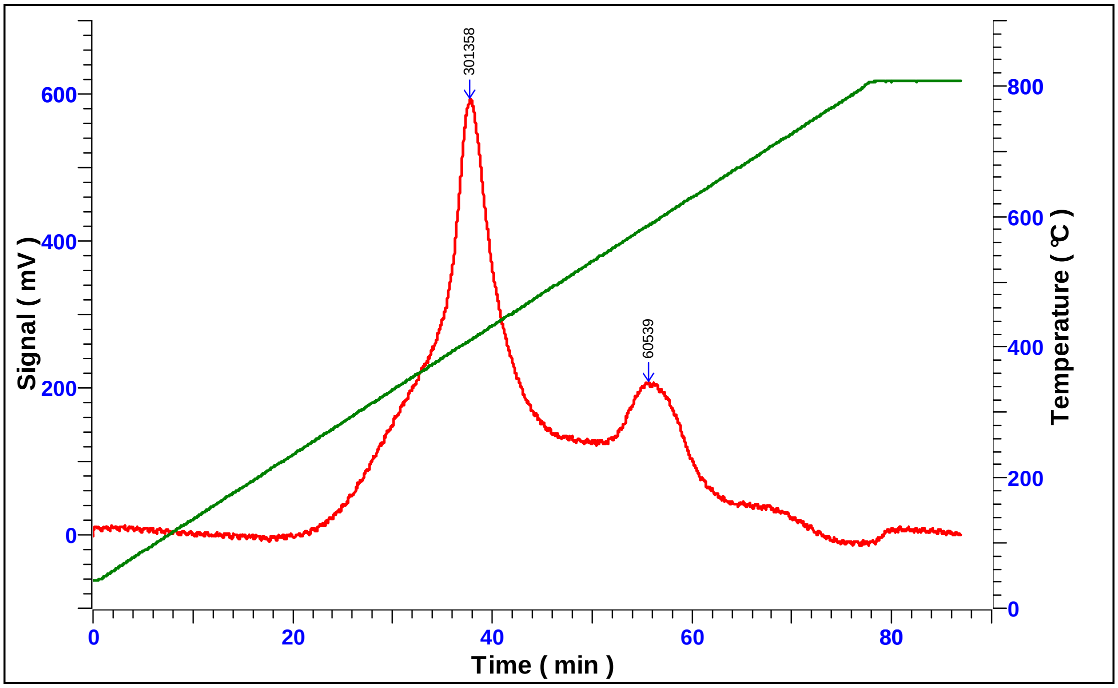

Results

Amount gas adsorbed : 209.16721 µmol/g
Stoichiometric factor : 2
Amount of metal reacted : 418.33441 µmol/g (sample)
Total metal surface :1.978 m^2
Metal surface :16.375 m^2/g (sample)
327.5 m^2/g (metal)
17.237 m^2/g (support)
Dispersion degree : 46.728%
Mean particle diameter : 2.331 nm (spheres)
Total Metal : 2.336 %

1.19 Baseline

Start at 0.0167 min -9.96908 mV, Stop at 86.9167 min 46.23413 mV

1.20 Calibration

Use Calibration Factor: 69.819292 ·10^{-9} mmol/mVs

1.21 Peaks

#	Start[min]	Stop[min]	Maximum[min]	T[°C]	Integral[mVs]	[%]	[µmol/g]
1	24.8500	45.3833	37.7667	411	301358.14	83.27	174.17725
2	55.2833	62.7667	55.6833	587	60538.94	16.73	34.98995

E.3.1 Example of Calculation

Percentage of Dispersion (%D) and Mean Particle Diameter (*d*)

E.3.1.1. Formula

Percentage of dispersion, % D = C_2X/fw [8]

Where,

C_2 = Constant

X = Chemisorptive H_2 uptake (μmol/g)

f = Fraction of active element present in metallic state

w = Weight percentage of the catalytic element present as either metal or oxide

E.3.1.2 Values

C_2 = 1.12 (Fe)

f = 100% (Assuming Fe particles reduced completely)

E.3.1.3 Calculation

% D = [1.12 x 209.16721 μmol/g] / [100(1) x (0.05)]

= 46.85 %

APPENDIX F

EDX ANALYSIS CALCULATION

Table F: EDX Data of α-Fe_2O_3 Nanocatalysts Prepared via Sol Gel Method at Different Stirring Periods Annealed at 300°C.

Method			1 day	1 week	1 month
Atomic (%)	Fe	Exp.	22.56	28.84	41.74
		Dev.	77.30	38.69	-4.16
	O	Exp.	31.35	71.16	58.26
		Dev.	91.38	-15.68	2.98
Weight (%)	Fe	Exp.	54.40	58.89	71.43
		Dev.	28.57	18.86	-2.08
	O	Exp.	31.58	41.40	28.57
		Dev.	-5.09	-37.80	4.92

A. Theoretical calculation based on α-Fe_2O_3

Atomic %

Fe = 2 Fe / (2 Fe + 3O)

= 2/5 x 100%

= 40%

O = 3O / (2 Fe + 3O)

= 3/5 x 100%

= 60%

Weight %

Fe = 2 x MRM for Fe ($gmole^{-1}$) / MRM ($gmole^{-1}$)[2Fe + 3O]

= 2(55.847) / [2(55.747)+3(15.994)]

= 0.70 x 100%

= 70%

O = 3 x MRM for O ($gmole^{-1}$) / MRM ($gmole^{-1}$) [2 Fe + 3O]

= 3(15.994) / [2(55.747)+3(15.994)]

= 30%

Atomic Percentage

Stirring period	Deviation (%) = (Theory – Experiment)/Experiment x 100%	
	Fe	O
1 day	= (40-22.56)/22.56 x 100% = 77.30%	=(60-31.35)/31.35x100% = 91.38%
1 week	= (40-28.84)/28.84 x 100% = 38.69%	=(60-71.16)/71.16x100% = -15.68%
1 month	= (40-41.74)/41.74 x 100% = -4.16%	=(60-58.26)/58.26x100% =2.98

Weight Percentage

Stirring period	Deviation (%) = (Theory – Experiment)/Experiment x 100%	
	Fe	O
1 day	=(70-54.40)/54.40x100% =28.67%	=(30-31.58)/31.58x100% =-5.00%
1 week	=(70-58.89)/58.89x100% =18.86%	=(30-41.40)/41.40x100% =-27.53%
1 month	=(70-71.43)/71.43x100% =-2%	=(30-28.57)/28.57x100% =5%

APPENDIX G

EDX-Elemental Mapping of Supported 5% α-Fe_2O_3/γ-Al_2O_3 Nanocatalysts

G.1.Supported 5% α-Fe_2O_3/γ-Al_2O_3 Nanocatalysts – Effect of Synthesis Period

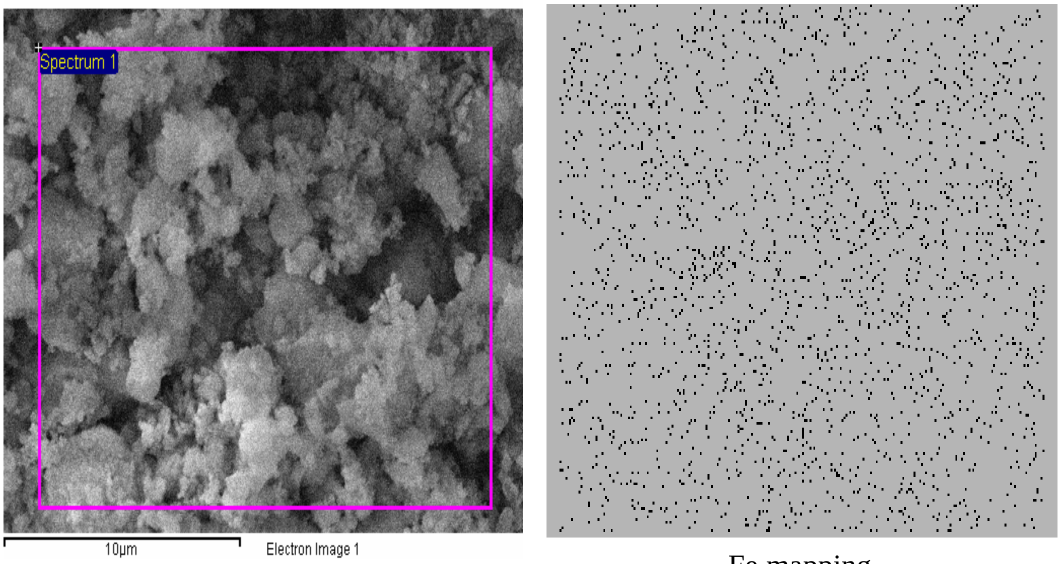

5% α-Fe_2O_3/γ-Al_2O_3

Fe mapping

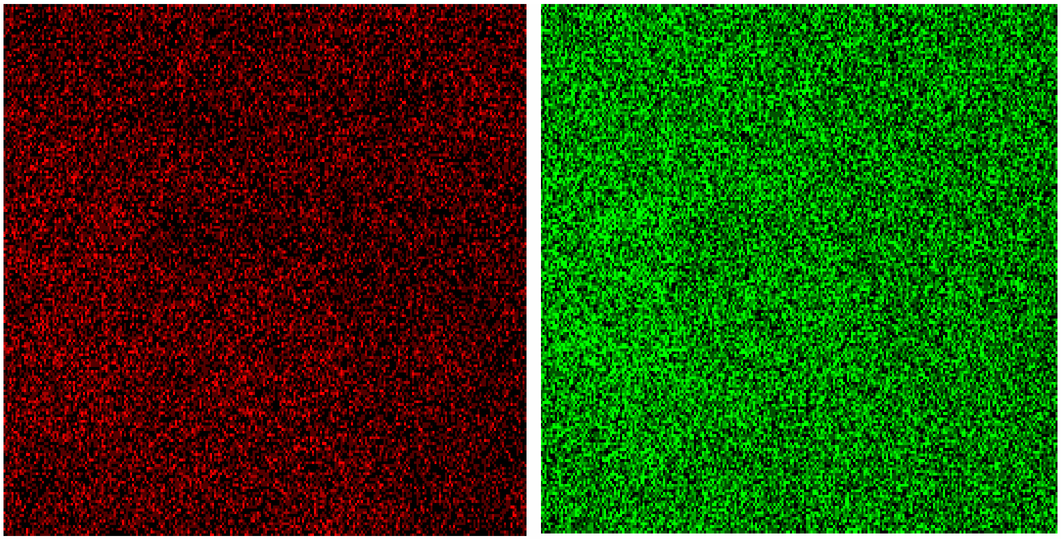

O mapping

Al mapping

Figure G.1.1: EDX mapping of 5% α-Fe_2O_3/γ-Al_2O_3 nanocatalyst prepared via sol gel-hydrothermal method in the absence of surfactant at 160°C for 1 hour.

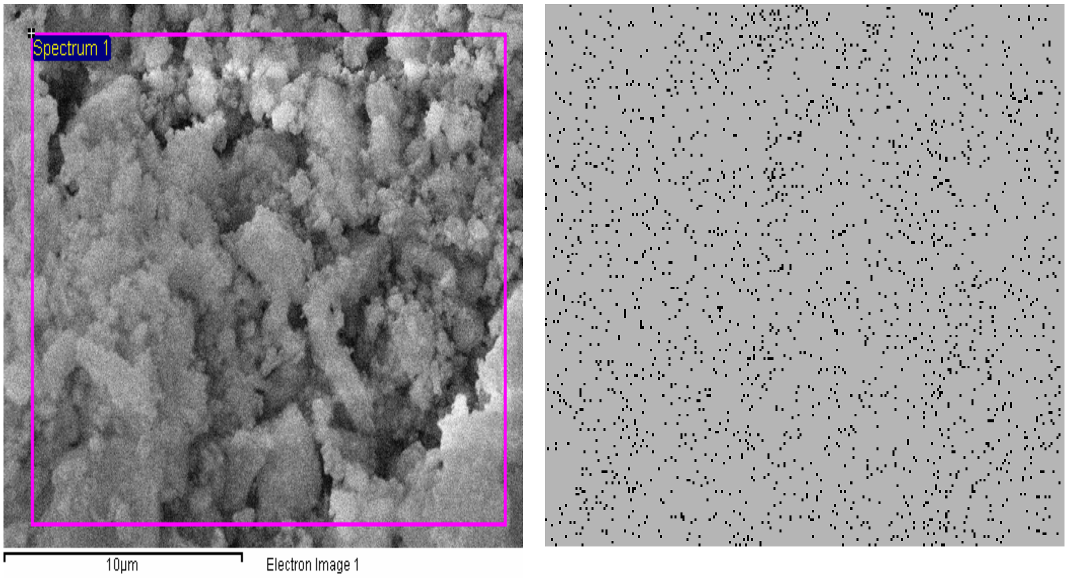

5% α-Fe_2O_3/γ-Al_2O_3 Fe mapping

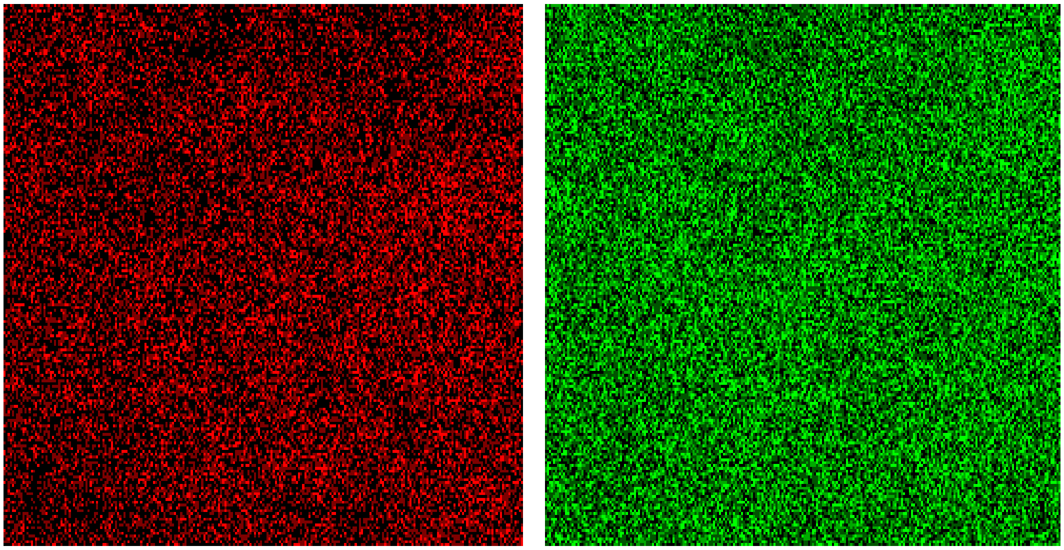

O mapping Al mapping

Figure G.1.2: EDX mapping of 5% α-Fe_2O_3/γ-Al_2O_3 nanocatalyst prepared via sol gel-hydrothermal method in the absence of surfactant at 160°C for 10 hours.

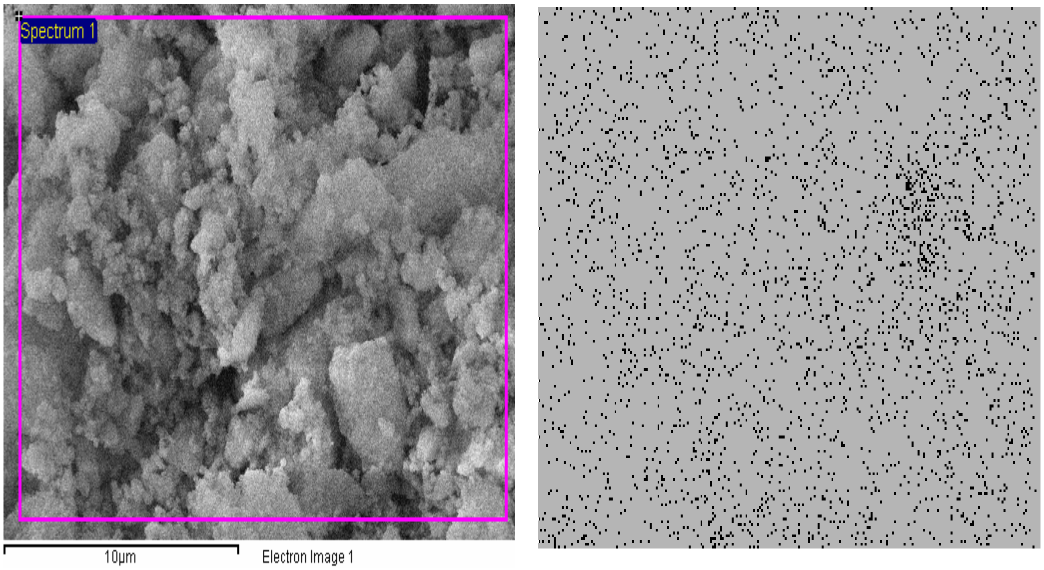

5% α-Fe_2O_3/γ-Al_2O_3

Fe mapping

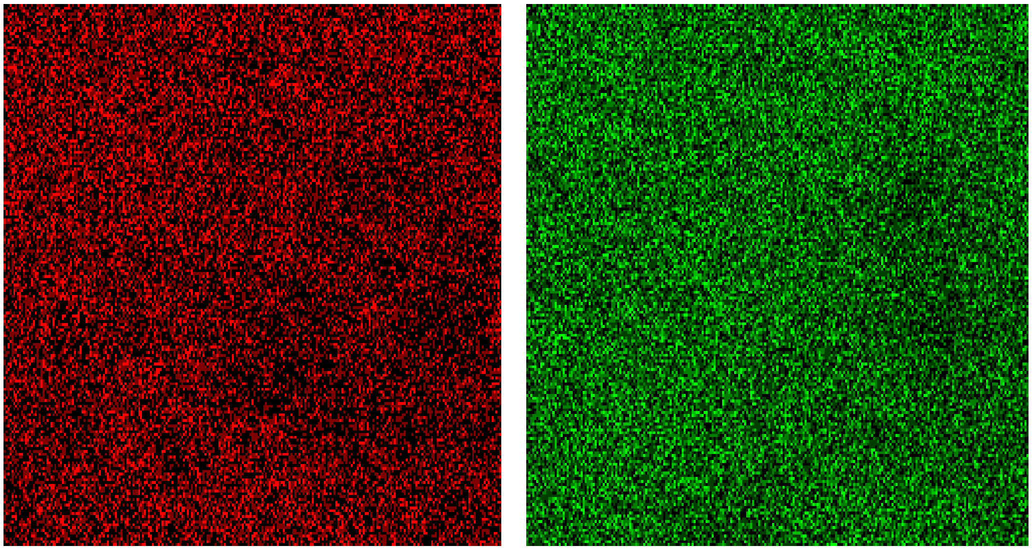

O mapping

Al mapping

Figure G.1.3: EDX mapping of 5% α-Fe_2O_3/γ-Al_2O_3 nanocatalyst prepared via sol gel-hydrothermal method in the absence of surfactant at 160°C for 1 day.

G.2. Supported 5% α-Fe_2O_3/γ-Al_2O_3 Nanocatalysts – Effect of Iron (III) Nitrate to Sodium Bis(2-ethylhexyl) Sulfosuccinate (SBS) Surfactant Ratio.

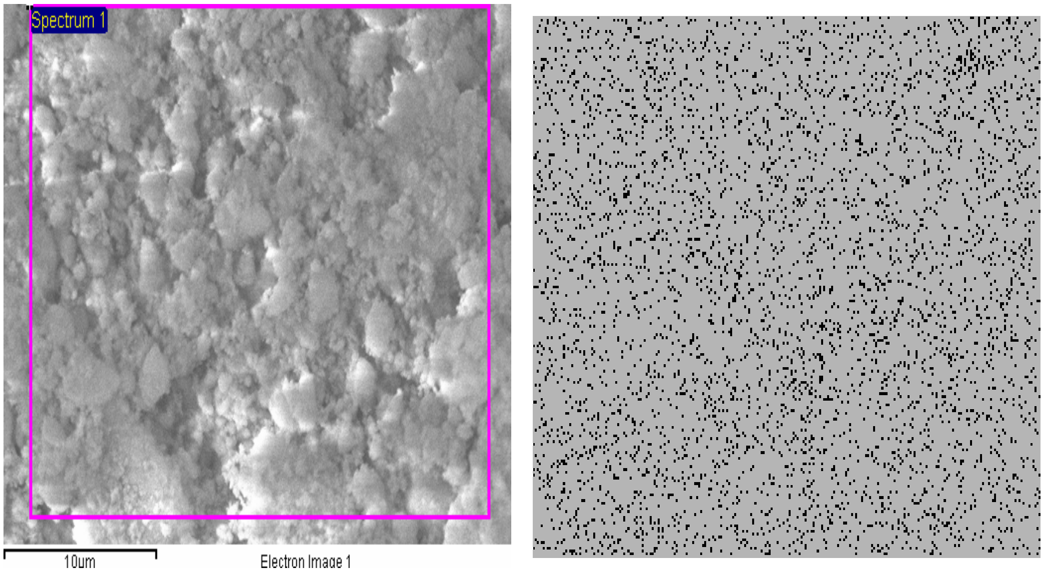

5% α-Fe_2O_3/γ-Al_2O_3 Fe mapping

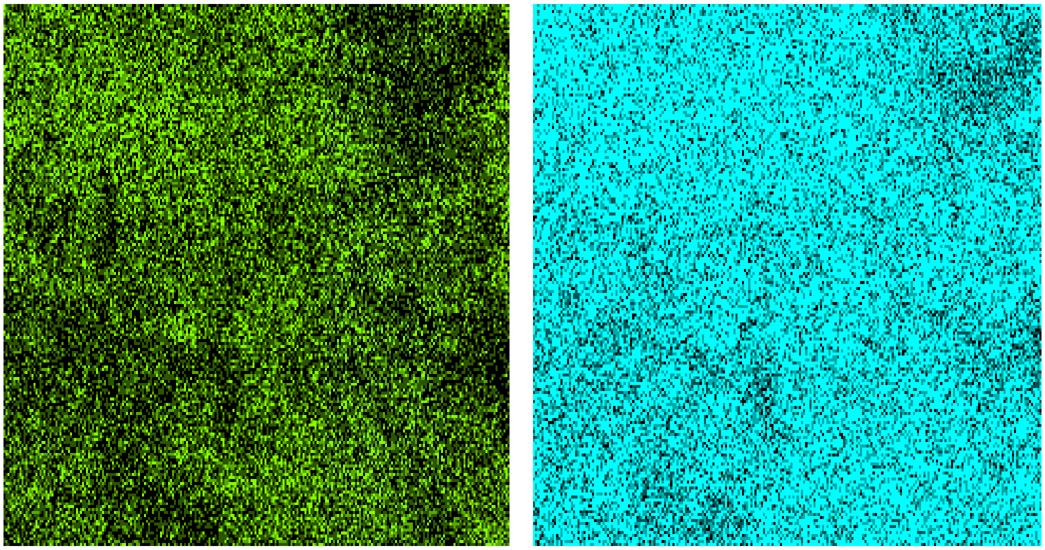

O mapping Al mapping

Figure G.2.1: EDX mapping for 5% α-Fe_2O_3/γ-Al_2O_3 nanocatalyst prepared via sol gel hydrothermal method at iron (III) nitrate to surfactant ($Fe(NO_3)_3$:Surf) ratios of 2:1

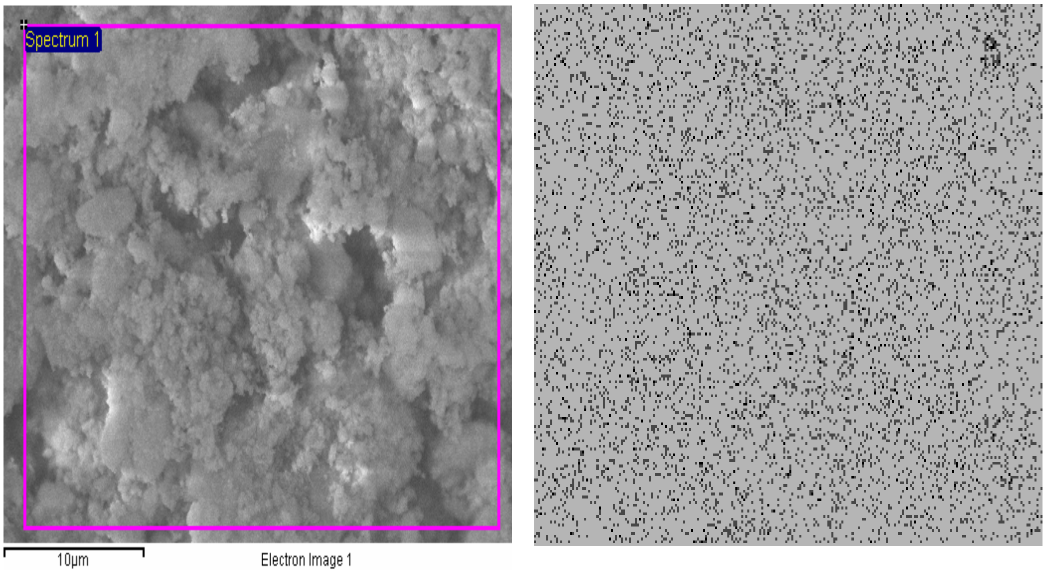

5% α-Fe_2O_3/γ-Al_2O_3 Fe mapping

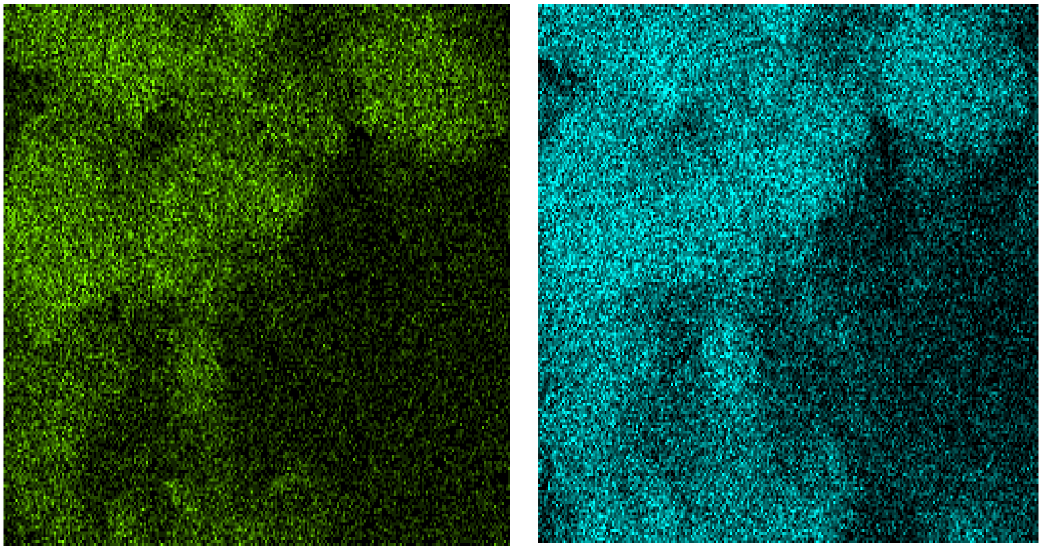

O mapping Al mapping

Figure G.2.2: EDX mapping for 5% α-Fe_2O_3/γ-Al_2O_3 nanocatalyst prepared via sol gel hydrothermal method at iron (III) nitrate to surfactant ($Fe(NO_3)_3$:Surf) ratios of 2:2.

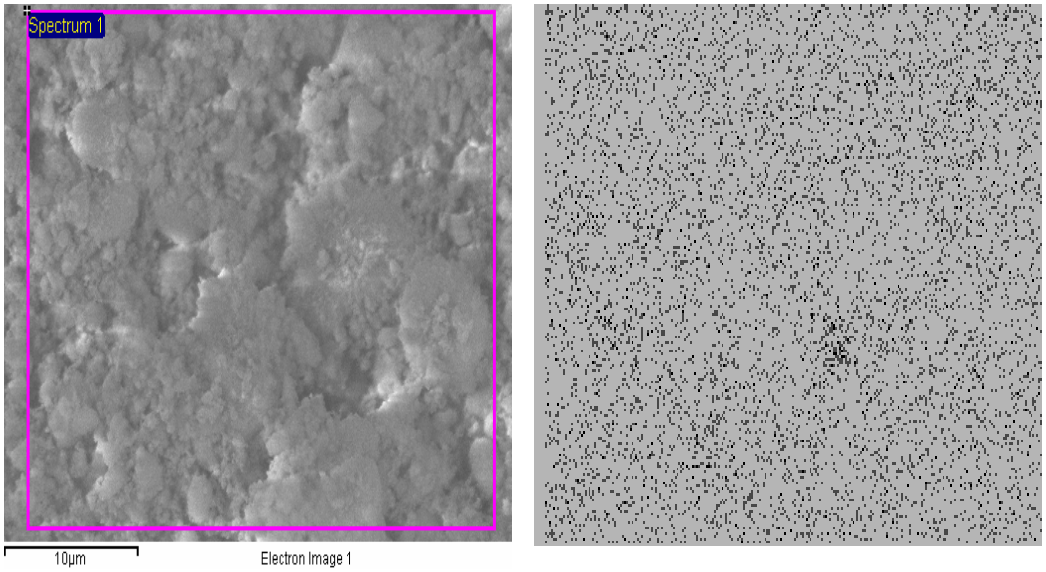

5% α-Fe_2O_3/γ-Al_2O_3 Fe mapping

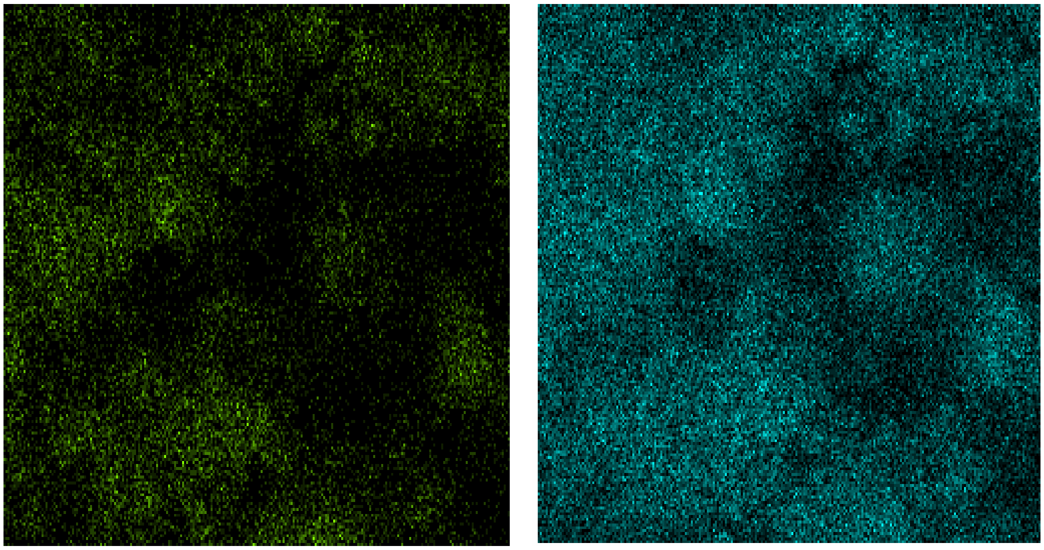

O mapping Al mapping

Figure G.2.3: EDX mapping for 5% α-Fe_2O_3/γ-Al_2O_3 nanocatalyst prepared via sol gel hydrothermal method at iron (III) nitrate to surfactant ($Fe(NO_3)_3$:Surf) ratios of 2:3.

APPENDIX H

Physical Adsorption

H.1 BET Surface Area

H.1.1. 5% α-Fe_2O_3/γ-Al_2O_3 Nanocatalyst (2:1)

Table H.1.1: BET surface area data of 5% α-Fe_2O_3/γ-Al_2O_3 nanocatalyst (2:1)

Relative Pressure (P/Po)	1/[Q(Po/P - 1)]
0.066343242	0.002188554
0.079519995	0.002574848
0.100211227	0.003172701
0.119876366	0.00373073
0.140146372	0.004302564
0.160100759	0.004864737
0.180142444	0.005431878
0.200136641	0.005996395
0.248925859	0.007395424

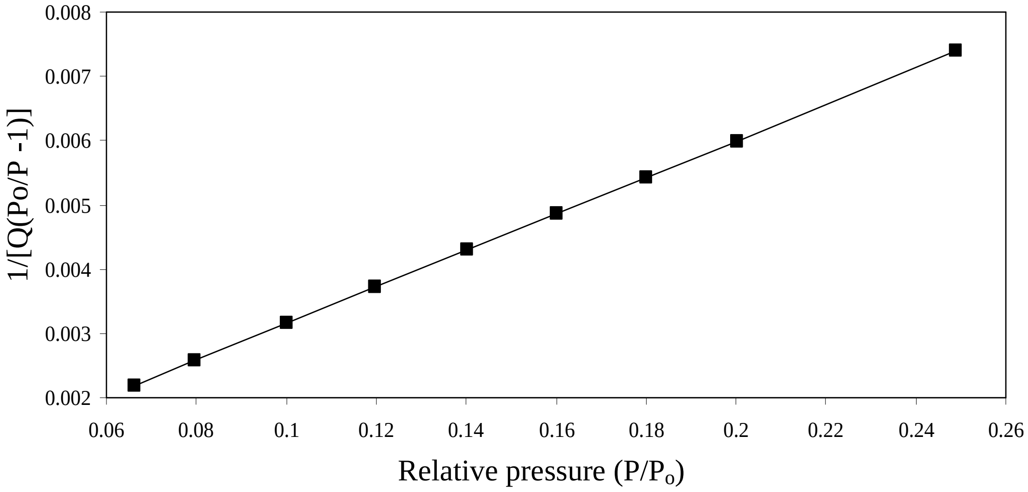

Figure H.1.1: BET surface area plot of 5% α-Fe_2O_3/γ-Al_2O_3 nanocatalyst (2:1).

H.1.2. 5% α-Fe_2O_3/γ-Al_2O_3 Nanocatalyst (2:2)

Table H.1.1: BET surface area data of 5% α-Fe_2O_3/γ-Al_2O_3 nanocatalyst (2:2)

Relative Pressure (P/Po)	1/[Q(Po/P - 1)]
0.065012	0.002418
0.07932	0.002888
0.099854	0.003552
0.119856	0.004189
0.139824	0.004821
0.16017	0.005464
0.179849	0.006086
0.200101	0.006723
0.248952	0.008279

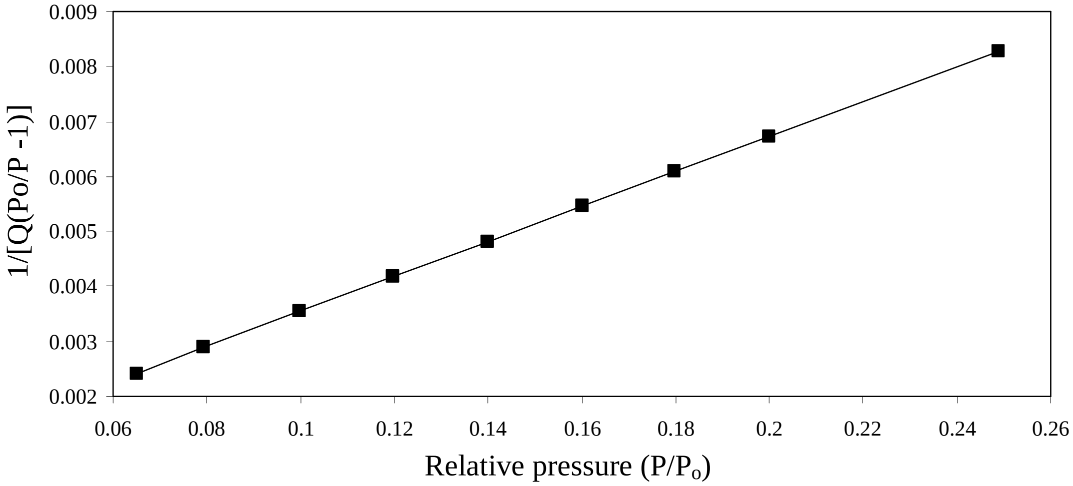

Figure H.1.2: BET surface area plot of 5% α-Fe_2O_3/γ-Al_2O_3 nanocatalyst (2:2)

H.1.3. 5% α-Fe_2O_3/γ-Al_2O_3 Nanocatalyst (2:3)

Table H.1.1: BET surface area data of 5% α-Fe_2O_3/γ-Al_2O_3 nanocatalyst (2:3)

Relative Pressure (P/Po)	1/[Q(Po/P - 1)]
0.064463	0.002281
0.079008	0.002739
0.100124	0.003393
0.119822	0.003998
0.140042	0.004615
0.15979	0.005214
0.179797	0.005823
0.199878	0.006438
0.248448	0.007948

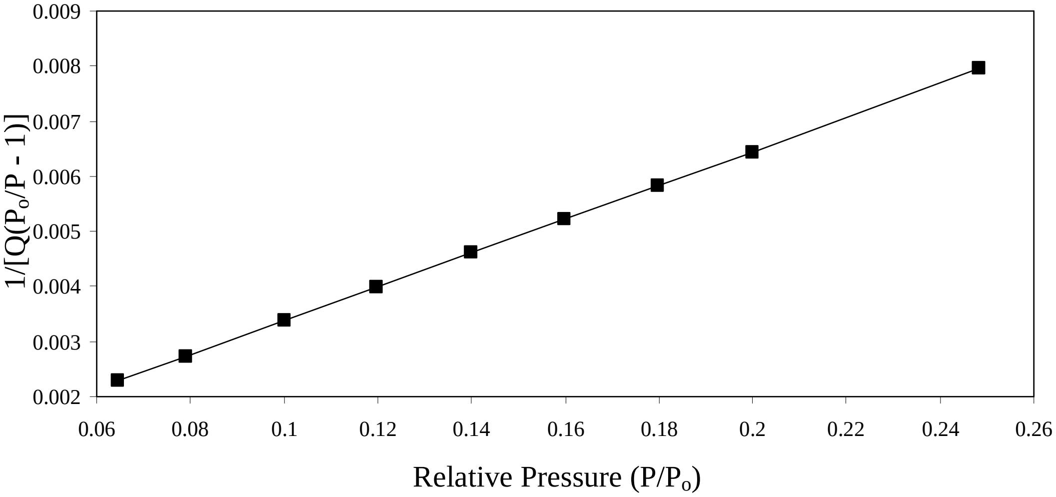

Figure H.1.3: BET surface area plot of 5% α-Fe_2O_3/γ-Al_2O_3 nanocatalyst (2:3)

APPENDIX I

Standard Operating Procedure of Microreactor

Loading the Catalyst

1. Load the catalyst between two layers of glass wool inside the tubular tube.

2. Couple the tubular tube with a pair of heating block. This forms a system namely tubular reactor system.

3. Loosen the screws of a pair of tube holder ring. Than, place the tubular reactor system into the rings and tighten up the screws.

4. Place a magnet block consisting of north and south poles. The location of the magnetic block and chamber is then adjusted so that both of them are in parallel position.

5. Connect two ends of the loaded tubular tube with inlet and out let gas tubes. Then, tighten the screws.

6. Place the thermocouple, heating rods and temperature indicator wire into the right channels at tubular reactor system.

A. Starting The Reactor

1. Connect regulator terminals of reactant gas (H_2 and N_2) to the gas ports of microreactor. Open the control valves of gas tanks as well needle valves of regulator.

2. Open the needle valves to flow the H_2 and N_2 into the system.

3. Adjust the control valves (H_2 and N_2) until the pressure gauge (H_2:N_2) indicators reach 1.2 barg.

4. Open the needle valves of flow meter. Then, set the flow rate of the feed gas (H_2 and N_2) according to the desired ratio using fine controller. The reactant gas is now flowed into the tubular reactor system.

5. Switch on the main control panel switch and set the temperature from 0^o to a desired value using temperature controller.

6. Turn on the magnetizer.

7. Turn the needle valve of gas outlet to "outlet" selection to bubble the outlet gas into hydrochloric acid.

B. Turn off the Reactor

1. Reduce the temperature of reaction to 25^oC using the temperature controller and then switch off the main switch of control panel.

2. Reduce the flow rate of the feed gas to zero and than turn off the fine controllers.

3. Reduce the pressure gauge reading (H_2 and N_2) to zero by adjusting the control valves. Then, close the needle valves.

4. Close the control vales of gas tanks as well needle valves of regulator.